EFFECT OF TRANSVERSE BASE RESTRAINT ON THE CRACKING BEHAVIOR OF MASSIVE CONCRETE

Adnan F. Ali **Omar Al-Farouq Al-Damluji** **Ala'a H. A. Al-Zuhairi**

Baghdad University **Baghdad University** **Baghdad University**

ABSTRACT

The effect of considering the third dimension in mass concrete members on its cracking behavior is investigated in this study. The investigation includes thermal and structural analyses of mass concrete structures. From thermal analysis, the actual temperature distribution throughout the mass concrete body was obtained due to the generation of heat as a result of cement hydration in addition to the ambient circumstances. This was performed via solving the differential equations of heat conduction and convection using the finite element method.

The finite element method was also implemented in the structural analysis adopting the concept of initial strain problem. Drying shrinkage volume changes were calculated using the procedure suggested by ACI Committee 209 and inverted to equivalent temperature differences to be added algebraically to the temperature differences obtained from thermal analysis.

Willam-Warnke model with five strength parameters is used in modeling of concrete material in which cracking and crushing behavior of concrete can be included. The ANSYS program was employed in a modified manner to perform the above analyses.

A thick concrete slab of 1.5m in thickness and 10m in length was analyzed for different widths 2, 4, 8, and 10m to produce different aspect ratios (B/L) of 0.2, 0.4, 0.8, and 1.0 respectively. The results of the analyses show an increase in cracking tendency of mass concrete member as the aspect ratio of the same member is increased due to the effect of transverse base restraint. Accordingly, such effect cannot be ignored in the analysis of base restrained mass concrete structures subjected to temperature and drying shrinkage volume changes.

تأثير تقييد القاعدة العرضي على سلوك تشقق الخرسانة الكتلية

الخلاصة

في هذا البحث، تم إجراء تحري عن تأثير أخذ البعد الثالث في أعضاء الخرسانة الكتلية بنظر الاعتبار على تشققها. وتتضمن الدراسة إجراء التحليل الحراري والإنشائي لمنشآت الخرسانة الكتلية. ويتم الحصول على التوزيع الحقيقي لدرجات الحرارة خلال جسم الخرسانة الكتلية من خلال التحليل الحراري للمسألة نتيجة للحرارة المتولدة جراء إماهة السمنت بالإضافة إلى الظروف الجوية المحيطة. وهذا يجرى من خلال حل المعادلتين التفاضليتين للتوصيل والحمل الحراري باستخدام طريقة العناصر المحددة.

كما إن طريقة العناصر المحددة أستخدمت أيضا في التحليل الأنشائي وذلك بتبني فكرة مسألة الأنفعال الابتدائي. كذلك يتم احتساب التقلصات الحجمية المرافقة لجفاف الخرسانة بالاعتماد على الطريقة المقترحة من قبل معهد الخرسانة الأمريكي لجنة 209 والتي يتم تحويلها إلى ما يكافئها من تغير في درجات الحرارة لتضاف جبريا إلى التغيرات بدرجات الحرارة التي تم الحصول عليها من التحليل الحراري.

لقد تم تبني نموذج ويلام–ورانك ذات خمسة معاملات مقاومة لتمثيل مادة الخرسانة إذ يتضمن هذا النموذج تصرف الخرسانة في حالتي التشقق والتهشم. هذا وتم استخدام برنامج ANSYS وبطريقة معدلة لإنجاز التحليلين المشار أليهما أعلاه.

تم تحليل بلاطة خرسانية بسمك 1.5م وطول 10م وبأعراض مختلفة 2، 4، 8 و10م لتحقيق نسب جانبية عرض/طول مختلفة 0,2، 0,4، 0,8و 1,0 على الترتيب. أظهرت نتائج التحليل زيادة في قابلية تشقق أعضاء الخرسانة الكتلية بزيادة النسب الجانبية بسبب تأثير تقييد القاعدة العرضي. وعليه، فأن مثل هذا التأثير لا يمكن إهماله في منشآت الخرسانة الكتلية التي تتعرض لتغيرات في درجات الحرارة و تقلص الجفاف.

KEYWORDS

Mass concrete, temperature difference, drying volume change, base restraint, concrete cracking.

INTRODUTION

Mass concrete is an expression usually used for any concrete structure with dimensions large enough to cause structural problems during and after the construction period. These problems are mainly the occurrence of cracking due to temperature variations and shrinkage volume changes. Like any solid material, concrete is affected by increase and decrease of temperature. The effect appears as a thermal strain that occurs within the concrete structure when it is prevented or restricted from motion, i.e., restrained. The second category of volume change is the drying shrinkage, which is related to the drying and shrinking of the cement gel.

ACI 207 Committee (ACI Committee 1995) suggested the following equations to be used to calculate the degree of restraint for rigid continuous base restraint.

$$\begin{aligned} K_R &= \left[(L/H-2)/(L/H+1)\right]^{h/H} \qquad for\ L/H \geq 2.5 \\ K_R &= \left[(L/H-1)/(L/H+10)\right]^{h/H} \qquad for\ L/H < 2.5 \end{aligned} \tag{1}$$

where

L/H = length to height ratio, and

h = the height at which the degree of restraint is calculated.

As can be noticed, ACI 207 Committee neglects the effect of the restraint in the transverse direction and hence, eq. (1) can be applied to the concrete walls only. Therefore, it is the objective of the present study to investigate the effect of transverse base restraint, i.e., effects of 3rd dimension on the behavior of massive concrete and therefore cracking tendency and cracking prevention in such structures.

THERMAL ANALYSIS

Based on Fourier's Law for heat transfer, the heat conduction equation can be expressed as follows (Holman, 1981):

$$k_x \frac{\partial^2 T}{\partial x^2} + k_y \frac{\partial^2 T}{\partial y^2} + k_z \frac{\partial^2 T}{\partial z^2} + \bar{q} = \rho c_p \frac{\partial T}{\partial t} \tag{2}$$

where,

k_x, k_y and k_z = heat conductivity of the material in x, y and z-direction respectively,

T = the difference between absolute and reference temperatures,

$\bar{q}$ = heat generation per unit volume,

c_p = specific heat, and

ρ = density.

On the other hand, heat may transfer by convection according to the following Newton formula (Holman, 1981):

$$q = \int_A h_{cv}(T - T_\infty)dA \quad (3)$$

where,

h_{cv} = convection heat transfer coefficient (film coefficient).

T_∞ = bulk fluid temperature.

T = temperature.

Both of the above equations may be descritized using Raylieh-Ritz variation process to derive an expression employing the finite difference method to overcome the time-rate nature of the problem, that is,

$$\left[K_e^*\right]\left\{\Delta\delta_{(t)}\right\} = \left\{F^*\right\} \quad (4)$$

where,

$$\left[K_e^*\right] = \left[K_e\right] + \frac{[C]}{\Delta t}$$

$$\left\{F^*\right\} = \left\{\Delta F_{(t)}\right\} + \frac{[C]}{\Delta t}\left\{\Delta\delta_{(t-\Delta t)}\right\}$$

Eq. (4) is used in the finite element method to predict the temperature distribution within the mass concrete body invoking the described initial and boundary temperatures as follows:

1. Initial temperature = concrete placement temperature = 20 ^oC.
2. Bulk ambient temperature T_∞ which is specified for Baghdad climate according to Kammouna, 2001, from:

$$T_\infty = 29.815 - 15.291*\cos(0.893t) \quad (5)$$

where, t is time in days.

SHRINKAGE STRAIN CALCULATION

Following the procedure recommended by (ACI Committee 209, 1992) and taking the ambient circumstances and concrete mixing and placing conditions, the drying shrinkage strains may be calculated as a function of time after curing period for concrete which is assumed to be seven days.

Quoting the concept of evaporable moisture content that was adopted by Carlson, 1937, the distribution of drying shrinkage strains may be assessed within the body of mass concrete member. Table (1) shows such distribution in which the values of drying shrinkage strains seem very low. Such observation may be related to the non-convenience of eq. (6) that was suggested by ACI 209 Committee (ACI Committee, 1992) and used to estimate shrinkage strain-time relation.

$$(\varepsilon_{sh})_t = \frac{t}{35+t}\ (\varepsilon_{sh})_u \quad (6)$$

where,

$(\varepsilon_{sh})_t$ = shrinkage strain at any time t (in days), and

$(\varepsilon_{sh})_u$ = ultimate shrinkage strain = $780*10^{-6}$.

As can be seen from eq. (6) 50% only of the ultimate shrinkage strain occurs at 35 days after curing. However, one can conclude from the trend of the drying shrinkage strains as they are

decreased with the increase in the width of the slab as the major cause of cracking in large mass concrete members is the temperature variation rather than shrinkage volume changes.

ADOPTED COSTITUTIVE RELATIONSHIP FOR CONCRETE

The concrete was modeled using Willam and Wranke model (Willam and Wranke, 1974) which predicts failure of brittle materials in which the cracking and crushing modes should be accounted for. The criterion for failure of concrete due to a multiaxial stress state can be expressed in the form:

$$\frac{F}{f_c'} - S \geq 0 \tag{7}$$

where,

F = a function of the principal stress state (σ_{xp}, σ_{yp}, σ_{zp}),

S = failure surface expressed in terms of principal stresses and five input strength parameters as follows:

f_t' = ultimate uniaxial tensile strength in MPa

f_c' = ultimate uniaxial compressive crushing strength in MPa,

f_{cb} = ultimate biaxial compressive strength in Mpa,

σ_h = ambient hydrostatic stress state in MPa,

f_1 = ambient hydrostatic stress state of biaxial superimposed on hydrostatic stress state in Mpa, and

f_2 = ambient hydrostatic stress state of uniaxial superimposed on hydrostatic stress state in Mpa.

For simplicity, Willam and Warnke, 1974, suggested the following equations to calculate three of strength parameters in terms of f_c' in case of $|\sigma_h| \leq \sqrt{3} f_c'$. Thus, the failure surface S can be specified with a minimum two constants, f_t' and f_c'.

$$\begin{aligned} f_{cb} &= 1.2 f_c' \\ f_1 &= 1.45 f_c' \\ f_2 &= 1.725 f_c' \end{aligned} \tag{8}$$

Failure of concrete is categorized into four domains. In each domain, independent functions were specified to describe the function F and the failure surface S. The failure surface S can be seen in Fig. (1).

Compression-Compression-Compression Domain($0 \leq \sigma_1 \leq \sigma_2 \leq \sigma_3$)

In this case, F takes the form:

$$F = F_1 = \frac{1}{\sqrt{15}} \left[(\sigma_1 - \sigma_2)^2 + (\sigma_2 - \sigma_3)^2 + (\sigma_3 - \sigma_1)^2 \right]^{\frac{1}{2}} \tag{9}$$

and the failure surface S is defined as:

$$S = S_1 = \frac{2r_2\left(r_2^2 - r_1^2\right)\cos\eta + r_2(2r_1 - r_2)\left[4\left(r_2^2 - r_1^2\right)\cos^2\eta + 5r_1^2 - 4r_1 r_2\right]^{\frac{1}{2}}}{4\left(r_2^2 - r_1^2\right)\cos^2\eta + (r_2 - 2r_1)^2} \tag{10}$$

where,

$$\cos\eta = \frac{2\sigma_1 - \sigma_2 - \sigma_3}{\sqrt{2}\left[(\sigma_1-\sigma_2)^2 + (\sigma_2-\sigma_3)^2 + (\sigma_3-\sigma_1)^2\right]^{\frac{1}{2}}}$$ in which η = angle of similarity, and

$$r_1 = a_0 + a_1\xi + a_2\xi^2$$

$$r_2 = b_0 + b_1\xi + b_2\xi^2$$

$$\xi = \frac{\sigma_h}{f_c'}$$

The undetermined coefficients a_0, a_1, a_2, b_0, b_1, and b_2 are discussed below.

When $\eta = 0^o$, S_1 in eq. (10) is equal to r_1 while if $\eta = 60^o$, S_1 is equal to r_2. Therefore, the function r_1 represents the failure surface of all stress states with $\eta = 0^o$.

The function r_1 is determined by adjusting a_0, a_1, and a_2 such that f_t', f_{cb} and f_1 all lie on the failure surface. Mathematically:

$$\begin{Bmatrix} \frac{F_1}{f_c'}(\sigma_1 = f_t', \sigma_2 = \sigma_3 = 0) \\ \frac{F_1}{f_c'}(\sigma_1 = 0, \sigma_2 = \sigma_3 = -f_{cb}) \\ \frac{F_1}{f_c'}(\sigma_1 = -\sigma_h^a, \sigma_2 = \sigma_3 = -\sigma_h^a - f_1) \end{Bmatrix} = \begin{bmatrix} 1 & \xi_t & \xi_t^2 \\ 1 & \xi_{cb} & \xi_{cb}^2 \\ 1 & \xi_1 & \xi_1^2 \end{bmatrix} \begin{Bmatrix} a_0 \\ a_1 \\ a_2 \end{Bmatrix} \quad (11)$$

in which $\xi_t = \frac{f_t'}{3f_c'}$, $\xi_{cb} = \frac{f_{cb}}{3f_c'}$, *and* $\xi_1 = -\frac{\sigma_h^a}{f_c'} - \frac{2f_1}{3f_c'}$.

The proper values for the coefficient a_0, a_1, and a_2 can be determined through the solution of the simultaneous equations given in eq. (11).

The function r_2 is calculated by adjusting b_0, b_1, and b_2 to satisfy the conditions:

$$\begin{Bmatrix} \frac{F_1}{f_c'}(\sigma_1 = \sigma_2 = 0, \sigma_3 = -f_c') \\ \frac{F_1}{f_c'}(\sigma_1 = \sigma_2 = -\sigma_h^a, \sigma_3 = -\sigma_h^a - f_2) \\ 0 \end{Bmatrix} = \begin{bmatrix} 1 & -\frac{1}{3} & \frac{1}{9} \\ 1 & \xi_2 & \xi_2^2 \\ 1 & \xi_0 & \xi_0^2 \end{bmatrix} \begin{Bmatrix} b_0 \\ b_1 \\ b_2 \end{Bmatrix} \quad (12)$$

where,

ξ_2 is defined by: $\xi_2 = -\frac{\sigma_h^a}{f_c'} - \frac{f_2}{3f_c'}$.

and ξ_0 is the positive root of the equation:

$$r_2(\xi_0) = a_0 + a_1\xi_0 + a_2\xi_0^2 \quad (13)$$

in which a_0, a_1, and a_2 are evaluated by eq. (11).

Since the failure surface must remain convex, the ratio r_1/r_2 is restricted to the range ($0.5<r_1/r_2<1.25$), although the upper bound is not considered to restriction since ($r_1/r_2 < 1.0$) for most materials. Also, the coefficients a_0, a_1, a_2, b_0, b_1, and b_2 must satisfy the conditions:

$a_0 > 0$, $a_1 \le 0$, $a_2 \le 0$

$b_0 > 0$, $b_1 \le 0$, $b_2 \le 0$

Therefore, the failure surface is closed and predicts failure under high hydrostatic pressure ($\xi < \xi_2$). This closure of the failure surface has not been verified experimentally and it has been suggested that Von Mises type cylinder is a more valid failure surface for large compressive σ_h-values. Consequently, it is recommended that values of f_1 and f_2 are selected at a hydrostatic stress level in the vicinity of or above the expected maximum hydrostatic stress encountered in the structure.

Eq. (9) describes the condition that the failure surface has an apex at $\xi = \xi_0$. A profile of r_1 and r_2 as a function of ξ is shown in Fig. (2).The lower curve represents all stress state such that $\eta = 0^o$ while the upper curve represents stress state such that $\eta = 60^o$. If the failure criterion is satisfied, the material is assumed to crush.

Tension-Compression-Compression Domain ($\sigma_1 \ge 0 \ge \sigma_2 \ge \sigma_3$)

In this regime, F takes the form:

$$F = F_2 = \frac{1}{\sqrt{15}}\left[(\sigma_2 - \sigma_3)^2 + \sigma_2^2 + \sigma_3^2\right]^{\frac{1}{2}} \tag{14}$$

and S is defined as:

$$S = S_2 = \left(1 - \frac{\sigma_1}{f_t'}\right)\frac{2p_2\left(p_2^2 - p_1^2\right)\cos\eta + p_2(2p_1 - p_2)\left[4\left(p_2^2 - p_1^2\right)\cos^2\eta + 5p_1^2 - 4p_1p_2\right]^{\frac{1}{2}}}{4\left(p_2^2 - p_1^2\right)\cos^2\eta + (p_2 - 2p_1)^2} \tag{15}$$

where $\cos\eta$ is already defined above, and

$$p_1 = a_0 + a_1\chi + a_2\chi^2$$

$$p_2 = b_0 + b_1\chi + b_2\chi^2$$

$$\chi = \frac{1}{3}(\sigma_2 + \sigma_3)$$

The coefficients a_0, a_1, a_2, b_0, b_1, and b_2 are defined by eq. (11) and eq. (12).

If the failure criterion is satisfied, cracking occurs in the plane perpendicular to the principal stress σ_1.

Tension- Tension -Compression Domain ($\sigma_1 \ge \sigma_2 \ge 0 \ge \sigma_3$)

Here the function F takes the form:

$$F = F_3 = \sigma_i \;\; ; i = 1,2 \tag{16}$$

and the failure surface S is defined as:

$$S = S_3 = \frac{f_t'}{f_c'}\left(1 + \frac{\sigma_3}{S_2(\sigma_i, 0, \sigma_3)}\right); i = 1,2 \tag{17}$$

If the failure criterion for both i = 1, 2 is satisfied, cracking occur in the planes perpendicular to principal stresses σ_1, σ_2. If the failure criterion is satisfied only for i = 1, cracking occurs only in the plane perpendicular to principal stress σ_1.

Tension- Tension - Tension Domain ($\sigma_1 \geq \sigma_2 \geq 0 \geq \sigma_3$)

In this regime, F takes the form:

$$F = F_4 = \sigma_i \quad ; i = 1,2,3 \tag{18}$$

and S is defined as:

$$S = S_4 = \frac{f_t'}{f_c'} \tag{19}$$

If the failure criterion is satisfied in directions1, 2, and 3, cracking occurs in the planes perpendicular to principal stresses σ_1, σ_2, and σ_3, otherwise, cracking occurs in plane or plane perpendicular to the directions of principal stresses where the failure criterion is satisfied.

IMPLEMENTATION OF THE FINITE ELEMENT METHOD

According to Fung, 1965, the effect of temperature changes on an elastic body subjected to external forces may be determined using one of the followings:

1. Solution of the discretized form of the coupled thermo-elastic equation in which the effect of both temperature and displacement on each other may be determined, i.e. the displacement due to unit temperature change and vice versa. However, this procedure is not usually used especially in problems where the temperature changes are not high enough like in mass concrete problem.
2. When the simplifying assumptions mentioned in (1) above are introduced, the theory is referred to as an uncoupled, quasi-static theory; it degenerates into heat conduction and thermoelasticity as two separate problems. Experience shows that the change of temperature of an elastic body due to adiabatic straining is, in general, very small. If this interaction between strain and temperature is ignored, then the only effects of elasticity on the temperature distribution are effects of change in dimensions of the body under investigation. The change in dimension of a body is of the order of product of the linear dimension of the body L, the temperature rise ΔT, and the coefficient of thermal expansion α. If L = 1m and $\Delta T = 100\ ^oC$, $\alpha = 10*10^{-6}$ per ^oC, the change in dimension is 10^{-3}m, which is negligible in problems of heat conduction.

The equivalent temperature changes to the estimated drying shrinkage strains may be calculated using the following simple relation:

$$\Delta T_{DS} = \frac{\varepsilon_{sh}}{\alpha_c} \tag{20}$$

where,

ΔT_{DS} = drying shrinkage equivalent temperature change,

ε_{sh} = shrinkage strain, and

α_c = coefficient of thermal expansion of concrete.

Then the equivalent temperature changes to drying shrinkage may be added algebraically to the temperature changes resulting from thermal analysis. The effect of this sum of temperatures, which appears as thermal stress and strain, may be detected using the second method described in (2) above. This means that the problem is treated as "an initial stress or strain" problem. The term *"initial stress"* signifies a stress present before deformations are allowed. Effectively, it is a

residual stress to be superposed on stress caused by deformation. The effect of temperature changes can be placed as initial strain ε_o, or initial stress and strain σ_o and ε_o. Both are viewed as alternative ways to express the same thing (Cook, 1989).

In a linear elastic material, the stress-strain relation is (Cook, 1989):

$$\varepsilon = \frac{\sigma}{E} + \varepsilon_o \tag{21}$$

where,

ε_o = initial strain = $\alpha_c \Delta T$

or,

$$\sigma = E(\varepsilon - \varepsilon_o) \tag{22}$$

The strain energy U_o is defined as (Cook, 1989):

$$U_o = \int_v \frac{\sigma\varepsilon}{2} dv \tag{23}$$

Substituting eq. (22) into eq. (23):

$$U_o = \int_v \frac{E}{2}(\varepsilon - \varepsilon_o)^2 dv$$

or,

$$U_o = \int_v \frac{E}{2}(\varepsilon^2 - 2\varepsilon\varepsilon_o + \varepsilon_o^2) dv \tag{24}$$

The third term in the parenthesis in eq. (24) can be omitted since it is independent of nodal displacements. Then its derivative is equal to zero. Thus,

$$U_o = \int_v \frac{E}{2}(\varepsilon^2 - 2\varepsilon\varepsilon_o) dv \tag{25}$$

Writing $u_o = \frac{E}{2}(\varepsilon^2 - 2\varepsilon\varepsilon_o) dv$ = is the energy per unit volume. Hence, for a state of multiaxial stresses:

$$u_o = \frac{1}{2}\lfloor \varepsilon \rfloor [D]\{\varepsilon\} - \lfloor \varepsilon \rfloor [D]\{\varepsilon_o\} \tag{26}$$

where

[D] = the constitutive relations matrix for concrete and is defined for linear-elastic material as follows (Cook, 1989):

$$[D]=\frac{E}{(1+\upsilon)(1-2\upsilon)}\begin{bmatrix}(1-\upsilon) & \upsilon & \upsilon & 0 & 0 & 0\\ \upsilon & (1-\upsilon) & \upsilon & 0 & 0 & 0\\ \upsilon & \upsilon & (1-\upsilon) & 0 & 0 & 0\\ 0 & 0 & 0 & \frac{1-2\upsilon}{2} & 0 & 0\\ 0 & 0 & 0 & 0 & \frac{1-2\upsilon}{2} & 0\\ 0 & 0 & 0 & 0 & 0 & \frac{1-2\upsilon}{2}\end{bmatrix} \quad (27)$$

The potential of external load may be expressed as:

$$\Omega_{ex}=-\lfloor u\rfloor\{\phi\} \quad (28)$$

where,

$\lfloor u\rfloor$ = the displacement field vector, and

$\{\phi\}$ = the load vector.

Furthermore, the potential of body forces is given by:

$$\Omega_{bf}=\lfloor u\rfloor\{\overline{F}\} \quad (29)$$

where

$\{\overline{F}\}$ = the body force vector, which is any force distributed over the entire volume of the body like the self-weight.

The total potential energy per unit volume can be written in the form (Cook, 1989):

$$\Pi_{p_0}=U_o+\Omega=\frac{1}{2}\lfloor\varepsilon\rfloor[D]\{\varepsilon\}-\lfloor\varepsilon\rfloor[D]\{\varepsilon_o\}-\lfloor u\rfloor\{\phi\}-\lfloor u\rfloor\{\overline{F}\} \quad (30)$$

The total potential within the element is:

$$\Pi_{p_e}=\int_v \Pi_{p_o}dv \quad (31)$$

or,

$$\Pi_{p_e}=\frac{1}{2}\int_v\lfloor\varepsilon\rfloor[D]\{\varepsilon\}dv-\int_v\lfloor\varepsilon\rfloor[D]\{\varepsilon_o\}dv-\int_s\lfloor u\rfloor\{\phi\}ds-\int_v\lfloor u\rfloor\{\overline{F}\}dv \quad (32)$$

Since,

$$\{u\}=[N]\{e\} \quad (33)$$

where,

[N] = shape function matrix, and

{e} = nodal displacement vector.

Also,

$$\{\varepsilon\} = [B]\{e\} \tag{34}$$

where,

[B] = strain-nodal displacement matrix.

Hence,

$$\Pi_{p_e} = \frac{1}{2}\int_v \lfloor e \rfloor [B]^T [D]\{e\}dv - \int_v \lfloor e \rfloor [B][D]\{\varepsilon_o\}dv - \int_s \lfloor e \rfloor [N]^T \{\phi\}ds - \int_v \lfloor e \rfloor [N]\{\overline{F}\}dv \tag{35}$$

which after simplification and introducing effects of externally applied nodal forces becomes:

$$\Pi_{p_e} = \frac{1}{2}\lfloor e \rfloor [K]\{e\} - \lfloor e \rfloor \{R\} - \lfloor e \rfloor \{F\} \tag{36}$$

where, {F} = externally applied nodal forces vector.

Applying the minimization of the total potential yields:

$$\frac{\partial \Pi_p}{\partial \{e\}} = 0$$

or,

$$[K]\{e\} = \{F\} + \{R\} \tag{37}$$

where, $\{R\} = \int_v [B]^T [D]\{\varepsilon_o\}dv + \int_v [N]^T \{\overline{F}\}dv + \int_s [N]^T \{\phi\}ds$

Eq. (37) will be used in the analysis of the mass concrete due to effects of temperature and drying shrinkage volume changes.

COMPUTER IMPLEMENTATION

Besides the "Graphical User Interface (GUI)" that is commonly used in software packages, ANSYS program proposes a programming language similar to some extent to the conventional FORTRAN language. The proposed language is referred as APDL (ANSYS Parametric Design Language).

A modified ANSYS program is adopted in this study. This consists of a main program and four subprograms. The main program contains the principal steps of analysis and required calls for subprograms. Each of these subprograms is responsible of some limit tasks like:

- Performing the thermal analysis,
- Storing temperature values in a pre-dimensioned array,
- Calculating drying shrinkage strains throughout the concrete body, and
- Conducting the nonlinear structural analysis by considering the effect of concrete aging via updating concrete strength parameters (f_t', f_c', E_c) after deleting the thermal finite element mesh and constructing a new structural one.

Two Types of elements are used in this program:

1. Thermal Solid 70: This element is an eight-noded brick element with one degree of freedom, temperature, at each node. The element is applicable to a three-dimensional, steady state or transient thermal analysis.
2. Structural Solid 65:This element is used for the three-dimensional modeling of the concrete with or without reinforcing bars. The element is defined by eight nodes having three degrees of freedom at each node: translations in the global x, y, and z directions. It is capable of considering cracking in tension and crushing in compression.

PROBLEM DESCRIPTION AND RESULTS

To investigate the effect of the transverse base restraint on the cracking behavior of mass concrete member due to temperature variation and drying shrinkage volume changes, a nonlinear finite element analysis was applied to base restrained thick concrete slab. Four different aspect ratios (width/length) were considered for the case of a slab with fixed bottom cast at the first of January (winter concrete placement) in Baghdad. The aspect ratios were 0.2, 0.4, 0.8, and 1.0 and obtained by fixing the length of the slab to 10 meters and varying the width as 2, 4, 8, and 10 meters. In all these cases, the thickness of the slab was taken as 1.5 m.

Thermal and structural analyses were conducted on the slab including all the surrounding circumstances and boundaries utilizing the finite element mesh shown in Fig. (3).

The temperature distribution in the central sections along the length and width directions at some times after concrete placement are shown in Figs. (4) to (15). The assessed final cracking pattern of the concrete slabs with different aspect ratios can be seen in Figs. (16) to (19).

CONCLUSIONS

The following conclusions can be drawn from the results of the analysis:

* Value of peak temperature increases with increasing aspect ratio (B/L) of the slab. This may be related to the increase in the magnitude of heat generated upon concrete placement due to volume increase.
* A small temperature drop at the 28^{th} day of concrete age is noticed as the ratio B/L is increased. This is related to the effect of the volume to surface ratio (V/S), since the temperature increases with increasing the aspect ratio (B/L).
* The number of primary cracks (cracks that extend over the entire thickness) increase with increasing width of the slab, i.e., the aspect ratio. This can be interpreted as a result of the considerable increase in restraint provided by the slab base and the increase in the maximum temperature due to the hydration process after concrete placement.
* The full-depth cracks are concentrated at the central portion of the slab where the maximum drop in temperature occurs.

From the above and since it was concluded previously that the major cause of cracking in the thick slabs is temperature drop, the effect of the third dimension (width) cannot be ignored when the response (stresses and cracking) of this type of structures is required. Unfortunately, most of the standards like ACI-Committee neglect the effect of the third dimension and assume a uniform temperature distribution.

Table (1) Drying shrinkage strains

d/H	Drying shrinkage strain (10^{-6})

(*)	Slab width = 2.0m					Slab width = 4.0m					Slab width = 8.0m					Slab width = 10.0m				
	After … days					After … days					After … days					After … days				
	8	14	28	90	180	8	14	28	90	180	8	14	28	90	180	8	14	28	90	180
0	0.5	3.2	7.5	18.0	24.3	0.2	1.3	3.0	7.1	9.6	0. 1	0.6	1.4	3.3	4.4	0.08	0.48	1.12	2.7	3.6
0.2	0.2	1.3	3.1	7.5	10.3	0.1	0.5	1.2	3.0	4.1	0.04	0.25	0.57	1.4	1.9	0.03	0.2	0.47	1.13	1.5
0.4	0.07	0.4	1.01	2.4	3.2	0.03	0.17	0.4	0.96	1.3	0.01	0.08	0.19	0.44	0.63	0.01	0.07	0.15	0.36	0.48
0.6	0.02	0.1	0.3	0.8	1.1	0.01	0.05	0.12	0.3	0.45	0	0.02	0.05	0.14	0.21	0	0.02	0.04	0.11	0.17
0.8	0	0	0	0	0	0	0	0	0	0	0	0	0	0	0	0	0	0	0	0
1.0	0	0	0	0	0	0	0	0	0	0	0	0	0	0	0	0	0	0	0	0

(*) d/H defines the ratio of the depth from top surface / the slab thickness H.

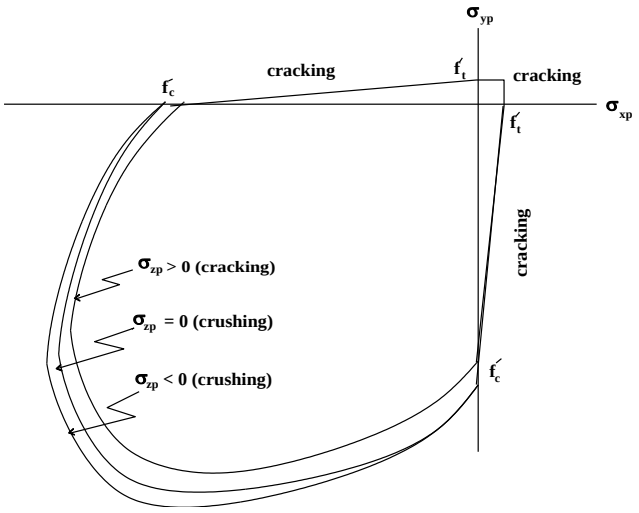

Fig.(1): Failure surface in principal stress space with nearly biaxial stress state, after ANSYS Inc.

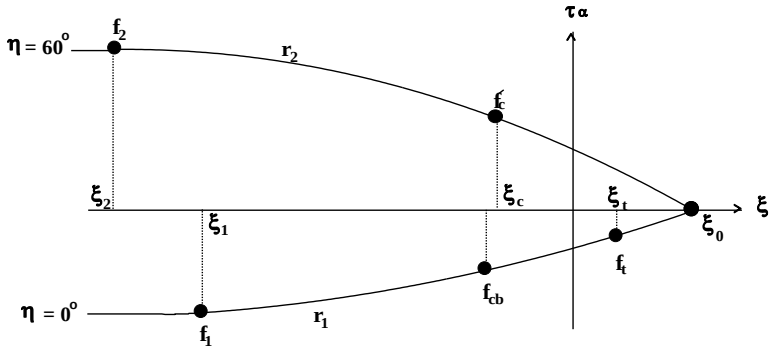

Fig. (2): A profile of the failure surface, after ANSYS Inc.

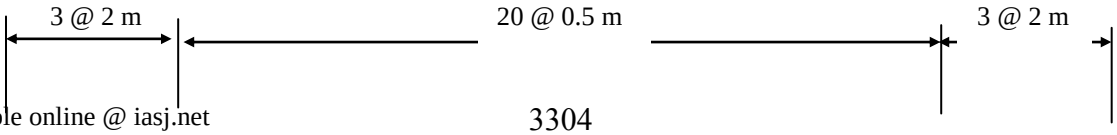

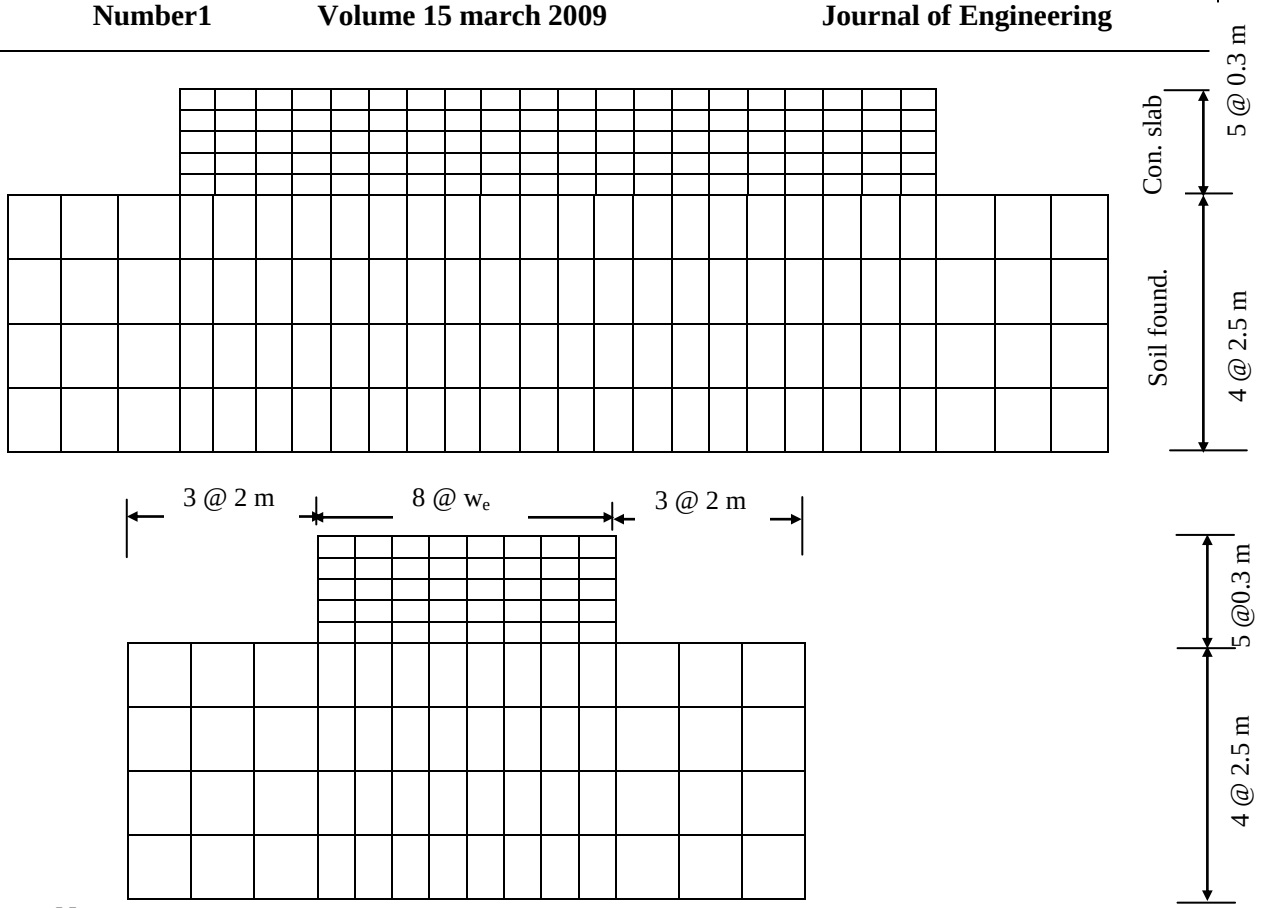

Notes:

- w_e = concrete element width (variable) = 0.25, 0.5, 1.0, or 1.5 m.
- Dimensions are not to scale.

Fig. (3): Finite element mesh for a thick concrete slab problem

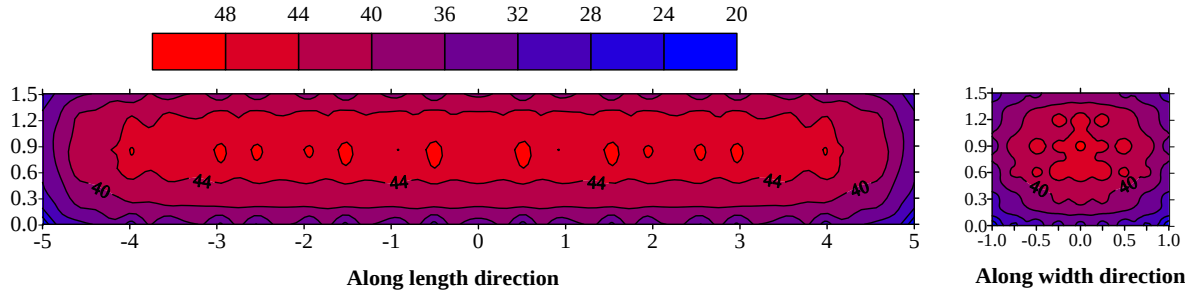

Note: Temperatures are in ^{o}C

Fig. (4): Temperature distribution in a slab with B/L=0.2 (3 days after placement)

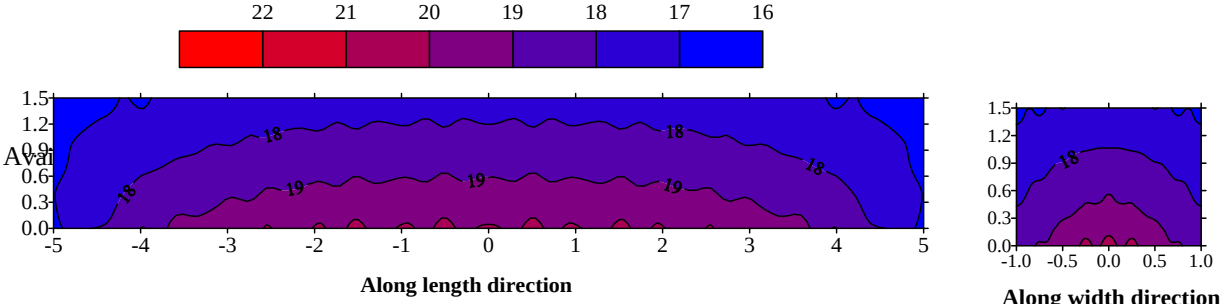

Note: Temperatures are in ^{o}C

Fig. (5): Temperature distribution in a slab with B/L=0.2 (28 days after placement)

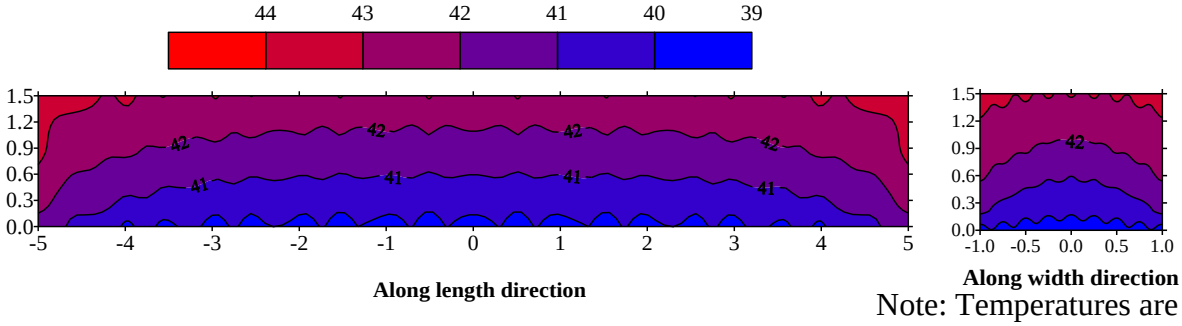

Note: Temperatures are in ^{o}C

Fig. (6): Temperature distribution in a slab with B/L=0.2 (180 days after placement)

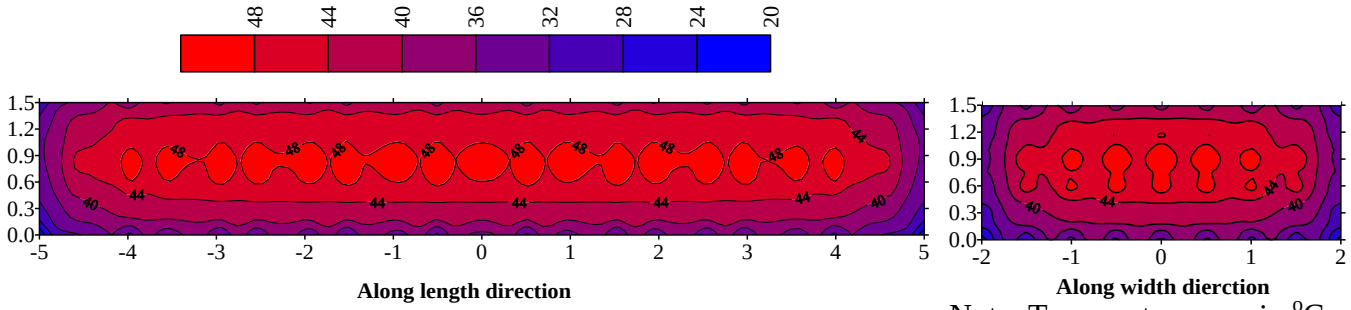

Note: Temperatures are in ^{o}C

Fig. (7): Temperature distribution in a slab with B/L=0.4 (3 days after placement)

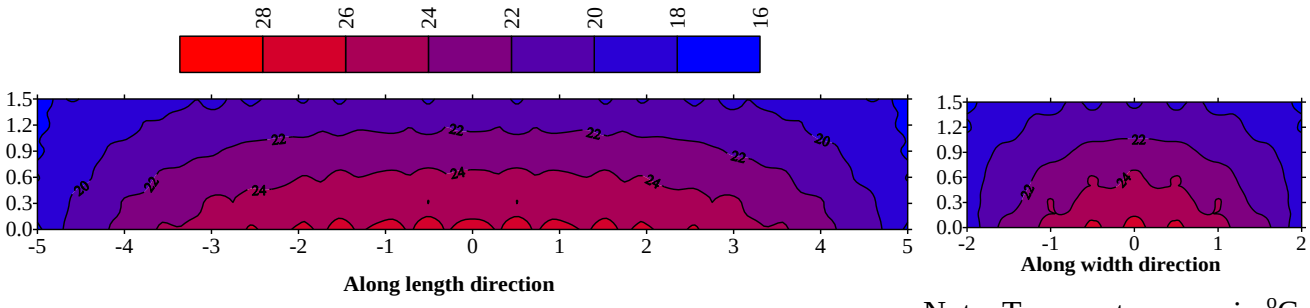

Note: Temperatures are in ^{o}C

Fig. (8): Temperature distribution in a slab with B/L=0.4 (28 days after placement)

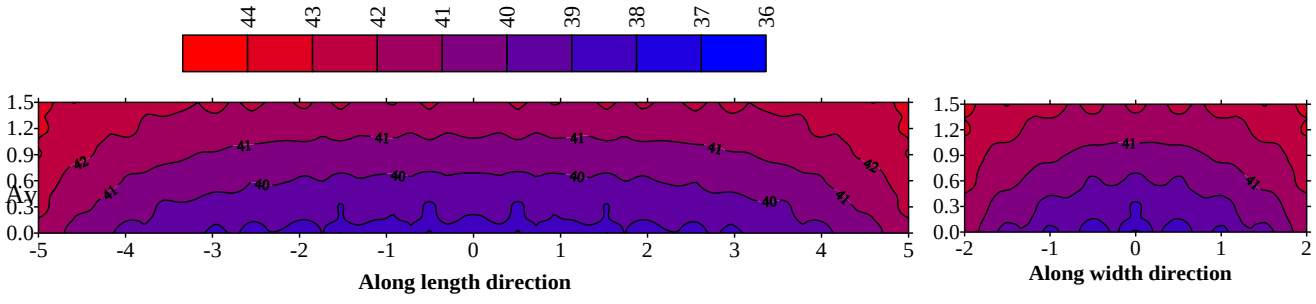

Avy

Note: Temperatures are in ^{o}C

Fig. (9): Temperature distribution in a slab with B/L=0.4 (180 days after placement)

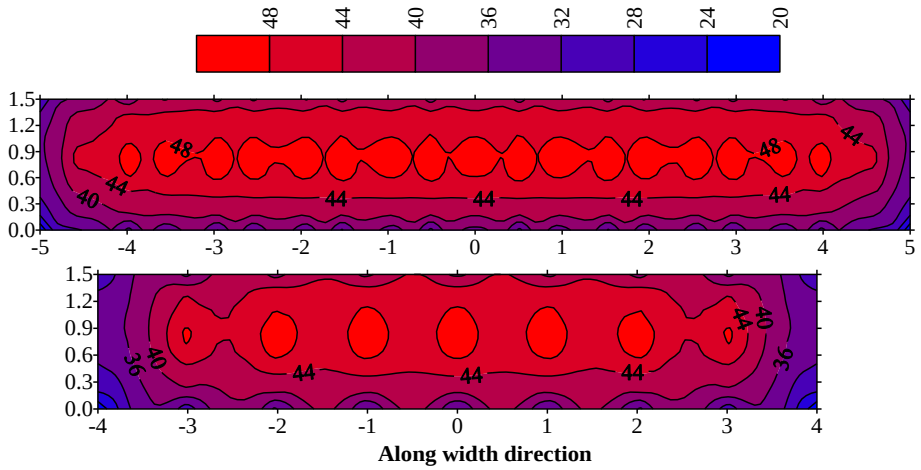

Note: Temperatures are in ^{o}C

Fig. (10): Temperature distribution in a slab with B/L=0.8 (3 days after placement)

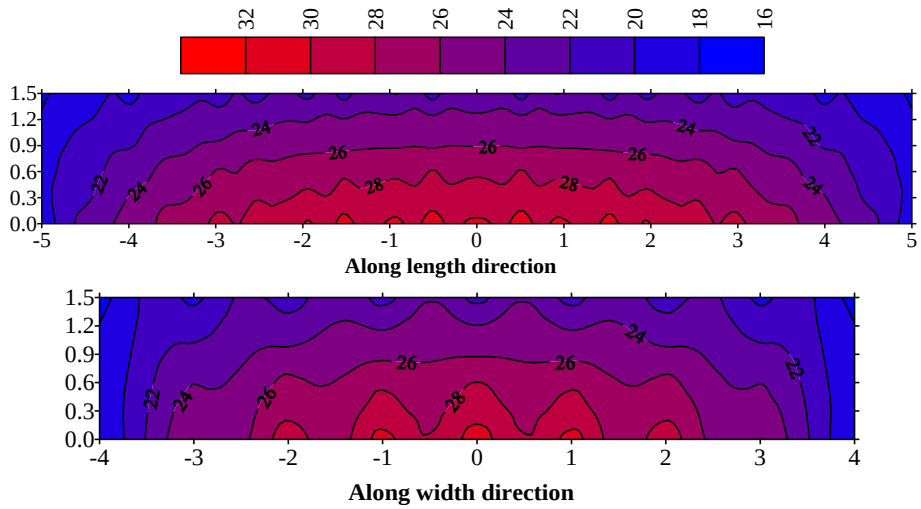

Note: Temperatures are in ^{o}C

Fig. (11): Temperature distribution in a slab with B/L=0.8 (28 days after placement)

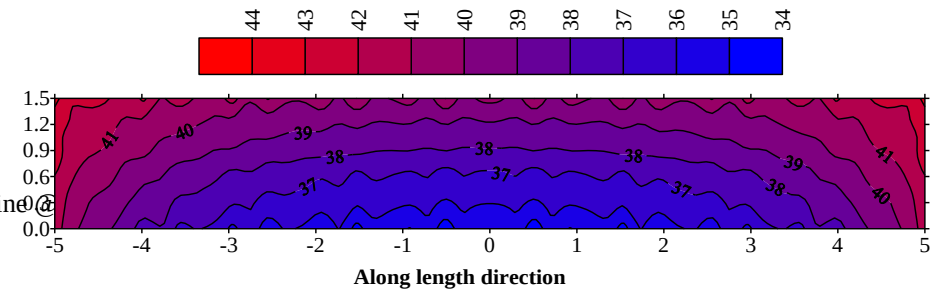

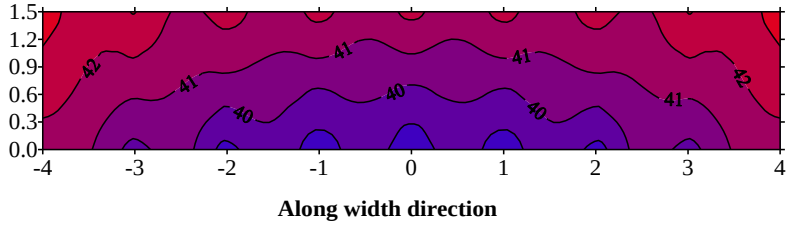

Note: Temperatures are in ^{o}C

Fig. (12): Temperature distribution in a slab with B/L=0.8 (180 days after placement)

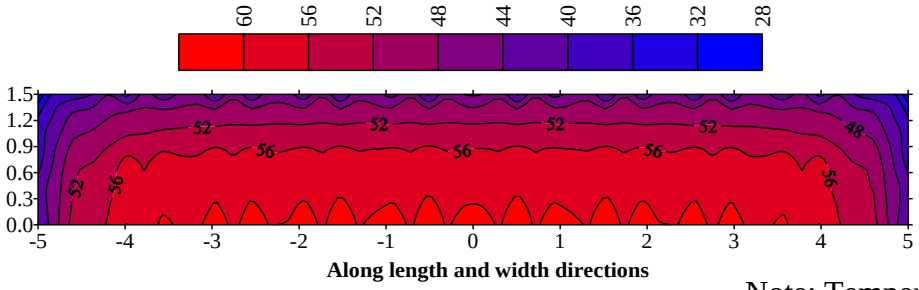

Note: Temperatures are in ^{o}C

Fig. (13): Temperature distribution in a slab with B/L=1.0 (3 days after placement)

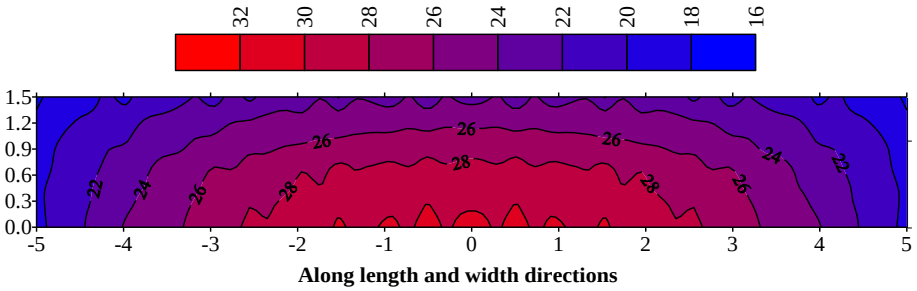

Note: Temperatures are in ^{o}C

Fig. (14): Temperature distribution in a slab with B/L=1.0 (28 days after placement)

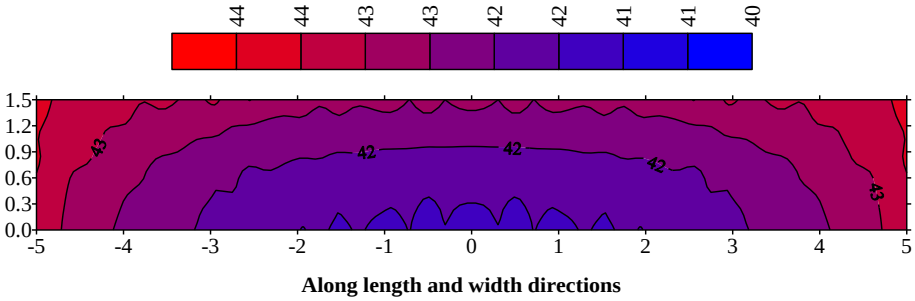

Note: Temperatures are in ^{o}C

Fig. (15): Temperature distribution in a slab with B/L=1.0 (180 days after placement)

Side view of the central section along length direction

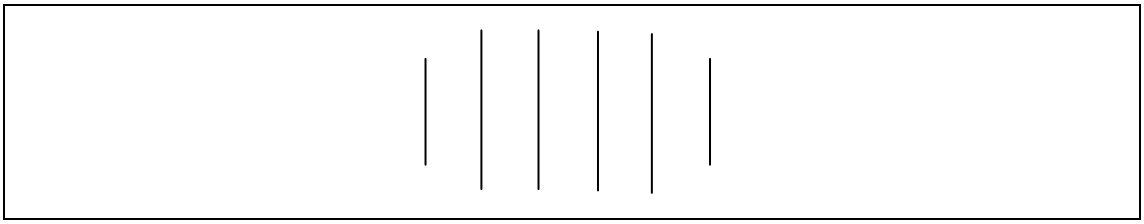

Top view

Fig. (16): Final cracking pattern for slab cast in winter with B/L=0.2

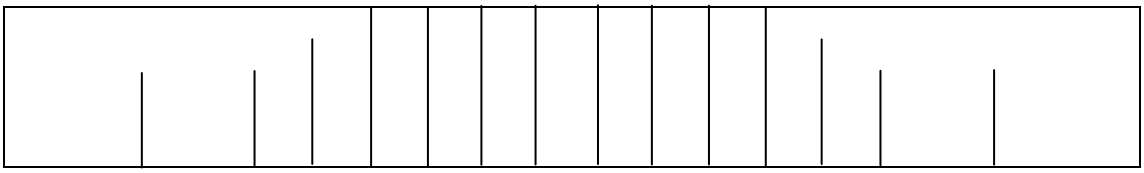

Side view of the central section along length direction

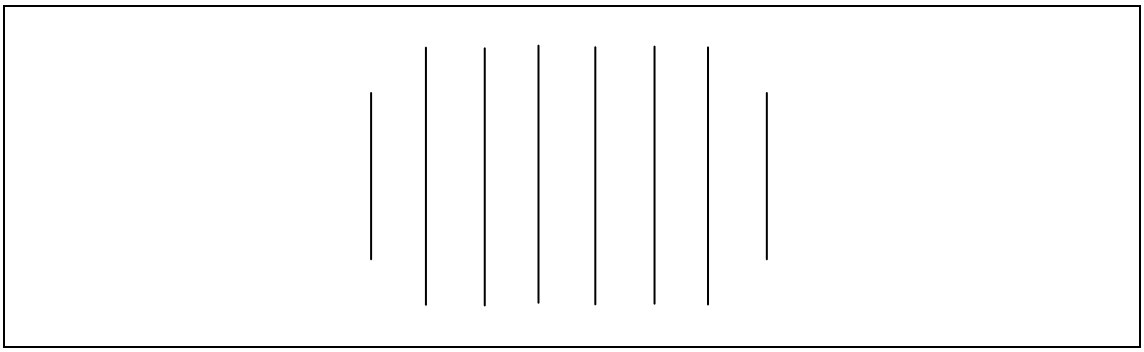

Top view

Fig. (17): Final cracking pattern for slab cast in winter with B/L=0.4

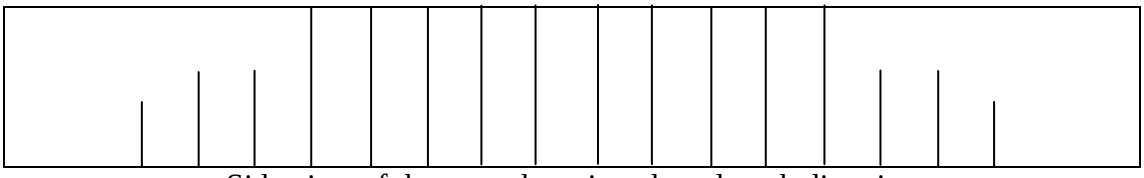

Side view of the central section along length direction

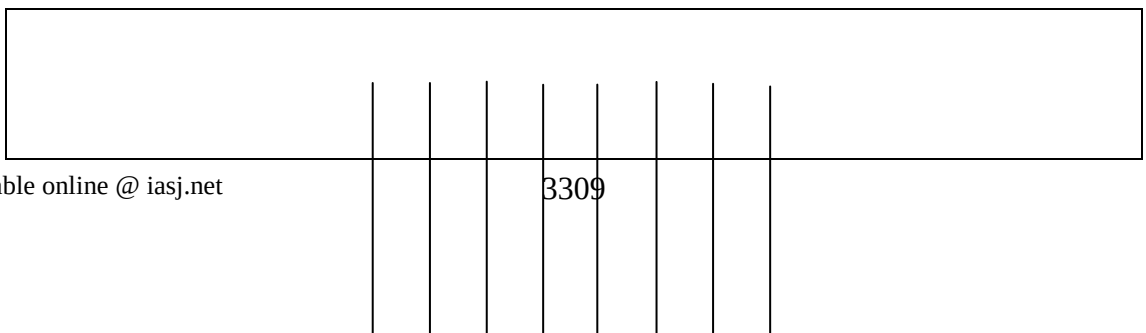

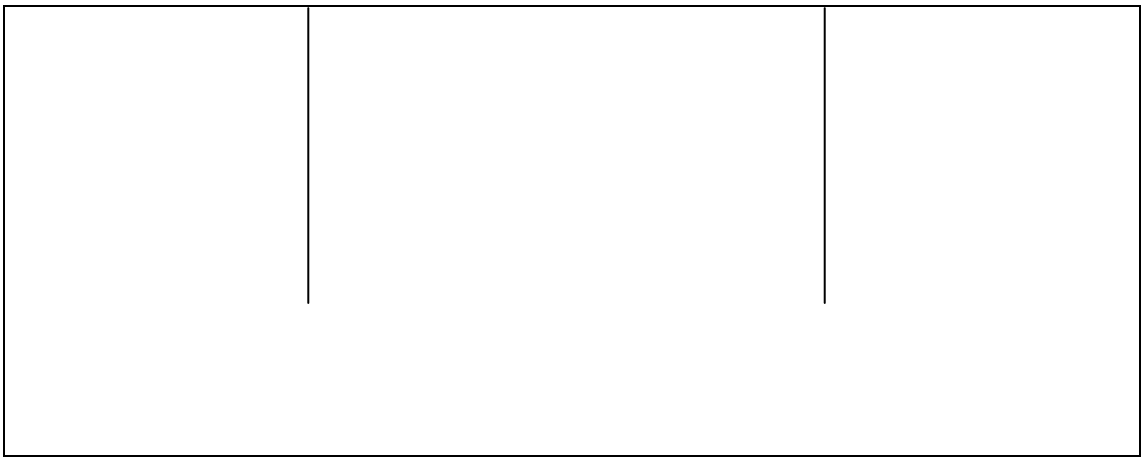

Top view

Fig. (18): Final cracking pattern for slab cast in winter with B/L=0.8

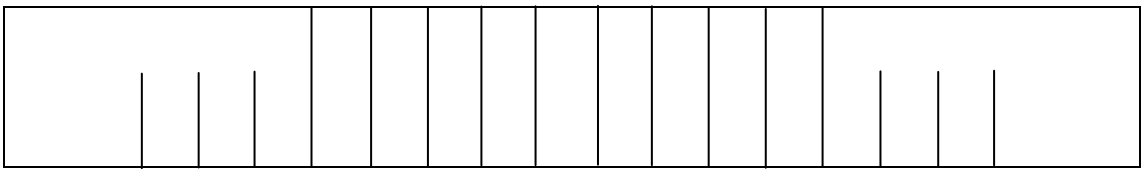

Side view of the central section along length direction

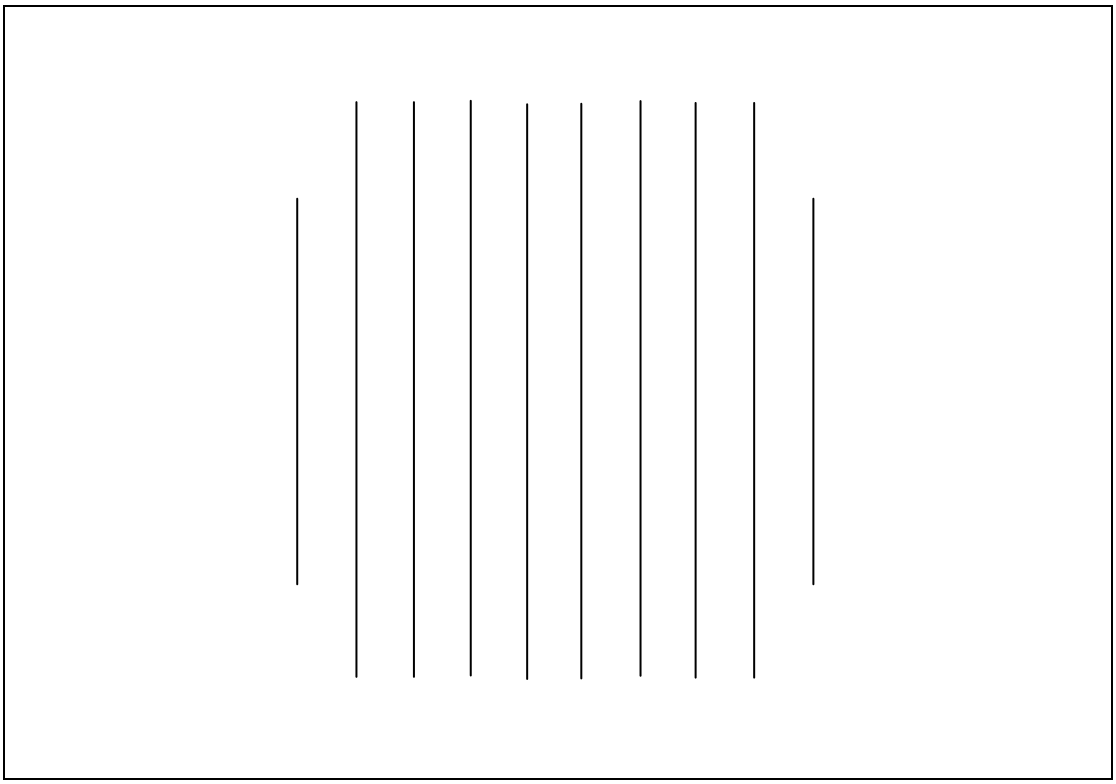

Top view

Fig. (19): Final cracking pattern for slab cast in winter with B/L=1.0

REFRENCES

* ACI Committee 207, "Effect of Restraint, Volume Change, and Reinforcement on Cracking in Massive Concrete", (ACI 207.2R-95). American Concrete Institute, Detroit, 1999, 26 pp.

* ACI Committee 209, "Prediction of Creep, Shrinkage, and Temperature Effects in Concrete Structures", (ACI 209R-92), (Reapproved 1997). American Concrete Institute, Detroit, 1999, 47 pp.

* ANSYS 5.4 Inc., "ANSYS Theory Reference", Eighth Edition, SAS IP, Inc. 1997, Chapter 4 pp. 48-56.

* Carlson, R. W., "Drying Shrinkage of Large Concrete Members" ACI Journal, Proceedings, Vol. 33, January-February 1937, pp.327-336.

* Cook, R. D., Malkas, D. S., and Plesha, M. E., "Concepts and Applications of Finite Element Analysis", John Wiley and Sons Inc., Third edition, 1989, 630 pp.

* Fung, Y. C., "Foundations of Solid Mechanics", Prentice-Hall Inc., Englewood Cliffs, New Jersey, 1965, 525 pp.

* Holman, J. P., "Heat Transfer", Fourth Edition, 1976, McGraw-Hill.
Kammouna, Z. M., "Development of A Mathematical Model for Creep of Concrete with Reference to Baghdad Climate", M.Sc. Thesis, Baghdad University, College of Engineering, 2001, 90 pp.

* Willam, K. J., and Warnke, E. D., "Constitutive Model for the Triaxial Behavior of Concrete", Proceedings, International Association for Bridge and Structural Engineering, Vol. 19, ISMES, Bergamo, Italy, p. 174 (1975).

الحلول التقليدية في التكيف المناخي المستدام وتوظيفها في السكن المعاصر

بهجت رشاد شاهين سالي فخري خلف عبدالله

جامعة بغداد – كلية الهندسة – قسم الهندسة المعمارية

الخلاصة :

يعني مفهوم الاستدامة تكامل الأنظمة الايكولوجية والتكنولوجية والاقتصادية والاجتماعية في تكوين البيئة الحضرية، وان تلك الأنظمة كفيلة بتلبية الاحتياجات الحالية والمستقبلية، لقد أكدت الاستدامة على عدة مبادئ أهمها الاستفادة من الطاقات الطبيعية، التعلم من العمارة التقليدية، وتقليل استهلاك المصادر وبالتالي تقليل الضرر بالبيئة المحيطة.

من أجل الوصول الى بعض خصوصيات السكن المعاصر في ظروف المناطق الحارة الجافة يحاول البحث الحالي دراسة وتحليل أهمية مايمكن للعمارة التقليدية أن تقدمه لنا لحل كثير من مشكلاتنا المعاصرة وفي مقدمتها السكن الملائم والمريح

سيتناول البحث أستعراض مكونات النسيج الحضري التقليدي في المناطق الحارة الجافة، حيث ان التجربة الحضرية في تلك المناطق توضح بأن الأشكال المتضامة هي التأثيرات المعدلة للاجهادات المناخية، وإن حاجة الإنسان للتكيف مع المناخ الحار الجاف، تؤدي إلى تطوير الأشكال الحضرية المتضامة، والتي تساعده في الحصول على مناخ موضعي معتدل. حيث إن الشوارع والأزقة الملتوية والضيقة تحجب أشعة الشمس والعواصف الترابية وتخزن الهواء البارد فيها مما يؤدي إلى حصول النسيم المعتدل.

سيحاول البحث استخلاص المؤشرات الفاعلة للاستدامة في النسيج الحضري التقليدي من الإطار النظري ومن ثم تطبيقها على عدد من المجمعات السكنية في المناطق الحارة الجافة، لاختبار فاعليتها واهميتها في تشكيل تجمعات سكنية مستدامة وملائمة لظروف تلك المناطق.

الكلمات الرئيسية: الاستدامة, الايكولوجيا، العمارة التقليدية، التكيف, الطاقات الطبيعية، التضام.

The traditional solutions in the sustainable climatic adaptation and its employment in the contemporary housing

ABSTRACT

Sustainability means, the integration between the ecological, technological, economical and social systems to forming the urban environment to maintain the resources for the future generations. Sustainability focuses on many principles: Using the natural energy, learning from the traditional architecture, minimizing the consumption of the resources.

To develop some criteria's for contemporary dwellings in hot dry climate, the research tried to study and analyze the traditional architecture to diagnose its importance and ability to solve contemporary problems, one of which is the lack of comfortable and suitable dwelling units in hot dry climate regions.

The research will study the traditional urban fabric components in the hot- arid zone, because the urban experiment in this zone emphasized on the compact forms and considered it the result of the human adaptation to create the comfortable microclimate.

The research concludes the effective indicators in the traditional urban fabric and employed it in many of housing clusters in hot arid zone to examine its importance and effect in the formalization of sustainable and suitable housing clusters.

المقدمة:

الاستدامة تعنى بملائمة البيئة والاستخدام الامثل للمواد والطاقات الطبيعية التي تعطي ديمومة الحياة. وتعنى أيضا بإنشاء البيئة الحضرية والسيطرة على عمليات التوسع والتطوير التي تعد من أقدم الفعاليات الإنسانية.

لقد ارتبط الإنسان منذ القدم ولحد ألان بالبيئة الطبيعية وذلك لأجل العيش والبقاء، وقد حاول التفاعل معها، حيث تعتبر العمارة هي نتيجة التفاعل بين الإنسان والبيئة المحيطة به. وتعتبر العمارة التقليدية هي اصدق صورة للعمارة البيئية حيث استطاع الإنسان أن يكيف عمارته مع البيئة المحيطة به مستفيداً من الإيجابيات الفعالة لمظاهر البيئة الطبيعية.

ان العمارة التقليدية عموماً، هي انعكاس لتلك العمارة ذات البيئة المحددة، والتي استطاعت تكوين شخصيتها والمحافظة على هويتها والاستفادة من التجارب السابقة ومن ثم المقدرة على تطويع المواد البنائية للتعبيرعن البيئة المحلية وسلوكيات المجتمع وبما يتماشى مع عقائده وتاريخه وبما يتلاءم مع العوامل الطبيعية والمناخية الخاصة به. حيث إن التكيّف الذكي للأبنية التقليدية مع ظروف المناخ يمثّل مفتاحاً مهمّاً من مفاتيح الأستدامة في العمارة، فهذه الصيغ التقليدية تمثّل تجارب متراكمة عبر الزمن، وقد جاءت هذه التجارب نتيجة مباشرة للحاجات الإنسانية والظروف المناخية القاسية

وبسبب الضغوط المناخية الشديدة للمناطق الحارة الجافة وضعف موازنة المنظومة الايكولوجية فيها، لذا أصبح من الضروري إيجاد منظومات خاصة ونظريات تحمل في ثناياها استراتيجيات تنطلق من صلب الواقع البيئي لمشاكل هذه المناطق وصولا إلى أفضل الحلول التصميمية والتخطيطية للمجمعات السكنية في هذه المناطق ويكون ذلك بتقييم الحلول البيئية وتبنيها وتعديلها وتطويرها وربطها بمبادئ الاستدامة لكي تتلاءم ومتطلبات العصر

فكـرة الاستدامـة

إن الأرض تعود إلى كل الأجيال التي تعيش عليها. لذلك ليس من الصحيح أن تقوم بعض الأجيال بالتعدي على حقوق أجيال أخرى وذلك باستنزاف ثرواتها.

إن للاستدامة جذوراً بيئية تقليدية منذ القدم. وهي تؤثر بالقوى التي تجعلها لا تستنزف وهذه القوى تتضمن تحديد استخدام مصادر الطاقة والتطور التكنولوجي عبر مبادئ الاقتصاد والترشيد واستغلال المبادئ الايكولوجية.

ومن أولويات الاستدامة هي الاستجابة إلى السياق الايكولوجي والاجتماعي وسياق المبنى الذي يتضمن القيم الجمالية للفضاء والشكل والمواد المستخدمة.

وان أساس الاستدامة هو دراسة العلاقة بين المبنى والطبيعة، بالطريقة التي تجعل هذه الأنظمة تعمل معاً وتتبادل المنفعة، حيث إن فائدة مقومات الطبيعة المحيطة للمبنى من خلال توفير الطاقة الشمسية عبر الموقع المناسب والمواد البنائية الصحيحة وصولاً إلى توفير المسكن اللائق للإنسان، ويستفاد المبنى من الطبيعة إذا تجاوب مع مقوماتها، أي احترام خصوصية المكان، وجغرافية الموقع، والبيئة الطبيعية المحيطة.(Pearlmuter,2001,p.23)

وبذلك يكون **تعريف الاستدامة:**هو تكامل النظم الذاتية الطبيعية (الايكولوجية) والنظم التكنولوجية والاقتصادية مع خصوصية المكان في خلق نسيج حضري أو مبنى منفرد متكيف مع بيئته المحيطة. وتشكل السياقات الثلاثة الايكولوجيا، المجتمع، المبنى، الإطار الذي يحدد التصميم ضمن سياق المكان.

-المبادئ الاساسية في تصميم الشكل الحضري للتخطيط المناخي المستدام

مبادئ تصميم الشكل الحضري الاساسية اقترحت من قبل (Golany 1983) والتي مثلت كمبادئ تصميمية لممارسات مقصودة اوغير مقصودة في العديد من المناطق وخصوصاً الحارة – الجافة لاجل البقاء.

- التجميع الحضري:

هذا المبدأ طبق كمظهر رئيسي للتصميم الحضري، حيث ان التجمع الحضري المستدام يؤكد اهداف التطوير المستدام وهو تحسين الاحساس بالمكان، التفاعل مع الطبيعة، الحفاظ على الطاقة والمصادر، تقليل الفضلات المطروحة الى البيئة الطبيعية، تحسين توزيع الشوارع والتنطيق (Zoning) حيث يساعد ذلك في ربط وتكامل العديد من مكونات المجتمع لتحقيق الاستدامة الحضرية (Public Mangement Magazine, 1995, p.12)

- التقارب في استعمالات الارض:

ان التقارب في استعمالات الارض وعدم ترك فراغات سالبة عادة يتوافق مع العادات الاجتماعية والثقافية والعرقية والمعتقدات الدينية فضلاً عن الملائمة في توفير مساحة الارض ويساعد في خلق مناخ موضعي متكيف، حيث ان أي جزء فارغ كبير من الارض داخل المدينة، يكون مصدر لتوليد الهواء الحار خلال النهار والهواء البارد خلال الليل، ومصدر لتوليد الغبار وان التقارب يساعد على خلق الراحة المناخية والملائمة الاجتماعية بالاضافة الى انه يحافظ على الارض ويعزز استخداماتها. (Al-Homoud,2000, p.127)

.التناسق الحضري

ان تنوع المعايير يساهم في خلق التناسق الحضري لاي نسيج حضري وخصوصاً التقليدي من حيث:

اولاً: الشكل الخارجي للنسيج الحضري (مورفولوجية المنطقة) والذي يتضمن خط السماء الافقي والمقطع العمودي له حيث ان النسيج الحضري التقليدي يكون نوعاً ما مستوي، ولا توجد عناصر عمودية ماعدا المنائر.

ثانياً: شبكة السابلة في النسيج حيث كانت الازقة الضيقة والملتوية تعطي الحد الادنى للتبادل الحراري، فتعمل على توفير الظلال في اوقات النهار والبرودة في اوقات الليل، وايضاً تقلل من سرعة تيارات الرياح الخارجية وتقلل من تأثير الغبار وتحتفظ بالرطوبة.

ثالثاً: توجيه الابنية بالنسبة الى دورة الشمس وتقليل تأثيرها صيفاً وضمان التحرك الهوائي الذاتي بتوجيه المبنى بأتجاه الرياح السائدة.

رابعاً: توقيع استعمالات الارض حسب علاقة بعضها مع البعض حيث تساعد على التهوية وتقليل سرعة الرياح السائدة والاحمال الحرارية. التناسق الكثيف للمدينة يساعد في خلق مناخ موضعي. حيث يفقد درجات الحرارة ببطء في المساء ويكتسبها ببطء خلال الصباح، حيث ينتج عن ذلك الليالي الدافئة والنهار البارد. (Al-Homoud,2000, p.127)

-التضـام

المدن المتضامة تطورت عبر التاريخ لاسباب متنوعة وهي التماسك الاجتماعي، الحماية من الاعداء، حماية الاراضي الزراعية والكفاءة الاقتصادية والتكيف مع المناخ القاسي.

والتضام هو التركيز او كثافة العلاقة بين الاجزاء حتى ضمن المسكن الواحد، والمدينة التقليدية تكون متضامة بكاملها لغرض الحماية من المناخ القاسي وخصوصاً في المناطق الحارة – الجافة وذلك لتقليل السطوح المعرضة لاشعة الشمس، وايضاً للسايكولوجيا الاجتماعية، ومع ذلك لايكون التضام على حساب الخصوصية حيث عالجت العمارة التقليدية ذلك بأنفتاح الوحدة السكنية على فناء داخلي خاص بها وعزل العام عن الخاص والخاص جداً. (Steemer,2003,p.39)

وقد أشار (Golany 1983) إلى ثلاثة معايير موجودة في العمارة التقليدية والتي تقود إلى تخطيط ذكي وكفوء مناخياً:

- تخطيط المدينة على أساس العلاقة مع حركة الشمس اليومية والفصلية.
- الأزقة المظللة والباردة طوال النهار، والتي تتحقق بواسطة التوجيه الصحيح وتضام النسيج العمراني.
- الأزقة الضيقة تحتفظ بالبرودة خلال النهار والدفء خلال الليل. والربط بين أجزاء النسيج يكون فقط بممرات ضيقة وملتوية (الأزقة) تنتشر بين مجموعات المساكن. حيث إن كفاءة هذه الأزقة في المحافظة على درجات الحرارة الواطئة وضمان تحرك هوائي مريح تفيد في خلق مناخ موضعي معتدل لعموم النسيج. (Ibid, p.120)

لاشك إن المناخ عامل مسيطر في التخطيط التقليدي للمدينة، لذا يلاحظ وجود انتظام في النسيج الحضري في كل المناطق الحارة الجافة. ويتميز تخطيط المدينة في تلك المناطق بمظهرين اثنين:

1. الشوارع أو الأزقة الضيقة.
2. الأفنية الواسعة نسبياً والمكشوفة والحدائق الداخلية. (فتحي،1988،ص118-119)

ان هذه الافنية تطغى على الشكل العام لتخطيط المدينة في العادة، حيث تعمل كخزانات للهواء النقي المعتدل البرودة، كما موجود في تخطيط العديد من المدن المتضامة والموضحة في الشكل (1).

تقوم الشوارع الضيقة التي تنفذ على عقد أو مجازات (Vistas) ذات نهايات مغلقة بالوظيفة ذاتها التي تقوم بها الأفنية الداخلية، فهي تخزن الهواء المعتدل البرودة في الليل، وتمنع تسربه مع هبوب الرياح.(المصدر السابق،ص120)

-.تصميم الفناءات المفتوحة:

الفناءات المفتوحة في المناطق الحارة – الجافة تكون دائماً صغيرة الحجم ومنتشرة لغرض تجنب حدوث التيارات الهوائية الحارة او الباردة، وتكون دائماً مزروعة ومظللة.

تتحدد الفناءات المفتوحة بالفناء الداخلي ضمن البيت الواحد او الفناءات العامة ضمن مجموعة مساكن.(Steemer,2003,p.38)

تعمل الفناءات الداخلية المفتوحة في النسيج الحضري التقليدي بشكل متضام ومتكامل عبر اختلافات الضغط الهوائي نتيجة ظهور الفناء المشمس الواسع والفناء المظلل الضيق وما بينهما من ازقة مظللة تعمل جميعاً على رفع ديناميكية التحرك الهوائي الذاتي وزيادة المناطق المظللة وتقليل الاحمال الحرارية وبدخول المزروعات والمياه تزيد من فاعلية هذه الفناءات الى مستوى الراحة المطلوبة. وتشكل هذه الفراغات منظومة بيئية متكاملة تسمى بالفراغ الانسيابي وسيتناول البحث دراسة هذه المنظومة في النسيج التقليدي لاهميتها في خلق مناخ موضعي مريح.

- الفراغ الانسيابي في النسيج الحضري التقليدي:

الفراغ الانسيابي هو عبارة عن منظومة متكاملة تتكون من الفناءات الحضرية والأزقة والفناءات الداخلية والتي تعمل على تلطيف المناخ الموضعي الخاص بالنسيج الحضري بصورة عامة وبالمبنى المنفرد بصورة خاصة. (شاهين،2006،ص4)

استخدم المعمار العربي مبدأين لضمان التحرك الهوائي الطبيعي خلال الفراغ الأنسيابي التكاملي لعموم المدينة العربية التقليدية حيث يعتمد المبدأ الأول على التباين في ضغط الهواء الناجم عن الأختلافات في سرعة الرياح (velocities)، الأمر الذي يؤدي إلى تدفق الهواء من منطقة الضغط العالي إلى الضغط المنخفض، أي حركة الهواء بفعل تباين الضغط وبالأعتماد على مبدأ (عملية فنتوري-Venturi action) المشتق أساساً عن ظاهرة تأثير(برنولي– Bernoulli Effect) ، كإطار نظري هام لفهم كيفية حدوث حركة الهواء بفعل تباين الضغط الناتج عن حركة الرياح. (المصدر السابق، ص5)

وتتلخص نظرية (برنولي) بأن ضغط المائع المتحرك (moving fluid) يقل بأزدياد سرعته(velocity) ويعتمد المبدأ الثاني على حركة الهواء بتأثير الحمل (Convection) الناتجة عن تسخين الهواء وصعوده إلى الأعلى، بما يقتضي حلول هواء أكثر برودة منه في مكانه. كما قد تؤدي العملية إلى ما يدعى بمفعول المدخنة (stack effect) فعندما يرتفع الهواء الدافيء يجب أن يستبدل بهواء أكثر برودة من محيطه. وبوجود مصدر الحرارة المستمر تتولد حركة دائمة في الهواء (فتحي،1988،ص102-103).

أ. الفضاءات الحضرية العامة ودورها في الفراغ الانسيابي:

تتميز الفضاءات المفتوحة في النسيج التقليدي بمواقعها ومقاييسها الملائمة وتكاملها مع التشكيل الكتلي للبيئة الحضرية حيث تعتبر أفضل واقرب تكوين للبيئة الطبيعية، ويمكن الاستفادة منه في السيطرة على استخدام الطاقة والموارد الطبيعية. (Moughtin,1996,p169)

يبدأ الفراغ الانسيابي بالفضاءات الحضرية العامة حيث يحصل أول أنخفاض واضح في الحمل الحراري الإجمالي المؤثر في عموم المنطقة.

أن الساحات العامة في النسيج الحضري التقليدي تتضمن مساحات خضراء ومسطحات مائية بينما تكون أجزاء أخرى منها مبلطة ومخصصة للتجمعات السكانية. وتتكون هذه الساحات من مساحات وأحجام مختلفة بعضها مظلل والبعض الأخر مشمس. هذه المواصفة في التشكيل الفضائي المفتوح لجميع الساحات العامة تخلق بطبيعة الحال أختلافاً واضحاً في الضغط تفرضه مبادىء الأختلاف في درجات الحرارة مابين فضاء وفضاء لتنساب التيارات الهوائية عبر الأزقة الضيقة المظللة والمتعرجة بأتجاه الفناءات الداخلية المشمسة والمظللة لتخلق تياراً هوائياً لعموم النسيج العمراني التقليدي. الشكل (2) (شاهين،2006،ص3-5)

ب. دور الأزقة في الفراغ الانسيابي داخل النسيج العمراني :

الزقاق لا يتسلسل تسلسلاً واعياً ولا عمدياً إذ أن تكوين البيت مع علاقته بالبيت الأخر جاء بصورة عفوية وقد تكون عشوائية. ولكن في النهاية يتحول الزقاق إلى وحدة مترابطة. (المصدر السابق،ص5)

والزقاق عبارة عن طريق خطي يضيق في بعض الأجزاء من النسيج الحضري ويتسع في أجزاء أخرى منه بصورة غير منتظمة، ليخلق من خلال هذا التنويع الفضائي مجالاً واسعاً في أختلاف الضغط العالي للهواء المظلل البارد. والذي يندفع إلى فضاءات الدور السكنية المطلة عليه من خلال مفاصل ذكية تساعد في تقوية شدة السحب الهوائي حيث يندفع الهواء من خلال المدخل المنكسر(المزور).ويكون هذا المفصل عبارة عن مرشح للهواء القادم من الزقاق، فضلاً عن أستبعاده للمناسيب الضوضائية التي ممكن أن تصدر من الأزقة والشوارع المحيطة، وكأنه منظومة عالية الدقة والتكوين ظهرت بشكل عفوي حكمته متطلبات الحياة وقوانين حرمة الدار. (المصدر السابق،ص6)

ج. دور الفناءات الداخلية في الفراغ الأنسيابي داخل النسيج العمراني.

الفناء الداخلي أو الفناء الوسطي يعد من أهم مميزات تصاميم الدور التقليدية حيث تتجمع حوله معظم فضاءات المسكن، والتي أجمع الباحثون على أهميتها الستراتيجية البيئية (تحرك الهواء وتواجد الضوء الطبيعي والحصول على فسحة مظللة ذات ضغط جوي عالي قابل للتحرك بأتجاه الفضاءات المعيشية المحيطة بالفضاء). حيث يعتبر الاختلال في الضغط من المبادئ الأساسية في عملية إدخال الهواء للمبنى، إذ تصل ديناميكية الهواء إلى (1.4) مرة أكثر من الاعتيادي عندما يكون هناك تلاعب بالضغط الهوائي، ويمكن الاستفادة من ظاهرة التحرك الهوائي باعتماد نظام التبريد التبخيري لضمان درجات حرارة نهارا بأقل نسبة رطوبة داخل المبنى، ويعد هذا المبدأ من أساسيات التصميم المستدام لاقتصاده بالطاقة.(المصدر السابق،ص6-7))

كانت النافورة (الفسقية) The Fountain في البيت العربي التقليدي توضع في وسط الفناء بحيث تطل عليها الايوانات وقاعات الجلوس، وكان للنافورة دائماً شكل رمزي (symbolic form) يتكون من مربع محيطه الداخلي ثماني أو سداسي الشكل. ويظهر الشكل (3) مخطط لأحد البيوت التقليدية في القاهرة تظهر فيه النافورة تتوسط الفناء الداخلي. حيث إن الماء مهم جداً لزيادة رطوبة الهواء، مما يساهم في توفير شروط الراحة المتعلقة بالمحيط الحراري في المناطق الحارة الجافة.(المصدر السابق،ص8)

أما في حالة انخفاض الضغط بحيث لا يكون كافياً لدفع المياه من رأس النافورة، يلجأ المعمار التقليدي دائماً إلى استبدال النافورة بالسلسبيل، وهو عبارة عن لوح رخامي متموج المظهر (wavy pattern) مستوحى من حركة الماء أو الريح. يوضع اللوح داخل فتحة (كوة) في الجدار المقابل للإيوان أو موضع الجلوس، ويكون اللوح مائلاً للسماح للماء بأن يتقطر فوق سطحه لتسهيل عملية التبخر وزيادة رطوبة الهواء. بعد ذلك تنساب المياه في مجرى رخامي، حتى تصل النافورة في وسط الفناء أو الدر قاعة.(فتحي،1988،ص96).

- <u>مؤشرات الاستدامة في النسيج الحضري التقليدي:</u>

إن المناطق الحارة الجافة كبيئة لها طابعها المعماري الخاص والمميز، والطابع المعماري لأي بيئة يتأثر بمجموعه من المقومات منها الاجتماعية والثقافية والمناخية والطبيعية، وان الحياة الاجتماعية والثقافية تتغير بالتقدم العلمي، ولكن استمرار الطابع والنمط يعتمد إلى حد كبير على المؤثرات الطبيعية والمناخية الثابتة حيث إن العمارة التقليدية في تلك المناطق هي انعكاس أو نتاج فطري لمقومات البيئة المناخية والحضرية، حيث عبرت عن صورة سليمة تعكس إمكانيات وظروف عصرها. (عيسى،2000،ص78)

جاءت العمارة التقليدية صادقة التعبير عن بيئتها حيث تعاملت مع الظروف المناخية مما أدى إلى ظهور نمط حقيقي ذا طابع مميز يلائم ظروف تلك البيئة، ويضم عدد من العوامل التي ساعدت في تكيفه وتشمل التضام و الفراغ الانسيابي والتكامل في المنظومة البيئية والاقتصاد في استعمالات الأرض بالإضافة إلى إدخال الطبيعة في التشكيل العمراني.

هذه العوامل تمثل استراتيجيات الاستدامة الحضرية حيث تحقق التكامل والتوافق مع البيئة الطبيعية والمناخية وبالتالي تقلل استهلاك الطاقة، ومما تقدم يمكن تلخيص عدد من النقاط التي تمثل استدلالات للاستدامة في التكيف المناخي على مستوى النسيج الحضري:

- النسيج الكثيف التضام: حيث إن التخطيط الحضري للمدينة هو الأداة الأولى للسيطرة على المناخ، لان المدينة المتضامة تقلل من المساحات السطحية المعرضة للظروف البيئية، بالإضافة إلى تقليل مساحات الأرض المكشوفة، وأيضا إن عرض وتوجيه الشوارع (الأزقة) يجعل واجهات الأبنية مظللة بالأبنية المقابلة.
- السيطرة الشمسية بواسطة التوجيه: حيث روعي توجيه الفناءات الحضرية والفناءات الداخلية بأتجاه الجنوب أو الجنوب الغربي، مع حماية السطوح المعرضة للشمس بواسطة البروزات والطارمات.
- الفراغ الانسيابي: الذي يعمل على خلق تيارات هوائية تلطف المناخ الموضعي للنسيج الحضري، والتي تبدأ من الفناءات الحضرية مروراً بالأزقة وانتهاءاً بالفناءات الداخلية.
- إدخال الطبيعة في النسيج العمراني (المناطق الخضراء): تميز النسيج التقليدي بأحتوائه على الفناءات العامة (الفضاءات الحضرية المفتوحة) بالإضافة إلى الفناءات الخاصة، والتي تحتوي على عنصري الماء (النافورة والسلسبيل) والنباتات الخضراء، حيث تعمل على تقليل ظاهرة الجزر الحرارية بسبب تقليل مساحة التبليط.
- الاقتصاد في استعمالات الأرض: حيث تحقق هذا العامل بسبب التراص بين الكتل البنائية.
- المنظومة الايكولوجية المتكاملة: وذلك بأعتماد التخطيط البيومناخي الحساس بالطاقة، واعتماد مستويات عالية للراحة في الفضاءات المفتوحة والمغلقة، والاعتماد على المواد البنائية الايكولوجية الاقتصادية، بالإضافة إلى توفير المتطلبات الاجتماعية، حيث يعتبر نموذجا للتكامل البيئي الإنساني.
- تشكيل الأبنية وبالخصوص الواجهة الحضرية: إن التشكيل المتضام أدى إلى خلق واجهة متضامة تتمتع بمورفولوجية التناسق، والصفة المميزة في تشكيل الواجهة الحضرية هو تظليل بعض الأبنية على البعض الأخر، وبالتالي العمل على خلق تيارات هوائية بين الأجزاء المظللة والمشمسة بسبب اختلال الضغط حيث يعمل على تقليل الأحمال الحرارية.

ويوضح الجدول (1) المفردات أو المؤشرات المنتخبة للاستدامة في التكيف المناخي التقليدي

الجدول (1)

المؤشرات الفاعلة

التشكيل المتضام (تقليل المساحات السطحية)
توجيه المباني والمجمعات السكنية على أساس العلاقة مع حركة الشمس اليومية والفصلية
مبدأ الانسياب الفراغي (اعتماد قاعدة فنتوري)
إدخال الطبيعة في التشكيل العمراني (استخدام المناطق الخضراء والمياه في الفناءات الحضرية)
الاقتصاد في استعمالات الأرض
التكامل في المنظومة البيئية
فصل حركة السابلة (الأزقة) عن حركة السيارات (الشوارع) (تحقيق الخصوصية)
تشكيل الواجهات الحضرية

المؤشرات الفاعلة للاستدامة في التكيف المناخي التقليدي (الباحث)

- **الإجراءات التطبيقية:**

تناقش هذه الفقرة الإجراءات والخطوات التي اتبعها البحث وصولاً إلى تحقيق أهداف البحث، بدءاً بوصف وتحديد عينة البحث، وقياس العلاقة بين المتغيرات، وانتقاء الوحدة التحليلية والأوجه المسحية وأخيراً معالجة النتائج.

أ. **العينة البحثية (Case Study):**

استند البحث إلى نظام الـ(Google Earth) وعدد من الكتب والمجلات في تحديد العينة البحثية ذات العلاقة بالتكيف المناخي الطبيعي التقليدي، حيث جرى انتقاء (8) مشاريع، روعي التباين في المصممين والتباين المكاني.

اقتصر البعد الوظيفي للعينة على المشاريع السكنية فقط تحقيقاً لهدف البحث. أما البعد المكاني للعينة فقد شمل دولاً غربية وعربية ومحلية تقع فقط ضمن بيئة المناطق الحارة–الجافة، أما البعد الزمني فلم يتحدد البحث ببعد معين.

والمشاريع المنتخبة وهي:

1. الكاظمية
2. دمشق القديمة
3. مشروع تطوير منطقة سكنية متدهورة في الجيزة
4. قرية للعمال الزراعيين بجناكليس
5. إعادة تعمير احد الأحياء القديمة بمدينة تونس
6. مشروع قرية باريس
7. مشروع البيت الكامل في اليمن
8. مشروع قرية مارين– كاليفورنيا

تكمن مسوغات هذا الاختيار في تغطية أنماط مختلفة لتجميعات حضرية تقليدية (قديمة) وحديثة. وتحت نفس الظروف الطبيعية. فقد اختيرت منطقتي الكاظمية ودمشق القديمة نظراً لكونهما لا تزالان تحتفظان بمعظم خصائص الشكل الفيزياوي والتقليدي.

أما بقية المشاريع فقد اختيرت للأسباب التالية:

- تمثل مشاريع سكنية صممت بالتكامل مع البيئة الطبيعية
- روعي في تصميم هذه المشاريع مفاهيم التكيف المناخي التقليدي والمستخلصة من دراسة الواقع البيئي والحضري للمناطق التقليدية.
- لقد مر على استخدام هذه المشاريع أكثر من عشر سنوات وهي مدة كافية لمعرفة مدى نجاح تلك المشاريع.

ب. وصف العينة البحثية (The Case Study Description):

تتطرق هذه الفقرة إلى تقديم شرح وافٍ عن العينات المنتخبة لأغراض القياس والتحليل.

مدينة الكاظمية:

اعتمد التنظيم الفراغي في المدينة على أساس وجود مرقد الإمامين (الكاظم والجواد) والذي يمثل مركزاً دينياً مهماً في العالم الإسلامي، لذا تركزت الوحدات السكنية حوله فشكلت تجمعاً حضرياً يشبه الشكل الدائري حيث يحتل المرقد المركز، في حين تمثل الشوارع المحيطة حدود المنطقة.

امتازت المنطقة بصورة عامة بالنسيج العضوي المتضام، حيث جاءت المساكن متلاصقة يفصل بينها بعض الأزقة الضيقة الملتوية والمظللة بشناشيل الدور المجاورة، بالإضافة إلى احتوائها على فناءات حضرية عامة تكون مع الفناء الداخلي منظومة بيئية متكاملة.الشكل (4) (Warren & Fathi,1982,p.27-83)

دمشق القديمة:

تأثر تخطيط مدينة دمشق بالفكر الإسلامي، حيث تحولت من النمط الشبكي إلى النمط المتضام، وامتازت الوحدات السكنية بالتراص يفصل بينها بعض الأزقة الضيقة الملتوية تنتهي هذه الأزقة بفناءات حضرية عامة تكون بالقرب من الجامع.

يرتبط الزقاق بالفناء الداخلي للمسكن عبر ممر مستقيم وذلك لان الطابق الأرضي مخصص للاستخدام العام لذلك لا يحتاج إلى الخصوصية، الشكل (5). (ميخائيل،2000،ص43-58)

مشروع تطوير منطقة سكنية متدهورة في الجيزة:

لقد حاول المصمم تدعيم التكوين الاجتماعي بالمنطقة فأتخذ من الأسرة "الخلية الأساسية" في تخطيطه لها فقسم المنطقة إلى مجموعة من وحدات الجيرة أساس كل منها مجموعة من الأسر يخدمها مجموعة من الخدمات والمرافق. واستخدم فكرة "الربع" أو "الحارة" الموجودة في المدينة العربية القديمة في التصميم، حيث تجمعت

الوحدات السكنية حول فضاء محدود المساحة "الربع" يستخدم لممارسة الفعاليات الاجتماعية، وتترابط هذه الفضاءات مع بعضها بمجموعة من الطرقات الضيقة والمتعرجة "الحارة" للمشاة – بعيدا عن الشوارع المخصصة لحركة السيارات– وذلك لتوفير الخصوصية للمشاة ولزيادة إحساسهم بالمقياس الإنساني. واستخدم المصمم المساحات الخضراء في الفراغات العامة والخاصة، كما استخدم مجموعة من الأحواض تمر فيها المياه ببطء معلقة على جدران الأفنية الداخلية للمساعدة على تلطيف درجة الحرارة من ناحية وخلق البيئة المناسبة للساكنين بتكامل المبنى مع العناصر الطبيعية.الشكل (6) (الخولي،1975،ص82–83)

قرية للعمال الزراعيين بشركة منتجات الكروم والتقطير المصرية بجناكليس:

تقع القرية بالقطاع الشمالي من الصحراء الغربية, بصورة عامة القرية ذات نسيج دقيق ومتضام التكوين(compact)، حيث مبانيها متلاصقة على امتداد طرقات ضيقة ومتعرجة وبين الحين والحين يفاجئ المرء ببعض الفراغات الكبيرة نسيبا. وذلك للتقليل من مساحة السطوح المعرضة لأشعة الشمس من ناحية ولتقصير المسافات بين أجزائها المختلفة من جهة أخرى، ولتسهيل الاتصال بين سكانها تدعيما لروابطهم الاجتماعية. تتكون القرية من مجموعة من الوحدات السكنية، كل مجموعة تتكون من ستة عشر مسكن يتوسطهم فراغ رئيسي وتربط الحارة (الزقاق) ما بين هذه الفراغات الرئيسية مما يؤدي في النهاية إلى الوصول في تخطيط القرية إلى وحدة ذات تكوين فراغي متكامل ونسيج متجانس مع ما يحيط به من طبيعة ريفية. الشكل (7) (الخولي،1975،ص88–89)

إعادة تعمير احد الأحياء القديمة بمدينة تونس:

يقع حي حفصية القديم ضمن حدود وسط المدينة، وكان الهدف الأساسي من التصميم هو الوصول إلى حل عصري يحقق المتطلبات الحياتية للسكان إلى جانب تدعيمه لطابع وتقاليد المنطقة.

اعتمد المصمم على مبدأ التضام (compact) في تشكيل الوحدات السكنية باعتباره الحل الأفضل لظروف المناطق الحارة الجافة، وحقق هذا التصميم التوازن بين استعمال السيارة كوسيلة عصرية للمواصلات وبين حركة المشاة وذلك بالفصل بين حركة السيارة والمشاة ومراعاة عدم التعارض بينهما، فأزدادت بذلك كفاءة السيارة في حركتها كما تحقق للمشاة إحساسهم بذاتهم، ولزيادة الكفاءة المناخية لممرات المشاة تم تسقيفها لحماية المارة من أشعة الشمس إضافة إلى تسقيف أجزاء من الشوارع بمساكن معلقة لتوفير التظليل والتخلص من الأحمال الحرارية التي تعاني منها تلك المناطق بالإضافة إلى الاقتصاد في استعمالات الأرض. الشكل (8) (الخولي،1975،ص77)

مشروع قرية باريس بمصر:

تقع قرية باريس في الواحات الخارجة بمصر، وتميزت بالتكيف مع البيئة المحيطة، حيث استطاع المعمار حسن فتحي توظيف معظم عناصر التكيف المناخي الذاتي التي امتازت بها العمارة التقليدية في تصميم القرية للاستفادة من الطاقات الطبيعية.

امتازت القرية بالتخطيط المتضام حيث كونت كل مجموعة من المساكن المتلاصقة وحدة جيرة تضم بينها فناء خاص بتلك الوحدة يرتاده الأطفال وكبار السن وترتبط تلك الأفنية مع بعضها بواسطة ممرات ضيقة مبلطة تشبه إلى حد كبير الحارة الموجودة في المدينة القديمة. بالإضافة إلى مراعاة عدم وصول السيارة إلى تلك ألاماكن، أي الفصل الصارم بين حركة السيارة وحركة المشاة. وقد تم توظيف عنصر التختبوش في القرية على مستوى النسيج الحضري، وذلك لتوفير مكان معتدل البرودة وملائم لجميع السكان، حيث يعمل على توفير حركة الهواء المطلوبة فتكون ملائمة للاستخدام في فصل الصيف.الشكل (9) (فتحي،1988،ص118-119)

مشروع البيت الكامل في اليمن

اختار المصمم اسم البيت الكامل من التقاليد اليمنية وهو البيت المتجه نحو الجنوب حيث إن البيت الناقص هو المتجه نحو الشمال والنصف كامل المتجه نحو الشرق أو الغرب، ومن تحليل المصمم إلى البيت التقليدي اليمني استطاع أن يتوصل إلى عدد من الثوابت في النسيج الحضري التقليدي, وتلك الثوابت تم تطبيقها في المشروع, حيث إن السكن في اليمن يختلف عن غيره وذلك بتجميعه العمودي حول حديقة مشتركة (بستان)، تلك المساكن التي تعرف بالمساكن البرجية أصبحت نتيجة لتطور التصميم تستفيد من ضوء الشمس والتهوية الطبيعية، وهي شبيهة بالأبراج المقسمة إلى عدة طوابق، حاول المصمم الاستفادة من الطاقات الطبيعية وذلك بالاستفادة القصوى من الواجهة الجنوبية، حيث ركز السكن على تلك الواجهة والخدمات على الواجهة الشمالية.الشكل (10) (انطانيوس،2000، ص139-138)

قرية مارين في كاليفورنيا:

الفلسفة التصميمية هي التي ساعدت في إنجاح المشروع، وأعطائه حيوية وصفة مميزة بكونه يعتمد على الطاقات الطبيعية، والهدف من ذلك هو الحصول على مجتمعات تخدم نفسها ذاتيا. يحتوي المشروع على (2000) وحدة سكنية، موزعة في خمس قطاعات متجاورة.

تخطيط القرية بصورة عامة امتاز بالتضام، حيث قُسمت القرية إلى عدد من وحدات الجيرة والتي تتكون من (12) مسكن حيث تكون متراصة مع بعضها وتضم بينها فناء وسطي خاص بتلك المجموعة وكل ست مجموعات تحتوي على فناء (فضاء مفتوح) خاص بها. ولأجل تحقيق الخصوصية لوحدات الجيرة فقد وضعت مواقف السيارات خارج هذه المناطق بحيث تكون المسافة بين تلك المواقف والمساكن لا تزيد عن (125)م. مع مراعاة الفصل بين حركة المشاة والسيارات. فضلا عن تصميم الفناءات المفتوحة في القرية وتحقيق العلاقة بينها للحصول على تيارات هوائية معتدلة. أما فيما يخص التوجيه فقد روعي أن تتجه المباني كلها (الأبنية العامة والمساكن) نحو الجنوب، ويتكون المسكن من طابقين تتخذ الفضاءات المعيشية الواجهة الجنوبية. الشكل (11) (www.desertknowlage.com.au)

ج. قياس العلاقة بين المتغيرات (Variable relationship measurement):

اعتمد البحث على الأسلوب الوصفي التحليلي والمستند على استمارة المسح لقياس العلاقة بين المتغيرات، لاحظ الجدول (2) يوضح المؤشرات بعد الترميز. علماً بأن المؤشرات خاصة فقط بالتصميم الحضري.

الجدول (2)

المؤشرات الفاعلة	الرمز
التشكيل المتضام	X1
توجيه المباني والمجمعات السكنية على أساس العلاقة مع حركة الشمس	X2
مبدأ الانسياب الفراغي	X3
إدخال الطبيعة في التشكيل العمراني	X4
الاقتصاد في استعمالات الأرض	X5
التكامل في المنظومة البيئية	X6
فصل حركة السابلة عن حركة السيارات (الخصوصية)	X7
تشكيل الواجهات الحضرية	X8

المؤشرات الفاعلة في النسيج الحضري المستدام (الباحث)

د. انتقاء الوحدة التحليلية:

جرى انتقاء النصوص (Texts) واللقطات التوضيحية (2D,3D) المعبرة عن المشاريع بوصفها أساساً للوحدة التحليلية.

هـ. الأوجه المسحية:

تضمنت العملية ثلاثة أوجه، بدءاً من عملية جمع العينات وانتهاءاً بالنتائج المستخلصة من الاختبار.

- **الوجه الأول (First Phase):**

هدفه تحديد العينات البحثية (مشاريع سكنية) مع إجراء التحليل الوصفي لها، للتوصل إلى استدامة التكيف المناخي التقليدي، إذ جرى جمع (15) مشروعاً باعتبارها مرحلة أولى ثم جرى تقليصها إلى (8) مشاريع.

- **الوجه الثاني (Second Phase):**

يهدف إلى إجراء المسح على العينات للتوصل إلى نسبة تفعيل كل مؤشر فيها وتثبيتها في استمارة المسح لغرض اختبارها. مع إجراء التحقق من صحة هذه النسب.

- **الوجه الثالث (Third Phase):**

يهدف إلى إجراء الاختبار الرئيس للعينة لتقويم كل مشروع على حدة ومن ثم تحديد معدل كل مؤشر بالنسبة للمشاريع ، لاستخراج فاعلية كل مؤشر على حدة، للتوصل إلى أهمية كل مؤشر بالنسبة للمؤشرات الباقية في التصميم الحضري، مع إجراء مقارنة بين النسيج التقليدي (الكاظمية، دمشق) بالمقارنة مع المشاريع الحديثة للتوصل إلى مدى نجاح تلك المشاريع في التكيف المناخي وفق مفاهيم العمارة التقليدية المستدامة.

و. معالجة النتائج (Results Treatment):

جرى تفريغ نتائج الاختبار على لوحة رئيسية (Master sheet) واعتمد البحث برنامج (EXCEL XP) لمعالجة البيانات.

- تحليل الإجراءات التطبيقية:

المرحلة التحليلية:

أوضحت نتائج الاختبار إلى استدامة النسيج الحضري التقليدي بالإضافة إلى استدامة العينات التي اعتمدت في تخطيطها على المؤشرات الفاعلة المستخلصة من النسيج التقليدي حيث اقتربت القيم المستخلصة من (1) وهي القيمة المفترضة للاستدامة، ومن مقارنة محصلة النسيج التقليدي(الكاظمية، دمشق) مع محصلة المشاريع الحديثة أثبتت النتائج التقارب الكبير بينهما مع تفوق النسيج التقليدي بنسبة ضئيلة جداً، وأوضحت نتائج البرنامج الحاسبي أيضا تفاوت أهمية المؤشرات الفاعلة من مؤشر إلى آخر في التصميم الحضري، حيث اخذ المؤشر الأول نسبة (14%)، المؤشر الثاني (13%)، المؤشر الثالث (13%)، المؤشر الرابع (11%)، الخامس (13%)، السادس (12%)، السابع (13%) والمؤشر الثامن (12%) علماً إن مجموع نسب هذه المؤشرات هو (100%).لاحظ الأشكال (12,13,14)

المعدل/المؤشر	X8	X7	X6	X5	X4	X3	X2	X1
معدل نسب المؤشرات	0.83	0.86	0.828	0.844	0.77	0.861	0.862	0.9456

حيث أثبتت نتائج الاختبار:

أن المؤشر الفاعل في العامل الأول هو X1 وقيمته 0.945

حيث إن X1: هو التشكيل الحضري المتضام.

والمؤشرات الفاعلة في العامل الثاني هي X7،X3،X2 وقيمتها على التوالي (0.862 ،0.861 ،0.86)

حيث إن

X2: توجيه المباني والمجمعات السكنية على أساس العلاقة مع حركة الشمس

X3 : الفراغ الانسيابي

X7: فصل حركة السابلة عن حركة السيارات (الخصوصية)

والمؤشرات الفاعلة في العامل الثالث هي X5، X6، X8 وقيمتها على التوالي (0.844، 0.828 ،0.83)

حيث إن

X5: الاقتصاد في استعمالات الأرض

X6: التكامل في المنظومة البيئية

X8: تشكيل الواجهات الحضرية

إما العامل الرابع فالمؤشرات الفاعلة فيه هي X4 وقيمتها 0.77

حيث إن

X4: إدخال الطبيعة في التشكيل العمراني

نتائج الدراسة العملية (البرنامج الحاسبي):

من خلال دراسة تسع عينات طبقت أسس التكيف المناخي التقليدي، أظهرت نتائج البرنامج الحاسبي، استدامة النسيج الحضري التقليدي بالإضافة إلى استدامة المشاريع التي اعتمدت في تصميمها على أسس التصميم الحضري المناخي التقليدي، وبالرغم من فاعلية جميع المؤشرات المستخلصة من النسيج التقليدي ، إلا إن الدراسة العملية أثبتت تفاوت أهمية هذه المؤشرات في خلق الاستدامة على مستوى النسيج الحضري.

حيث أثبتت الدراسة إن أهم مؤشر في تحقيق الاستدامة الحضرية هو التضام وبذلك يكون من ضمن العامل الأول، واخذ العامل الثاني كل من مراعاة التوجيه، مبدأ الانسياب الفضائي والفصل بين حركة السابلة والسيارات. واخذ العامل الثالث كل من الاقتصاد في استعمالات الأرض، التكامل في المنظومة البيئية وتشكيل الواجهات، وضم العامل الرابع إدخال الطبيعة التشكيل العمراني. لاحظ الجدول (3).

الجدول (3)

المؤشرات الفاعلة	الرمز	العامل الأول	العامل الثاني	العامل الثالث	العامل الرابع
التشكيل المتضام	**X1**	*			
توجيه المباني والمجمعات السكنية على أساس العلاقة مع حركة الشمس	**X2**		*		
مبدأ الانسياب الفراغي	**X3**		*		
إدخال الطبيعة في التشكيل العمراني	**X4**				*
الاقتصاد في استعمالات الأرض	**X5**			*	
التكامل في المنظومة البيئية	**X6**			*	
فصل حركة السابلة عن حركة السيارات (الخصوصية)	**X7**		*		
تشكيل الواجهات الحضرية	**X8**			*	

نتائج الدراسة العملية

- الاستنتاجات:

- فاعلية استخدام أنظمة التكيف المناخي التقليدي على مستوى النسيج الحضري والمبنى المنفرد.
- أكدت استراتيجيات الاستدامة على التفكير ضمن النطاق المحلي، والحفاظ على مصادر المصادر الطبيعية، وتقليل استهلاك الطاقات الناضبة، بالإضافة إلى التعلم من القديم لخلق الجديد، وتعتبر هذه المفردات من أهم اعتبارات العمارة المستدامة لخلق عمارة تحترم خصوصية المكان، وتتلاءم مع المحددات المحيطة بها.

- اعتماد مبادئ الاستدامة على مبادئ العمارة التقليدية (أسس تشكيل العمارة التقليدية) ذات الطابع الديناميكي بسبب علاقتها بالبيئة الطبيعية المحيطة من جهة وتلبية متطلبات الشاغلين من جهة أخرى. حيث إن العمارة التقليدية هي استجابة صريحة للمؤثرات المناخية والطبيعية المحيطة بها. وبذلك تعتبر من أكثر الأنماط تلائماً مع البيئة حيث ينعكس هذا التلاؤم على مستوى النسيج الحضري وعلى مستوى المبنى المنفرد.
- تكامل المبنى المنفرد مع النسيج المحيط به حيث يكون جزء من المنظومة البيئية المتكاملة، بالإضافة إلى احتواءه على العديد من العناصر التي زادت من تكيفه بالاعتماد على الطاقات الطبيعية وهذه العناصر هي الأفنية الداخلية والمستويات المتعددة والملاقف والمشربيات والبروزات والطارمات، بالإضافة إلى المواد البنائية الطبيعية ذات السعة الحرارية العالية التي زادت من تكيف المبنى مع البيئة المحيطة وتقليل استهلاكه للمصادر الناضبة وبالتالي حققت استدامة المبنى.
- فاعلية الأسس التصميمية المستدامة المعتمدة في النسيج الحضري التقليدي المتمثلة بـ أولا: التجميع الحضري الذي يحقق مبادئ الاستدامة من حيث التفاعل مع البيئة الطبيعية، والإحساس بهوية المكان، والحفاظ على الطاقة، ثانيا: التناسق الحضري التقليدي الذي يضم توزيع الأبنية وشبكة الأزقة في النسيج الحضري، بالإضافة إلى توجيه الأبنية حسب العلاقة مع حركة الشمس اليومية والفصلية، وتوقيع استعمالات الأرض حسب علاقتها مع بعضها، ثالثا: التقارب في استعمالات الأرض حيث إن هذا التقارب يتوافق مع العادات الاجتماعية والمعتقدات الدينية بالإضافة إلى خلق مناخ موضعي مريح، حيث إن المناطق المفتوحة في المناخ الحار تسبب بأحداث التيارات الحارة نهاراً والباردة ليلاً. وهذا التقارب يؤدي إلى التضام في النسيج التقليدي والذي يعمل على تقليل المساحات السطحية المعرضة لأشعة الشمس، وان للتضام مشاكل عديدة منها تقليل الخصوصية، لذلك عالجت العمارة التقليدية ذلك بالانفتاح على الفناء الداخلي الذي يوفر الخصوصية للوحدة السكنية بالإضافة إلى توفير الإضاءة والتهوية الطبيعية، حيث يعمل على خلق مناخ موضعي مريح للمسكن. وخامساً: تصميم الفناءات المفتوحة والتي تعتبر جزء من المنظومة الايكولوجية الحضرية التقليدية والتي تكون بداية الفراغ الانسيابي في النسيج الحضري وترتبط بالفناء الداخلي من خلال الزقاق.

متوفر

شكل (1) اشكال مختلفة للمدن المتضامة
(الخولي 1975, ص36 ,Google Earth)

شكل (2) الفراغ الانسيابي في النسيج الحضري
التقليدي (شاهين،2006،ص6)

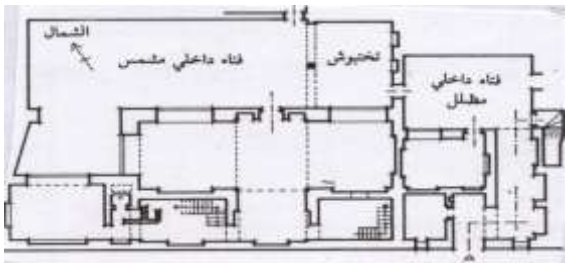

الشكل (3) استخدام النافورة في الفناء لتلطيف الجو
(فتحي،1988، ص201)

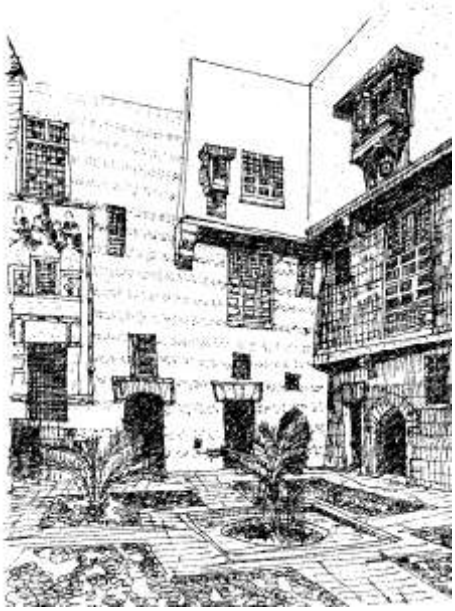

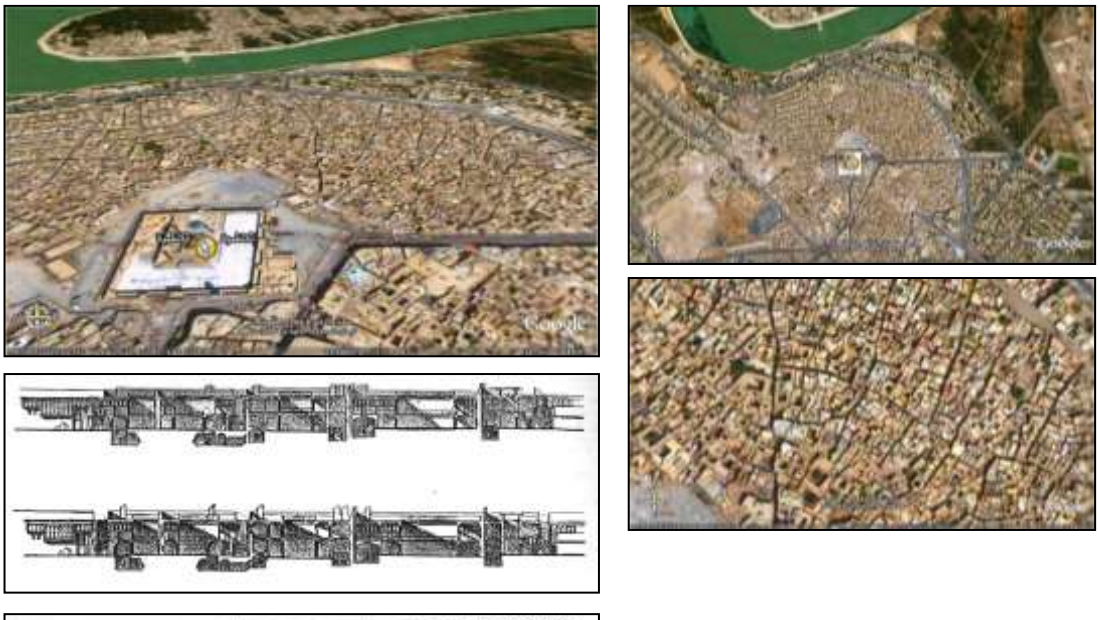

شكل (4) مدينة الكاظمية(Google Earth، Al-Kaissi.1983)

شكل (5) مدينة دمشق القديمة (عبد العال، 1987، ص49-67، Google Earth)

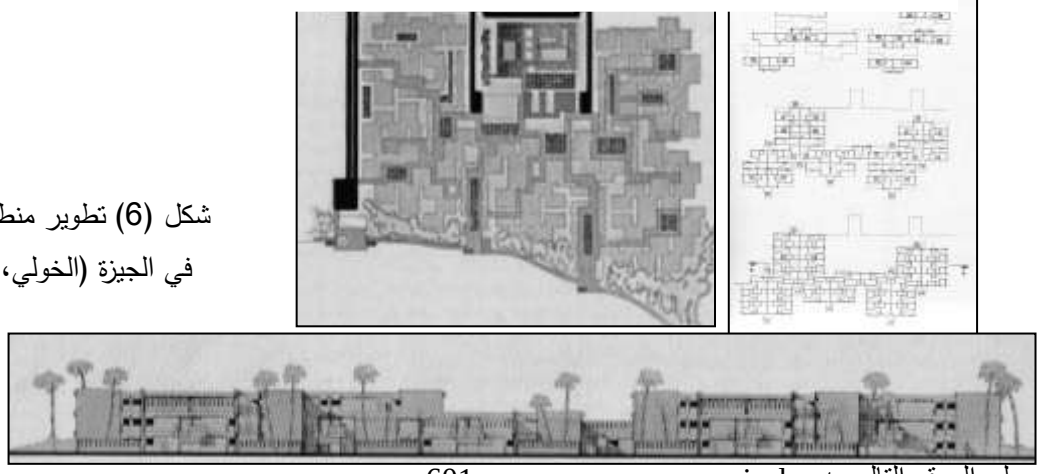

شكل (6) تطوير منطقة متدهورة في الجيزة (الخولي، 1975)

شكل (7) مشروع قرية للعمال
الزراعيين– بجنكاليس
(الخولي،1975، ص91–93)

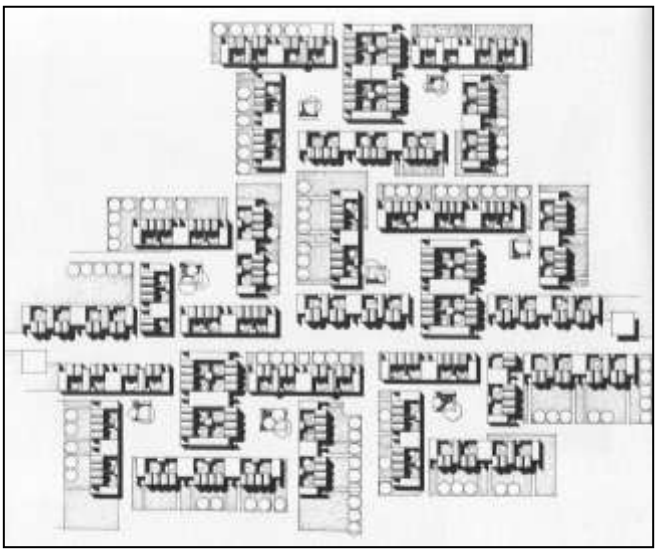

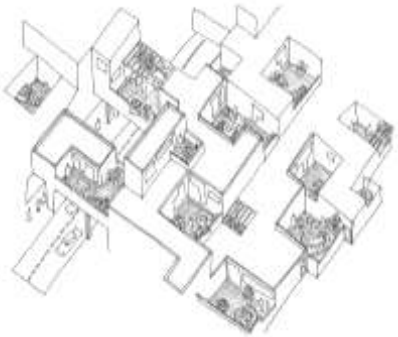

شكل (8) احياء حي حفصية– في تونس
(الخولي،1972،ص78–79)

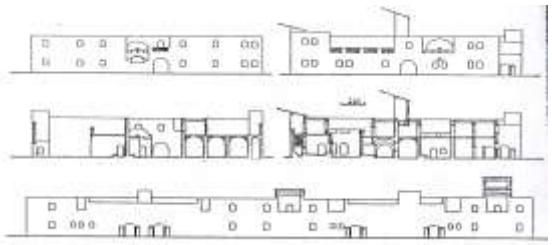

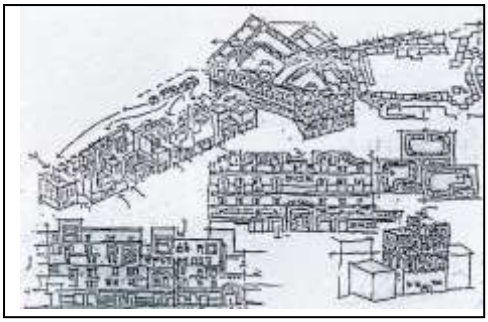

شكل (10) مشروع البيت الكامل في اليمن
(انطانيوس،2000،ص126)

شكل (9) قرية باريس في الواحات الخارجة بمصر
(فتحي،1987،ص195)

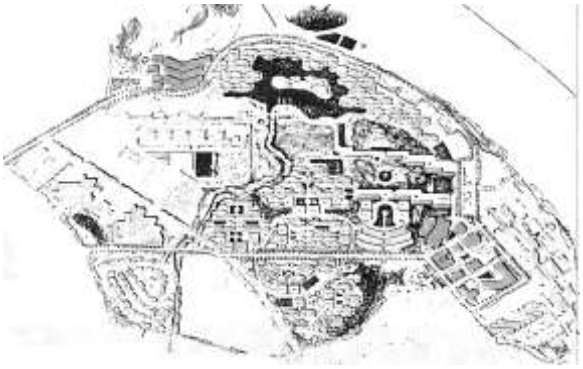

شكل (11) قرية مارين في كاليفورنيا
(Pearlmutter,2000,p.20)

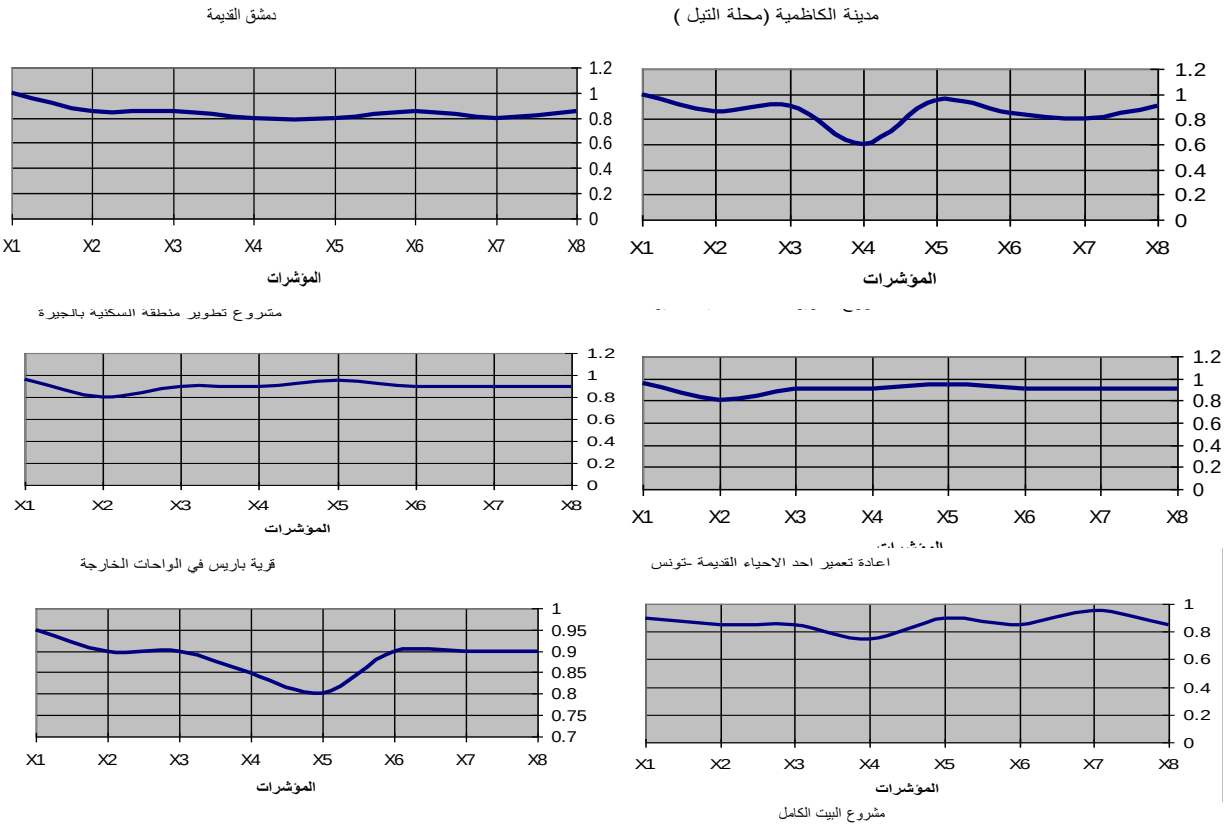

شكل (12) نتائج البرنامج الحاسبي

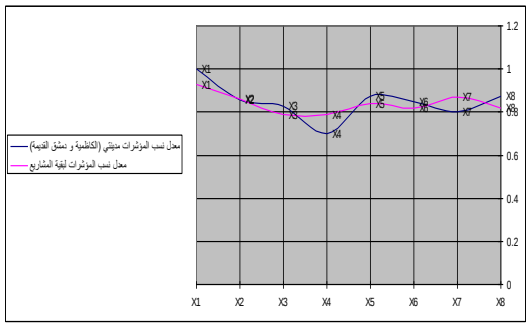

شكل (13) مقارنة بين محصلة النسيج التقليدي والنسيج الحديث

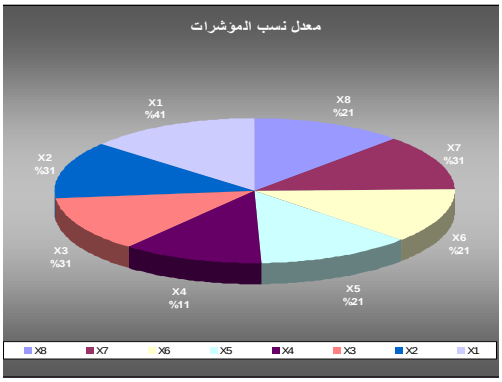

شكل (14) نسب تفاوت المؤشرات الفاعلة الدراسة

مصادر:

- الخولي،بدر الدين "المؤثرات البيئية والعمارة العربية"، جامعة بيروت العربية،1975.
- انطانيوس، غيداء منيف "بين الاصالة والعولمة.. المعالجات البيئية التقليدية وتطبيقاتها في العمارة العربية المعاصرة" المؤتمر المعماري الأردني الثاني، الجزء الأول، 2000.
- شاهين، د.بهجت رشاد " بعض خصوصيات السكن العربي المعاصر في المناطق الحارة–الجافة" كلية الهندسة، جامعة بغداد،2006.
- عبد المتطلب، احمد محمد، "ملامح الفكر البيئي للمسكن التراثي بين النظرية والتطبيق لعمارة الصحراء"، المؤتمر المعماري الأردني الثاني، الجزء الأول، 2000.
- عيسى، ابراهيم، " الاعتبارات البيئية في تشكيل الملامح المعمارية البحرينية" مؤتمر العمارة المستدامة، الجزء الثاني,2000
- فتحي، حسن "الطاقات الطبيعية والعمارة التقليدية" المؤسسة العربية للدراسات والنشر، 1988م.
- ميخائيل، سلوى، "المدينة والمسكن في الإسلام وعلاقتها بخصوصية الحياة العائلية كسلوك اجتماعي" المؤتمر المعماري الاردني الثاني "نحو عمارة مستدامة،2000

-AL-Homoud, M., "Sustainable Urban Planning of Historical Jawa" Analysis the physical and social pattern, Jordan Engineers Association, Part 1, 2000

-Golany. G, "Design for Arid Regions Urban form Design for Arid Regions", Van Nostrand Reinhold Company: New York, 1983.

-Moughtin, C. "Urban Design: Green Dimensions" Architectural press, 1996.

-Pearlmutter, D., "Patterns of Sustainability in desert Architecture" ARIDLAND, No. 47, May, 2001

- Public Management Magazine, "Development Sustainable Communities", 1995

-Steemer, K. "Building Form and Environmental Performance: Archetype analysis and an arid climate", Environmental Science,2003

-Warren, J & Fethi, I. "Tradition Houses in Baghdad", Coach publishing House Ltd, 1982

تثبيت نظام المعلومات الجغرافية GIS في العراق

بهجت رشاد شاهين
جامعة بغداد - كلية الهندسة
قسم الهندسة المعمارية

عامر ناجي صالح
جامعة بغداد - كلية الهندسة
قسم الهندسة المعمارية

ABSTRACT

Growth of cities made Urban Designers and Planners determine to the extent that need to knew solutions appear to maintain and analyze data, especially regarding dealing with 3D geometrical information and concepts integration on building them to enable analysis and ensure 3D rapid visualization as complication and mutual relations among various data types (3D spatial and non -spatial) and users vary greatly that current information systems face difficulty in dealing with, analyses and completing them, confusing the process of Urban Planning and conduct nowadays rather than a decade ago; it was necessary to set an attempt to combine available technology components and develop new concepts to conclude a system that meets users' requirements and solves problems of urban planning and of information users better . Therefore, focus was on a 3D system to conclude the concept of building objects and their attributes to allow efficient recovery and display, where focus is on 3D spatial objects; since demand of 3D spatial information is the most urgent.

So , the aim is identifying the conceptual model capable of dealing with a variety of object and relations of interest for urban planners appropriately to analysis and 3D interactional visualization using current technological developments , so that object of no spatial range are combined in the database according to objective classification , so that spatial object , classification with objective characteristics can work according to hierarchy in semantic and geometrical domains

this to be integrated by possibility of introduction of this public system to Iraq in general and Baghdad in particular by attempting suggesting conducting that system as a start to be the responsible for its application for real .

The research was finished with cooperation of many parties abroad to reach its desired aim.

الخلاصة

لقد عقد نمو المدن مهام المصممين والمخططين الحضريين الى حد ظهور الحاجة لحلول جديدة للمحافظة على البيانات وتحليلها خصوصاً ما يتعلق بمعاملة المعلومات الهندسية ثلاثية الابعاد وتكامل المفاهيم حول بناءها لتمكين التحليل وضمان التخيل السريع ثلاثي الأبعاد. وحيث يتفاوت التعقيد والعلاقات المتبادلة بين انواع البيانات المختلفة (المكانية واللامكانية ثلاثية الابعاد) و المستخدمين الى حد كبير جداً بحيث تواجه انظمة

المعلومات الحالية صعوبة في معالجتها وتحليلها لاكمالها، مما يشوش عملية التخطيط والادارة الحضريين في الوقت الحاضر ولاكثر من عقد مضى، كان من الضروري وضع محاولة لتوحيد مكونات التكنولوجيا المتوفرة وتطوير مفاهيم جديدة للوصول الى نظام يفي بشكل افضل بمتطلبات المستخدمين ويحل مشاكل التخطيط الحضري ومشاكل الذين يستخدمون المعلومات ، لذا تم التركيز على نظام المعلومات الجغرافية (GIS) ثلاثي الابعاد، للوصول الى مفهوم لبناء الاشياء وخصائصها مما يسمح باسترداد وعرض وافيين، يكون التركيز فيه على الاشياء المكانية ثلاثية الابعاد مادام الطلب على المعلومات المكانية ثلاثية الابعاد هو الاكثر الحاحاً.

ليكون الهدف هو تحديد النموذج المفاهيمي القادر على معاملة تشكيلية من الاشياء والعلاقات ذات الاهمية للمخططين الحضريين بطريقة مناسبة للتحليل والتخيل التفاعلي ثلاثي الابعاد اللذين يستخدمان تطورات التكنولوجيا الحالية، ليصار الى توحيد الاشياء التي تكون بدون مدى مكاني في قاعدة البيانات حسب خصائصها الموضوعية ويتم تصنيفها حسب التصنيف الموضوعي، ليعمل تصنيف الاشياء المكانية التي تمتلك صفات مميزة موضوعية حسب التسلسلات الهرمية في الحقول الدلالية والهندسية وتلك الخاصة بالموضوع وليتكامل ذلك بامكانية طرح هذه المنظومة العامة على العراق بالعموم وعلى بغداد بالخصوص بمحاولة اقتراح ادارة تلك المنظومة بداية لتكون الكفيل بتطبيقها حقاً.

وقد اتمم البحث بالتعاون مع عدة جهات خارج البلد للوصول الى اهدافه المبتغاة.

هدف البحث :

يهدف البحث الى تقديم الحلول من اجل التطوير المستقبلي للـ GIS في العراق عموماً وذلك لتأسيس نظام GIS متكامل، والبحث يوفر مقترحاً لتأسيس مؤسسة على المستوى الوطني لخدمة المجتمع بمعطيات جغرافية وخدمات ذات فائدة مشتركة، فضلاً عن ذلك فانه يقدم المتطلبات وستراتيجية التنفيذ والبرامج المطلوبة لتنفيذ هذا المقترح، للوصول الى توصيات عامة بهدف تطبيق النظام على العراق عموماً وعلى بغداد خصوصاً كونها نواة المدن العراقية والاهم فيما بينها على الاطلاق.

المقدمة :

إن اغلب الوظائف ضمن عملية التخطيط، تكون متعلقة بصنع القرار ومستندة الى وقائع الحالة الموضوعية، وهذا يدل ضمناً على ان الوظائف تعتمد على انظمة للامداد بالمعلومات وقبل كل شيء انتاج الخرائط، ماعدا مقترحات التخطيط الصرف، وعلى اعتبار ان وظائف المعلومات الجغرافية GIS من المنظور الاقليمي والوطني، والانظمة المساحية (وضع خرائط الاملاك) ومعالجة النظام، يكون التركيز فيها على التخطيط الاستراتيجي لاستخدام الأرض ، فإنها ستقتضي وظائف العمليات الاتية:-

أ- نظام تخطيط ستراتيجي لمراقبة التطوير وتخطيط التطوير المستقبلي، وهذا النظام يجب ان ينسجم مع نظام المعلومات الستراتيجية، والذي يجب ان يتضمن برامج التطوير الحضري والموارد الطبيعية والتخطيط والبرمجة الاقليميين والتخطيط والبرمجة الوطنيين. (Martin,1990,p.95).

ب- انظمة عمليات صنع القرار الروتيني طبقاً لمهام التخطيط قصير المدى، وهذا يجب ان يتضمن الاستثمار والبرمجة الاجتماعية ونظام دعم القرار، وقد يتضمن هذا الموافقة على خطة البداية والامداد بالمعلومات. (Van Helden,1993,p.244).

ان انشطة نظام المعلومات الجغرافية GIS ضمن المؤسسات الحكومية يجب وقبل كل شيء، ضمن هذه الخطوط العامة، حصرها بالاستخدام الاعتيادي لقاعدة نظام المعلومات الجغرافية GIS وعملية التحليل وادوات التقييم، كدعم لجهود التخطيط الاقليمي والوطني، وهذا يعني ان معرفة عمليات نظام المعلومات الجغرافية GIS يجب ان تكون جزءاً من تشكيلة الوسائل العامة لاغلب اعضاء ملاك التخطيط المحترف. (Martin,1990,p.105).

ولايمكن مناقشة التطوير المستقبلي لنظام المعلومات الجغرافية GIS دون الاخذ بنظر الاعتبار سلسلة GIS-chain GIS والتي تتضمن : الخبرة والمعطيات المبنية والتنظيم ومعدات الكومبيوتر/ البرامجيات (Bernhardsen,1992,p.96) و مكونات نظام المعلومات الجغرافية GIS : وهي معدات الكومبيوتر والبرامجيات وقواعد المعلومات ومعدات التنظيم والمعدات الحياتية. واضعين في الاعتبار دور الـGIS كنظام

دعم للتخطيط في مناقشات التنظيم المستقبلي وتوزيع المهام على المؤسسات الحكومية لتعمل مجموعة نظم GIS الموجودة كوحدة دعم تخطيطية رئيسة. (Haugan,1998,p.102).

على اعتبار ان عمليات نظام المعلومات الجغرافية GIS هي متكاملة شاملة تستلزم قدرات ادارية للمعطيات المعززة **"المعطيات المبينة"**، وهذا يتضمن القدرة على اشتقاق المعطيات من مصادر مختلفة لتخطيط وظائف معلومات الاقسام وتنظيم وتنسيق "معدات تنظيم" الاقسام والملاك الذي يجب ان ينفذ وظائف هذه العمليات، بحيث ان نشاط نظام المعلومات الجغرافية GIS يجب ان يدمج جميع المعطيات والانتاج المجهز من الكيانات الخارجية والمؤسسات الحكومية الاخرى بصفة معطيات لمختلف الأغراض ، مما يتطلب مسؤوليات اكثر وضوحاً لبعض الكيانات الحكومية العاملة في حقل انتاج وتحديث المعطيات، والعلاقات المتبادلة بين هذه الكيانات التي يجب ان تصنع اولوية متقدمة في تحديات مهام ابنية وهيئات المؤسسات الحكومية. , لهذا فان قدرة الانتاج المتواضعة يجب الحفاظ عليها ضمن المنظمات الحكومية وذلك لانجازعمليات تصنيع وثائق الخطة والحفاظ على قواعد المعلومات، التي يجب ان تكون جزءاً من مسؤوليات الحكومة (كأرشيف للخطة الماضية والحالية) وللتزويد بالمعطيات الاستثنائية لهذا الغرض (Bernhardsen,1992,p.66).

ان عملية بدء العمل الناتج من عمليات نظام المعلومات الجغرافية GIS يعتمد على توازن متعقل للتكنولوجيا والتنظيم والملاك والمهام، وهذه المكونات فضلاً عن المعطيات والمعلومات التي لايمكن فصلها، حتى خلال مناقشات نظام المعلومات الجغرافية GIS في المستقبل (Bernhardsen,1992,p.107).

وبموجب هذا, فان المعلومات الاساسية يجب ان تكون دقيقة ويمكن تحمل تكاليفها، ومربحة وغير مقحمة وقبل كل شيء يجب ان تكون سهلة الوصول اليها، وعند البحث فان النظام يجب ان يوفر المعلومات مع توفيره "معدات الكومبيوتر والبرامجيات"، وبينما تتواصل اهمية الكومبيوتر بالنمو فانه سيعوض التعقيد المتزايد للانظمة، مما يؤدي إلى مواكبة متواصلة للتطورات الجديدة تتفاوت وكفاءة عمليات نظام المعلومات الجغرافية GIS الخاصة بملاك التخطيط المحترف داخل المؤسسات الحكومية, لذا لابد من التدريب على نظام المعلومات الجغرافية GIS الاساسي مع الاستخدام المتواتر للادوات والبرامجيات. (Haugan,1998,p.120).

وعلى اعتبار ان المهارات الادارية لنظام المعلومات الجغرافية GIS والممثلة ضمن المؤسسات الحكومية تكون محدودة جداً، فانه يجب اعطاء برنامج تدريب شامل على نظام GIS ضمن هذه المؤسسات، على اساس تقدير الحالة الفعلية، تماشياً مع وظائف ملاك التخطيط المحترف وكفاءاته والبرامجيات الجديدة المقدمة في المؤسسات (Bernhardsen,1992,p.215).

ان الغرض من هكذا برامج تدريبية، هو لتعزيز القدرات الاجمالية للملاك والمسماة "بالمعدات الحياتية Live ware" التي تعمل طبقاً للمعايير الاتية:-

اولاً: يجب ان تكون لدى كل محترفي التخطيط معرفة عملية بالادوات، اي ان يكونوا قادرين على استخدام نظام المعلومات الجغرافية GIS المكيف للتخطيط في عملهم اليومي الاعتيادي من اجل عمل الخرائط والتقديمات Presentations ولاغراض التحليل البسيط.

ثانياً: يجب اختيار ملاك التخطيط المحترف فيما بين 3-4 اشخاص لتحمل مسؤوليات خاصة لوظائف نظام المعلومات الجغرافية GIS الادارية , لتكمن في ادارة وتأسيس وبناء والحفاظ على قواعد المعلومات المكيفة للتخطيط، ويجب ان يتم توزيع وظائف ادارة GIS توزيعاً تفصيلياً داخل الاقسام المختلفة للمؤسسات.

ثالثاً: ومن بين الملاك الفني يجب اعطاء مسؤولية محددة لشخص واحد لخدمات انتاج عمليات نظام المعلومات الجغرافية GIS والتي تتضمن التحول الى اشكال رقمية ومداولات وتحويلات التصاميم وتحرير قواعد معلومات الرموز وقواعد المعلومات الجغرافية. (Bernhardsen,1992,p.221).

ان تقنية GIS وتقنيات المعلومات المكانية الاخرى (مثل التصوير المساحي الضوئي Photo grammetry ونظام الموقع الجغرافي GPS)، ستصبح كامنة في الكثير من العمليات اليومية للمؤسسات الحكومية، حيث سيساهم الاستفهام عن المعطيات المكانية في اكمال صنع القرار، ومن خلال ادخال الاستفهام

الالي عن المعطيات المكانية سيقوم نظام المعلومات الجغرافية GIS بمساهمة اساسية في هذا الامر ليصبح واقعياً. (Bernhardsen,1992,p.222).

كذلك فان الشبكة الدولية (الانترنت Internet) والشبكة الداخلية لما بين المستخدمين سيساهم بشكل كبير في هذا التطوير عن طريق زيادة المسافة بين الكومبيوتر والمستخدم النهائي مادياً وذهنياً بشكل رئيسي. بمعنى انه سيتم الوصول الى الكثير من التطبيقات دون وجوب الشعور بادنى قلق حول التقنية الاساسية مهما كان هذا الامر معقداً، وفي هذا السياق فان شبكة الخدمة (NT server) في نظام المعلومات الجغرافية GIS المركزية ستضم كل المعطيات المتوفرة والمعلومات وخرائط التخطيط التي يجب ان تكون (شبكة الخدمة) التي من الممكن الوصول إليها، ليس بالنسبة للملاك الحكومي وحسب , بل كذلك لكل المحترفين والمهتمين من الخارج (جمعة ، 1998, ص11).

وطبقاً للادخال السابق بخصوص الافكار التي قد تساعد على تطوير نظام المعلومات الجغرافية GIS في عموم رقعة العراق وبسبب الاحتياجات المتزايدة لنظام GIS المركزي لتجهيز كل الناس والمؤسسات بالمعطيات المتوفرة والمعلومات وخرائط التخطيط لاستخدامها في الميادين المختلفة، فان اقتراح تأسيس سلطة حكومية لوضع الخرائط (Mapping Authority of government: MAG) مرتبط مباشرةً بمكتب رئيس الجمهورية ويديرها مدير عام، هو امر ضروري جداً مما سيلي ذكره بالتفصيل.

*** مقترح لتطوير الـGIS لعموم رقعة العراق:**

- <u>امكانية تثبيت نظام GIS:</u>

لاسباب تاريخية قام عدد كبير من الحكومات وعلى شتى المستويات في ارجاء العالم بعملية جمع المعطيات ولامد طويل ، وعلى اعتبار ان انشطة وضع الخرائط كانت وماتزال في بعض الدول تعتبر نشاطاً عسكرياً، وتنسيق الانشطة على المستوى القومي في معظم البلدان تتولاه سلطة وضع الخرائط القومية او وحدة تنظيمية مشابهة ، فقد كان الهدف الرئيس للتنظيم هو تنفيذ الوظائف ذات المصلحة العامة للمجتمع المتعلقة بالمعطيات الجغرافية. ولقد توسع الاهتمام بامور سياسة المعطيات والمعلومات توسعاً كبيراً في السنوات الاخيرة، ومع ذلك مازال موقع سلطة وضع الخرائط القومية موقعاً قوياً في اغلب البلدان ولايمكن مناقشة الحاجة لهذا النوع من المنظمات ولكن مسؤولية المنظمة متغيرة طبقاً للسياسات الجديدة، اما استحداث سياسة المعطيات الجغرافية فتسيرها عدة عوامل مثل(Bernhardsen,1992,p.251):-

- تأثير التقنية الجديدة على جمع المعطيات وتوزيعها.
- التغييرات السريعة في توقعات المستخدمين (الزبائن) وفي السوق التابع.
- التغيرات في قيم المجتمع والإصلاحات الحكومية.

ونتيجة لتطور التقنية , تغير التركيز من انتاج الخرائط الى قواعد المعلومات، مستنداً الى التعاون والتكامل مع الانترنت الذي يتطور بصفته قناة توزيع جديدة للمعطيات، وفيما تغيرت توقعات المستخدمين ومتطلباتهم، يتطور السوق التجاري في مجال المعطيات الجغرافية ، مما احدث وفي العديد من الدول تغير في المسؤوليات من الحكومات ذات المستوى الاعلى الى الادنى، مما أثر على مسؤولية سلطة وضع الخرائط القومية . واعتماداً إلى تنظيم الإنتاج والسوق (المستخدم) فقد يقع اختيار سلطات وضع الخرائط القومية، على طريق من طرق العمل المختلفة الآتية (Bernhardsen,1992,p.245):-

1- إنتاج المعطيات الأساسية وتوزيعها لمعطيات الخرائط الاساس الى كل المستخدمين.
2- توزيع المعطيات الاساسية مترافقة مع المعطيات القياسية الاخرى (معطيات العناوين والمعطيات المساحية والمعطيات المعدة لاغراض متعددة ...الخ) الى كل المستخدمين بانتاج واسع للخرائط.
3- توزيع المعطيات الاساسية مترافقة مع المعطيات القياسية الاخرى والمعطيات للمستخدمين المعينين لتصنيف منتجات المستخدمين المصنوعة لغرض معين (الأنشطة ذات القيمة المضافة) .
4- تنسيق تبادل المعطيات دون الدخول في عملية الإنتاج وإنما التركيز في المسؤولية عن المقايسة.

واليوم تركز سلطات وضع الخرائط القومية على ادارة سياسات الخرائط العامة وادارة البنى التحتية للمعطيات الاساسية ومقايسة المعطيات الجغرافية، مما اعطى الى حد ما تخفيضاً في طاقة الإنتاج القصوى الى

حدها الادنى لصالح الشركات الخاصة، وكذلك المنظمات العامة الاخرى. وفي السوق الخاص بالمنتجات ذات القيمة المضافة , تتنافس سلطات وضع الخرائط القومية مع الشركات الخاصة ، ومادام اكتساب المعطيات الجغرافية ومعاملتها وتوزيعها يستلزم في احوال كثيرة كلاً من السلطات القومية والمحلية فضلاً عن المصالح التجارية والشركات الخاصة ، فان بضعة دول قد بادرت الى انشاء شراكة لحل مثل هذه المهام، علماً ان سلطات وضع الخرائط القومية يجب ان تكون هي المؤسسة الوحيدة المسؤولة عن الشبكة الجيوديسية القومية في البلاد. (MOPIC,2000,p.222).

وهذا هو الوضع في دول ذات الباع والتجربة العتيدة في وضع الخرائط وادارة المعطيات الجغرافية، اما في العراق وبغداد خاصة فان الوضع لايمكن مقارنته بشكل مباشر مع هذه الدول، كونه يتميز بالافتقار الى المعطيات ومجموعة الانشطة المنسقة وبامتلاكه سوقاً غير متجانس ومجاميع مستخدمين ذات كفاءة متدنية مع الافتقار الى المؤسسات التي يمكنها ان تلعب دوراً مناسباً، لذا فان التحدي الرئيسي في العراق هو بناء بنى تحتية لمؤسسات قادرة على البقاء وقواعد معلومات ذات اطار زمني معقول، مع انشاء قواعد السوق الرصينة، بحيث تؤمن ما يجب القيام به عندما تكون الوظائف الاساسية والمعطيات الرئيسية في الموضع الصحيح وبكفاءة معززة، ولكن من الضروري الاخذ بالحسبان ان الهدف هو خدمة المجتمع وان احتياجات المستخدم يجب ان تكون الاساس لكل الستراتيجيات، اما الوظائف والمعطيات التي لاحاجة لها فيجب عدم اشراكها مما يعني ان بعض انواع تحاليل الكلفة والفائدة يجب تنفيذها عند اختيار الإستراتيجيات.(جمعة ، 1998, ص37).

الاطار العام لانشاء سلطة وضع الخرائط الحكومية:

(Mapping Authority of Government: MAG)

بلدنا وكحال الدول الاخرى، تحتاج الى مؤسسة على المستوى القومي لخدمة المجتمع بالمعطيات الجغرافية والخدمات ذات النفع العام، مما يتوجب انشاء بنى تحتية لمؤسسات وقواعد المعلومات فضلا عن سلطة وضع الخرائط الحكومية (MAG). وقد اثبتت التجربة العالمية انه يجب اختيار الستراتيجيات المتنوعة لمرحلة التأسيس ومرحلة التشغيل للمؤسسات و قواعد المعلومات (MOPIC,2000,p.222).

ويجب تنفيذ تاسيس المؤسسة الجديدة خلال مشروع عمل حقيقي للتمكن من تطوير المعرفة الفنية لتعاون الادارة والمعطيات ذات الصلة. كما يجب ترتيب الاطار المالي والاطار الزمني لمشروع كهذا قبل ان يبدأ، ويجب تقسيم المشروع الى مراحل حيث يكون النجاح في المرحلة السابقة متطلباً اساسياً واضحاً قبل التحرك للمرحلة الثالثة، كما وينبغي تمويل المشروع مع اشتراك القطاعات الخاص والعام والاكاديمي والمنظمات غير الحكومية معاً (MOPIC,2000,p.223).

- وظائف سلطة وضع الخرائط الحكومية (MAG):

وبموجب ما تقدم يجب ان تكون الوظائف الاتية هي مسؤولية سلطة وضع الخرائط الحكومية(MAG):-

1- ادارة سياسات الخرائط العامة/ المعطيات الجغرافية.
2- ادارة البنى التحتية للمعطيات القومية وتنسيقها.
3- تطوير المعايير القومية للمعطيات الجغرافية.
4- تطوير الشبكة الجيوديسية القومية وصيانتها.
5- جمع المعطيات الاساسية (التصوير المساحي الضوئي والاستشعار عن بعد...الخ) في كل مجالات مقياس الخرائط.
6- ادارة قاعدة المعلومات (وضع الخرائط ونظام المعلومات الجغرافية GIS).
7- خدمات الزبائن- توزيع مجموعات المعطيات الأساسية.

اما النشاط الثاني "جمع المعطيات" فيجب ان تنفذه بصورة مشتركة بين الشركات الخاصة والحكومية، ويجب تنظيم سلطة وضع الخرائط الحكومية(MAG) لتغطية هذه الوظائف (PECDAR,2000,p.101).

- بنية المؤسسات المقترحة:

استنادا الى ما تقدم , يجب استحداث سلطة وضع الخرائط الحكومية (MAG) التي تكون مرتبطة مباشرةً بمكتب رئيس الجمهورية ، لتشتمل على تأسيس سلطة وضع الخرائط الحكومية Mapping Authority of Government: MAG التي تكون مسؤولة عن سلطة سجل الاراضي الحكومية الممسوحة (Cadastre Authority: CA) وقد تتوحد سلطتي (MAG و CA) الا انه يكون من الممكن تنفيذ تطوير اسرع في وحدتين منفصلتين عند بداية العمل كونه حديث الوضع. (PECDAR,2000,p.110).

وان السبب في جعل ورفع سلطة وضع الخرائط الحكومية MAG الى مستوى مكتب رئيس الجمهورية يستند الى حقيقة ان وضع الخرائط يمثل وظائف مهمة في البنى التحتية للمعلومات القومية، لتكون الوظائف بشكل نموذجي على المستوى ما بين الوزارات وذات اهمية كبيرة للتطوير الاقتصادي . وهنا يجب ان يشرف على سلطة وضع الخرائط الحكومية MAG مجلس مكون من عدة وزارات ويرأسه مدير عام تابع لمكتب رئيس الدولة ، سيكون الغرض من المجلس المؤلف من عدة وزارات هو ضمان لاحتياجات المستخدمين للوزارات المختلفة لتعلمها وتدعمها سلطة وضع الخرائط الحكومية MAG ، لاستعمال المعرفة والقدرة الموجودة . وبهذا ستكون خطوة باتجاه ادخال ادارة اكثر شفافية وديمقراطية ، من عدة وزارات بمجلس يستند الى مهام GIS ووضع الخرائط المطلوبة، وكذلك يجب تضمين ممثلين من القطاعات الاكاديمية والمنظمات غير الحكومية (NGO) ممن يكونوا ذوي امتيازات محدودة في القرار. (MOPIC,2000,p.241).(شكل-1).

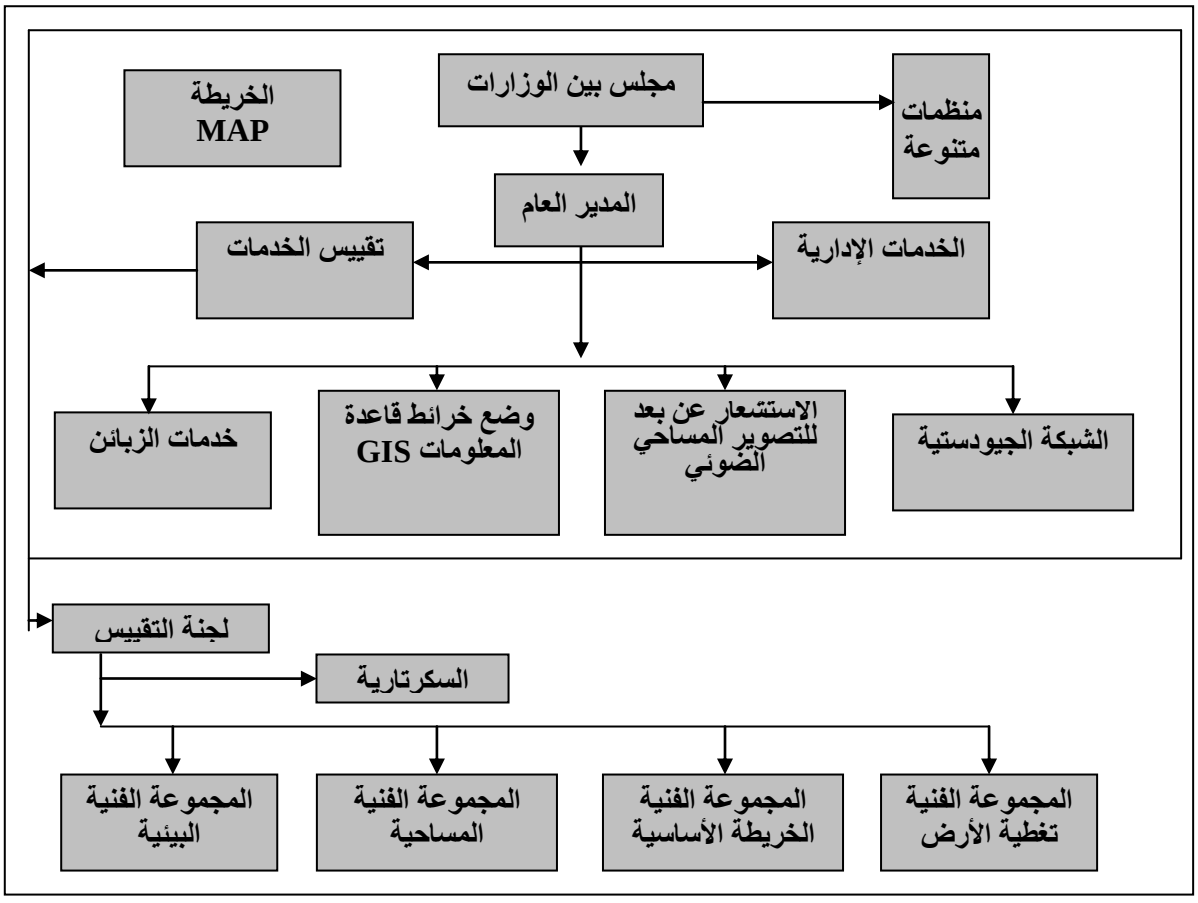

شكل (1) بنية المؤسسات (MOPIC,2000,p.28)

إن الكثير من الوزارات ستحتاج قدرة GIS الخاصة بهم لانجاز وظائفهم الرئيسية، بتقاطع عملها وتكامله مع مجموعات البلديات في مناطق مختلفة من البلاد، لهذا يجب ان يتم شمول عدد من البلديات مع

الوحدة الخاصة في مشروع (GIS) المقترح كخطوة بداية, وان بعض الامثلة للاحتياجات البلدية الاساسية التي يجب تنسيقها على المستوى القومي هي (MOPIC,2000,p.2158):-

1- الشبكة الجيوديسية.
2- الوصول الى المعلومات المساحية.
3- الدعم لشراء معطيات خرائط كبيرة المقياس.
4- الدعم لاجل السيطرة على نوعية المعطيات كبيرة المقياس.
5- الوصول الى خطط اقليمية وقومية لاجل التخطيط المحلي.
6- المعلومات الاحصائية.
7- تطوير وصيانة انظمة خطوط الانابيب للامداد بالماء والكهرباء والخدمات العامة.

والنقطة الأخيرة هي مثال للاهمية القومية، حيث يكون GIS اداة فعالة لوضع الخرائط والادارة، والمطلوب هو تعيين انظمة المعلومات لمثل هذه الاغراض. (MOPIC,2000,p. 160).

- متطلبات تأدية الوظائف:

يجب ان تعتمد الوظائف على اطار قانوني وبضمنه المتطلبات الادارية والتنظيمية، مما يتطلب تقسيم موارد المشاريع المستقبلية حسب مسؤولية الوحدة التي يجب ان تكون تحت طائلة ادارة محترفة حديثة بقيادة قوية وباشخاص ذوي كفاءة عالية , كما يجب ان تكون الوحدة مجهزة تجهيزاً كفوءاً، ويجب ان تتمتع بدعم عالي مستقر طويل الامد، مع احتياجها الى استشاريين لمدة زمنية طويلة. (MOPIC,2000,p. 161).

وفي ضوء هذا فان سلطة وضع الخرائط الحكومية MAG ستكون بحاجة الى تزويدها بالمعرفة من المؤسسات الحكومية الداخلية والخارجية. وللايفاء بمتطلبات سلطة وضع الخرائط القومية الحديثة ، يكون من المطلوب المعرفة والخبرة في مجالات علوم الجيوديسي والتقييس والتصوير المساحي الضوئي وادارة قاعدة المعلومات الجغرافية وتصميمها والسيطرة النوعية والاستشعار عن بعد ووضع الخرائط العام على مستوى نظري رفيع , كما يجب توفير معدات حاسوبية وبرامجيات معينة لمسح ووضع الخرائط على نطاق قومي ، ويتضمن هذا معدات المسح الجيوديسية وبرامجياته (GPS) ، ومعدات حاسبة التصوير المساحي الضوئي الرقمي وبرامجياته , مع قابليات انتاج خرائط بنوعية عالية (image setters) ومختبرات تصوير فوتوغرافي وطباعة بالاوفسيت) وما الى ذلك من متطلبات انشاء مختبرات نظام المعلومات الجغرافية (GIS) (PECDAR,2000,p.124)

- القطاع الاكاديمي:

ولتحقيق ذلك , يتوجب بداية أن يتم تطوير مؤسسين فقط على المستوى الجامعي في العراق لتكون نواة المؤسسات الرئيسة لخدمة المجتمع العراقي , بمرشحين في حقل المسح ووضع الخرائط والتصوير المساحي الضوئي وعلم رسم الخرائط وGIS...الخ. ويمكن للمعهد العالي للتخطيط الحضري والاقليمي – بغداد وجامعة بغداد ان تكونا مرشحتين لهذا الموقع ، وهذا يجب ان لا يستثني الجامعات الاخرى من الدورات المقامة في هذا المجال، ولكن يجب ان لا تتمتع هذه الجامعات بنفس الاولوية فيما يخص التمويل على اعتبار ان الانشاء والحفاظ على قابلية التعليم في علوم الجيوديسي وعلى المستوى الجامعي , من الارجح انها ستكلف اكثر مما تعطي كمنافع ، لذا يتوجب استقدام او شراء هذه القابلية من خارج العراق عند الحاجة ، عن طريق إرسال الطلبة الى جامعات تتمتع بسمعة جيدة في خارج البلاد وعند دول متقدمة في هذا المجال. (PECDAR,2000,p.125).

وهنا يتحتم أن يتم تطوير مؤسسة واحدة فقط على مستوى كلية في جامعة بغداد، لتكون (المؤسسة) الرئيسة لخدمة المجتمع العراقي بمرشحين في حقول المسح ووضع الخرائط والتصوير المساحي الضوئي وعلم رسم الخرائط وGIS...الخ ، ويمكن لكلية الهندسة ان تاخذ الدور الاول في الترشيح لهذا الموقع وهذا لا يجب ان يستثنى الكليات اخرى من الدورات المقامة في هذه الحقول ، ولكن هذه الكليات يجب ان لا تتمتع بنفس الاولوية فيما يخص التمويل كما سبق الاشارة اليه. (PECDAR,2000,p.126).

وقد أظهرت التجربة العالمية ان التقنية تتطور سريعا في هذا الحقل وستكون هناك حاجة مستمرة لانعاش المعرفة ، ويمكن تغطية ذلك بدورات قصيرة ما بعد الخبرة تنفذها مؤسسات اكاديمية متنوعة ، بالاضافة الى دورات التعليم الاكاديمي التي ستنفذها مؤسسة متخصصة لتدريب الملاك ، وسيتم تنفيذ هذه الدورات عند الحاجة (ولأغراض داخلية) وليس ثمة حاجة لتنسيق قومي لهذه الدورات.(PECDAR,2000,p.126).

ولجمع المصلحة الاحترافية في ميدان GIS ، يتوجب أنشاء جمعية قومية مشابهة لجمعية المعلومات الجغرافية (Association of Geographic Information) في انكلترا، تعنى هذه الجمعية بالمصلحة فيما يخص التعليم ما بعد التخرج , لتقوم بتخريج وتنظيم دورات واجتماعات احترافية وتقيم الاحكام والمعاييرالتي تطورها الوزارات...الخ، وتشترك في العمل والاجتماعات الدولية، وهذا الموقع قد يكون مسؤولية المنظمات غير الحكومية (NGO),(PECDAR,2000,p.167).

- القطاع الخاص:

سيكون الدور الرئيس للقطاع الخاص هو انتاج المعطيات، مع توفير القابلية لإنتاج التصوير المساحي الضوئي , فضلاً عن مسح الاراضي التقليدي وقياسات GPS، وتعديل البرامجيات الاساسية حسب طلب الزبائن مع تطوير التطبيق . لتكون هذه الانشطة هي المهمة الموكلة التي ينفذها القطاع الخاص والذي بموجبها لا يحتاج نهائيا لأن يطور قابليته للانتاج ضمن الاستشعار عن بعد وطباعة الخرائط وثيق الصلة بالمعرفة الاحترافية الشاملة لعلوم الجيولوجي والزراعة والبيئة...الخ . (PECDAR,2000,p.188).

- التنفيذ:

اعتماداً الى ما تقدم وبقصد وضع إجراءات التنفيذ لـ(MAG) عن طريق وضع المتطلبات الرئيسة لستراتيجية التنفيذ وبرنامج التنفيذ، فلابد من الآتي (PECDAR,2000,p.189):-

- إستراتيجية التنفيذ العامة:

يجب ان يتم التنسيق ما بين تحقيق سلطة وضع الخرائط الحكومية MAG وتطوير البنى التحتية القومية للمعطيات الجغرافية وتنفيذها ضمن فترة تتراوح بين 5– 10 سنوات وبمراحل مختلفة، تشمل الاتي(PECDAR,2000,p.188):-

المرحلة الأولى:- برنامج قصير الامد
المرحلة الثانية:- برنامج متوسط الامد
المرحلة الثالثة:- برنامج طويل الامد

وستتميز المراحل الثلاثة على التوالي بالتقدم في التنفيذ لتضم الاولى: التحضير والثانية: الانتاج والثالثة: التحديث/العمليات لتعكس هذه المراحل كذلك ضرورة التأسيس التدريجي لسلطة وضع الخرائط الحكومية MAG , ووفقا للتجربة العالمية فأن التشغيل الكامل والتزويد بالعاملين لن يتم الوصول اليه قبل 5-6 سنوات، ولذا ستتحكم بالمرحلتين الاولى والثانية تنظيم مشروع للانشطة في حين ان البنية التنظيمية الدائمية ستتحكم بالمرحلة الثالثة. (PECDAR,2000,p.190).

وبهذا يمكن تقسيم استراتيجية التنفيذ الى ثلاث فئات هي:-

1- الطريقة التقنية (حيث ان افضل تقنية تعطي على الأغلب أفضل نتيجة للمنظمات).
2- الطريقة التخطيطية (اذ ان الخطة المعدة جيدا تعطي دائما افضل نتيجة للمنظمات).
3- الطريقة الموجهة العملية (وفيها يكون التنفيذ غير قابل للتنبؤ وعلى المنظمات ان تحصل على الخبرة خلال عملية التعليم). (PECDAR,2000,p.190)

وقد أظهرت التجربة العالمية ان (90%) من المشاكل في هذا النوع من المشاريع، مرتبطة بمسائل تنظيمية في حين أن (10%) منها مرتبط بمسائل تقنية ، وهذا يشير الى انه يجب ابقاء التركيز على المسائل التنظيمية، لذا لابد من اختيار طريقة التخطيط بحيث يكون المشروع مرنا وقابلا للتعديل للخبرة العملية التي يتم الحصول عليها خلال فترة المشروع والتي يرافقها استعداداً وقدرةً على حل المسائل التنظيمية. (PALGRIC,2000,p.92) من خلال اعتماد الاتي:-

أ) البنية التحتية القومية للمعطيات الجغرافية:

يجب ان يتضمن تطوير بنية تحتية قومية للمعطيات الجغرافية على كل المستويات التنظيمية شاملة المستوى القومي والمستوى البلدي والقطاع الاكاديمي والقطاع الخاص والمنظمات غير الحكومية(NGO)، ويجب تحديد مسؤولية المؤسسات المختلفة (PALGRIC,2000,p.93) (جدول - 1).

(جدول - 1) أدوار التوزيعات في البنية التحتية القومية المستقبلية للمعلومات الجغرافية (PALGRIC,2000,p.95)

المؤسسة	المسؤوليات	الارتباط التنظيمي
MAG	- ادارة سياسات الخرائط العامة / المعطيات الجغرافية. - ادارة وتنسيق البنية التحتية للمعطيات القومية. - تطوير المعايير القومية للمعطيات الجغرافية. - تطوير وصيانة الشبكة الجيوديسية القومية. - جمع المعطيات الاساسية (التصوير المساحي الضوئي والاستشعارعن بعد ..الخ) في كل مساحات مقياس الخرائط. - ادارة قاعدة المعلومات (وضع الخرائط وGIS) -خدمات الزبائن – توزع مجموعات المعطيات الاساسية.	مكتب رئيس الجمهورية
قسم (إدارة) المساحة	- جمع المعطيات المساحية. - ادارة المعلومات المساحية. - خدمات الزبائن – توزيع المعطيات المساحية.	وزارة الاسكان
الوحدة الفنية الخاصة	- جمع معطيات التخطيط والمعطيات ذات الصلة. - انتاج معلومات التخطيط وادارتها. - خدمات الزبائن – توزيع معطيات التخطيط.	وزارة التخطيط
قسم معلومات النقل GLGRIC	- جمع معطيات النقل والمواصلات (transport). - انتاج معلومات النقل والمواصلات وادارتها. - خدمات الزبائن – توزيع المعطيات الاحصائية.	وزارة النقل والمواصلات
مكتب الاحصاء	- جمع المعطيات الاحصائية وادارتها. - انتاج المعلومات الاحصائية. - خدمات الزبائن – توزيع المعطيات الاحصائية.	مكتب رئيس الجمهورية
البلديات	- جمع معطيات تسهيلات الامداد بالماء والمجاري وادارتها. - انتاج معلومات تسهيلات الامداد بالماء والمجاري وادارتها. - خدمات الزبائن - توزيع معطيات تسهيلات الامداد بالماء والمجاري.	وزارة البلديات والاشغال
مالكوا مؤسسات النفع العام الاخرى (الكهرباء والاتصالات والغاز)	- جمع معطيات مؤسسات النفع العام. - انتاج معلومات مؤسسات النفع العام وادارتها. - خدمات الزبائن – توزيع معطيات مؤسسات النفع العام.	موؤسسات الكهرباء والاتصالات والغاز
المنظمات غير الحكومية (NGOs)	- جمع المعطيات الجغرافية وادارتها. - انتاج المعلومات الجغرافية وادارتها. - خدمات الزبائن – توزيع المعطيات الجغرافية.	القطاع الخاص

ب) التطوير القادر على البقاء (المستدام sustainable):

ان التطوير القابل للبقاء لسلطة وضع الخرائط الحكومية MAG والمؤسسات الأخرى سيعتمد على الوصول الى القابلية والجدارة المحلية، المترافقة مع الموارد البشرية العالمية ذات العدد والكفاءة الجيدة وبكل انواع المهن المختلفة التي يجب تغطيتها , وقد أظهرت التجربة العالمية ان التدريب المترافق مع الانتاج الحقيقي هو طريقة كفوءة لبناء هذه القابلية للبقاء، وتؤكد هذه الطريقة على بقاء التركيز على المستخدمين والتقدم المرتبط بالمواعيد و (السقف الزمني)، لذا لابد من استخدام هذه الطريقة كأحد العناصر لبناء سلطة وضع الخرائط الحكومية MAG والمؤسسات الاخرى المسؤولة عن المعطيات الجغرافية، فبناء المؤسسات هو النشاط الموجه للعمليات، بأخطائها وتصحيحاتها، لتكون السلطة العليا قابلة لتنفيذ وادارة المشروع وصنع القرار لاجل تنفيذ البرامج طبقا للتصميم المعد والمأمول , مترافقا ومتزامنا مع عملية الاشراف المحترف الذي يجب ان ينفذه فريق الاستشاريين الدوليين الذين يجب ان يكون عددهم محدوداً ضمن برنامج التخطيط. (PECDAR,2000,p. 431).

- برنامج التنفيذ:

حتى لو كان تنفيذ MAG والبنى التحتية المحيطة من حيث المبدأ منقسماً الى 3 مراحل ، فلن يكون هناك فصلاً جلياً بين المراحل المختلفة ، اذ ستبدأ بعض الانشطة في مرحلة وتنتهي في أخرى . لذا يجب وضع تصميم المشروع المفضل بتنسيق وثيق بين المانحين الفعليين والسلطات المحلية وبالاعتماد على التجارب العالمية. ولإظهار مستوى موارد الملاك والاستثمار المطلوب فسيقدم البحث الحالي مسودة مقترح للمراحل الثلاثة المختلفة، مع اعتبار الاستثمار المطلوب والموارد البشرية التقريبية التي يجب معاملتها كمؤشرات وليست كأرقام نهائية، وذلك للوصول الى تطوير البنية التحتية القابلة للبقاء والفعالة التي تستوجب دعم MAG والمؤسسات المشمولة بموارد الملاك والمعدات والبرامجيات وتخصيص الموارد لكل مؤسسة مذكورة مع اعتبار هذا التخصيص كمؤشرات لبناء مؤسسة (GIS) المطلوبة . (PALGRIC,2000,p. 66).

أولا - المرحلة الأولى "البرنامج قصير الامد" :

(1) الجدول الزمني: السنة الاولى والثانية (فترة امدها سنتان).

من المفترض تزويد سلطة وضع الخرائط الحكومية MAG والمؤسسات الاخرى بالعاملين ليتم البدء بالعمل في السنة الاولى من فترة التنفيذ ولكن بعد فترة تحضير امدها (4- 6 اشهر)، والملاك يجب ان يكون النقطة الرئيسة لذا لابد من تجنيده من المؤسسات الحكومية الموجودة ، وهذا يعني ان مؤسسة MAG الاساسية لن تضيف كلفة ملاك جديد بالنسبة للمجتمع، مع الافتراض مقدماً بتخفيض مشابه لنسبة (الشخص / السنة) في المؤسسات .(PALGRIC,2000,p. 67).

اما موارد الملاك في القطاع الخاص فتكون متضمنة في القوائم (جدول – 2) و (جدول - 3) للاشارة الى المستوى المطلوب، التي كلفتها ستغطيها الخدمات التي تشتريها (MAG) والتي تكون حينئذ متضمنة في ارقام الاستثمار لسلطة وضع الخرائط الحكومية MAG . ومن الضروري وعند المرحلة الاولى من برنامج التنفيذ البدء بتطوير قاعدة المعلومات ولكن ليس قبل تصميم قاعدة المعلومات المباشرة، ليكون التصميم مستنداً الى متطلبات المستخدمين الحقيقية (PALGRIC,2000,p. 66).

ثانيا - المرحلة الثانية "البرنامج متوسط الامد" :

- **الجدول الزمني: السنة الثالثة الى الخامسة (فترة امدها 3 سنوات).**

من المفترض أن تكون سلطة وضع الخرائط الحكومية MAG في حالة تشغيل كامل في بداية هذه المرحلة ، وستهيمن أنشطة الإنتاج عليها في MAG والمؤسسات الفعلية الأخرى ، ويفترض (كاشتراط محدد لدقة الخرائط كما وضعت عالمياً) من المخطط ان يكون تأسيس قواعد المعلومات في مساحة مقياس خريطة (1000:1) و (10000:1) كأحد الأنشطة الرئيسية لـ MAG في المرحلة الثانية مادامت كل حالات تأسيس قاعدة المعلومات يجب ان تستند الى احتياجات المستخدمين الحقيقية ، ولكن إنتاج هذه الخرائط يتم تحديده مبكراً كنشاط فعلي وهذا الانتاج ضروري ليس لاغراض التخطيط وحسب , بل كذلك لوضع الخرائط المعدة

لاغراض متعددة ، ولتقديم المعلومات المساحية ولتوثيق الوضع الفعلي الميداني فيما يخص الموافقات على البناء وما شابه. (PALGRIC,2000,p. 91).

(جدول – 2) الأنشطة والموارد الرئيسية المطلوبة لتنفيذ المرحلة الاولى للعراق الباحث عن (PALGRIC,2000,P.91), (MOPIC, 2000, P.134)

	النشـاط الحكومـي	موارد الملاك لكل مرحلة (شخص-سنة)	الملاحظات
1	القبول بانشاء مؤسسة لـMAG (سلطة حكومية لوضع الخرائط) وتنظيم تنفيذ العملية	2	ملاك عراقي متنوع الاختصاصات
2	توضيح المسؤوليات للمؤسسات المختلفة بخصوص ادارة المعطيات الجغرافية	4	ملاك عراقي متنوع الاختصاصات
3	تطوير مجموعة تمويلية لاجل انشاء الـMAG والبنى التحتية المحيطة بها	2	ملاك عراقي متنوع الاختصاصات
	انشاء الـMAG – مجلس ادارة موجه – تجنيد ملاك	2	ملاك عراقي متنوع الاختصاصات
4	– توصيف الوظائف – تطوير روتين الادارة – تدبير المعدات المكتبية و تجهيزاتها – تدبير معدات الانتاج	 2 1 1	ملاك الـMAG ملاك الـMAG ملاك الـMAG
5	ادارة متنوعة الاختصاصات للـMAG	5	ملاك الـMAG
6	تطوير برامج التعليم – دورات موجهة للانتاج القصير – برامج اكاديمية طويلة الامد	2	ملاك الـMAG
7	تقوية القطاع الاكاديمي – تجنيد الملاك الجامعي و تدبير المعدات المكتبية...الخ	5	
8	انجاز برامج التعليم الاولي – دورات موجهة للانتاج القصير – برامج اكاديمية طويلة المدى	(25-20) (15-10) (3)	ملاك الـMAG والملاك العراقي المتنوع
9	تحديد متطلبات المستخدمين المتعلقة بالمعلومات الجغرافية	5	ملاك الـMAG
10	وصف مفصل للانشطة الموجهة للانتاج – الشبكة الجيوديسية – التقييس – انتاج الخرائط الاساسية – جمع المعطيات و تطوير قاعدة المعلومات – وضع الخرائط المعدة لاغراض متعددة	1	ملاك الـMAG والمستشارون
11	تحديث الشبكة الجيوديسية وشبكة الشاخص الدقيق	4	ملاك الـMAG والمستشارون والقطاع الخاص
12	تطوير المعايير القومية للمعلومات الجغرافية	6	ملاك الـMAG والمستشارون
13	تصميم قاعدة معلومات قواعد معلومات بمقياس مساحة 1:50000	1	ملاك الـMAG والمستشارون
14	جمع المعطيات وتطوير قواعد المعلومات القومية بمقياس مساحة 1:50000	9	ملاك الـMAG والمستشارون والقطاع الخاص
15	خدمة الزبائن عند الـMAG	3	ملاك الـMAG
16	تطوير اضافي لخدمات سجل الاراضي الممسوحة	2	ملاك قسم المسح
17	ادارة اجمالية لمرحلة التنفيذ	1	ملاك عراقي

			ومستشارون
18	دعم اجمالي لمرحلة التنفيذ	1	ملاك عراقي ومستشارون
19	انشطة غير معينة وعناصر التكاليف	3	ملاكات لـMAG وملاك عراقي ومستشارون اخرون
	المجـــموع	88	

(جدول – 3) الانشطة والموارد الرئيسة المطلوبة لتنفيذ المرحلة الثانية
الباحث عن (PALGRIC,2000, MOPIC,2000)

	النشـــاط	موارد الملاك التقديرية في المرحلة (شخص-سنة)	الملاحظات
1	ادارة لـMAG	20	ملاك الـMAG
2	خدمة الزبائن في الـMAG	14	ملاك الـMAG
3	صيانة الشبكة الجيوديسية في الـMAG	8	ملاك الـMAG
4	تقوية القطاع الاكاديمي المتواصل من البرنامج قصير المدى	12	الملاك الجامعي
5	انجاز برامج التعليم- المتواصل من البرنامج قصير الامد – دورات موجهة للانتاج القصير – برامج اكاديمية طويلة الامد – التعليم الدولي	(40-30) (25-20) (3)	
6	تطوير المعايير القومية للمعلومات الجغرافية/ الخدمة الفنية في الـMAG- المتواصل من البرنامج قصير الامد	19	ملاك الـMAG
7	جمع المعطيات/تطوير قواعد معلومات قومية بمقياس مساحة 1:50000 –المتواصل من البرنامج قصير الامد	2	ملاك الـMAG والقطاع الخاص
8	تحديث قواعد المعلومات بمقياس مساحة 1:50000	6	ملاك الـMAG
9	تصميم قاعدة المعلومات - قواعد معلومات بمقياس مساحة 1:10000	1 1	ملاك الـMAG والمستشارون
10	جمع المعطيات/وضع الخرائط وتطوير قواعد المعلومات بمقياس مساحة 1:10000	12	ملاك الـMAG والقطاع الخاص
11	جمع المعطيات/وضع الخرائط وتطوير قواعد المعلومات بمقياس مساحة 1:1000	12	ملاك الـMAG والقطاع الخاص
12	تصميم قاعدة المعلومات (وضع الخرائط المعد لاغراض متعددة)	2	ملاك الـMAG والقطاع البلدي والمستشارون
13	تقوية القطاع البلدي في مجال المعطيات الجغرافية – معطيات معدة لاغراض متعددة – معطيات تخطيط مادي – معطيات مساحية – معطيات خرائط اساسية	2	ملاك الـMAG والمستشارون
14	تطوير الروتين لوضع الخرائط المعدة لاغراض متعددة والمياه والمجاري	1	القطاع البلدي والمستشارون
15	جمع المعطيات المعدة لاغراض متعددة وتطوير قواعد المعلومات المعدة لاغراض متعددة والمياه والمجاري	10	القطاع البلدي والقطاع الخاص

16	الادارة الاجمالية لمرحلة التنفيذ-المتواصل من البرنامج قصير الامد	2	الملاك والمستشارون العراقيون
17	الادارة الاجمالية لمرحلة التنفيذ-المتواصل من البرنامج قصير الامد	2	الملاك والمستشارون العراقيون
18	الانشطة الاخرى غير المحددة وما يلحقها موقعيا من عناصر التكاليف	8	ملاك الـMAG والملاك والمستشارون العراقيون الاخرون
	المجـــموع	187	

ثالثاً - المرحلة الثالثة "البرنامج طويل الامد":

- **(1) الجدول الزمني : من السنة السادسة الى التاسعة (مرحلة امدها 4 سنوات).**

من المفترض ان البنية التحتية الجغرافية القومية في البرنامج طويل الامد، ستتحول الى بنية تنظيمية مستقلة، وستصل MAG مستواها المخطط له للتزويد بالعاملين ، وستكون هذه مرحلة حاسمة وقاطعة بالنسبة لقابلية بقاء المنظمات المختلفة المعينة . وستهيمن على المرحلة ادارة المعطيات وتوزيعها، ومادامت هذه المرحلة تستمر 4 سنوات قدماً ، لذا من غير المناسب وضع خطة مفصلة للمرحلة , والانشطة المدرجة في (جدول – 4) عامة نسبياً . (PALGRIC,2000,p.206).

(جدول - 4) الأنشطة والموارد الرئيسية المطلوبة لتنفيذ المرحلة الثالثة الباحث عن (PALGRIC,2000, MOPIC,2000)

	النشـــاط	موارد الملاك التقديرية في المرحلة (شخص-سنة)	الملاحظات
1	ادارة وعملية الـMAG	32	ملاك الـMAG
2	خدمة الزبائن في الـMAG	24	ملاك الـMAG
3	صيانة الشبكة الجيوديسية في الـMAG	12	ملاك الـMAG
4	انجاز برامج التعليم-المتواصل من البرنامج متوسط الامد – دورات موجهة للانتاج القصير – برامج اكاديمية طويلة الامد – التعليم الدولي	(20- 40) (20- 30) (3)	
5	تطوير المعايير القومية للمعلومات الجغرافية/ الخدمة الفنية في الـMAG- المتواصل من البرنامج متوسط الامد	28	ملاك الـMAG
6	– جمع قاعدة المعلومات والتصوير المساحي الضوئي والاستشعار عن بعد- المتواصل من البرنامج متوسط الامد	32	MAG
7	ادارة قاعدة المعلومات ووضع الخرائط و GIS-- المتواصل من البرنامج متوسط الامد	64	MAG
8	تقوية القطاع البلدي - المتواصل من البرنامج متوسط الامد	2	ملاك الـMAG والمستشارون
9	جمع المعطيات وتطوير قواعد المعلومات المعدة لاغراض متعددة والمياه والمجاري- المتواصل من البرنامج متوسط الامد	10	القطاع البلدي والقطاع الخاص

10	تحديث عملية قواعد المعلومات المعدة لاغراض متعددة والمياه والمجاري	6	القطاع البلدي
11	الادارة الاجمالية لمرحلة التنفيذ-المتواصل من البرنامج متوسط الامد	2	الملاك والمستشارون العراقيون
12	الدعم الاجمالي لمرحلة التنفيذ- المتواصل من البرنامج متوسط الامد	2	الملاك والمستشارون العراقيون
13	الانشطة الاخرى غير المحددة وما يلحقها موقعيا من عناصر التكاليف	12	الملاك العراقي

- ولوضع برنامج التنفيذ الذي امده (10 سنوات) فيجب ان يتم احتساب اجمالي ما يقارب (400 شخص - سنة) والاستثمار احتساباً دقيقاً ، ويجب تخصيص الاجزاء الكبرى من الموارد والاستثمارات الى MAG مع ضمان بنية تحتية قابلة للبقاء ومن ثم لخدمة المجتمع بطريقة صحيحة داعماً كل المؤسسات الاخرى ، حيث ينبغي احتسابها بدقة، مع تحديد كل المصطلحات والتفاصيل . (جدول – 5). (PALGRIC,2000,p.208).

(جدول - 5) نظام برنامج التنفيذ الذي امده 10 سنوات
الباحث عن (PALGRIC,2000,p.209)

المؤسسة	المرحلة الأولى "قصيرة الأمد"		المرحلة الثانية "متوسط الامد"		المرحلة الثالثة "طويل الأمد"		برنامج التنفيذ الإجمالي	
	الموارد البشرية (شخص-سنة)	الاستثمار بملايين الدولار	الموارد البشرية (شخص-سنة)	الاستثمار بملايين الدولار	الموارد البشرية (شخص-سنة)	الاستثمار بملايين الدولار	الموارد البشرية (شخص-سنة)	الموارد البشرية (شخص-سنة)
MAG	32		100		132		184	316
الجامعات	5		12		18		16	33
المعاهد	3		6		9		8	17
القطاع الخاص	4		10		18		16	30
الاستشاريون	4		5		7		1	10
المجموع	48		133		183		225	406

- الاستنتاجات:-

يركز البحث على تثبيت النموذج المفاهيمي لنظام المعلومات الجغرافية GIS ، معتمداً على تثبيت بضعة اعتبارات اساسية لتحديد مجاله وكما يلي:

1- ان عملية تثبيت وتطوير نظام المعلومات الجغرافية (GIS) ، يفترض ان كل خطوة يجب ان يتم اكمالها بالتفاصيل قبل البدء بالخطوة الاتية، شاملاً بذلك تحليل كل المتطلبات لاعطاء معطيات حقيقية وتصميم مفصل شامل يمكن من وضع خارطة الاساس قبل استخدام التطبيقات.
2- يمكن لنظام المعلومات الجغرافية GIS المطبق بصورة تفصيلية حقيقية شاملة ، ان يعطي الخطط البديلة للتطوير المستقبلي مع تحديد اولويات احتياجات التخطيط، لدعم التخطيط الحضري والاقليمي وحماية استخدام الارض وادارته مع المحافظة على البيئة ومواردها الطبيعية والطاقوية .
3- يجب الاعداد قبل البدء بخطة تثبيت نظام المعلومات الجغرافية GIS، شاملاً ذلك اعداد الكفاءات البشرية والقيادية من الخبراء والمخططين القادرين على ادارة النظام وتنفيذه مع اعطاء الاهمية

للتجهيزات الحاسوبية والبرامجيات الاساس وما يحيط ذلك من المؤسسات والمنظمات الساندة والتابعة القادرة على مواكبة التكنولوجيا والتقنية الحديثة.

4- لتحقيق نظام المعلومات الجغرافية GIS قادر على الانتاج، يجب انشاء ما يسمى بـ(مجلس التخطيط الاعلى) الذي تنطوي مهمته بالمصادقة على التخطيط الوطني والاقليمي المقدم من وزارة التخطيط، يرتبط ويشرف هذا (المجلس) على اللجان المركزية المنتشرة في المحافظات والتي تعمل تحت طائلته، يضاف لها كل ماهو تابع لها من المخططين الاهليين والمجالس البلدية ومجالس القرى والارياف .

5- لذا وبضوء ما تقدم يوصي البحث بأعتماد ماطرحته من منظومة هيكلية وجدولية كاملة لعموم الهيكل التنظيمي والوظائفي لادارة وتثبيت نظام (GIS) على المدن , وبشكل ماتم طرحه من موظفين وادرايين وفنيين , مما يستلزم القيام بمجموعة من الدراسات تعمل على محورين يتعلق الاول بدراسة متكاملة لمدينة بغداد مع اعادة طرحها وبشكل تصميم متكامل ضمن مفاهيم واليات نظام المعلومات الجغرافية (GIS) , اما المحور الثاني فيقصد العراق بصفة عامة , بغية جعل المحورين اساساً جديداً في الطرح التخطيطي الحديث المعتمد على مجموعة متكاملة ومحدثة من المعلومات التفصيلية عن كل مايخص مدينة بغداد خصوصاً والمدن الاخرى عموماً .

- المصادر العربية :

- عامر ناجي صالح , تأثير نظام المعلومات الجغرافية في التخطيط العمراني في العراق , رسالة ماجستير,جامعة بغداد , كلية الهندسة , قسم الهندسة المعمارية ,2007 .

– المصادر الاجنبية :

- Bernhardsen, Tor, "Geographic Information System" , VIAK IT and Norwegian Mapping Authority, Norway, 1992

- Haugan, Frank, "Reorganizing Management, map use and Geographic System (GIS) ", none published article,london 1998.

- Martin J," Information Engineering ", Introduction Prentice Hall, Englewood Cliffs, N.J., 1990.

- MOPIC, "Regional Plan for West Bank and Ghaza", Physical development Plan Project, Palestine, 2000.

- PALGRIC, "Final Proposed Program about GIS Development Project" , uncompleted Project, Jordan, 2000.

- PECDAR, Geographic Information System Development Project, TR, 1238, Jordan, 2000.

-Van Helden P: "The Development and Management of an integrated Information System for Urban Planning at a Local Authority ", University of Pretoria,USA, 1993.

FINITE ELEMENT ANALYSIS OF EMBANKMENTS ON SOFT CLAYS - CASE STUDIES

Yousif J. al-shakarchi
University of Baghdad
College of Eng., Civil Eng. Dept

Mohammed Yousif Fattah
University of Technology
Building and Construction Eng. Dept

Ahmed S. Jawad Al- Shammary
University of Baghdad
College of Eng., Civil Eng. Dept.

ABSTRACT

In order to design structures on soft soils, it is necessary to predict the behavior of the soft soil under imposed structure load. The high excessive settlements of the soft soil can cause many problems for the structures built on the soil like cracking and breakup of pavements, railway, highway embankments, etc...

In this work, the finite element method is utilized as a tool for carrying out different analyses of embankments on soft ground with different conditions. The computer program CRISP (CRItical State Program) is developed to suit the problem requirements. CRISP uses the finite element technique and allows predictions to be made of soil deformations using the critical state theory.

Eight-node isoparametric quadrilateral element has been added to the program. The program was used to analyze fully coupled (Biot) consolidation of two-dimensional plane strain problems. The finite element predictions of displacements and excess pore water pressures were compared with field measurements.

It was concluded that the maximum vertical movement occurs below the centerline of the embankment. The settlement decreases slightly as the toe of the embankment is approached and decreases rapidly as the distance away from the toe increases. Upward movement of the surface far from the toe is observed. The maximum horizontal movement occurs near the top boundary. The rate of horizontal movement at the top of the foundation is greater than at the bottom. This behavior may be due to the flexibility and free movement condition of the vertical boundary in the top half

التحليل بالعناصر المحددة للتعليات الترابيية على تربة طينية رخوة – دراسات حالة

الخلاصة

لغرض تصميم المنشات التي تستند على ترب رخوة, من الضروري التنبوء بسلوك هذه الترب تحت تأثير احمال المنشأت. ان الهبوط المفرط العالي للترب الرخوة قد يؤدى الى حدوث مشاكل للمنشات المشيدة عليها مثل التشققات و تكسر طبقات التبليط و خطوط السكك و الطرق السريعة و السداد الترابية (التعليات) و غيرها.

في هذا البحث, استعملت طريقة العناصر المحددة كطريقة لاجراء عدد من التحليلات لسداد ترابية (تعليات) مشيدة على ترب رخوة و لحالات مختلفة. و قد طور برنامج الحاسبة المسمى (CRISP) ليناسب متطلبات المسالة. ان برنامج (CRISP) يستعمل تقنية العناصر المحددة و يسمح باجراء تخمين للتشوهات التي تحدث في التربة اعتمادا على نظرية الحالة الحرجة. و قد اضيف عنصر ثماني العقد رباعي الشكل إلى البرنامج. و استعمل البرنامج لتحليل مزدوج للانضمام حسب نظرية بيوت لمسائل ثنائية الابعاد ذات انفعال مستوي و قد قورنت نتائج طريقة العناصر المحددة للازاحات و ضغط ماء المسام الاضافي مع القياسات الحقلية .

لقد وجد أن الإزاحة الشاقولية العظمى تحدث تحت الخط المركزي للسداد (التعلية) و تتناقص هذه الازاحة كلما تم الاقتراب من حافة السدة ثم تتناقص بشكل سريع عند الابتعاد عن حافة السدة و قد لوحظ حدوث ازاحات شاقولية للأعلى لسطح التربة الواقع بعيداً عن جسم السدة (التعلية).

كما تحدث الازاحة الافقية العظمى بالقرب من الحدود العليا لطبقة تربة الاساس. ان معدل الازاحة الافقية في النصف العلوي من الاساس يكون اعلى من قيمته في النصف السفلي. ان هذا التصرف يمكن ان يعزى الى مرونة الحركة و الشرط الحدودي الحر للسطح العلوي من الاساس.

KEY WORDS
Finite Elements, Embankment, Soft soil, Cam Clay, Consolidation analysis.

INTRODUCTION

The increase in the world population and the consequent demand on new areas for construction forced the civil engineer to construct on large lands that have been avoided in the past because of their inadequacy as foundation ground. This means that land which was formerly considered unsuitable has now been utilized by building over. However, before this can be done, the problems which made the land unsuitable in the first instance have to be overcome by the engineer either by special design or ground improvement.

In order to design structures on soft soils, it is necessary to predict the behavior of the soft ground under impose of structure load. The high excessive settlements of the soft soil can cause many problems for the structures built on the soft soils like cracking and breakup of pavements, railway, highway embankments, etc...

The engineering properties of the soft clay may be improved to make the soil suitable for construction; several techniques have been suggested to improve the engineering properties of the soft soil.

PROBLEMS IN PREDICTING SETTLEMENT OF EMBANKMENTS ON SOFT CLAY

The major uncertainties in predicting settlement of embankments on soft clays are list:

1. Uncertain stratigraphy and drainage boundaries.

2. Uncertain time history of loading.
3. Mass movements due to shearing stresses.
4. Economical problems that restrict exploration, testing, and other analyses.

Other problems that clearly influence the accuracy of predicting include (Olson and Fellow, 1998):

1. Effects of secondary compression. Field data documenting long-term behavior are required. Many field observations terminate when a structure (pavement, bridge, tank, etc...) is constructed, because the instrumentation is destroyed. The client is not interested in paying for continued readings, and the engineer does not wish to risk for being used based on the documented movements.
2. Sampling disturbance compared with disturbance introduced in the field such as during wick installation.

Use over simplified and analytical procedure, or performing the design based on "Engineering Judgment" with minimal exploration and testing, is an effort to underbid the complication.

THE COMPUTER PROGRAM CRISP

CRISP (CRItical State Program) was developed at Cambridge University, Engineering Department, Soil Mechanics Group, in 1975. Later after making necessary modifications on (CRISP), it was republished in 1987.

CRISP uses the finite element technique and allows predictions to be made on ground deformation using critical state theories.

CRISP is used in this work for the analysis of embankment problems after making necessary developments. These developments include the following (Al-Shammary, 2006):

1. Eight-node isoparametric quadrilateral element is added with all necessary modifications in corresponding matrices.
2. Some subroutines are rearranged and organized.

Summary of Facilities:

Solution techniques:

There is a number of techniques for analysis of non–linear problems using the finite elements. CRISP uses the incremental or tangent stiffness approach. The user divides the total load acting into a number of small increments and the program applies each of these incremental loads in turn. During each increment, the stiffness properties appropriate for the current stress level are used in the calculations.

Excavation, Construction and Increment Blocks:

A finite element program intended for geotechnical analysis should be capable of analyzing problems where soil is excavated or soil structures (e.g. embankments) are constructed. This is not a standard feature found in finite element programs in other branches of engineering. CRISP allows elements to be removed to simulate excavation and elements to be added to simulate construction. The applied loadings for these cases are automatically calculated by the program.

When performing a non-linear analysis involving excavation or construction, the requirement for relatively small applied loads in each increment still applies. The way of achieving this is the removal or addition of a large number of layers of "thin" elements due to the large number of elements, and possible numerical conditioning problems associated with elements that have large aspect ratios. CRISP circumvents this problem by allowing the effect of element removal or addition to be spread over several increments in an "increment block" which is a series of ordinary increments grouped together in the input data for the program.

CASE STUDY PROBLEMS

The construction of embankments on soft clays will be simulated by using the eight-node isoparametric elements.

SIGMA Test Embankment Problem

This is one of the basic problems of the computer program GeoSlope. In this problem, the subsurface clay stratum is 9 m deep and the water table is 1 m below the ground surface.

The 1 m-layer above the water table is highly weathered desiccated and fissured making the behavior similar to a fine granular soil.

The embankment to be analyzed is shown in Fig. 1 and is constructed of relatively sandy soil. The height of the embankment is 5 m with 3:1 side slopes and 10 m crest width. Due to symmetry about the center, only half of the cross section is modeled in the analysis. Part of the underlying soil (clay) is considered in the analysis.

The bottom of the problem is fixed, while both vertical ends are allowed to move vertically but not horizontally. The finite element mesh of the embankment and its foundation is shown in Fig.1

Clay Properties

The clay is modeled as a modified Cam –clay (MCC). It is highly plastic with liquid limit (LL) of 61%. The compression index, Cc, can be estimated from the well-known equation (Skempton, 1944):

$$C_c=0.009*(\text{LL-10 percent}) \quad (1)$$

The slope of the normal consolidation line, λ, can be computed from $\lambda = C_C/2.303$ (Atkinson and Bransby, 1978). A summary of the soil properties is provided in Table 1.

Sand Properties

The embankment and the upper one meter of subsoil is modeled as highly permeable. Linear elastic model can be used for this material, which can be considered adequate since the major settlement issue arises in the underlying compressible clay. The properties adopted for sand are also given in Table 1.

Table 1 The properties of foundation and embankment of problem (Manual of the program Geo-Slope).

Type of soil	Model	Parameter	Value
Clay	MCC	Liquid limit (LL)	61%
		Compression index (C_C)	0.46
		Slope of normal consolidation line (λ)	0.2
		Slope of swelling line (κ)	0.04
		Coefficient of volume compressibility (m_v)	$3*10^{-4}$ (1/kPa)
		Hydraulic conductivity (k)	$5*10^{-3}$(m/day)
		Effective friction angle (ϕ)	26°
		Slope of critical state line (M)	1
		Coefficient of earth pressure at rest (K_0)	0.56
		Poisson' s ratio (ν)	0.36
		Over-consolidation ratio (OCR)	1.2
		Unit weight (γ)	20 kN/m^3
Sand	Linear elastic	Modulus of elasticity (E)	2000kPa
		Poisson' s ratio (ν)	0.36
		Hydraulic conductivity (k)	1 m/day
		Coefficient of volume compressibility (m_v)	$3*10^{-4}$ (1/kPa)
		Unit weight (γ)	20 kN/m^3

In Situ-Stresses

An essential feature when using the modified Cam clay (MCC) soil model is to establish the initial yield surface. Any changes due to the embankment loading are relative to the yield surfaces that exist prior to loading. The initial yield surface is related to the initial in-situ stress and over–consolidation ratio (OCR). The (OCR) is specified as a soil property but the in-situ stress must be computed in a separate step.

The total and effective horizontal stress profiles in the sub-soil before starting the embankment fill placement are shown in Fig.2.

Loading sequence

The embankment fill is going to be placed in five stages as follows:

Fill lift	Elapsed time (days)	Height (m)
1st	1	1
2nd	7	2
3rd	13	3
4th	19	4
5th	25	5

Results and Discussion

Comparison of Results

Fig. 3 shows a comparison between the settlements that occur at the centerline at the water table elevation predicted by the CRISP program which is used in this study and those by SIGMA program. It can be seen that the settlement predicted by the two programs is similar during construction of the test embankment. The excess pore water pressure changes with time at a specified location one meter to the right of center line and two meters below the water table (point B in Fig. 1) are compared in Fig. 4 for both programs. The SIGMA program shows lesser excess pore water pressure during construction, while, after construction, the two results tend to be similar.

The pore water pressure starts to dissipate immediately after construction of each fill lift, then its value increases when the next fill is constructed and dissipation continues.

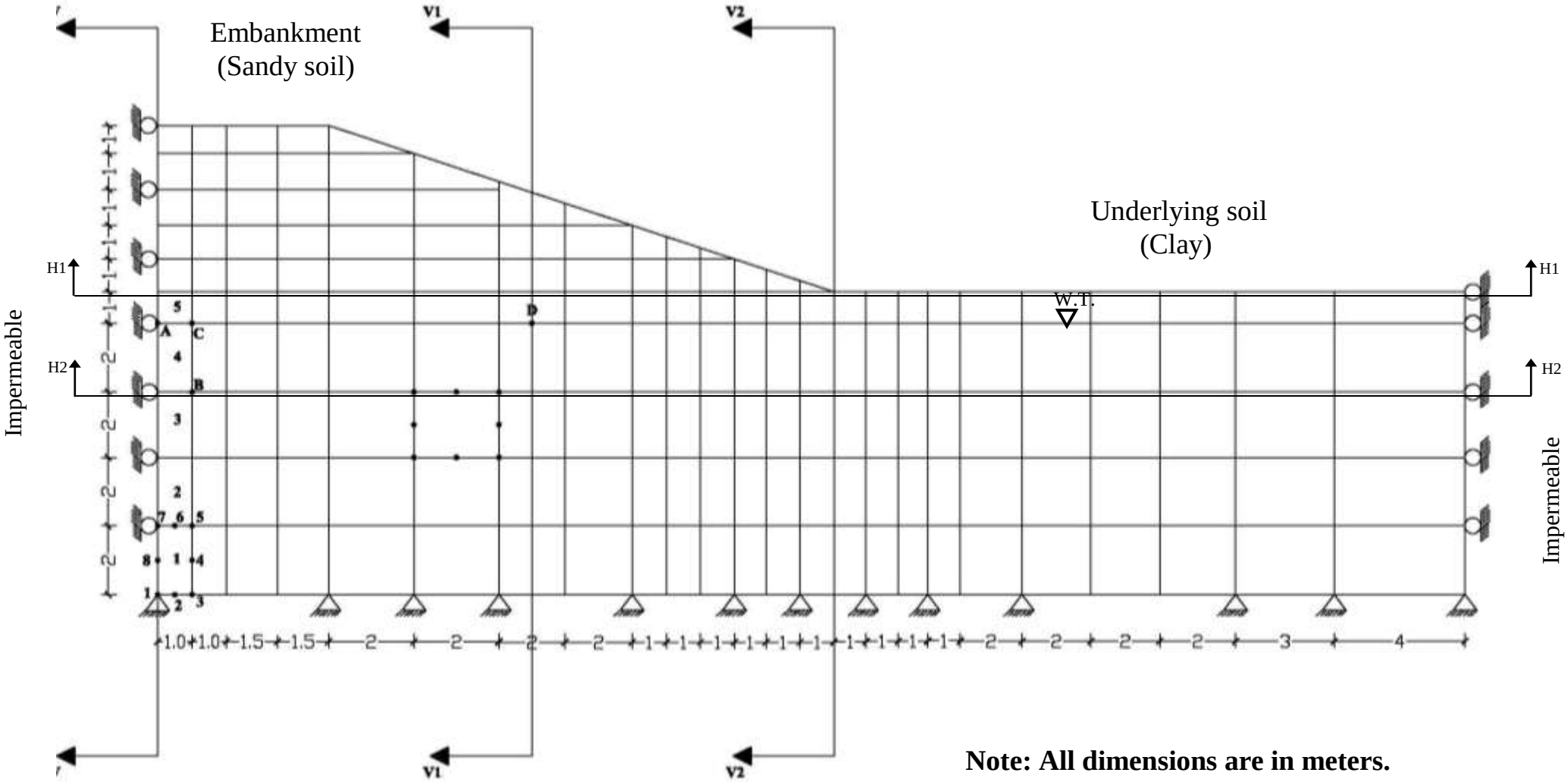

Fig.1 The finite element mesh of SIGMA embankment.

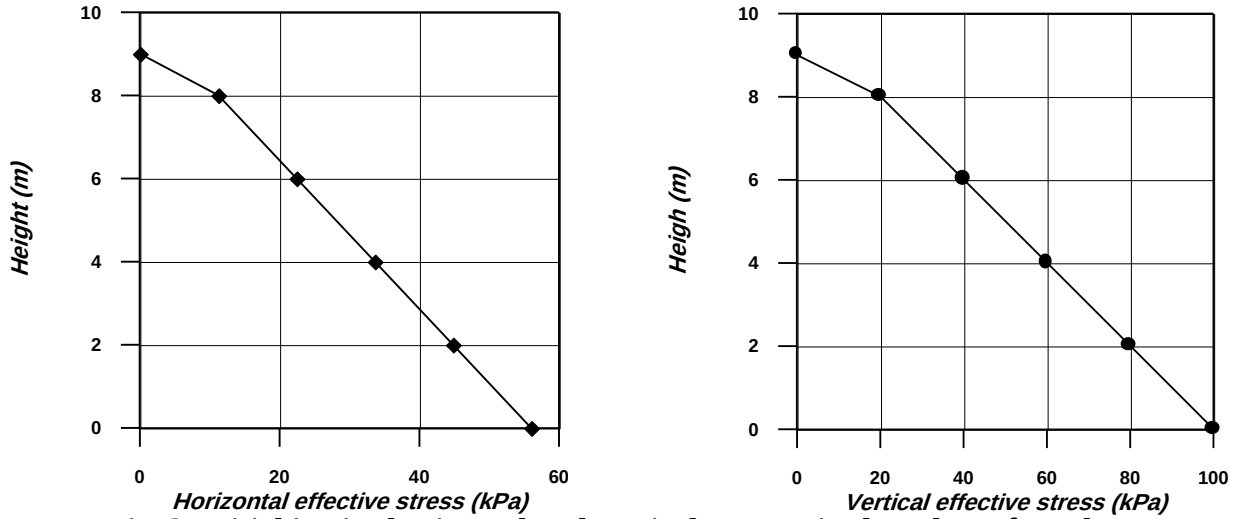

Fig. 2 Initial in-situ horizontal and vertical stresses in the sub-surface clay.

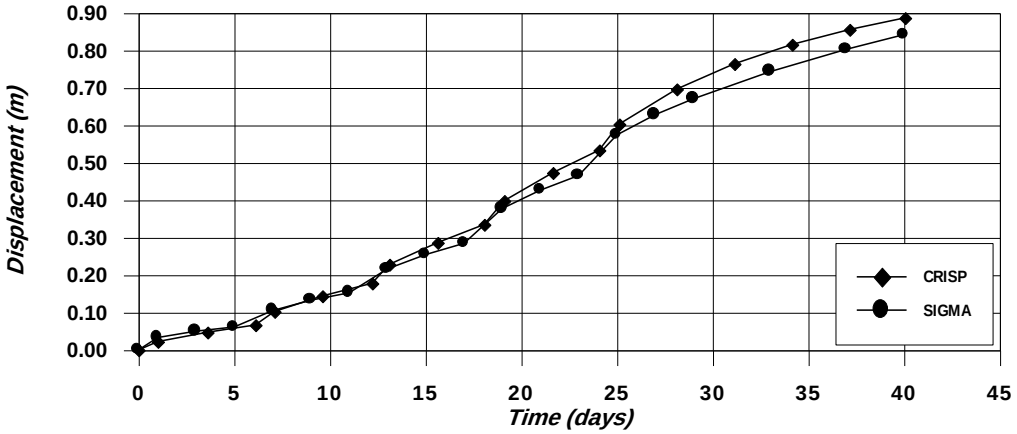

Fig. 3 Vertical displacement at node (A) of SIGMA test embankment.

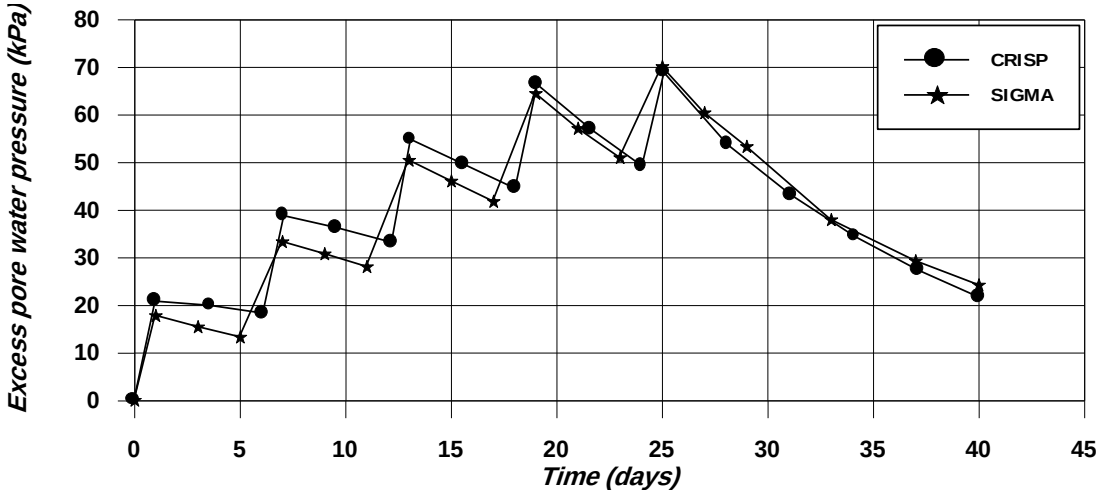

Fig. 4 Excess pore water pressure at node (B) of SIGMA test embankment.

Vertical Displacement

In Figures (5 and 6) the finite element analysis results of the vertical displacements along horizontal sections (H1-H1), (H2-H2) (as shown in Fig. 1) during construction are presented. The maximum

settlement does not occur along the centerline but is located more towards the outer edge of the fill in the early stages of loading. This behavior is due to the zone of lower effective horizontal stresses. In addition, the toe of the fill has been lifted up slightly because the zone near the toe is a high shear stress zone. Upward movement of the surface far from the toe is observed due to the large load applied at the centerline of the foundation. This upheaval decreases slightly towards the toe of the embankment and decreases significantly as the distance away from the toe becomes large.

The vertical settlement along the vertical sections (V1-V1) and (V2-V2) and the centerline are shown in Figures (7, 8 and 9). From all these figures, the maximum vertical displacement was found at elevation 9 m because this level will be exposed to load directly. After construction, the maximum settlement will occur at the centerline as shown in Figs. (10 and 11). This behavior is due to the fact that the zone near the center of embankment suffers from concentration of stresses. In Fig. 9, the maximum settlement is found at elevation 4 m because this region is affected by all strains developed above this level resulted from the loads applied above this level. On completion of the embankment, the staged construction is halted and the load remained constant. In this stage, the consolidation of the soil will occur without any increase in the applied load.

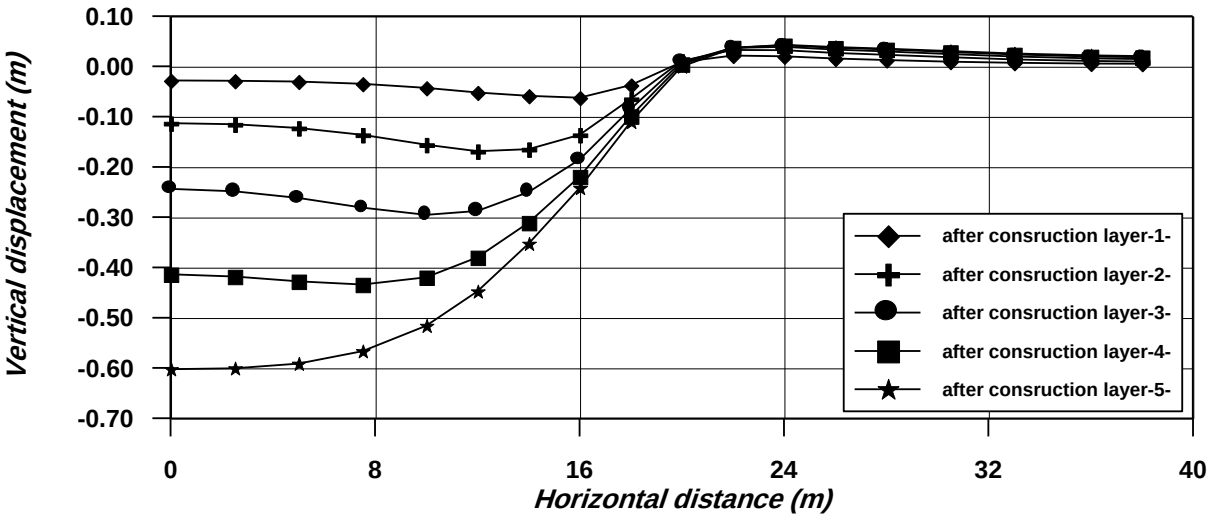

Fig. 5 Vertical displacement along section (H1-H1) during construction of SIGMA test embankment.

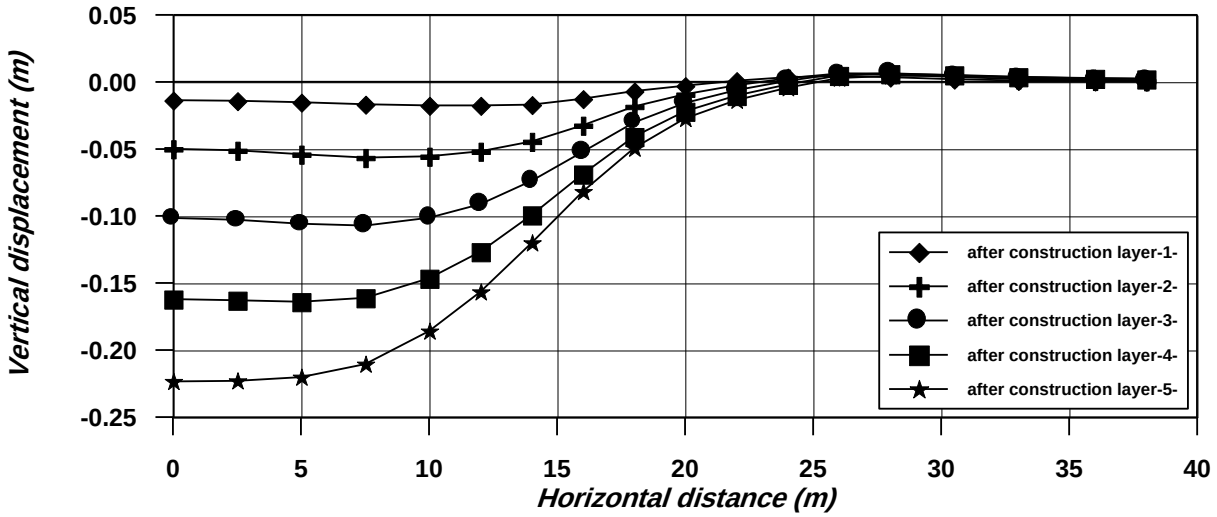

Fig.6 Vertical displacement along section (H2-H2) during construction of SIGMA test embankment.

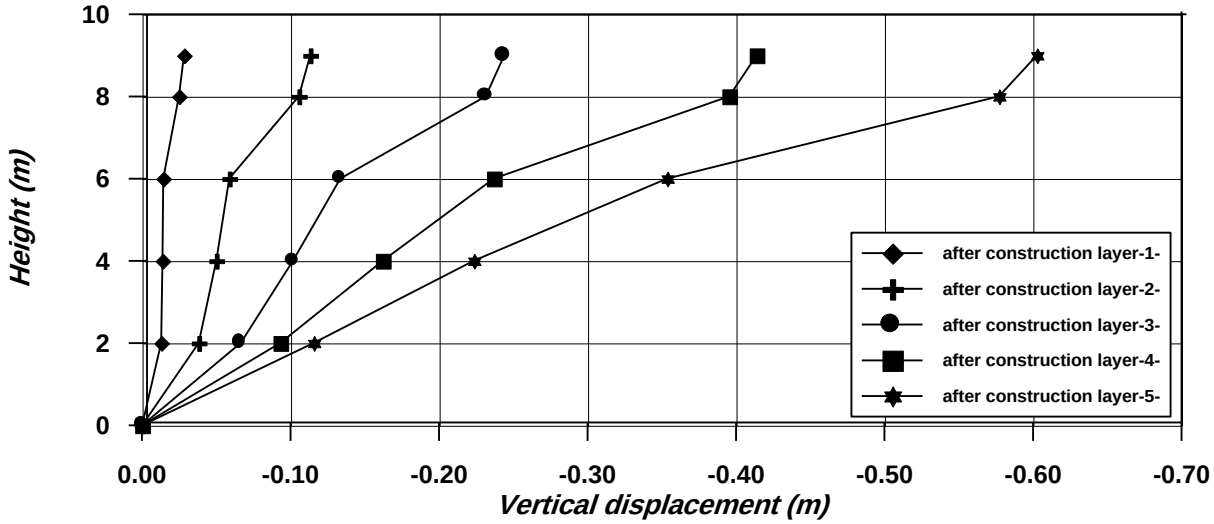

Fig.7 Vertical displacement along the centerline during construction of SIGMA test embankment.

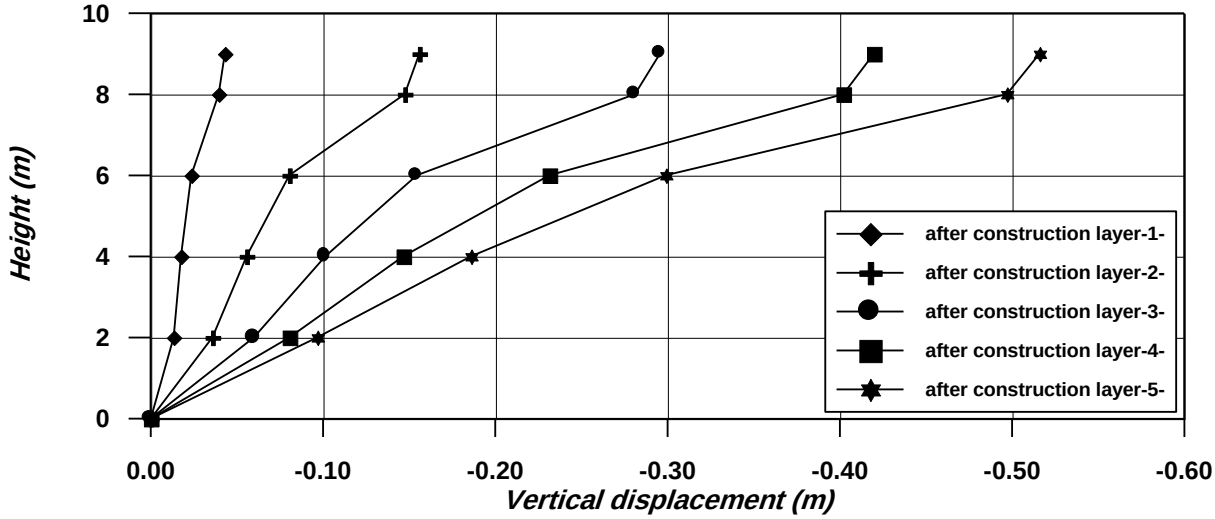

Fig. 8 Vertical displacement along section (V1-V1) during construction of SIGMA test embankment.

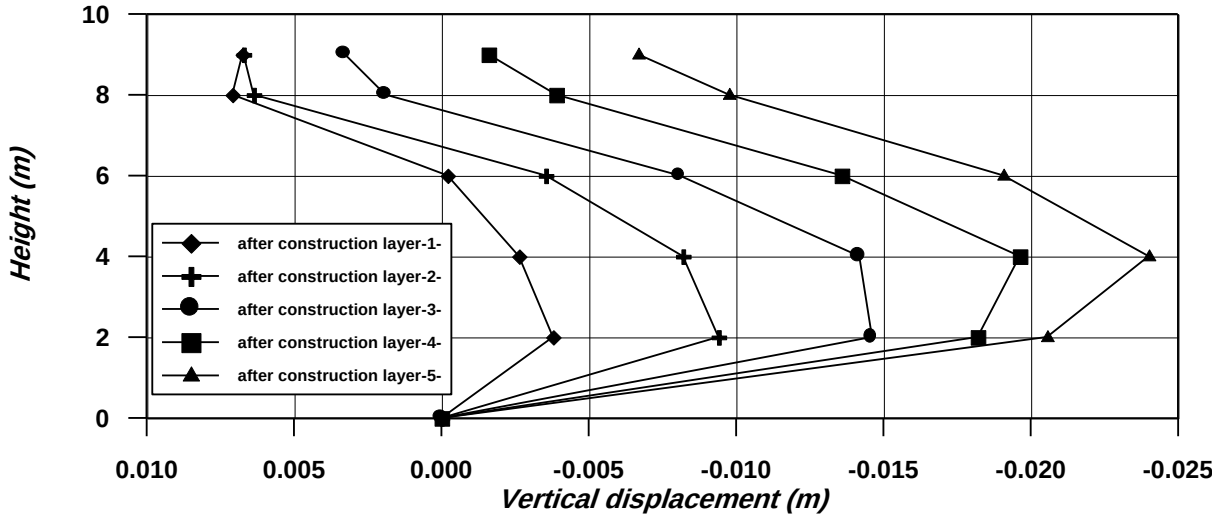

Fig. 9 Vertical displacement along section (V2-V2) during construction of SIGMA test

embankment.

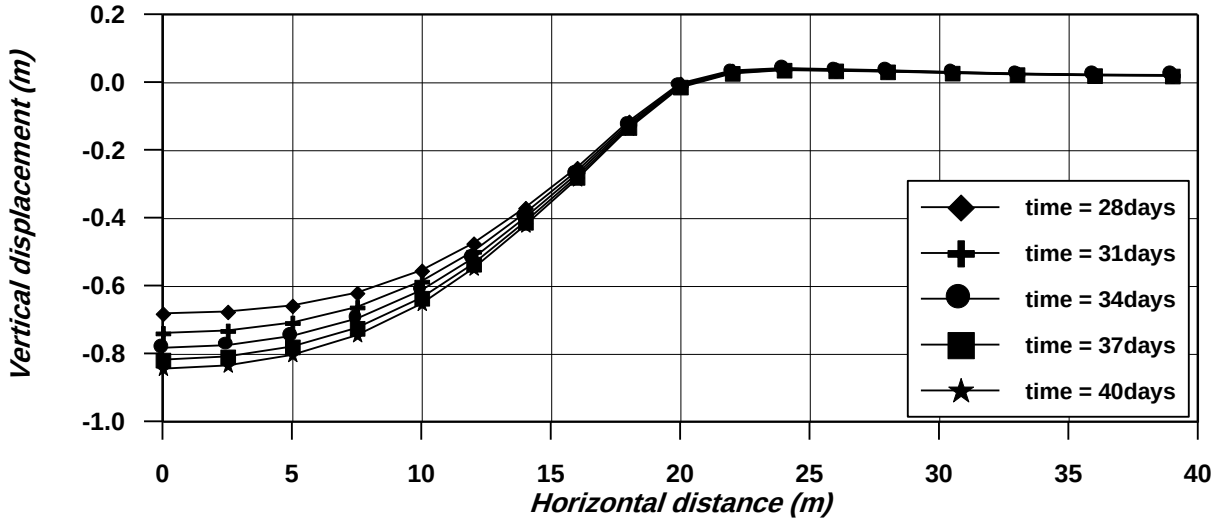

Fig. 10 Vertical displacement along section (H1-H1) after construction of SIGMA test embankment.

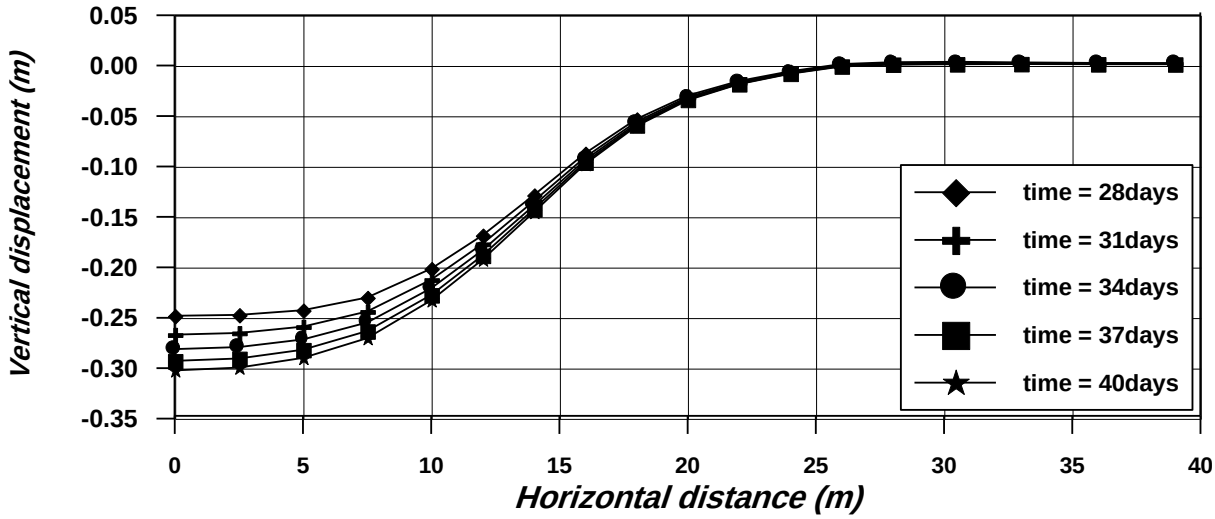

Fig. 11 Vertical displacement along section (H2-H2) after construction of SIGMA test embankment.

Horizontal Displacement

The horizontal movements along two vertical sections, (V1-V1) and (V2-V2) are presented in Figures (12 and 13) during construction. In general, it is seen in these figures that the maximum horizontal displacement occurs near the top boundary. The rate of horizontal movement at the top of the foundation is greater than that at the bottom. This behavior may be due to the flexibility of the top boundary assumed for horizontal movement. It can also be seen that section (V1-V1) near the toe shows the maximum horizontal displacement in comparison with the other section (V2-V2). This behavior is due to the large difference between the vertical load concentration on the left and right hand sides of section (V1-V1).

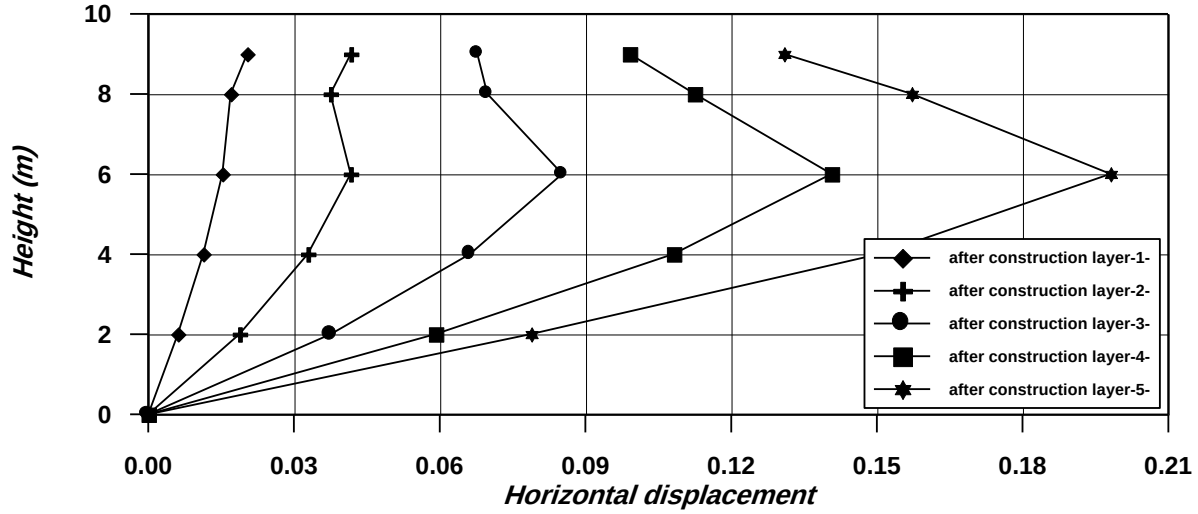

Fig. 12 Horizontal displacement along section (V1-V1) during construction of SIGMA test embankment.

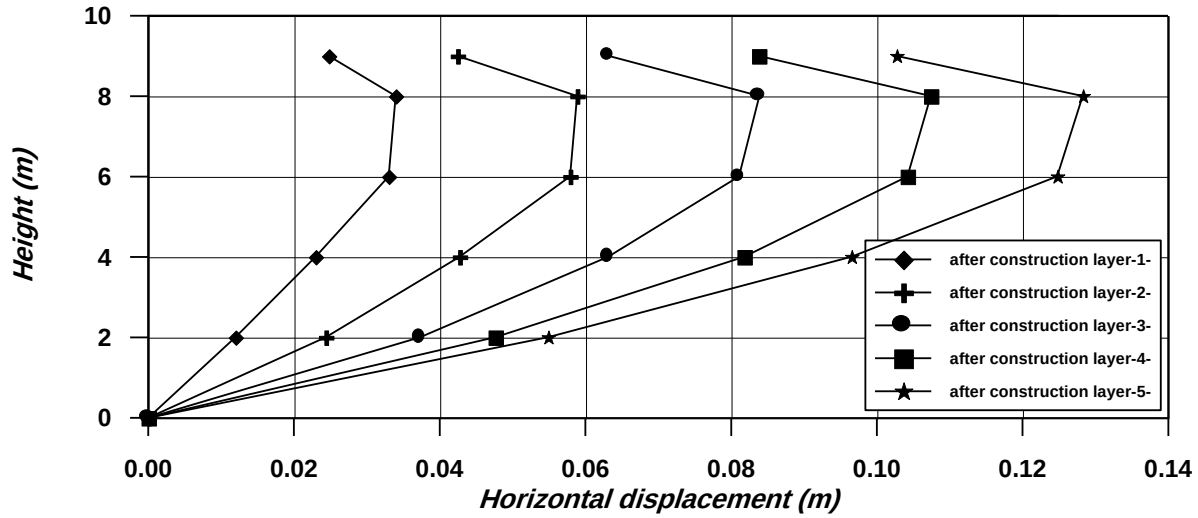

Fig. 13 Horizontal displacement along section (V2-V2) during construction of SIGMA test embankment.

Excess Pore Water Pressure

The excess pore water pressure dissipation along the centerline, sections (V1-V1) and (V2-V2) are shown in Figures (14 to 19). The curves show the isochrones of excess pore water pressure during construction and after construction at times 28, 31, 34, 38 and 40 days. As it is shown, the isochrones of excess pore water pressure give symmetric curves with maximum values near the middle of the foundation soil. This behavior is due to the two–way drainage assumption. The analysis predicts pore water pressure at centerline of the embankment greater than at the other two sections. This behavior is expected and it is due to the concentration of the load at the centerline of the embankment.

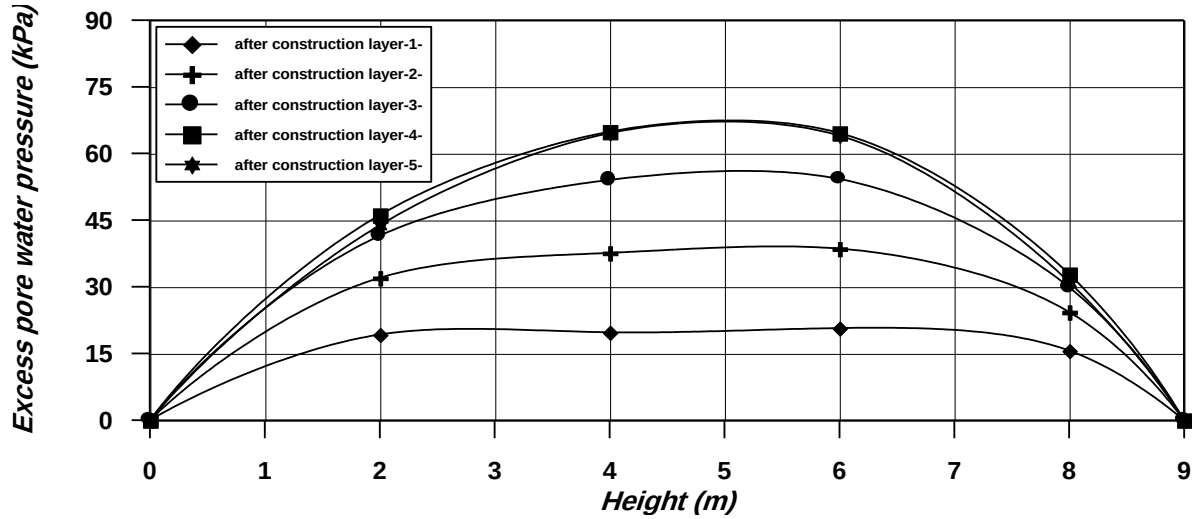

Fig. 14 Excess pore water pressure along the centerline during construction of SIGMA test embankment.

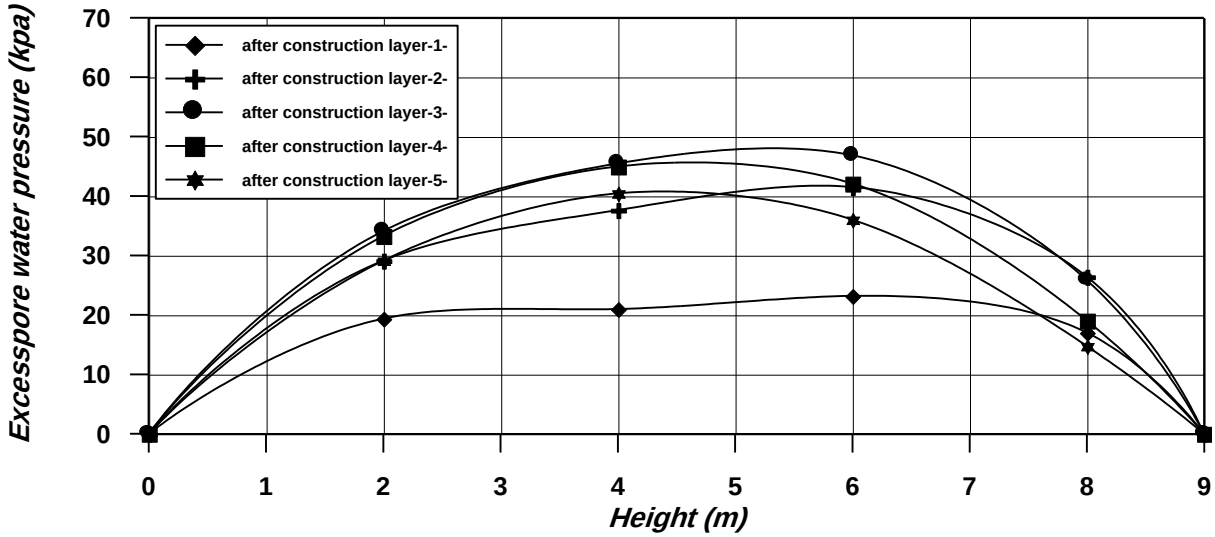

Fig. 15 Excess pore water pressure along section (V1-V1) during construction of SIGMA test embankment.

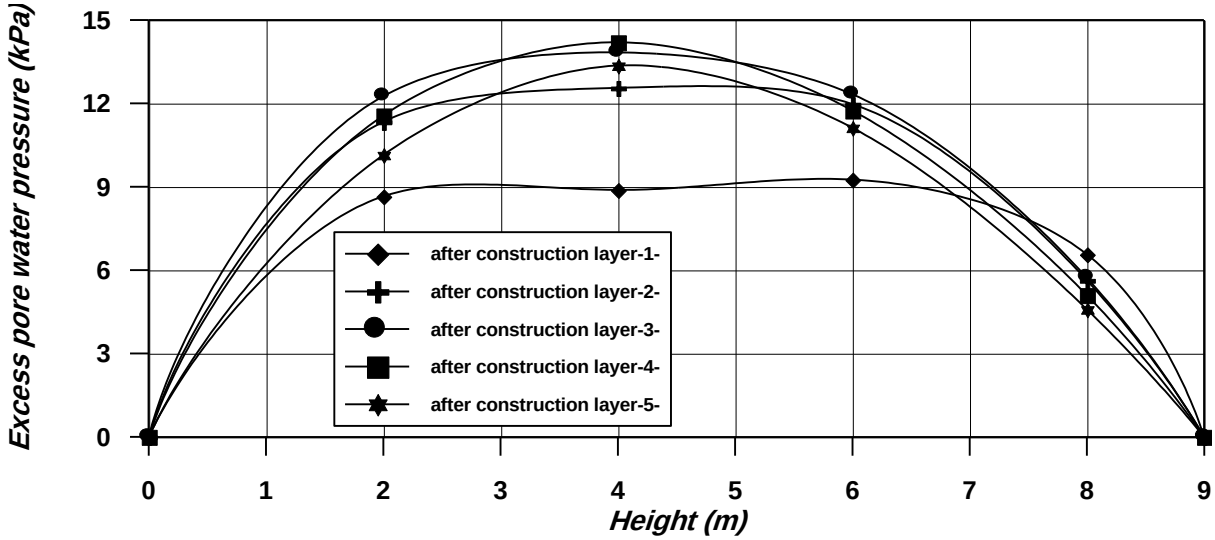

Fig. 16 Excess pore water pressure along section (V2-V2) during construction of SIGMA test embankment.

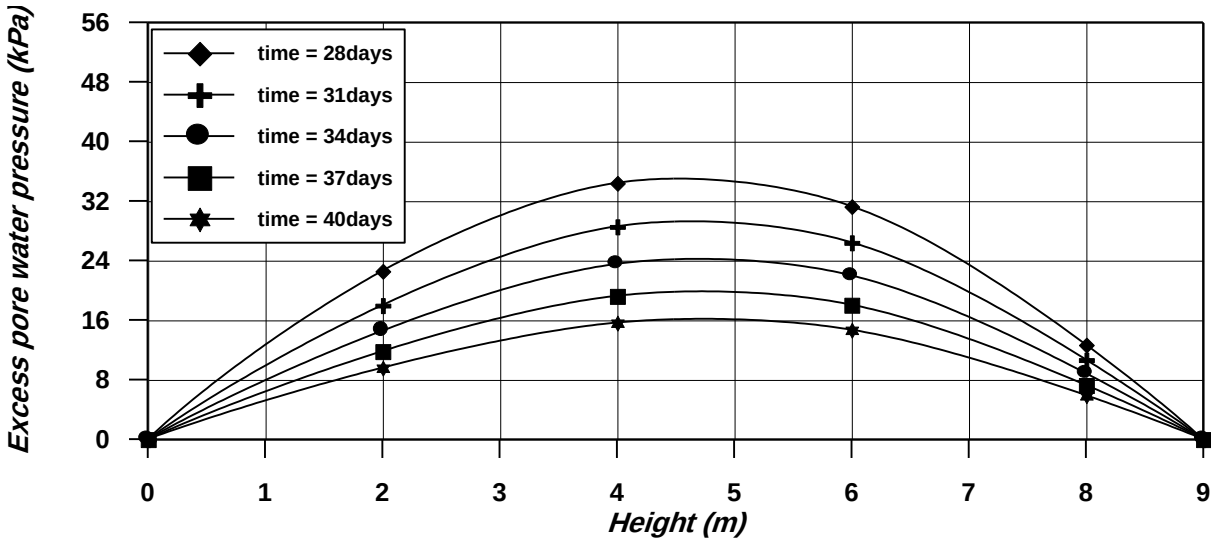

Fig. 17 Excess pore water pressure along section (V1-V1) after construction of SIGMA test embankment.

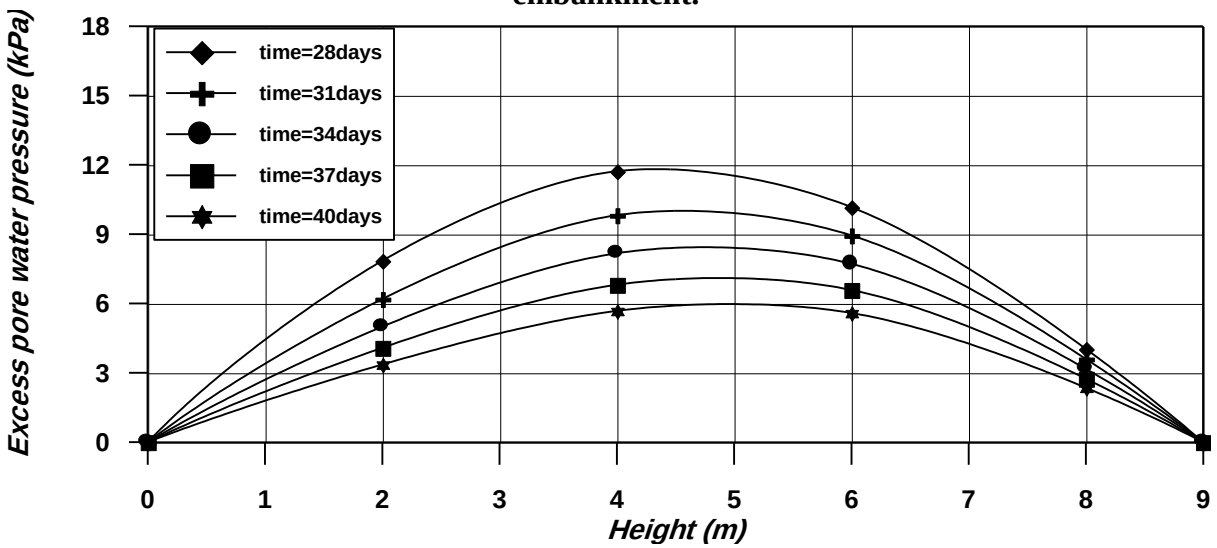

Fig. 18 Excess pore water pressure along section (V2-V2) after construction of SIGMA test embankment.

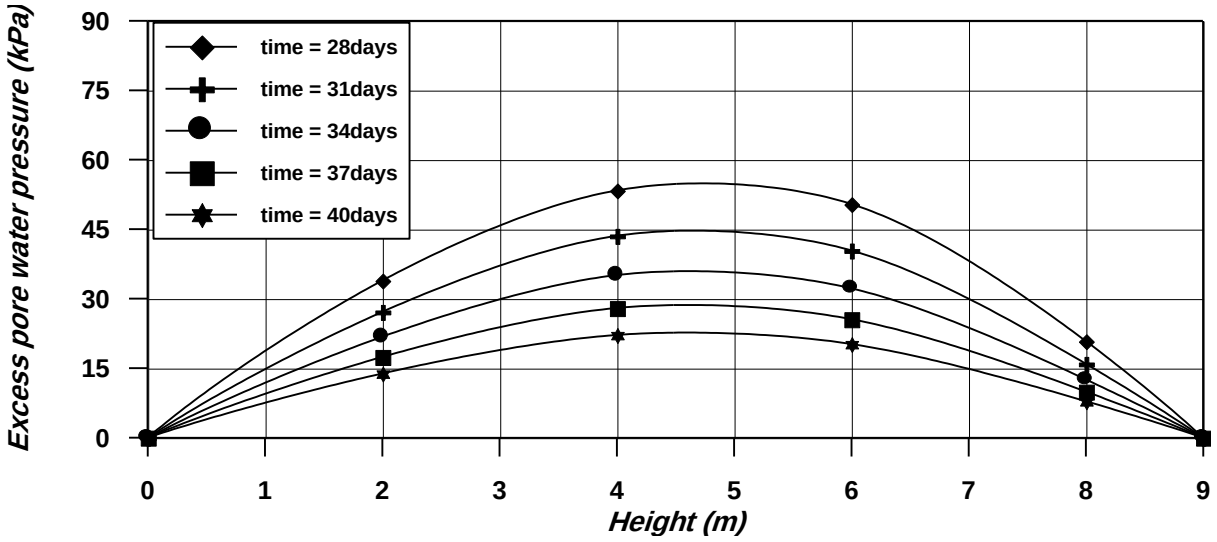

Fig. 19 Excess pore water pressure along centerline after construction of SIGMA test embankment.

Skä Edbey Embankment

Project Description: -

The test embankment was built on the site of Skä Edbey about 25 km west of Stockholm in the year 1961, to study the long-term behavior of Swedish clays and the suitability of the site for construction of an airport.

The embankment has a height of 1.5 m with crest width of 4 m and side slope 1:1.5. It was constructed in three stages as indicated in Fig.18, and the embankment was completed in little over one month. The cross section of the embankment and foundation soil is shown in Fig.19.

The stress applied by the fill was about 27 kN/m^{2}and based on the original shear strength of the clay. The factor of safety against failure was about 1.5, still from elastic theory; the maximum shear stresses under the edge of the embankment were quite high and may have locally exceeded the shear strength.

Instrumentation was installed near the middle of the embankment at locations shown in Fig. 19. Two types of gages were used to measure settlements. Those were placed on the ground surface under the fill where simply steel rods welded to plates with settlement recording made by precise leveling. The gages for measuring settlements at depth considered of rod to firm bottom width in pipe welded to earth screw. Dial indicators determined relative movements. Horizontal movements at the sides of the embankment were measured in plastic tubes by the (SGI) inclinometer (Kallstenius And Berqau, 1961).

Soil Properties

The geotechnical profile for the soil under embankment is shown in Fig. 20 (Holtz, 1972). The soft soil was divided into 8 sub-layers with different compressibility parameters and (OCR) (Neher et al., 1999) as shown in Table 2.

Table (2) Soil parameters for Skä Edbey embankment (from Neher et al., 1999).

<table>
<tr><th>Layer</th><th>γ_t (kN/m^3)</th><th>k (m/day)</th><th>λ</th><th>OCR</th><th>M</th><th>ϕ</th></tr>
<tr><td>A</td><td>14.2</td><td rowspan="2">$8.64*10^{-5}$</td><td>0.106</td><td>14.1</td><td rowspan="9">1.61</td><td rowspan="9">30°</td></tr>
<tr><td>B</td><td rowspan="2">14.4</td><td>0.096</td><td>2</td></tr>
<tr><td>C</td><td>$7.0*10^{-5}$</td><td>0.083</td><td>1.2</td></tr>
<tr><td>D</td><td rowspan="5">16.1</td><td>$6.22*10^{-5}$</td><td rowspan="3">0.076</td><td rowspan="4">1.0</td></tr>
<tr><td>E</td><td>$5.44*10^{-5}$</td></tr>
<tr><td>F</td><td>$5.01*10^{-5}$</td></tr>
<tr><td>G</td><td rowspan="2">$4.75*10^{-5}$</td><td rowspan="2">0.069</td></tr>
<tr><td>H</td></tr>
</table>

Comparison of Results with Observation: -

The predicted and measured vertical settlement at node A (as shown in Fig. 20), and excess pore water pressure at section (V1-V1) at time 10 years after construction and horizontal displacements along section (V2-V2) at time 20 years are shown in Figs. (23, 24 and 25).

It can be seen that the results obtained using the CRISP program are in good agreement with those obtained by PLAXIS program by adopting the modified Cam clay model. The accuracy of models used and the correctness of the input property of the soil, typically for soft ground, is a big topic of soil mechanics, since the elasto-plastic, visco-plastic, and reheology behavior of the soft clay make it extremely difficult to model the soft soil stress- strain relationship. Normally, increasing the model parameters may increase the accuracy of the model, but also increase the difficulties for input parameters evaluation. At present, some of the model parameters, such as compressibility, can be determined from high quality laboratory triaxial or consolidation tests with confidence. However, some other parameters, such as permeability, are very difficult to be determined accurately. For this kind of parameters, the most reliable way is to derive the parameter values from back- analysis of existing case histories.

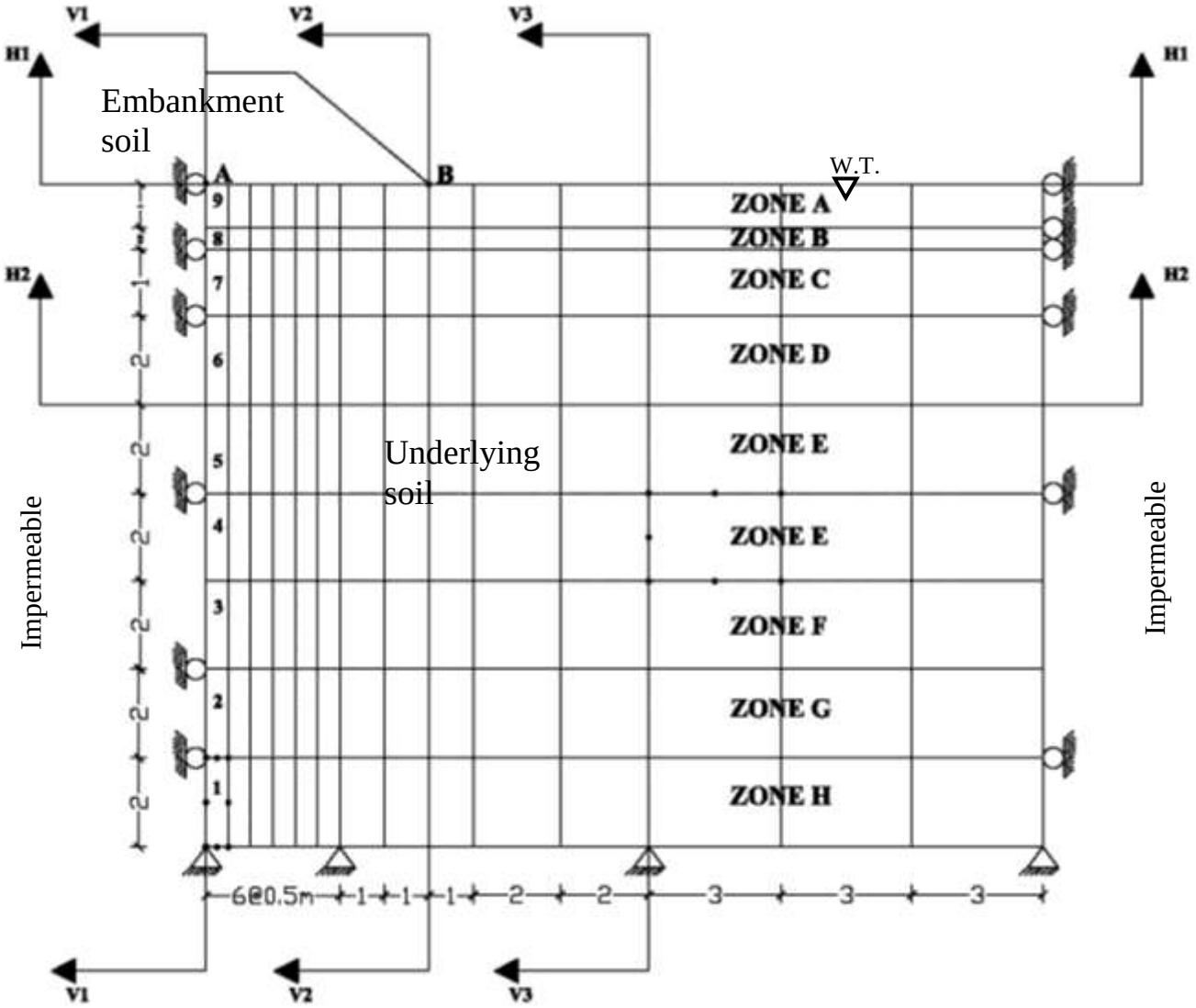
V1
V2
V3
H1
H2
Embankment soil
A
B
W.T.
ZONE A
ZONE B
ZONE C
ZONE D
ZONE E
ZONE E
ZONE F
ZONE G
ZONE H
Underlying soil
Impermeable
Impermeable
6@0.5m
1
2
3
9
8
7
6
5
4
3
2
1

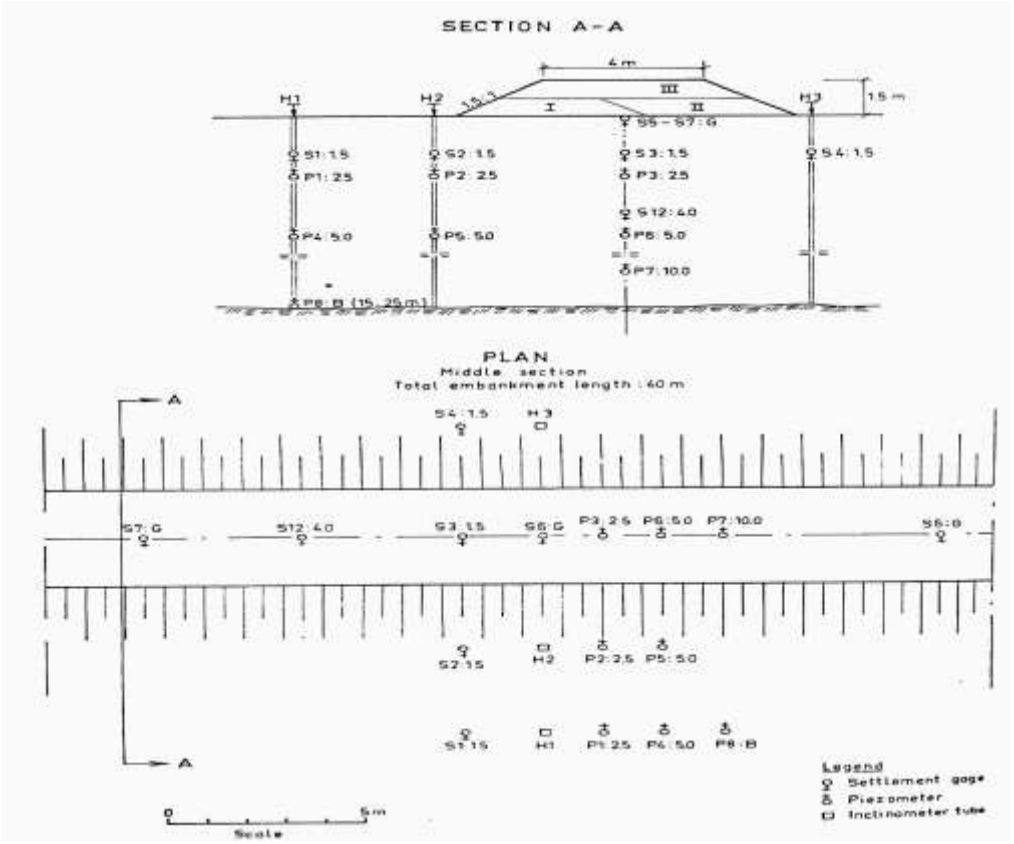

Fig. 21 Plan and section of Skä Edbey embankment showing gage locations and depth below ground surface in meters) (from Holtz, 1972).

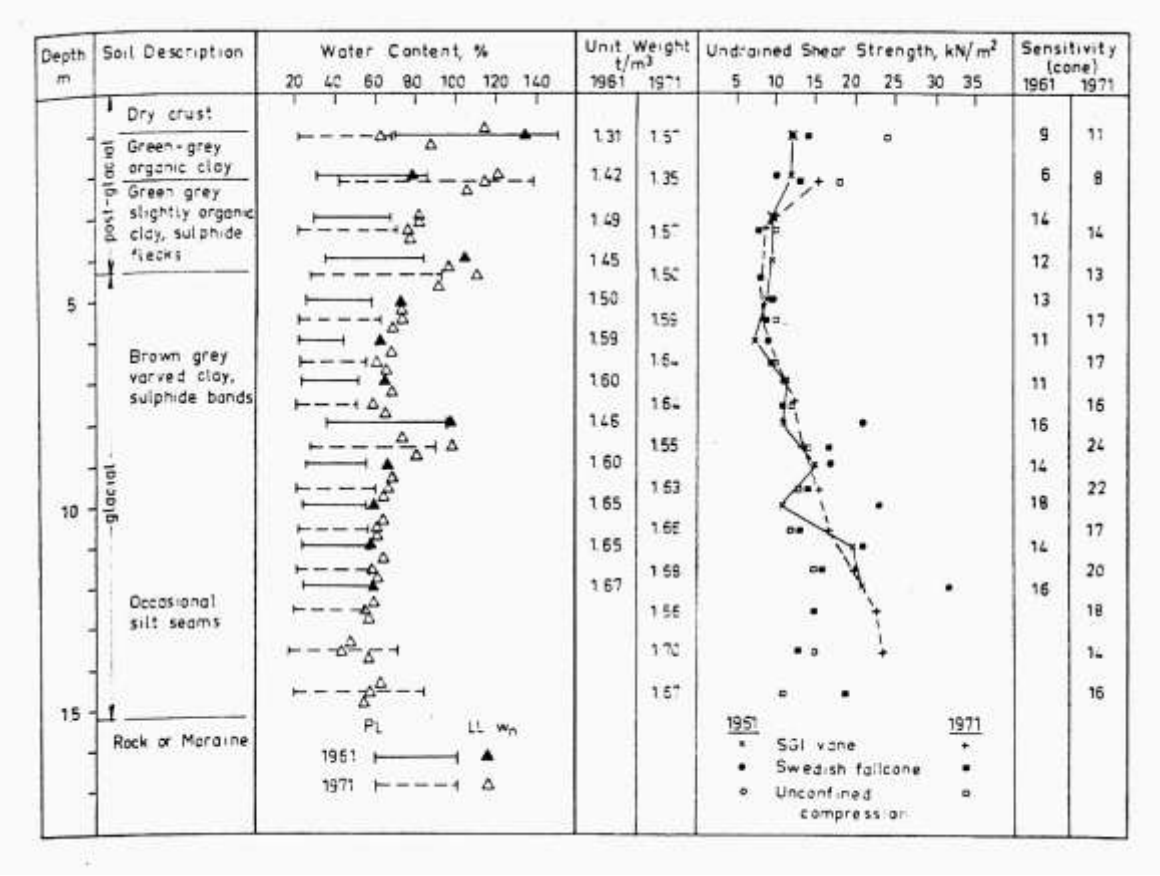

Fig. 22 Geotechnical profile for Säk Edbey embankment (from Holtz, 1972).

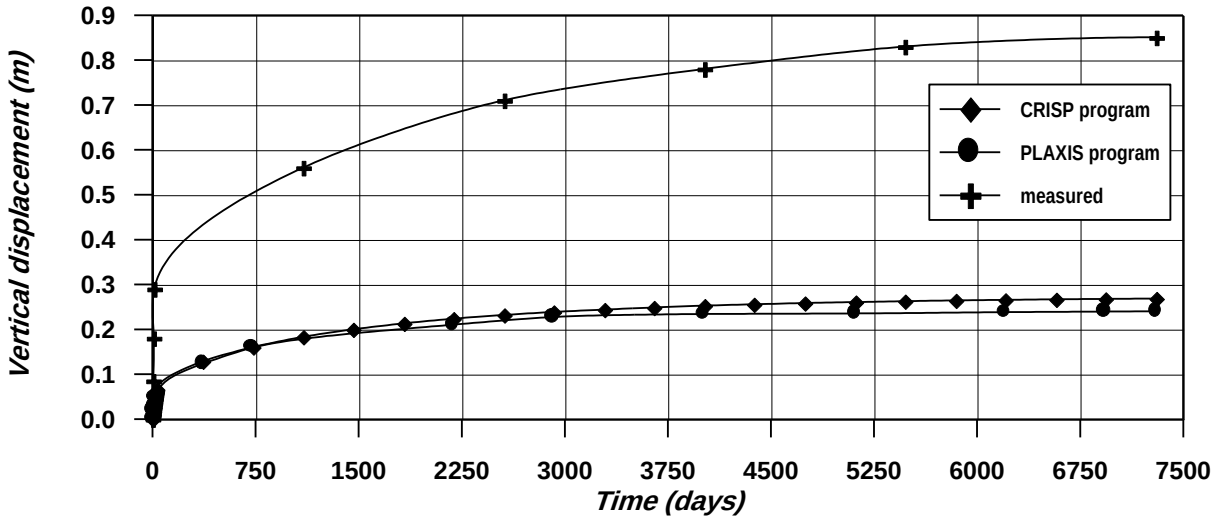

Fig.23 Vertical displacement at point (A) at 20 years after construction of Skä Edbey test embankment.

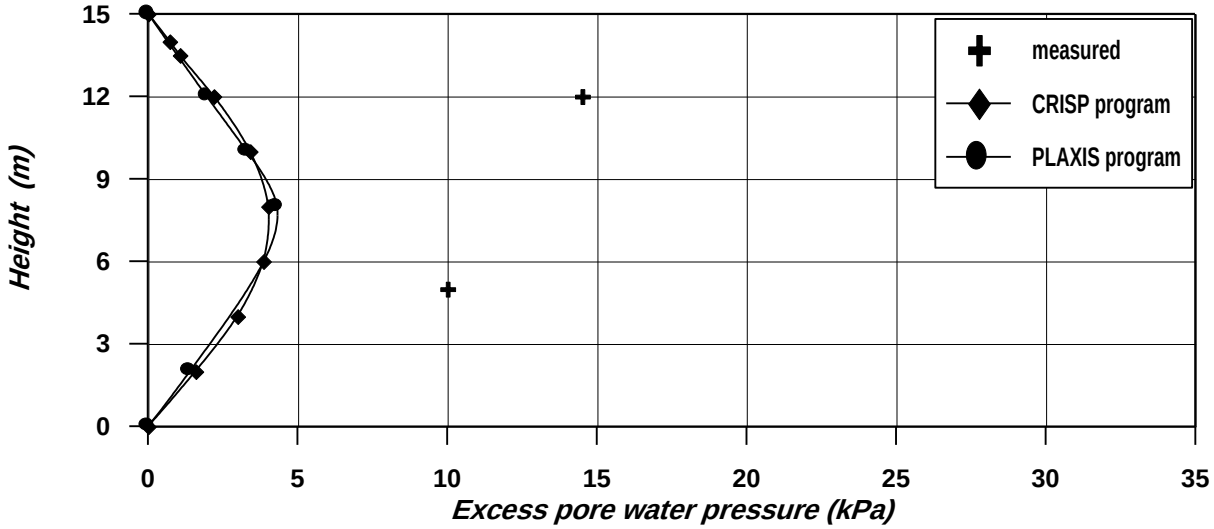

Fig. 24 Excess pore water pressure along section (V1-V1) at 10 years after construction of Skä Edbey test embankment.

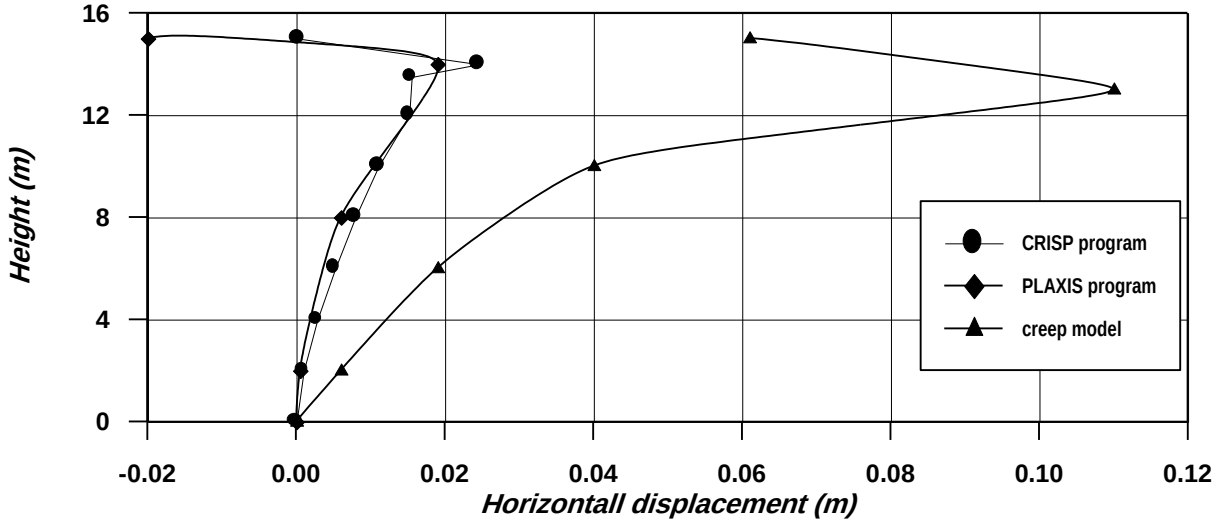

Fig. 25 Horizontal displacement along section (V2-V2) at 20 years after construction of Skä Edbey test embankment.

-Vertical Settlement

For the Skä Edbey test embankment, the vertical movements at the ground surface, sections (H1-H1) and (H2-H2) (shown in Fig. 20) are presented in Figs. (26 and 27). As can be seen, the maximum vertical settlement occurred below the centerline of the embankment. The settlement decreases slightly as the toe of the embankment is approached and decreases rapidly as the distance away from the toe increases. Upward movement of the surface far from the toe is observed. This behavior is due to the loading concentration at the center part of the embankment.

Vertical displacements along sections (V1-V1), (V2-V2) and (V3-V3) are shown in Figs. (28, 29 and 30).

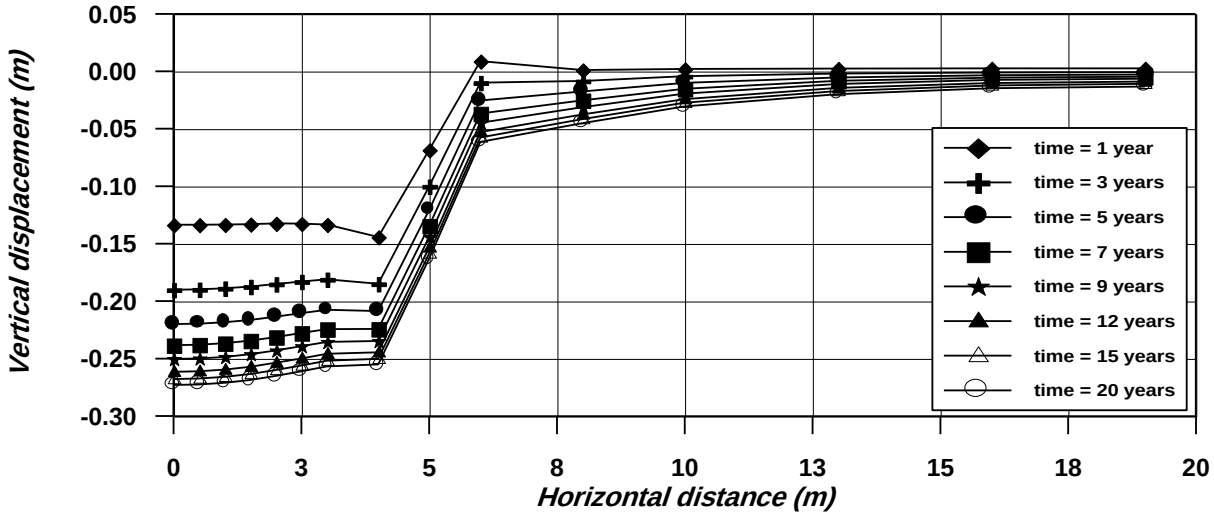

Fig. 26 Vertical displacement along section (H1-H1) after construction of Skä Edbey test embankment.

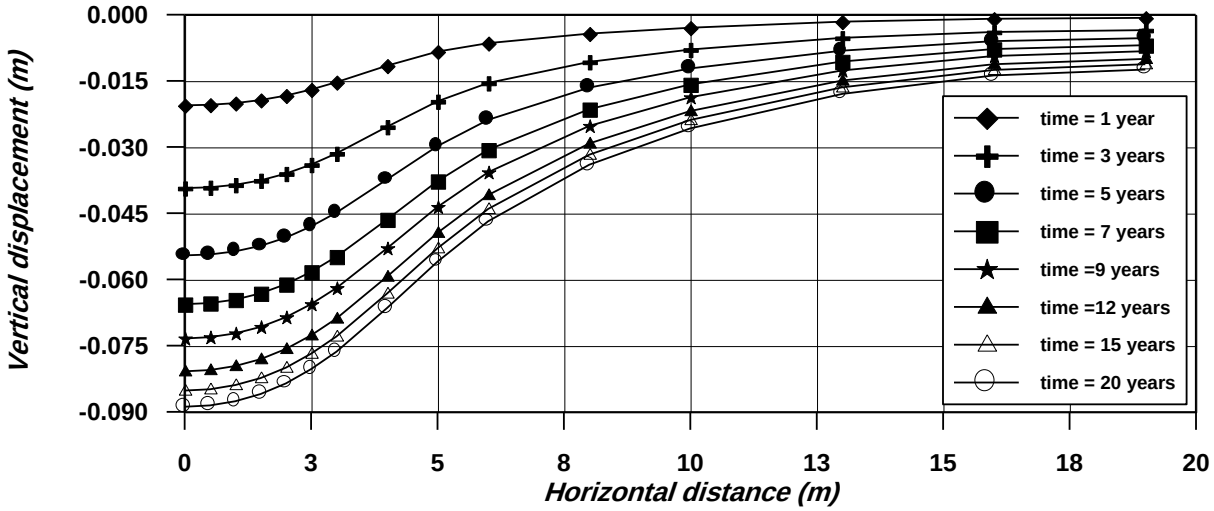

Fig. 27 Vertical displacement along section (H2-H2) after construction of Skä Edbey test embankment.

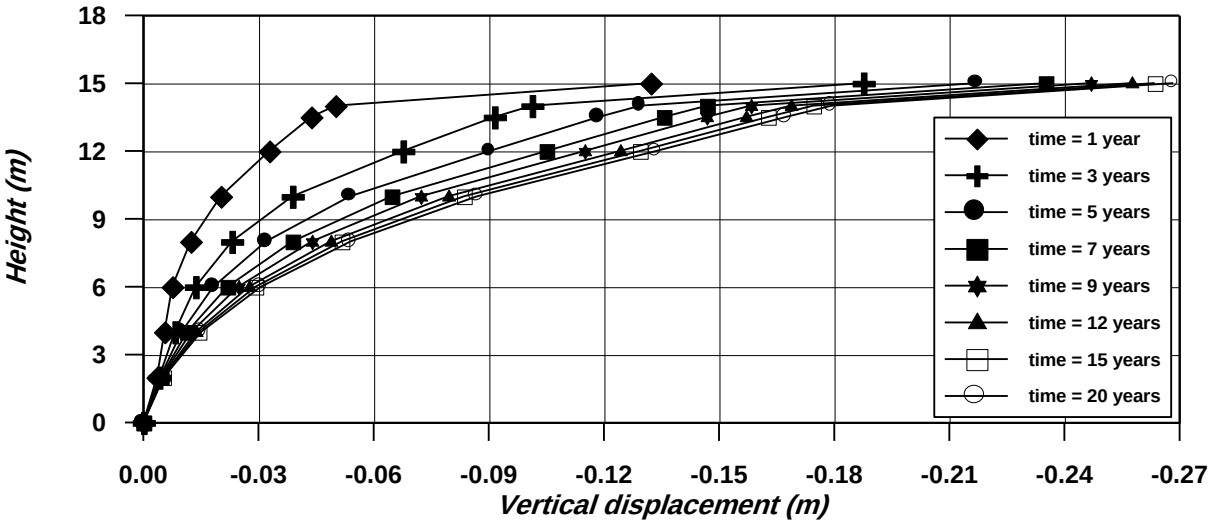

Fig. 28 Vertical displacement along section (V1-V1) after construction of Skä Edbey test embankment.

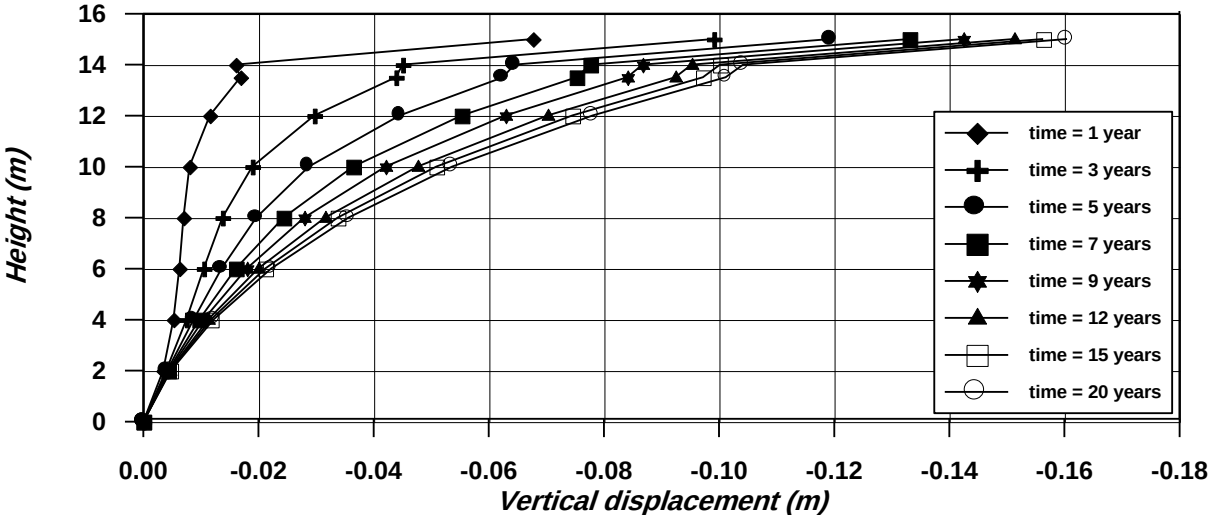

Fig. 29 Vertical displacement along section (V2-V2) after construction of Skä Edbey test embankment.

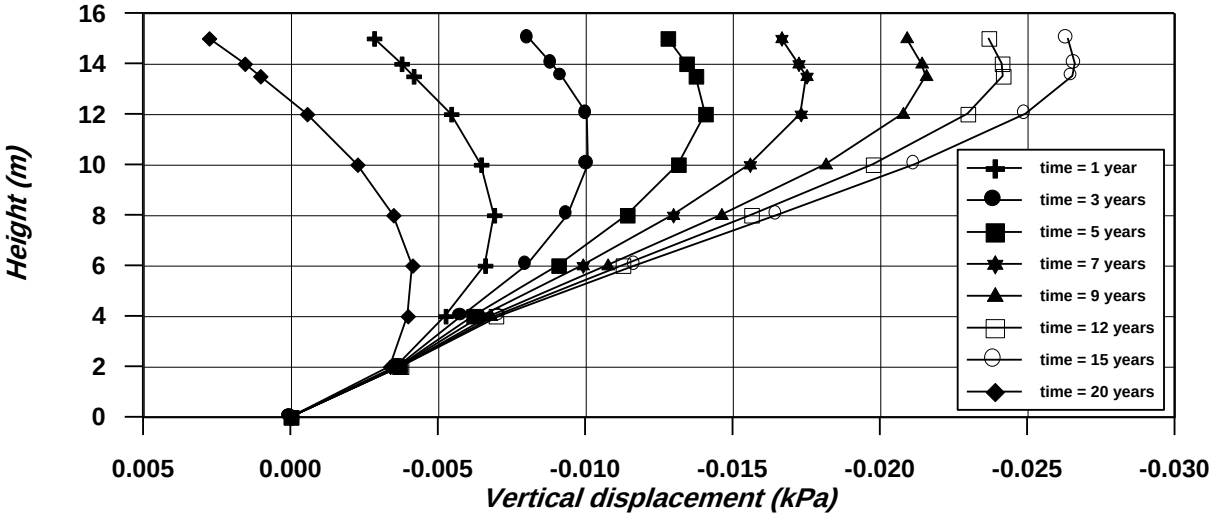

Fig. 30 Vertical displacement along section (V3-V3) after construction of Skä Edbey test embankment.

Horizontal Displacement

The horizontal movement along two vertical sections, which are (V2-V2) and (V3-V3) shown in Fig. 20 are presented in Figs. (31 and 32) after construction at different times. In general, it can be seen that the maximum horizontal displacement occurs near the top boundary. The rate of horizontal movement at top of the foundation is greater than that at the bottom. This behavior may be due to the flexibility of the top boundary that is assumed for horizontal movement. It can also be seen that section (V2-V2) at the toe, shows the maximum horizontal displacement compared with the other section. This behavior is due to the large difference between the vertical load on the left and right hand sides of section (V2-V2).

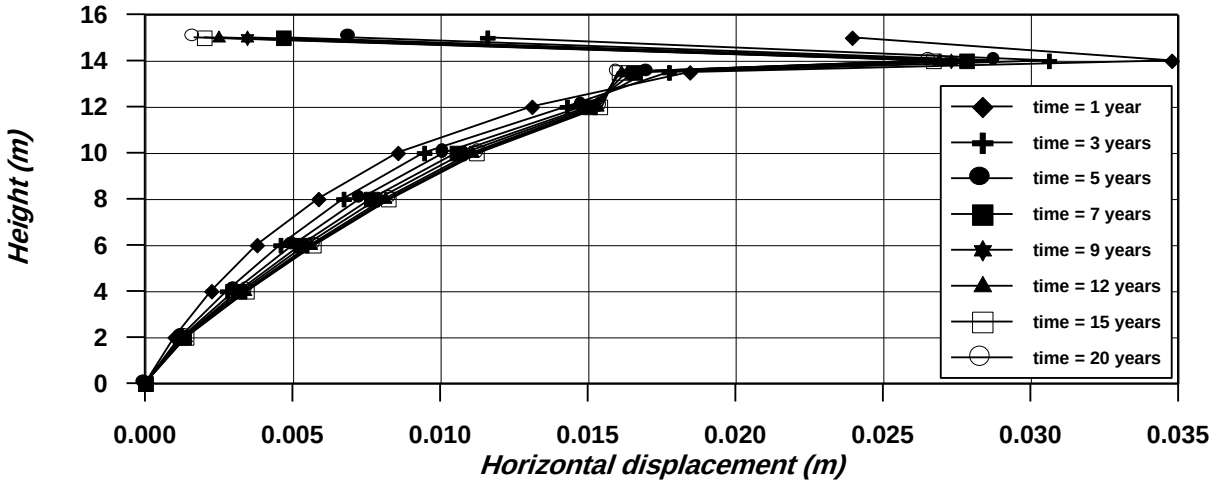

Fig. 31 Horizontal displacement along section (V2-V2) after construction of Skä Edbey test embankment.

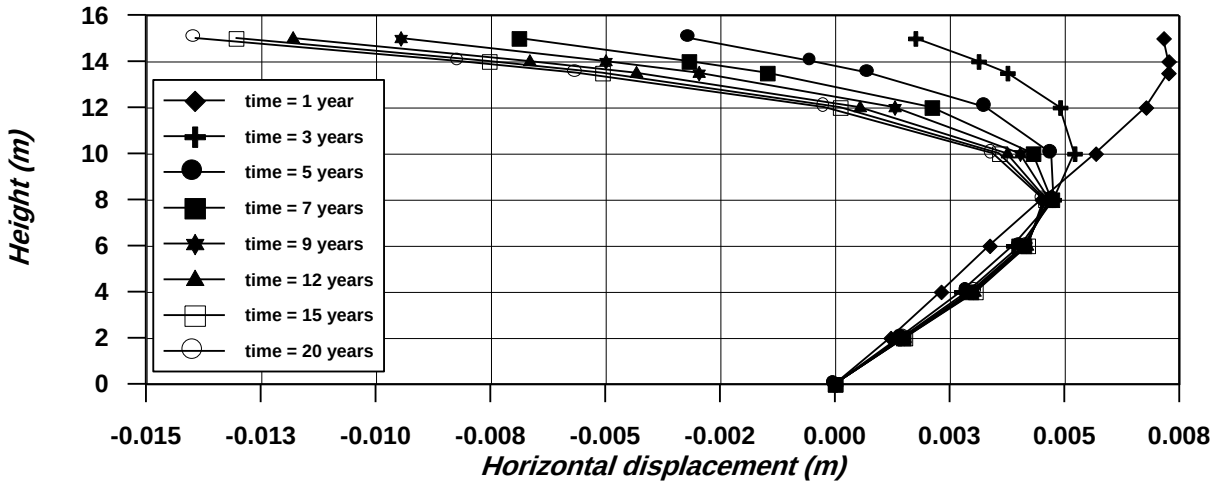

Fig. 32 Horizontal displacement along section (V3-V3) after construction of Skä Edbey test embankment.

Pore Water Pressure

The excess pore water pressure dissipation with time at sections (V1-V1), (V2-V2) and (V3-V3) is shown in Figs. (33, 34 and 35).

As shown in the figures, there is no symmetry in excess pore water pressure isochrones in spite of tow- way drainage condition. This may be attributed to the non-homogeneity in the foundation soil and the differences in the permeability values for different types of foundation layers. The dissipation of excess pore water pressure in the upper layer was faster than at the bottom

layer. This is because that the upper layer has permeability greater than that of the underling layers.

The excess pore water pressure along section (V1-V1) is higher than of the two other sections (V2-V2) and (V3-V3). Such behavior is clearly due to the location of the embankment loads, which are more concentrated on the centerline of the embankment.

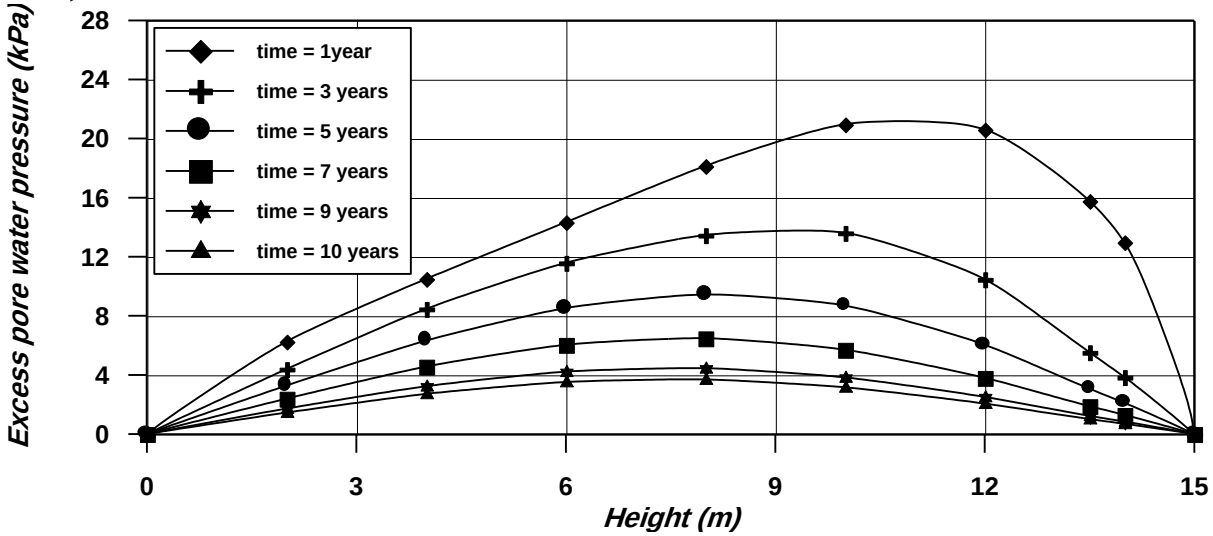

Fig. 33 Excess pore water pressure along section (V1-V1) after construction of Skä Edbey test embankment.

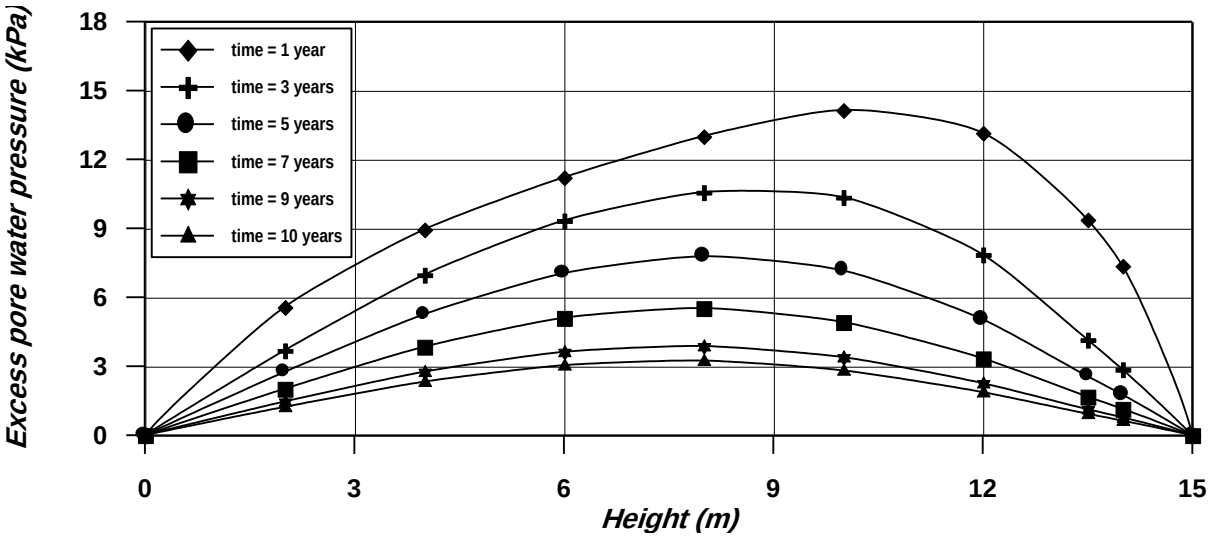

Fig. 34 Excess pore water pressure along section (V2-V2) after construction of Skä Edbey test embankment.

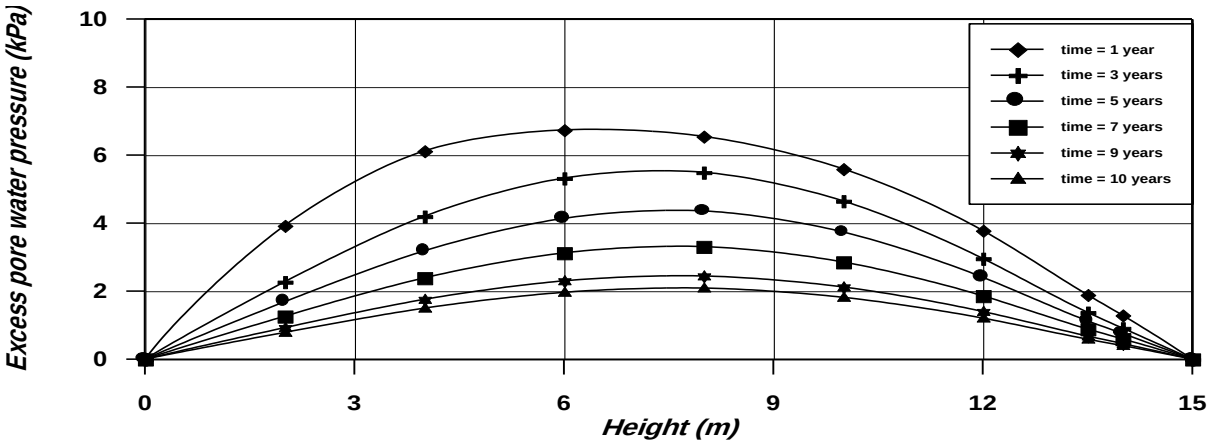

Fig. 35 Excess pore water pressure along section (V3-V3) after construction of Skä Edbey test

embankment.

-Stress State

Figs. (36 and 37) trace the stress path for points A and B (shown in Fig. 20), respectively. It can be seen that isotropic hardening takes place upon loading and new yield surface is always generated at each load increment. The hardening at point (A) which is located at the centerline of the embankment is greater than that at point (B) at its toe. In addition, due to the upward movement of point (B), the stress state may over-pass the critical state line at some stages, and hence dilation might occur at the point. The soil behaves as overconsolidated at that stage.

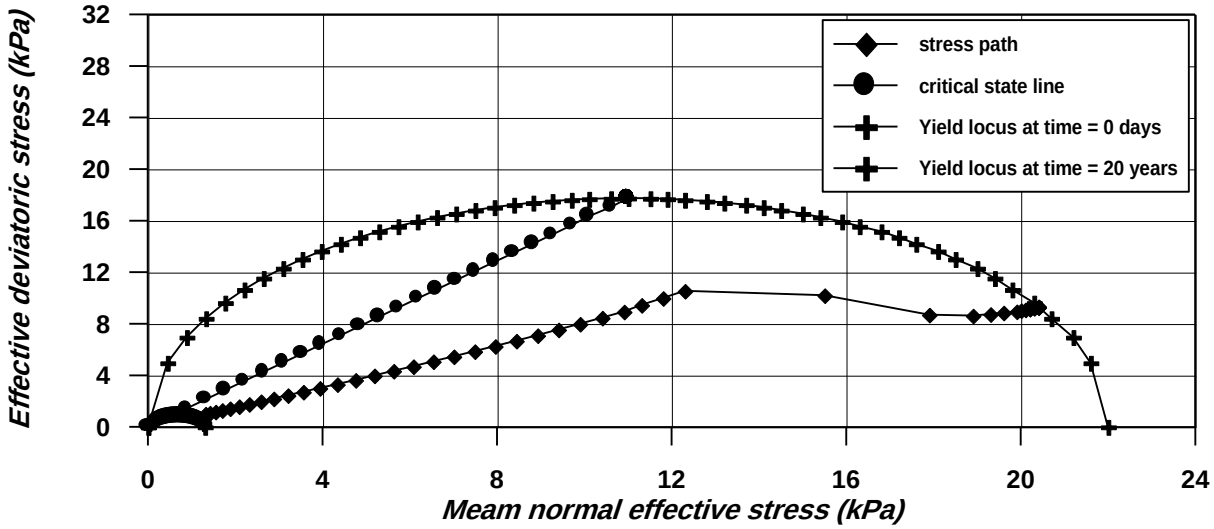

Fig. 36 Stress state at node (A).

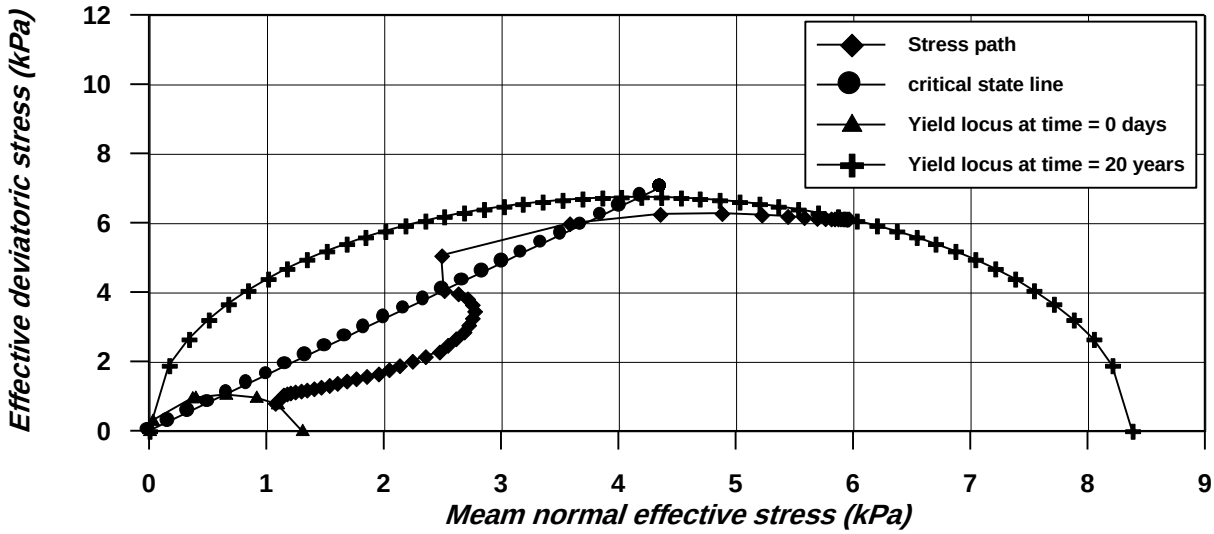

Fig. 37 Stress state at node (B).

CONCLUSIONS

The analysis of two study embankments on soft ground by using the finite element method is achieved. The embankment material is assumed to behave as elastic or elastic-plastic material while foundation soil behavior is considered to follow the modified-Cam clay model. The following conclusions can be drawn:

1. The modified-Cam clay model can simulate the soil behavior successfuly. When the results of analysis are compared with the measured values, good agreement was obtained.

2. The maximum vertical movement occurs below the centerline of the embankment. The settlement decreases slightly as the toe of the embankment is approached and decreases rapidly as the distance away from the toe increases. Upward movement of the surface far from the toe is observed.
3. The maximum horizontal movement occurs near the top boundary. The rate of horizontal movement at the top of the foundation is greater than at the bottom. This behavior may be due to the flexibility and free movement condition of the vertical boundary in the top half.

REFERENCES

* Al-Shammary, A.S. (2006), "*Effect of Lightweight Materials on the Consolidation Characteristics of Embankment on Soft Soils*", M.Sc. Thesis, College of Engineering, Civil Engineering Department, University of Baghdad.

* Atkinson, J.H. and Bransby, P.L. (1978), "*The Mechanics of Soils an Introduction to Critical State Soil Mechanics*", Mc Graw-Hill Book Company, U.K.

* Holtz, R. P. (1972), "*Soil Movement below a Test Embankment*", ASCE, Especialty Conference on Performance of Earth and Earth Supported Structure, Purdue, Vol.2, PP.273-289.

* Kallstenius, T., and Berqau, W. (1961), "*In-situ Determination of Horizontal Ground Movements*", Proceedings, 5th International Conference on Soil Mechanics and Foundation Engineering, Paris, Vol.1, PP.418-485.

* Neher, h. P. and Wehnert, M. and Bonnier, P. G. (1999), "*In Evaluation of Soft Soil Models Based on Trial Embankments*", from Internet, http://www.neher/veroeffentlichungenl/arizonanehaeo.dvi.

* Olson, E. and Fellow, A. (1998), "*Settlement of Embankment on Soft Ground*" Journal of Geotechnical and Geoenvironmental Engineering, ASCE, Vol. 124, No.4, PP. 278-287.

* SIGMA/W for Finite Element Stress and Deformation Analysis-Version 5 User's Guide, Geo-Slope International Ltd., (2002), from Internet, http://www.geoslope.com.

* Skempton, A.W., (1944), ""Notes on the compressibilities of clays," Quarterly Journal of Geological. Soc, London, C (C: Parts 1 & 2).

BUILDING AN INTEGRATED SYSTEM FOR MANAGEMENT OF PROJECTS ((SOME WATER PROJECTS AS A CASE STUDY))

Rafa H. Al- Suhaili **Ziyad J. Fadhal**
Dept. of Civil Eng., College of Engineering
University of Baghdad

ABSTRACT
Many useful softwares in projects management are available now. Ms Project and Primavera are some examples of these softwares. Those programs need to be fed by information by the user. The users usually collect this information from the project and design documents. This collection process needs considerable time and efforts, and usually accompanied of some errors in data transfer process.
In order to reduce the required time and efforts and to eliminate individual errors in data transfer process, an Integrated System is needed. This Integrated System can extract the graphical information from an AutoCAD drawing and transfer it to a digital form suitable for processing in the project management softwares such as Excel and Ms Project.
In this research an Integrated System (IS) was built, to connect three softwares, AutoCAD, Excel and Ms Project, using Active X data transfer technology. The Integrated System was tested using three case studies. Al-Nahrain University waste water network, the Islamic University water supply network, and an irrigation and drainage project. The results indicated the capability of the system to transfer the graphical data into digital data, and to conduct the quantity of survey of the selected projects.
It is worthy to mention that this system requires some modification that is should be adopted in the AutoCAD drawings. The drawings should be performed using layers, and definition blocks for objects. These modifications are simple and can be done easily. Moreover the system was built in a way that gives the ability of adding other case studies (i.e., other types of projects).

الخلاصة
تتوفر العديد من البرامجيات الهندسية المفيده في ادارة المشاريع. مثل هذه البرامج على سبيل الذكر هي (Ms project, Primavera) وغيرها . أن هذه البرامجيات تحتاج الى التغذيه بالمعلومات من قبل المستخدم حيث يقوم المستخدم عادة بجمع المعلومات من المصادر المطلوبه مثل وثائق المقاوله ومخططات التصميم وغيرها. ان عملية جمع هذه المعلومات وادخالها يصاحبها جهد ووقت وقد تتعرض هذه العمليه الى حدوث اخطاء في نقل المعلومات.
ولتوفير الجهد والوقت وتقليل الاخطاء في نقل المعلومات يتطلب انشاء نظام متكامل يقوم باستخلاص المعلومات قدر الامكان من وثائق ومخططات المقاوله وتحويلها من صيغتها الفعليه الى الصيغه الملائمه لتشغيل برامجيات

ادارة المشاريع. Iهذا النظام المتكامل بامكانه استخلاص المعلومات الرسوميه من مخططات ال (AutoCAD) وتحويلها الى ارقام مناسبه للمعالجه في برامج ادارة المشاريع مثل (Excel and Ms Project)
في هذا البحث تم بناء نموذج متكامل لربط البرامجيات (برنامج اوتوكاد، مايكروسوفت أكسيل و مايكروسوفت بروجيكت) بحيث يقوم النموذج باستقراء المعلومات من المخططات التصميميه المرسومه ببرنامج (AutoCAD)وتحويلها مباشره الى برنامج (Excel) وبرنامج(Ms Project) بصيغه عدديه بحيث يمكن التعامل معها بسهوله لايجاد الكميات وبناء نظم اداره المشروع بشكل سريع ومباشر.تم بناء النموذج المتكامل باستخدام البرامجيات اعلاه وربطها بتقنيه (Active X) التلقائيه. تم تجربه النموذج المتكامل على ثلاث حالات دراسيه وهي شبكة مجاري لموقع جامعة النهرين وشبكة ماء لموقع الجامعه الاسلاميه وشبكة قنوات الري والبزل. اثبتت النتائج فعالية النموذج في تحويل المعلومات من صيغتها الرسوميه الى صيغ عدديه يمكن التعامل معها بسهوله ويسر بالبرامجيات المشموله بها.
ومن الجدير بالذكر بان النموذج يتطلب ان يتم رسم المخططات التصميميه ببرنامج الاوتوكاد مع بعض التاشيرات الطفيفه في هذا البرنامج لكي يتمكن النظام بالعمل المطلوب ، مثل اجراء الرسومات بصيغ الطبقات ال(Layers) وحصر الاشكال (Objects) بلوحات التعريف (Blocks) وهي متطلبات بسيطه يمكن تنفيذها بسهوله.كما ان النظام تم بناءه بطريقه مرنه بحيث يمكن اضافة اي حاله اخرى (اي مشاريع اخرى).

KEY WORDS
Integrated System, AutoCAD, Excel, Ms Project, Active X Technology

INTRODUCTION

Construction was a collaborative activity involving a multi-disciplinary team including client, architect, engineer, consultant, contractor, etc. Each member of this team was responsible for certain aspects of the project. Different professions used their own unique processes to undertake their tasks, but often had to rely on information supplied by others. At present, the communication problem between the team members is often a cause for project delay and building defects. Improving the communication link had been identified as crucial to further efficiency gain in construction. (Sun and Aouad: 1999).

With the wide use of Architecture, Engineering, Construction (AEC) software, the traditional cross discipline communication is increasingly manifested as an issue of data exchanged and data sharing between different software applications. (Sun and Aouad: 1999).

The increasing technical complexity of projects created a demand for the integration of construction project information .The development and deployment of new construction industry software applications, improvements in network technology, the application of robotics to the building process, the development of new modeling methodologies and languages and the definition of standards for information exchange all created new opportunities for integration. (Dikbas, Morten and Yitmen: 2000).

Integrated construction management systems had their early start with the automation of scheduling and planning through the use of emerging Artificial Intelligence (AI) techniques (e.g., Levitt et al. 1988; Waugh 1990) as mentioned by (Rankin, Forese and Waugh: 1999). It was found that starting from so-called "first principles" and regenerating all the necessary information that was required for a single application, let alone integrated applications, was a challenging task. Work in this area then took a turn towards integrating the applications that were more widely accepted (scheduling and estimating), through the application of broader information technology approaches, with a higher level of information representation and use of templates or libraries of knowledge structures (e.g., Yamazaki 1995; Strumpf et al. 1996) as mentioned by (Rankin, Forese and Waugh: 1999).

To date, it is generally accepted that integrated construction management systems will be conceptually based on a central information source with which integrated applications and the industry participants

will interact (O'Brien 1997) as mentioned by (Rankin, Forese and Waugh: 1999). (Rankin, Forese and Waugh: 1999).

Limitations of Using Stand-alone AutoCAD in Construction Management:

1. in the AEC industry have used today's CAD systems as simply automated drafting tools
2. Information is scattered about the project in an uncontrolled and uncoordinated way, on a variety of information systems and media, so that the design cannot be viewed as a complete entity

3. A problem with these stand-alone CAD applications for construction management is that they are typically used primarily as drawing tools, and are not used to store construction management related data within the drawing. (Marir, Aouad and Cooper: 1998)

Limitations of the Current Traditional Project Management Softwares:

1. These softwares provide sophisticated functions of analyzing the network models of a project so as to scheduling the project
2. these softwares are applicable only to a prepared network model of a project
3. They are mainly used to carry out computations on input data provided by the construction planner. The input data required normally comprise an activity list complete with their estimated durations and logic dependencies
4. Even if the design is CAD-based, the data needed for establishing such model can not be extracted directly by these softwares from the data existing already in the CAD drawings generated at design phase while have to be re-input by the planner

If the construction schedule of a building can be generated directly and automatically from its drawings provided at design phase, it will benefit in at least two ways:

a) To predict the construction schedule at design phase, hence to optimize the design from construction view;

b) To fully utilize the data existing in the drawings for managerial purposes in construction phase, such as scheduling and cost estimating, so as to reduce the tedious human manipulation of data and the potential source for numerous errors. (Wang: 2001)

COMPUTER INTEGRATED CONSTRUCTION SYSTEMS

Computer integrated construction (CIC) systems had a tremendous potential to improve the productivity of the construction industry. (Elzarka: 2001).

Computer Integrated Construction (CIC) as an example of how research and development could deliver significant savings to the construction industry. The concept of (CIC) was that technical information was entered into the computer system once and instantly made available electronically to all project team members. (Frederick and Nancy: 2000).

Elzarka had defined the (CIC) as the use of computer system to integrate the management, planning, design, construction, and operation of constructed facilities. CIC systems automate many of the labor-intensive tasks associated with construction management of new facilities. Through the integration of (3d, 2d) CAD models, database management systems and expert systems , CIC systems allow users to automatically calculate material quantities from CAD models, test the constructability of the design before actual construction; report construction progress graphically and improve collaboration between project member. (Elzarka: 2001)

The main objective of CIC system is to communicate data to all project participants, throughout the project's entire life cycle and across business functions. (Elzarka: 2001)

The followings are the benefits of (CIC) systems:

An architect transmitted Computer-Aided Design (CAD) files to a construction manager, who automatically extracted areas and quantities for an accurate progress estimate and schedule. As the design was refined, so were the estimate and the schedule.

1. Estimate quantities electronically linked to the schedule for projecting the value of work in place. This allowed for easier and faster construction of a cost-loaded critical path schedule.
2. Suppliers' data bases were made electronically available to designers and builders, who extracted specifications, pricing, and availability information. For example, using a common symbol library, a designer clicked the "door" symbol; all door suppliers were listed. The designer clicked a particular price; availability information was listed.
3. A project's filed office was electronically linked to the home office and design consultants for communicating up-to-date design, schedule, and cost information. For example, a design consultant in a remote location transmitted, rotated, and explained a construction detail on a field superintendent's computer. (Frederick and Nancy: 2000).

SYSTEM INTEGRATION DEFINITIONS

There are many definitions to system integration and the researcher will view the following:
(Thomas: 1992) had define the system integration as "a spectrum of application-linking and data-sharing capabilities".
(Wang: 2000) had define system integration as "the pass of information from one application to another in a way that the information required can directly be used as the input for another application".
(Sun: 1999) had define system integration as "the exchange of data between Architecture, Engineering, and Construction applications".
The researcher defines the system integration as "a system integration that allow various applications to interoperate and exchange data with other applications"

DEVELOPMENT OF THE INTEGRATED SYSTEM

The integration of stand alone AutoCAD, Ms Excel and Ms Project using Visual Basic and Active X Automation technology is proposed as an alternative approach to developing the Integrated Construction System (ICS).
The integration of stand-alone CAD, spreadsheet, and scheduling software using Visual Basic is proposed as an alternative approach to developing integrated systems. One advantage of this approach is that the integration of existing software, already familiar to the user, achieves dramatic reductions in the development effort as well as training time over conventional programming for systems with similar scope.
The program was designed by using Visual Basic as control tool for sharing data between AutoCAD, Ms Excel and Ms Project

THE SOFTWARE USED IN PROGRAM

1. Visual Basic and Visual Basic for Applications
   - Stand-alone visual Basic is designed for general application development
   - Visual Basic for Applications is the edition of Microsoft Visual Basic designed specifically to provide development capabilities inside an off-the-shelf application
   - One of the most advantage of programs developed using VB lies in their graphical user interface GUI, which has the familiar Windows look that users are accustomed to. The same features and controls, like list boxes, dialog boxes, option buttons, and command buttons, can

be incorporated into the applications' screen displays. Visual Basic is a graphically oriented language, so mush of our program can be accomplished with the click of a mouse.

2. Auto Cad
   - AutoCAD is one of the most widely used computer-aided design/drafting (CAD) products on the market today. One of the main reasons for AutoCAD's popularity is its flexibility
   - Computer-aided design (CAD) has been widely used in the construction industry. Its use however has been limited to drafting for so many years that it is sometimes referred to as computer aided drafting.
3. Ms Excel
   - Ms excel spreadsheets have gained wide acceptance for calculation and data analysis
   - Tapping into the increasing capabilities modern computers, spreadsheet applications have been up graded significantly in the last few years to include additional capabilities and presentation options

4. MS project
   - Ms Project is one of the famous programs that used mainly for scheduling of projects. It is used as scheduling tools for construction projects and all other projects in the other disciplines.
   - Ms Project has multi view like critical path and Gant chart can be drawn.
   - Various options like early start, late start or scheduling back words from the completion date are available
   - Important events may be highlighted by specifying them as "milestones"
   - Various sub-projects or multiple networks can also be handled.

TYPES OF CONNECTIONS BETWEEN THE SOFTWARES

1. Dynamic Data Exchange (DDE)
   - Originally created to allow two windows applications to communicate and exchange data
   - DDE is the mechanism that allows two applications to "talk" to each other by continuously exchanging data.
   - In a DDE conversation, one application called the destination application, or client, initiates a conversation with another application called the source application, or server.
   - The information generally flows from the server, or source, to the client. If necessary, the process can be reversed, where the client sends information back to the server.
2. Object Linking and Embedding (OLE)
   - Object linking and embedding (OLE) has taken the capabilities of (DDE) a step further. Instead of simply passing information from one application to another (OLE) allows information to be presented in the same way it would appear in the original application
   - The information can be embedded by simply copying it to the windows clipboard and pasting it into another windows application
3. Active X Automation
   - Active X is Microsoft's term for "activating the internet" using the same technology used in other windows application on the computer
   - Using Active X Automation, the AutoCAD objects can be created and manipulated from any application that serves as an automation controller.

- It enables cross application macro programming-the ability to control one application, such as AutoCAD, from a macro developed in another application, such as Microsoft Excel
- With Active X Automation, the features of many applications can be combined in a single application.
- An Active X controls is a device created to perform a specific task in the used application

THE PROGRAM REQUIRMENTS

The program is built according to some requirements as follows:

1. AutoCAD drawing requirements

For water system and waste water system:

- Each pipe diameter should be drawn in a separate layer (for example pipe of diameter 300mm draw in layer named DIM300).
- Each fitting should be drawn as a block (for example A-angle fitting drawn as block named A).
- For pump station and Gate valve also should be drawn as a block named (PUMP).
- Each manholes should be drawn as a block (for example AS manhole draw as block named AS)

For Irrigation project:

- All channel type should be drawn in one layer named (LC).
- The name of each channel should be entered directly after the draw of channel.
- The name of each channel should be putted in layer named ID like (LC1/DC1/WC1).
- The channels should be drawn in a sequence start from (LC) and then (DC) and (WC).
- The cross sections drawing should be contain the (top level value, ground level value, and bed level value); these values entered as text in different layer name like (TL for the top level value), and so on.
- The sections should be named according to the related channel; the name should be entered in a layer named (ADDRESS).
- The sections should be drawn in a sequence from the first section to the last.
- The channels and sections should be drawn in one drawing

2. AutoCAD scale should be (1:1).
3. The cost of the activities is estimated using material quantities that extracted from the AutoCAD drawing and the cost information entered by the user (the information cost should be as unit cost /meter).
4. The production rate for an activity is assumed to be fixed along the activity duration (production rate should be as quantity/day).
5. The duration of the activities is estimated using material quantities that extracted from the AutoCAD drawing and the productivity rate information entered by the user.
6. The precedence of the activities should be entered by the user.

THE PROGRAM DESCRIPTION

The Integrated Construction System (ICS) is developed to facilitate the construction management of (water system, waste water system, and irrigation system) as case studies projects by integrating the following off-the shelf applications:

1. AutoCAD for reading the required information and data of design.
2. Microsoft Excel spreadsheet to report the bill of quantities in a convenient spreadsheet format for subsequent manipulation and printing.
3. Microsoft Project scheduling system to scheduling the project.

All components of the program are integrated using Visual Basic and Active X Automation technology. Figure (1) illustrates the integration achieved in the program.

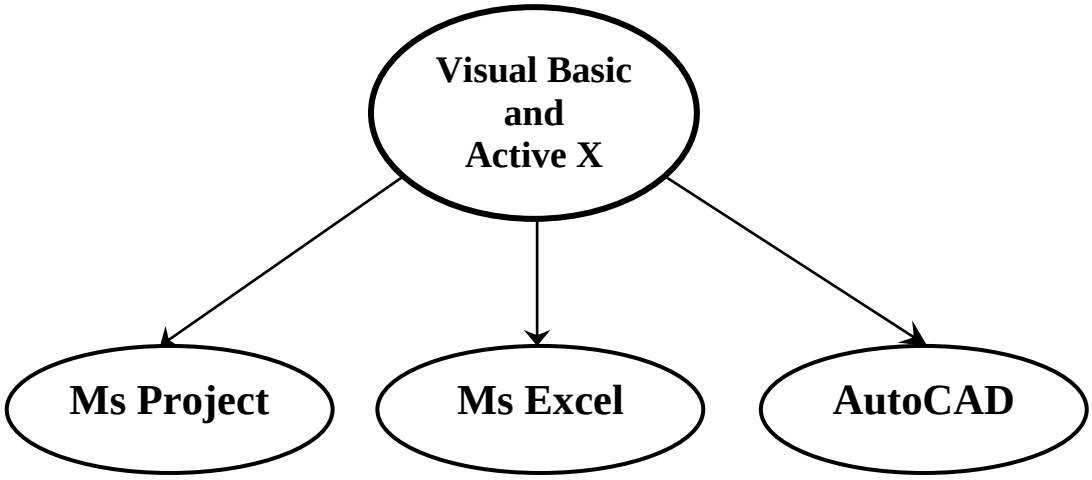

Fig (1) The integration model

To make another application's objects available in the developed VB code, there is a need to set a reference to that application's object library. This can be done by clicking on the project command in VB menu bar and selecting references. The references dialog box lists the references available to the project. To add the AutoCAD objects, the check box next to the AutoCAD name should be selected. The same process can be followed to make other application's objects available in the code of the program like MS Excel and Ms Project. As shown in figure (2).

Since AutoCAD drawing is essentially a data base, extracting and conveying information about drawing entities is not necessary difficult. Active X Automation can be used to obtain key information about the exposed AutoCAD objects and to send this information to a VBA-enabled application like Excel. This approach is useful for the generation of tables like a bill of material or quantity summary.

When the list command is used in AutoCAD, certain characteristics are displayed for the entities selected. For line, the values for the beginning point, end point, and length, as well as the layer name and, of course, the entity type, and line can be seen. The access of much of same information with Active X Automation can be preformed and put in to use in various ways, such as counting the number of entities in a certain layer, or tallying up the total length of certain lines.

The AutoCAD data base is the central repository of all data is stored in the AutoCAD model. It contains the information required to support the activities of cost estimating and scheduling.

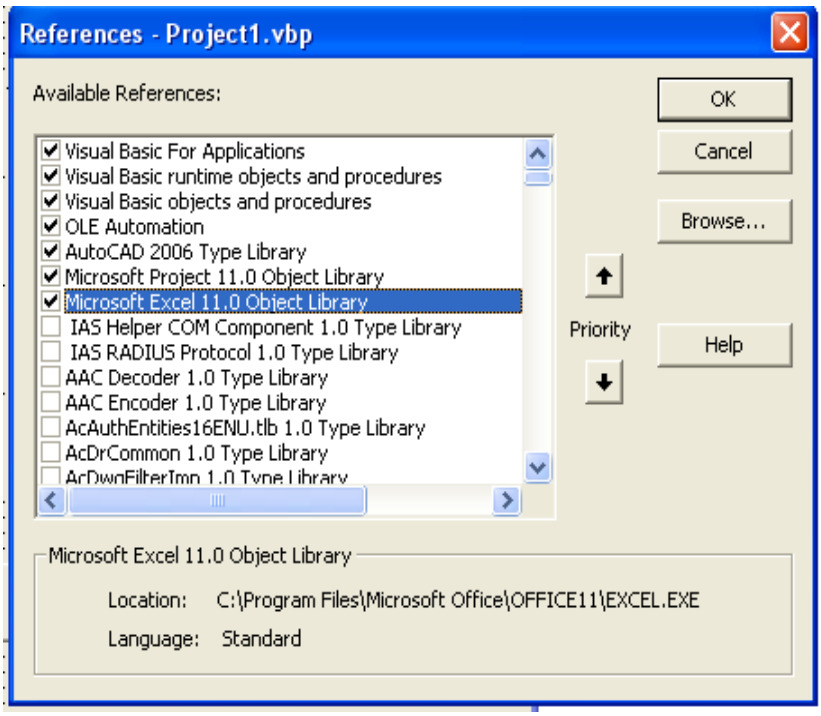

Figure (2) References dialog box

THE IMPLEMENTATION OF THE PROGRAM

Case Study One (Water System Network)

The layout drawing of the water system network is shown in figure (3) for the water system of the Islamic University in Baghdad. The output of the program is as follows:

Figure (3) The Islamic University in Baghdad water system network

1. Excel presentation quantity takes off: as shown in table (1) below

Table (1) The Excel presentation quantity takes off of program

Item	qty	unit	Cost	UNIT	DURATION	UNIT
DIM100	1029.00	meter	10290	ID	21	DAY
DIM150	283.00	meter	2830	ID	6	DAY
DIM200	255.00	meter	2550	ID	5	DAY
DIM250	301.00	meter	3010	ID	6	DAY
DIM300	267.00	meter	2670	ID	5	DAY
J	2.00	each	20	ID	1	DAY
A	12.00	each	120	ID	6	DAY
T	36.00	each	360	ID	18	DAY
GATE VALVE	3.00	each	30	ID	2	DAY
PUMP	2.00	each	20	ID	1	DAY

2. Ms Project scheduling presentation: as shown in table (2) below

Table (2) The Ms Project scheduling presentation of program

ID	Task Name	Duration	Start
1	DIM100	21 days	Mon 2/6/06
2	DIM150	6 days	Wed 2/8/06
3	DIM200	5 days	Thu 2/16/06
4	DIM250	6 days	Thu 2/23/06
5	DIM300	5 days	Fri 3/3/06
6	J	1 day	Fri 3/10/06
7	A	6 days	Mon 3/13/06
8	T	18 days	Fri 3/10/06
9	GATE VALVE	2 days	Wed 4/5/06

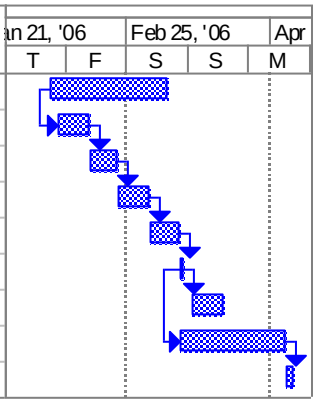

The hand calculations as shown in table (3) below:

Table (3) The quantity takes off by hand calculation

Dim 250 (meter)	Dim 300 (meter)	Dim 200(meter)	Dim 150(meter)	Dim 100(meter)	J-junction
69.79	147.47	24.32	33.98	23.24	**SUM=2 unit**
62.03	96.73	56.03	33.81	39.63	**A-angle**
19.25	10.87	21.3	25.21	89.75	**SUM=12 unit**
38.12	6.05	27.69	29.61	28.48	**T-node**
18.8	2.48	96.86	42.59	42.56	**SUM=36unit**
92.7	2.45	28.65	36.53	30.98	**GATE VALVE**
		254.85	28.2	16.68	**SUM=3unit**
SUM=300.69m	**SUM=266.05m**	**SUM=254.85m**	35.48	42.96	**PUMP**
			17.16	151.55	**SUM=2unit**
				91.26	
			SUM=282.57m	179.03	
				20.53	
				21.22	
				39.57	
				17.84	
				57.02	
				99.58	
				36.53	
				SUM=1028.41 m	

Case study two (Waste Water System Network)

The layout drawing of the waste water system network is shown in figure (4) for the waste water system of the Al-Nahrain University. The output of the program is as follows:

1. Excel presentation quantity takes off: as shown in table (4) below

Table (4) The Excel presentation quantity takes off of program

Item	qty	unit	cost	UNIT	DURATION	UNIT
DIM250	1211633.00	meter	12116330	ID	121	DAY
DIM300	602171.00	meter	6021710	ID	60	DAY
DIM400	430863.00	meter	4308630	ID	43	DAY
AS	26.00	each	260	ID	26	DAY
BS	19.00	each	190	ID	19	DAY
CS	1.00	each	10	ID	1	DAY
BD	5.00	each	50	ID	5	DAY
CD	1.00	each	10	ID	1	DAY
PUMP STATION	1.00	each	10	ID	1	DAY
VENT PIPE	1.00	each	10	ID	1	DAY

2. Ms Project scheduling presentation: as shown in table (5) below

Table (5) The Ms Project scheduling presentation of program

ID		Task Name	Duration
1		DIM250	121 days
2		DIM300	60 days
3		DIM400	43 days
4		AS	26 days
5		BS	19 days
6		CS	1 day
7		BD	5 days
8		CD	1 day
9		PUMP STATION	1 day
10		VENT PIPE	1 day

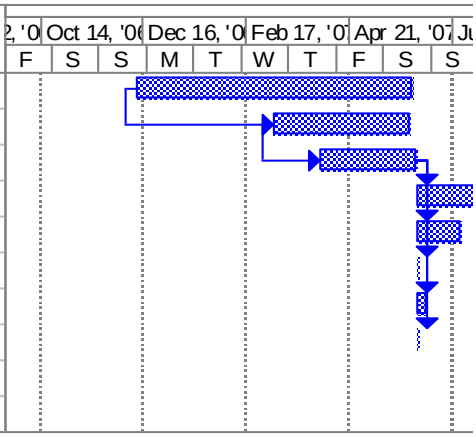

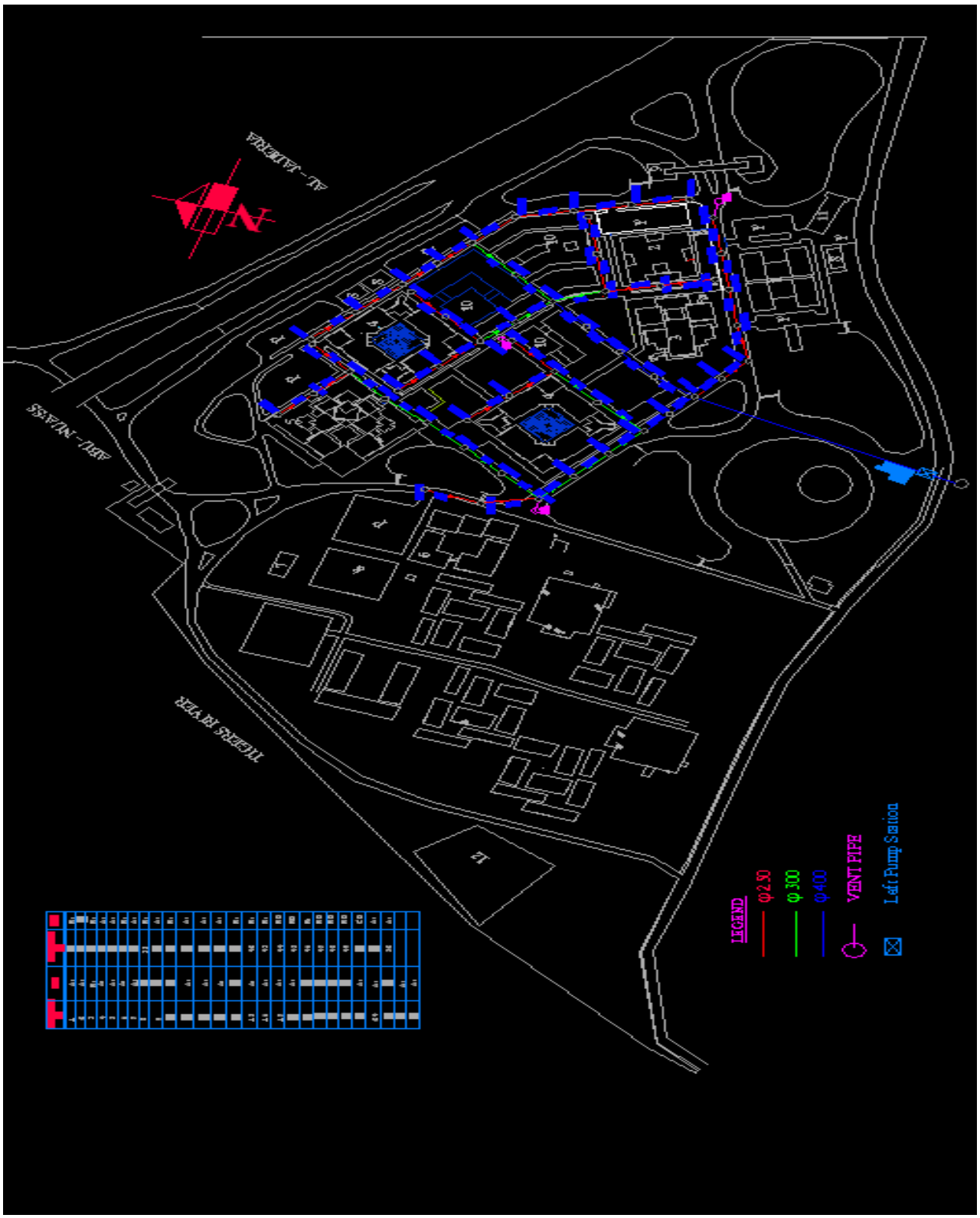

Figure (4) The Al-Nahrain University waste water system network

The hand calculations as shown in table (6) below:

Table (6) The quantity takes off by hand calculation

Dim400(meter)	Dim300(meter)	Dim250(meter)	AS
37299	39809	35043	**SUM=26unit**
37372	33809	35764	**BS**
37354	34402	41643	**SUM=19unit**
25049	40509	45452	**CS**
24876	49574	47509	**SUM=19unit**
211278	40803	34262	**BD**
20165	40879	33849	**SUM=5unit**
36955	39810	43803	**CD**
515	39811	43800	**SUM=1unit**
SUM=430863meter	39750	43806	**PUMP STATION**
	48158	43807	**SUM=1unit**
	48107	41183	**VENT PIPE**
	35747	41334	**SUM=1unit**
	35508	37370	
	35495	37370	
	SUM=602171meter	42373	
		42374	
		41340	
		41340	
		44863	
		43803	
		40885	
		40885	
		40989	
		40995	
		41379	
		43804	
		48002	
		26303	
		26303	
		SUM=1211633 meter	

Case study three (Irrigation System)

The layout of the irrigation system is shown in figure (5a, b). This layout is a proposal. Three sections for each canal were taken. The output of the program is as follows:

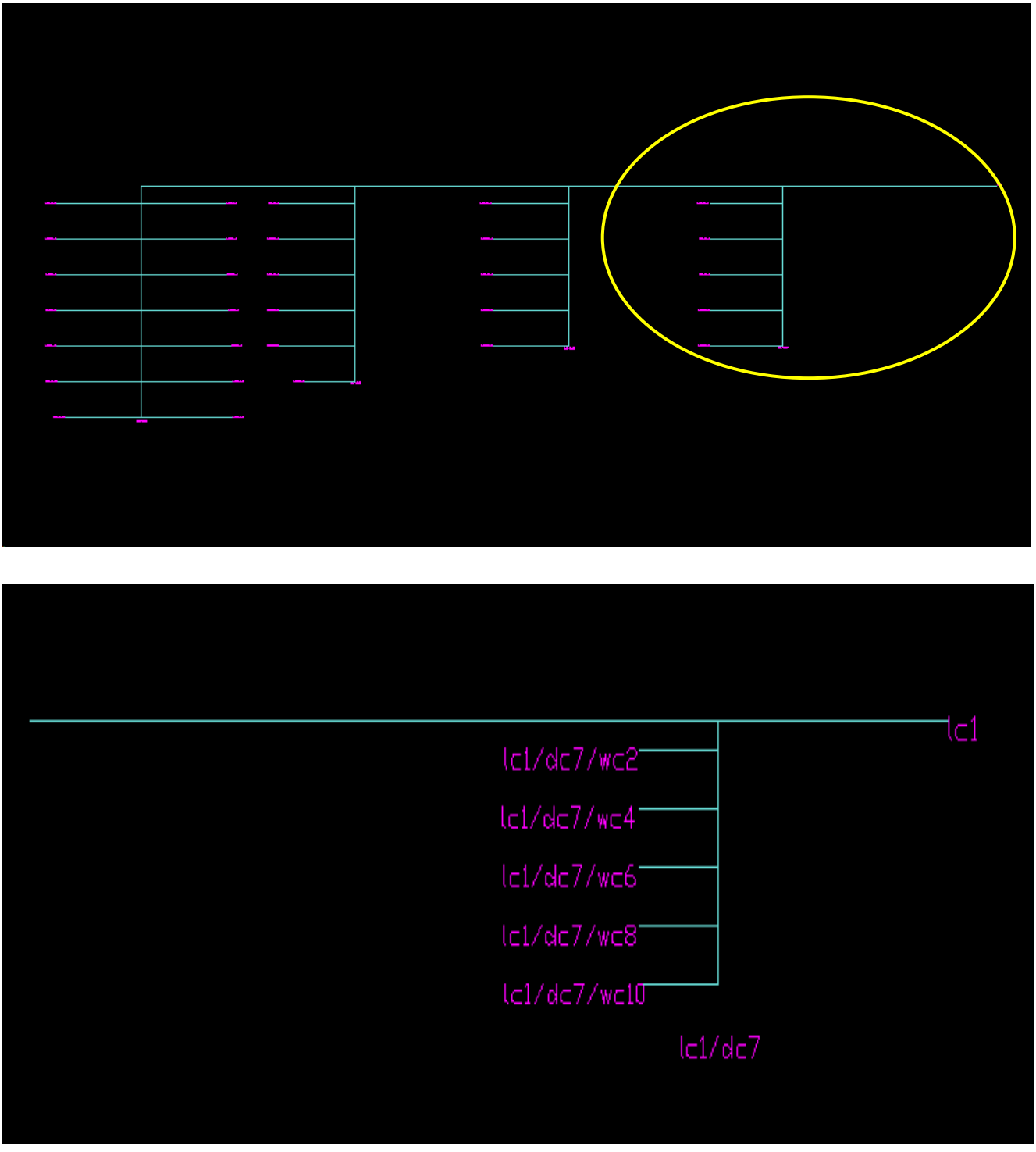

Figure (5a) The proposed irrigation system

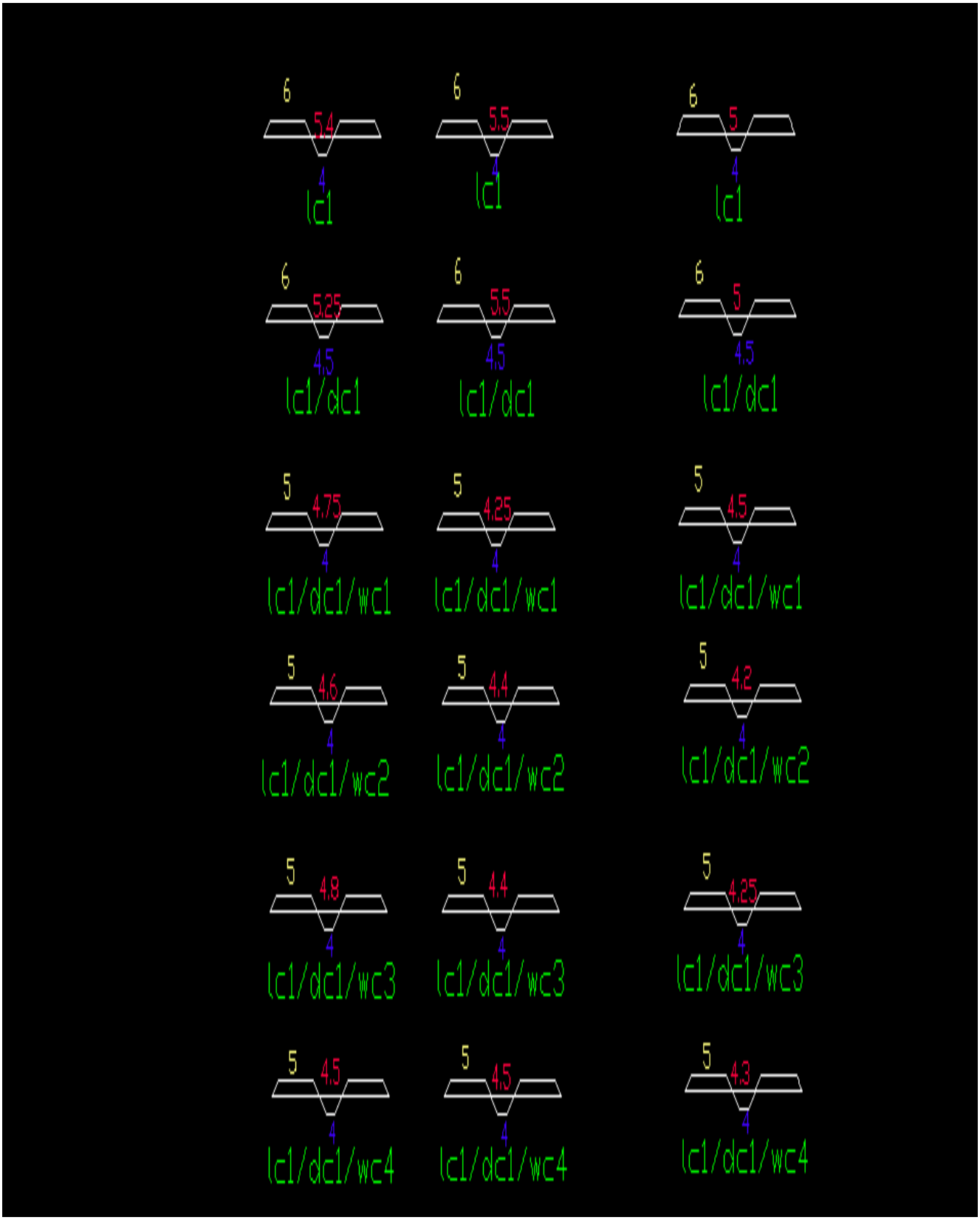
6
5.4
4
lc1
6
5.5
4
lc1
6
5
4
lc1
6
5.25
4.5
lc1/dc1
6
5.5
4.5
lc1/dc1
6
5
4.5
lc1/dc1
5
4.75
4
lc1/dc1/wc1
5
4.25
4
lc1/dc1/wc1
5
4.5
4
lc1/dc1/wc1
5
4.6
4
lc1/dc1/wc2
5
4.4
4
lc1/dc1/wc2
5
4.2
4
lc1/dc1/wc2
5
4.8
4
lc1/dc1/wc3
5
4.4
4
lc1/dc1/wc3
5
4.25
4
lc1/dc1/wc3
5
4.5
4
lc1/dc1/wc4
5
4.5
4
lc1/dc1/wc4
5
4.3
4
lc1/dc1/wc4

Figure (5B) The proposed irrigation system

1. Excel presentation quantity takes off: as shown in table (7a) and (7b) below:

Table (7a) The Excel presentation quantity takes off of program

ID	length	UNIT	AC	AF	UNIT	VC	VF	UNIT
lc1	12000.00	meter	6.43	12.26	sq. meter	643.00	1226.00	meter^3
lc1/dc1	3250.00	meter	3.03	13.06	sq. meter	303.13	1306.25	meter^3
lc1/dc1/wc1	1180.00	meter	1.34	10.44	sq. meter	134.38	1043.75	meter^3
lc1/dc1/wc2	1195.00	meter	1.16	11.12	sq. meter	116.00	1112.00	meter^3
lc1/dc1/wc3	1190.00	meter	1.44	9.92	sq. meter	143.63	992.25	meter^3
lc1/dc1/wc4	1195.00	meter	1.32	10.04	sq. meter	132.00	1004.00	meter^3
lc1/dc1/wc5	1200.00	meter	1.20	10.84	sq. meter	119.63	1084.25	meter^3
lc1/dc1/wc6	1195.00	meter	1.20	10.84	sq. meter	119.63	1084.25	meter^3
lc1/dc1/wc7	1220.00	meter	1.72	8.39	sq. meter	172.13	839.25	meter^3
lc1/dc1/wc8	1195.00	meter	1.13	11.06	sq. meter	112.75	1105.50	meter^3
lc1/dc1/wc9	1260.00	meter	2.33	5.40	sq. meter	232.63	540.25	meter^3
lc1/dc1/wc10	1195.00	meter	1.96	7.12	sq. meter	196.00	712.00	meter^3
lc1/dc1/wc11	1275.00	meter	1.94	7.09	sq. meter	194.25	708.50	meter^3
lc1/dc1/wc12	1195.00	meter	2.09	6.34	sq. meter	209.38	633.75	meter^3
lc1/dc1/wc13	1275.00	meter	1.03	11.90	sq. meter	102.63	1190.25	meter^3
lc1/dc1/wc14	1075.00	meter	2.32	5.73	sq. meter	231.50	573.00	meter^3
lc1/dc3	2750.00	meter	2.59	14.99	sq. meter	259.25	1498.50	meter^3
lc1/dc3/wc2	1070.00	meter	1.62	8.55	sq. meter	162.25	854.50	meter^3
lc1/dc3/wc4	1070.00	meter	1.27	10.98	sq. meter	126.63	1098.25	meter^3
lc1/dc3/wc6	1070.00	meter	1.34	10.42	sq. meter	133.63	1042.25	meter^3
lc1/dc3/wc8	1070.00	meter	1.14	11.44	sq. meter	114.38	1143.75	meter^3
lc1/dc3/wc10	1070.00	meter	1.00	12.20	sq. meter	100.00	1220.00	meter^3
lc1/dc3/wc12	700.00	meter	1.42	9.53	sq. meter	141.50	953.00	meter^3
lc1/dc5	2250.00	meter	2.67	14.34	sq. meter	267.00	1434.00	meter^3
lc1/dc5/wc2	1070.00	meter	1.34	10.77	sq. meter	133.50	1077.00	meter^3
lc1/dc5/wc4	1070.00	meter	1.72	7.96	sq. meter	171.56	796.11	meter^3
lc1/dc5/wc6	1070.00	meter	1.19	10.76	sq. meter	119.18	1076.36	meter^3
lc1/dc5/wc8	1070.00	meter	2.67	4.34	sq. meter	266.75	433.50	meter^3
lc1/dc5/wc10	1070.00	meter	0.81	13.22	sq. meter	80.75	1321.50	meter^3
lc1/dc7	2250.00	meter	1.38	22.15	sq. meter	137.50	2215.00	meter^3
lc1/dc7/wc2	1020.00	meter	2.15	6.11	sq. meter	215.25	610.50	meter^3
lc1/dc7/wc4	1020.00	meter	0.96	12.46	sq. meter	95.63	1246.25	meter^3
lc1/dc7/wc6	1020.00	meter	0.99	12.18	sq. meter	99.00	1218.00	meter^3
lc1/dc7/wc8	1020.00	meter	2.01	6.87	sq. meter	200.88	686.75	meter^3
lc1/dc7/wc10	1020.00	meter	1.09	11.34	sq. meter	109.38	1133.75	meter^3

Table (7b) The Excel presentation quantity takes off of program

CUT COST	UNIT	FILL COST	UNIT	duration	UNIT
6430	ID	12260	ID	120	day
3031.25	ID	13062.5	ID	33	day
1343.75	ID	10437.5	ID	12	day
1160	ID	11120	ID	12	day
1436.25	ID	9922.5	ID	12	day
1320	ID	10040	ID	12	day
1196.25	ID	10842.5	ID	12	day
1196.25	ID	10842.5	ID	12	day
1721.25	ID	8392.5	ID	12	day
1127.5	ID	11055	ID	12	day
2326.25	ID	5402.5	ID	13	day
1960	ID	7120	ID	12	day
1942.5	ID	7085	ID	13	day
2093.75	ID	6337.5	ID	12	day
1026.25	ID	11902.5	ID	13	day
2315	ID	5730	ID	11	day
2592.5	ID	14985	ID	28	day
1622.5	ID	8545	ID	11	day
1266.25	ID	10982.5	ID	11	day
1336.25	ID	10422.5	ID	11	day
1143.75	ID	11437.5	ID	11	day
1000	ID	12200	ID	11	day
1415	ID	9530	ID	7	day
2670	ID	14340	ID	23	day
1335	ID	10770	ID	11	day
1715.55	ID	7961.1	ID	11	day
1191.8	ID	10763.6	ID	11	day
2667.5	ID	4335	ID	11	day
807.5	ID	13215	ID	11	day
1375	ID	22150	ID	23	day
2152.5	ID	6105	ID	10	day
956.25	ID	12462.5	ID	10	day
990	ID	12180	ID	10	day
2008.75	ID	6867.5	ID	10	day
1093.75	ID	11337.5	ID	10	day

2. Ms Project scheduling presentation: as shown in table (8) below

Table (8) The Ms Project scheduling presentation of program

ID	Task Name	Duration	Start
1	Ic1	120 days	Mon 10/23/06
2	Ic1/dc1	33 days	Mon 11/20/06
3	Ic1/dc1/wc1	12 days	Mon 11/27/06
4	Ic1/dc1/wc2	12 days	Mon 11/27/06
5	Ic1/dc1/wc3	12 days	Thu 11/30/06
6	Ic1/dc1/wc4	12 days	Thu 11/30/06
7	Ic1/dc1/wc5	12 days	Wed 12/6/06
8	Ic1/dc1/wc6	12 days	Wed 12/6/06
9	Ic1/dc1/wc7	12 days	Mon 12/11/06
10	Ic1/dc1/wc8	12 days	Mon 12/11/06
11	Ic1/dc1/wc9	13 days	Mon 12/18/06
12	Ic1/dc1/wc10	12 days	Mon 12/18/06
13	Ic1/dc1/wc11	13 days	Mon 12/25/06
14	Ic1/dc1/wc12	12 days	Mon 12/25/06
15	Ic1/dc1/wc13	13 days	Mon 1/1/07
16	Ic1/dc1/wc14	11 days	Mon 1/1/07
17	Ic1/dc3	28 days	Mon 12/18/06
18	Ic1/dc3/wc2	11 days	Thu 12/21/06
19	Ic1/dc3/wc4	11 days	Tue 12/26/06
20	Ic1/dc3/wc6	11 days	Fri 12/29/06
21	Ic1/dc3/wc8	11 days	Wed 1/3/07
22	Ic1/dc3/wc10	11 days	Mon 1/8/07
23	Ic1/dc3/wc12	7 days	Thu 1/11/07
24	Ic1/dc5	23 days	Mon 1/29/07
25	Ic1/dc5/wc2	11 days	Thu 2/1/07
26	Ic1/dc5/wc4	11 days	Tue 2/6/07
27	Ic1/dc5/wc6	11 days	Fri 2/9/07
28	Ic1/dc5/wc8	11 days	Wed 2/14/07
29	Ic1/dc5/wc10	11 days	Mon 2/19/07
30	Ic1/dc7	23 days	Mon 3/12/07
31	Ic1/dc7/wc2	10 days	Fri 3/16/07
32	Ic1/dc7/wc4	10 days	Thu 3/22/07
33	Ic1/dc7/wc6	10 days	Wed 3/28/07

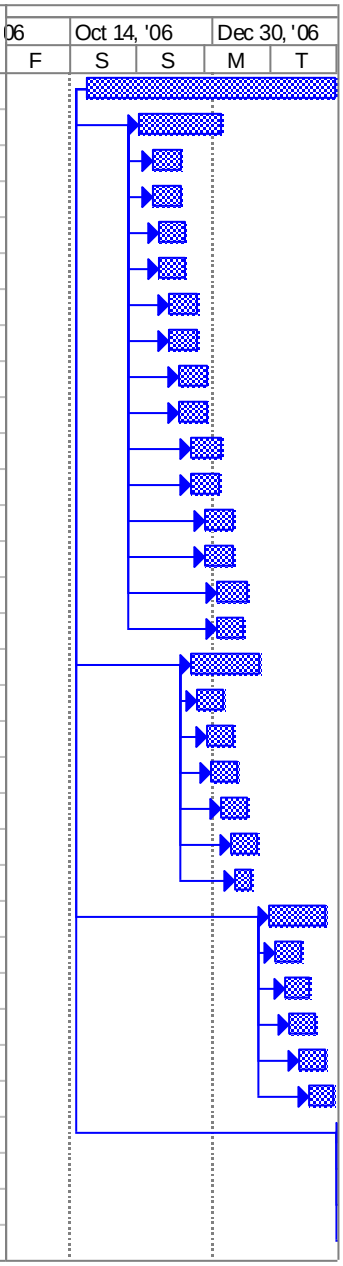

The hand calculations as shown in table (9) below:

Table (4-12) The quantity takes off by hand calculation

ID	length	UNIT	AC	AF	UNIT	VC	VF	UNIT
lc1	12000.00	meter	6.43	12.26	sq. meter	321.50	613.00	meter^3
lc1/dc1	3250.00	meter	3.03	13.06	sq. meter	151.56	653.13	meter^3
lc1/dc1/wc1	1180.00	meter	1.34	10.44	sq. meter	67.19	521.88	meter^3

CUT COST	UNIT	FILL COST	UNIT	duration	UNIT
3215	ID	6130	ID	240	day
1515.625	ID	6531.25	ID	65	day
671.875	ID	5218.75	ID	23	day

As shown from the two out put of the program and hand calculation there is no any difference between the two estimates of quantities. But the estimate of the program can achieve in easy way and in short time.

CONCLUSIONS

1. This research described in details the development and application of a Computer Integrated System (CIS) aiming at illuminating the idea of data sharing in construction management phases of a project.
2. (CIS) which was developed with Visual Basic and Active X Automation technique, can automatically interpret AutoCAD drawing of a (water system, waste water system, and irrigation system), extract the data needed for construction management and generate a bill of quantities and schedule.
3. The presented examples shows that the bill of quantities and the schedule generated by (CIS) for the sample projects are practical and applicable and the integrated system do the work efficiently.
4. The process of the developed system is so easy and can be achieved by just a mouse clicking and entering the required information's for cost and duration estimation.
5. The ability to develop a Computer Integrated System (CIS) should entice more contractors to use these systems. The AutoCAD software available today, with its ability to link to external programs has made such development possible. The utilization of (CIS) systems will become more and more important as the popularity of the design/build project delivery system continues to increase. In the design/build approach, more business functions are performed by the same company and as a result, their integration to share data becomes more vital.
6. (CIS) has automatically changed the drawing items to digital numbers and the user can deal with these digital numbers in an easy way more than the drawing items.
7. If there is any change in the design of drawings the project manger can easily re-run the program to get the correct quantities again and to check it before and after change with respect to cost and duration.

REFERENCES

* Dikbas A., B. Morten,I. Yitmen, 2000,"An integrated management information system for construction projects", Construction Information Digital Library .http://itc.scix.net/paper_w78-2000-277.content

* Elzarka H.,2001,"Computer integrated construction for small and medium contractors",ASC Proceedings of the 37th annual conference, University of Denver-Denver, Colorado, April 4-7,2001 pp255-262 http://www.asceditor.usm.edu/archives/2001/elzarka01.html

* Marir F.,Ghassan Aouad and Grahame Cooper, 1998, "OSCONCAD: A model-based cad system integrated with computer applications", ITcon Vol.3 (1998) http://www.itcon.org/1998/3/paper.pdf

* Nancy E.J. and Frederick E. G., 2000, "Construction project management", Prentice Hall upper Saddle River, New Jersey, Columbus, Ohio

* Rankin J.H., T.M. Forese and L.M. Waugh, 1999, "Application of case-based reasoning to computer-assisted construction planning", 8th International Conference On Durability Of Building materials And Components May 30-June 3,1999 Vancouver, Canada

* Sun M., G. Aouad, 1999," Control mechanism for information sharing in an integrated construction environment" research centre for built human environment, University of Salford, UK, Version of 9 July 1999 http://cic.vtt.fi/cec99/abstracts/sun01.html

* Thomas M.F.,1992, " Integrated computer-aided project management through standard object-oriented models" ,PhD. thesis, university of Stanford
http://www.civil.ubc.ca/~tfroese/pubs/fro92a_thesis/fro92a.pdf#search='construction%20integrated%20system'

* Wang S.Q., 2001, "ESSCAD: Expert System Integrated Construction Scheduling With Cad Drawing", Construction Information Digital Library. http://itc.scix.net/paper w78-2001-46.content

ANALYSIS OF CONSOLIDATION BEHAVIOR OF SUBSOILS UNDER CYCLIC TRAPEZOIDAL LOADING

Zainab Ahmed Alkaissi
Al-Mustansiriya University
College of Eng.

Duraid Ali Al Khafagy
University of Babylon
College of Eng.

ABSTRACT:

This paper is aiming to develop a numerical procedure using the finite element method for the analysis of soil consolidation by taking into consideration the loading and unloading cycles with particular emphases on the pore pressure built up. The study is concerned with trapezoidal cyclic loading. The shear stresses that are developed in the subsoil due to cyclic loading cause shear strains and change in the mean normal stresses due to distortion of soil element. Biot's consolidation theory that adopted in this study may be able to take these changes into consideration. The results indicated that the excess pore water pressure increases with load cycles and finally, a steady state conditions are reached. This may be attributed to the undrained cyclic shearing stresses to the origin initial cyclic shear stress ratio. Also it can be explained that when the load is applied very fast the collapse load approaches that undrained conditions, whereas when the load is applied very slowly the collapse load approaches that under drained conditions. When the elastoplastic model is considered the pore pressure are considerably larger than those predicted by the elastic consolidation analysis. This can be attributed to the plastic volume strain that have been taken into consideration in the elastoplastic model.

الخلاصة:

الهدف من هذه الدراسة هو لايجاد طريقة عددية باستخدام العناصر المحددة لتحليل انظمام التربة مع الاخذ بنظر الاعتبار دورات التحميل واللاتحميل مع التركيز على تولد ضغط الماء المسامي. هذه الدراسة تتعامل مع دورات الحمل شبة المنحرفة. ان اجهادات القص المتولدة في التربة التحتية نتيجة دورات التحميل تسبب انفعالات قص وتغيير في معدل الاجهادات العمودية بسبب التشوه الحاصل بالتربة. نظرية Biot's لظاهرة الانضمام تم تبنيها في هذه الدراسة والتي بامكانها اخذ بنظر الاعتبار التغيرات الحاصلة في الانضمام . وقد اظهرت النتائج ان ضغط الماء المسامي يزداد مع دورات التحميل الى ان تصل الى حالة الثبوت. وهذا يعزى الى نسبة اجهادات القص المتكررة الي اجهادات القص الاولية. كذلك ان تسليط الحمل بسرعة يؤدي الي وصول الفشل في الحالة الغير مبزولة وعندما يسلط الحمل ببطء فان الفشل يصل الى الحالة المبزولة وعند استخدام نموذج المرونة-اللدونة فان ضغط الماء المسامي يكون اكبر منه في حالة استخدام نموذج المرونة لظاهرة الانضمام. وهذا يعزي الى انفعالات اللدونة الحجمية التي تاخذ بنظر الاعتبار في نموذج المرونة-اللدونة.

KEY WORDS:
Finite element; Biot's consolidation; trapezoidal loading; unload cycles; plasticity; pore pressure; subsoil; collapse load.

INTRODUCTION

An important subject in soil mechanics and geotechnical engineering is to analyze the deformation behavior of soils, which may be fully or partially saturated with water. The deformation is coupled with the generation of pore water pressure. This kind of behavior is generally called consolidation.

It is obvious that both quality and performance of roads and other geotechnical structures will largely depend on the mechanical behavior of subsoils, especially the time-dependent response under cyclic loading. Computer modeling with finite element method is one of the most popular numerical methods currently used in modeling response of road subsoil. In this paper the term subsoil means the natural soil below a road embankment, and the term embankment includes all soil layers above natural ground surface.

A large number of constitutive models have been proposed to describe the deformation behavior of soils. Most of these models can be classified into one of the following categories: elastic, elastoplastic, elasto-viscoplastic models. Among the elastoplastic models there are perfectly plastic, isotropic hardening and kinematic hardening models. Since the constitutive models presented in this study will be used mainly for analysis of soils under monotonic trapezoidal cyclic loading, the isotropic hardening models will suffice for the purpose.

Schiffman (1958) first obtained a general solution of soil consolidation considering loading increase linearly with time. ***Wilson and Elgohary (1974)*** presented an analytical solution of one-dimensional consolidation of saturated soil subjected to cyclic loading based on Terzighi's linear consolidation theory.

Alonso and Krizek (1974) considered the settlement of elastic soft soil under stochastic loading. ***Baligh and Levadoux (1978)*** developed a simple prediction method for one-dimensional consolidation of clay layer subjected to cyclic rectangular loading with the superposition principle.

More recently, ***Favaretti and Soranzo (1995)***, ***Guan et.al. (2003)*** derived some solution for different types of cyclic loading.

* BIOT CONSOLIDATION THEORY

Consolidation theory is the mathematical theory describing the dissipation of excess pore pressure and associated deformation of the soil ***(Lambe and Whitman, 1969)***. Most of the consolidation problems in two and three dimensions are analyzed based on two basic approaches. The first was developed from diffusion theory by Terzighi and Rendulic. The second was developed directly from elastic theory by Biot ***(Scott, 1978)***. In Biot consolidation theory the soil skeleton is treated as a porous elastic solid and the laminar porefluid is coupled to the solid by the conditions of compressibility and continuity ***(Smith and Griffithes ,1998)***.

Biot's covering equations for two or three dimensional consolidations theory is given by:

$$\frac{\partial u}{\partial t} = C_v \nabla^2 u + \frac{\partial \sigma_m}{\partial t} \qquad (1)$$

Where:

u : excess pore water pressure.

σ : mean normal stress = $\frac{1}{3}(\sigma_{xx}+\sigma_{yy}+\sigma_{zz})$

$\frac{\partial u}{\partial t}$: variation of pore pressure with time.

∇^2: Laplace's operator.

C_v: coefficient of consolidation.

Mandel (1953), showed the same behavior by solving Biot equations for a rectangular section with drainage permitted along both sides only ***(Scott, 1978)***.

Smith and Hoobbs(1976), implemented Biot's theory of consolidation by means of finite elements in the solution of field consolidation problems. The method allows for simultaneous changes in geometry, loading and material properties during and after construction and the calculated results are compared with field measurements.The shear stresses that are developed in the subgrade soil or subsoft soil due to cyclic trapezoidal loading cause shear strains and change in the mean normal stresses due to distortion of soil element. Biot's consolidation theory may be able to take these changes into consideration. For this reason this theory is adopted in the present study.

*** FINITE ELEMENT SOLUTION OF COUPLED PROBLEM:**

The finite element method is the most powerful technique for numerical analysis. It can be used to solve many classes of problems and also it can take into account both linear and non-linear material properties which may be formulated in terms of either total or effective stress ***(Scott, 1978)***.

In the analysis of Biot consolidation theory, the soil is treated as a porous elastic solid and the laminar pore fluid is coupled to the solid by the conditions of compressibility and continuity ***(Smith and Griffithes, 1998)***.

Thus the Biot's governing equation is given by:

$$\frac{K'}{\gamma_w}\left[k_x\frac{\partial^2 u_w}{\partial x^2}+k_y\frac{\partial^2 u_w}{\partial y^2}+k_z\frac{\partial^2 u_w}{\partial z^2}\right]=\frac{\partial u_w}{\partial t}-\frac{\partial p}{\partial t} \qquad (2)$$

Where:

K' : soil bulk modulus.

p : mean total stress.

Kx: permeability in the x-direction.

Ky: permeability in the y-direction.

Kz: permeability in the z-direction.

Due to coupling of fluid and solid phases the applied total stress (σ_t) are divided between a portion carried by the soil skeleton called the effective stress (σ') and a portion carried by the pore water called the pore pressure and denoted by (u_w).

In the absence of body forces, and for z- dimension problems, the equations to be solved are the following:

1) EQUILIBRIUM

The gradient of effective stress is given in equation below ***(Timoshinko and Goodier, 1970)***:

$$\frac{\partial \sigma_x}{\partial x}+\frac{\partial \tau_{xy}}{\partial y}+F_x=0$$

$$\frac{\partial \tau_{xy}}{\partial x}+\frac{\partial \sigma_y}{\partial y}+F_y=0 \qquad (3)$$

The gradients of the fluid pressure (u_w) are given as:

$$\frac{\partial \sigma'_x}{\partial x}+\frac{\partial \tau_{xy}}{\partial y}+\frac{\partial u_w}{\partial x}=0$$

$$\frac{\partial \tau_{xy}}{\partial x}+\frac{\partial \sigma'_r}{\partial y}+\frac{\partial u_w}{\partial y}=0 \qquad (4)$$

2) Constitutive Relation

The constitutive laws for the solid and fluid respectively, are shown below for plane strain **(Smith and Griffiths, 1998)**:

$$\begin{Bmatrix}\sigma_x\\ \sigma_y\\ \tau_{xy}\end{Bmatrix}=\frac{E}{1-\upsilon}\begin{bmatrix}1 & \upsilon & 0\\ \upsilon & 1 & 0\\ 0 & 0 & \frac{1-\upsilon}{2}\end{bmatrix}\begin{Bmatrix}\varepsilon_x\\ \varepsilon_y\\ \gamma_{xy}\end{Bmatrix} \qquad (5)$$

$$\begin{bmatrix}q_x\\ q_y\end{bmatrix}=\frac{1}{\gamma_w}\begin{bmatrix}k_x & 0\\ 0 & k_y\end{bmatrix}\begin{Bmatrix}\frac{\partial u_w}{\partial x}\\ \frac{\partial u_w}{\partial y}\end{Bmatrix} \qquad (6)$$

Where:

q_x, q_y : the volumetric flow rate per unit area into and out of the element.

γ_w : the unit weight of water.

In the case of incompressibility the out flow from an element of soil equals the reduction in volume of the element:

$$\frac{\partial q_x}{\partial x}+\frac{\partial q_y}{\partial z}=-\frac{\partial}{\partial t}\left(\frac{\partial u}{\partial x}+\frac{\partial w}{\partial y}+\frac{\partial v}{\partial \theta}\right) \qquad (7)$$

From (Eq.6), the third differential equation is given by:

$$\frac{k_x}{\gamma_w}\frac{\partial^2 u_w}{\partial x^2}+\frac{k_y}{\gamma_w}\frac{\partial^2 u_w}{\partial y^2}+\frac{\partial}{\partial t}\left(\frac{\partial u}{\partial x}+\frac{\partial w}{\partial y}+\frac{\partial v}{\partial \theta}\right)=0 \qquad (8)$$

The equilibrium and continuity equations for Biot consolidation are given by:

$$[KM]x+[C]u_w=f \qquad (9)$$

$$[C]^T\frac{\partial x}{\partial t}-[KP]u_w=0$$

Where:

(KM) and (KP) are the solid and fluid stiffness respectively.

For the same linear shape functions govern the variation of pore water pressure and displacements within an element, the connection coupling matrix C is given as shown **(Smith and Griffiths,1998):**

$$C = \iint vol * FUNxdxdy \qquad (10)$$

Where:

FUN : array held the shape function in terms of local coordinates.

Vol : volumetric strain vector of an element.

The matrix product is called VOLF and C is numerically integrated as:

$$C = \sum_{I=1}^{NIP} DET_I * weights(i) * VOLF_I * R \qquad (11)$$

Where:

NIP : is the number of integrated points.

DET : is the determinant of Jacobian matrix.

Weights(I) : is the weighting coefficient corresponding to the particular integrating point.

R : the radial coordinate of each Gauss point.

After assembly into global matrices, equation (9) must be integrated in time using finite differences method as shown by:

$$\theta KMx_1 - \theta Cu_{w1} = (\theta - 1)KMx_0 + (\theta - 1)Cu_{w0} + f \qquad (12)$$

$$\theta C^T x_1 - \theta^2 \Delta tKPu_{w1} = \theta C^T x_0 - \theta(\theta - 1)\Delta tKPu_{w0}$$

Where:

f : is the total force applied

θ : parameter in implicit time-stepping $(\frac{1}{2} \le \theta \le 1)$.

* EXPERIMENTAL WORK

Undrained Triaxial Test

In undrained triaxial test the vertical and horizontal stresses are kept constant, after an initial shear stress, q has been applied. The properties of soil specimen are shown in Table (1), Under relatively small applied shear stresses (about 30% of the shear strength as determined in conventional tests) the creep movements are small while the excess pore water pressure increases. Under shear stresses of still higher intensity, an acceleration of the creep rate takes place followed by complete failure of the specimen (creep rupture).

As for the constant strain rate tests, the triaxial test had been completed by initially consolidating the samples under an effective confining pressure of 525 kPa and the test were performed at the constant shear stress of q=278.3 kPa. The results of the triaxial test were obtained and used for verification of the finite element program ***(ZCONS)***.

A comparison is made between the results obtained by the present finite element analysis and the triaxial test results. A good agreement is indicated as shown in Fig. (1).

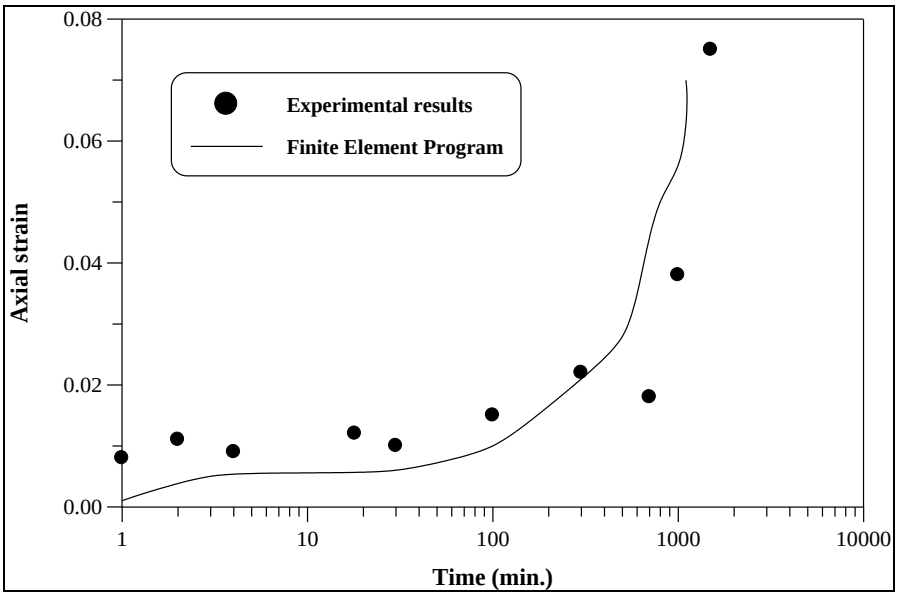

Fig. 1 Verification of Finite Element Computer Program ZCONS.

* RESULTS AND DISCUSSIONS

Finite Element Program

The computer oriented finite element method has become one of the most powerful tools in the analysis of the engineering problems. It has unified the analysis of any type of structures under boundary and loading conditions to one basic fundamental procedure. To carry out the analysis of this study, the finite element program ZCONS written in Fortran 90 language is developed. Which is primarily based on the program presented by (AL-Kaissi, 2001) for the analysis of elasto plastic constitutive relations. Extensive modifications and newly added subroutines are found necessary to incorporate the case study. ID program is divided into ten major parts with subroutine hierarchy ,as shown in Appendix (A). The basic finite steps are performed by primary subroutines, which rely on auxiliary subroutines to carry out secondary operations. An auxiliary subroutine may be required by more than subroutine, as shown in Appendix (A). The order of calling of the primary subroutine is controlled by a main or master routine.

The finite element program is utilized in conjunction with Biot's consolidation theory and the soil is treated as an elasto-plastic material basing on Mohr-Coulomb failure criterion. A quadrilateral hybrid element eight nodded regarding displacement four nodded for pore water pressure is adopted in the present analysis. The finite element method has been used together with Crank-Nicolson time discrietization and constant time steps. The displacement, rate of consolidation and pore pressure are evaluated by means of computer program which is modified to suit the objectives of this study.

CASE STUDY

Application of the proposed finite element program to a case study, the values of soil parameters used in the analysis where obtained from previous study presented by (Mannesmanne, 1974) regarding the soil investigation report about the Fao region in the far south part of Iraq. Table (1) displays the parameters regarding the clay layer and the finite element mesh used for analysis is shown in Fig. 2.

Table 1. Material Properties of the Soil.

Soil Parameters	Silty Clay
E(kN/m^2)	2108
ν	0.35
k_x (m/day)	4.33×10^{-4}
k_y (m/day)	8.67×10^{-6}
C (kN/m^2)	9.2
ϕ'	30.0
ψ'	0.0

This study deals with the generation and dissipation of pore water pressure and the rate of consolidation under loading and unloading cycle and their influences in the subsoils layer. This paper presents the finite element numerical procedure to study the consolidation problem by taking into consideration the loading and unloading cycles with particular emphases on the pore pressure built up. The model used to simulate this problem assumes a soil stratum with thickness H, vertical and radial permeability coefficient k_x, k_y as shown in Table (1) with the others parameters regarding the clay layer that have been used in the finite element program ***ZCONS***.

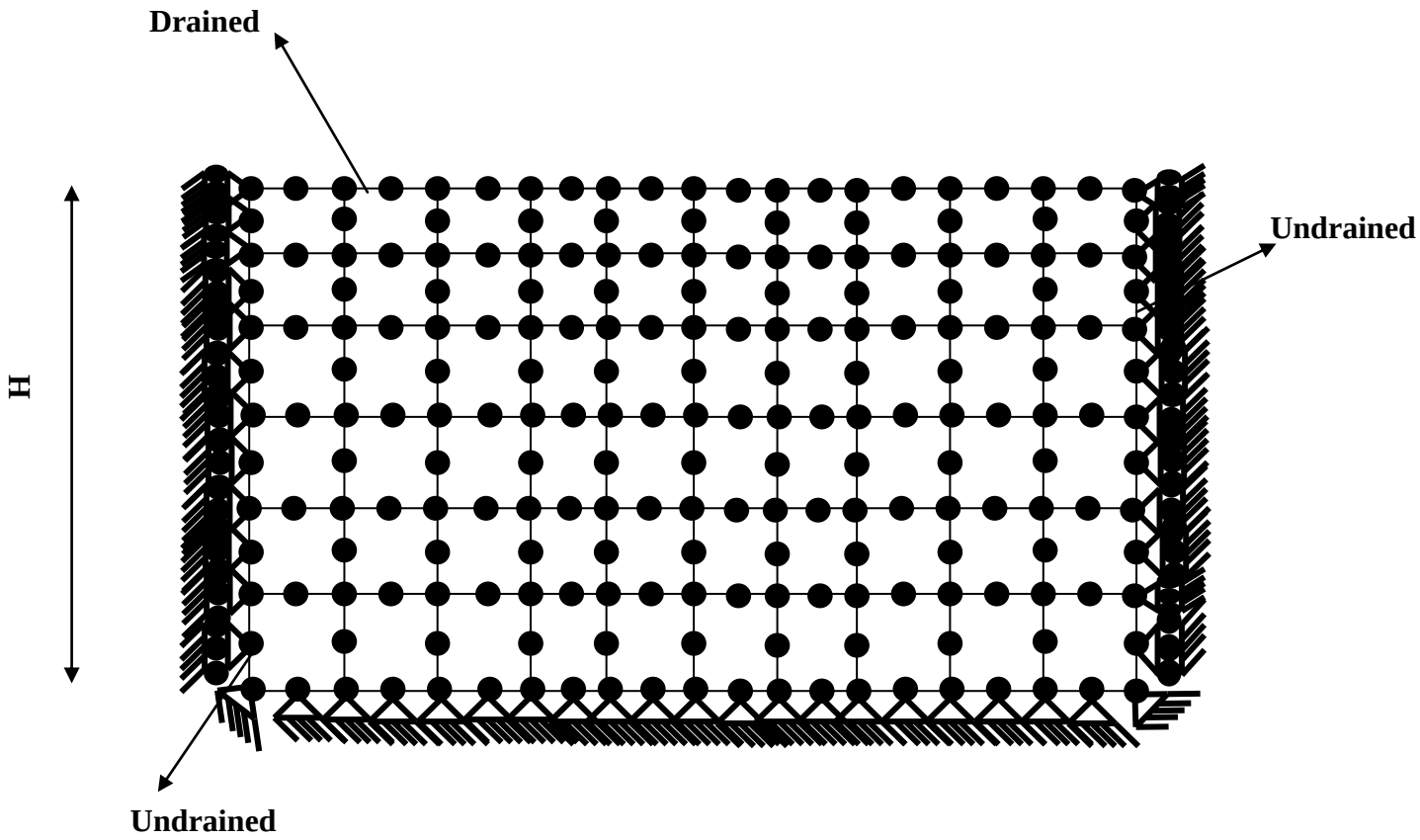

Fig. 2 The Finite Element Mesh.

The soil layer is subjected to a vertical trapezoidal loading as shown in Fig. (3), also the rectangular cyclic loading also considered in this study. In which q_0 is the maximum load, t_L is cyclic loading time. Fig. (4) shows the variation of consolidation with load cycles (loading and unloading). It can be seen from this figure, that for a given load cycle, the degree of consolidation for each cycle reaches the maximum value at the end of the constant loading phase and the minimum value at the beginning of the next cycle (i.e. at the end of the unloading cycle).

In Fig. (5) the effect of loading type is shown. The influence of loading type on consolidation process, from which it can be seen that it more significant for trapezoidal loading. (Since it simulate the actual traffic loading on soil). Fig. (6) was plotted to investigate the influence of construction time on consolidation, here Tv time factor is varying, it can be seen that the longer the construction time which means the greater time factor, the slower the rate of consolidation.

Also Fig. (7) presents the excess pore water pressure distribution with depth at maximum applied load of one cycle for different number of load cycles. We obtain from this figure that pore pressures build up increase. Additionally, a steady state conditions is reached between cycles (4) to (7). Since the excess pore water pressure is affected by changes in mean total stress, it may continue to increase for some time after the application of load cycle. This may be attributed to the undrained cyclic shearing stresses with the origin initial cyclic shear stress ratio, where shear stress ratio is defined as the cyclic shear stress on the horizontal plane over the initial vertical stress.

Figs. (8) and (9) show the analysis of collapse load response with the axial deformation. For the applied stress or load on the soil, the load is assumed to be as shown in Fig. (3).

At some given rate of loading, this is defined as:

$$\omega = \frac{dq}{dTv} \qquad (13)$$

Where Tv is the non-dimensional time factor, with H (one way drainage conditions) being the drainage length. And different values are used to obtain different rates of loading.

The collapse load under drained and undrained conditions can be estimated. The load deformation curves obtained for two different loading rates are shown in Fig. (8) and (9). From these figures it can obtained that when the load is applied very fast the collapse load approaches that undrained conditions, where as the load is applied very slowly the collapse load approaches that under drained conditions.

To study the effects of plasticity model of soil on consolidation analysis, elastic and elastoplastic consolidation model are compared as shown in Fig. (10) and (11) respectively.

From these figures it can be seen that when the elastoplastic model is considered the pore pressure are considerably larger than those predicted by the elastic consolidation model analysis as shown in Fig. (10), which may be attributed to the plastic strain that have been taken into consideration in the elastoplastic model.

Also Fig. (11) shows that the rate of consolidation takes a longer time to complete when the nonlinear elastoplastic model is considered.

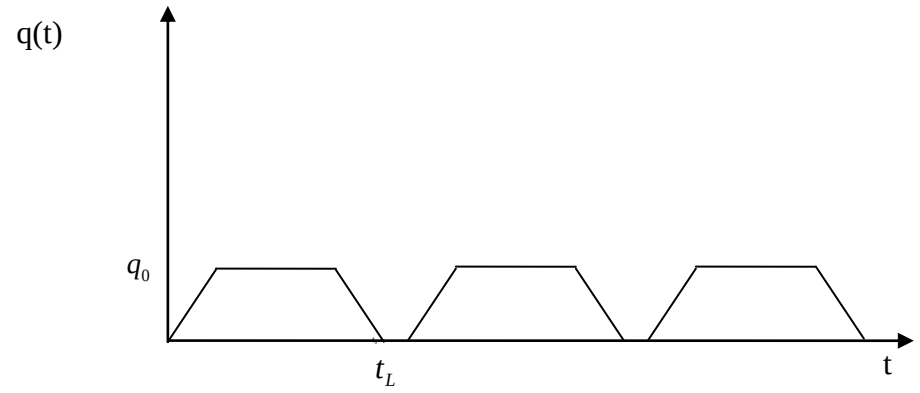

(a) Trapezoidal, t_L :time of loading

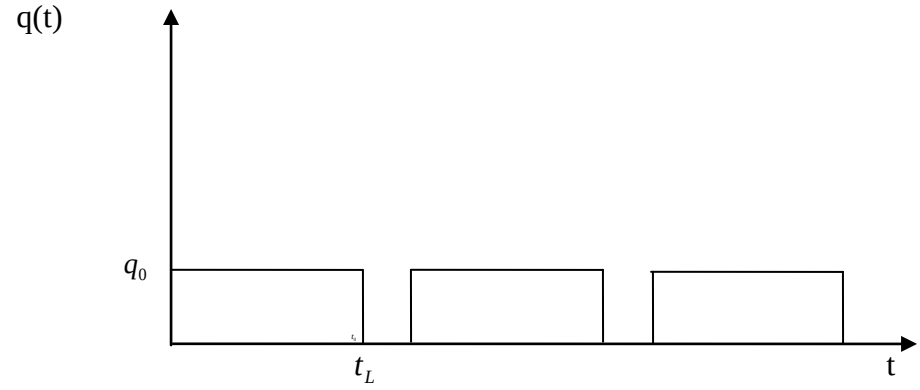

(b) Rectangular

Fig. 3 Loading Types: a) Trapezoidal loading
b) Rectangular loading

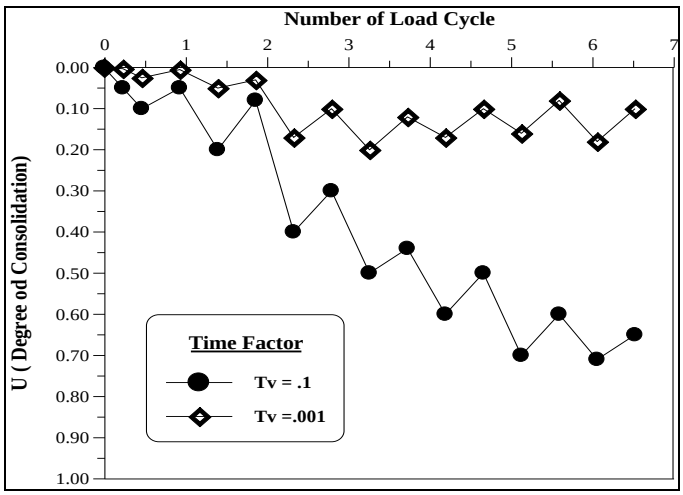

Fig. 4 Variation of Degree of Consolidation with Load Cycles.

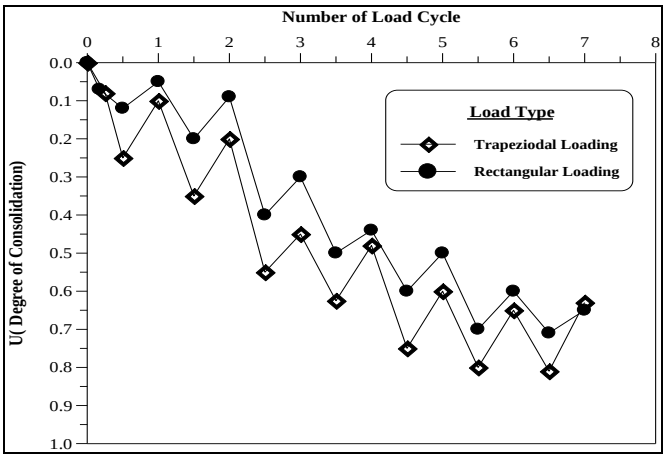

Fig. 5 Effect of Loading Type on Rate of Consolidation.

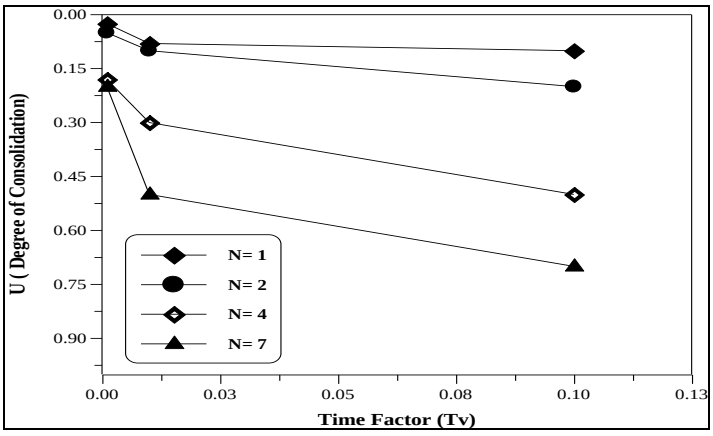

Fig. 6 Effect of Time Factor on Consolidation Rate for different number of load cycles)

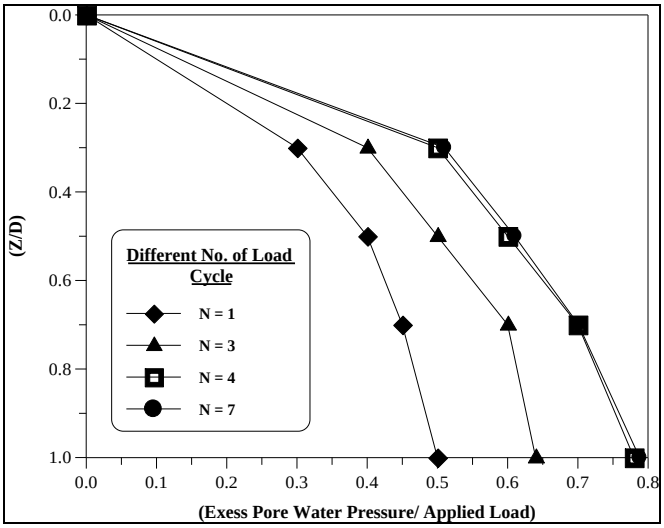

Fig. 7 Distribution of Excess Pore Water Pressure with Depth for Different Load Cycles.

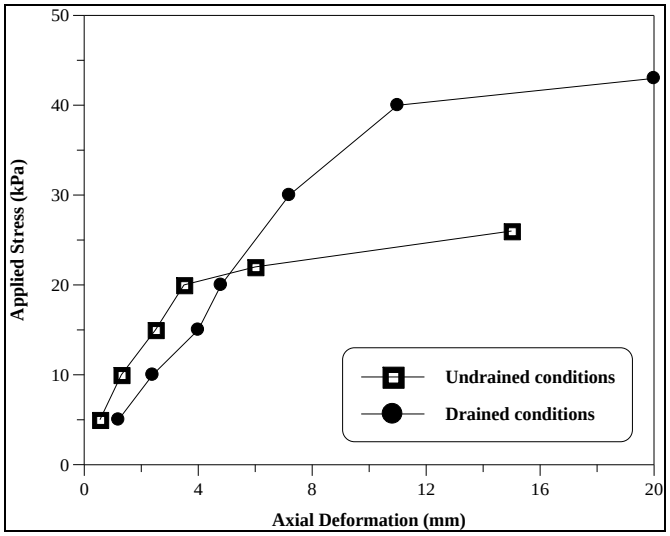

Fig. 8 Response of Collapse Load at fast rates of Loading and under the loading center.

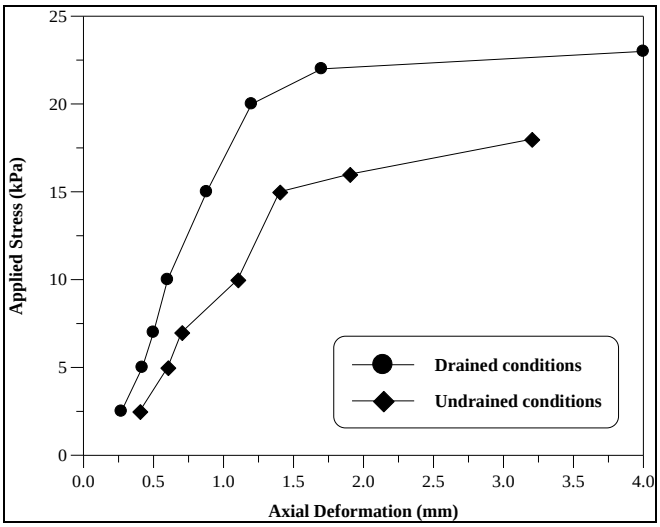

Fig. 9 Response of Collapse Load at slow rate of Loading.

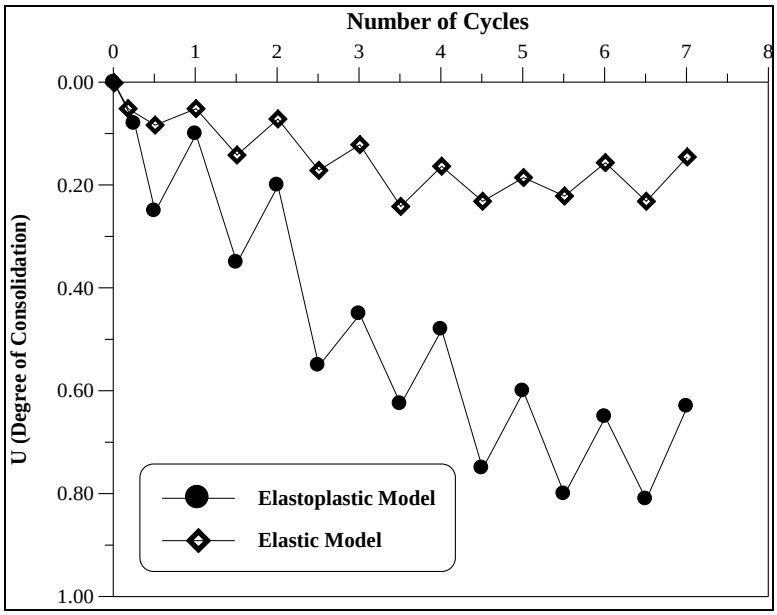

Fig. 10 Comparisons of Consolidations for Two Models.

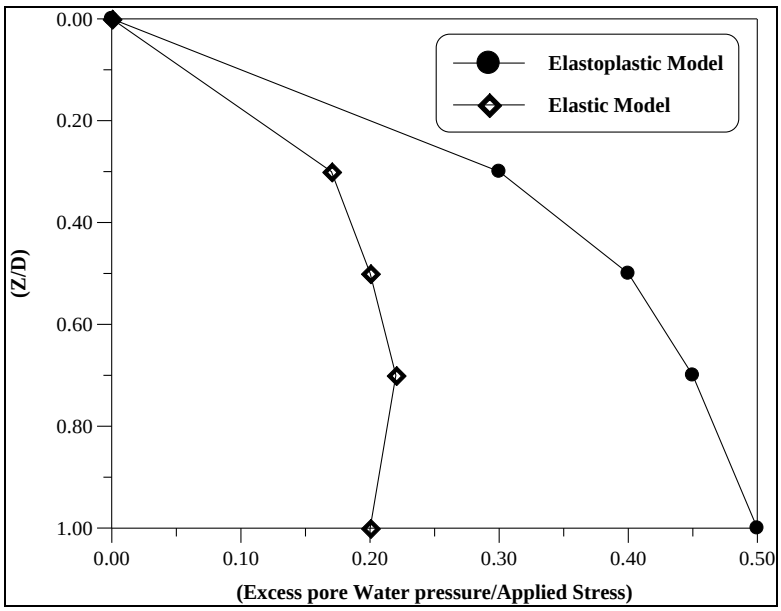

Fig. 11 Comparisons of Pore water Pressure for Two Models.

* CONCLUSIONS

The main conclusions that can be drawn from this study are the following:

1. For a given load cycle, the degree of consolidation for each cycle reaches the maximum value at the end of the constant loading phase and the minimum value at the beginning of the next cycle (i.e. at the end of the unloading cycle).
2. The excess pore water pressure increased with load cycles and finally, steady state conditions are reached between cycles 4 to 7. Since the excess pore water pressure is affected by changes in

mean total stress, it may continue to increase for some time after the application of load cycle. This may be attributed to the undrained cyclic shearing stresses with the origin initial cyclic shear stress ratio, where shear stress ratio is defined as the cyclic shear stress on the horizontal plane over the initial vertical stress.

3. The loading type affects the consolidation process, from results it can be seen that it is more significant for trapezoidal loading. (Since it simulate the actual repeated traffic loading on soil).
4. Analysis on collapse load has been carried out, it can be obtained that when the load is applied very fast the collapse load approaches that undrained conditions, where as the load is applied very slowly the collapse load approaches that under drained conditions.
5. When the elastoplastic model is considered the pore pressures are considerably larger than those predicted by the elastic consolidation model analysis. This can be attributed to the plastic volume strain that have been taken into consideration in the elastoplastic model. Also the rate of consolidation takes a longer time to complete when the nonlinear elastoplastic model is considered.

REFERENCES

. Alonso, E.E., and Krizek, R.J. (1974): "Randomness of Settlement Rate under Stochastic Load". Journal of Geotechnical Division, ASCE, 100(EM6):1211-1226.

. Al-Kaissi, Z.A (2001): "Behavior of Friction Piles in Clay". M.Sc. Thesis, Al-Nahrain University, College of Engineering.

. Baligh, M.M., Levadoux, J.N. (1978): "Consolidation Theory of Cyclic Loading". Journal of Geotechnical Engineering Division, ASCE, 104(GT4):415-431.

. Chen, J.Z., Zhu,X.R., Xie,K.H., Zeng, G.x. (1996): " One Dimensional Consolidation of Soft Clay under Trapezoidal Cyclic Loading". Proc. Of the Second International Conference on Soft Soil Engineering, Nanjing, p.211-216.

. Favaretti, M., Soranzo, M. (1995): "A Simplified Consolidation Theory in Cyclic Loading Condition". Proc. of Int. Symposium on Compression and Consolidation of Clayey Soils, Japan, p.405-409.

. Guan, S.H., Xie,K.H., Hu, A.F. (2003): " An Analysis on One Dimensional Consolidation Behavior of Soils under Cyclic Loading". Rock &Soil Mechanics, 24(5):849-853.

. Lambe, T.W., and, Whiteman, R.V. (1969): "Soil Mechanics". John Wiley and Sons Inc., New York.

. Mannesmanne, (1974): "The report of Settlement Survey during Construction and Water Filling Test".

. Schiffman, R.L. (1958): "Consolidation of Soil under Time-Dependent Loading and Varying Permeability". Proceedings, Highway Research Board, Washington, 37:584-617.

. Scott, C.R. (1978): "Developments in Soil Mechanics". Applied Science Puplishers Ltd., London.

. Smith,I.M., and, Hoobs, R. (1976): "Biot Analysis of Consolidation beneath Embankments". Geotechnique, Vol.26, No.1, pp.149-171.

. Smith, I.M., and, Griffiths, D.V. (1998): "Programming the Finite Element Method". Second Edition, John Wiley and Sons Ltd.

. Timoshinko, S.P., and Goodier, J.N. (1970): "Theory of Elasticity". Third Edition, Mc Graw-Hill Book Company, Inc. New York.

. Wilson, N.E., Elgohary,M.M. (1974): "Consolidation of Soils under Cyclic Loading". Canadian Geotechnical Journal, 11(3):420-423.

List of Symbols

Symbols	Description
E	Modulus of elasticity
ν	Poisson's ratio
C	Cohesion
C_v	Coefficient of consolidation
u_w	Excess pore water pressure
σ_m	Mean normal stress
∇^2	Laplace's operator
K'	Soil bulk modulus
q_x, q_y	Volumetric flow rate per unit area
k_x, k_y	Permeability in x, y direction
γ_w	Unit weight of water
$[KM], [KP]$	Solid and fluid stiffness matrices
FUN	Array held the shape function
VOL	Volumetric strain vector of an element
DET	Determinant of Jacobian matrix
NIP	Number of Gauss
θ	Parameter in implicit time-stepping
Δt	Time interval
$\sigma_x, \sigma_y, \sigma_z$	Total normal stress in x,y and z direction
τ	Shear stress
ϕ'	Angle of shearing resistance
ψ'	Angle of dilation

Appendix A
Flow Chart of Computer Program (ZCONS)

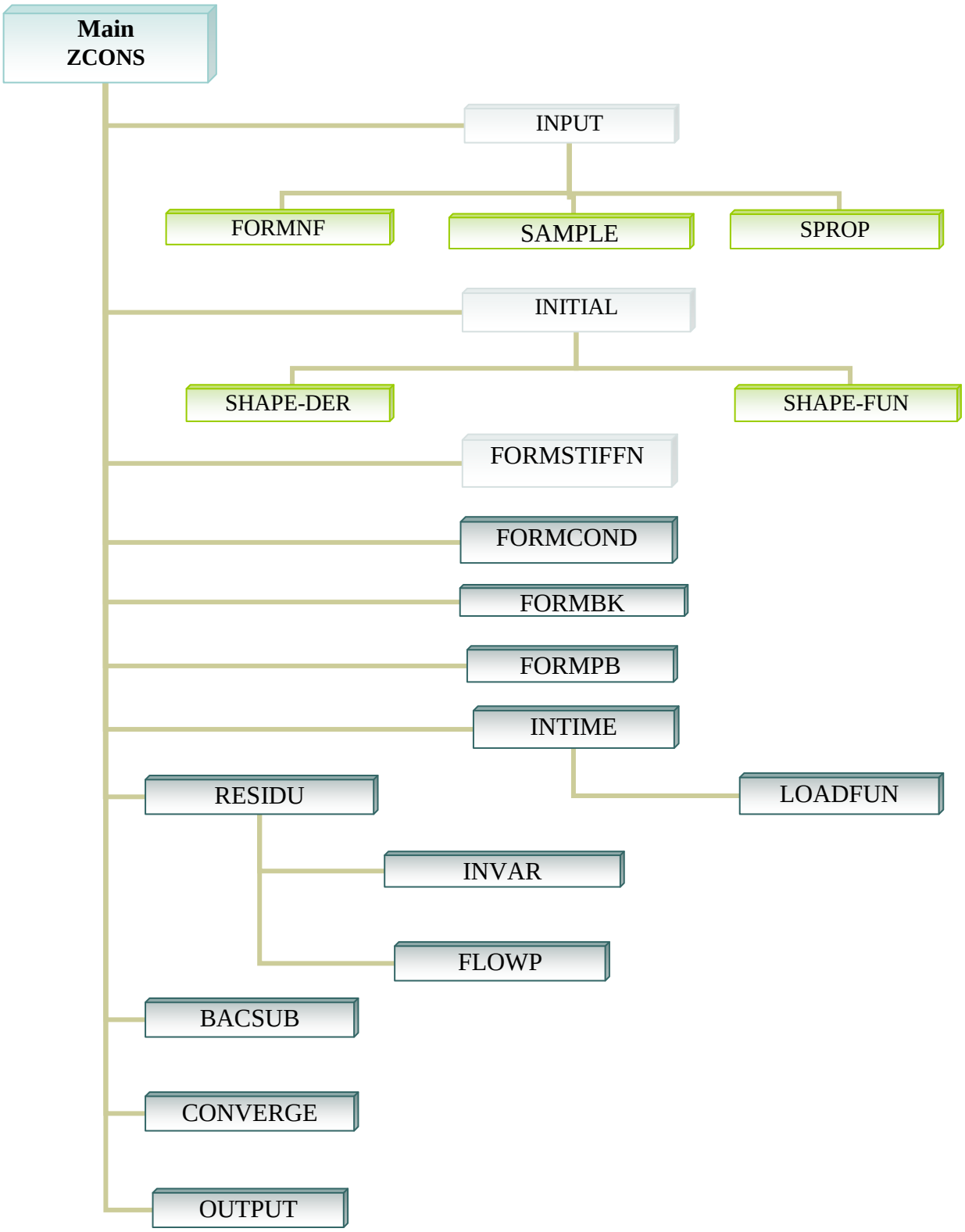

انتاج خرسانة عالية الاداء باستخدام انواع مختلفة من البوزولانات المحلية

ندى مهدي فوزي علياء فالح حمد
القسم المدني-كلية الهندسة-جامعة بغداد

الخلاصة

تعتبر الخرسانة عالية الاداء واحدة من اهم المنتجات التي شهدتها الصناعة الانشائية في السنوات الاخيرة في مجال انتاج انواع جديدة ومتطورة من الخرسانة. وان لهذا النوع الجديد من الخرسانة اهمية بالغة لما لها من خواص عالية من ناحية مقاومة الانضغاط والديمومة ومقاومة مهاجمة الاملاح الخارجية حيث لها نفاذية واطئة للغاية.

يتناول هذا البحث تجارب مختبرية لتقييم أداء خرسانة عالية الأداء بإستخدام نوع جديد من البوزولان المتوفر محليا مثل الميتاكاؤولين وخبث الافران ومقارنة تأثير إضافته مع أنواع أخرى من البوزولان المعروفة مثل دقيق السليكا. كأمكانية تنشيطها لتحسين نوعيته وتشمل التجارب دراسة المادة من حيث التحليل الكيمياوي وايجاد النسبة المثلى للإضافة ومدى تأثيرها على الخواص الميكانيكية وخواص الخرسانة في الحالة الطرية والمتصلبة وتأثير المضاف على الانكماش والتي تعطي فكرة عن ديمومة الخرسانة.

ABSTRACT

High Performance Concrete (HPC) is considered as one of the most important products known by the construction industries during the last years in the field of producing new and improved types of concrete. This new type of concrete has an essential importance due to its high compressive strength, superior resistance for external salt attack and its low permeability.

This paper is concerned with experimental investigations for evaluation of high performance concrete using a new type, locally available pozzolan. The results are compared with that obtained from using well known micro silica. The experimental work also includes the possibility of activation in order to improve the quality of HPC; the experiments mainly deal with the chemical analysis and the selection for the optimum dosages of additive. The properties of HPC are studied in both fresh and

hardened stages. The effect of pozzolan additive on shrinkage was also considered to provide an index for the durability of concrete.

ـ المقدمة

البوزولانا POZZOLANA

تعريفها

البوزولانا هي مواد سليكونية او سليكونية والومينية لا تملك لوحدها خواص أسمنتية او قد تكون ذات خواص أسمنتية قليلة ولكن عندما تكون بدرجة عالية من النعومة وبوجود الرطوبة تتفاعل كيميائيا مع هيدروكسيد الكالسيوم بدرجات الحرارةالاعتيادية لتكون مركبات ذات خواص أسمنتية او هي سليكات او الومينات نشطة تخلط مع الاسمنت او الجير (النورة) وتكسب الخرسانة مقاومة أضافية ضد هجوم الأملاح الكبريتية [1].

والمواد البوزولانية تتفاعل مع اوكسيد الكالسيوم الحر الناتج من تفاعل السمنت مع الماء مكونة مركبات غير قابلة للذوبان مثل سليكات والومينات الكالسيوم والتي تعمل على سد الفجوات الداخلية والمسام الشعرية ومن امثلتها الميتاكاؤولين ودقيق السليكا وخبث الافران المستعملة في هذا البحث.

تطبيقات البوزولانا

يمكن استخدام المواد البوزولانية بأنواعها المتعددة لإغراض مختلفة وذلك في الخرسانة وهذه بعض التطبيقات لمضاف البوزولانا

1- خبث الفرن العالي : يستخدم كمضاف في الخرسانة الكتلية وكمادة أولية في تصنيع الاسمنت البوروتلاندي. يتكون الخبث من اربعة اكاسيد رئيسية مطابقة للاكاسيد الموجودة في مادة السمنت ولكن بنسب مختلفة واشكال بلورية مختلفة وهي السليكا والالومينا والموجودة في تراب الحديد واكاسيد الكالسيوم والمغنيسيوم ومصادرها المواد المساعدة للصهر [3,2]

ان الخبث في العراق ينتج من افران القوس الكهربائي من مخلفات صناعة الحديد، وخواص الخبث الناتج وفعاليته الكيميائية تعتمد على طريقة معالجة منصهر الخبث حين خروجه من الفرن.

2- الميتاكاؤولين : هي اطيان معدنية منشطة بدرجات حرارية (650-800)^0 م وتحتوي في تركيبها الكيمياوي على السليكا والالومينا ويكون تفاعل هذه المادة في الخرسانة كما يلي

$$C3S/C2S+H2O = Calcium\ Silicate\ Hydrates(C\text{-}S\text{-}H) + Ca(OH)2$$

$$Ca(OH)2+MK + (C\text{-}S\text{-}H)$$

3- دقيق السليكا: تعتبر من المواد البوزولانية العالية الفعالية وهي ناتج عرضي من افران القوس الكهربائي في صناعة معادن السليكون او سبائك الحديد والسليكون ، وهي عبارة عن حبيبات كروية الشكل غير متبلورة ذات مقاس 0.1 مايكرون[4] وللسليكا اهمية كبيرة في انتاج الخرسانة حيث انها تتفاعل مع هيدروكسيد الكالسيوم الناتج من اماهة C3S,C2S لتكون جل سمنتي يعمل على تقليل سمك الطبقة البينية الموجودة بين السمنت والركام مما يزيد من مقاومة انضغاط الخرسانة.

- دراسات سابقة

هناك العديد من الدراسات والبحوث التي تناولت موضوع المضافات الخرسانية وبالاخص المضافات البوزولانية وتأثيراتهما على الخرسانة ،وكانت هذه الدراسات أما متعلقة بالمضافات البوزولانية لوحدها او تشمل معها مضاف او مضافات اخرى ويتم عمل المقارنات بين نتائج التأثير الفردي والمشترك لهذه المضافات على الخرسانة عند الاستخدام . وتكون الدراسة ذات طابع عام او طابع محلي تحت ظروف معينة حسب خصائص كل بلد .

ومن هذه الدراسات المحلية درس محمد مصلح[5] في عام 1987 تأثير اضافة بعض المواد المحلية على التغيرات البعدية والتشقق في الخرسانة وعنيت هذه الدراسة بمضافي الجبس والبوزولانا وتناولت تأثيراتهما على الخرسانة .
ومن أهم الاستنتاجات هو **ان** مضا ف البوزولانا او البوزولانا مع الجبس الى الاسمنت عموما تعمل على تقليل مقاومة الانضغاط في الاعمار المبكرة ، ولكن مع الاستمرار بعملية الإنضاج بالماء لفترات طويلة سوف يحسن مقاومة الانضغاط للخرسانة مع المضافات .

واستخدم(Justice.J.M.et al) [6] نوعين من الميتاكاؤولين بمساحة سطحية مختلفة (11.1 و 25.4 م^2/غم)وبين بان النوعين من البوزولانا الناعمة جدا تعمل على تحسين خواص الخرسانة ومقارنتها مع اداء دقيق السليكا في تحسين خواص الخرسانة.

ودرس Jianxin [7] الخرسانه ذات الاداء العالي والتي تصل مقاومة الانضغاط الى 150 ميكا باسكال بسبب اضافة مواد مثل السيليكا والتي تعمل على تحسين الخواص الفيزياويه للخرسانه وذلك بتقوية المنطقه الفاصله بين المادة المالئه والركام وبالتالي الحصول على كثافات عاليه
كما ذكر Mehta[8] ان الملدنات المتفوقة تمتلك شحنات سالبة قوية تؤدي الى تنافر عالي يساعد في تقليل الشد السطحي لجاذبية الماء وعليه يعزز بشكل كبير انسيابية النظام وبنفس الوقت فان كمية الماء المطلوبة للحصول على قابلية تشغيل معينة تكون قليلة.

-المواد المستعملة والتجارب المختبرية

المواد المستعملة :-

1- السمنت :- استخدم السمنت البورتلاندي الاعتيادي من انتاج لبنان علامة ترابة السبع ويبين الجدول (3-1) التحليل الكيمياوي للسمنت البورتلاندي والجدول (3-2) يبين الفحوصات الفيزياوية للسمنت.

2- الماء : استخدم ماء الإسالة في جميع الفحوصات المختبرية .

3-الركام الناعم :- استخدم الرمل النهري المأخوذ من مقالع منطقة العسيلة ويبين الجدول (3-3) الفحوصات الخاصة بالرمل المستعمل.

4- **الركام الخشن :-** يستعمل الركام النهري المكسر ويبين الجدول (3-4) فحوصات الركام الخشن المستعمل .

5- الملدن المتفوق :الملدن المتفوق المستعمل في هذا البحث لتقليل الماء بدرجة متفوقة من النوع ايكوبيت VZ من انتاج شركة الكيمياويات السويسرية مطابق للمواصفة الامريكية ASTM C494 Type G

6-المواد المضافة المستعملة:

أستعملت ثلاثة أنواع من المضافات هي المايكروسليكا مستوردة وخبث الافران ومتوفر في العراق في الفرن الكهربائي لمصانع صهر الحديد والميتاكاوؤلين وهو من منطقة ارضمة قرب الانبار .ويبين جدول (3-5) التحليل الكيمياوي لكل من هذه المواد المضافة المستعملة في البحث .

التجارب المختبرية:-

1- معامل الفعالية البوزولانية للمايكروسليكا وخبث الافران والميتاكاؤولين :-

تم أستعمال المواد البوزولانية التالية (المايكروسليكا وخبث الافران والميتاكاؤولين)وهي مطابقة للمواصفة الامريكية ASTM C 618 [9]كاستبدال جزئي للسمنت البورتولاندي الاعتيادي ،وتم فحص الفعالية البوزولانية بموجب المواصفة الأمريكية ((ASTM C(311-02)[10] وكانت النتائج كما في الجدول (3-6) .

2- **تصميم الخلطة الخرسانية** : تم تصميم الخلطة الخرسانية بموجب المواصفة الامريكية ACI 211 [11] وكانت نسب الخلط (1: 1.75:1.25) وبنسبة ماء الى سمنت 0.28 وذلك باستخدام الملدن المتفوق لجميع الخلطات. ومحتوى سمنت 400 Kg/m3 للحصول على مقاومة انضغاط بمقدار 70 ميكاباسكال وهذه هي الخلطة المرجعية للمقارنة مع بقية الخلطات ,أما الخلطات الاخرى فتمت بنفس الطريقة السابقة مع إضافة (5 ،10)% من المواد البوزولانية التالية (المايكروسليكا ،خبث الافران ،والميتاكاؤولين).

3- مقاومة الانضغاط :-تم اعداد مكعبات بابعاد (15x15x15)cm من الخرسانة باستعمال نسب مختلفة من الاستبدال الجزئي للمواد المضافة وتم فحص مقاومة الانضغاط لهذه النماذج ويبين الجدول (3-7) نتائج هذه الفحوصات .

4- معاير الكسر :-تم اعداد نماذج موشورية بابعاد (10*10*50) cm من الخرسانة ويبين الجدول (3-7) نتائج هذه الفحوصات .

5- فحص الذبذبات فوق الصوتية :-تم فحص النماذج الموشورية المعدة لفحص معاير الكسر وكذلك تم فحص النما ذج المعدة لفحص مقاومة الانضغاط بفحص الذبذبات فوق الصوتية بجهاز (PUNDIT) لايجاد سرعة مرور الذبذبات فوق الصوتية خلال النماذج وكذلك فحص كثافة كل نموذج وكانت معدل هذه النتائج مبينة في الجدول (3-7) .

6- يمكن ايجاد E_D من معادلة رقم (1) [12]

$$E_D=22+2.8\sqrt{F_{cu}} \quad \text{----------(1)}$$

حيث أن
F_{cu} : مقاومة الانضغاط بوحدة الميكاباسكال
E_D : معامل المرونة الديناميكي بوحدات الكيكاباسكال

جدول(3-1) التحليل الكيماوي للسمنت البورتلاندي الاعتيادي*

اسم الاوكسيد	المحتوى%	حدود المواصفة العراقية م.ق.ع رقم 1984/5
CaO	64.1	
SiO2	21.0	
Al2O3	4.6	
Fe2O3	3.0	
MgO	2.4	حد أعلى 5 %
SO3	2.7	حد أعلى 2.8 %
Na2O	0.4	
K2O	0.2	
L.O.I	1.5	حد أعلى 4%
C3S	58.9	
C2S	15.8	
C3A	7.0	
C4AF	9.1	

*تم الفحص الكيمياوي في التقييس والسيطرة النوعية

الفحوصات			التدرج المطلوب بموجب المواصفة العراقية (أ ق ع 1984/45)			
1-التدرج	العابر%	فتحة المنخل	منطقة تدرج رقم (1)	منطقة تدرج رقم (2)	منطقة تدرج رقم (3)	منطقة تدرج رقم (4)
	100	10	100	100	100	100
	97.58	4.75	100-90	100-90	100-90	100-95
	89.91	2.36	95-60	100-75	100-90	100-95
	80.4	1.18	70-30	90-55	100-85	100-90
	66.3	0.6	34-15	59-35	79-60	100-80
	22.00	0.3	20-5	30-8	40-12	50-15
	7.89	0.15	10-0	10-0	10-0	15-0
2- الأملاح so3الكبريتية	0.1		حد أعلى 0.5%			

جدول (3-2) الخواص الفيزياوية للسمنت البورتولاندي الاعتيادي

جدول (3-3) تدرج الركام الناعم

الخواص	النموذج المستعمل	المواصفة رقم 5 لسنة1984
النعومة (سم2/غم) (بطريقة blaine)	3500	لاتقل عن 2300
زمن التماسك الابتدائي (دقيقة) النهائي (ساعة)	60 دقيقة 6.30 ساعة	لا تقل عن 45 دقيقة لا تزيد عن 10ساعة
مقاومة الانضغاط (Mpa) بعمر3 أيام بعمر7 أيام	20 32	15 23

جدول (3- 4) تدرج الركام الخشن

الفحوصات			حدود المواصفة العراقية رقم 45 لسنة 1984	
1- التدرج	العابر %	فتحة المنخل	(5-20) mm	(5-40) mm
	100	37.5	100	100-95
	90.0	20	100-95	60-35
	39.84	10	55-25	40-10
	0.75	4.75	10-0	10-0
2- الأملاح الكبريتية so3	0.02		حد أعلى % 0.1	

جدول (3-5) التحليل الكيماوي للمايكروسليكا وخبث الافران والميتاكاؤولين المستعمل في البحث

اسم الاوكسيد	%المايكروسليكا	%خبث الافران	% الميتاكاؤولين
SiO2	93	32	51.34
Al2O3	0.06	25	41.8
Fe2O3	0.45	2	0.52
CaO	0.5	35	0.34
L.O.I	2.2	1.5	0.72

جدول (3-6) معامل الفعاليه للمواد المستعمله

نوع الخلطة	مقاومة الانضغاط (MPa)			معامل الفعالية بموجب ASTM C(311-02)
	بعمر28يوم	بعمر 60	بعمر90يوم	
الخلطة المرجعية (مونة سمنتية)	30	37	43	100
مونة مايكروسليكا (MS)	32,4	44	53	108
مونة خبث الافران (S)	31,5	40	50	105
مونة ميتاكاؤولين (MK)	34,5	47	58	115

جدول (3-7) نتائج الفحوصات المختبريه

رقم الخلطة	المايكروسليكا (%)	خبث الأفران (%)	الميتاكاؤولين (%)	معدل مقاومة الانضغاط (MPA)		معاير الكسر (MPA)	نسبة الامتصاص (%)	معدل سرعة الذبذبات فوق الصوتية Km/sec	معامل المرونة (E) (Gpa)
				بعمر 28 يوم	بعمر 90 يوم				
1	0	0	0	72	78	7.3	10.2	4.5	45
	5	0	0	85	100	12	7.1	4.9	48
	10	0	0	93	110	14.8	5.2	5.0	50
2	0	5	0	80	90	11	8.1	4.6	46
	0	10	0	88.5	96.5	13.5	7.2	4.8	47
3	0	0	5	87	100	15	6.1	4.9	49
	0	0	10	95	110	16.5	5.0	5.0	51

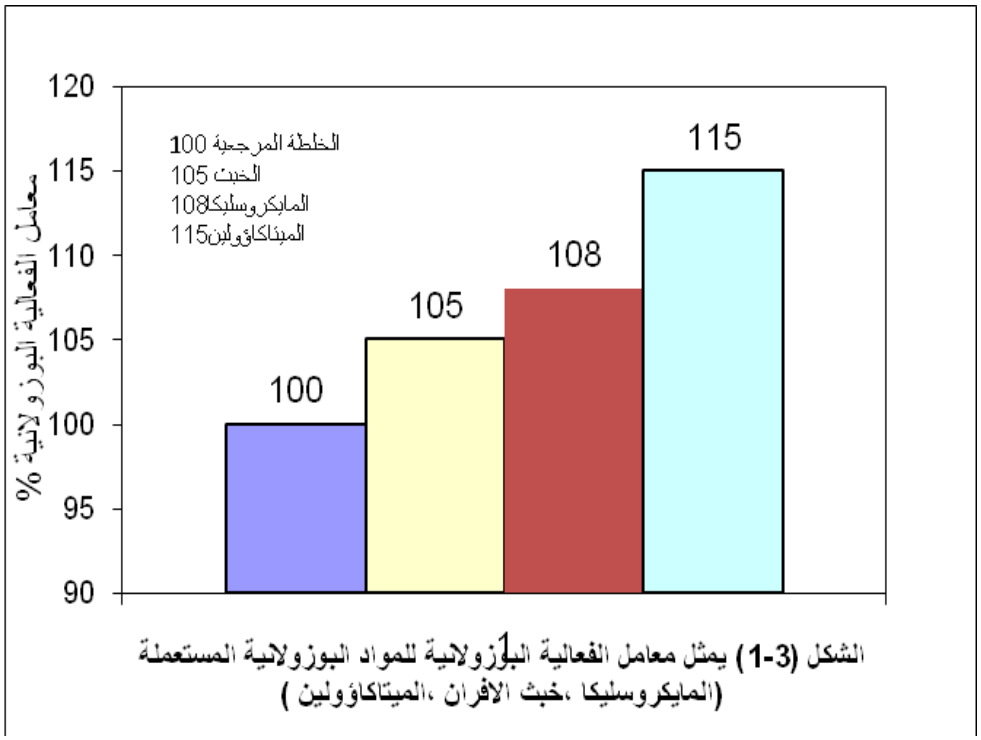

الشكل (3-1) يمثل معامل الفعالية البوزولانية للمواد البوزولانية المستعملة (المايكروسليكا ،خبث الافران ،الميتاكاؤولين)

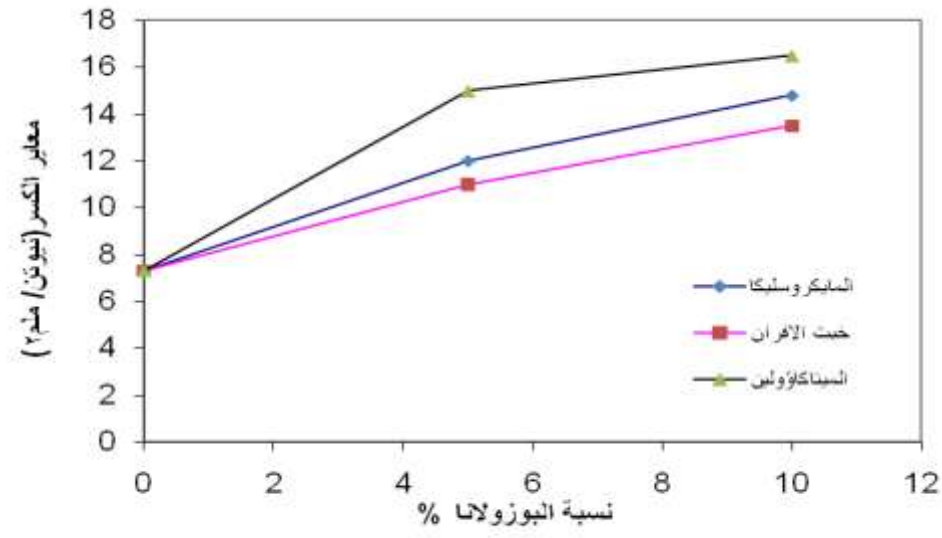

الشكل (٣-٢) يمثل العلاقة بين معاير الكسر ونسبة البوزولانا

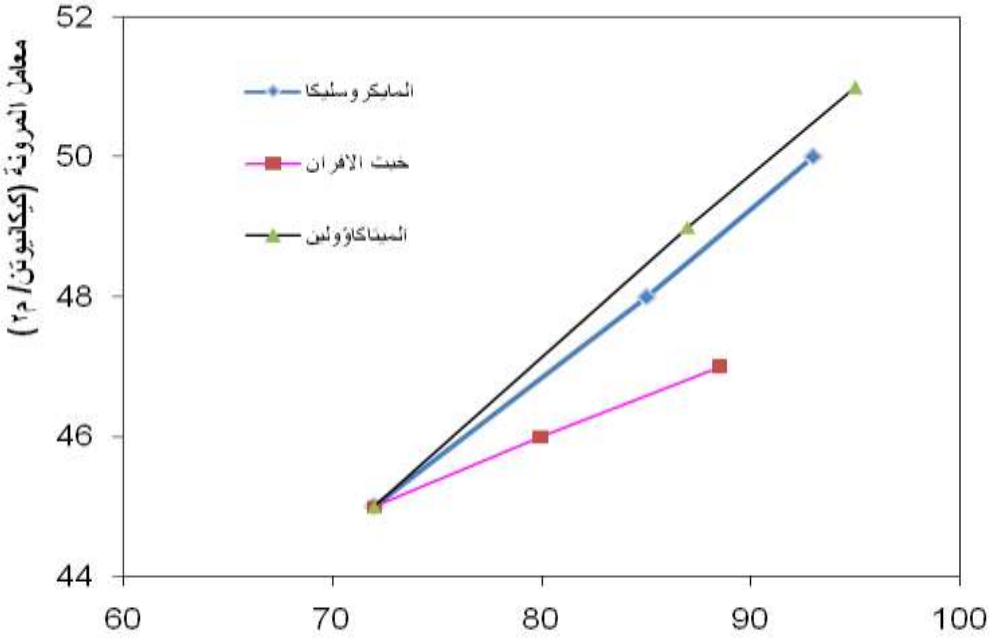

الشكل (٣-٣) يمثل العلاقة بين معامل المرونة ومقاومة الانضغاط بعمر ٢٨ يوم

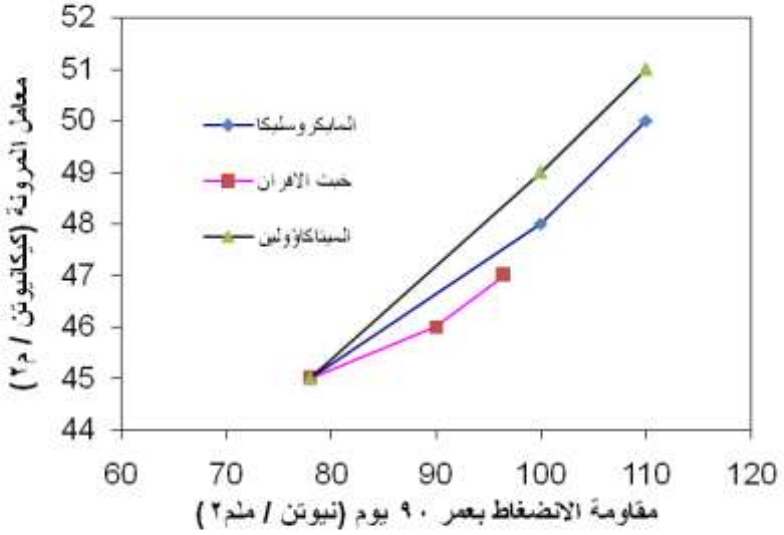

الشكل (٣-٤) يمثل العلاقة بين معامل المرونة ومقاومة الانضغاط بعمر ٩٠ يوم

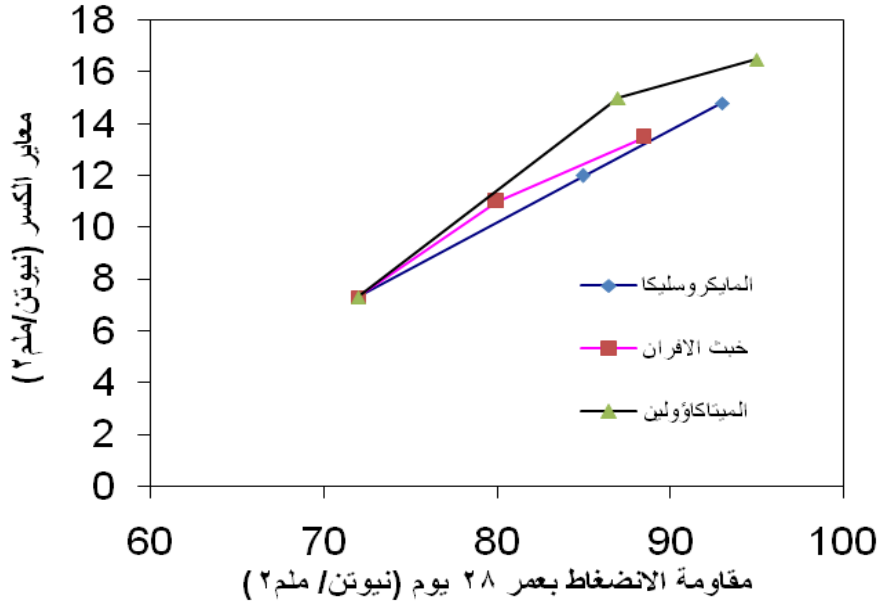

الشكل (٣-٥) يمثل العلاقة بين معاير الكسر ومقاومة الانضغاط بعمر ٢٨ يوم

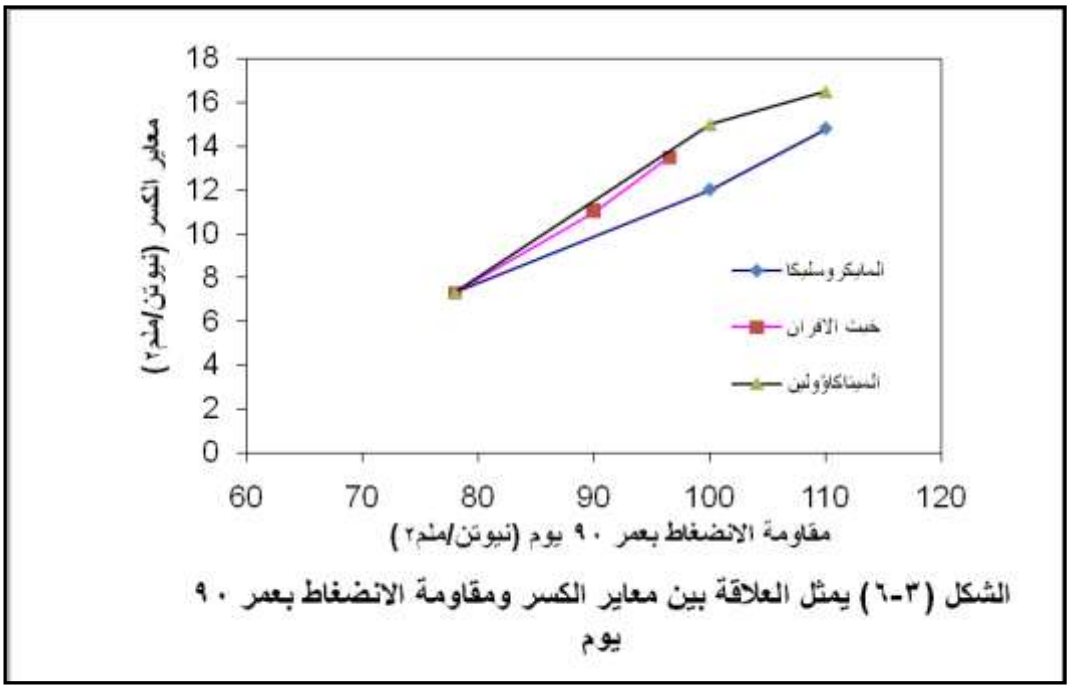

الشكل (٣-٦) يمثل العلاقة بين معاير الكسر ومقاومة الانضغاط بعمر ٩٠ يوم

ـ مناقشة النتائج

1-يبين الشكل (3-2) نتائج مقاومة الانضغاط للخلطات الخرسانية المستخدمة في هذا البحث والحاوية على الانواع الثلاثة من البوزولانات ومقارنتها بالخلطة المرجعية وقد لوحظ من الشكل ان الخلطات الحاوية على البوزولانا المحلية كانت ذات كلفة قليلة وذات مقاومة انضغاط قريبة من البوزولانا المستوردة (المايكروسليكا) . ومن هذا ممكن التعويض عن البوزولانا المستوردة بالمحلية.

2- من الشكل(3-3)نلاحظ نتائج معاير الكسر ونستنتج كذلك بامكانية استخدام البوزولانا المحلية ذات الكلفة القليلة واستبدالها بجزء من السمنت .

3-ويبين الشكلين (3-4) ، (3-5) بان معامل المرونة للخلطات الحاوية على الميتاكاؤولين المحلي تكون اعلى من باقي الخلطات وكذلك بالنسبة للامتصاص لهذه الخلطات تكون اقل اي المسامية لهذا النوع من الخرسانة تكون قليلة.

ـ الاستنتاجات

1- أن إضافة المادة البوزولانية تؤدي إلى تحسين الخواص الفيزياوية للخرسانة المصنوعة منها والالومينا(SiO_2)وهذا بسبب كيمياوي حيث أن التركيب الكيمياوي للمادة البوزولانية هو السليكا المتبقي غير المتفاعل وتكون مركبات سمنتية (CaO)هذه المركبات تتفاعل مع (Al_2O_3) مفيدة تزيد من قوة الخرسانة.

2- أن اضافة هذه المواد الدقيقة التجزئة (نعومتها تعادل حوالي خمسة امثال نعومة السمنت الاعتيادي) تعمل على تقوية هيكل المادة الخرسانية مما تؤدي الى سد كثير من الفراغات الموجودة في هيكل الخرسانة وتقليل الامتصاص والمسامية للخرسانة وبذلك تزيد من المقاومة والديمومة للخرسانة.

3- تعمل على تقوية المناطق البينية بين السمنت والركام،ولذلك يلاحظ ان مقاومة الانضغاط للخرسانة تصل الى 110 ميكاباسكال وبذلك فهي متوافقة مع الخرسانة عالية الاداء .

4- يمكن استخدام الميتاكاؤولين المحلي المتوفرحاليا حيث أن كلفته فقط هي في الطحن ويطحن عن طريق العصف بكميات كبيرة ويعطي خواص فيزياوية للخرسانة المصنوعة منها مقاربة إلى المايكروسليكا المستورد وخبث الافران أيضا وهو ناتج عرضي من أفران صهر الحديد أيضا نتائجه مقاربة إلى المايكروسليكا وهو لايحتاج إلى طحن فيمكن بذلك الحصول على خرسانة عالية الأداء من استخدام مواد محلية رخيصة وتقلل من كمية السمنت وبذلك يؤدي إلى نقص في الكلفة .

REFERENCES

- Neville A. M."Properties of Concrete", Long Man Group Limited, London, Fourth Edition, 1995.

- Mohammed Musluh" The effect of addition of some local materials on dimensional changes and cracking of a concrete "MSc. Baghdad University 1987.

-J.M. Justice, et al. "Comparison of Two Metakaolins And A Silica Fume Used As Supplementary Cementitious Materials "Article to be published in: Proc. Seventh International Symposium on Utilization of high-Strength\high Performance Concrete, to be held in Washington D.C. ,June 20-24, 2005.

-Jianxin Ma1; Holger Schneider1 "Properties of Ultra-High-Performance Concrete" LACER No. 7, 2002

- Mehta P. Kumar" Concrete Structure, Properties and Materials" University of California 1986.

-ASTM C618-03,"Coal Fly Ash and Raw or Calcined Natural Pozzolan for Use in Concrete " Annual Book of Standard American Society For Testing and Material, Vol.0402,2003.

- ASTM C311-02,"Standard Test Methods for Sampling and Testing Fly Ash or Natural Pozzolan for use in Portland – Cement Concrete " Annual Book of Standard American Society For Testing and Material, Vol.0402,2003.

-ACI 211.1-91 "Standard Practice For Selecting Proportions for Normal Heavyweight and Mass Concrete" Reported by ACI Committee 1997.

- زين العابدين رؤوف، مفيد السامرائي(الفحوص غير الاتلافية للخرسانة" الامارات العربية المتحدة 1999.

- يوسف، موفق زين العابدين"انتاج خرسانة ذات مقاومة عالية التحمل باستخدام خبث افران الصهر"وزارة الاسكان , مركز بحوث البناء والزجاج ،كانون الاول1999.

- الملا،جمال احمد " تأثير استخدام الخبث العراقي في صناعة الخرسانة" اطروحة ماجستير، جامعة بغداد 1992.

- الخلف، مؤيد ويوسف، هناء عبد "مضافات الخرسانة، مطبعة جامعة الموصل 1991 .

NONLINEAR ANALYSES OF PARTIALLY COMPOSITE STEEL BEAMS ENCASED IN CONCRETE WITH INNOVATIVE POSITION OF STUD BOLTS

Raad K. Shukur
Asst. Profesor /Civil Eng. Dept.
College of Eng. / University of Baghdad.

ABSTRACT:

Static behavior of three partially encased composite steel beams with cambering under flexural condition is investigated in the context of studying some alternative positions for the headed studs. Shear resistance between the cambered I-shaped beam and the concrete was provided by headed studs in two positions: vertically welded on the bottom flange and horizontally welded on the faces of the web. In the present study, a nonlinear three-dimensional finite element analysis has been used to predict the load-deflection and moment-rotation behaviors of composite encased beams consisting of steel sections using the finite element computer program (**ANSYS V. 10**). Composite encased beams are analyzed and a comparison is made with available experimental load-deflection curves, good agreement with the experimental results is observed. Cambering of steel section is introduced on the steel section of the composite beams encased in concrete. It is found that using of steel section with cambering can increase the ultimate load capacity of the composite encased beam by relatively (15%) and also it is found that deflection are nearly (65% to 80%) the deflection of the same beam without cambering. Parametric studies have been carried out to study the increasing of the moment-carrying capacity due to the use of encased concrete; meanwhile the slip along the beams length is studied. The strain distributions along the steel section and encased concrete depth are also examined. The effects of concrete compressive strength on the stiffness of the composite encased beams are also investigated with the Poisson's ratio of concrete and the effect of cambering of steel-section.

KEYWORDS
Nonlinear Analysis, Composite beam, Flexural behavior, Cambering .

الخلاصة:

في البحث الحالي, تم التحري حول سلوك ثلاث نماذج من العتبات المركبة المثنية و المغلفة جزئياً بالخرسانة تحث تأثير الاحمال الساكنة ضمن نهج عام يتمحور حول دراسة الموقع الافضل لوضع روابط القص (Shear Studs). تم توليد مقاومة القص بين الكونكريت و المقطع الفولاذي المثني و من خلال روابط القص عن طريق موضعين رئيسين: الروابط الملحومه طولياً و الروابط الملحومه أفقياً. أستخدم في الدراسة الحالية, طريقة العناصر المحددة للتحليل اللاخطي ثلاثي الابعاد

و ذلك لغرض تحري علاقة كل من الحمل بالهطول و كذلك العزم بالدوران للعتبات المركبة و التي تحتوي على عنصر فولاذي مثني مغلف بالخرسانة وباستخدام برنامج العناصر المحددة للتحليل الانشائي الـ(**ANSYS**). تم تحليل العتبات المركبة ذوات المقاطع المغلفة و تمت مقارنة نتائج منحنيات القوة و الهطول مع النتائج العملية المتوفرة, تم ملاحظة توافق جيد بين النتائج المستحصلة من البرنامج و النتائج العملية. تم توليد تحديب (أنثناء) في المقطع الفولاذي للعتبات المركبة المغلفة بالخرسانة. لقد لوحظ بأن استخدام المقاطع المثنية في العتبات المركبة و المغلفة بالخرسانة يؤدي الى زيادة قابلية تحمل تلك العتبات بمقدار (١٥٪), و كذلك لوحظ بأن الهطول الدوران يتراوح مابين (٦٥٪ الى ٨٠٪) من هطول الدوران للعتبات التي تحتوي على مقاطع مثنية. تم دراسة تأثير وجود الخرسانة المغلفة على زيادة قابلية تحمل العزوم للعتبات القشرية المركبة و المغلفة جزئياً بالخرسانة, في تلك الاثناء تم دراسة التزحلق الذي يحدث في سطح الاتصال و على طول العتب للعتبات المركبة أيضاً. بالاظافة الى ذلك تم دراسة نمطية توزيع الانفعالات على العمق الكامل للمقاطع الفولاذية و كذلك الخرسانة المغلفة. تم التحري عن مدى تاثير مقاومة أنضغاط الخرسانة على جسائة العتيات المركبة و المغلفة بالخرسانة.. و اخيراً, تم التحقق من تاثير كل من (Poisson's ratio), مقدار تحدب (ثني) المقطع الفولاذي و مقدار نعومة (دقة) النموذج المعمول بالـ(**ANSYS**) على قابليات تحمل العتبات المركبة.

INTRODUCTION:

Steel–concrete composite structures have been used more frequently in modern constructions, especially in multi-storey buildings. These materials combine the strength of steel with the compressive strength and the stiffness of concrete, producing a highly economical and interesting structural system. From the beginning, the most common type of composite beam in use has been an I-steel profile connected to the concrete slab or profiled steel-concrete composite slab. Given its importance, this traditional composite beam (Fig. 1(a)) has already been incorporated by design code procedures [1–3]. The composite action between the concrete and steel profile can be achieved by means of mechanical shear connectors as headed studs, proving to be an efficient shear connector. However, in several situations, it can be interesting to reduce the overall depth of the floor using the beams contained within the depth of the floor (Fig. 1(b)). The concrete between the flanges of the beam results in several advantages, such as high fire-resistance and load capacity, as well as a significant increase in the bending stiffness compared to a steel beam. The local buckling strength also increases in relation to the steel section, and the overall height of both composite beam and composite floor is reduced. In addition, lower construction cost compared to reinforced concrete (RC) or steel frame system and shorter construction time compared to RC can be obtained using encased beams. Therefore, the concrete cast in the flanges of the steel beam is an innovative and interesting alternative that needs to be investigated in details, as each detail of the components can modify the behavior of the encased beam. Despite the advantages in terms of structural behavior and costs, the encased beam is a constructive solution not totally understood yet, especially in relation to the headed studs contribution to load capacity and composite behavior. Currently, only the details shown in (Fig. 1(a) and (e)) are included in standard codes [1–3]. Comparing traditional composite beams (Fig. 1(a)) and partially encased beams (Fig. 1(e)), we note that the reinforced concrete between flanges increases the bending stiffness and reduces the vertical displacements. Among the innovative solutions shown in (Fig. 1), the focus here is on the contribution of the headed studs for the composite action.

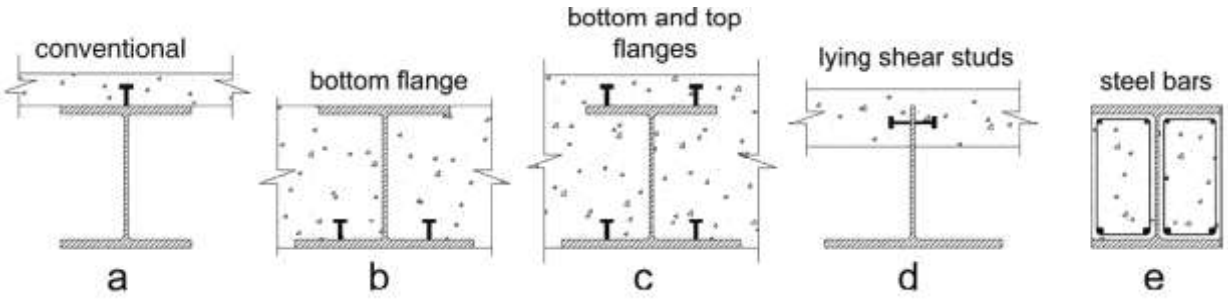

Fig. 1. Examples of composite beams.

*** PRECAMBERED STEEL BEAM:**

This type of steel composite beam is maximizing the structural advantage of both steel frame and reinforced concrete; it is produced by cambering the steel beam upwards over the span using suitable propping or jacking systems. Preflex beams have been used successfully in a number of road bridges as well as building structures. The typical construction sequence of a precambered beam is as follows [4], see (Fig. 2):

a. In the plant, setup a steel I-girder with a precamber supported at each end.
b. Prebend the steel girder by applying two concentrated loads at one-third of the span from both sides.
c. Cast the first phase of concrete at the level of the bottom flange of the steel girder while keeping in place the loads of the prebending phase of the girder.
d. Two days after casting the concrete, remove the prebending loads. As a result, the beam goes up, the precamber becomes smaller than the original precamber and the concrete is now subjected to compression.
e. Cast the second phase concrete on site [4].

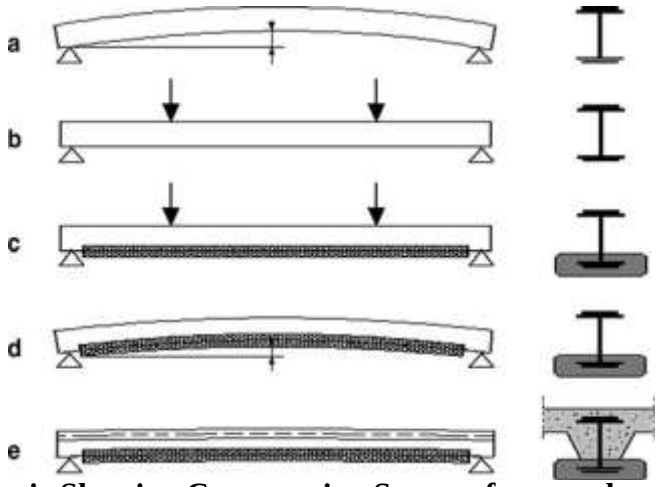

Fig. 2. Schematic Showing Construction Stages of precambered Beam [4].

STEEL-CONCRETE COMPOSITE BEHAVIOR IN ENCASED BEAMS:

Shear connectors are necessary when the natural bond is inefficient to achieve the desired steel-concrete interaction. Among the several types of available shear connectors used to provide composite action, the headed shear stud is the most common. In addition, headed shear studs are widely used welded on the upper flange of the steel profile in the vertical position. However, some new and interesting positions have been suggested. For example, studs vertically welded on the bottom flange or on both flanges [5], or horizontally on the web [6], see (Fig. 1(a), (b) and (d)). Many studies have been conducted for composite beams with headed

shear studs welded in vertical position. However, very little experimental data is available for the case of headed studs horizontally welded on the web of the steel beam to achieve the composite action between steel and concrete. **Breuninger** [6] proposed an innovative composite cross section where the top flange of the steel beam is eliminated and the headed studs are directly welded to the web in the horizontal position, see (Fig. 1(d)). The headed studs in the horizontal position are called lying studs and experimental results showed that the load capacity is limited by: splitting of the concrete slab, splitting of the concrete slab, and tear-off or pull-out of the studs. The splitting failure of the lying studs is the most important failure mode; however, the design rules in standard codes are based on test results for only conventional studs and do not cover this failure type. Parameters such as concrete strength, thickness of concrete slab, distance, diameter and length of the studs, number and diameter of the stirrups, and reinforcement of slabs showed to be very important [6]. Among these parameters, the reinforcement of slab and the stirrups are the most important, mainly regarding the intersection between reinforcement and stirrups. Despite that the contribution of the headed studs to the composite action is unquestionable; **Dipaola et al.** [7] suggest the shear transfer mechanisms may be only provided by the adhesion and friction resistances of the steel-concrete interface (Fig. 3(a)). In the absence of bending moment, the area of the steel web is the shear resistant section, and for bending moment, the transference of shear forces is attributed to adhesion and friction resistant mechanisms [7]. When the upper flange of the steel beam is removed and lying studs are welded on the web, the shear strength of the beam decreases due to the small distance from the studs to the surface of the reinforced concrete slab (Fig. 3(b)). Using strut-and-tie models, **Kuhlmann and Kürschner** [8] showed the mechanism of shear transfer is a result of the load transferred by the studs and by the friction, but the latter is the most dominant mechanism. The contribution of the friction to the horizontal shear load capacity is only due to the web area and the horizontal studs. On the other hand, the vertical shear capacity depends on the web, concrete and stirrups. An interesting slim floor system is proposed by **Ju and Kim** [9] to minimize storey height and consists of inverted T-section steel beam and precast concrete rested on the bottom flange. Stirrups and lying studs on the top web are used to provide the composite action (Fig. 3(c)). In other research, where reinforcing bars and headed shear studs were combined to provide the composite action, the longitudinal shear force transfer occurred mainly by friction forces acting at the interface among the concrete encasement and the structural steel [9]. Additionally, pull-out test results of **Hegger and Goralski** [10] showed the load carrying capacity is higher for larger profiles due to the larger contact surface between the flange and the concrete encasement and also by the lower shortening of the concrete due to the shrinkage (Fig. 3(d)). The confinement effect of the steel profile in some areas of the concrete also increases the load carrying capacity. Regarding the failure modes, the absence of the reinforcement or headed studs leads to a failure without diagonal cracks. With reinforcing bars, the behavior becomes more ductile, and with headed studs, the failure is achieved by splitting the concrete around the studs [10].

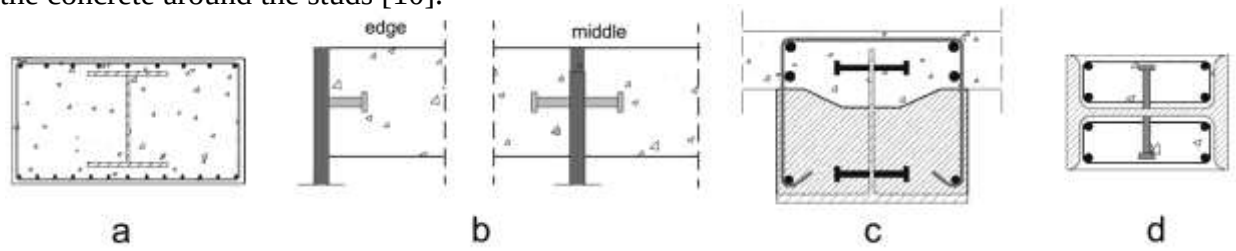

Fig. 3. Arrangement of headed shear studs;
(a) without headed studs [6]; (b) horizontally welded on the web [7]; (c) steel profile without top flange and (d) reinforcing bars and headed studs [10].

*** AVAILABLE EXPERIMENTAL RESEARCH**:

Works on encased composite beams dates back to the beginning of the last century, a series of testes have been conducted on this type of composite beam to study the influence of the concrete encasement on the behavior of steel beam section under different loading conditions. In the present study, **De Nardin and Lucia H.C., in (2008) [11]**, tested specimens (PEB-B, PEB-W and PEB) are chosen to verify the applicability of **ANSYS** computer program to analyze the encased composite beams and also to investigate the main parameters that affected it's the behavior.

- DETAILS OF THE TEST SPECIMENS:

A total of three simply supported (full-scale) composite partially encased beams with an asymmetrical structural (built-in) steel section and concrete filling were tested under two concentrated load, one of them being a beam without shear studs (specimen PEB) as a reference, and the remaining two beams are with studs, vertically welded on the top of the bottom flange, specimen (PEB-B), and horizontally welded on two opposite sides of the steel web, specimen (PEB-W). Five headed studs of (19 mm) diameter and total post-weld height (75 mm) were directly welded on each side of the web or bottom flange of the steel section, the centre-to-centre spacing of the studs was kept constant and equal to (480 mm). As the main parameter to be investigated was the shear stud position, all the three specimens of asymmetric steel beam were designed with exactly the same geometry. No longitudinal or transverse reinforcements were used in the specimens. The cross-sections and loading arrangement for the tested specimens are shown in (Fig. 4); the dimensions of steel sections, gross-sections and failure mode are given in (Table 1). The material properties are given in (Table 2).

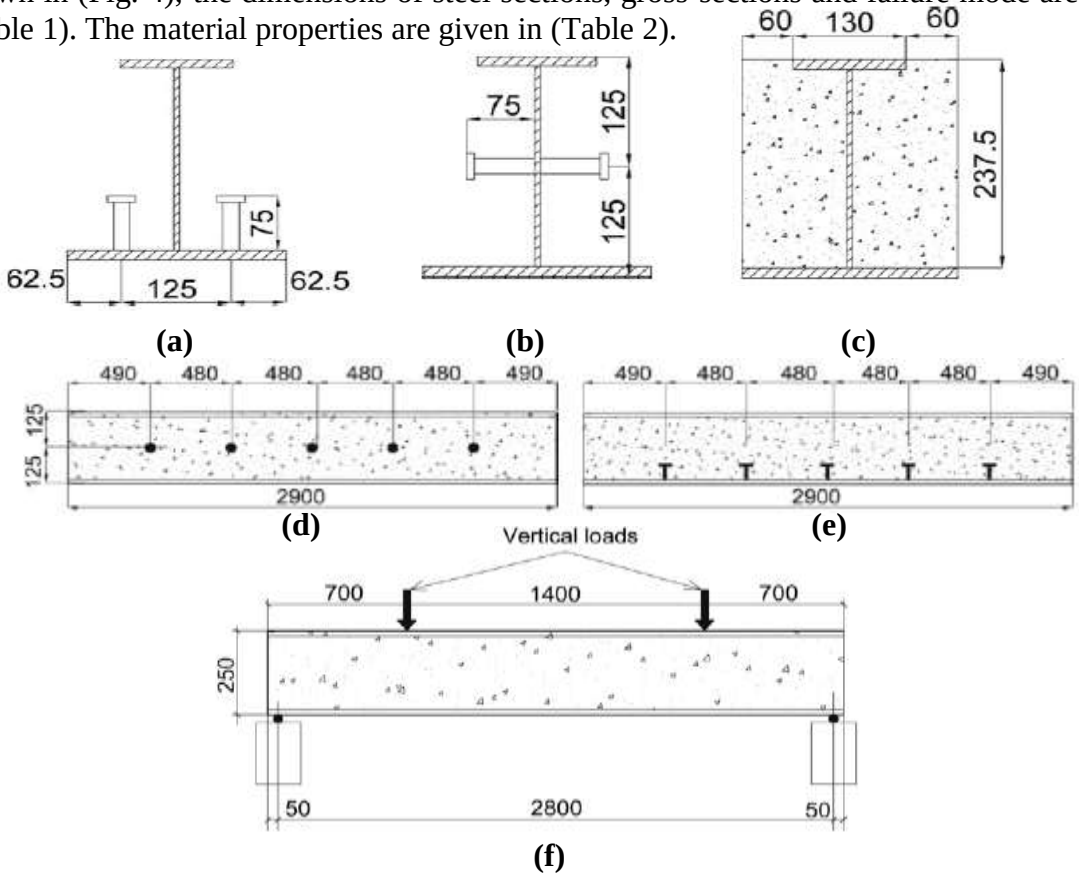

Fig. 4. Geometry of the Partially Encased Tested Specimens [11]:
(a) PEB-B Specimen Cross-Section, (b) PEB-W Specimen Cross-Section,

(c) Typical Cross-Section, (d) PEB-W: Studs on the Web, (e) PEB-B: Studs on the Bottom Flange, (f) Loading Arrangement, (All dimensions in mm).

Table 1: Descriptions, Dimensions of Steel Sections and Dimensions of Gross-Sections of the Tested Specimens.

Analyzed (Tested) specimen	Steel shape (ds×bf×tw×tf) (mm)	Cross-Section Dimensions(mm)
PEB	….	(250X250)
PEB-B	{250X(U=130, B=250)X6.3X12.5}	(250X250)
PEB-W	{250X(U=130, B=250)X6.3X12.5}	(250X250)

Table 2: Material Properties of the Analyzed (Tested) Specimens.

Analyzed (Tested) specimen	PEB	PEB-B	PEB-W
Concrete			
Compressive strength-(f'c)-(N/mm2)(♦)	46.540	46.540	46.540
Tensile strength-(fcr)-(N/mm2)(♥)	4.240	4.240	4.240
Young modulus- (Ec)-(N/mm2) (♣)	32288.6	32288.6	32288.6
Poisson's ratio-(ν)(♠)	0.2	0.2	0.2
Steel section			
Yield stress of steel-(fy)-(N/mm2)(♦)	….	308	308
Ultimate stress of steel-(fy)-(N/mm2)(♦)	….	469	469
Young modulus- (Es)-(N/mm2) (♠)	….	200000	200000
Poisson's ratio-(ν)(♠)	….	0.3	0.3
Shear connector (studs)	….	D19 mm	D19 mm
Yield stress of steel-(fy)-(N/mm2)(♠)	….	500	500
Young modulus- (Es)-(N/mm2)(♠)	….	200000	200000
Poisson's ratio-(ν)(♠)	….	0.3	0.3
Notation			
Symbol	Description		
(♣)	Equation (1)		
(♠)	Assumed		
(♥)	Equation (2)		
(♦)	From test		

- $E_c = 4733\sqrt{f_c}$ ……..……..……..…….....….. (1)

- $f_{cr} = 0.622 \sqrt{\acute{f}_c}$ ……..……..…….. (2)

Where:
E_c = Modulus of elasticity of concrete in (MPa).
$\acute{f}_c$= Cylinder uniaxial compressive strength (MPa).
f_{cr}= tensile strength of concrete (MPa).

*** FINITE ELEMENT MODEL:**

- SOFTWARE, ELEMENT TYPES AND MESH CONSTRUCTION:

Advances in computational features and software have brought the finite element method within reach of both academic research and engineers in practice by means of general-purpose nonlinear finite element analysis packages, with one of the most used nowadays being **ANSYS**. The program offers a wide range of options regarding element types, material behaviors and numerical solution controls, as well as graphic user interfaces (known as GUIs), auto-meshers, and sophisticated postprocessors and graphics to speed the analyses. In the present study, the structural system modeling is based on the use of this commercial software. The finite element types considered in the model are as follows: elastic-plastic shell **(SHELL43)** and solid **(SOLID65)** elements for the steel section and the concrete slab, respectively, and nonlinear springs **(COMBIN39)** to represent the shear connectors. Both longitudinal and transverse reinforcing bars are modeled as discrete using **(LINK8)** element. Rigid-to-flexible contact mechanisms are used to model the interface contact surface between the structural steel section and the encased concrete. The rigid target surface (encased steel section which is represented by **(SHELL43)** element) modeled with **(TARGE170)** elements, while the contact flexible surface (concrete encasement which is represented by **(SOLID65)** elements) modeled with **(CONTA173)** elements. The element **(SHELL43)** is defined by four nodes having six degrees of freedom at each node. The deformation shapes are linear in both in-plane directions. The element allows for plasticity, creep, stress stiffening, large deflections, and large strain capabilities [12]. The element **(SOLID65)** is used for three dimensional modeling of solids with or without reinforcing bars (rebars capability). The element has eight nodes and three degrees of freedom (translations) at each node. The concrete is capable of cracking (in three orthogonal directions), crushing, plastic deformation, and creep [12]. The rebars **(LINK8)** element are capable of sustaining tension and compression forces, but not shear, being also capable of plastic deformation and creep and have two nodes with three translation degrees of freedom at each node. The element **(COMBIN39)** is defined by two node points and a generalized force–deflection curve and has longitudinal or torsional capability. The longitudinal option is a uniaxial tension–compression element with up to three degrees of freedom (translations) at each node. Symmetry of the composite encased (straight and preflex) beams is taken into account by modeling a full scale beam span. A typical finite element mesh for a composite encased beam is shown in (Fig. 5).

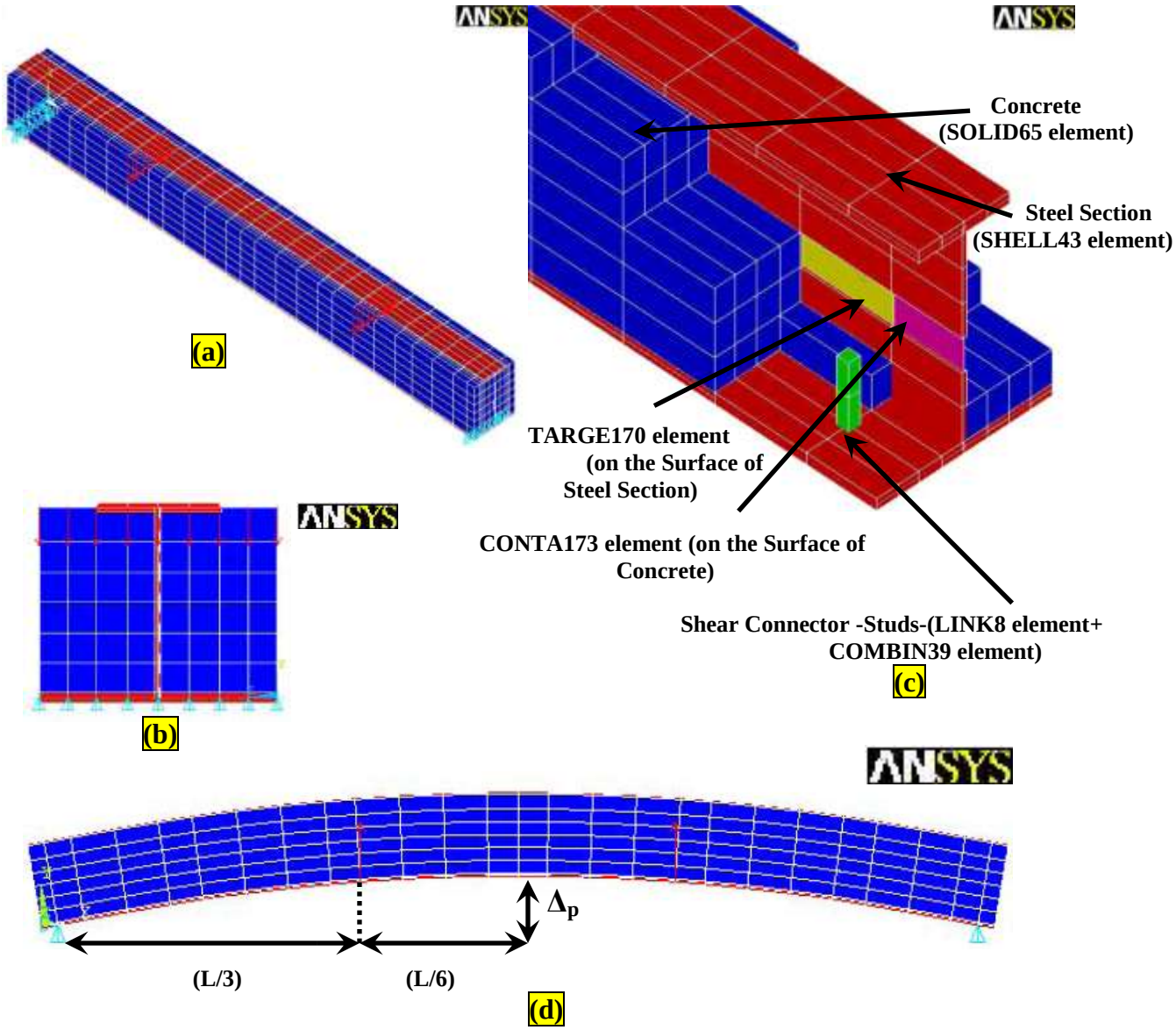

Fig. 5. Finite Element Mesh for (PEB-B) Model:
(a) Isometric-View, (b) Front-View, (c) Internal Section, (d) Precambered Shape.

The following equations used to calculate the amount of forces required to produce the upward movement (cambering) of simply support steel section subjected into two forces at distance (L/3) from its two ends for a given allowable compressive stress in the steel beam [13].

Upward deflection $\Delta_p = \frac{23PL^3}{648EI}$ ..... (3)

Bending moment $M = \frac{PL}{3}$ ..... (4)

Compression flange stress $\sigma = \frac{My}{I}$ ..... (5)

By substituting in equation (6.3):

$$\Delta_p = \frac{23\sigma L^2}{216Ey} \quad \text{.....(6)}$$

$$P = \frac{3\sigma I}{Ly} \quad \text{.....(7)}$$

Where:

Δ_p in **(mm)**= cambering produced in the steel section.

P= force applied to the a steel section to produced cambering.

σ= Allowable compressive stress in the steel beam - (N/mm2).

L= Clear span of the tested specimens-(mm).

E=Es= (Young modulus of steel=200,000 N/mm2).

y= Distance from the steel section centroid to the top surface of compression flange in (mm).

- MATERIAL MODELING:

The von Mises yield criterion with isotropic hardening rule (multilinear work-hardening material) is used to represent the steel beam (flanges and web) behavior. The stress–strain relationship is linear elastic up to yielding, perfectly plastic between the elastic limit and the beginning of strain hardening. The von Mises yield criterion with isotropic hardening rule is also used for the reinforcing steel. An elastic-linear-work hardening material is considered, with tangent modulus being equal to (1/10000) of the elastic modulus, in order to avoid numerical problems. The values measured in the experimental tests for the material properties of the steel components (steel beam and reinforcing bars) are used in the finite element analyses. The concrete encasement behavior is modeled by a multilinear isotropic hardening relationship, using the von Mises yield criterion coupled with an isotropic work hardening assumption. The uniaxial behavior is described by a piece-wise linear total stress–total strain curve, starting at the origin, with positive stress and strain values, considering the concrete compressive strength ($\acute{f}_c$) corresponding to a compressive strain of (0.2%). The stress–strain curve also assumes a total increase of (0.05 N/mm2) in the compressive strength up to the concrete strain of (0.35%) to avoid numerical problems due to an unrestricted yielding flow. The concrete element shear transfer coefficients considered are: (0.25) for open crack and (0.8) for closed crack. Typical values range from (0 to 1), where (0) represents a smooth crack (complete loss of shear transfer) and (1) a rough crack (no loss of shear transfer). The default value of (0.6) is used as the stress relaxation coefficient (a device that helps accelerate convergence when cracking is imminent). The crushing capability of the concrete element is also disabled to improve convergence. The concrete encasement compressive strength is taken as the actual cylinder strength test value. The concrete tensile strength and the Poisson's ratio are assumed as (1/10) of its compressive strength and (0.2), respectively. The concrete elastic modulus is evaluated according to equation (1) mentioned above. The model allows for any pattern of stud distribution to be considered. In all analyses, the number/spacing of studs adopted in the experimental programmers is utilized. As far as the shear connector behavior is concerned, the load–slip curves for the studs are used (obtained from available push-out tests) by defining a table of force values and relative displacements (slip) as input data for the nonlinear springs. These springs are modeled at the steel–concrete interface [14], as shown in (Fig. 6). the behavior of the interface surface of contact between the steel section and concrete encasement is modeled according to the basic **Coulomb friction model**, in which, two contacting surfaces can carry shear stresses up to a certain magnitude across their interface before they start sliding relative to each other. This state is known as sticking. The **Coulomb friction model** defines an equivalent shear stress (τ), at which sliding on the surface begins as a fraction of the contact pressure (p) as [12]:

$\tau_{lim} = \mu p + COHE$, $|\tau| \leq \tau_{lim}$ ..... (8)

where:

τ_{lim} = limit shear stress, τ= equivalent shear stress, μ= the friction coefficient, P= constant normal pressure, COHE= cohesion sliding resistance (stress unite).

Once the shear stress is exceeded, the two surfaces will slide relative to each other. This state is known as sliding. The sticking/sliding calculations determine when a point transitions from sticking to sliding, see (Fig. 7). **ANSYS** provides two models for Coulomb friction [12]: Isotropic friction (2-D and 3-D contact): which is based on a single coefficient of friction (MU) and the Orthotropic friction (3-D contact): which is based on two coefficients of friction (MU1 and MU2). In the present study, (3-D) Isotropic friction model is used with single coefficient of friction (MU), and the cohesion sliding resistance (COHE) set to (0.00) making (Fig. 7(a)) change to (Fig. 7(b)).

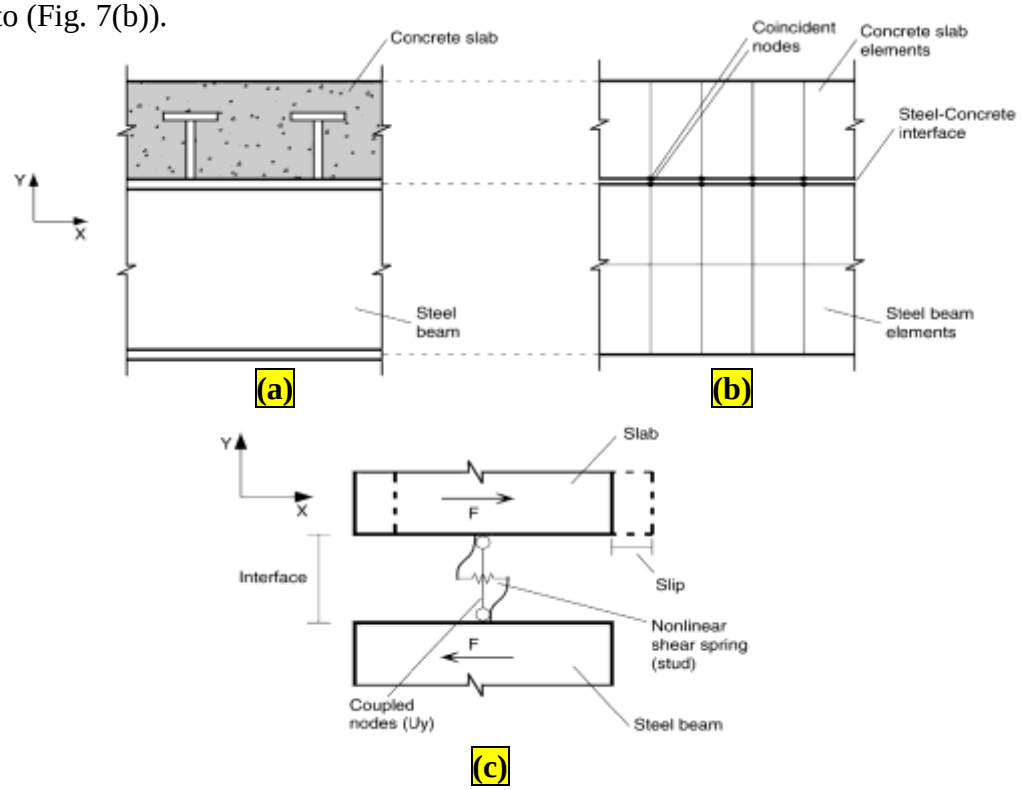

Fig. 6. Modelling of shear connectors (longitudinal view) [14]:
(a) Shear studs in a typical composite beam. (b) Shear studs in a typical composite beam finite elementmesh. (c) Representation of the shear stud model.

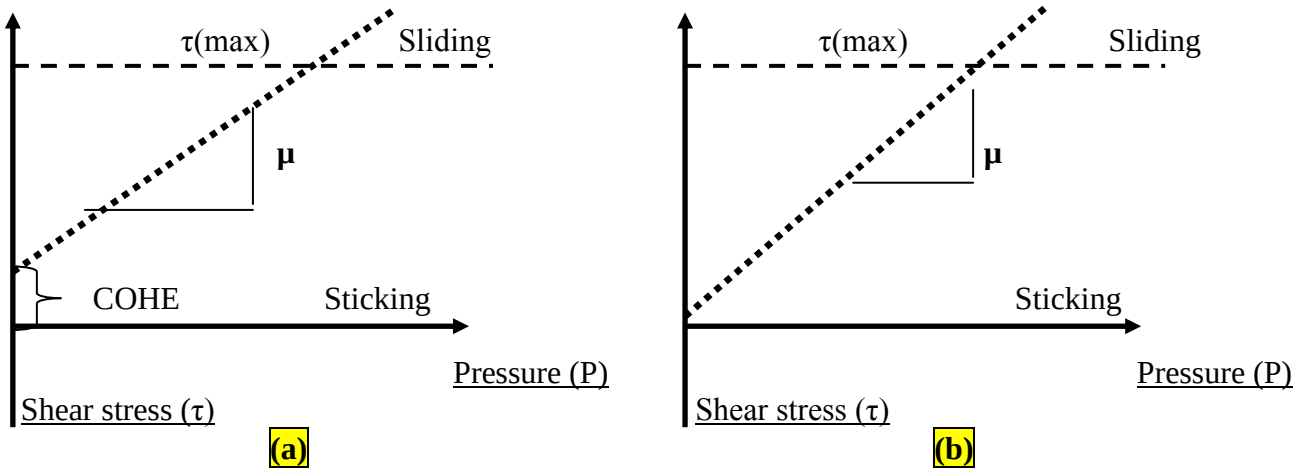

Fig. 7. Frictional Models [12].

APPLICATION OF LOAD AND NUMERICAL CONTROL:

Regarding application of load, concentrated loads are incrementally applied to the model by means of an equivalent displacement to overcome convergence problems (displacement control). For the convergence criterion, the **L2-Norm** (square root sum of the squares) of displacements is considered. Concentrated loads are represented by means of point loads applied at nodes. These concentrated loads are also applied to the model incrementally using the load control strategy and the **L2-Norm**. The tolerance associated with this convergence criterion (**CNVTOL** command of **ANSYS**) and the load step increments are varied in order to solve potential numerical problems. Whenever the solution does not converge for the set of parameters considered, as far as load step size and converge criterion are concerned, the **RESTART** command is used in conjunction with the **CNVTOL** option. **ANSYS** allows two different types of restart: the single-frame restart and the multi-frame restart, which can be used for static or full transient structural analyses. The single-frame restart only allows the user to resume a job at the point it stopped. The multi-frame restart can resume a job at any point in the analysis for which information is saved. This capability enables multiple model analyses, presenting more options for data retrieval after an undesired aborted solution. The second approach is used throughout the present analyses. For the case in which only one point load is applied to the system, there is a direct relationship between force and displacement, making the displacement control method easier to be utilized. The load control method is, however, less efficient than the displacement control method in nonlinear analyses. This fact is observed especially when the applied load approaches the ultimate load of the system, as an incremental increase in the load leads to a significant increase in the corresponding displacements, causing difficulties in terms of numerical convergence. For the type and size of the finite element problem investigated, the load control method demanded, on average, (70%) more disk space and took (150%) longer to be processed than similar displacement control solutions. The finite element analysis of the models was set up to examine two main behaviors: (initial cracking of the composite encased beams and the strength limit state). The Full Newton-Raphson method of analysis is used to compute the nonlinear response. The application of the loads up to failure was done incrementally as required by the Newton-Raphson procedure.

*** ANALYSIS PROCESS FOR THE ANALYZED FINITE ELEMENT MODELS:**

- ANALYSIS OF THE STRAIGHT ENCASED COMPOSITE BEAMS:

The finite element analyses for the straight simply support composite encased beams under concentrated forces have been carried out using static analysis type. The solution controls command dictates the use of a linear or non-linear solution for the finite element model. The program behavior upon non-convergence for this analysis was set such that the program will terminate but not exit. The most important typical commands utilized in a nonlinear static analysis are shown in (Table 3). The rest of the commands were set to defaults.

Table 3: The Most Important Commands Used to Control Nonlinear Analysis.

Commands	Description
solution printout controls	all solution items such as {nodal DOF solution, nodal reaction loads, element solution (element nodal stresses+element elastic and plastic strains…etc),…etc}
print frequency	write every substep
controls for database and results file written.	all solution items such as {nodal DOF solution, nodal reaction loads, element solution (Element nodal stresses+element elastic and plastic strains…etc),…etc}
print frequency	write every substep
time at end of loadstep	(experimental failure load)X(1.1)
time Step size	(1%) from the time at end of loadstep
automatic time stepping	on
max no. of substeps	time Step size
min no. of substeps	(10%) from the max no. of substeps

At first trials for the analysis, the values for the convergence criteria (force and displacement) are set to defaults except for the tolerances. The tolerances for force and displacement are set as (15 times) the default values as shown in (Table 4), which represent the commands used for the nonlinear algorithm and convergence criteria. However, when the composite encased beams began cracking, convergence for the non-linear analysis was impossible with the default values. The displacements converged, but the forces did not. Therefore, the convergence criterion for force was dropped and the reference value for the Displacement criteria was changed to (5), this value is then multiplied by the tolerance value of (0.01) to produce a criterion of (0.05) during the nonlinear solution for convergence. A small criterion must be used to capture correct response.

Table 4: Nonlinear Algorithm and Convergence Criteria Parameters.

Commands	Description	
equilibrium iteration	100	
criteria to stop an analysis	stop and stay	
Set Convergence Criteria		
Label	F (force)	U (displacements)

reference value	calculated	calculated
convergence tolerance	0.001	0.010
Norm	L2 (SRSS value)	L2(SRSS value)
Minimum reference value	not applicable	not applicable

- ANALYSIS OF THE PRECAMBERED ENCASED COMPOSITE BEAMS:

Analyses for the precambered encased composite beams were similar to the analyses of the straight encased composite beams. However, different load steps were used. The first load step taken was to produce camber in the steel beam only in which the upward movement of the beam resulted, meanwhile all others element consisting the encased beams considered to be a **(DEAD ELEMENTS)** according to **ANSYS** options. **RESTART** command then used to re-analyze the beams due to its original state of loading **(Experimental Researches paper)**, during this, the flexural reinforcements, shear reinforcements, concrete and shear studs elements are re-activated and the two preflexing forces are neutralized by two forces having the same magnitude but opposite direction. The preflexing loads are removed. As a result, the beam goes down a little due to self weight (gravity-loads) and the stress recovery of the steel beam, the precamber amount becomes smaller than the original cambering, and the concrete is now subjected to compression. The load-deflection curves for analyzed composite partially encased beams {{(PEB-B+PEB-W) **De Nardin** and **Lucia H.C.,** (2008) [11]}} which were obtained numerically by the finite element method using **ANSYS (V.10)** computer program for straight and preflex steel section and compared with the experimental results are presented in (Fig. 8) through (Fig. 11); respectively. The goal of the comparison of the finite element models and the beams experimental works is to ensure that the elements types, meshing, material properties, real constants and convergence criteria are adequate to model the response of the beams.

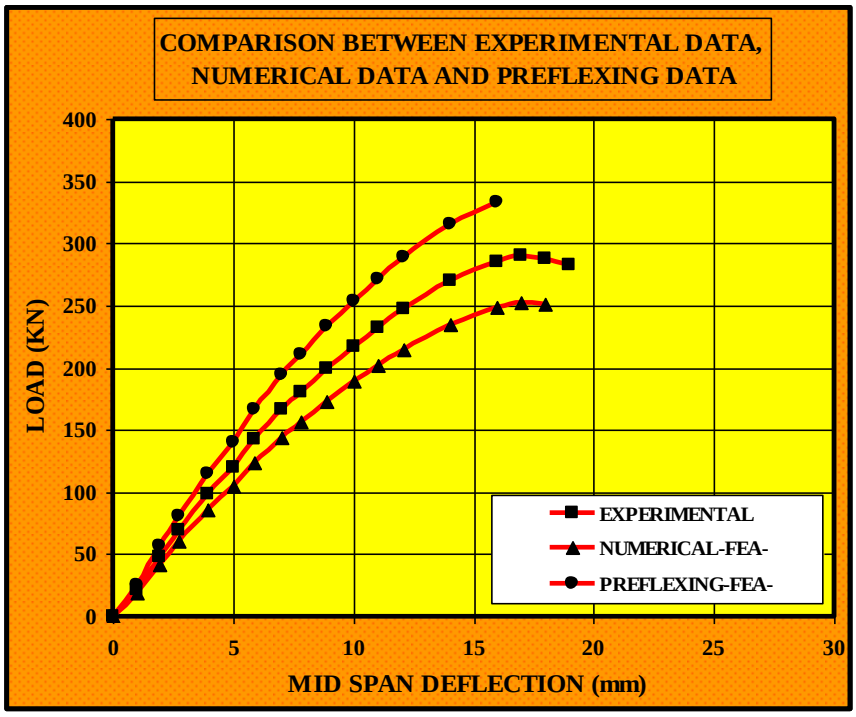

Fig. 8. Finite Element Analysis Result for Model (PEB).

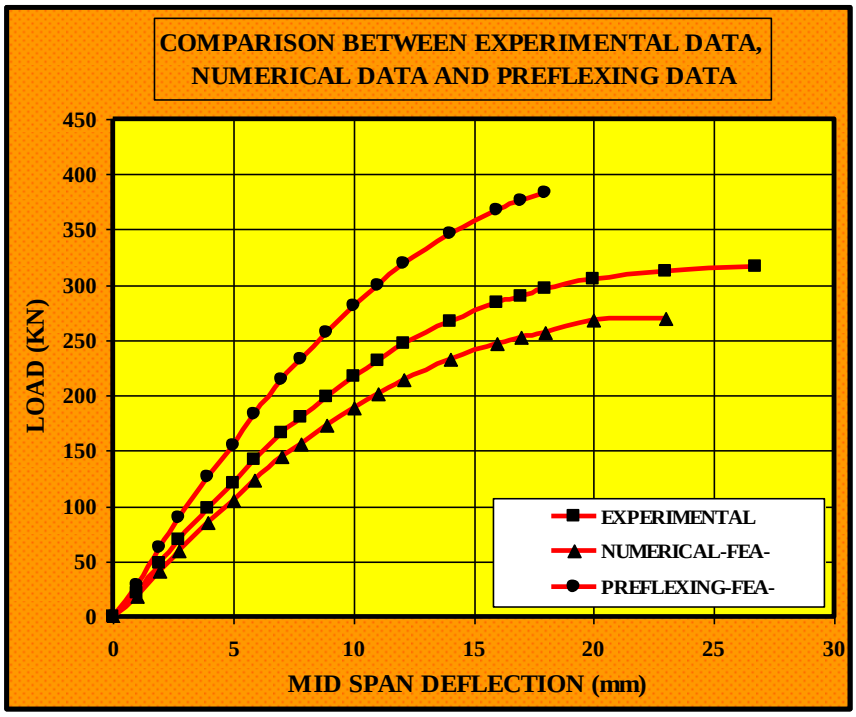

Fig. 9. Finite Element Analysis Result for Model (PEB-B).

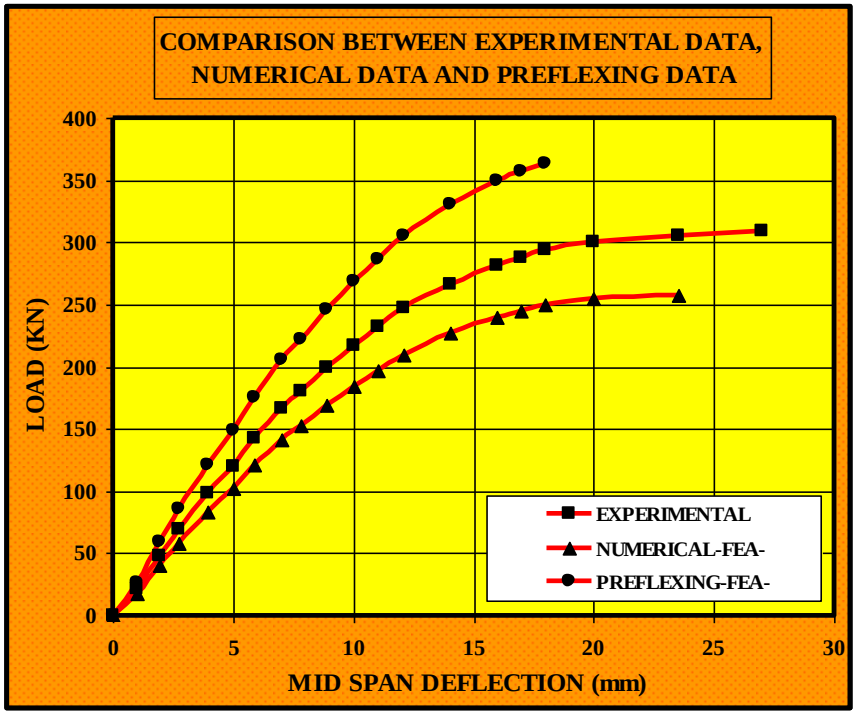

Fig. 10. Finite Element Analysis Result for Model (PEB-W).

BEHAVIOR AT ULTIMATE LOADS:

The analytical and experimental values of the ultimate loads for straight and preflex composite encased beams which presented in (Fig. 8) through (Fig. 10); respectively, are

summarized in (Table 5). (Table 5) showed that The preflex load for the analyzed specimen (PEB-B) is higher than the preflex load of the analyzed specimen (PEB-W), this is due to the presence of vertical studs {specimen-(PEB-B)} which are more efficient than horizontal ones {specimen-(PEB-W)} in providing the composite action between the steel profile and the concrete encasement, because the vertical stresses from concrete encasement acting on the surface of bottom flange and also the friction forces developed in the same surface is tremendously higher than that developed in the surface of steel section web. The analyses finished (Done) for the partially encased composite analyzed specimens (PEB-B+PEB-W) due to the excessive cracking in the constant moment region.

Table 5: Comparison between Analytical and Experimental Values of the Ultimate Loads.

Tested specimen	Experimental (ultimate loads)	Analytical (ultimate loads)-straight beams	A%	Analytical (ultimate loads and)-preflex beams	B%
PEB	288	252	12.5	330	12.7
PEB-B	317	270	14.8	382.7	17.2
PEB-W	309	258	16.5	363.5	15.1
Notation					
Symbol	Description				
A%	$\frac{(P_u)_{exp} - (P_u)_{ANSYS\text{-}Straight}}{(P_u)_{exp}}$				
B%	$\frac{(P_u)_{ANSYS\text{ - }Preflex} - (P_u)_{exp}}{(P_u)_{ANSYS\text{ - }Preflex}}$				

BEHAVIOR AT MAXIMUM DEFLECTIONS:

The analytical and experimental values of the maximum deflections for straight and preflex composite encased beams are summarized in (Table 6). The load-deflection curves which presented in (Fig. 8) through (Fig. 11); respectively, for the analyzed specimens in which the corresponding experimental, theoretical and preflexing curves are superimposed, show that the curves are lie very close to each other at initial stages for all the specimens. However, there seems to be some deviation between the results near the failure. The discrepancy may be due to the inadequacy in concrete and interface behavior modeling. It was found that the deflections are nearly (85% to 95%) the deflections of the same experimental beam for straight beam situation, and (65% to 80%) of the same experimental beam for preflexed beam situation.

Table 6: Comparison between Analytical and Experimental Values of the Maximum Deflections.

Tested specimen	Experimental Deflections	Analytical (Deflections) straight beams	Analytical (Deflections) preflex beams
PEB	18.5	16	15
PEB-B	26.7	23	18
PEB-W	27.36	23.8	19

*** THE PARAMETRIC STUDY:**

A parametric study has been done on the same samples that have been analyzed. Many parameters can be studied in the analyzed models to examine the effect of each parameter on the behavior of the models results. Some models were chosen to study the effect of encased concrete in the increasing of moment-bearing capacity, meanwhile other are chosen to study the slip along the composite partially encased beams length. The strain distributions along the steel section and encased concrete depth are also examined. The Poisson's ratio of concrete and the effect of cambering of steel-section are also investigated.

- THE EVALUATION OF SLIPS ALONG THE COMPOSITE ENCASED BEAMS INTERFACE:

The partially encased beams (PEB), (PEB-B) and (PEB-W) which were described in (Fig. 4) and (Fig. 5) are chosen for the evaluation of the slip along the steel-encased concrete interface surface length under different loading magnitudes. The first part of the curves presented a stiff behavior corresponding to an initial bond provided by the concrete–steel connection. It is named "adhesion" or "chemical bond", and corresponds to a small part of the bond strength, which is active mainly in the early stages of loading, when the displacements are small. As shown in details in (Fig. 11), for Specimen (PEB), the adhesion broke when the load was approximately (10 kN). The rupture of the adhesion was not clearly identified for the specimens with mechanical connectors (PEB-B and PEB-W). In these specimens, it can also be seen that the presence of the mechanical connectors contributes to increasing the maximum load and slightly changes the applied load-slip relationship. Although all specimens behaved in a similar way in both pre-peak and post-peak branches, specimen (PEB) presented a slight reduction of the load capacity after the ultimate load had been reached. In the pre-peak branch, the specimens with mechanical connectors behaved in a stiffer manner and the specimen with vertical headed studs was stiffer than the specimen with horizontal studs. Therefore, the results indicated that the end slips of the specimens with studs were smaller than the specimen without studs and these mechanical shear connectors were more effective when the applied load was increased. Comparing the end slips in all specimens, the vertical position of the studs on the bottom flange was the most effective in all loading stages. It should be mentioned that the values of the slips were obtained from the (DOF solution, X-component of displacement).

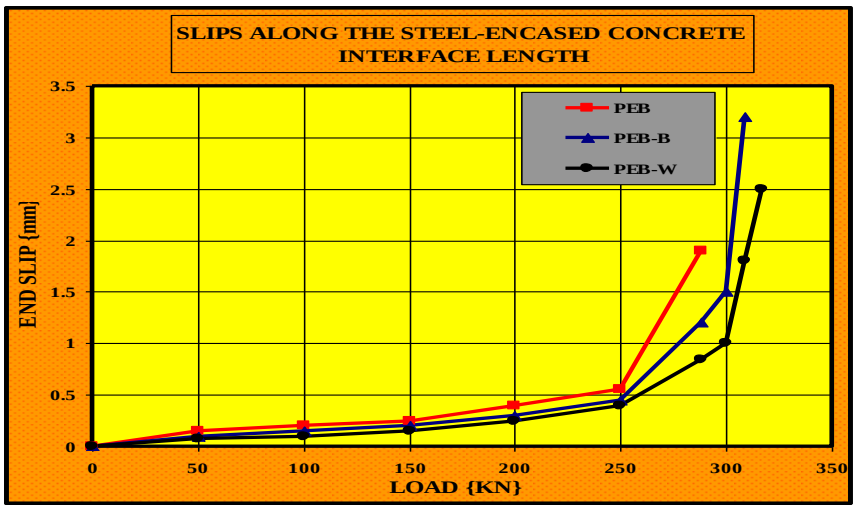

Fig. 11. Finite Element Results of Model (PEB, PEB-B and PEB-W) to Show the End Slips along the Steel-Encased Concrete Interface.

- THE EVALUATION OF STRAIN DISTRIBUTIONS ALONG THE STEEL SECTION AND ENCASED CONCRETE DEPTH:

The laminated encased beams (PEB), (PEB-B) and (PEB-W) which were described in (Fig. 5) are chosen to examine the strain distributions along the depth of both steel section and concrete encasement under different loading magnitudes as shown in (Fig. 12) through (Fig. 17). In the case of Specimen (PEB), without mechanical shear connectors, the strains of the steel profile increased with the same ratio until the ultimate state (when the applied load was equal to Fu)-(Fig. 12). Additionally, the strains on the bottom and top flanges presented approximately the same values. On the other hand, the strains of Specimen (PEB-B) presented an abrupt change in the tension zone, which did not occur in the compression zone and the increased proportionally to the neutral axis distance (Fig. 13). Additionally, the change of the strain behavior became more expressive when the applied load in each loading point reached (250 KN). The behavior of Specimen (PEB-W) was very similar to (PEB), including the values of the strains. Apparently, the horizontal studs were less effective than the vertical ones in providing the composite action and increasing the load carrying capacity (Fig. 14). By means of the neutral axis, the encasement concrete was more effective for Specimen (PEB-B), as such an axis was higher than in the other specimens.

- STRAINS IN THE BENDING AND SHEAR ZONES OF THE BEAM:

A SPECIMEN (PEB): WITHOUT SHEAR MECHANICAL CONNECTORS:

For the specimen without mechanical connectors (PEB), the strains increased proportionally to the neutral axis distance until (250 Kn) at a zone under constant shear. For the ultimate load (Fu), the strains in some points presented a sudden change (Fig. 15). Comparing the strain results for Specimen (PEB at (35 cm) of the end and mid-length, the sudden change could be only observed at the first zone, where the shear was constant. Probably, the natural bond at the interface between the steel profile and the concrete encasement was destroyed by the shear stress. Therefore, it can be said that the partially encased beam only behaved as a composite beam until the load of (250 KN). After that, the natural bond of the steel-concrete interface was broken, this was more evident in the length of the beam under shear constant. Regarding the strains at the mid-length of the beam, the natural bond was not broken in the constant moment zone, where the shear stresses are zero.

B SPECIMEN (PEB-B): WITH VERTICAL HEADED STUDS WELDED ON THE BOTTOM FLANGE:

The strains of Specimen (PEB-B) presented a large variation of the distribution in both moment and shear constant zones (Fig. 16). Apparently, the presence of vertical studs in the tensile zone modified the contribution of the natural bond and Specimen (PEB-B) did not behave as a composite beam from the first stages of loading. The sudden change of the strains was more expressive in the constant shear zone.

C SPECIMEN (PEB-W): WITH HORIZONTAL HEADED STUDS WELDED ON THE WEB:

The strains of the specimen with horizontal studs behaved as the specimen without mechanical shear connectors in the mid-length of the beam (Fig. 14). At (35 cm) of the beam end, abrupt changes could be observed from the first stages of loading, especially in the compressive zone (Fig. 17). These results showed that the headed studs horizontally welded on the web were not efficient regarding composite action.

Finally, all tested specimens showed a sudden change of the strains in the shear constant zone. Furthermore, the changes of strains occurred at the same points of the measurement but for different levels of the loading. Additionally, the change of the strains was first recorded in Specimen (PEB-W) and with a lower loading level.

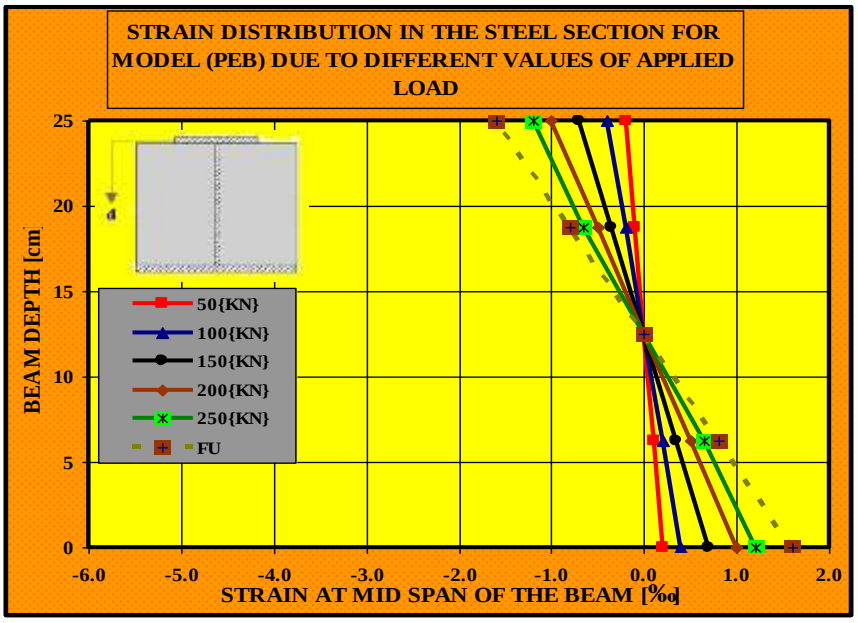

Fig. 12. Strain Distribution along the Depth of Steel Section for Model (PEB).

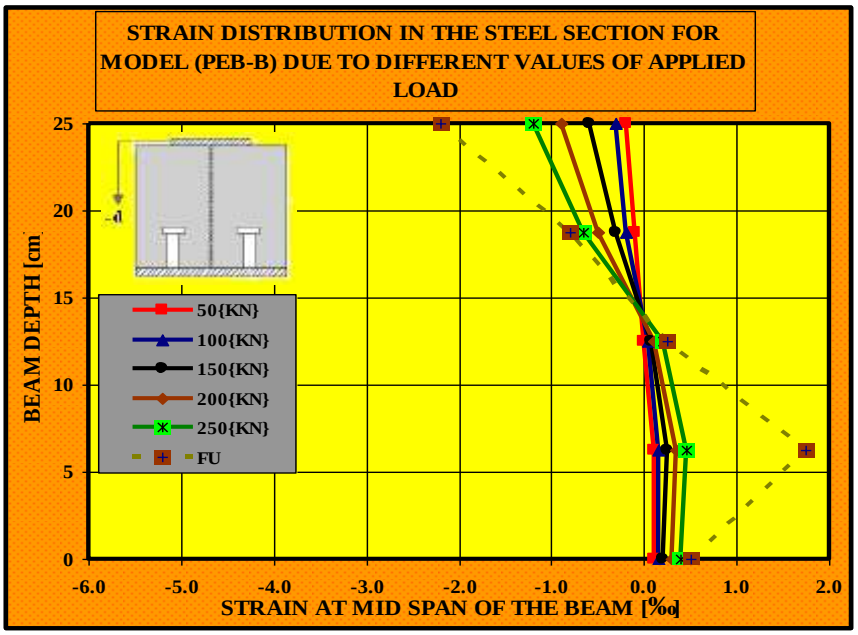

Fig. 13. Strain Distribution along the Depth of Steel Section for Model (PEB-B).

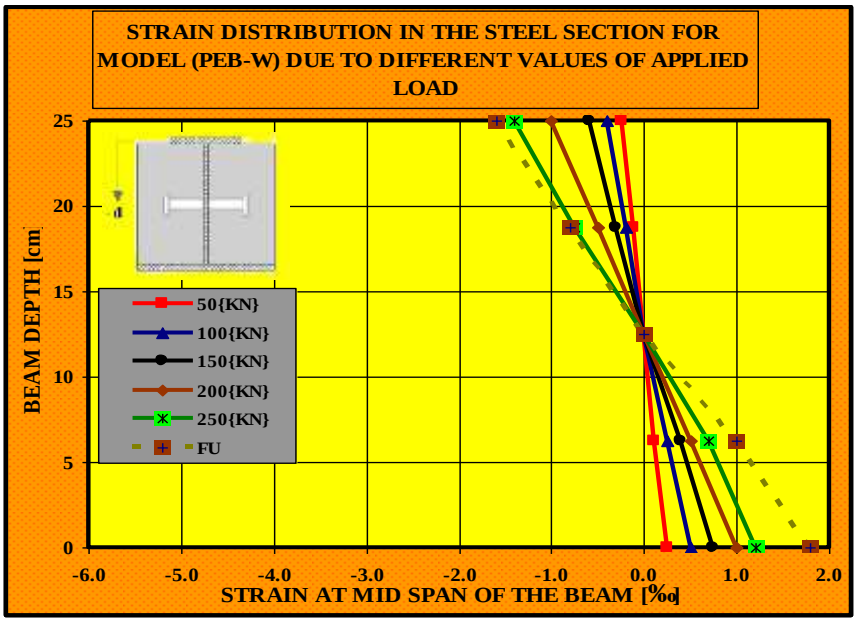

Fig. 14. Strain Distribution along the Depth of Steel Section for Model (PEB-W).

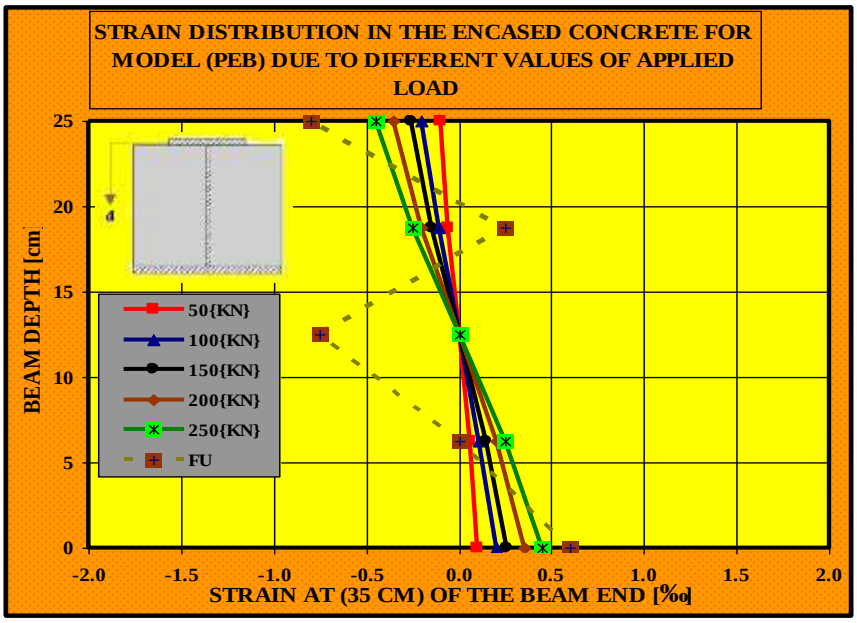

Fig. 15. Strain Distribution along the Depth of Encased Concrete for Model (PEB).

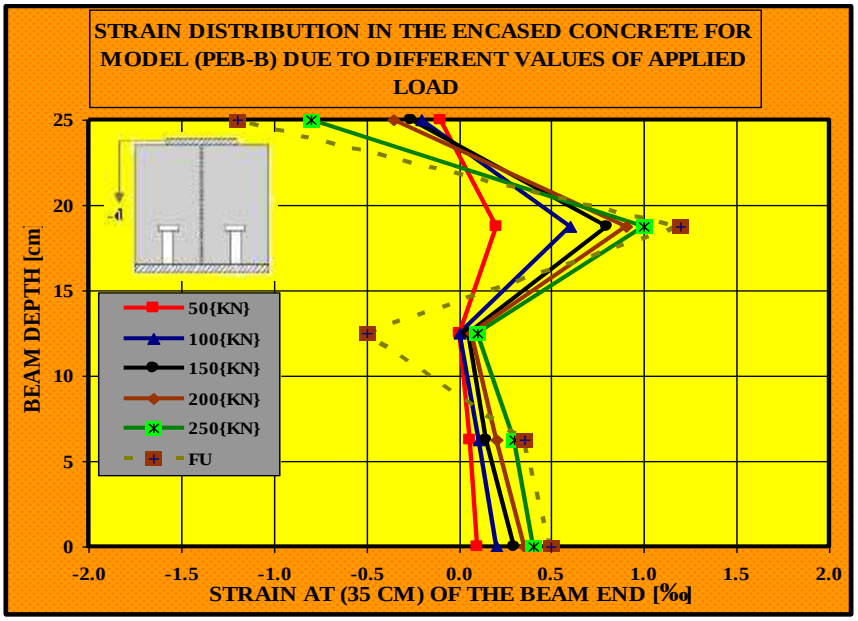

Fig. 16. Strain Distribution along the Depth of Encased Concrete for Model (PEB-B).

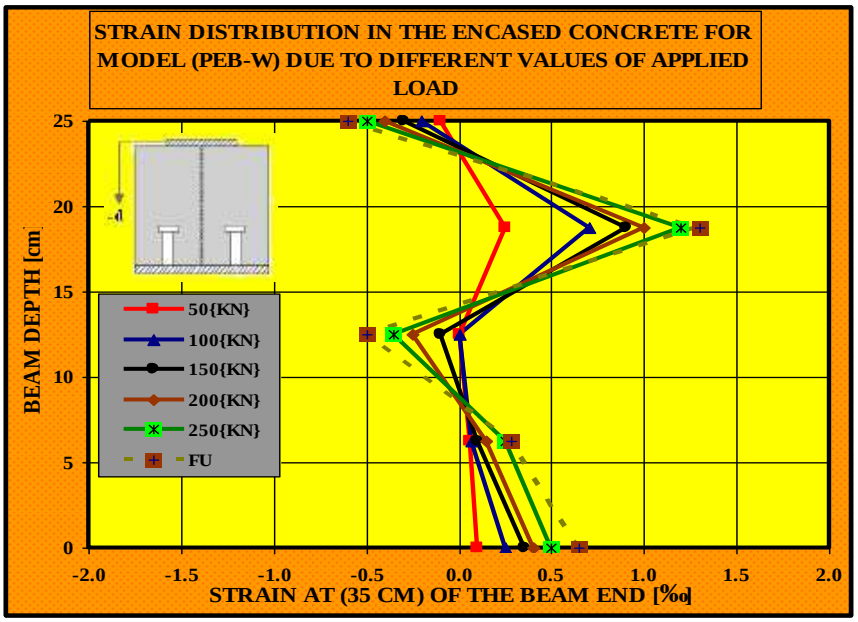

Fig. 17. Strain Distribution along the Depth of Encased Concrete for Model (PEB-W).

--EFFECT OF CONCRETE POISSON'S RATIO ON THE BEHAVIOR OF MODEL (PEB-W):

The composite partially encased beam (PEB-W) has been chosen to study the effect of variation of the concrete Poisson's Ratio on its behavior. This beam is described in details in (Figure 5). The beam (PEB-W) has an assumed concrete Poisson's Ratio equal to (ν=0.2) and it has been reanalyzed for values of (0.17 and 0.15). As shown in (Fig. 18). the ultimate load capacity of this beam has insignificant effect with reduction of Poisson's ratio value. The reduction in the ultimate load capacity is not more than (3 % and 5%) for the concrete Poisson's ratio values (0.17 and 0.15) respectively.

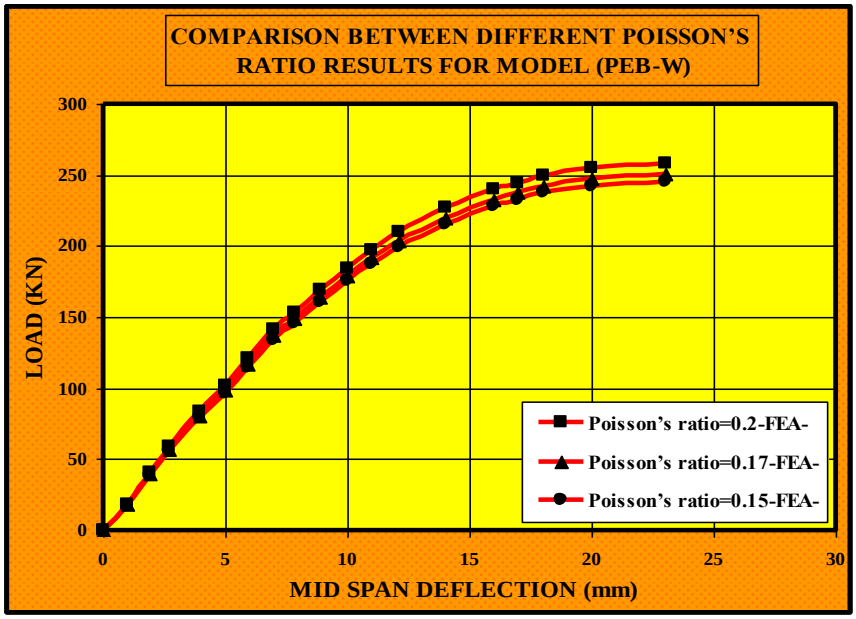

Fig. 18. Effect of Poisson's Ratio on the Behavior of Model (PEB-W).

- EFFECT OF THE COMPRESSIVE STRENGTH OF CONCRETE ON MODEL (PEB-B):

The composite partially encased beam (PEB-B) has been chosen to study the effect of variation of the compressive strength of concrete on its behavior. This beam is described in details in (Figure 5). The beam (PEB-B) has an experimental compressive strength of concrete equal to (46.540 N/mm2) and it has been reanalyzed for values of concrete compressive strength (f'_c) of (30, 60 and 70 N/mm2) as shown in (Fig. 19). The behavior of this beam with high compressive strength seems to be stiffer than those having smaller strength. The predicted ultimate load of this beam is increased by (12% and 18.1%) for concrete compressive strength values of (60 and 70)-(N/mm2), respectively, and reduced by (11.6%) for compressive strength value of (30 N/mm2) relative to the tested result.

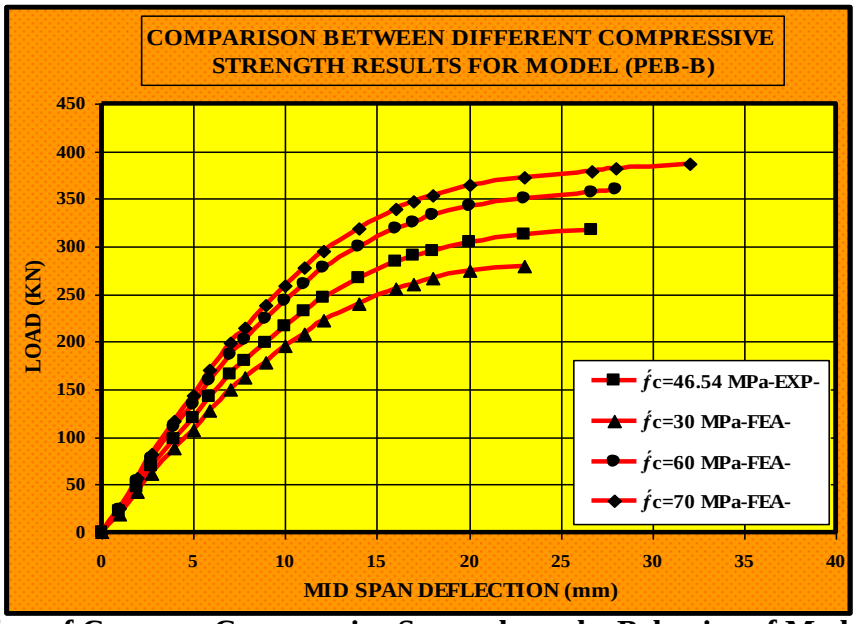

Fig. 19. Effect of Concrete Compressive Strength on the Behavior of Model (PEB-B).

*** CONCLUSIONS:**

Based on the results of this investigation, the following conclusions can be drawn:

1. The modeling of concrete by eight-node brick elements (**SOLID65** element), the I-steel section by the four-node shell element (**SHELL43** element), the steel reinforcement by two-node bar element (**LINK8** element), the shear stud by two-node nonlinear spring element (**COMBIN39** element) and the interface model by both (**SOLID65** element) on the surface of encased concrete and (**TARGE170** element) on the surface of steel section gives results which are close to the experimental results for the analysis of composite encased beams consisting of preflex steel section.
2. The failure load given by **ANSYS** computer program are close to that measured during experimental test.
3. The analyzed partially encased specimen with vertical studs {studs on bottom flange} are more efficient than the horizontal ones {studs on web} in providing the composite action between the steel profile and the concrete encasement, because the vertical stresses from concrete encasement acting on the surface of bottom flange and also the friction forces developed in the same surface is tremendously higher than that developed in the surface of steel section web.
4. According to the Applied load vs. End slip behavior, the specimens with headed studs can be considered ductile and the behavior is almost elastic-plastic, while the specimen without shear connectors slightly decreased in the applied load after the ultimate load capacity was reached. Therefore, both headed studs horizontally and vertically welded on the steel profile can be effectively used to provide composite action.
5. The values of strains at the steel-encased concrete surface (contact plane) for the models with full shear connection are nearly the same in comparative with the same model without shear studs were the strains values at the contact plane showing miner diverging.
6. The finite element results show that the Poisson's ratio has insignificant effect on the increasing or decreasing the ultimate load of the composite encased beams.

NOTATIONS:

1-D	One Dimensional Mode
2-D	Two Dimensional Mode
3-D	Three Dimensional Mode
Ec	Modulus of Elasticity of Concrete
Es	Modulus of Elasticity of Steel
f	Function
f'_c	Uniaxial Compressive Strength of Concrete
f_t	Uniaxial Tensile Strength of Concrete
P	Applied Concentrated Load
ε	Strain
ε_{cu}	Ultimate Strain
ν	Poisson's Ratio
τ	Shear Stress
Δ_p	Cambering Produced in the Steel Section
Δ	Deflection
y	Distance from the Steel Section Centroid to the Top Surface of Compression Plange
I	Moment of Inertia
M	Bending Moment

REFEENCES:

***** EUROCODE 4. In: Design of composite steel and concrete structures – Part 1-1: General Rules and rules for buildings. European Committee for Standardization; 2004.

***** ANSI/AISC 360-05. In: Specification for structural steel buildings. American Institute of Steel Construction; 2005.

***]** PR NBR 8800. In: Design of steel and composite structures for buildings. Brazilian Association of Standard Codes; 2007.

***** N. Roussel, S. Staquet, L. D'Aloia Schwarzentruber, R. Le Roy, and F. Toutlemonde, "SCC Casting Prediction for the Realization of Prototype VHPC-Precambered Composite Beams", Materials and Structures, Vol. 40, 2007, pp.877–887 .

***** Bernuzzi C, Zandonini R. In: Buckner D, Shahrooz BM, editors. Slim floor steel–concrete Composite systems. Composite construction in steel and concrete, vol. III. Germany: ASCE; 1996. p. 486–99.

***** Breuninger U. Design of lying studs with longitudinal shear force. In: International Symposium on connections between steel and concrete; 2001. p.1015–24.

***** Dipaola V, Prete F, Prete G. The elasto-plastic behaviour of encased composite beams for Slim floors in multi-storey buildings. In: 2nd international congress–Fib. Naples: FIB. 2006. p. 1–12 (ID 5-24).

***** Kuhlmann U, Kürschner K. Structural behaviour of horizontally lying shear studs. In: 5th International conference in composite construction in steel and concrete. South Africa; 2005. p. 534–43.

***** Ju Y-K, Kim S-D. Structural behavior of alternative low floor height system using structural Tee, half precast concrete, and horizontal stud. Canadian J. Civil Engineering 2005;32(2):329–38.

***** Hegger J, Goralski C. Structural behavior of partially concrete encased composite sections With high strength concrete. In: 5th international conference in composite construction in Steel and concrete. South Africa; 2005, p. 346–55.

***** Silvana De Nardin, and Ana Lucia H.C. El Debs, "Study of Partially Encased Composite Beams with Innovative Position of Stud Bolts"Journal of Constructional Steel Research, March-2008, pp.1–9 .

***** Swanson Analysis Systems, ANSYS. Online manual, version10.0 (2005) and Theory Reference.10th ed. Swanson Analysis Systems, s.1., s.d.

***** Method of Manufacturing Preflex Beams", World Intellectual Property Organization (International Bureau), International Publication Number: WO 01/18319 A1, International Publication Date: 15 March 2001, pp 1-56.

***** F.D. Queiroza, P.C.G.S. Vellascob, and D.A. Nethercota, "Finite Element Modeling of Composite Beams with Full and Partial Shear Connection", Journal of Constructional Steel Research, Vol.63, 2007, pp.505–521.

PERFORMANCE ANALYSIS OF INVERTER-FED SINGLE-PHASE INDUCTION MOTOR

Ali M. Saleh Amer O. Kareem
College of Engineering, University of Baghdad

ABSTRACT

This study investigates the effects of the presences of harmonics in the exciting voltage when using a dc/ac inverter on the performance of a single-phase induction motor, the investigation includes theoretical and experimental parts and together with performance comparison of the motor with the nominal sinusoidal input voltage. The computed performance of the motor depend on the theoretical equivalent circuits which are modified to take into account the existence of harmonics in the inverter output to compute the performance at each harmonic order. It conclude from the analysis that the pulsating torque is inherent in single-phase induction motor even when supplied from a sinusoidal voltage source. Particular attention has been devoted to the pulsating torque when the motor is supplied from an inverter and the most important pulsations have been identified. The comparisons of simulation and measured results show good correlation between them in addition that it highlight and identify the cumulative effects of harmonics on the motor performance.

KEYWORDS
Harmonics, Single-Phase Induction Motor, Inverter

الخلاصة : يتناول البحث دراسة تأثيرات المحتوى التوافقي للفولتية المحتثة من عاكسة (dc/ac Inverter) على أداء محرك حثي أحادي الطور، يتألف البحث من أجزاء نظرية و عملية تقارن أداء المحرك باستخدام فولتية جيبية و فولتية العاكس. تم استخدام مبدأ الدوائر المكافئة في عملية حساب الأداء النظري للمحرك، حيث تمت عملية تعديل على هذه الدوائر لكي تتناسب مع حساب الأداء لكل مركبات التوافقيات(Harmonic Order). إن الاستنتاج التحليلي أكد تأصل وجود العزم النبضي في المحرك الحثي أحادي الطور حتى عند تغذية المحرك بمصدر جيبي الفولتية. تم تكريس الاهتمام بالعزم النبضي للمحرك المجهز من العاكسة مع دراسة و تعريف (Pulsation) الأهم في هذه الحالة. إن مقارنة النتائج النظرية و القيم العملية بينت اتفاق جيد بالإضافة الى تركيز الاهتمام و تحديد تأثيرات تراكم التوافقيات الأكثر أهمية على أداء المحرك.

INTRODUCTION

The single-phase induction motor is widely used in low-power and variety applications such as domestic refrigerators and a wide variety of pumping applications, since this machine is logically least expensive, lowest maintenance and operates with a single-phase power supply. Almost 90 per cent of induction motors are squirrel cage rotor type, since this type of rotor has the simplest and most rugged construction imaginable and almost indestructible[1]. In special application, the dc power supply or special batteries are the main

source type which only exist to drive the AC induction motor. Then, the available power has to be converted to an AC power for driving the AC induction motors, and for this aim one can use the electromechanical rotary converters or the static dc/ac converters (inverters). The last type of converter is started replacing the old rotary converters, since the use of a rotary type is associated with increase in machine size, weight and losses, while the static inverter has higher accuracy, better reliability, reduced maintenance, higher efficiency and lower in cost than the old rotary converter[2]. The output voltage waveform of the inverter is non-sinusoidal since the principle operation of the inverter is based on the switching techniques. Using the Fourier analysis shows that the output voltage and current waveforms of the inverter are rich in harmonics which may have serious problems and influences the performance of the motor. At least, the harmonics can be a source of extra losses in induction motor in addition to higher noise level.

The work presented in this study deals with steady state operation condition of the inverter-fed single-phase induction motor, and the equivalent circuit model which has been adopted in this study has been modified in order to predict the performance of the motor under load conditions.

ANALYSIS OF INVERTER-FED SINGLE-PHASE INDUCTION MOTOR

For the purpose of generality, the work presented in this study considers a single-phase induction motor fed from an inverter of a quasi-square waveform output voltage**.** Analyzing this waveform is given in Appendix[A]and shows that such a waveform which is the stator voltage of the motor which have a fundamental component and a series of harmonics. Thus, the overall performance of the motor can be described as it is connected to an independent generators all in series supplying the motor. Since each harmonic current will be independent of all the others, a series of independent equivalent circuits (one for each harmonic) can thus be used to calculate the complete steady state performance of the motor. If the magnetic saturation is neglected, the motor can be regarded as a linear device and the principle of superposition can be applied [2,3,4,5,6]. That is the motor's behavior can be analyzed independently for the fundamental and for each other harmonics term [7].

SINGLE-PHASE INDUCTION MOTOR WITH SINUSOIDAL VOLTAGE SUPPLY

The per-phase equivalent circuit referred to the stator windings (i.e. the main winding) of the single-phase induction motor for a sinusoidal voltage supply is shown in figure(1) Which realized from the symmetrical component theory. The core loss is neglected in the magnetizing branch. The magnetic flux mutual to both stator and rotor has two sequence magnetizing currents flow: I_{mp} and I_{mn}. The effect of motor speed is reflected by the presence of slip in the rotor impedance in the equivalent circuit. In this circuit the motor input impedance is given by:-

$$Z = 2Z_m + Z_{2p} + Z_{2n} \quad \ldots\ldots\ldots\ldots (1)$$

Where:-

$Z_m = r_1 + jx_1$, $Z_{2p} = jX_m \,//\, ((r_2 / s) + j x_2)$, $Z_{2n} = jX_m \,//\, (r_2 /(2- s) + j x_2)$

The sequence currents are :-

$$I_p = I_n = V \,/\, Z \quad \ldots\ldots\ldots\ldots (2)$$

Then, the stator winding input current is:-

$$I = I_p + I_n \quad \ldots\ldots\ldots\ldots (3)$$

And the total input power is :-

$$P_{i/p} = V\ |I|\ \cos(\theta) \quad \ldots\ldots\ldots\ldots (4)$$

The air-gap power is:-

$P_g = P_{gp} - P_{gn} = 2(| I_p |^2 \ R_{2p} - | I_n |^2 \ R_{2n}) = 0.5 |I|^2 \ [R_{2p} - R_{2n}]$ ..……..……(5)

While the rotor loss is :-

$$P_{rcu} = s\, P_{gp} + (2-s)\, P_{gn} \quad \text{……..……..……..……(6)}$$

The developed gross output power is :-

$$P = (1-s)\, P_g \quad \text{……..……..……(7)}$$

The net developed torque measured in Nm is :-

$$T = P_g \ / \ \omega_s \quad \text{……..……..……..……(8)}$$

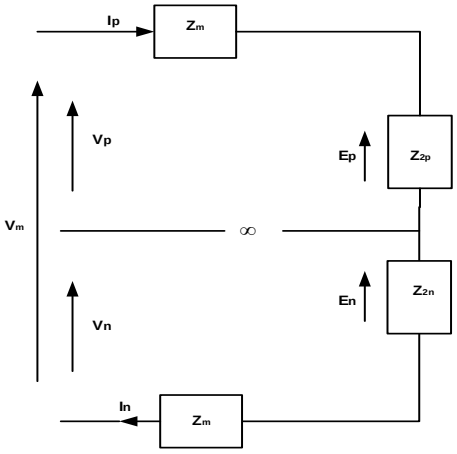

Figure(1) Fundamental equivalent circuit of single-phase induction motor

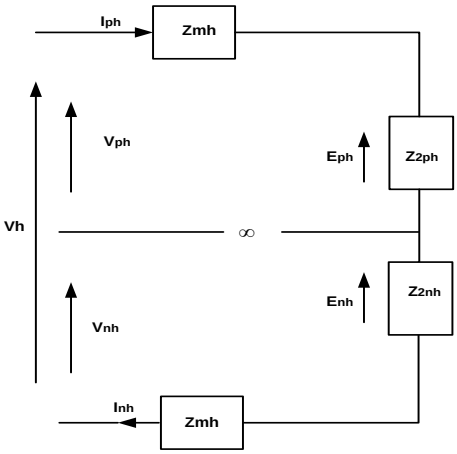

Figure(2) The harmonic equivalent circuit of single-phase induction motor

SINGLE-PHASE INDUCTION MOTOR WITH NON-SINUSOIDAL SUPPLY

It is well know that a single-phase induction motor can be run on a non-sinusoidal supply. If the physical non-linearities of the induction motor (the magnetic saturation) is considered of negligible effects then the motor may be regarded as a linear device. Thus, the periodic non-sinusoidal supply voltage waveform could be resolved using the Fourier Series method**.** The behavior of the machine is obtained by superposing the effects of the fundamental and harmonics. This method provides information about individual harmonic performance.

According to Appendix[A], there will be no even order harmonics (i.e. $h \neq 2, 4, 6$…etc) for the quasi-square waveform, since the waveform is symmetrical. Then the only order of harmonics which exist are h=1, 3, 5……etc. and these are the only orders of harmonic that could affect the motor performance. For convenience, the existing harmonics can be expressed as:-

$$h \text{ (harmonic order)} = |4k \pm 1| \quad \text{……..……..(9)}$$

Where k=0, 1, 2, 3….etc (constant) The harmonics of orders h=4k+1 (i.e. h=5,9,13,17,…etc) travels in the same direction as the fundamental at a speed equal to (4k+1)Ns. The harmonics of order h=4k-1 (i.e. h=3,7,11,…..,etc) travel in the opposite direction of the fundamental field with speed of rotation equal to (4k-1)Ns. Equation (9) could be written in the form for more convenience :-

$$h = 1 \pm 4k \quad \text{……..……..……(10)}$$

in order to specify the direction of each harmonic, too.

Frequency of Harmonic Rotor Current

The fundamental frequency equivalent circuit of the single-phase induction motor is shown in figure(1) must be modified in order to take into consideration the harmonic frequencies. This modification can be performed by introducing the following changes[3, 8]:-

1. All the reactances have a value of "h" times their value at the fundamental frequency .
2. The operation slip is the s_h.

A time harmonic of order "h" have a harmonic synchronous speed (h N_s) while the machine is rotating at speed "N_r". Thus the "h^{th}" harmonic slip of motor is :-

$$s_h = \frac{h \pm (1-s)}{h} \qquad \text{……………………………………………….….(11)}$$

Where:-

s is the fundamental slip.
s_h "h^{th}" harmonic slip of motor.
N_r rotating speed of the machine (rpm).
N_s synchronous speed (rpm).

The frequency of rotor current have positive and negative components. Then the frequency of the "h^{th}" harmonic positive sequence current component is:-

$$f_{2ph} = s_h\,(h\ \ f_1) = (\,h-1+s\,)\,f_1 \qquad \text{………..………………….…….(12)}$$

while the frequency of the "h^{th}" harmonic negative sequence current component is:-

$$f_{2nh} = (2-s_h)\,(h\,f_1) = (h+1-s)\,f_1 \qquad \text{……………………………..(13)}$$

where f_1 is the Stator supply frequency (Hz)

Harmonic Equivalent Circuit

For any harmonic voltage (V_h) at frequency (h f_1), the rotor equivalent circuit of single-phase induction motor will appear as shown in figure(2). The parameters of the circuit are:-

$Z_{mh} = r_{1h} + j\,x_{1h}$, $Z_{2ph} = jX_{mh} \,//\, ((r_{2h} / s_h) + j\,x_{2h})$, $Z_{2nh} = jX_{mh} \,//\, (r_{2h} /(2-s_h) + j\,x_{2h})$

The rotor of the machine which is used in the work presented in this study is a cage type rotor. The crowding of current at the top of the bars increases with rotor current frequency. However the effective resistance of cage-rotor is only slightly larger than the ohmic resistance unless the bars are very deep[3, 9]. Therefore, with a low saturation level one can assume that:-

$$x_{1h} = h\,x_1 \qquad x_{2h} = h\,x_2 \qquad X_{mh} = h\,X_m \qquad r_{1h} = r_1 \qquad r_{2h} = r_2$$

Then the parameters of the circuit which shown in figure(2) will be modified as below:-

$Z_{mh} = r_1 + jhx_1$

$Z_{2ph} = (jh\,X_m) \,//\, ((r_2/ s_h)+jh\,x_2)$

$Z_{2nh} = (jh\,X_m) \,//\, (r_2/(2-s_h)+jh\,x_2)$

The positive and negative harmonic current components I_{ph} and I_{nh} are respectively given by :-

$$I_{ph} = I_{nh} = V_h / (2\,Z_{mh} + Z_{2ph} + Z_{2nh}) \qquad \text{…..……..………….(14)}$$

The harmonic input current component :-

$$I_{mh} = I_{ph} + I_{nh} \qquad \text{…………………………………….………….(15)}$$

Then the r.m.s value of total input current is :-

$$I_m = \sqrt{\sum_{h=1,3,5}^{h=\infty} |\,I_{mh}\,|^2} \qquad \text{………………………………………….….(16)}$$

OBVIOUS HARMONIC EFFECTS (LOSS INCREASE)

In general, harmonics are usually defined as a periodic steady state distortion of voltage and/or current waveforms in power system[10]. The effects of the harmonics are highly variable, which in range of non-significance effect to equipment destruction, but in general the harmonics always decrease both the efficiency and effective power factor of the load and the harmonics currents cause increased heating and audible noise in motors and magnetic devices[11]. Harmonic voltages produce harmonic currents that in turn, generate not only torque pulsation but also increase the losses in the form of copper and core losses. The additional losses due to the harmonics tax the thermal capability of the motor[2]. The conventional induction motor has the following losses[12, 13, 14] :-

(i) Stator copper loss;
(ii) Rotor copper loss;
(iii) Core loss;
(iv) Friction and windage loss;
(v) Stray loss.

The presence of harmonics causes the stator and rotor copper losses to increase, as for the core loss. Magnetic loss in metallic parts caused by harmonic leakage flux is difficult to estimate. It is believed that ignoring these losses can introduce negligible error compared to the harmonic copper losses[3,15]. The frictional and windage losses are independent on the harmonics [4].

Stator Copper Loss

The total harmonic current is:-

$$I_{har} = \sqrt{(|I_{m3}|^2 + |I_{m5}|^2 + \ldots + |I_{mh}|^2)} \quad \ldots\ldots(17)$$

Then the stator copper loss is (neglect the effects of the skin factor) :-

$$P_{scu} = I_m^2 \; r_1 \quad \ldots\ldots(18)$$

Where I_m is the r.m.s value of total input current. Then:-

$$P_{scu} = (I_{m1})^2 r_1 + (I_{har})^2 r_1 = \sum_{h=1,3,..}^{h=\infty} P_{scuh} = P_{scu1} + \sum_{h=3,5,..}^{h=\infty} P_{scuh} \quad \ldots\ldots(19)$$

The term $[(I_{har})^2 r_1]$ is representing the extra harmonic stator copper loss. This additional losses will increase the conductor temperature due to higher current density.

Rotor Copper Loss

The rotor copper loss is evaluated independently for each h^{th} harmonic:-

$$P_{rcuh} = 0.5 \; |I_{mh}|^2 \; (s_h \; R_{2ph} + (2 - s_h) R_{2nh}) \quad \ldots\ldots(20)$$

The total harmonic copper loss is calculated as a summation of the harmonic contributions.

$$P_{rcu} = \sum_{h=1,3}^{h=\infty} P_{rcuh} \quad \ldots\ldots(21)$$

Also :-

$$P_{rcu} = P_{rcu1} + \sum_{h=3,5}^{h=\infty} P_{rcuh} \quad \ldots\ldots(22)$$

It's clear that the second term in the (22) is representing the additional rotor copper loss due to harmonic currents.

AVERAGE DEVELOPED TORQUE

The interaction between the components of the air-gap flux and the rotor current of the same harmonic frequency generates steady torques. From the harmonic equivalent circuit in figure(2), it is clear that each harmonic component produce an air-gap power (corresponding to the harmonic torque) in both positive and negative sequence directions (namely τ_{ph}, τ_{nh} respectively) acting at a speed of "h ω_s" (radian per second). The sequence component of the air-gap power is given by the following formula:-

$$\tau_{ph} \; h \; \omega_s = 2 \; |I_{ph}|^2 \; R_{2ph} \quad \ldots\ldots(23)$$

$$\tau_{nh} \; h \; \omega_s = 2 \; |I_{nh}|^2 \; R_{2nh} \quad \ldots\ldots(24)$$

Since $I_{ph} = I_{nh}$ for the motor under investigation, the "h^{th}" harmonic equivalent torque (in synchronous watt) referred to the fundamental frequency given by:-

$$\tau_h = (\tau_{ph} - \tau_{nh}) / h = 2 \; |I_{ph}|^2 \; (R_{2ph} - R_{2nh}) / h \quad \ldots\ldots(25)$$

The order of the harmonic defines the direction of the net developed torque, and therefore the torque will act in the positive direction for the orders 1, 5, 9,….,etc, and having a positive value. For negative direction rotating fields (of order 3,7,11,….,etc,) the net torque is having a negative value (braking) and then the net develop torque due to the fundamental and harmonic current are :-

$$\tau = \sum_{h=1,3}^{h=\infty} \tau_h \quad \ldots\ldots\ldots\ldots\ldots\ldots\ldots\ldots\ldots\ldots(26)$$

Obviously, τ_h becomes very small as "h" increased and thus the most important torque contribution arises from the low order harmonics.

TORQUE PULSATION

Sinusoidal Supply

With a sinusoidal supply, the input current of the single-phase induction motor, produces negative and positive sequence field components. Then in addition to the developed steady torques by these components a pulsating torque is exist with an average value of zero. The pulsation is a result of the interaction between the "fundamental" positive and negative sequence flux components with the "fundamental" negative and positive sequence rotor current components, respectively. The frequency of the generated torque is the difference between the corresponding frequency of the producing flux and currents[2,3], i.e. it is (2f). Table(1) Summaries the possible interaction of the present components with each other and the frequency of the pulsating torque or the direction of the resulting average torque, whichever is applicable. The flux components are replaced in this table by the air-gap voltages produced by them.

The general expression of the pulsation torque resulting from the different sequence field components:-

$$t_{pulsation} = t_{vn} + t_{vp} \quad \ldots\ldots\ldots\ldots\ldots\ldots\ldots\ldots\ldots\ldots(27)$$

where :-

$$t_{vn} = p\ L_m\ |I_{mp1}|\ |I_{2n1}|\ \sin(2wt + x) \quad \ldots\ldots\ldots\ldots\ldots\ldots(28)$$

$$t_{vp} = -p\ L_m\ |I_{mn1}|\ |I_{2p1}|\ \sin(2wt + y) \quad \ldots\ldots\ldots\ldots\ldots\ldots(29)$$

And:-

$$x = 90 - (\arg(E_{n1}) - \arg(I_{2n1})) \quad \ldots\ldots\ldots\ldots\ldots\ldots\ldots\ldots(30)$$

$$y = 90 - (\arg(E_{p1}) - \arg(I_{2p1})) \quad \ldots\ldots\ldots\ldots\ldots\ldots\ldots\ldots(31)$$

Non-Sinusoidal Supply

The presence of the harmonic currents can generate (in addition to the steady-torque) parasitic torques which are superimposed with the fundamental useful steady-state torque. These generated harmonic torques are two types :-

(i) Steady torque; resulting from the interaction between the harmonic current with harmonic flux of the same order. This type is usually of little importance since:-

- Harmonic currents and harmonic flux, both are relatively small in magnitude as compared to the fundamental (depends on the layout of windage).
- The forward torque produced by the positive sequence components will be partially reduced by the reverse torque that produced by the negative sequence components.

(ii) Oscillatory (pulsating) torques (with zero average value); resulting from the interaction of each harmonic current with the harmonic flux of the different orders. However, the oscillatory torques which produced by the interaction of harmonic currents with the fundamental flux (the most significant flux in the single-phase induction motor) will be predominant.

Table(2), shows a sample of the pulsation torque being considered for analysis in this study. The frequency of the pulsating torque is the difference between the frequencies under consideration[3]. From this tablehe instantaneous pulsation torque is given by:-

$$t_{puls} = t_{vn} + t_{vp} \quad \text{.....(32)}$$

Where:-

$$t_{vn} = p\, L_m\, |I_{mp1}|\{\, |I_{2n1}|\sin(2wt + x) + |I_{2p3}|\sin(2wt + i)\,\} \quad \text{.....(33)}$$

$$t_{vp} = -\, p\, L_m\, |I_{mn1}|\{|I_{2p1}|\sin(2wt + y) + |I_{2n3}|\sin(2wt + e)\,\} \quad \text{.....(34)}$$

And:-

$$x = 90 - (\arg(E_{n1}) - \arg(I_{2n1})) \quad \text{.....(35)}$$

$$y = 90 - (\arg(E_{p1}) - \arg(I_{2p1})) \quad \text{.....(36)}$$

$$i = 90 - (\arg(E_{p3}) - \arg(I_{2p3})) \quad \text{.....(37)}$$

$$e = 90 - (\arg(E_{n3}) - \arg(I_{2n3})) \quad \text{.....(38)}$$

THEORETICAL AND EXPERIMENTAL RESULTS

The results of the simulation programs which are based on the theoretical analysis are compared with the experimental results, in order to demonstrate the validity of the theoretical model analysis. The tests with sinusoidal and inverter excitation are compared, too. The conclusions derived for such comparisons will identify the effects of feeding a single-phase induction motor upon it's operation with much more confidence. The practical measurements fall into two types, depending on the type of the supply that used to feed the motor. One of them is the sinusoidal voltage waveform while the other is the quasi–square voltage waveform. The experiments are divided into two sets of tests, each one of them measured the performance of the motor at various loads while only the main winding is in operation with rated voltage at rated frequency.

Table (1) Interaction between the air-gap flux and rotor current components in case of sinusoidal.

Stator	Rotor	Torque	Direction/frequency of pulsation
E_{p1}	I_{2p1}	Steady	Forward
E_{p1}	I_{2n1}	Pulsation	2f
E_{n1}	I_{2p1}	Pulsation	2f
E_{n1}	I_{2n1}	Steady	Backward

Table(2) Reaction of stator and rotor harmonics for nonsinusoidal

Stato	Rote	Torq	Direction/freq pulsatio
E_p	I_{2p}	Steady	Forward
E_p	I_{2n}	Pulsat	2f
E_n	I_{2p}	Pulsat	2f
E_n	I_{2n}	Steady	Backward
E_p	I_{2p}	Pulsat	2f
E_p	I_{2n}	Pulsat	4f
E_n	I_{2p}	Pulsat	4f
E_n	I_{2n}	Pulsat	2f
E_p	I_{2p}	Pulsat	4f
E_p	I_{2n}	Pulsat	6f
E_n	I_{2p}	Pulsat	6f
E_n	I_{2n}	Pulsat	4f

Operation with Sinusoidal-Waveform Supply

The measurements of the stator input current and the computed stator losses are plotted as a function of slip as shown in figure(3) and (4), the corresponding theoretically predicted current and losses as shown on the same figures, too. Both of these figures have a good agreement with the simulation results.

Measured and computed input power are shown in figure(5). This figure shows that the measured values slightly higher than the computed values with no more that 7% which may be attributed to neglecting of the core losses assessment in the analytical model.

The measured results of the output torque is plotted in figure(6) together with the calculated developed motor torque. The difference between the measured and calculated values is less than 14% at the worst case since the mechanical losses where not include in the mathematical model.

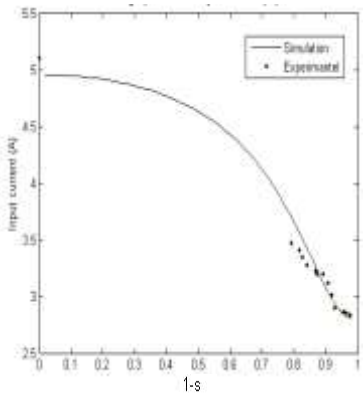

Figure(3) Input current

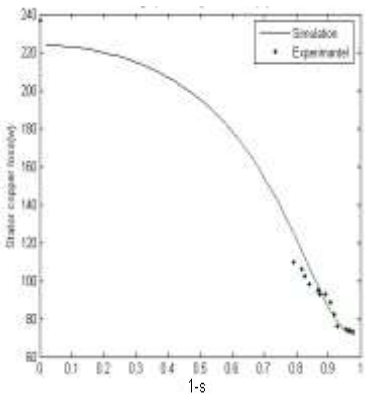

Figure(4) Stator loss

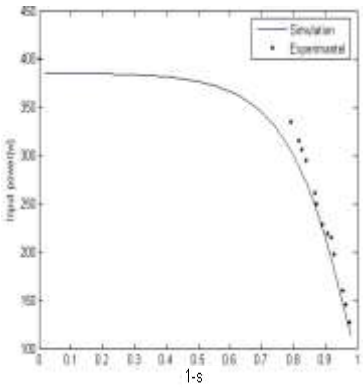

Figure (5) Input power

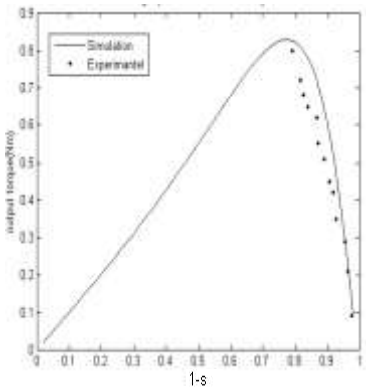

Figure(6)Output torque

Operation with Quasi-Square Waveform Supply

In this test the single-phase induction motor is supplied by a 50Hz inverter of a quasi-square waveform voltage, such that the fundamental voltage component is equal to the rated value. Figure(7.a) shows the experimental applied voltage waveform at the terminals of the motor at load conditions. Figure(7.b,c) shows that the harmonic order 5,15,…etc are not exist, since the ON-time ratio of the quasi-square voltage of the used inverter is 80%**.** Figures(8) and (9) show the experimental and simulation waveforms of the supply input current with it's harmonic spectrum**.** Good agreement between the simulation and experimental oscillogram of the input current graph is shown, noting that the simulation program plot the algebraic summation of the fundamental and harmonic spectrums of the input current up to 19th

harmonic order. Inclusion of harmonics orders higher than the 19th was found to be of little importance.

The supply line current harmonics as a percentage of the fundamental line current (I_h/I_1) are shown in figure(10) for different loading conditions. It shows that with load increase; the percentage harmonic current are decrease, since the increase in the fundamental current component.

-a- -b- -c-

Figure(7) Input terminal voltage of the motor(a)Experimental waveform(100v/div,5ms/div) (b)Spectrum analyzer (c)Harmonic simulation components

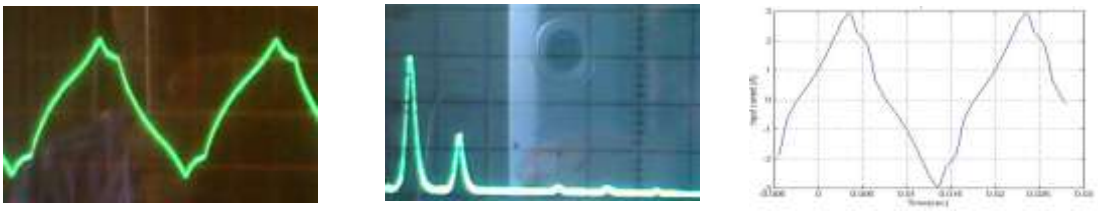

-a- -b- -c-

Figure(8) Input current to the motor at s=0.05 (a) Experimental waveform of current (2A/div, 5ms/div)(b) Spectrum analyzer(c)Simulation waveform of current

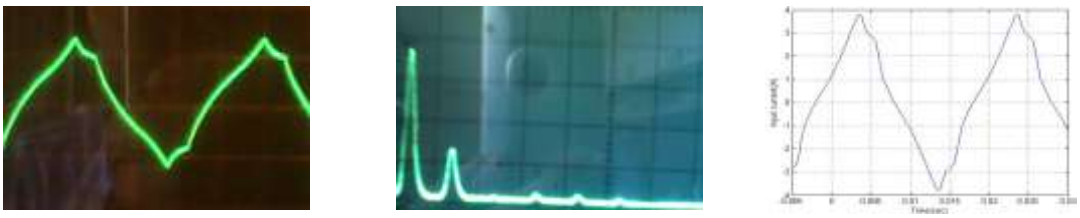

-a- -b- -c-

Figure(9) Input current to the motor at s=0.2 (a) Experimental waveform of current (2A/div, 5ms/div)(b) Spectrum analyzer(c) Simulation waveform of current

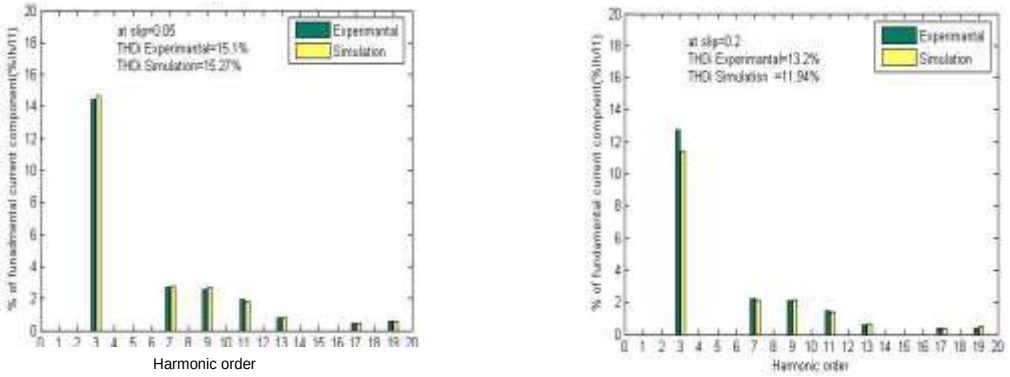

-a- -b-

Figure (10) Comparison of the simulation and experimental results of the input current harmonics as a percentage of the fundamental at (a)s=0.05, (b)s=0.2.

The measured and computed stator input current as a function of slip is shown in figure(11) with a good a agreement. The stator loss have slightly higher difference between the simulation and experimental results as shown in figure(12). The input power results have a significant difference between the simulation and experimental results as shown in figure(13) within 9.7% error. In figure(14) the torque measurements are lower than the computation outcomes by 18.5%. The mechanical losses are neglecting in the simulation analysis, and the difference is expected.

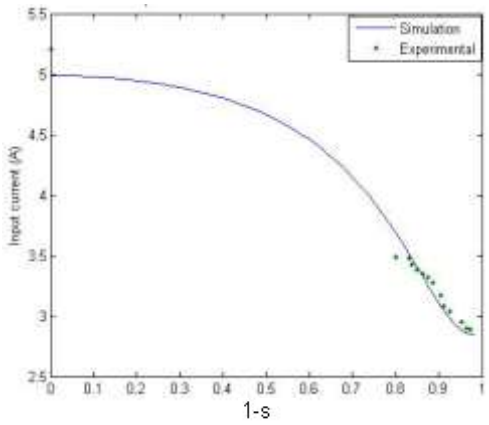

Figure(11) Input current

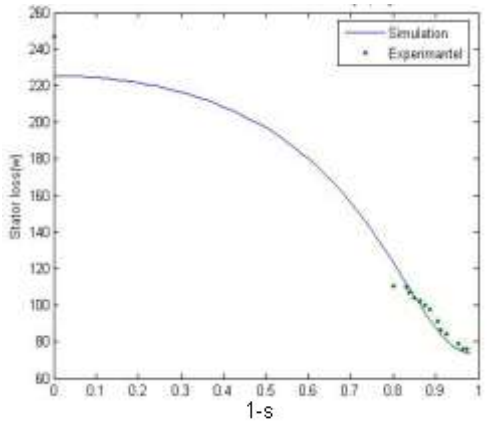

Figure(12) Stator loss

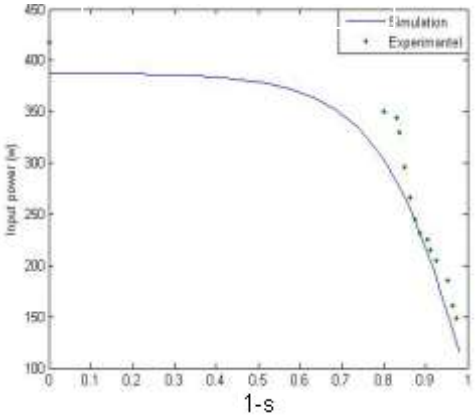

Figure(13) Input power

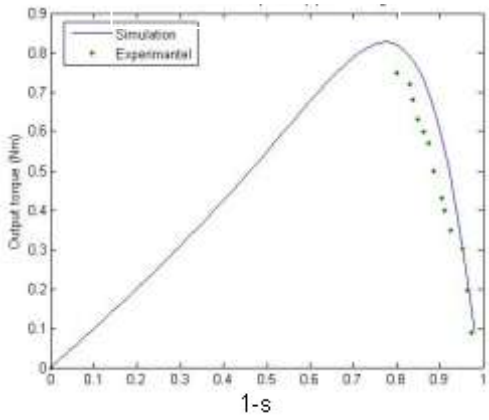

Figure(14)Output torque

SIMULATION RESULTS

Since the experimental tests cannot be performed beyond the point of the maximum torque, it is believed that using the simulation results is very useful to determine the operational parameters of single-phase induction motor with two types of supplies down to zero speed. This will be very useful in realizing the cumulative influences of harmonics existence on the performance of motor.

Figure(15) shows the motor input current for the two types of supplies. It is clear from this graph that there is a small increase in current due to the presence of harmonics. Figure(16) illustrates the increase in the stator loss of the motor, as a result of the increase in the rms input current, slightly greater than the sinusoidal supply. For the same reasoning, it can be noted in figure(17) the slightly difference between the simulation graph of input power.

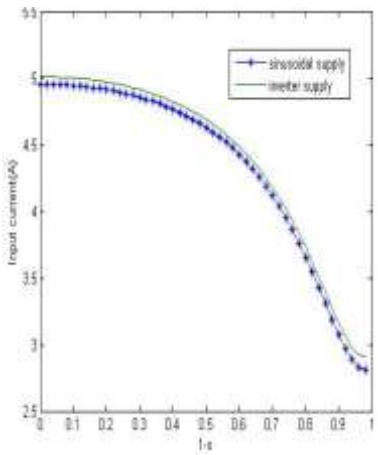

Figure(15) Variation of Input current

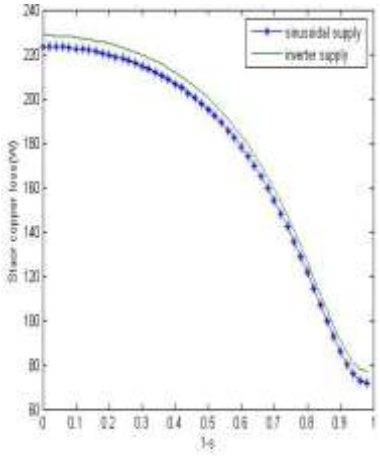

Figure(16) Variation of stator loss

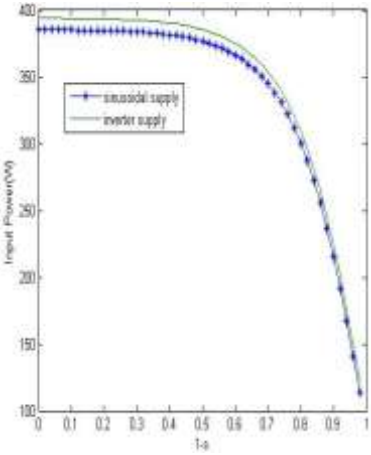

Figure(17) Variation of input power

The simulation results of the torque pulsation are computed for single-phase induction motor at the sinusoidal and inverter excitation, and then plotted as a functions of time for each type of feeding. It is clear from the graphs shown in figures (18) and (19), that the torque pulsation of the inverter-fed motor is larger than that of the sinusoidal supply, as a results of the presence of harmonics.

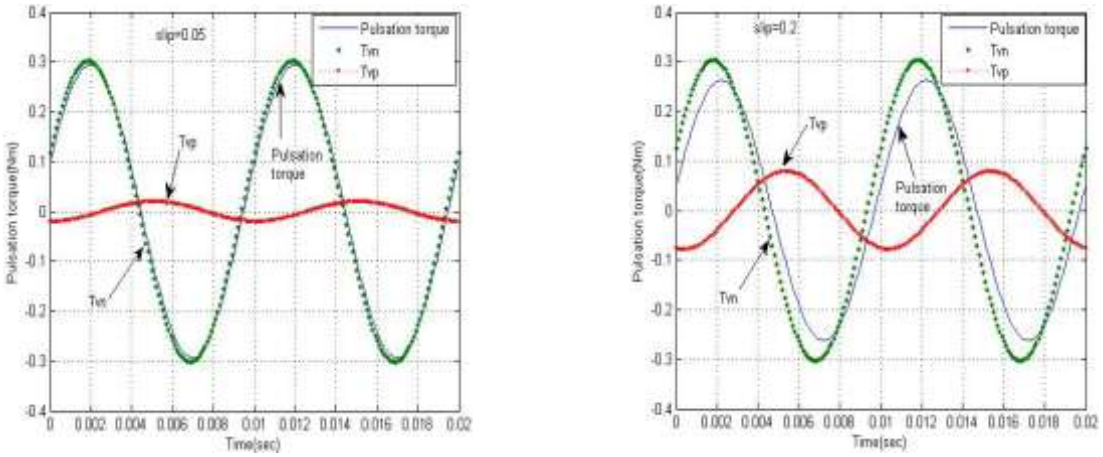

Figure (18) Instantaneous pulsation torque at different loading condition of single-phase induction motor at sinusoidal supply

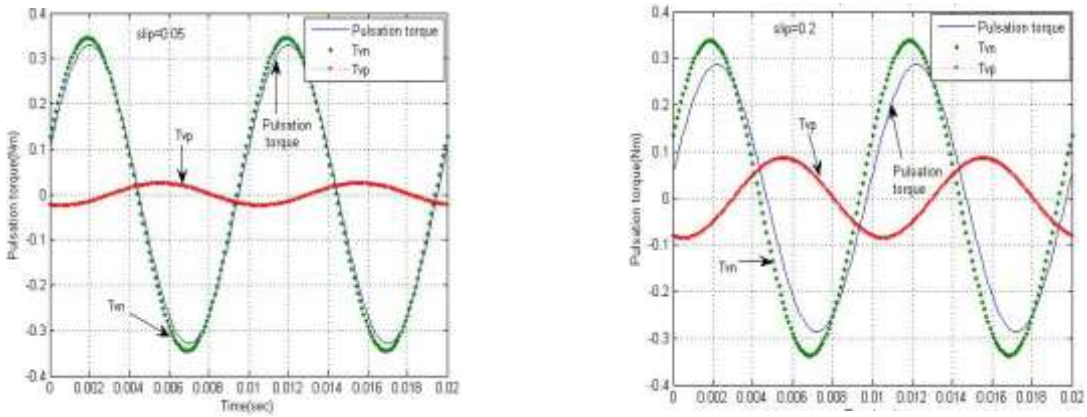

Figure(19) Instantaneous pulsation torque at different loading condition of single-phase induction motor at inverter supply

CONCLUSIONS

From the comparisons of the theoretical and experimental results one can conclude that the theoretical analysis developed in this study can reasonably simulate the motor performance. The harmonics voltages and currents lead to increase in the input current, input power and motor losses and consequently lead to a drop of the efficiency as a result of the decrease in the output torque. The increase of the input power is mainly consumed in the motor as losses representing an additional source of heat, which in turn lead to increases in stator and rotor resistance and thus reduces the fundamental torque and decreasing the thermal capability of the motor. The interaction of the harmonic currents with harmonic flux of the same order produces a steady torque which could be positive or negative. However, the harmonic currents and harmonic fluxes are relatively small as compared with the fundamental and each pair of them torques are acting against each other, which may decrease each other and the net torques is too small.

The pulsation torque is inherent in single-phase motors, even when supplied from sinusoidal voltage source. With a non–sinusoidal voltage supply, the peak value of the pulsating torque is higher than that of the sinusoidal supply as a result of the presence of harmonics. The most important torque pulsation is that at two times the fundamental frequency. All the present orders of harmonics are contributing in the generation of the pulsating torque through their interaction with the other orders(including the fundamental). Thus, the torque pulsation is not confined to (2f), but higher frequency torque pulsations are also exist. However, there pulsations are of small amplitude and their net is reducing with the order of the contributing harmonic, and therefore they are of little importance.

REFERENCES

- C. G. Veinott; "Fractional and sub-fractional horsepower electric motors", MC Graw–Hill Book company; Third Edition, 1970.

- J. M. D. Murphy; "Thyristor Control of A.C. Motors", Pergamon Press Ltd., Headington Hill Hall, Oxford, 1973.

- A. M. Saleh; "Effects of Time Harmonics on Induction Gyromotors", IJCCCE, No. 2, Vol.2, pp. 1-11, 2001.

- R. Krishnan; "Electric motor drives, modeling, analysis and control", Prentice Hall Electronics and VLSI series released, Feb. 2001.

- S. K. Biswas and D. P. Sen Gupta; "Performance Analysis of an Asymmetrical Phase-Converter Fed Induction Motor", IEEE Transactions on Industry Applications, Vol.34 , No.5, pp. 1049-1058, Sep/Oct, 1998.

- P. C. Sen and G. Premchandran; "Improved PWM Control Strategy For Inverters and Induction Motor Drives", IEEE Transactions on Industrial Electronics, Vol.IE-31, No.1, pp. 43-50, February, 1984.

- Z. Y. Walid; "Thyristor Control of A Single Phase Induction Motor", M.sc. Thesis; Baghdad University ,June,1977.

- B. J. Chalmers and B. R. Sarkar : "Induction–Motor Losses due to Non-sinusoidal Supply Waveforms", IEE,Vol.115, No. 12, pp. 1777-1782. December, 1968.

-T. A. Lipo; "An-improved weighted total harmonic distortion index for induction motor drives", OPTIM. Brasov; Romania; 2000, vol.2, pp.311-322, (lipo@engr.wisc.edu).

- G. C. Jain; "The Effect of Voltage Waveshape on the Performance of a 3-Phase Induction Motor", IEEE Transactions on Power application and system, Vol. 83, pp. 561-566, June, 1964.

- B. L. Theraja and A. K. Theraja; "Electrical Technology", Ram Nagar, New Delhi, 1989.

-K. S. Al-Sabagh; "Performance And Design of Single Phase Induction Motors", M.sc. Thesis ; Baghdad University, 1976.

-W. S. Wood; "Theory of Electrical Machines", Butterworth's Scientific Publications, London, 1958.

- K. S. Rama Rao and M. Ramamoorty; "Design optimization of inverter fed 3-phase squirrel cage induction motor", National conference on computer–Aided Design, India, pp. 1-5, 1999.

-A. T. Radhi ; "Effect of Harmonics on Solid-Rotor Induction Motor", M.sc. Thesis, Baghdad University, 2004.

APPENDIX[A]

Consider the general form for the quasi-square wave, shown in figure(A.1), where **ß** is the conduction period. This rectangle waveform can be analyzed by using Fourier series using.

$$v(wt)=\begin{cases} -E & -(\pi+\beta)/2 < wt < -(\pi-\beta)/2 \\ 0 & -(\pi-\beta)/2 < wt < (\pi-\beta)/2 \\ E & (\pi-\beta)/2 < wt < (\pi+\beta)/2 \end{cases}$$

This function is an odd function since $v(-wt)=-v(wt)$, therefore a_h =0, i.e., no cosine term.

The function have symmetry a bout the x-axis, therefore a_0 =0, and since the wave has symmetry about each half cycle (i.e., $v(wt+\pi)=-v(wt)$) so there are no-even harmonic, therefore :-

$$b_h=\frac{2}{\pi}\int_{(\pi-\beta)/2}^{(\pi+\beta)/2} E\sin(hwt)d(wt)$$

Hence:-

$$b_h=\frac{4E\sin\left(\frac{h\beta}{2}\right)}{h\pi} \qquad \text{.....(A.12)}$$

The instantaneous value of "v" can be expressed as:-

Figure(5)
Input power

$$v(wt) = \sum_{h=1,3}^{h=\infty} \frac{4E \sin\left(\frac{h\beta}{2}\right)\sin(hwt)}{h\pi} \quad \text{.....(A.13)}$$

The peak and rms values of the fundamental component are; respectively :-

$\hat{V}_f = \hat{V}_1 = 4E \sin(ß/2) / \pi$ .....(A.14)

$V_f = V_1 = 2\sqrt{2}\, E \sin(ß/2) / \pi$ .....(A.15)

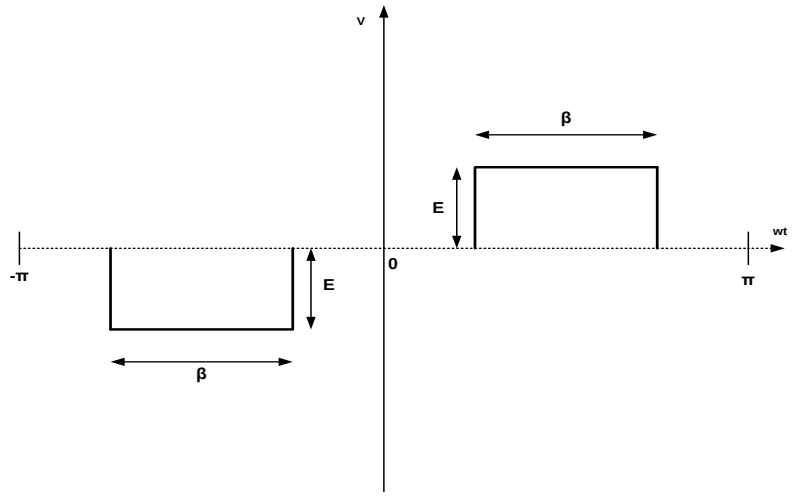

Figure(A.1) Quasi-square waveform.

Appendix [B]
Motor and Inverter Specifications

Main winding resistance, r_{1m}, Ω	9.1
Main winding reactance, x_{1m}, Ω	11.646
Auxiliary winding resistance, r_{1a}, Ω	18.1
Auxiliary winding reactance, x_{1a}, Ω	23.7
Stator magnetizing reactance, X_M, Ω	59.4
Rotor resistance referred to main, r_2, Ω	9.59
Rotor reactance referred to main, x_2 , Ω	11.646
Turn ratio	1.15
β (ON-time rating of the output voltage of the inverter)	80%

PID CONTROLLER DESIGN FOR THE SATELLITE ATTITUDE CONTROL SYSTEM

Sami Kadhim Hasan Ar-Ramahi
College of Information Engineering,
Nahrain University,
Baghdad- IRAQ.

ABSTRACT

A PID controller satellite attitude yaw-axis control system was designed to step the angle of the satellite body via actuating a precise angular position of a DC motor as quickly and accurately as most optimally possible. The (PID) controller was advantageously chosen for its quick transient response and zero steady-state error. A mathematical model has been derived for the whole satellite attitude yaw-axis control system. Then, the computation power of the MATLAB is utilized to obtain a generalized optimal controller design that enables the satellite attitude yaw-axis control system to have the quickest settling time without excessive overshoot and zero steady state error.

الخلاصة

تم تصميم مسيطر ثلاثي الانشطة (تناسبي / تكاملي / تفاضلي) لمنظومة السيطرة حول المحورالعمودي (الانعراج) لموقع القمر الاصطناعي بحيث يتم وضع جسم القمر الاصطناعي بالزاوية المطلوبة عبر محرّك مباشر التيار بامثل سرعة وافضل دقّة .تم اختيار المسيطر ثلاثي الانشطة لانفراده بسرعة اجتيازه للاستجابة العابرة وانعدام الخطأ في الحالة المستقرة.

تم اشتقاق النموذج الرياضي الكلي لمنظومة السيطرة حول المحورالعمودي (الانعراج) لموقع القمر الاصطناعي . ثم استثمرت القدرة الحاسوبية لبرامجيات **الماثلاب** للتوصّل لتصميم المسيطر ثلاثي الانشطة الامثل الذي يستطيع جعل منظومة السيطرة حول المحورالعمودي (الانعراج) لموقع القمر الاصطناعي ذات زمن استقرار اسرع بدون المرور عبر استجابات متجاوزة لنقطة الضبط وانعدام الخطأ في الحالة المستقرة.

KEY WORDS

PID controller, ACS mathematical model, satellite attitude yaw-axis control system, ACS

INTRODUCTION

The control task of the satellite attitude control system demands an optimal controller capable of precisely rotating the satellite body into the desired attitude. The researches concerning satellite attitude control system are now conducted within the premises of international space centers like NASA, The Danish Ørsted Geomagnetic Research center / ESA , and charted universities / institutions like Princeton Satellite

Systems, Inc., CTA Space Systems, Inc. [1], engineering college of swarthmore of sccs .

Although some international efforts had been recently reported in the design of attitude control system such as the Ørsted satellite attitude control system (ACS) project [5] [6] [7] [8] for its 65 kg micro-satellite, and a mutual project paper issued by Princeton Satellite Systems, Inc., together with CTA Space Systems, Inc., the development of Satellite Attitude Control System architecture, called the SPACECRAFTC ONTROL SYSTEM [1]. However this research paper reports an alternative powerful optimal controller design for the satellite ACS empowered by the computational tools of MATHLAB [3].

The satellite attitude control system manipulates, in this paper, the angular position of the satellite body around the yaw axis. A DC motor is advantageously selected [2] [5] as the actuating element to rotate the satellite body to the desired yaw angle. An amplifier is saturated by the correcting signal from the designed optimal PID controller [1] [2] [4] to obtain the quickest response with zero steady state error.

The mathematical model of the whole satellite system has been derived. A PID controller is optimally designed accordingly via a powerful MATLAB program and a Nyquist stability analysis is conducted.

SATELLITE SYSTEM MATHEMATICAL MODEL:

The satellite attitude control system can diagrammatically be represented by the following block diagram;

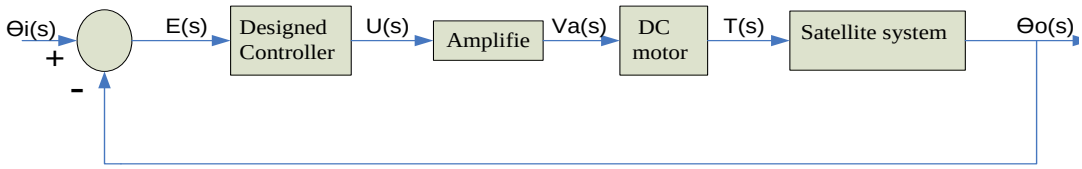

Fig.(1) The Satellite attitude control system

The moment of inertia of the entire system is J, which encompasses both the satellite body moment of inertia about the axis of rotation at the center of mass (J_f) and that's of the motors' armature (J_a). There is a viscous friction, B, as part of the load elements.

Let us first obtain the transfer function of the satellite system. The angular displacement $\theta_o(s)$ of the satellite body around the yaw-axis is the output of the satellite system and the DC motor torque T(s) is the input. Thus the transfer function of the satellite attitude system is ($\theta_o(s)$/ T(s)).

The differential equation for the load elements is; $J(\frac{d^2\theta_o}{dt^2}) + B(\frac{d\theta_o}{dt}) = T$ .. (1)

Taking the Laplace transforms of both sides of equation (1) and assuming zero initial conditions, we get after rearranging; $s(s+\frac{B}{L})\theta_o(s) = \frac{T(s)}{J}$ ..... (2)

Directly from equation (2), $\frac{\theta_o(s)}{T(s)} = \frac{1/J}{s(s+\frac{B}{J})}$ ……(3)

Next, the transfer function of the DC motor can be obtained as the torque T(**s**) is the output form the motor, and the input is the amplifier voltage (Va(**s**)), which supplies current (i_a) to the resistance (R) and inductance of the armature winding, consequently, the motor creates a back-emf, v_m. Thus, by applying the kirchhoff's voltage law, the differential equation for the DC motor armature circuit is;

$L(\frac{di_a}{dt}) + Ri_a = (v_a - v_m)$ ……. (4)

Taking the Laplace transforms of both sides of equation (4) and assuming zero initial conditions, we get; $I_a(s) = \frac{(V_a(s) - V_m(s))}{L(s+\frac{R}{L})}$ …….. (5)

Since the motor's torque (T) is proportional to the armature current, (i_a). Then,
$T=K_T i_a$ …….. (6)

Taking the Laplace transforms of both sides and Substituting, we get;

$$T(s) = \frac{K_T}{L}\frac{(V_a(s) - V_m(s))}{(s+\frac{R}{L})} \quad \text{…….. (7)}$$

Where, $K_{T;}$ is the torque gain.

And the angular velocity from the motor is proportional to the back-emf, v_m, thus;

$$v_m = K_m \frac{d\theta}{dt} \quad \text{…… (8)}$$

Where, $K_{m;}$ is the back-emf, (v_m), gain.

Since at steady state, the angular acceleration term = zero, in equation (1), so we get;

$$T = B\frac{d\theta}{dt} \quad \text{…… (9)}$$

From equations (8) & (9) we get, $v_m = \frac{K_m}{B}T$ …… (10)

Taking the Laplace transforms of both sides, substituting, and rearranging we get;

$$T(s) = \frac{K_T}{BL}\frac{(BV_a(s) - K_m T(s))}{(s + \frac{R}{L})} \quad \text{…….. (11)}$$

$$BL(s + \frac{R}{L})T(s) = (BV_a(s) - K_m T(s)) \text{ …….. (12)}$$

$$(BLs + BR + K_T K_m)T(s) = K_T BV_a(s) \quad \text{……. (13)}$$

$$(s + \frac{(BR + K_T K_m)}{BL})BLT(s) = K_T BV_a(s) \quad \text{…….. (14)}$$

$$T(s) = \frac{K_T}{L}\frac{1}{(s + \frac{(BR + K_T K_m)}{BL})}V_a(s) \quad \text{…….. (15)}$$

Hence, the DC motor has a first order transfer function; $\frac{T(s)}{V_a(s)} = \frac{K_k}{(s+b)}$ ….. (16)

Where, $K_k = \frac{K_T}{L}$, and, $b = \frac{(BR + K_T K_m)}{BL}$

Now, the control signal, U(s), is the feeding signal to the isolating amplifier of the DC motor, and its output, V_a (s), equals the input signal multiplied by the amplifier gain, $\mathbf{K_{amp}}$, hence the amplifier's transfer function is; $\frac{V_a(s)}{U(s)} = K_{amp}$ ... (17)

Therefore, the satellite attitude system transfer function $\frac{\theta_o(s)}{U(s)}$ can be obtained from equations. (3), (19) & (20), with the angular displacement θ_o(s) of the satellite body around the yaw axis is the output of the satellite system and the control signal, U(s), is the input as following; $\frac{\theta_o(s)}{U(s)} = \frac{K_{ak}}{s(s + \frac{B}{L})(s+b)}$ …… (18)

Where, $K_{ak} = \frac{K_{amp} K_k}{L}$

Equation (18) represents the satellite system transfer function which is a type one system.

The gains and the constant parameters within the general transfer function, as presented in equ (21), of the satellite system may be determined by selecting the closed loop pole locations. When selecting the pole locations, it is important to consider first the numerical values of the particular satellite body inertia, the DC motor armature inertia and electrical & electronics components, and the amplifier gain

value. Hence, the following numerical values will be accounted for in this paper to go forward in the optimal controller design; $\frac{\theta_o(s)}{U(s)} = \frac{1}{s(s+2(s+5)}$ …… (19)

PID CONTROLLER DESIGN:

The satellite attitude control problem, in this paper, is to design a PID controller, able to step the yaw-axes angle so that the satellite body can be rotated into the desired attitude with little overshoot as quickly as less than two second settling time estimated for an approximately 90 degree step. The settling time criterion was within 98% of the final value.

The PID controller might be designed, as the control platform scheme for the satellite attitude control system. The controller transfer function, $G_c(s)$, is;

$$G_c(s) = \frac{E(s)}{U(s)} = K_p(1 + \frac{1}{T_i s} + T_d s) \quad \text{…….. (20)}$$

Where, K_p = the proportional gain, T_i = the integration time, T_d = the derivative time. Since the satellite attitude transfer system has an integrator, equ (22), hence the PID design starts with the second method of the Ziegler-Nichols tuning rule [7] [9]; and the controller transfer function become; $G_c(s) = K\frac{(s+a)^2}{s}$ ……. (21)

And the control problem is to determine the values of, K, and, a, such that the unit step response will exhibit the maximum overshoot, m, between 5% and 0%, and the settling time, ts, will be less than 2 sec.

A MATHLAB program is written to set the search region as;

$2 \le K \le 40$ $0.05 \le a \le 0.5$

The step size for, K, to be 1 and that for, a, to be 0.05, so that to find the first set of variable (K) and (a) that will satisfy the satellite attitude control specifications.

The closed loop transfer function $\frac{\theta_o(s)}{\theta_i(s)}$ is given by;

$$\frac{\theta_o(s)}{\theta_i(s)} = \frac{(Ks^2 + 2Kas + Ka^2)}{(s^4 + 6s^3 + (5+K)s^2 + 2Kas + Ka^2)} \quad \text{…….. (22)}$$

A possible MATLAB program that produces the first optimal set of variable (K,a) and that will satisfy the given specifications is shown in appendix (1). The optimal values obtained by this program are; K = 21.0000, a = 0.3000, m% =4.71%, ts = 1.8100 sec. The resulting unit-step response curve is shown in appendix (2).

STABILITY ANALYSIS:

The designed optimal controller satellite attitude system may confidently be verified further by the stability analysis via Nyquist diagram. Thus, the open loop gain is given below: $G_c(s)G_{sat}(s) = \frac{K(s+a)^2}{s^2(s+1)(s+5)}$ ……. (23)

Substituting the optimal values (K, a) of the PID controller in the above equ., and re-write it into a polynomial form, we get; $G_c(s)G_{sat}(s) = \frac{(21s^2 + 1.26s + 1.89)}{(s^4 + 6s^3 + 5s)}$ … (24)

Consequently, the Nyquist plot is shown in appendix (4) as a result of running the MATLAB program in appendix (3).

Since the (-1) point is not encircled, the system is stable, which is confirmed by the obtained step response of the satellite attitude control system, as the unit step response exhibits the maximum overshoot, m, between 5% and 0%, the settling time, ts, is less than 2 sec, and zero steady state error. Thus the satellite did not lose control of itself when performing the real life operations in space.

COCLUSION

A PID controller is optimally designed for the satellite attitude control system so that the satellite body can be rotated around the desired Yaw-axis attitude of (90) degrees as quickly as less than (2) second settling time without excessive overshoot of not more than 4.71 %. A mathematical model for the satellite attitude control system is derived to be repeatedly utilized in analysis and design of the PID controller.

The powerful MATHLAB was the tool for the design and stability analysis stage. The outcome is a MATHLAB program which outputs an optimal PID controller parameters (K, a) to suite the control requirements of any satellite attitude control system.

REFERENCES

* W. I. Sullivan, M. A. Paluszek; Princeton Satellite Systems, Inc., W. K. Daniel; CTA Space Systems, Inc.: "A New Satellite Attitude Control System",14 PDF Pages, **2007**.
* K. Ogata, "Modern Control Engineering, "4th Ed: Person Education International, **2002**.
* K. Ogata, "Solving Control Engineering Problems with MATHLAB," Upper Saddle River, NJ: Prentice Hall, **1994**.
* R. C. Dorf, and R. h. Bishop, "Modern Control systems, "11th Ed: Upper Saddle River, NJ: Prentice Hall, **2008**.
* R. Wisniewski," Satellite Attitude Control Using Only Electromagnetic Actuation" Alborg University, Ph.D. Thesis **1997**, Department of Control Engineering, Denmark.
* S., R. Bøgh, T. Bak Wisniewski:" Autonomous attitude control system," IFAC Workshop on Control of Small Spacecraft, Breckenridge, USA, 5. February **1997.**

* T. Bak, R. Wisniewski, and M. Blanke: :" Autonomous attitude determination and control system for the Orsted," 1996 IEEE Aerospace Application Conference. Colorado, Feb.**1996**.
* S.A Bøgh, and M. Blanke, "Fault-Tolerant Control - a Case Study of the Ørsted Satellite", IEE Colloquium on Fault Diagnosis in Process Systems, York, UK, April **1997**

```
%%%%%%    PID controller for the SAC system %%%%%%%%%%%%%%%%%
t=0:0.01:2.5;
for k = 40:-1:2;%start outer loop to vary the k values
   for a = 0.5:-0.05:0.05;%start inner loop to vary the k values
      num = [0 0 k 2*k*a k*a^2];
      den = [1 6 5+k 2*k*a k*a^2];
       y = step(num,den,t);
       m = max(y);
       s = 251; while y(s)>0.98&y(s)< 1.02;
          s = s-1;end;
       ts = (s-1)*0.01;
       if m<1.05 & m > 1.00 & ts < 2.0
          break;% breaks the inner loop
       end
   end
   if m<1.05 & m > 1.00 & ts < 2.0
          break;% breaks the outer loop
       end
   end
   plot(t,y); grid; title( 'the satellite attitude control system unit step response')
   xlabel('t  sec'); ylabel(' the satellite angular yaw axis position')
  solution = [k;a;m;ts]

solution =

  21.0000
   0.3000
   1.0471
   1.8100
```

Appendix (1): a MATHLAB program to obtain the optimal PID controller parameters (K, a) that meets the satellite attitude control system.

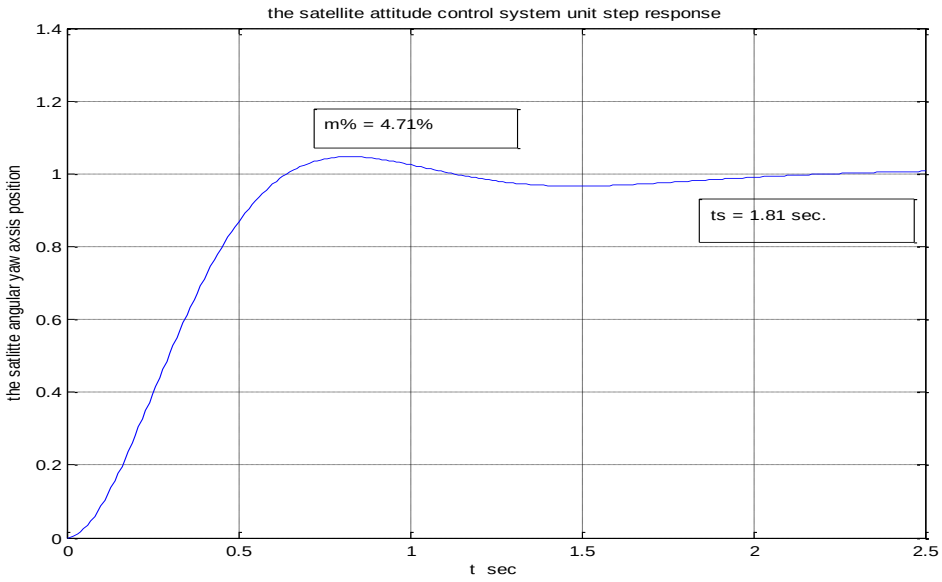

Appendix (2): The unit step response of the SAC system.

```
%%%%%%% Nyquist plot of the SAC system open-loop transfer function %%%%%
%%%%% Gc(s)Gsat(s) = (21s2+1.26s+1.89)/(s4+6s3+5s2)%%%%%% %%%%%%%

num = [0 0 21 1.26 1.89];
den = [1 6 5 0 0];
nyquist(num,den)
v = [-2 2 -5 5];axis(v)
grid
title('Nyquist plot of Gc(s)Gsat(s)')
```

Appendix (3): MATLAB program to plot the Nyquist Stability Diagram for the PID-controlled satellite attitude system.

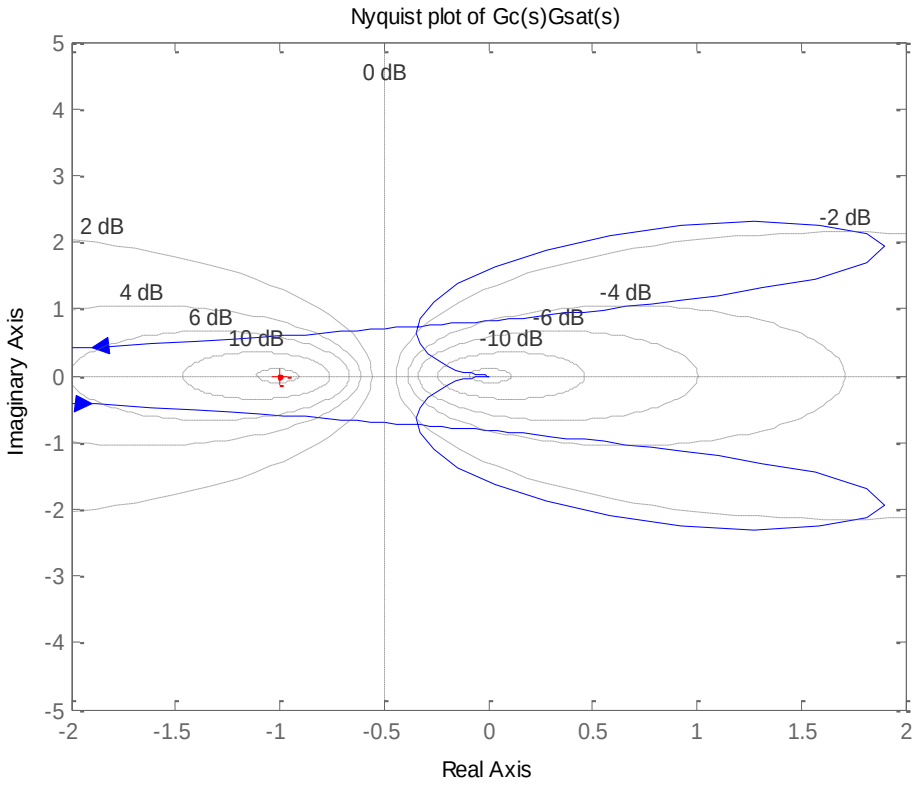

Appendix (4): Nyquist Stability Diagram for the PID-controlled satellite attitude system.

IMPROVED DATA DETECTION PROCESSES USING RETRAINING OVER TELEPHONE LINES

Sarcote.N..Abdullah
Electronic & Communication
Eng.Dept.College of Eng.
Baghdad University

ABSTRACT:
This paper describes two new developed detection processes for a modem over the public switched telephone network. The modem is a synchronous serial system using a 16-point QAM signal with a detector. The detector is preceded by an adaptive filter that is adjusted to make the sampled impulse response of the channel and filter minimum phase. The idea of these two new detectors is to transmit a known retraining data every specified interval and make use of these known data to improve the conventional nonlinear equalizer and near maximum likelihood detector.
Results of computer simulation tests are presented comparing tolerance to additive white Gaussian noise with retraining and with out retraining. The detectors with retraining achieve a better noise performance than conventional detectors. Furthermore the amount of retraining data is varied to find the best compromise between efficiency of data transmission and performance improvement

خلاصة:-
يصف هذا البحث طريقتين لعملية الكشف لمودم يعمل على خط التلفون: المودم يستعمل (16-QAM) مع الكاشف. يسبق الكاشف مرشح متكيف لجعل استجابة القناة المقطعة مع المرشح ذات حد ادنى للطور. فكرة هذان الكاشفان هو ارسال معلومات متفق عليها بشكل دورى والاستفادة من هذه المعلومات لتحسين اداء الكاشف نتائج المحاكاة باستخدام الحاسبة قدمت حيث تمت المقارنة بين اداء الكاشف مع إرسال المعلومات المتفق عليها وبدونها.استخدام المعلومات المتفق عليها ادى الى تحسن اداء الكاشفين بالنسبة للضوضاء. تم ايضا تغيرنسبة المعلومات المتفق عليها لايجاد افضل نسبة التى تجمع بين كفاءة الارسال مع جودة الاداء بالنسبة للضوضاء

KEYWORDS:
Detection,Equalizers,simulation,telephone channel,data transmission

INTRODUCTION:
In the search for a data- transmission system that achieves the fastest possible transmission over a linear channel ,a study must be made of the detection processes that

are the most tolerant to a considerable reduction in the bandwidth of the transmitted signal and hence a considerable intersymbol interference. The intersymbol interference can be removed by means of an equalizer which may be linear or nonlinear. But a better tolerance to noise is achieved through the use of a maximum likelihood sequence estimation implemented with Viterbi algorithm in place of the equalizer (Forney, 1972; Proakis,2001).

Unfortunately with severe intersymbol interference Viterbi algorithm becomes unacceptably complex, so that a simpler but somewhat less effective detector must be used. Considerable advances have been achieved in the development of a potentially cost effective detector, for the application just mentioned (Eyuboglu andQuereshi,1988;Duel-Hallen and Heegard,1989;Gerstacker and Schober,2002;Kamel and Bar-Ness,1994;Olivier et al,2003)(Xiang-guo and Zhi,2005)

A promising technique for overcoming this problem is to modify the Viterbi algorithm detector in such a way as to reduce both the amount of storage required and the number of operations per received data symbol but without reducing greatly the tolerance of the detector to noise, such systems are referred to as near maximum likelihood detector. These detectors, operate basically similar to the Viterbi algorithm but using a different selection process for the stored sequence of possible data symbol values, and only a very few of these sequences (typically 4-16) are stored with the corresponding costs (Clark et al ,1978;Clark and Fairfield,1981;Clark and Clayden,1984;Clark et al 1985;Clark and Abdullah,1987;Alhakim and Abduulah,1990)

* **System model**:

A model of the synchronous serial data transmission is shown in fig.1.

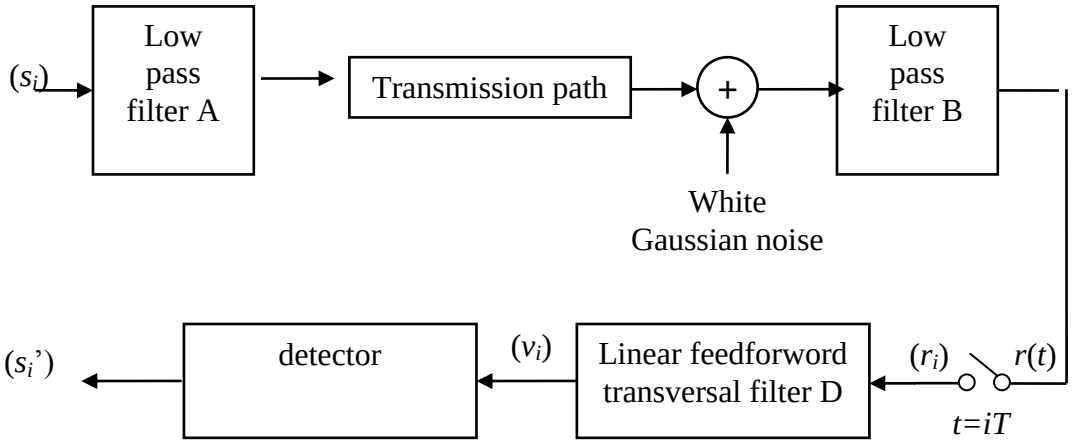

Fig.1 Model of data transmission system

The information to be transmitted is carried by the data symbol $\{s_i\}$ where

$$s_i = a_i + jb_i \qquad (1)$$

And $j = \sqrt{-1}$, a_i = ±1 or ±3 and b_i= ±1 or ±3 .

The $\{s_i\}$ values are statistically independent and equally likely to have any of their 16 possible values (16 point QAM). It is assumed that $s_i = 0$ for $i<0$, so that s_i is the $(i+1)^{th}$ transmitted data symbol (Fig.2).QAM is used because it is a bandwidth efficient modulation technique

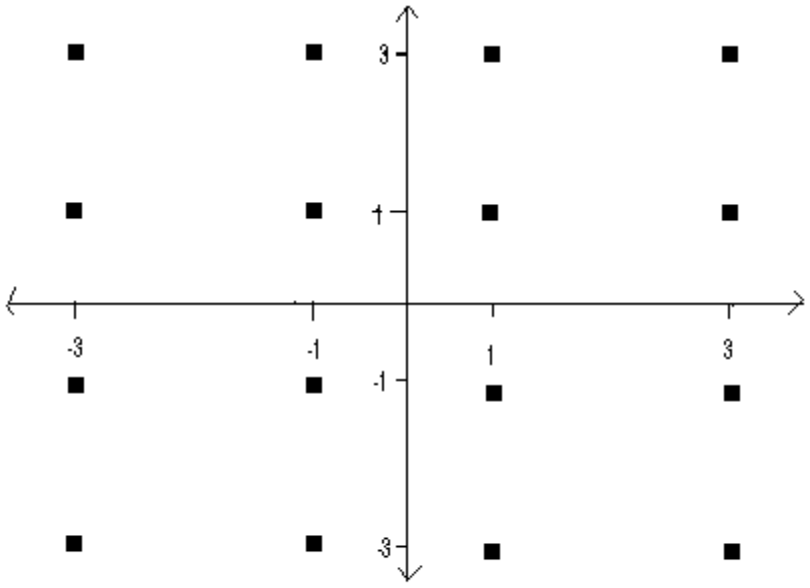

Fig. 2 16-point QAM signal constellation

.

The linear baseband channel includes a low-pass filter A (transmitter output filter),a linear baseband transmission path and a low pass filter B(receiver input filter).The transmission path includes a telephone circuit, together with a linear modulator at the transmitter and a linear demodulator at the receiver. The resultant channel has an impulse response $y(t)$,which has ,for practical purposes, a finite duration while Gaussian noise is added to the data signal at the output of the transmission path to give the bandlimited Gaussian noise waveform $w(t)$,with zero mean and fixed variance, at the output of the low pass filter B. The output waveform for the linear baseband channel is

$$r(t) = \sum_i s_i y(t - iT) + w(t) \qquad (2)$$

where $r(t)$, $y(t\text{-}iT)$ and $w(t)$ are complex valued in the case of telephone circuits, the shape of $y(t\text{-}iT)$ is independent of iT, such that $y(t\text{-}iT)$ is $y(t)$ delayed by iT seconds. The received waveform $r(t)$ is sampled at the time instants$\{iT\}$ to give the samples $\{r_i\}$, which are fed to the linear feedforward filter D, whose corresponding output samples are the $\{v_i\}$. The real and imaginary parts of the noise components in the $\{r_i\}$ are statistically independent Gaussian random variable with zero mean and fixed variance. The resultant sampled impulse response of the linear baseband channel and filter is given by the vector (sequence)

$$\boldsymbol{E}=[\ 1\ e_1\ e_2\ \ldots\ldots\ e_g\ ] \qquad (3)$$

The delay in transmission over the channel and filter D, other than that involved in the time dispersion of the signal, is neglected here, so that the first component of E (with value unity)is taken to have no delay. Also e_i =0 for $i < 0$ and $i > g$.
The linear filter D is an all pass network that adjusts the sampled impulse response of the channel and filter to be minimum phase .This filter may be adjusted adaptively without too much complexity(clark and hau,1987).The ideal adjustment of the filter is assumed throughout this paper. The signal at the output of the filter D, at time $t=iT$, is

$$v_i = \sum_{n=0}^{g} s_{i-h} e_h + u_i \qquad (4)$$

Where the real and imaginary parts of the $\{u_i\}$ are statistically independent Gaussian random variable with zero mean and fixed variance σ^2. The detector has exact prior knowledge of E and the possible values of s_i. It uses this prior knowledge to determine the detected values of $\{s`_i\}$ from its input signals $\{\ v_i\ \}$.

CONVENTIONAL NONLINEAR EQUALIZER:
In the conventional nonlinear equalizer just prior to the detection of si, the equalizer form

$$z_i = \sum_{n=1}^{g} \acute{s}_{i-h} e_h \qquad (5)$$

This is an estimate of the intersymbol interference in z_i and is subtracted from v_i to give the equalized signal

$$f_i = v_i - z_i \qquad (6)$$

Which is fed to a threshold level detector, with correct detection of the data symbols s_{i-1} ,s_{i-2}, ……, s_{i-g} the equalized signal becomes

$$f_i = s`_i\, e_o + w_i \qquad (7)$$

s_i is now detected as its possible value $s`_i$ such that $s`_i\, e_o$ is closest to f_i. The incorrect detection of one or more of the data symbols s_{i-1} ,s_{i-2}, ……, s_{i-g} leads to intersymbol interference in f_i and so greatly increase the probability of error in s_i. Errors in the detected data symbols therefore tend to occur in bursts (Clark and clayden, 1984)

CONVENTIONAL NONLINEAR EQUALIZER WITH RETRAINING:
Here it is similar to the conventional nonlinear equalizer except that at the end of training period it starts with correct detected data symbols $\{s_i\}$(fig. 3)from the known retraining period. Hence there will be a correct cancellation of intersymbol interference at each retraining period (eq. 6) .Fig.3 shows how the sequence of information data and training is transmitted. Furthermore it shows the various amount of training that is transmitted in each case

Retraining is already used in communication systems(such as GSM)(Olivier et al,2003).This detector makes use of it.

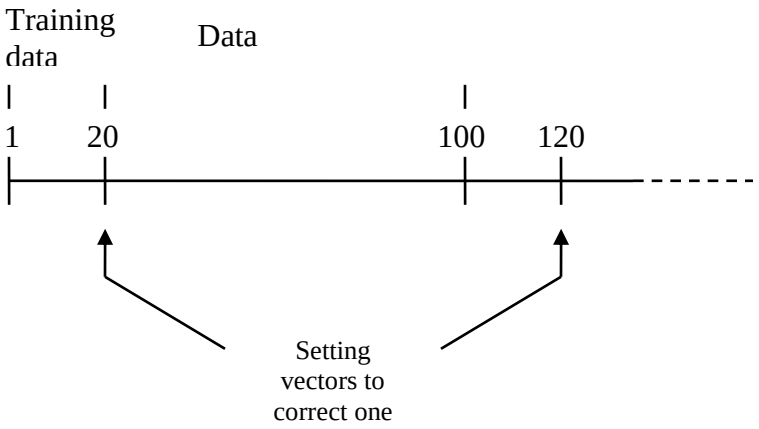

(a)

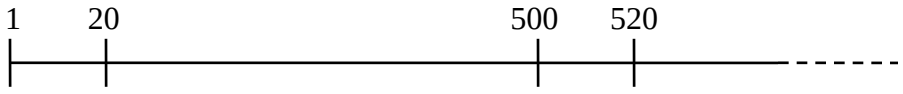

(b)

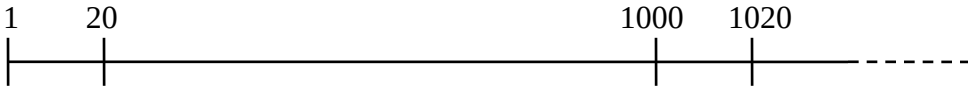

(c)

Fig.3 Different retraining cases **(a)** 20-100, **(b)** 20-500, and **(c)** 20-1000

NEAR MAXIMUM LIKELIHOOD DETECTOR (CLARK AND ABDULLAH, 1987):

The data transmission is as shown in fig.1, just prior to the receipt of the signal v_i from the filter D. The detector holds in store 16 n-component vector (sequence)$\{Q_{i-1}\}$where

$$Q_{i-1} = [x_{i-n} \;\; x_{i-n+1} \;\; \ldots \; x_{i-1} \;] \qquad (8)$$

And x_{i-h} takes on a possible value of s_{i-h} for h=1,2,… n. Each vector Q_{i-1} represents a possible sequence of values of the data symbols s_{i-n} s_{i-n+1} … s_{i-1}. Each of these vectors is first expanded to give the corresponding vector P_i

$$P_i = [x_{i-n} \; x_{i-n+1} \; \ldots \; x_{i-1} \; x_i] \qquad (9)$$

And hence the corresponding vector Q_i with the smallest cost. The cost is calculated from the equation

$$C_i = C_{i-1} + \left| v_i - \sum x_{i-n} e_n \right|^2 \qquad (10)$$

Where C_{i-1} is the cost of the vector Q_{i-1} from which P_i was derived. Three vectors $\{Q_i\}$ are added to each of the two smallest cost vectors, that differ only in the last component and with smallest cost. One vector Q_i is added to the third and fourth smallest costs of the set of 16,differing only in the last component and with smallest cost. No vectors are added to the four vectors $\{Q_i\}$ having the fifth to eighth smallest cost of the original set of 16 and the remaining eight of this set of vectors are discarded. There are now 16 vectors $\{Q_i\}$ together with their costs. The detected. Value s_{i-n}' of the data symbol s_{i-n} is now taken as the value x_{i-n} in the vector Q_i with smallest cost in the final set of 16 vectors

NEAR MAXIMUM LIKELIHOOD DETECTOR WITH RETRAINING:

Its operation is similar to near maximum likelihood detector above except that at the end of every training period the $\{Q_i\}$ vectors are set to the correct one (correct s_{i-1}, $s_{i-2,}$ …, s_{i-g}) (during the training period the data transmitted is known so it starts with correct vector) During normal data transmission if due to noise the minimum cost vector becomes different from the correct one the training period reinitializes it with correct one to start again from a correct vector(fresh start)

COMPUTER SIMULATION TESTS:

Computer simulation tests have been carried out on the various systems described here to determine their relative tolerance to additive white Gaussian noise when operating over models of two different telephone circuits. The systems are as shown in fig.1 and described in sections 3-6The telephone circuits 1 and 2 are close to the typical worst circuits on the public telephone network in the UK. Table 1 shows the sampled impulse response of the linear baseband channel and adaptive filter in fig 1.

Figs 3-6 show the performance of the various systems over the telephone circuits 1 and 2.The signal to noise ratio (SNR)is here taken to be ψ dB where

$$\psi = 10 \log \frac{5}{\sigma^2} \qquad (11)$$

The mean-square value of s_i being 10 and the variance of v_i being $2\sigma^2$

The delay in detection for near maximum likelihood detector has been set equal to n=20

Table 1 : Sampled impulse response of baseband channel and adaptive filter in fig. 1, for each of the two telephone circuits(Clark and clayden,1984)

Telephone circuit 1		Telephone circuit 2	
Real part	Imaginary part	Real part	Imaginary part
1.0000	0.0000	1.0000	0.0000
0.4861	1.0988	0.2544	1.9941
-0.5980	0.0703	-1.7394	-0.2019
0.1702	-0.1938	0.6795	-0.8086
-0.0245	0.1000	0.0408	0.5113
0.0100	-0.0258	-0.1189	-0.1463
-0.0134	0.0110	0.0343	0.0420
0.0056	-0.0042	-0.0185	-0.0364
0.0003	0.0003	0.0139	0.0261
-0.0008	0.0041	-0.0102	-0.0009
0.0000	-0.0061	-0.0019	-0.0034
0.0007	-0.0007	0.0037	-0.0046
0.0037	0.0002	-0.0028	-0.0006
-0.0019	-0.0025	-0.0019	-0.0046
0.0020	0.0008	0.0083	0.0022
0.0005	-0.0002	-0.0056	0.0059
-0.0022	0.0002	-0.0046	-0.0028
0.0007	-0.0005	0.0049	-0.0019
-0.0008	0.0002	-0.0009	0.0037
0.0005	0.0005	-0.0009	0.0003

It can be seen from figs 4 and 5 for nonlinear equalizer with various amount of retraining that for telephone circuit1 at an error rate of 10^{-3} an improvement of around 3 db is gained by using 20% retraining(20-100).Furthermore 1.5 db is gained for 4% retraining(20-500)

For telephone circuit 2 which has more severe intersymbol interference at error rate 10^{-3} there is around 4 db improvement when using 20% retraining and 2 db for 4% retraining

Furthermore in the case of near maximum likelihood detector figs 6 and 7 for telephone circuit 1 at 10^{-3} error rate there is around 1.5 db improvement for 20% retraining over no retraining, and 1 db for 4% retraining

Finally for telephone circuit 2 and near maximum likelihood detector there is 2 db improvement for 20% retraining over the conventional near maximum likelihood detector(no retraining) at an error rate of 10^{-3} and 1 db for 4%retraining

Error rate in the [s_i]

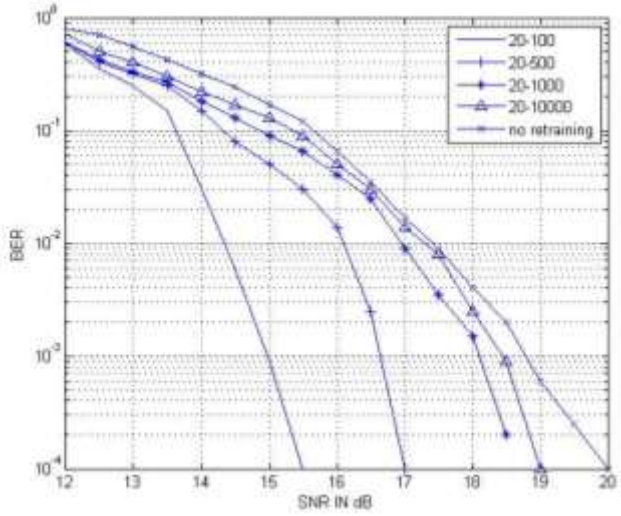

Fig4 Variation of error rate with SNR for nonlinear equalizer over telephone circuit 1

Error rate in the [s_i]

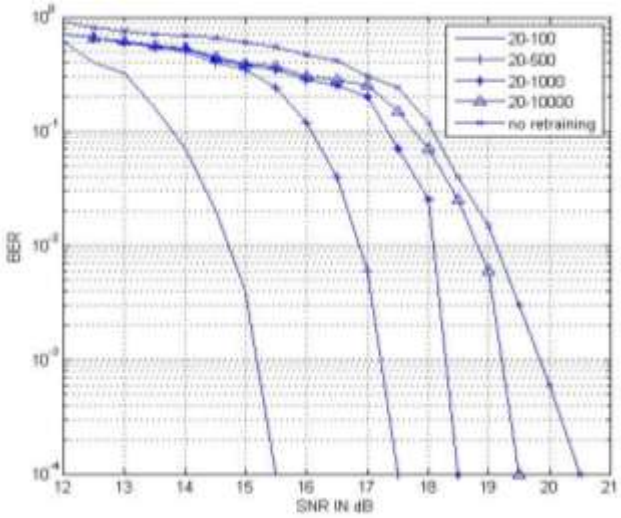

Fig5 Variation of error rate with SNR for nonlinear equalizer over telephone circuit 2

Error rate in the [s_i]

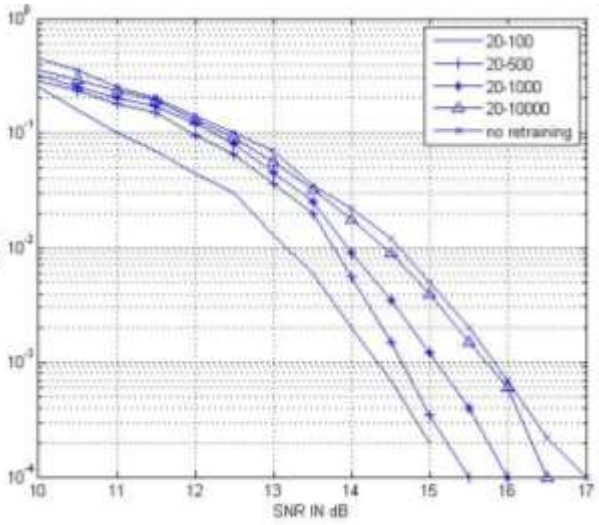

Fig6 Variation of error rate with SNR for near maximum likelihood over telephone circuit 1

Error rate in the [s_i]

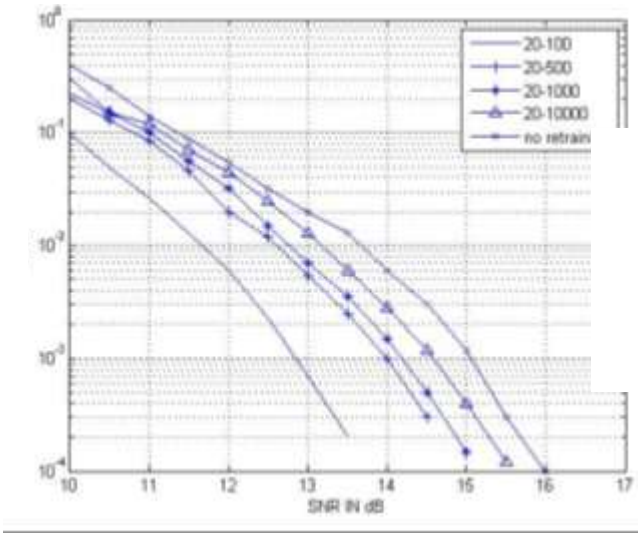

Fig7 Variation of error rate with SNR for near maximum likelihood over telephone circuit 2

CONCLUSIONS:

Retraining of near maximum likelihood detector and conventional nonlinear equalizer improves its noise performance at the expense of reducing efficiency of data transmission. Furthermore it can be concluded that the improvement obtained in the case of nonlinear equalizer is more than that of near maximum likelihood detector. The nonlinear equalizer with retraining seems to be a promising detector that combines both simplicity and performance. The retraining amount could be decided according to the application

Future work may include using retraining with Viterbi algorithm to improve its performance. Also fading channels may be used instead of telephone circuits

REFERENCES:

Alhakim S.S and Abdullah S.N(1990)"Flexible pseudo binary and psudo quaternary detector for 9600 bit/s modem"IEE Proc.Vol 137 .pt.I No.2

Clark A.P and Fairfield M.J(1981)"Detection processes for a 9600 bit/s modem"Radio & Electron.Eng.,Vol. 51,pp.455-465

Clark A.P,.Harvey J.D and.Driscoll J.P(1978):"Near maximum likelihood detetion processes for distorted digital signals"Radio&Electron.Eng. Vol. 48,pp.301-309

Clark A.P.,and Clayden M(1984):"Psudobinary Viterbi detector"IEE Proc.F,Commun.,Radar &signal process, Vol 131,(2),pp.208-218

Clark A.P, Abdullah S.N, Jayasinghe.S.Gand Sun: K.H.(1985)"Pseudobinary and pseudoquaternary detection processes for linearly distorted multi level QAM signals",IEEE Trans, COM-33,pp.639-645

Clark A.P and.Abdullah S.N(1987):"Near maximum likelihood detectors for voiceband channels"IEE.F,Commun.,Radar & signal prosesses"Vol. 134,(3),pp.217-226

Clark A.P and Hau S.F(1984)"Adaptive adjustment of receivers for distorted digital signals"IEE Proc.F,Commun.,Radar & signal process,Vol. 131,(5),pp.526-536

Duel-Hallen .D.and Heegard C(1989)"Delayed decision feedback sequence estimation"IEEE Trans.Comm.,Vol 37,pp428-436

Eyuboglu V.M and S.U.Quereshi S.U.(1988)"Reduced-state sequence estimation with set portioning and decision feedback"IEEE Trans.Comm.Vol 36 ,pp 13-20

FORNEY G.D.(1972):"Maximum Likelihood Sequence Estimation for digital sequences in the presence of intersymbol interference"IEEE Trans. IT-18,pp.363-378

Gerstacker W.H. and. Schober R.(2002)"Equalization concepts for EDGE"IEEE Trans. Wireless Comm.Vol 1.pp.189-199
Kamel R.E and Bar-Ness Y.(1994)"Reduced-state sequence estimation of digital sequences in dispersive channels using state partioning"Electronic Letters.Vol.30 No.1

Olivier J.C.ang-Yick leong,chengshan Xiao and Mann K.D(2003)"Efficient equalization and symbol detection for 8-psk EDGE cellular system"IEEE Trans.on Vehicular technology.Vol 52.No 3.

Proakis .J (2001),"Digital communications"Fourth ed New York,McGraw Hill
Xiang-guo Tang,Zhi Ding(2005)"Low-complexity Itertative equalization for EDGE with bidirectional processing"IEEE transactions on Wireless communication,vol.4No.5

EFFECT OF AL HUWAYZA MARSH BOUNDARY CONFIGURATION ON THE VELOCITY PATTERNS AND WATER QUALITY DISTRIBUTION

Riyadh Z. Al Zubaidy
Shaimaa U. Kareem
Department of Water Resources, University of Baghdad

ABSTRACT

A two-dimensional depth-averaged hydrodynamic model and a two-dimensional water quality parameters transport model were developed to simulate the characteristics of Al Huwayza Marsh, which is considered the largest and most important marsh in the south of Iraq. The hydrodynamic model for Al Huwayza Marsh was built by using RMA2 model, while the water quality model was built by using RMA4 model. These two models are part of Surface Water Modeling System, SMS, software package.

To investigate the effect of the marsh boundary configuration on the variation of the velocity pattern and the water quality within the marsh, both of the hydrodynamic and the water quality models were applied to three cases of boundary configuration of Al Huwayza Marsh. The first case represents the natural extension of the marsh boundary. The second case represents the existing boundary configuration of the marsh, in which the south west of the marsh is bounded by a dyke. The third case represents the Iraqi part of the marsh bounded by the south west dyke and a dyke along the Iraq-Iranian borders, which when completed will separate the marsh into two parts.

Models runs were based on above cases of Al Huwayza Marsh boundary configuration and topographical survey, hydrological measurements and routing, and water quality measurements carried out by the Center of Rehabilitation of Iraqi Marshlands. Discharges of all feeders and stages of the outlets are considered for wet, normal, and dry years. Feeder's seasonal discharges were averaged. High and low concentrations of three selected water quality parameters of the marsh feeders were adopted in the model runs.

Generally, it was found that the flow velocities are relatively high at the inlets and outlets of the marsh. The construction of the dyke along the Iraqi-Iranian border leads to variation in the direction of water flow in all portions of the marsh and a great reduction in AsSuwayb River discharge. While, a slight effect was noticed in the mixing process of the feeders' water of different concentration in case three compared to other cases

الخلاصة:

تم اعداد نموذج هيدروديناميكي ثنائي البعد ونموذج نوعية المياه لتمثيل خصائص هور الحويزة الذي يعد من اكبر واهم اهوار العراق الجنوبيه. تم بناء النموذج الهيدروديناميكي لهور الحويزة باستخدام نموذج RMA2. أما نموذج نوعية المياه فقد تم بناؤه باستخدام نموذج RMA4 وهما جزء من نماذج النظام البرمجي Surface Water Modeling System.

تم تطبيق النموذج الهيدرولكي ونموذج نوعية المياه على ثلاث حالات من حدود هور الحويزة لبيان اثر حالة حدود الهورعلى تغاير انماط السرع ونوعية المياه داخل الهور. الحالة الاولى تمثل وضع امتداد حدود الهور الطبيعية. والحالة الثانية تمثل الوضع الحالي لحدود الهور وهي حالة وجود سدة جنوب غرب الهور. والحالة الثالثة تمثل وضع الهور ضمن الحدود العراقية بعد اكمال انشاء السدة على امتداد الحدود العراقية الايرانية ضمن هور الحويزة والتي ستقسم الهور الى جزئين.

اعتمدت تطبيق النماذج على وضعية حدود هور الحويزة ونتائج القياسات الهيدرولوجيه وعلى نتائج استتباع الجريان و المسح الطوبوغرافي الذي تم تنفيذه من قبل مركزانعاش الاهوار العراقيه. تم التعامل مع قيم التصاريف للمداخل والمخارج على اساس السنوات الرطبة والمعتدلة والجافه حيث تم اخذ المعدلات الفصليه لتلك التصاريف، اما في نموذج نوعية المياه فقد تم اعتماد اعلى واقل التراكيز لبعض معايير مختارة لنوعية مياه مغذيات الهور.

عموما، تم ملاحظة كون سرع الجريان عالية نسبيا عند مداخل ومخارج هور الحويزة. ان انشاء سدة على امتداد الحدود العراقية الايرانية سيؤدي تغير في اتجاهات جريان الماء في معظم الهور وقلة كبيرة في تصاريف نهر السويب. بينما كان التاثير قليل على عملية الخلط داخل الهور لمياه المغذيات المختلفة التراكيز في الحالة الثالثة مقارنة ببقية الحالات.

KEY WORDS
Al Huwayza Marsh, RMA2, RMA4, Hydrodynamic model, Water quality model.

INTRODUCTION

The Iraqi marshlands are the largest wetland ecosystem in the Middle East and Western Eurasia. These marshes began to decline as a result of the increasing water demand for different uses and dam building upstream Tigris and Euphrates Rivers in Turkey, Syria and Iraq, which attenuated the rivers natural flows. Iraq attempts to restore these marshes through the actions of the Center of Restoration of the Iraqi Marshlands, CRIM, of the Ministry of Water Resources and some of interested international organizations.

Al Huwayza Marsh, which is considered as the largest Iraqi marshland, spreads on the east side of Tigris River within Misan Governorate crossing the Iraqi-Iranian borders. The major part of the marsh lies within the Iraqi borders.

During the eighties of the last century, dykes were constructed west of Al- Huwayza Marsh for flood protection and military purposes. Recently, construction of a new dyke has been started along the Iraq-Iranian borders within the marsh area that will separate the marsh into two parts.

Generally, this study is focused on building both hydraulic and water quality models of Al Huwayza Marsh to investigate the effects of the change in the marsh boundaries, due to the constructed dykes, on the velocity distribution, circulation, and the water quality variations of some selected contaminants.

GENERAL DISCRIPTION OF AL HUWAYZAH MARSH

Al Huwayza Marsh is located to the east of the Tigris River in Misan Governorate and extended to the Iraqi-Iranian borders as shown in **Fig.1.** The total length of Al Huwayza Marsh is about 80*km* measured from the northern bank of the marsh close to Ghzayla-AshSheeb check point road down to Southern bank at AsSuwayb River. The average width of this marsh is about30*km*, measured from the flood protection dykes along its west bank to the Iranian lands at its east bank.

Al Musharah, Al Ka'hla River, Al Karkheh River, and AsSanna'f Marsh are the main feeders, while Al Kassara and AsSuwayb Rivers are the main discharge outlets of the marsh.

The total area of Al Huwayza varies between 2350 and 3500km^2 in the flood season, and it is reduced to the half during the dry season, Mohamed, 1999. Only the deep parts of marsh that remain forming water ponds such as Al Huwayza, Um -Elniaj and Al Adhaim, these water ponds are connected to each other by water paths that pass through dense areas of Weeds, Reeds, Papyrus and other water bushes types, Al Furat Center, 2003.

The water level elevations during autumn vary between 1 to 2*m* a.m.s.l. then increase to about 4.5*m* at the western part of the marsh in the end of spring and the early summer. The deepest part of the marsh is at its northern part, including permanent lakes were the depth of water exceeds 6-8*m*, the depth of water reduce going towards the south. However, in major parts of the marsh, particularly that at the Iranian part of the marsh, the depth of water is less than 3*m*, allowing the growth of reed.

Fig.1. General view of Al Huwayza Marsh.

THE MATHEMATICAL MODELS

The Surface Water Modeling System, SMS, RMA2 is a two-dimensional, finite element hydrodynamic modeling code that supports subcritical flow analysis. It computes a finite element solution of the depth-integrated equations of fluid mass and momentum conservation in two horizontal directions. Friction is calculated with the Manning's or Chezy's formula, and eddy viscosity coefficients are used to define turbulence characteristics **Donnell, 2004 a.** RMA2 model was used to compute the water surface elevation and velocity variation over Al Huwayza Marsh.

The Surface Water Modeling System, SMS, RMA4, is a companion model to RMA2, is a finite element water quality transport numerical model. RMA4 is applied to represent the transport of a contaminant, salinity intrusion in a system. RMA4 was used to investigate the movement of some of the water quality parameters inside Al Huwayza Marsh.

THE BOUNDARY CONDITIONS

Fig. 2 shows a schematic diagram of the boundary conditions of Al Huwayza marsh that were applied in the hydraulic analysis. Feeders flow assigned values were used at the upstream boundary and the marsh outlets stage hydrographs were used as downstream boundary.

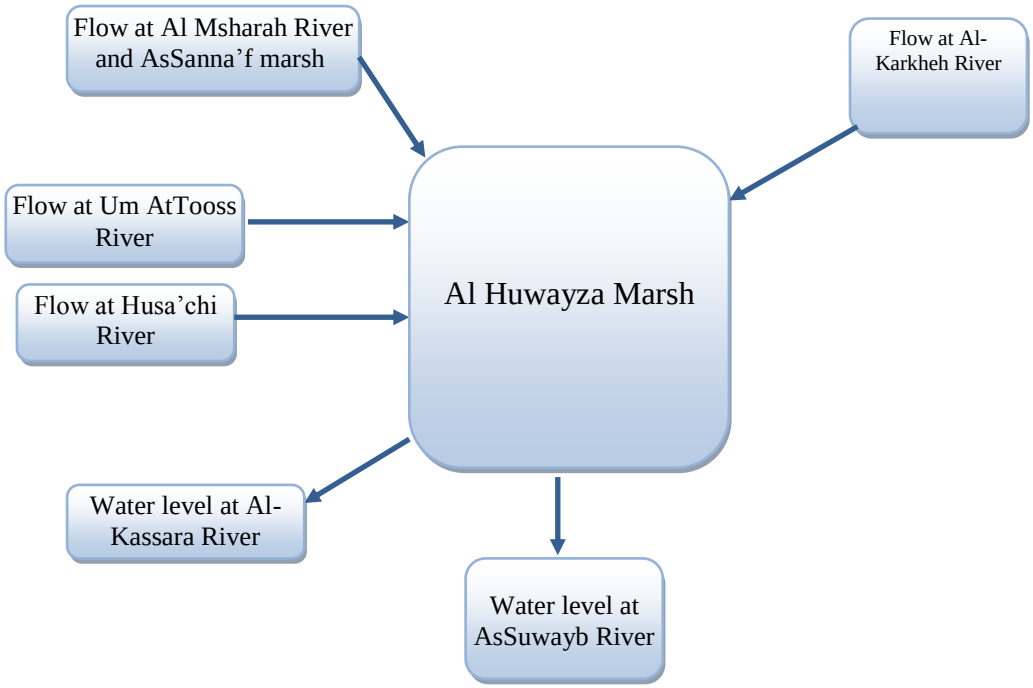

Fig.2. Boundary conditions schematic diagram of Al Huwayza Marsh.

CASES STUDIES

Three cases were taken into consideration, which depend on the Al Huwayza Marsh boundaries configuration. The first case represents the natural extension of the Al Huwayza Marsh boundaries, the second; represent the present situation of marsh boundaries where the south-west dykes limiting the natural extension of the marsh, and the third case represents the Iraqi part of the Al Huwayza Marsh only after completion of the east dyke along the Iraqi-Iranian borders.

Case One

In this case study, Al Huwayza Marsh extends beyond the current existing south-west dykes as shown in **Fig. 3,** which represents the natural extension of the marsh. The south-west dykes were constructed for military purposes during the first gulf war The maximum surface area of Al Huwayza Marsh for this case, when the water level at 7m a.m.s.l., is about 1800km^2 with a storage capacity of about 5896 million m^3. Al Huwayza Marsh with this boundary configuration was studied by CRIM in year 2006. The study carried out hydrologic and hydraulic investigations and water quality field measurements. Discharges were estimated to be assigned for the marsh, this estimation depending on the results of the hydrological routing scenario for wet, normal, and dry years.

Case Two

In this case study, Al Huwayza Marsh is bounded by the south-west dykes as shown in **Fig 3.** This case represents the existing boundary configuration of the marsh. The maximum surface area of Al Huwayza Marsh for this case is about 1240km^2 with a storage capacity of about 4400 million m^3.

Case Three

This case study includes the Iraqi side of Al Huwayza Marsh only because of Iran has planned and started constructing a dyke along its borders with Iraq within the marsh area, which when will be completed will separate the marsh into two parts. The total area of Al Huwayza Marsh within the Iraqi borders is about 1013km^2 with a storage capacity of about 3735million m^3.

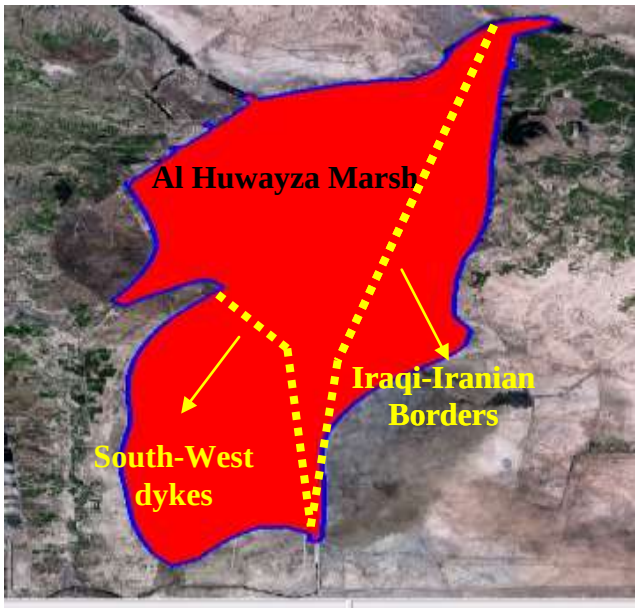

Fig.3. Sketch to define Al Huwayza Marsh boundaries.

REQUIRED DATA

Discharge of all feeders and stages at the outlet were considered for for wet, normal and dry years. The discharges of all feeders are presented in **Table 1**. The averaged inflow from the Karkheh River into the marsh has been obtained from the Azadegan Environmental Baseline studies, Iranian Ministry of Environment 2004, where the maximum flow entering the marsh was 220m^3/sec during April and the minimum value of flow during October was 19m^3/sec. The stages at the outlets were considered from the hydrologic routing achieved in the study of CRIM, 2006

Water quality analysis was based on the highest and lowest concentrations of the water quality measurements at the marsh feeders that were carried out by CRIM during the period from January to July 2006, which are presented in **Table 2**.

Table 1. The averaged seasonal discharges in m^3/sec of each feeder during wet, normal and dry years, *after CRIM, 2006*.

Season		Feeder			
		Al Husachi	**Um AtTooss**	**Al Msharah and AsSanna'f Marsh**	**Al Karkheh**
Wet year	Winter	96	60	184	130
	Spring	75	53	37	207
	Summer	38	25	18	55
	Autumn	77	51	32	30
Normal Year	Winter	56	37	72	83
	Spring	25	19	17	145
	Summer	18	12	9	32
	Autumn	27	18	13	20
Dry Year	Winter	6	4	3	45
	Spring	4	3	5	68
	Summer	5	3	4	19
	Autumn	7	4	5	12

Table 2. High and low concentrations of contaminants , after CRIM, 2006.

River	Contaminant									
	High Concentrations					Low Concentrations				
	PH	TDS (mg/l)	NO_3 (mg/l)	TURB. (NTU)	SO_4 (mg/l)	PH	TDS (mg/l)	NO_3 (mg/l)	TURB. (NTU)	SO_4 (mg/l)
Al Msharah	8.2	2670	9.8	145	280	7	430	2.8	1.02	90
Um AtTooss	8.3	1310	10	3136	260	7.4	540	0.88	26.69	165
Al Husachi	8.3	1390	8.86	359	280	7.3	530	3.24	14.17	110
Al Karkheh	8	1400	0.5	50	290	7.2	900	0.28	7	200

Topographical survey of the Al Huwayza Marshwas carried out by CRIM, 2006, and is presented in **Fig. 4.** Based on the topographical survey, the area elevation and storage elevation relations for case one and two were computed and presented by CRIM, 2006. While, the area elevation and storage elevation relations for case three was computed and presented in **Figs 5** and **6**, respectively.

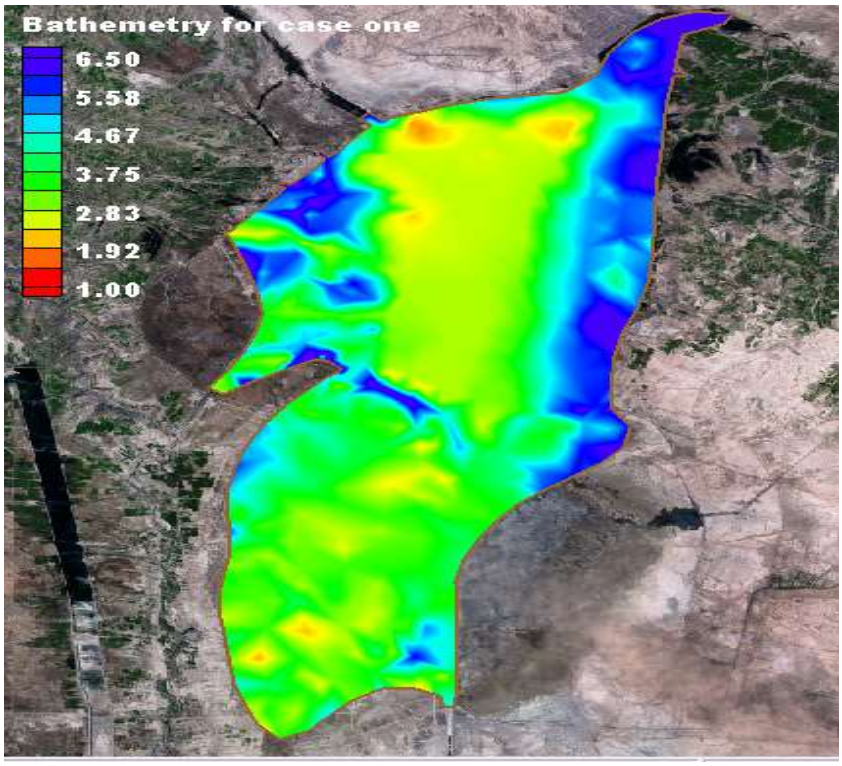

Fig. 4. Bed elevation of Al Huwyzah Marsh, *after CRIM, 2006*.

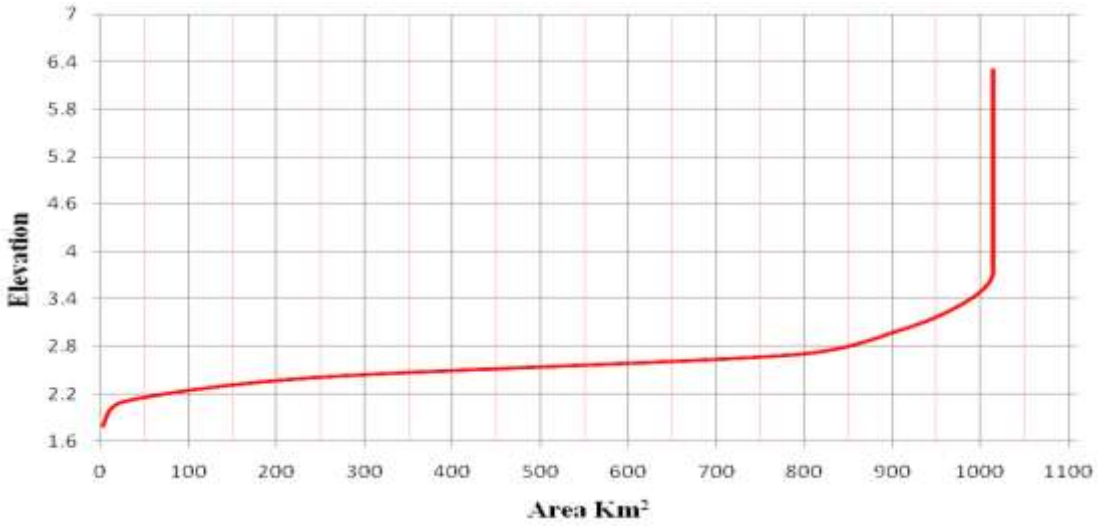

Fig 5. Computed Area- Elevation curve of Al Huwayza Marsh, case three.

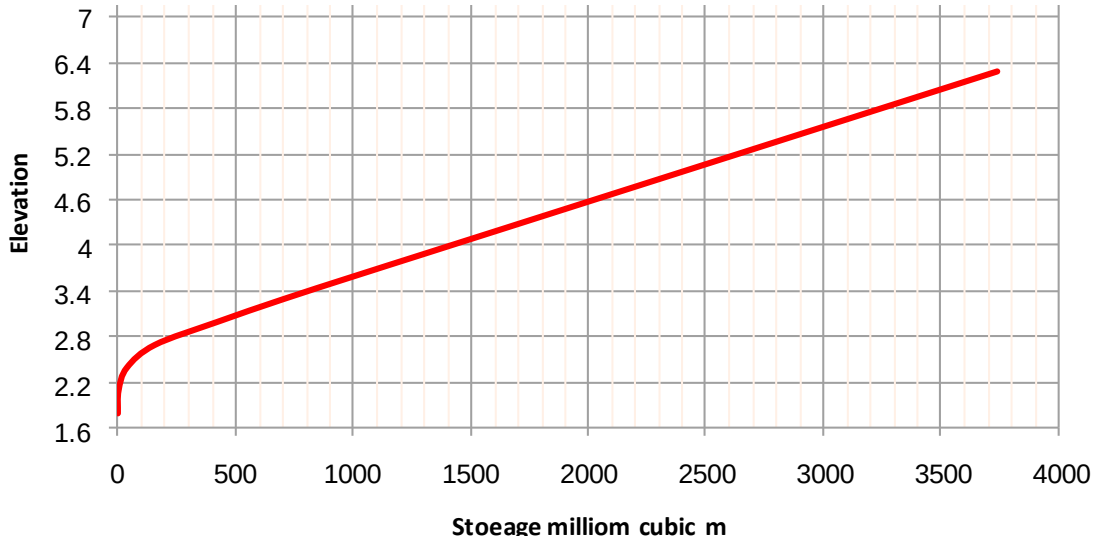

Fig 6. Computed storage- Elevation curve of Al Huwayza Marsh, case three.

Manning roughness coefficient was used to define the bed friction of marsh and a value of 0.045 were used for shallow non vegetated part and 0.07 for shallow vegetated part of the marsh. Typha and reed are the major aquatic plants within the marsh, theses aquatic plants cannot grow when the water depth is greater than 2m. This is the criteria used to separate the vegetated from non vegetated zones within the marsh. The Manning roughness coefficient as a function of depth that was obtained from RMA2 model is shown in **Fig. 7**.

The eddy viscosity is an addition coefficient that must be specified in the implementation of the model. The value of eddy viscosity affects stability and turbulent fluid characteristics. More than one technique was adapted in the definition of the eddy viscosity number.

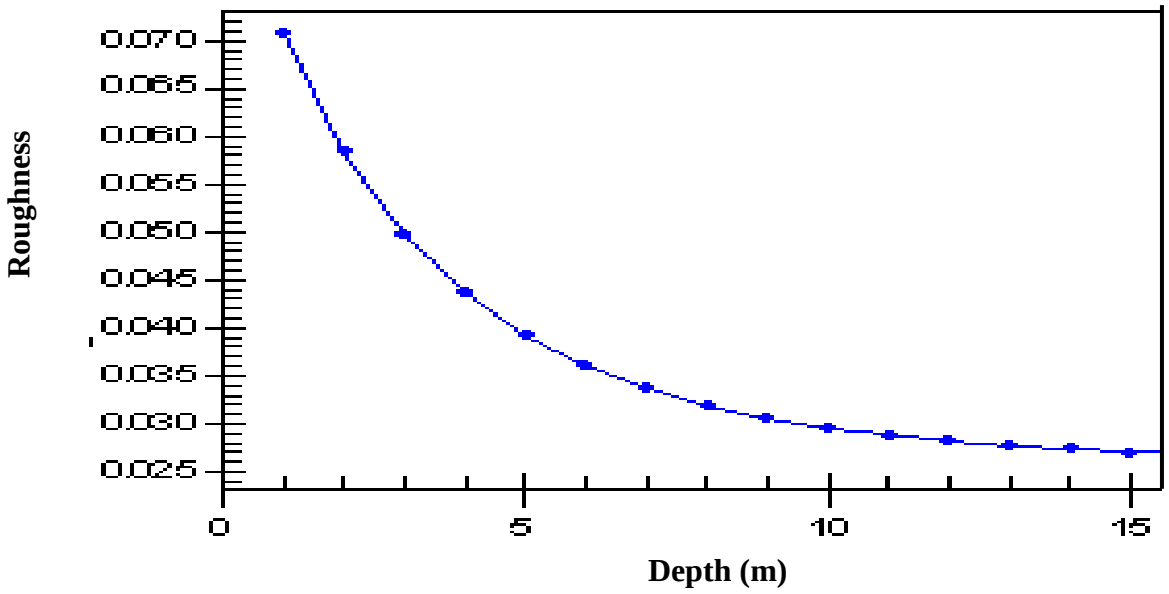

Fig. 7. Roughness values of Al Huwayza Marsh.

VERIFICATION OF THE HYDRAULIC MODEL

The verification consists of comparing field water surface elevation at two locations in Al Huwayza marsh which are Al-Adhaim and AsSodda bridge. **Fig. 8** shows a good satisfactory between the model predicted data and field measurement data at the two gauge stations.

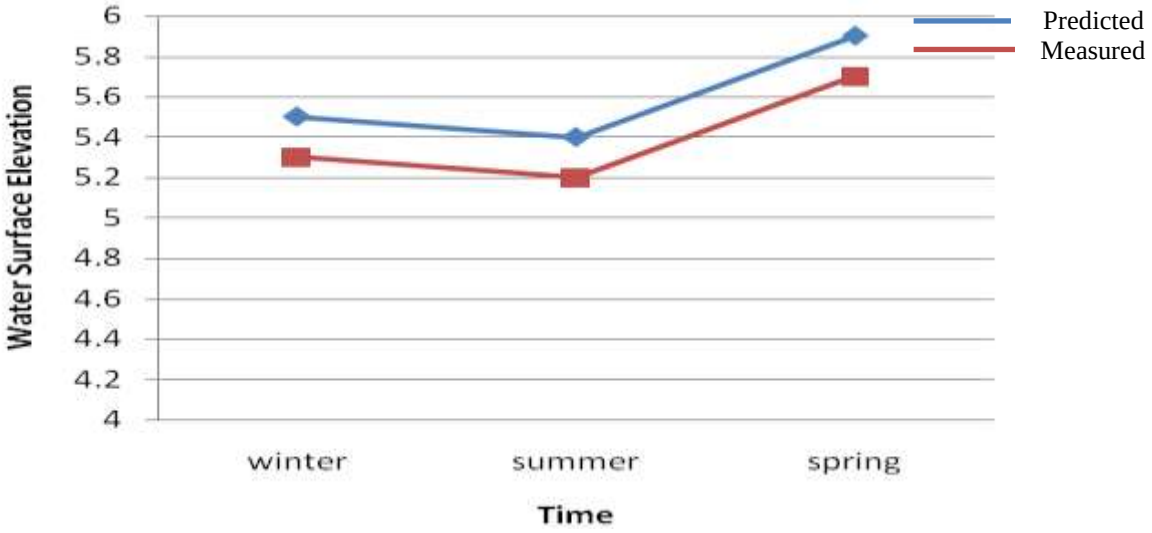

a- at AsSodda Bridge station

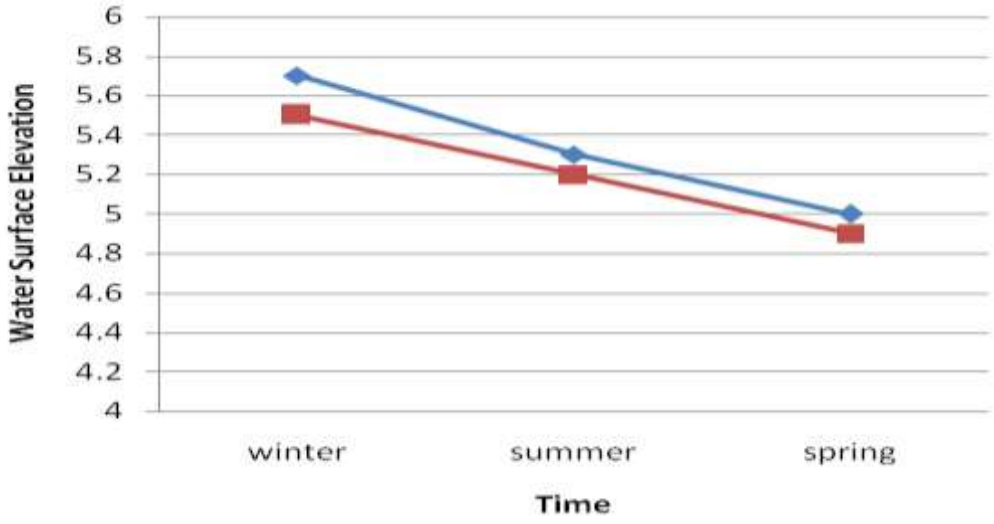

b- at Al Adhaim station.

Fig. 8. Water surface elevation comparison at selected measuring stations.

ANALYSIS OF THE CASE STUDIES

The velocity pattern and the water quality distribution of the three cases of boundary configuration of Al Huwayza Marsh were analyzed as follows:

Case one

The flow velocity patterns were analyzed for wet, normal and dry years as shown in **Figs. 9** to **11**, respectively. It is clear that the topographic of the marsh bed (refer to **Fig. 4**), inflow (season) and the outlets capacities affecting the velocity profiles. The velocities are higher at the inlets and outlets of the marsh than that at the interior part of the marsh. The maximum velocities are at the outlets of the marsh, Al Kassara and AsSuwayb.

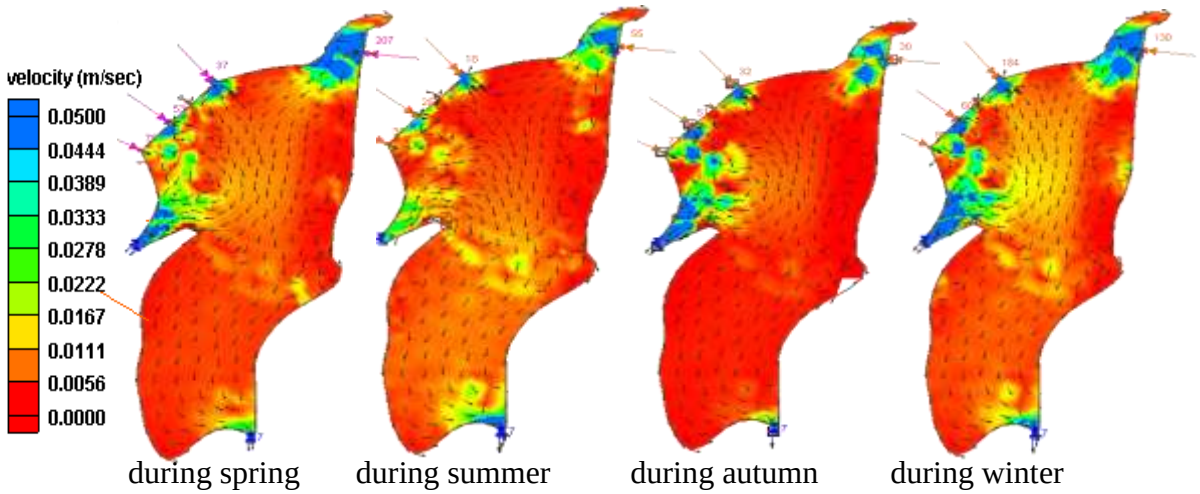

Fig.9. Velocity pattern within the marsh during a wet year, case one.

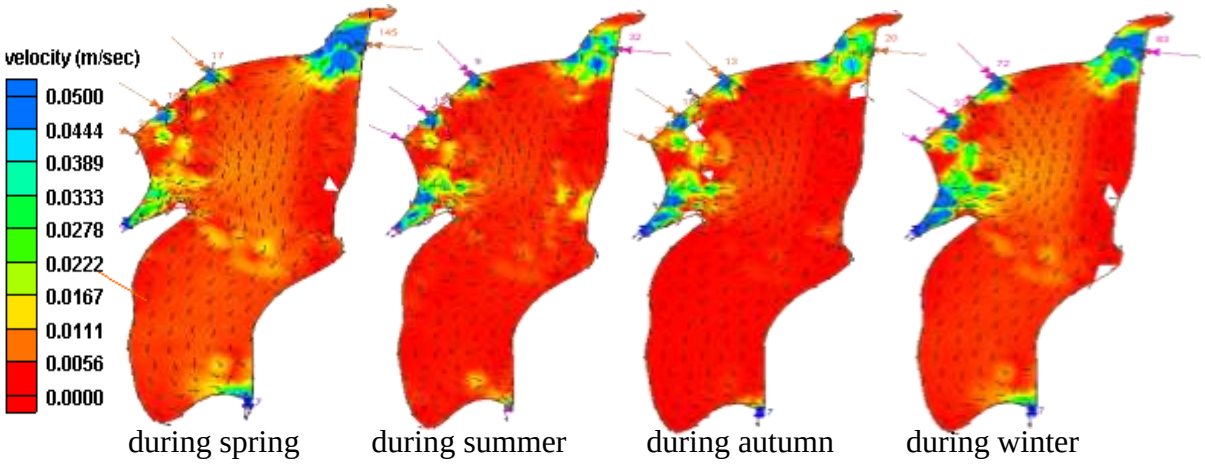

Fig.10. Velocity pattern within the marsh during a normal year, case one.

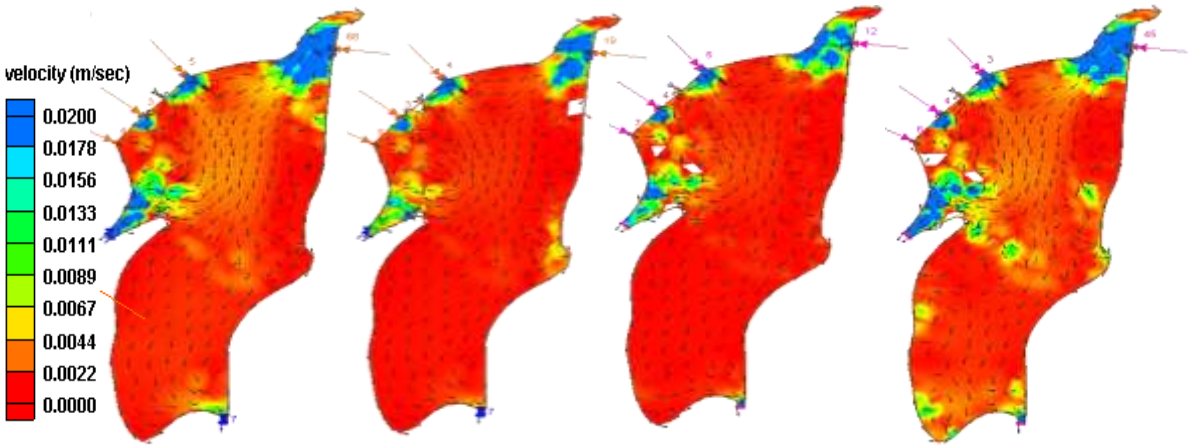

Fig.11. Velocity pattern within the marsh during a dry year, case one

Case Two

Fig. 12 to **14** shows the flow velocity pattern for wet, normal and dry years of case two, respectively. In addition to the above mentioned factors affecting the velocities within the marsh the marsh boundary configuration is an additional factor that affects the velocity variation within the marsh. Velocities of water are relatively high at outlets of the marsh but the velocities at some of the inlets are reduced compared to that of case one. This reduction may be referred to the increase in water level elevation within and the overall change in the velocity patterns within the marsh.

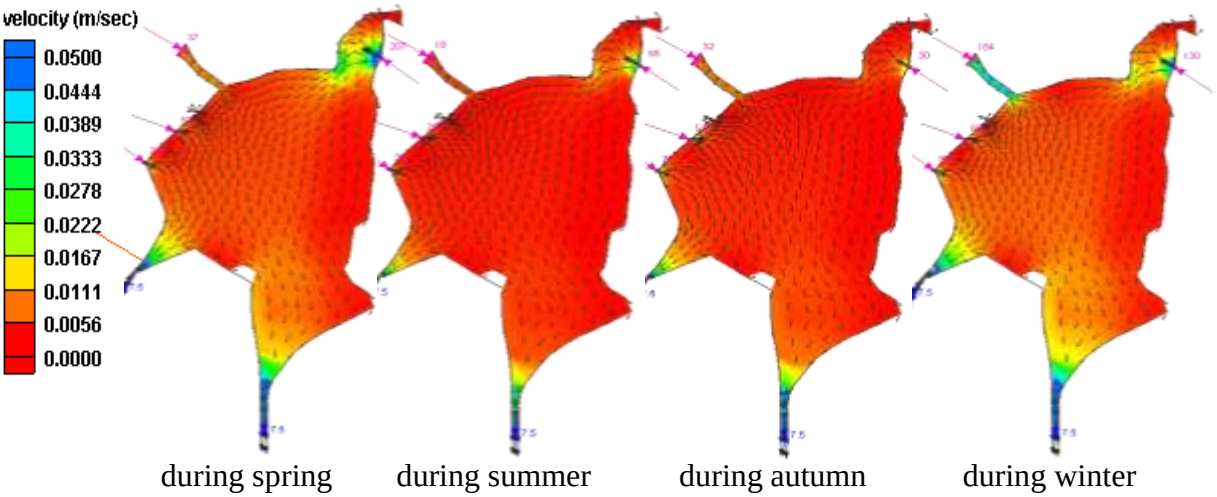

Fig.12. Velocity pattern within the marsh during a wet year, case two.

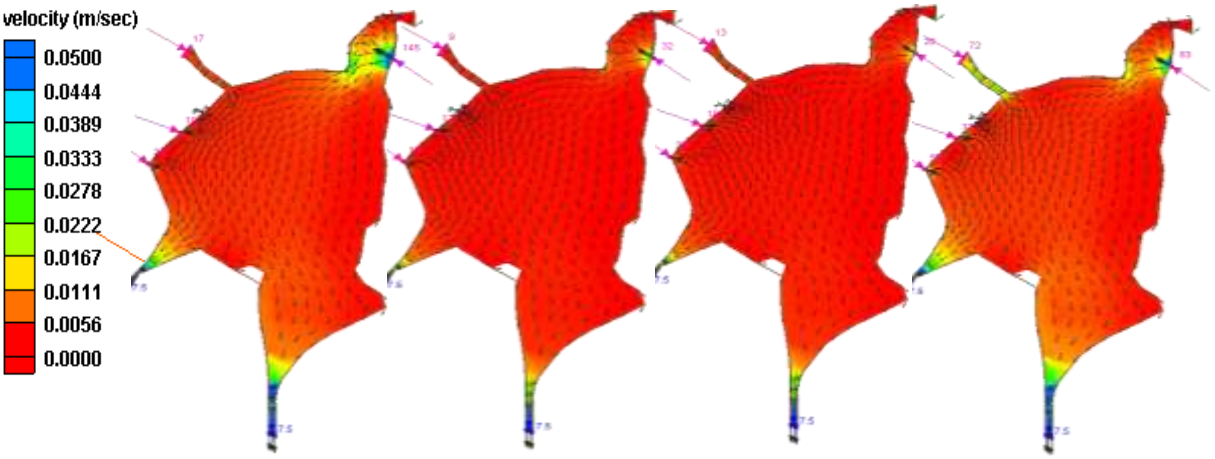

Fig.13. Velocity pattern within the marsh during a normal year, case two.

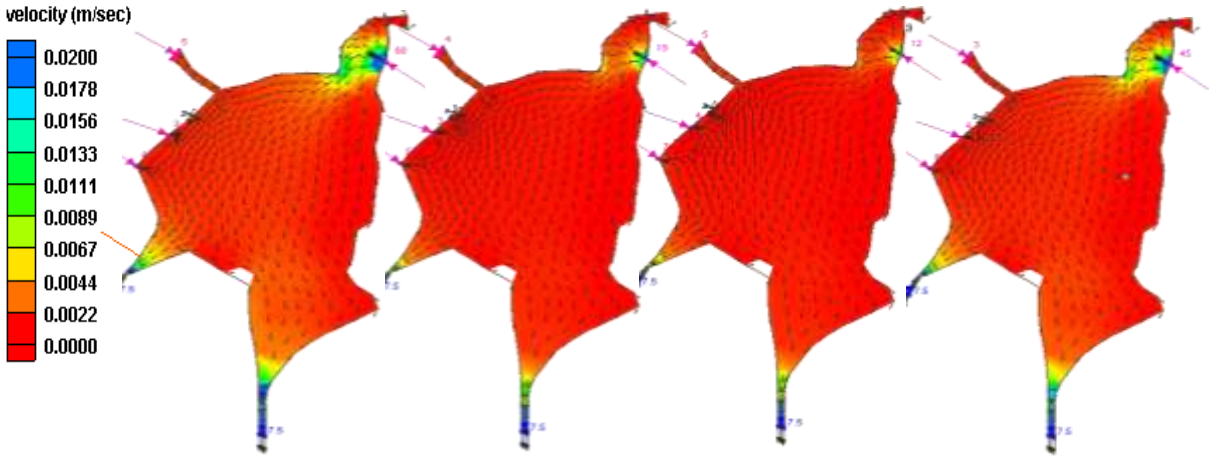

Fig.14. Velocity pattern within the marsh during a dry year, case two

Case Three

The velocity patterns within the marsh for wet, normal, and dry years are analyzed as shown in **Figs.15 to 17,** respectively. The velocity values Al Kassara River is of the high velocity. Most of the out flow in this case is through Al Kassara River, while the flow towards AsSuwayb River is reduced greatly and is approaches zero flow. The velocities at the north east of the marsh near Al Karkheh River toward AsSuwayb River at the south along the Iraqi-Iranian borders are reduced greatly, the water in this area is considered shallow and of very low level of water because of the construction of the dyke in this area. Some of the marsh areas are left dry.

By comparing the velocity profiles of case three with that of case one and two, a high changes in velocity profiles can be notice at all parts of Al Huwayza Marsh for all of flow conditions as a result of construction of the dyke along the Iraqi-Iranian borders.

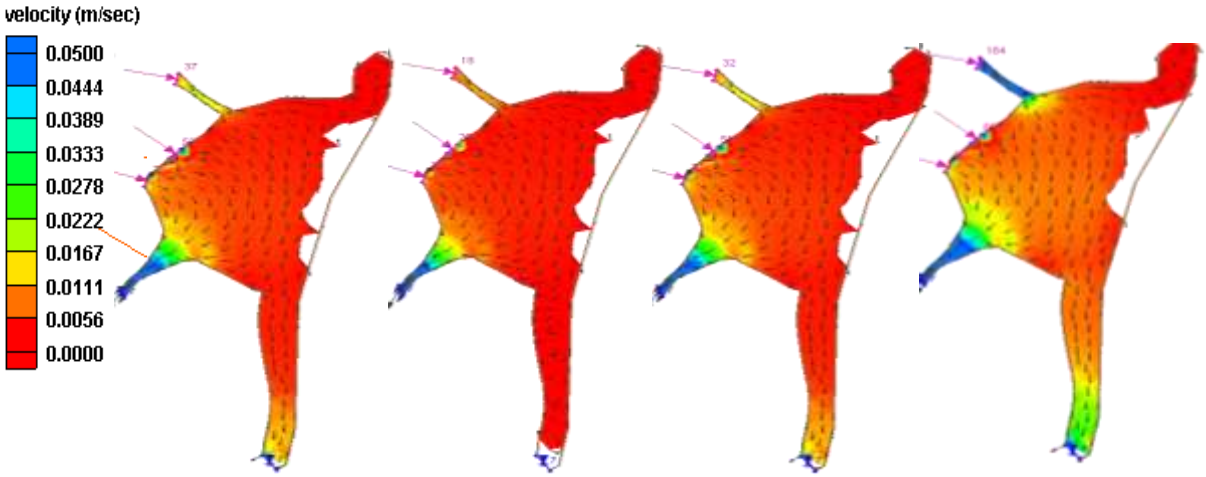

Fig.15. Velocity pattern within the marsh during a wet year, case three.

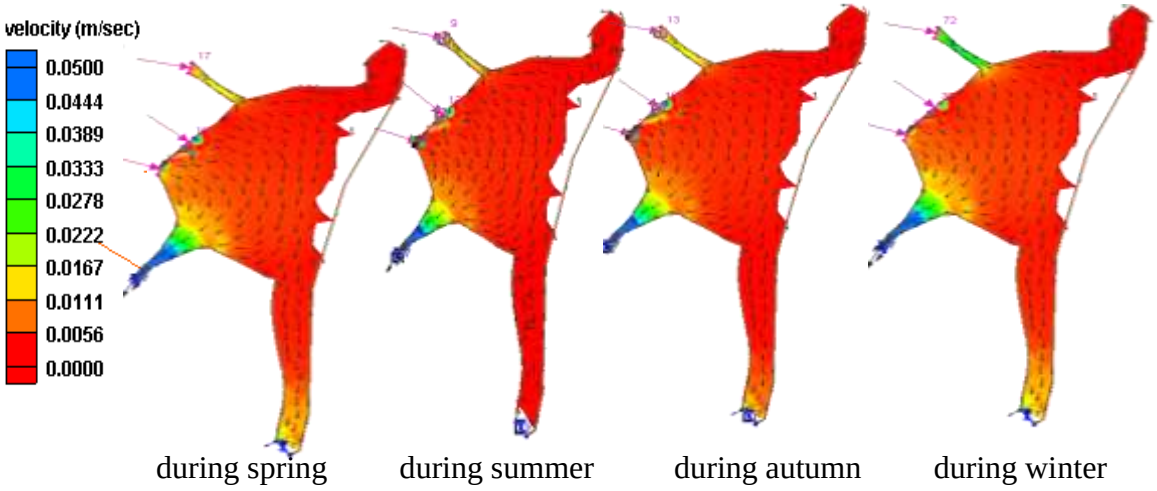

Fig.16. Velocity pattern within the marsh during a normal year, case three.

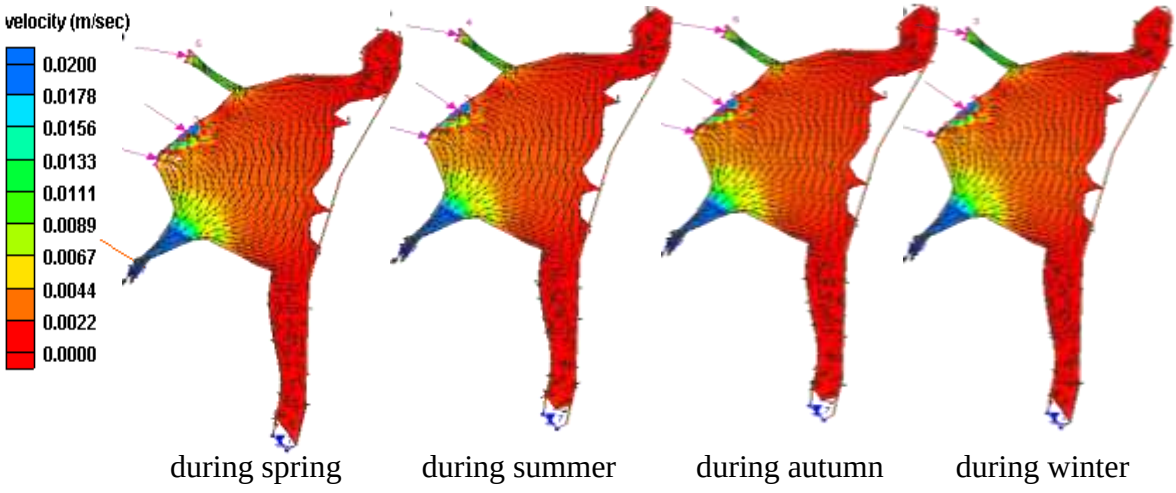

Fig.17. Velocity pattern within the marsh during a dry year, case three.

EFFECT BOUNDARY CONFIGURATION ON OUTLETS DISCHARGES

The discharges throughout Al Kassara and AsSuwayb Rivers are affected greatly by the boundary configuration of Al Huwayza Marsh. **Table 3,** shows the discharges through these two outlets for the three cases of boundary configuration. The great impact is in case three because of the construction of dyke along the line of the Iraqi-Iranian borders, in this case the velocities are reduced where the minimum value is at AsSuwayb River and the discharges in this river will reduced greatly.

Table 3. The discharges in m^3/sec of Al Kassara and AsSuwayb outlet during wet, normal, and dry years.

Year		Cases Study					
		Case 1		Case 2		Case 3	
		Al Kassara	AsSuwayb	Al Kassara	AsSuwayb	Al Kassara	AsSuwayb
Wet	Winter	354	116	217.3	253	300	40
	Spring	229	143	174.5	197.5	156.5	8.5
	Summer	50	86	59	77	75	6
	Autumn	71	119	67.5	122.5	153.3	6.7
Normal	Winter	135	113	105	143	157.3	7.7
	Spring	85	121	91	115	56.5	4.5
	Summer	53	22	21	50	35	4
	Autumn	60	18	30	48	55.3	2.7
Dry	Winter	31	24	32	26	12.7	0.35
	Spring	55	25	31	49	12.1	0.89
	Summer	20.7	10	11	20	14	5
	Autumn	17.8	10.4	10	18	15.3	0.61

WATER QUALITY ANALYSIS OF THE CASE STUDIES

Steady state water quality model was applied to the three cases of boundary configuration of Al Huwayza Marsh. This model depends on the hydrodynamic model and advection–diffusion equation to obtain a solution. Based on the set of initial conditions that represent the concentrations at the feeders of Al Huwayza Marsh, **Table 2,** the model used to calculate the variation of the concentration of three water quality parameters, PH, TDS, and NO_3, within the marsh. Flow of a normal year only was used in the model because the actual field measurement for water quality model was during this year and the initial conditions were applied for only the highest concentrations and lowest concentrations to show the variations of the concentrations in these critical cases.

Case one

The PH variation within Al Huwayza Marsh for this case study can be shown in **Fig. 18**. Salinity variation, represented by TDS, within Al Huwayza Marsh is shown in **Fig.19. Fig.20** represents nitrate changes during spring and winter seasons. The concentration of all contaminates within the marsh reaches a common value within short distances from the marsh feeders; this is an indication to a good mixing process take place within the marsh.

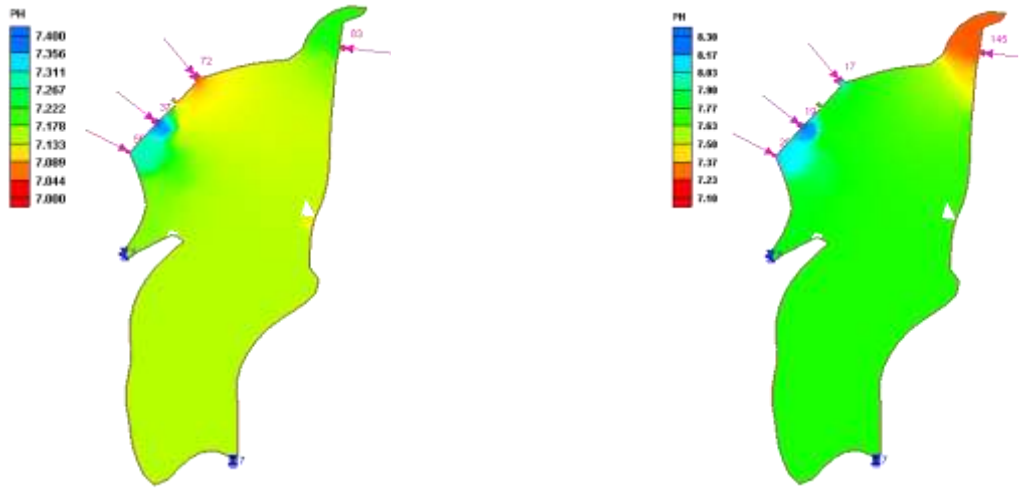

a-during winter b- during Spring

Fig. 18. Variation of PH within the Al Huwayza Marsh.

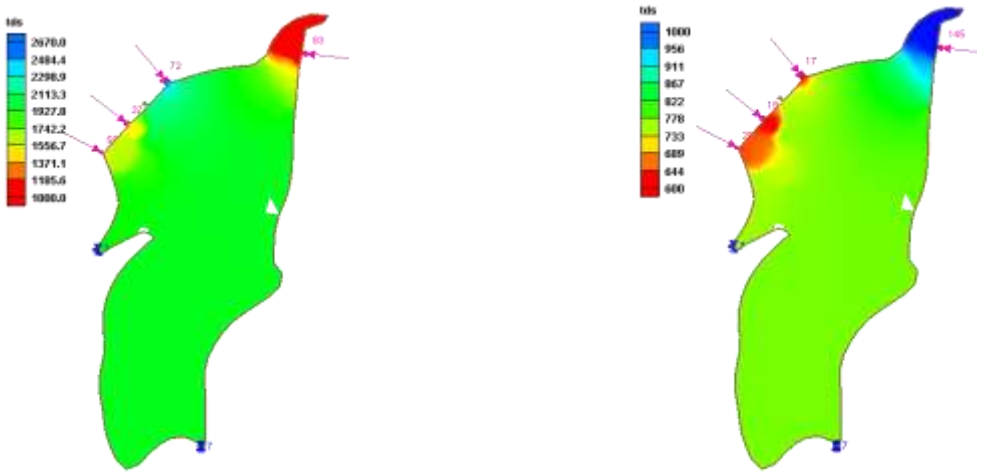

a- during winter

b- during spring

Fig.19. Variation of TDS within the marsh.

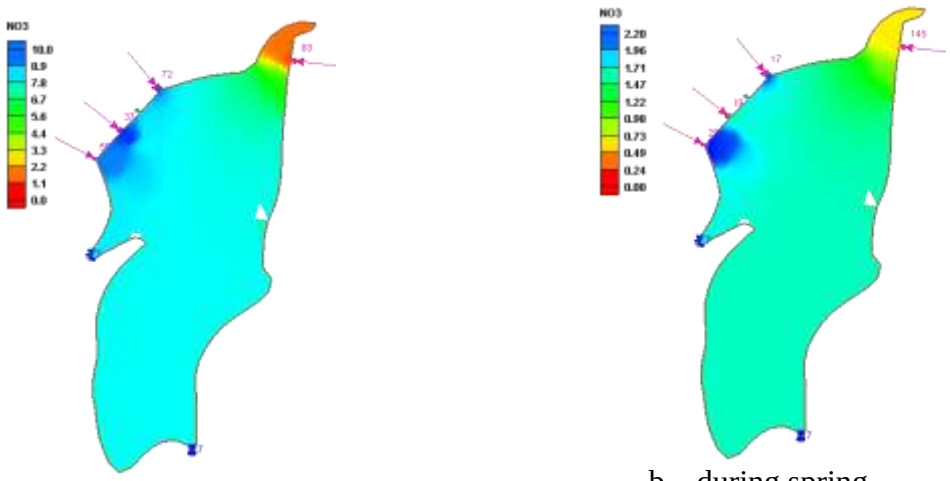

a- during winter

b- during spring

Fig. 20. Variation of NO_3 within Al Huwayza Marsh.

Case Two

Fig.21 shows the values of PH variation within Al Huwayza Marsh. Salinity in Al Huwayza Marsh is shown in **Fig.22.** **Fig.23** shows the nitrate changes for this case study. The mixing process within the marsh still good.

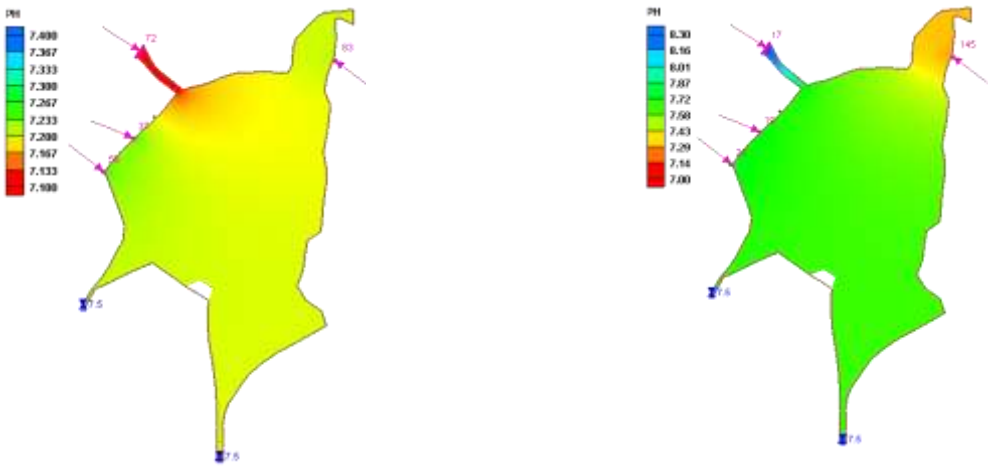

a- during winter b- during spring

Fig.21. Variation of PH within Al Huwayza Marsh.

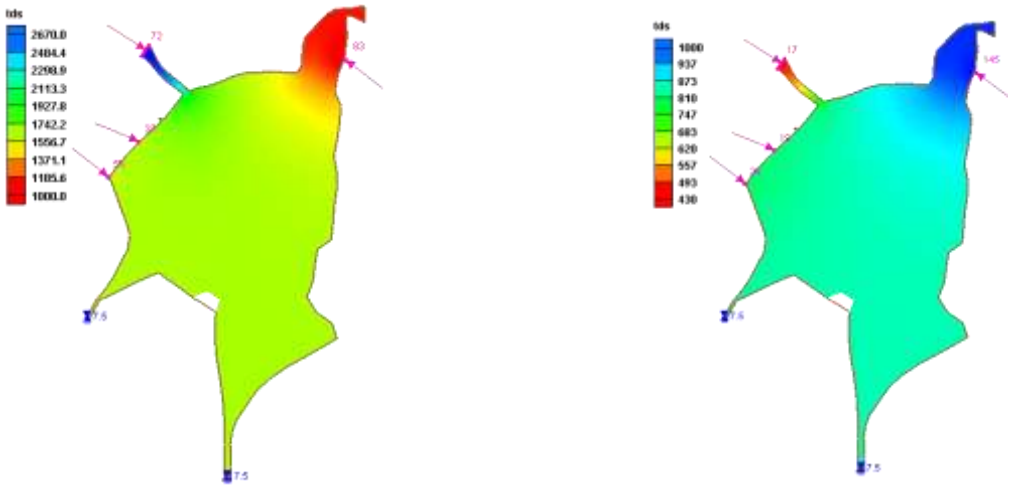

a- during winter b- during spring

Fig.22. Variation of TDS within Al Huwayza Marsh

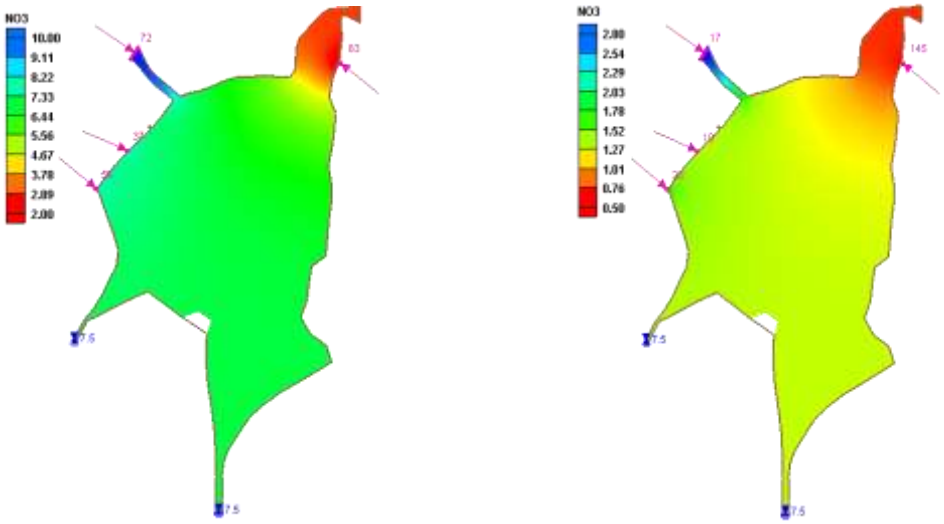

c- during winter b- during spring

Fig.23. Variation of NO_3 within Al Huwayza Marsh

Case Three

The PH variation for this case study is shown in **Fig. 24.** **Fig.25** shows that TDS concentrations in Al Huwayza Marsh. **Fig.26** represents nitrate variation for this case study. A slight effect may be notice in the mixing process of the feeders water of different concentration compared to other cases which may be referred to the change in flow patterns.

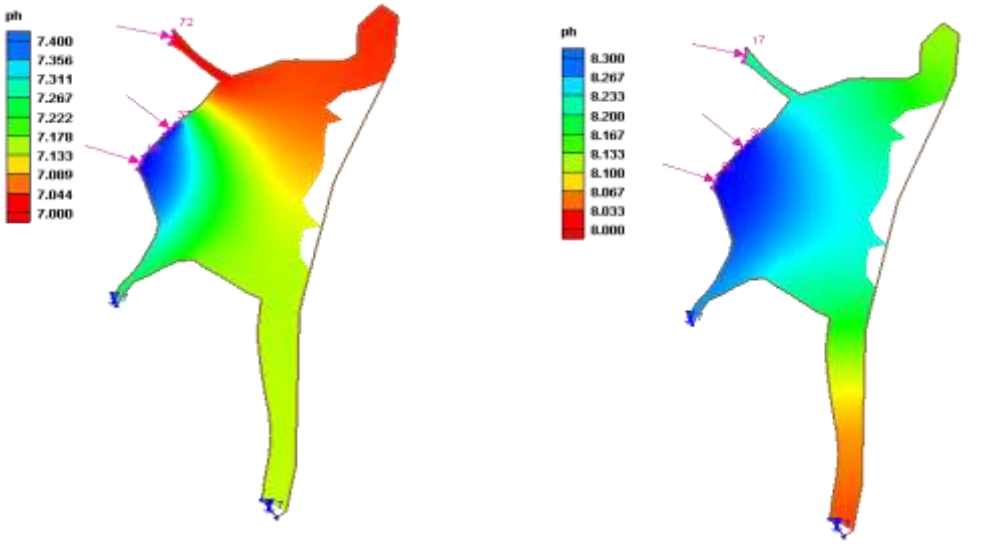

a- during winter b- during spring

Fig.24. Variation of PH within Al Huwayza Marsh.

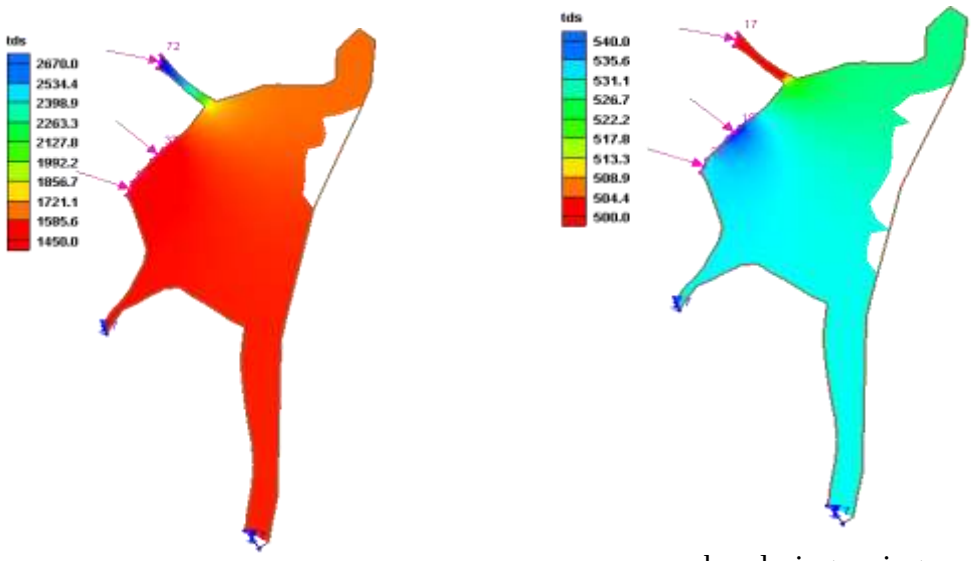

a- during winter b- during spring

Fig.25. Variation of TDS within Al Huwayza Marsh.

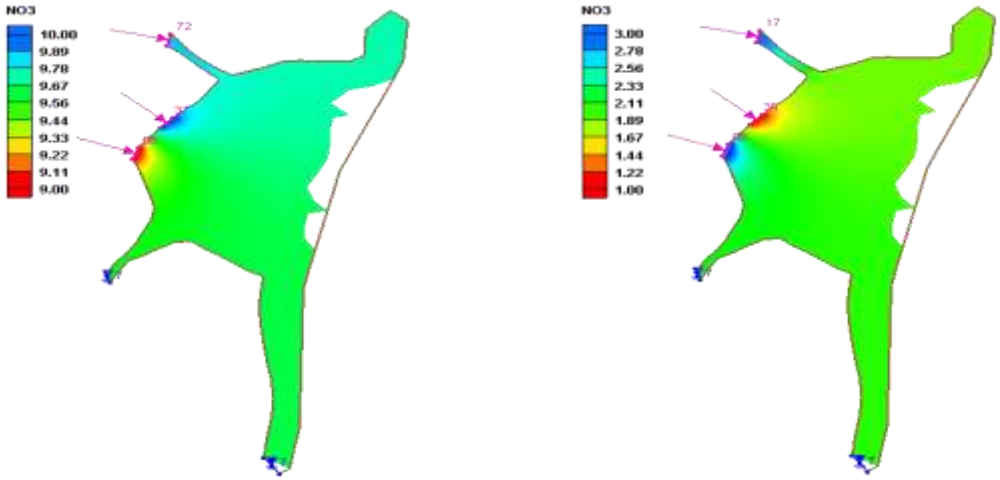

a- during winter b- during spring

Fig.26 Variation of NO_3 within Al Huwayza Marsh.

CONCLUSIONS

The study has come out with the following conclusions:

- The flow velocity is relatively high near the inlets and outlets of Al Huwayza Marsh.
- A high changes in velocity patterns and the overall water circulation was noticed at all parts of Al Huwayza Marsh for all of the flow conditions as a result of construction of the dyke along the Iraqi-Iranian borders within the marsh.
- The discharge values increase at AsSuwayb River outlet of the marsh in case two. While a great reduction in the discharges of this outlet was noticed in case three.
- A slight effect was noticed in the mixing process of the feeders' water of different concentration in case three compared to other cases.
- RMA2 and RMA4 models found to be a powerful tool in simulating the flow and water quality and could be applied to study other Iraqi marshlands.

REFERENCE

- Al Furat Center for Studies and Designs of Irrigation Projects, 2003, ***A Study of Reflooding Southern Marshes***, Ministry of Water Resources, Iraq.
- Azadegan, 2004, ***Azadegan Environmental Baseline Studies: The Natural Environment, Iran***.
- Donnell, B. P., 2004 (a), ***User Guide to WES-RMA2 Version 4.5, Waterways Experiment Station***, Costal and Hydraulics Laboratory, California, Davis, U.S.A.
- Donnell, B. P., 2004 (b), ***User Guide to WES-RMA4 Version 4.5, Waterways Experiment Station***, Costal and Hydraulics Laboratory, California, Davis, U.S.A.
- Center for the Restoration of Iraqi Marshlands, CRIM, 2006***, Study the Rehabilitation of AL Huwayza Marsh Ecological System*** , Iraq **.**
- Italian Ministry for the Environmental and Territory, Free Iraq Foundation, 2005, ***Hydological Modeling of Abu Zirig Marsh Using RMA2 Model***, United Nations.
- Iranian Ministry of Environment, 2004, ***Azadegan Environmental Baseline Studies: The Natural Environment,*** Iran
- Mohamed, Jafer, 1999, ***Modern Irrigation and Drainage projects in Mayssan and DheKar Governorates, A study of Water Resources Geographic***, Ph. D. Thiess, University of Baghdad, Translated from Arabic.
- Swenson, H.A., and Baldwin, H.L., 1965, ***A primary on Water Quality***, Washington U.S printing office.

PREPARATION OF Nd – FLUORIDE LASER GLASS AND INVESTIGATION OF ITS CHARACTERISTICS

Saad S. Rahmatallah and Ziyad H. Rasheed
Dept. of Nuclear Engineering University of Baghdad

ABSTRACT

Fluorophosphate neodymium laser glass has been prepared by discontinuous melting technique. Special melting and casting conditions were followed to prevent devitrification of glass samples. Furnace melting followed by slow cooling resulted formation of non vitreous glass. Problems of high viscosity melt and incomplete solubility and immiscibility of glass components were encountered by adjusting composition of glass components. X-ray diffraction analysis of the prepared glass samples proved the formation of amorphous phase. The prepared Nd – fluoride glass has low refractive index which is an important parameter for high power laser application. Optical properties of Nd – fluoride glass samples were investigated. UV – visible spectra showed almost total absorbance of light at wave length below 400 nm, while in the visible range a typical spectrum of Nd^{3+} ions covers the entire range. Infra – red spectral properties of these samples were studied. Transmission of the glass was found to be dependent on neodymium concentration.

KEYWORDS

Nd- laser Glass, Refractive Index, Optical Absorption, Infra- Red Measurement, Glass Density, X-ray Diffraction, Glass Casting and Phosphate Glass.

الخلاصة

زجاج ليزر النيوديميوم الفلوروفوسفاتي تم تحضيره بطريقة الصهر الغير مستمر. وقد اتبعت ظروف خاصة لعمليتي الصهر و الصب (القولبة) لمنع حدوث ظاهرة التبلور في نماذج الزجاج. عند إجراء عملية الصهر في الفرن يتبع ذلك التبريد البطئ لوحظ حدوث ظاهرة التبلور(اللازجاجية) في نماذج الزجاج. تم معالجة مشكلتي اللزوجة العالية للمنصهر وعدم الذوبانية الكاملة والامتزاج التام لمكونات الخليط الزجاجي بالسيطرة على مكونات الخليط الزجاجي. أظهرت نتيجة الفحص بطريقة حيود الأشعة السينية إن النماذج الزجاجية المحضرة عشوائية التركيب والتكوين. إن نماذج زجاج النيوديميوم- الفلوريدي المحضرة كانت تتميز بانخفاض معامل الانكسار الضوئي وهو شرط مهم في تطبيقات زجاج القدرة العالية. الخواص الضوئية لزجاج النيوديميوم- الفلوريدي جرت دراستها حيث تبين إن الضوء يمتص كليا في منطقة الطول ألموجي الأقل من 400 نانومتر من الطيف المرئي – فوق البنفسجي بينما في منطقة الضوء المرئي فان طيف ايون النيوديميوم يغطي غالبية المدى من الطول ألموجي. أما الخواص الضوئية للزجاج في منطقة تحت الحمراء فقد تمت دراستها حيث وجد إن نفوذية الضوء تعتمد على تركيز النيوديميوم وبدرجات مختلفة وحسب الطول ألموجي.

INTRODUCTION

The glass laser currently provides pulse of high power, energy, and radiance, and shorter duration **(Young 1967)**. There are several characteristics of the glass host which are important.

Glass host is isotropic, durable, can accept large dipping concentration uniformly, and can be fabricated inexpensively in various shapes and large sizes with diffraction limited optical quality **(Snitzer and Young 1968)**. The index of refraction of host glass can be varied from 1.4 to almost 2.0 and the thermal properties can be selected to minimize the optical aberrations caused by temperature variation in the laser rod **(Loh 1966)**. One of the most useful laser systems is that which results when the Nd^{3+} ion present as an impurity atom in glass **(Snitzer and Young 1968)** and **(Johnson and Nassau 1961)**. The first report of laser action using a glass host material was by Snitzer in 1961 using a potassium barium silicate glass containing 2-wt% neodymium oxide **(Snitzer 1966)**. Since then much research has been carried out to determine the effects of glass composition on the parameters which affect the laser performance of glasses doped with rare earth ions **(Patek and Edwards 1970)**. The Nd^{3+} doped glasses have been studied in most detail but the behavior of other fluorescents rare earth ions has also been examined, e.g. Yb^{3+}, Ho^{3+}, and Er^{3+} **(Young 1984)**.

In addition to oxide host glasses (including tellurite and germanate as well as the more familiar silicate, borate and phosphate systems) the work has included a number of halide and oxyhalide systems **(Weber 1983)**

The small refractive index of some fluoride glasses makes them a prime material for high powered lasers, such as those used for nuclear fusion research. A good fluoride glasses may be defined as one that has a low refractive index, resistant to moisture attack, and can be made into a large block without devitrification. Pure BeF_2 glasses would be ideal if it where not for the fact that BeF_2 is hygroscopic. Other less soluble fluorides such as CaF_2, MgF_2, etc. must be incorporated to raise the resistance to moisture attack, even though their presence increases the probability of devitrification.

In the binary systems of fluoride glasses containing BeF_2 and alkali fluoride or alkaline earth fluoride, a large mole fraction of BeF_2 has to be present in order to form a glass **(Rawson 1967)**. This requirement is also the case in the ternary systems; alkali / alkaline earth / Be fluorides found by Vogel **(Vogel 1971)**. The resulting glasses are sensitive towards moisture attack. To over come this problem is by reducing BeF_2 fraction but this may lead to devitrification of glass and loss of its optical properties. Sun found that this problem can be solved by substitution of AlF_3 for BeF_2 **(Sun 1949), (Sun 1949) and (Sun and Huggins 1951)**.

One glass made by Imoka has the mol % composition 12 BeF_2, 32 AlF_3, 29 CdF_2, and 27 PbF_2 **(Imaoka 1954)**. These results indicate that AlF_3 is a good intermediate in a glass formation; it yields glasses with superior optical quality, stable with respect to moisture attack and devitrification.

The refractive index of fluoride glasses varies with their composition. Goldstein and Sun reviewed refractive index values and composition of 114 fluoride glasses **(Poulin et al. 1977) and (Vogel 1966)**.

Sun developed a composition of vitreous fluorophosphate systems on the base metaphosphate aluminum and fluorides of metal from the first and second group of the periodic table of the chemical elements **(Goldschmidt 1972), (Heyne and Anorg 1933), (Mackenzie and Baldwin 1976) and (Sun 1950)**. Several authors have studied domains of glass forming and some physicochemical and optical properties in fluorophosphate glasses. IR spectroscopic investigations of the glasses show that structural lattices of these glasses have phosphate, fluoride and fluorophosphates groups **(Golubtsov et al. 1969), (Golubtsov et al. 1971)**, **(Golubtsov et al. 1970) and (Golubtsov et al. 1971)**. The presence of different rare earth ions at different mole percentages were investigated **(Kolobkov et al. 1971), (Chalilev et al. 1979) and (Chlilev et al. 1978)**.

In this work phosphate – borate based Nd doped fluoride glasses were prepared. Formations of vitreous phase were examined together with some optical properties.

EXPERIMENTAL WORK

Materials, Equipments and Instruments

Chemical compounds: the following compounds were used: B_2O_3 (as H_3BO_3), P_2O_5, MgF_2, NaF and Nd_2O_3. Their purity is the highest available, but not less than 99%.
Crucibles: made from platinum, nickel, porcelain, silica, alumina, graphite and Pyrex.
Melting equipments: electrical furnace type (Nabertherm FRG) and high temperature torch (Butane – oxygen) were used.
Analytical balance: type: Sartorious (FRG) sensitivity 0.1 mg was used for weighing process of the raw materials. It was used for density measurement.
Refractive Index Measurements: a traveling microscope was used. Method described else were **(Krylova and Poluehktov 1995)**.
X-Ray Diffraction: measurements were carried out using Phillips XRD machine type PW-1840 with copper target.
Optical Measurements: SHIMADZU spectrophotometer type (UV – 1650 PC) (Japan) was used for ultra- violet to visible range spectra absorption measurements in the wave length range 200 – 1100 nm.
SHIMADZU spectrophotometer type (FTIR -8000) (Japan) was used for recording transmission of the glass samples in the frequency range 500 – 4000 cm^{-1}.

Preparation of glass samples

The aim of the experimental work is to find a successful combination of different working parameters that ultimately yield a glass sample suitable for examination and presentation as a laser glass medium. These parameters involve:

1. The selection of chemical formulation which contain adverse materials or compounds that differ in;
    - Thermal stability, during heating and melting.
    - Solubility and miscibility with other compounds.
    - Do not suffer segregation or phase separation upon cooling.
    - Resistance to devitrification, which usually results a non-glass medium.
2. Suitable heating, melting and cooling steps.
3. Inertness towards atmospheric attack, so it is easier practically to carry out the work under normal atmosphere and no further complication for need of inert atmosphere or special containment.
4. Due to the presence of fluoride ions in the glass melt, only platinum crucibles are suitable for melting and graphite mould for casting.
5. Only melting furnace or gas torch is suitable to carry out melting steps which is followed by pouring out the melt into the graphite mould.

As mentioned above there is a need for a compromise to yield a proper glass sample suitable for optical examination.

RESULTS AND DISCUSSION

Glasses can be made from many substances oxide and non oxide. Traditionally, glass must contain a major percentage of silica which is the glass forming oxide. Attempts to find a new glass forming oxide have led to the discovery of phosphate and borate glasses. Recently, new types of glasses are prepared to meet specific requirements and applications, these are germinate, arsenate, tellurite, tungestate, titanate, molybdate, vanadate and plumbate glasses **(Snitzer and Young 1968)**. The non oxide glasses systems mainly chlorides and fluorides. These glasses transmit to longer wave length in the infra – red than do the silicate glass, and may eventually replace silica – based fibers in optical communication systems **(Drexhage 1985) and (Trans et al. 1984)**.

Upon addition of aluminum oxide or fluoride to silica, the cation Al^{3+} substitutes for Si^{4+} in the lattice thereby leads to the stability of the network, and thus is referred as network intermediate. Neodymium oxide or fluoride which is an intermediate acts as active medium in the lasing process.

The previously mentioned compositional facts have found to affect the properties of the prepared glass. Many experiments were carried out aimed to prepare neodymium containing glass of fluorophosphate base by discontinuous melting technique. The glass mixture is heated rapidly to a temperature higher than the melting point of its components, stirred and mixed well to assure complete mixing and miscibility of mixture, and then cast rapidly in a graphite mould i.e. quenched.

Only platinum crucible was found suitable for this work. Porcelain, quartz and silica crucibles were cracked while nickel and stainless steel crucibles were attacked vigorously due to reaction of the melt (fluoride ions) with nickel and iron at high temperature **(Trans et al. 1984)**.

Many experiments were carried out to achieve the proper composition of the glass components. A new formula containing nearly 50 wt % of both glasses formers (B_2O_3, P_2O_5) and glass intermediate (AlF_3, MgF_2, NaF, Nd_2O_3) gave successfully glass samples suitable for laser work. The chemical composition is given in **table (1)**. Nd_2O_3 varies as in the following (LG9: 4wt %, LG10: 2wt %, LG11: 1wt% and LG12: 0wt %). Glass samples LG9 has intense violet color, the color intensity decreases as the concentration of the Nd_2O_3 is decreased, as shown in **Fig. (1)**.

In laser glass research, the aim is to manufacture a low refractive index glass. This target was found to be possible with fluoride glasses but the refractive index varies with their composition. In the prepared glass, the average value of index of refraction Nd = 1.392 ± 0.053 and thus, the refraction loss R = 2.7 %, and the transmitted light is 94.6 %.

Since fluoride glass is a mixture of many compounds; therefore, it is expected that the glass density is an average figure of fractional densities of its components. The measured densities of the prepared fluoride glass samples have an average value in the range 2.5±0.07. Glass density is an important technological factor; it is a critical factor in melting as in casting processes. It affects the refractive index and other optical properties.

To prove the formation of glass material from non – oxide or non – silicate compounds mixture, a blend of known composition was taken, sodium and magnesium fluoride added to it boron oxide (as boric acid) and phosphorous pentoxide. The compounds of this blend were mixed thoroughly and examined using x-ray diffraction technique which revealed clear pattern of these compounds. This is shown in **Fig. (2)**. When the mixture was melted, cast and cooled, then examined by x-ray diffraction technique. The spectrum showed no pattern, only amorphous phase which is an evidence for glass formation; this is shown in **Fig. (3) (ASTM Cards)**. Thus fluoride glass can be formed when alkali and alkaline earth fluorides are melted together with boron oxide and phosphorous pentoxide (glass formers) in the presence of aluminum oxide or better aluminum fluoride, the glass intermediate which plays the role of glass modifier. Furthermore, rapid cooling of the melt prevents devitrification process and thus only glass phase is formed **table (2)**.

Optical properties of Nd fluoride glasses

Developments of new optical materials become necessary when measurement and discrimination of electromagnetic radiation reached beyond the visible spectrum into ultraviolet and infra–red.

The spectral range of transmission is limited on the short wavelength side by electronic resonances and on the long wavelength side by atomic resonances. Light intensity is reduced by reflection which depends on the refractive index of the material, angle of incidence of the light, and in the absorption region on the absorption coefficient **(McCarthy 1963)** .

Further intensity losses are caused by light scattering resulting from irregularities on the surface or inclusions inside the material. For laser applications, absorption coefficient measurements can insure that the specific wavelength absorption of the laser beam is below required level.

Spectral absorbencies for glass samples LG9, LG10, LG11, and LG12 were measured in the uv-visible range between 200 and 1100 nm. The results of all samples are shown in **Fig. (4)- (7)**, the following observation can be made:

- Light is completely absorbed in the wavelength below 300 nm and partially absorbed between 300 –400 nm. This case is similar to that found in window glass (soda lime glass) which has a composition $Na_2O - CaO - SiO_2$.
- In relatively pure quartz the absorption edge is placed approximately at the wavelength λ=190 nm in the ultra – violet region of the spectrum **(Sigel 1973)**, Pure sodium fluoride and magnesium fluoride do not absorb uv-light, their absorption edge are 140 nm and 110 nm for single crystal respectively. Vitreous boron trioxide with an absorption edge at 170 nm transmits well in the ultra-violet region of the spectrum **(Vaughen 1944)**. Boron oxide and aluminum fluoride, both of them are trivalent, thus furnish the glass matrix with pairs of free electrons which enhanced resonances of the radiation with frequencies of electrons of various level of bonding. Therefore, the location of the absorption edge in the ultra-violet region of the spectrum depends upon the composition of the glass as well as the chemical nature of its components **(Nc Swain 1963)**.
- Glass LG12 does not contain absorbing component, thus it is transmitive for radiation in the visible region of the spectrum, see **Fig. (7)**.
- Nd doping of fluoride glass is necessary factor in laser application, thus glasses LG9, LG10 and LG11 are doped with 4, 2 and 1 % Nd as Nd_2O_3 respectively. The violet fluoride glasses revealed complex absorption spectra in the visible region which is a characteristic spectrum of rare-earth ion **(Stewart and Kato 1958)**; this complex spectrum is due to strong absorption due to transitions between different electronic configurations. In rare-earth ions in solid matrix, the 4f levels are strongly shielded from the crystal field by filled 5s and 5p shells and as a result, the emission lines are well defined sharp and narrow and the level structure varies slightly from one host to another **(Dieke 1958)**.
- A plot of absorption maxima of Nd^{3+} ion in the glass of different wavelength against neodymium concentration is shown in **Fig. (8)**. The absorption increases as the concentration is increased, but the rate of increased is lowered at 4% Nd concentration which means that higher Nd concentration is not useful, but trouble may be faced regarding solubility of glass components and its transparency. The figure implies that all spectra lines are due to neodymium since the absorbencies increase with the Nd concentration.

The energy of most molecular vibrations corresponds to that of the infrared region of the electromagnetic spectrum. Quanta of infrared radiation can excite atoms to vibrate directly, thus, the absorption of infrared radiation gives rise to the infrared spectrum. The largest vibrations are exhibited by the charges of the so called dipoles in resonance **(Banwell 1972)**.

The IR spectra of the glasses contain characteristic bands related to alkaline metaphosphate which are observed in the spectral range 1425 – 1350 cm^{-1} **(Corbridge and Lowe 1954)**. Wassilac et al investigated properties, structure and spectroscopy of fluorophosphate glasses doped with Nd. They established correlation between shift in spectral lines and concentration of fluorides in the glass **(Kolobkav et al. 1977)**. The presence of bands in 760 – 730 cm^{-1} is due to P-O-P vibration or P-F bands in monofluorophosphate anion **(Margaryan and Arutunyan 1973)**. **Fig. (9)** to **(12)** show the infrared spectra of fluoride glasses of the system $B_2O_3 - P_2O_5 - AlF_3 - MgF_2 - NaF$ prepared in our laboratory. Glasses LG9, LG10 and LG11 are shown in **Fig. (9)**, **(10)** and **(11)** respectively. The spectra are identical but differ in percentage of transmission. They are characterized by the appearance of the spectral bands at 3450, 2450, 1750, 1650, 1550, 1300, 1100, 650 and 500 cm^{-1}. The transmission of these bands increase as the neodymium concentration is increased. Glass LG12 which is free from Nd shows different IR spectrum especially in the range 800 -1600 cm^{-1}.

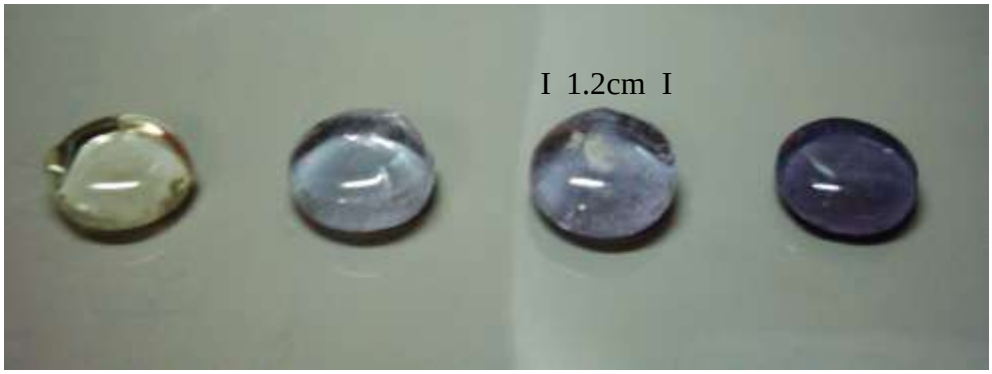

LG12 LG11 LG10 LG9

Fig. (1) Samples LG9-LG12

Table (1)

Composition of fluorophosphate laser glass LG9

Compound	Weight %		Mole fraction %	
AlF_3	30	50	27.8	58.9
NaF	10		18.6	
MgF_2	10		12.5	
Nd_2O_3	4		0.9	
B_2O_3	26	46	29.1	40.1
P_2O_5	20		11.0	
Element	**Weight %**		**Mole fraction %**	
Al	9.6		6.7	
Na	5.5		4.4	
Mg	3.9		3.0	
Nd	3.6		0.48	
B	8.2	16.9	14.1	19.4
P	8.7		5.3	
F	31.0		31.0	
O	29.5		35.0	
F/P	3.56		5.85	
F/B	3.78		2.20	
B/P	0.94		2.66	

Table (2)

X-ray diffraction lines of infused glass
LG9 components **Fig. (2)**

Angle 2θ	Spacing d	compound
14.7	5.984	AlF_3
14.7	5.980	B_2O_3
16.0	5.515	AlF_3
27.3	3.261	B_2O_3
27.7	3.210	B_2O_3
28.8	3.091	AlF_3
35.1	2.545	MgF_2
40.4	2.227	MgF_2
43.8	2.062	MgF_2
49.9	1.823	B_2O_3
53.4	1.712	MgF_2
56.8	1.617	MgF_2

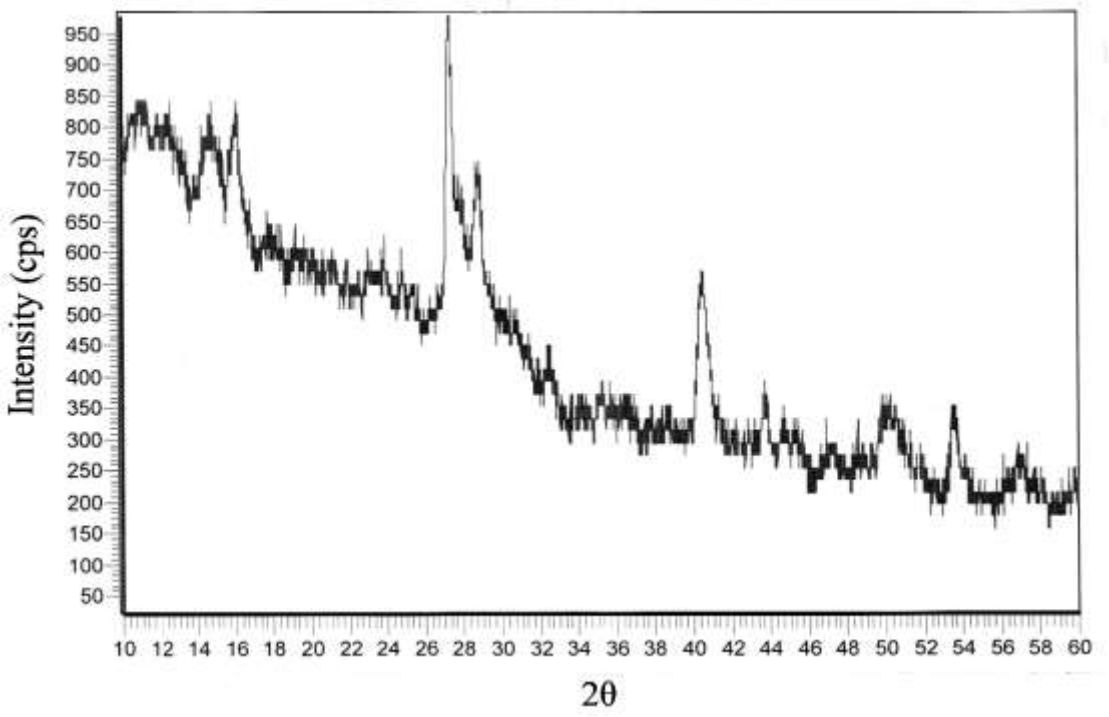

Fig. (2). X-ray diffraction for the sample LG9 (before melting)

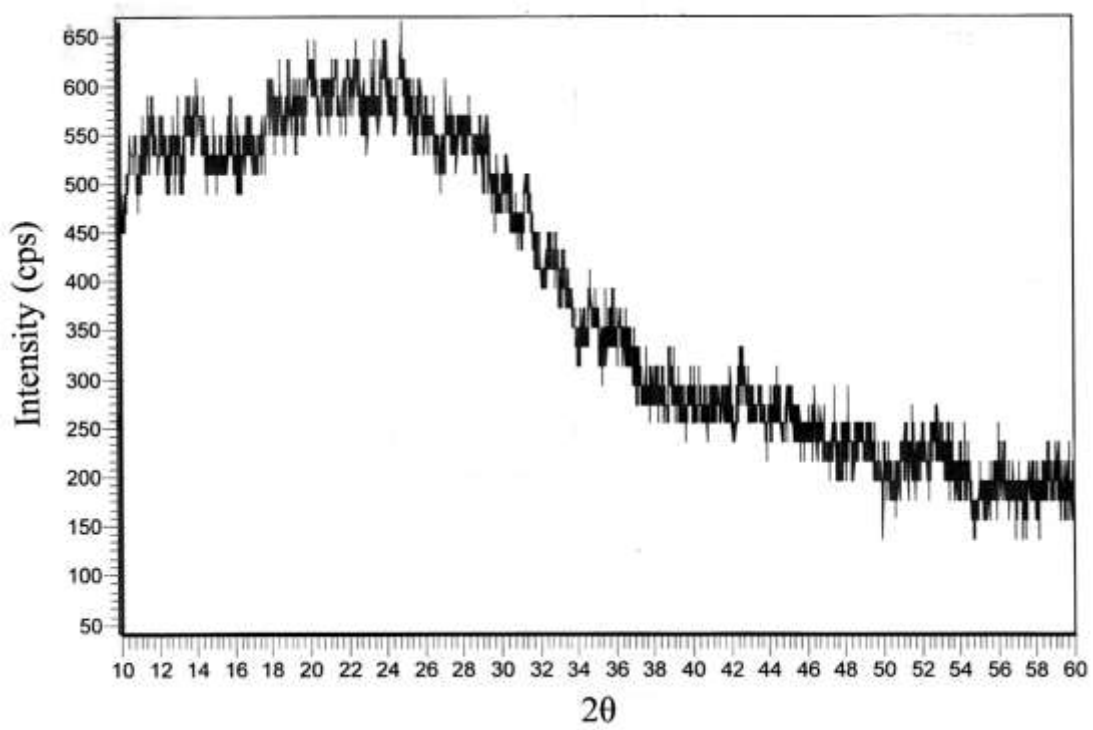

Fig. (3). X-ray diffraction for the sample LG9 (after melting)

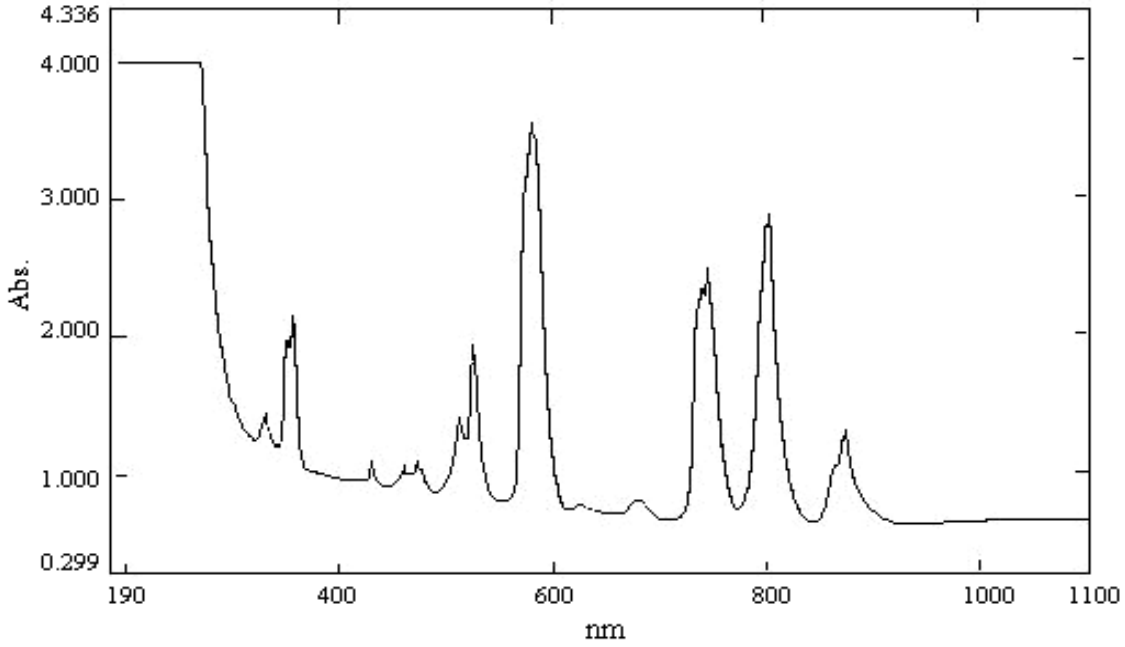

Fig. (4) uv-visible spectrum of Nd- glass sample LG9

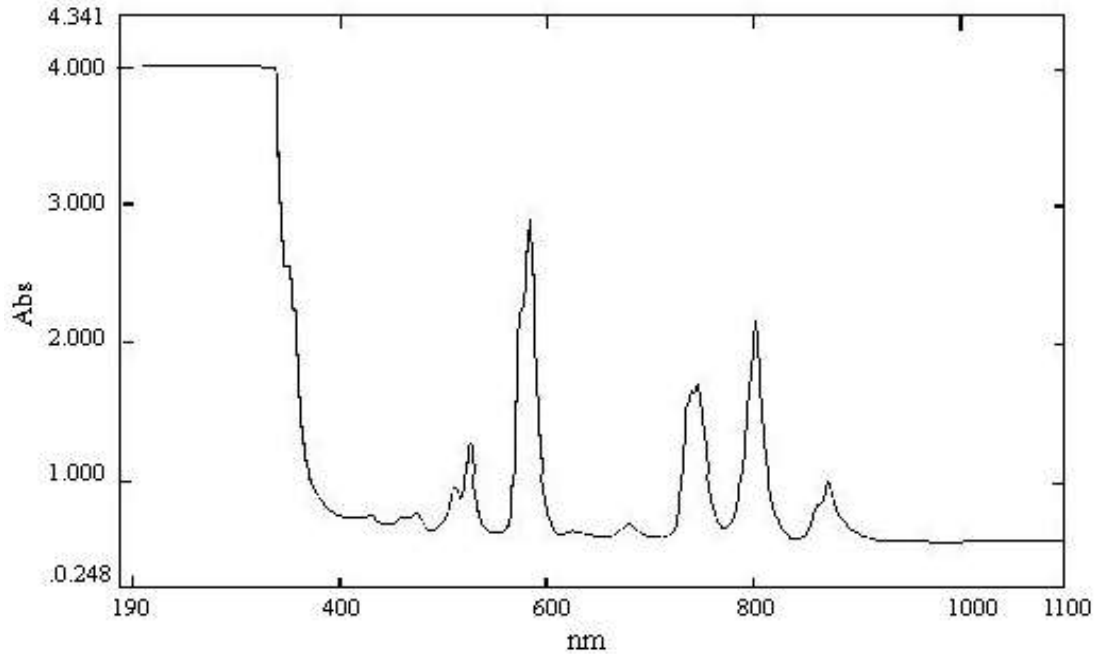

Fig. (5) uv-visible spectrum of Nd glass sample LG10

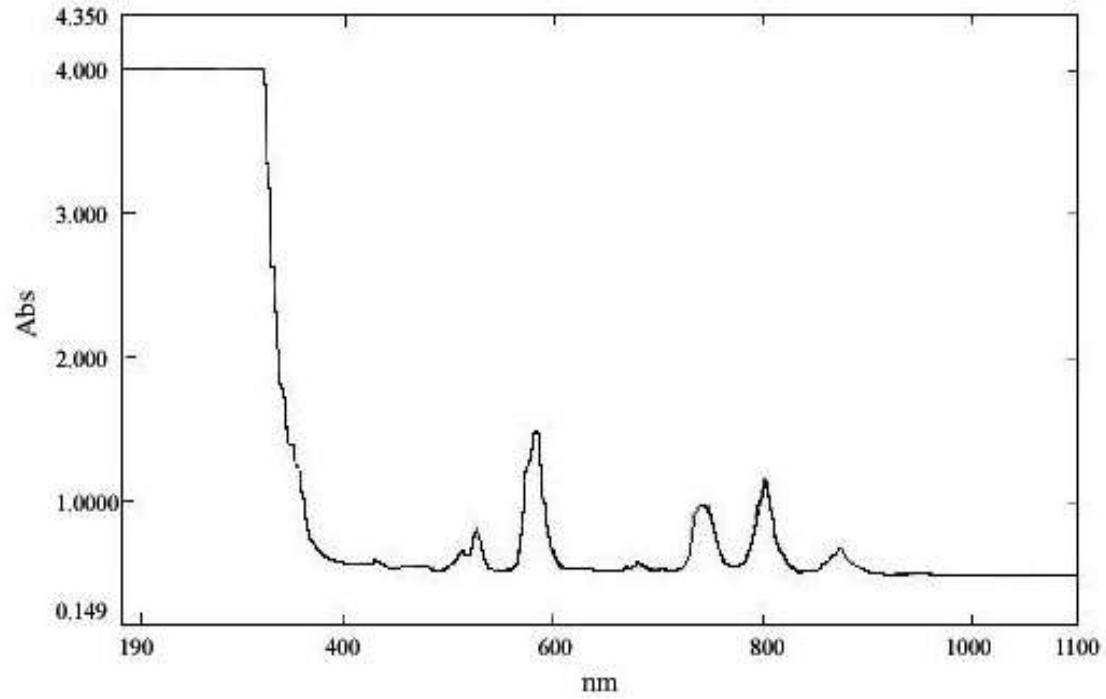

Fig. (6) uv-visible spectrum of Nd glass sample LG11

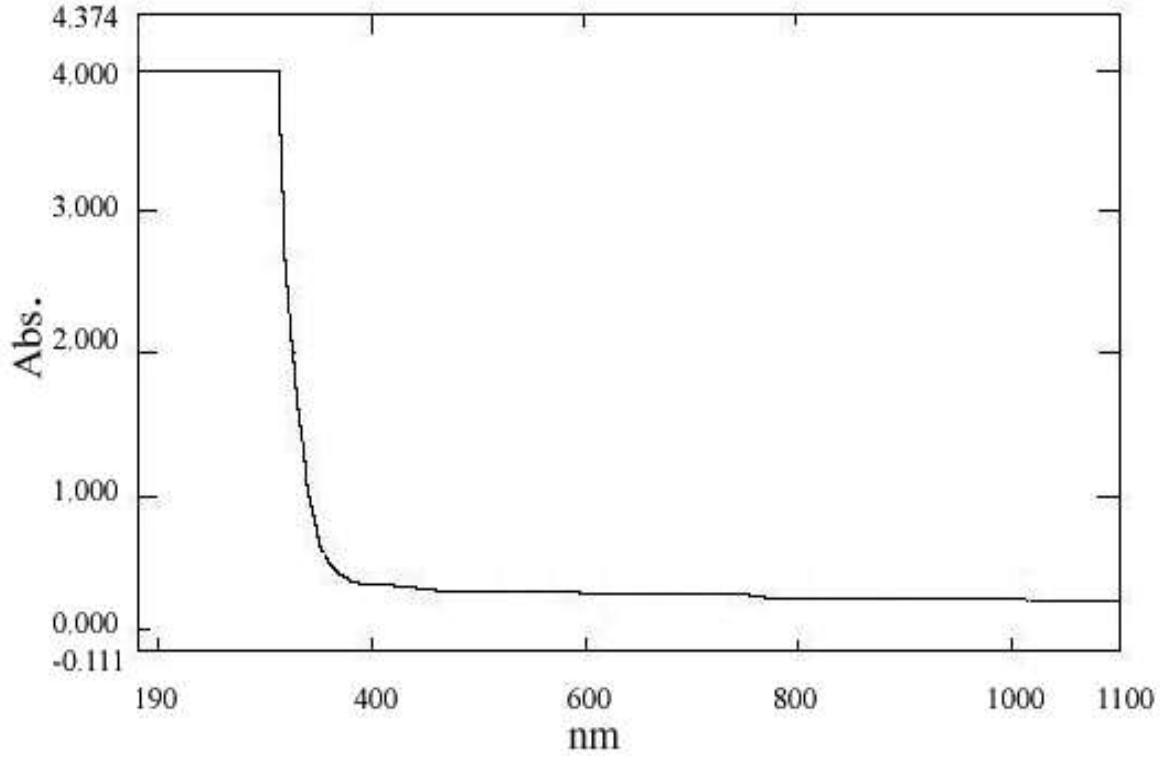

Fig. (7) uv-visible spectrum of Nd glass sample LG12

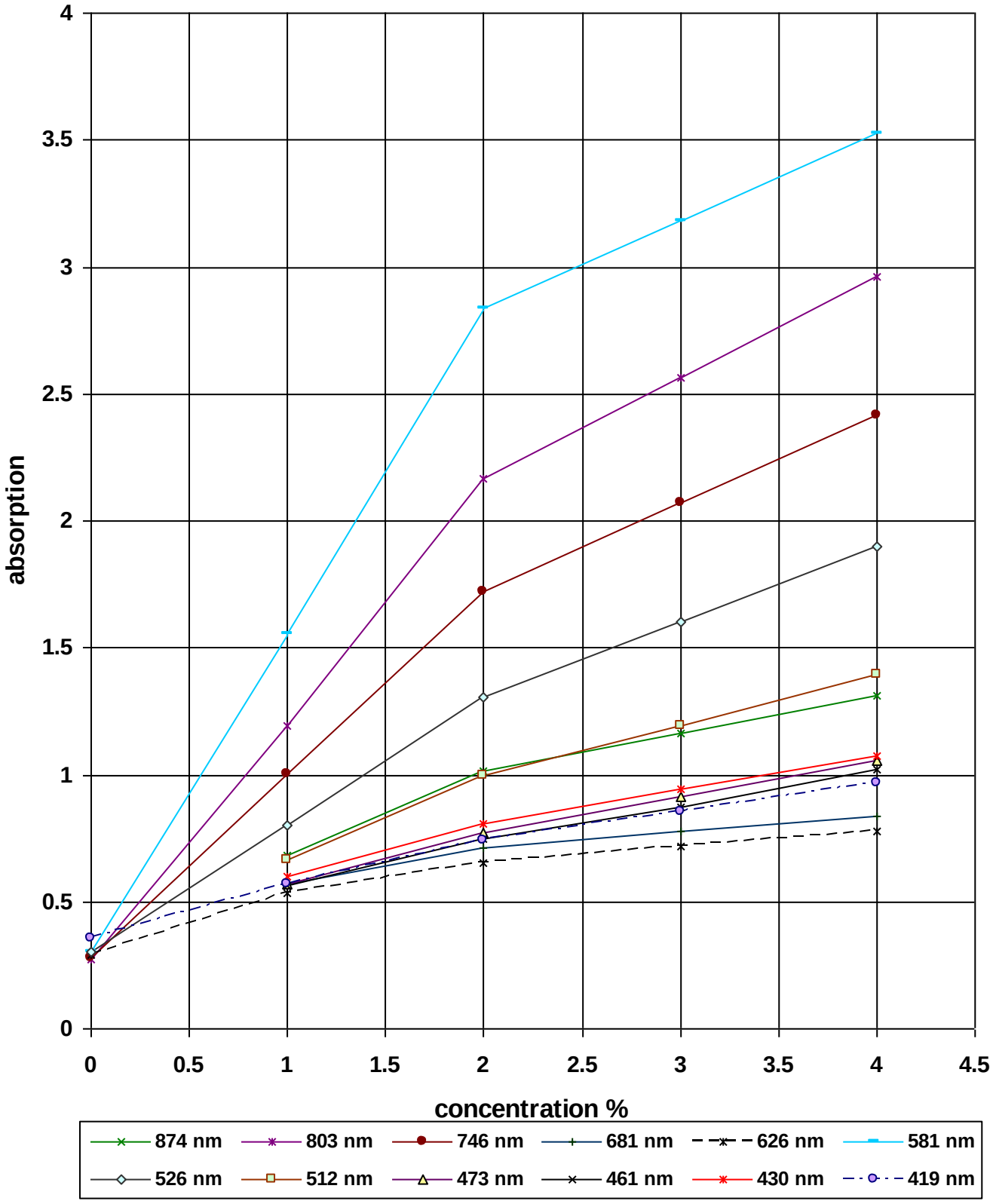
absorption
concentration %
0
0.5
1
1.5
2
2.5
3
3.5
4
4.5
874 nm
803 nm
746 nm
681 nm
626 nm
581 nm
526 nm
512 nm
473 nm
461 nm
430 nm
419 nm

Fig. (8) Dependence of uv-visible absorption maxima on neodymium concentration

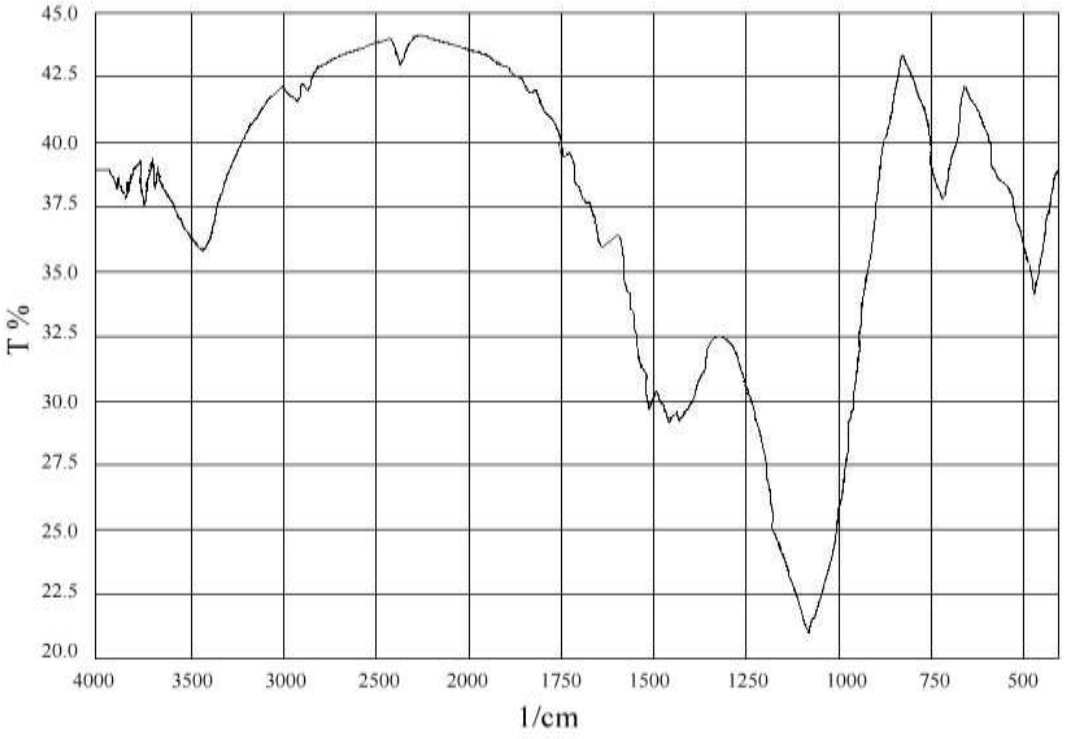

Fig. (9) IR- spectral of Nd glass sample LG9

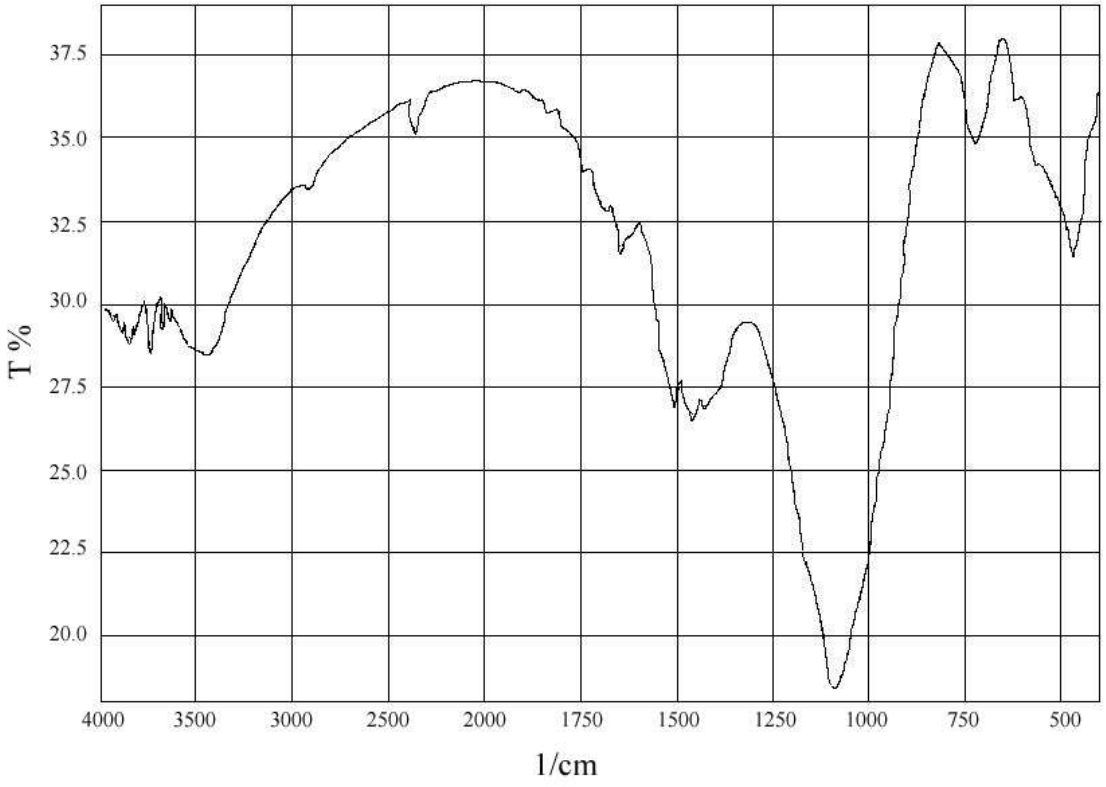

Fig. (10) IR- spectral of Nd glass sample LG10

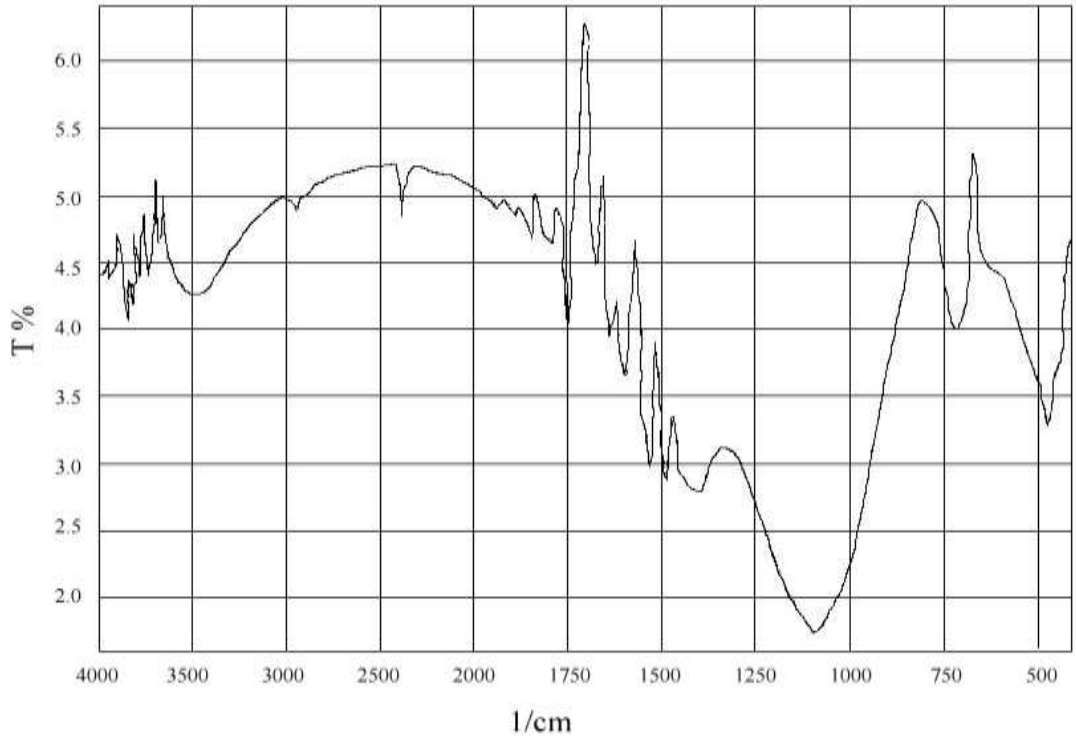

Fig. (11) IR- spectral of Nd glass sample LG11

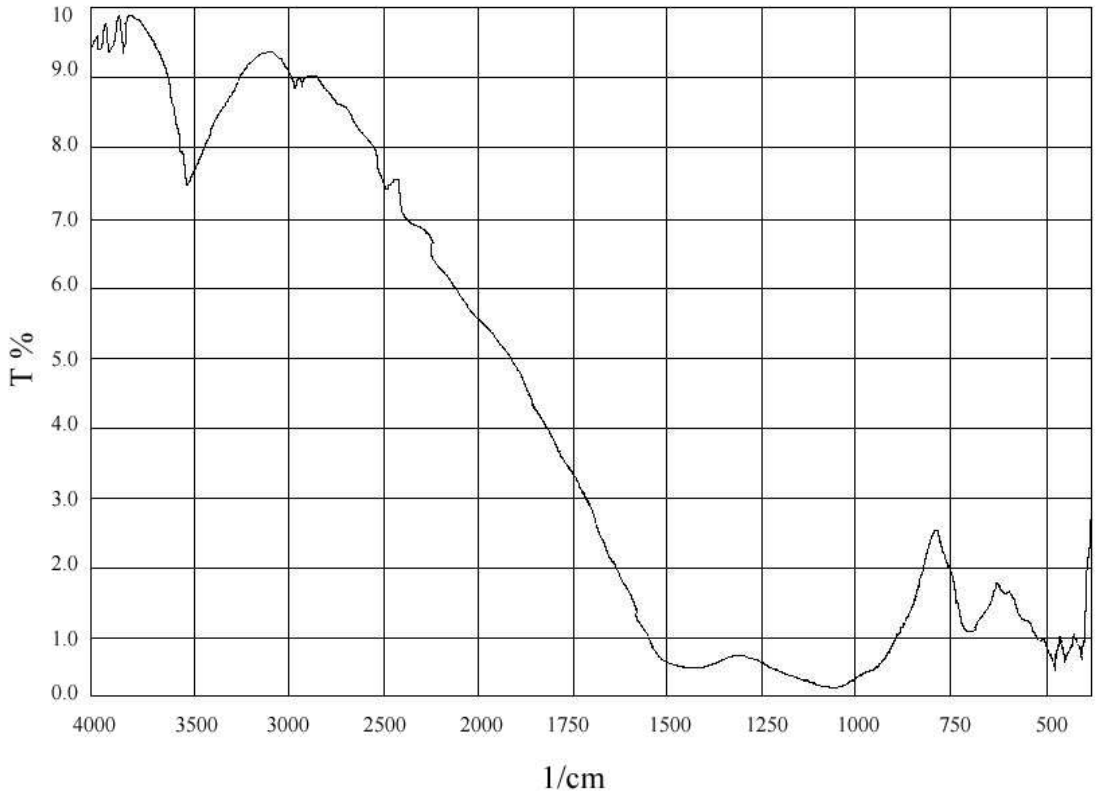

Fig. (12) IR-spectral of Nd glass sample LG12

REFERENCES

ASTM card No. 6-0290 for MgF_2
ASTM card No. 1-0213 for P_2O_5
ASTM card No. 6-0297 for B_2O_3

REFERENCES

Banwell C.N., *Fundamentals of Molecular Spectroscopy,* McGrow Hill *(*1972).

Boyd D.C. et al., Initial Report to ERDA under contract No. **EY-76-C-02-**4079 (1977).

Chalilev V. D., Pronkin A. A., Vakhrameev V. I., and Wassilac Y. P., *"Electroconductivity and structure of non-alkaline fluoride glasses"*, Physics and Chemistry of Glass (USSR), **5 :**188(1979).

Chalilev V. D., Wassilac Y. P., Melnikova O. V., Morozov I. N., Kolobkov V.P., and Vakhrameev V. I., "*IR – spectroscopic and Roentgen phase analyses non-alkaline fluorophosphate glasses and products of their crystallizations"*, Physics and Chemistry of Glass (USSR), **4 :**42(1978).

Corbridge D. E. C., and Lowe E. J., "*The infrared spectra of some inorganic phosphorus compounds*", J. Chem. Soc., 493 and 4555 (1954).

Depalis P.F., U.S. Patent **2819977**, (1958).
Dieke G., *Spectra and Energy Levels of Rare Earth Ions in Crystals*, Interscience (1958).

Drexhage M.G., *Heavy Metal Fluoride Glasses n "Treatise on Materials Science and Technology"* Academic Press, (1985).

Goldschmidt V.M., Z. Tech. Phys. **8:251**, (1972).

Golubtsov L. A., Chalilev V. D., and Evstropev K. S., *"Some Physicochemical properties of ternary non-alkaline fluorophosphate glasses"*, J. Optico-Mech. Ind. (USSR), **4:**59 (1969).

Golubtsov L. A., Chalilev V. D., Evstrpev K. S., and Ivanova E. N., *"Glass formation and some physicochemical properties of glass in the systems $Al(PO_3)_3 – BaF_2 – RF_2$, where R-Mg, Ca, Sr"*, J. Appl. Chemistry (USSR), **44:**180 (1971).

Golubtsov L. A., Chalilev V. D., and Petrovski G. T., "*Optical glass"*, Patent USSR, **No268619**, (1970).

Golubtsov L. A., Chalilev V. D., and Evstropev K. S., "*Investigation of structure of fluorophosphate glasses by IR spectroscopy"*, In: Glass Forming State (Nuka Press, Leningrad), **262**(1971)**.**

Heyne G., Z. Anorg. Allg. Chem. **46:**473, (1933).

Imaoka M., J. Jap. Ceram. Soc. **62:**38, (1954).

Imaoka M. and Mizusawa S., J. Jap. Ceram. Soc. **61:21,** (1953).

J. Non Cryst. Solids, *Fluorescence and Glass Lasers* **47**(1982) 117:134.

Johnson L.F. and Nassau K., Proc. IRE. **49**:1704, (1961).

Kolobkov V. P., Chalilev V. D., Wassilac Y. P., Vkhrameev V. I., Zhmirieva I. A., and

Kovalieva I. V., "*Spectral-luminescent investigations of fluorophosphate glasses, doped rare earth elements*", Physics and Chemistry of Glass (USSR), **3 :**249(1977).

Kolobkov V. P., Chalilev V. D., Wassilac Y. P., Vakhrameev V. I., Zhmirieva I. A., and

Kovalieva I. V., "*Spectral-luminescent investigations of fluorophosphate glasses, doped rare earth elements"*, Physics and Chemistry of Glass (USSR), **3** :249(1971).

Krylova N. V., and Poluehktov P. P., *"Characteristics of solidified high-level wastes as one of the barrier indisposal system"*, Atomnaya Ehnergiya, **78:**93(1995).

Loh E., Phys. Rev. **147**:493, (1966).

McCarthy D.E., applied optics, **2, 6** (1963).

Mackenzie J.D. and Baldwin C., UCLA-ENG **76103**, (1976).

Margaryan A. A., and Arutunyan D. S., "*Investigation of $P_2O_5 – LaF_3 – RF_2$ systems*", In: Materials Conf. Of Young Scientist and Specialists of Inst. Ge. And Inorgan Chem. Of Akad. Science of Arm. SSR (Akad. Sci. Arm. SSR, Yerevan) 166 (1973).

Nc Swain B.D., Phys. Chem. Glasses, **4:**1 (1963).

Patek K, "*glass laser*" Ed. J. G. Edwards CRC Press, (1970).

Poulin M., Chanthanasinh M. and Lucas J., Mater. Res. Bull. **12:151**, (1977).

Rawson H., *Inorganic Glass Forming System,* Academic press. N.Y. (1967).

Sigel G.H., J. None. Crys. Solids, **13**:373 (1973).

Snitzer E. and Young C.G. *Glass Laser*, in Laser Vol.**2**, A.K.Levin Ed N.Y., (1968).

Snitzer E., Proc. IEEE, **54**:1249, (1966).

Snitzer, E. and Young C.G.,"*Glass Laser*" in "*Advanced in Laser*" Vd2 Ed. A. Levine, Dekker (1968).

Stewart D.C. and Kato D., Anal. Chem. **30:**164 (1958).

Sun K. H., "*Fluorophosphate glass*", Patent USA, **No2511225,** 1950.

Sun K.H., U.S. Patent **2466509**, (1949).

Sun K.H., U.S. Patent **2466507**, (1949).

Sun K.H. and Huggins, M.L., U.S.Patent **2578325**, (1951).

Trans D.C., et al., J. Light Wave Technology, **LT – 2:**566(1984).

Vogel W., *Structure and Crystallization of Glasses,* Pergamon Press. N.Y. (1971).

Vogel W., West German Patent **1 086 866**, (1960).

Voughen T.C., Glass Ind. **25:259:**278 (1944).

Weber M., *Oxide and Halide Laser Glasses,* 2nd International Schott Colloquium, Jena Math. Nat. **32**(1983) 239:250.

Young C., Laser Focus, **3**:36, (1967).

Young C.G., Microwaves, **7**, 69 (1984).

VIBRATION ANALYSIS OF ROTATING PRE-TWISTED CANTILEVER PLATE BY USING THE FINITE ELEMENT METHOD

Oday I. Abdullah
University of Baghdad / College of Engineering
Nuclear Engineering Department

Abstract:

In this paper the finite element method has been used to determine the fundamental natural frequencies of a pre-twisted plate mounted on the periphery of a rotating disc. Three dimensional, finite element programs was built using three noded triangular shell element as a discretization element for cantilever plate, this element has six degrees of freedom at each node. All formulations and computations are coded in (FORTRAN-77). The investigation covers the effect of speed of rotation, disc radius, aspect ratio, pre-twist angle and skew angle on the vibration characteristics of rotating cantilever plate. For this analysis, the initial stress effect (geometric stiffness) and other rotational effects except the corioles acceleration effect have been included. The eigenvalues have been extracted by using simultaneous iteration technique. Results shown that the natural frequencies increase when; angular speed and disc radius are increases.

الخلاصة:

استخدمت في هذا البحث تقنية العناصر المحددة لحساب الترددات الطبيعية الاساسية لصفيحة ملتوية مثبته بقرص دوار. تم تمثيل هذه الصفيحة كقشرة دوارة, باستعمال العنصر المثلث كعنصر تجزئة لهيكل الصفيحة, حيث يحتوي هذا العنصر على ثلاث عقد لكل عقدة ست درجات من الحرية. تم الحصول على كل النتائج باستخدام برنامج حاسوب بلغة (FORTRAN-77). البحث درس تأثير عدة متغيرات مثل سرعة الدوران و نصف قطر القرص و نسبة الطول إلى العرض و زاوية الالتواء و زاوية التثبيت على خصائص الاهتزاز في الصفائح الدوارة. في هذا التحليل تمت دراسة تأثير الإجهاد الابتدائي (الجسأة الهندسية) و التأثير ألدوراني بدون الأخذ بنظر الاعتبار وجود تأثير تعجيل كيريولس (Coriolis acceleration), وباستخدام تقنية التكرار المتزامن لحساب الترددات الطبيعية. تبين النَتائِجَ بأنّ الترددات الطبيعيةَ تَزِيدُ بزيادة السرعةِ الزاويةِ ونصفِ قطر القرصِ.

KEY WORDS
rotating pre-twist plate, natural frequency, geometric stiffness, FEM.

INTRODUCTION:

The natural frequencies of rotating turbomachinery blades are known to be significantly higher than those of the non- rotating blades. For reliable and economic designs of the structures, it is necessary to estimate the dynamic characteristics of those structures accurately and efficiently. Since the blades are generally idealized as cantilever beams (a few investigations assumed the blade as a cantilever plate), the vibrations of rotating cantilever beams have been studied in several

investigations. An early analytical model to calculate natural frequencies of a rotating cantilever beam was suggested by (**Southwell** 1921). Based on the Rayleigh energy theorem, a simple equation that relates the natural frequency to the rotating frequency of a beam was suggested. This equation is known as the Southwell equation, and widely used by many engineers nowadays. Later, to obtain more accurate natural frequencies, a linear partial differential equation that governs bending vibration of a rotating beam was derived by **(Schilhansl** 1958). Applying the Ritz method to the equation, more accurate coefficients for the Southwell equation could be obtained. Since the early 1970s, due to the progress of computing technologies, a large number of papers based on numerical approaches have been published. For instance, in references (**Bauer** 1980), approximation methods for the modal analysis of rotating beams were employed. More complex shapes and the effects of beams were also considered. The effects of tip mass (**Wright** 1982), elastic foundation and cross-sectional variation (**Kuo** 1994), shear deformation (**Yokoyama** 1988), pre-twist and orientation of a blade (**Subrahmanyam** 1987), and gyroscopic damping effect (**Yoo** 1998) on the modal characteristics of rotating cantilever beams were studied. Survey papers for the vibration analysis of rotating structures are available (**RAO** 1987). The most widely used modeling method for the transient analysis of structures is the classical linear modeling method (**Bodley** 1978). This modeling method employs the Cartesian deformation variables and the linear Cauchy strain measures. It has several merits such as simplicity of formulation, ease of implementation in finite elements methods, and efficiency of computation, which results from the use of co-ordinate reduction techniques (**Hale** 1980). This modeling method, however, often provides erroneous results when structures undergo overall motion such as rotation. To resolve the problem of the classical linear modeling method, several non-linear modeling methods (**Christensen** 1986) have been developed. With these non-linear modeling methods, the problem of accuracy can be resolved. However, serious computational inefficiency results from the non-linearity that disables the co-ordinate reduction techniques. More recently, a new linear modeling method for the dynamic analysis of a flexible beam undergoing overall motion was introduced (**Yoo** 1995).

THEORETICAL BACK GROUND:

The formulation follows a pattern similar to that in (**Henry** 1974). Two Cartesian co-ordinate systems are used, an absolute fixed system $R_0\,(X_0Y_0Z_0)$ and a local system $R_1\,(X\ Y\ Z\ )$ (see **Fig. 1**) attached to the rotating disc.

The potential strain energy U and kinetic T are, respectively,

$$U = \frac{1}{2}\int_{vol} \varepsilon^t\, \sigma\, d(vol) \qquad (1)$$

$$T = \frac{1}{2}\int_{vol} \rho \bar{V}^2\, d(vol) \qquad (2)$$

For plate bending problems, according to **(Zienkiewicz** 1979), the strains are given by:

$$\{\varepsilon\} = \begin{Bmatrix} \varepsilon_p \\ \varepsilon_f \end{Bmatrix} + \begin{Bmatrix} \varepsilon_g \\ 0 \end{Bmatrix} \qquad (3)$$

ε_p and ε_f are strains due to in-plane and bending displacements respectively and ε_g is the effect of bending displacements on mid-surface strains.

The stresses are given by,

$$\{\sigma\} = \begin{Bmatrix} \sigma_p \\ \sigma_f \end{Bmatrix} \qquad (4)$$

Where $\{\sigma_p\}$ and $\{\sigma_f\}$ are in – plane stress resultants and bending and twisting moments, respectively.
With the definitions for stresses and strains U is given by,

$$U = P_1 + P_2 + P_3 \qquad (5)$$

Where P_1, P_2 plane stress, bending strain energy and P_3 supplementary strain energy due to the effect of bending displacement on mid-surface strains, more expressions for P_1, P_2 and P_3 are standard (**Timoshenko** 1959).
At rest the co-ordinates of a typical Point M on the mid-surface are $(x, y, 0)$. Due to the displacement,

$$\{d\} = [u, v, w]^t \qquad (6)$$

The instantaneous co-ordinates of M are $(x+u, y+v, z+w)$, and then

$$\overrightarrow{OM}^{R_1} = \overrightarrow{OI}^{R_1} + \overrightarrow{IM}^{R_1} = \begin{Bmatrix} x_i \\ y_i \\ z_i \end{Bmatrix} \begin{Bmatrix} x+u \\ y+v \\ w \end{Bmatrix} = \begin{Bmatrix} x_i + x + u \\ y_i + y + v \\ z_i + w \end{Bmatrix} \qquad (7)$$

The angular velocity in the R_1 system is

$$\vec{\Omega}^{R_1} = [\Omega_1 \ \Omega_2 \ \Omega_3]^t \qquad (8)$$

And the absolute velocity of the point M is given by,

$$\vec{V} = \frac{\partial \overrightarrow{OM}^{R_1}}{\partial t_{R_0}} = \begin{Bmatrix} u^{\bullet} \\ v^{\bullet} \\ w^{\bullet} \end{Bmatrix} + \begin{Bmatrix} \Omega_1 \\ \Omega_2 \\ \Omega_3 \end{Bmatrix} \times \begin{Bmatrix} x_i + x + u \\ y_i + y + v \\ z_i + w \end{Bmatrix} = \begin{bmatrix} u^{\bullet} + \Omega_1 (z_i + w) - \Omega_3 (y_i + y + v) \\ v^{\bullet} + \Omega_3 (x_i + x + u) - \Omega_1 (z_i + w) \\ w^{\bullet} + \Omega_1 (y_i + y + v) - \Omega_2 (x_i + x + u) \end{bmatrix} \qquad (9)$$

Computing $\vec{V}^2$ $(i.e., \vec{V}^t \vec{V})$, canceling the terms like those proportional to z_i^2 which give no contribution when Lagrange's equations are applied, and substituting the result in **Eq.(2)** one can write the kinetic energy as (**Timoshenko** 1959),

$$T=\frac{1}{2}\int_{vol}\rho\begin{Bmatrix}u^{\bullet}\\v^{\bullet}\\w^{\bullet}\end{Bmatrix}^{t}\begin{Bmatrix}u^{\bullet}\\v^{\bullet}\\w^{\bullet}\end{Bmatrix}d(vol)+\frac{1}{2}\int_{vol}\rho\begin{Bmatrix}u^{\bullet}\\v^{\bullet}\\w^{\bullet}\end{Bmatrix}^{t}[A_1]\begin{Bmatrix}u\\v\\w\end{Bmatrix}d(vol)+$$
$$\frac{1}{2}\int_{vol}\rho\begin{Bmatrix}u^{\bullet}\\v^{\bullet}\\w^{\bullet}\end{Bmatrix}^{t}[A_2]\begin{Bmatrix}u^{\bullet}\\v^{\bullet}\\w^{\bullet}\end{Bmatrix}d(vol)+\frac{1}{2}\int_{vol}\rho\begin{Bmatrix}x_i+x\\y_i+y\\z_i\end{Bmatrix}^{t}[A_2]\begin{Bmatrix}u\\v\\w\end{Bmatrix}d(vol) \quad (10)$$

$$[A_1]=\begin{bmatrix}0 & -2\Omega_3 & 2\Omega_2\\ 2\Omega_3 & 0 & -2\Omega_1\\ -2\Omega_2 & 2\Omega_1 & 0\end{bmatrix} \quad (11)$$

$$[A_2]=\begin{bmatrix}\Omega_2^2+\Omega_3^2 & -\Omega_1\Omega_2 & -\Omega_1\Omega_3\\ -\Omega_1\Omega_2 & \Omega_1^2+\Omega_3^2 & -\Omega_3\Omega_2\\ -\Omega_1\Omega_3 & -\Omega_3\Omega_2 & \Omega_2^2+\Omega_2^2\end{bmatrix} \quad (12)$$

DERIVATION OF THE STIFFNESS MATRIX:

The polynomials for the displacements u and v are linear in $L_1, L_2 \text{ and } L_3$ while for the displacements w the polynomial assumed is cubic (**Zienkiewicz** 1979).
The in – plane nodal displacements are defined by,

$$\{q_1\}=\begin{bmatrix}u_1 & v_1 & u_2 & v_2 & u_3 & v_3\end{bmatrix}^t \quad (13)$$

And the bending nodal displacements are defined by,

$$\{q_2\}=\begin{bmatrix}w_1,\theta_{x_1},\theta_{y_1},w_2,\theta_{x_2},\theta_{y_2},w_3,\theta_{x_3},\theta_{y_3}\end{bmatrix}^t \quad (14)$$

$$\theta_{x_i}=-\left(\partial w/\partial y\right)_i,\ \theta_{y_i}=-\left(\partial w/\partial x\right)_i \quad (15)$$

After standard finite elements procedure one arrives at,

$$\begin{Bmatrix}u\\v\end{Bmatrix}=[N_1]\{q_1\},[N_2]=\begin{bmatrix}L_1 & 0 & L_2 & 0 & L_3 & 0\\ 0 & L_1 & 0 & L_2 & 0 & L_3\end{bmatrix} \quad (16, 17)$$

$$\{w\}=[N_2]\{q_2\},[N_2]=[N_{b_1}\ N_{b_2}....N_{b_9}]^t \quad (18, 19)$$

$$N_{b_1}=L_1+L_1^2L_2+L_1^2L_3-L_1L_2^2-L_1L_3^2 \quad (20)$$

$$N_{b_2}=b_3(L_1^2L_2+\frac{1}{2}L_1L_2L_3)-b_2(L_3L_1^2+\frac{1}{2}L_1L_2L_3) \quad (21)$$

$$N_{b_3} = a_3(L_1^2 L_2 + \frac{1}{2} L_1 L_2 L_3) - a_2 (L_3 L_1^2 + \frac{1}{2} L_1 L_2 L_3) \quad (22)$$

The other shape functions for nodes 2 or 3, can be written down by a cyclic permutation of the suffixes 1, 2, 3.

L_1, L_2, L_3 and the area co–ordinates, and a_i and b_i, are defined in **Fig.2**.

Once one knows the expression for the strain and the shape functions, then k_p the in–plane stiffness matrix, and k_f, the bending stiffness matrix can be easily derived. The integration is performed by using numerical three-point integration (**Cowper** 1973) over the triangular area.

DERIVATION OF GEOMETRIC STIFFNESS MATRIX:

Owing to the presence of the in–plane stresses σ_x^0, σ_y^0 and τ_{xy}^0 in the middle surface caused by rotation, the additional strain energy stored in the element is given by P_3. This additional strain energy results in an increase in the stiffness of the elements by an amount,

$$\{k_g\} = \int\int_A [G]^t \begin{bmatrix} \sigma_x^0 & \tau_{xy}^0 \\ \tau_{xy}^0 & \sigma_y^0 \end{bmatrix} [G] h \, dA \quad (23)$$

Where $[G]$ is defined by

$$\begin{Bmatrix} \frac{\partial w}{ax} \\ \frac{\partial w}{ax} \end{Bmatrix} = [G]\{q_2\} \quad (24)$$

For details, see (**Zienkiewicz** 1979). It is easy to show that,

$$U = \frac{1}{2} q^{\,t}[k + k_f]q + \frac{1}{2} q^t k_G \, q, \quad \{q\} = [q_1, q_2]^t \quad (25, 26)$$

Therefore,

$$\partial U / \partial q = [k + k_f]q + k_G \, q \quad (27)$$

DERIVATION OF MASS, CORIOLES AND SUPPLEMENTARY MATRICES, AND THE LOAD VECTOR:

By using **Eq. (16 and 18)** in **Eq. (10)** and then applying Lagrange's equations one obtain,

$$(d / dt)[\partial T / \partial q^{\bullet}] - [\partial T / \partial q] = m_E \, q^{\bullet\bullet} + c \, q^{\bullet} + k_R \, q - F \quad (28)$$

With $[N]$ defined by,

$$\begin{bmatrix} N_1 & 0 \\ 0 & N_2 \end{bmatrix} = [N]$$

The element mass matrix is,

$$[m_E] = \rho \int_{vol} [N]^t [N] d(vol) \qquad (29)$$

The element Coriolis matrix is

$$[C] = \rho \int_{vol} [N]^t [A_1][N] d(vol) \qquad (30)$$

The element supplementary or rotational stiffness matrix is,

$$[k_R] = \rho \int_{vol} [N]^t [A_2][N] d(vol) \qquad (31)$$

Moreover, the force vector is,

$$\{F\} = \rho \int_{vol} [N]^t [A_2] \begin{Bmatrix} x_i + x \\ y_i + y \\ z \end{Bmatrix} d(vol) \qquad (32)$$

FINAL MATRICES AFTER ASSEMBLY:

Adding expressions **Eq. (27** and **28)** and equating the result to zero gives the final differential equation of the structure after assembly in from,

$$M_E \ddot{q} + C\dot{q} + [K_E + K_G + K_R] q = \vec{F}(\Omega^2) \qquad (33)$$

The matrix K_G depends on the initial stress distribution. Initially the stresses are taken as zero and the equation.

$$[K_E + K_R] q = \vec{F}(\Omega^2) \qquad (34)$$

Is solved for the initial stress distribution σ_0. Then the solution of,

$$(K_E + K_G(\sigma_0) + K_R) q = \vec{F}(\Omega^2) \qquad (35)$$

Gives a new stress distribution σ. The stress values were found to converge within two iterations. Finally the frequencies and eigenvectors are found for the deformed configuration. The equation of motion of the structure, with the cariolis matrix neglected, is

$$M_E \ddot{q} + [K_E + K_G(\sigma) + K_R] q = 0 \qquad (36)$$

Assuming harmonic vibrations, $q = q_o\ e^{iwt}$, one has

$$[K_E + K_G(\sigma) + K_R - \omega^2 M_E] q_o = 0 \qquad (37)$$

In which M_E and $K_E + K_G + K_R$ are symmetric and positive definite matrices **Eq. (37)** is standard eigenvalue problem and is solved for the eigenvalues and eigenvectors by using a simultaneous iteration technique (**Jennings** 1977).
The tapered and skewed plate can be also be modeled by triangular shell elements, the variation in thickness being accounted for by defining the thickness of the element at the three nodes. For formulating all the matrices the element thickness can by taken as the mean of the nodal thicknesses.

VERFICATION TEST:

The present works were comparing with the numerical results in (**Rao** 1999) to find the fundamental non-dimensional frequency of vibration for rotating cantilever plate. **Table. (1)** explains the current results with numerical results in (**Rao** 1999), and the values of percentage error with numerical results. In this table, the maximum error not exceeds (2%). The data for the verification case are:

$$E = 217\mathbf{G}pa,\ \rho = 7850\,Kg/m^3, \upsilon = 0.3,\ b = 35mm, t = 3mm, l/b = 2, t/b = 0.0625, r/b = 4, \alpha = \theta = 30^\circ$$

RESULTS AND DISCUSSIONS:

The fundamental bending frequencies with out Coriolis effect are computed for pre- twisted cantilevers plates of two different aspect ratios (1 and 2), and for various values of non-dimensional speed of rotation $\left(\overline{\Omega}\ from\, 0\, to\, 1\right)$, of pre-twist angle $\left(\alpha = 0^\circ, 45^\circ\ and\ 90^\circ\right)$, of skew angle $\left(\theta = 0^\circ, 45^\circ\ and\ 90^\circ\right)$ and non-dimensional disc radius $\left(\bar{r} = r/l,\ from\, 0\ to\ 1.5\right)$. **Fig. 3** show the suitable mesh sizes where chosen for aspect ratios (1 and 2) in this analysis (The suitable mesh for the aspect ratio 1 and 2, which obtained after convergence test). In all computations, Poisson's ratio was taken as (0.3), and the material of the plate has been assumed homogeneous and isotropic $(E = 200{*}10^9\ N/m^2, \rho = 7850\,Kg/m^3)$ and the dimensions of the cantilever plate were $(b = 40mm,\ t = 2mm)$.

Figs. (4 and 5) show the variation of non-dimensional frequency of vibration (β) with non-dimensional speed of rotation $\left(\overline{\Omega}\right)$ for different twist and skew angles corresponding to the aspect ratios (1 and 2) respectively, for plate having $\left(\bar{r} = 0\right)$. The second set of results will initiate the tendency of change of (β) with $\left(\bar{r}\right)$ for different twist and skew angles were show in **Figs. (6 and 7)** corresponding for aspect ratios (1 and 2) respectively, for plate having $\left(\overline{\Omega} = 0.5\right)$.

The frequencies of all results are independent of skew angle and disc radius but dependent on pre-twist when the structure is stationary. The all-natural frequencies increase with increase in non-dimensional speed of rotation $\left(\overline{\Omega}\right)$ for all combinations of three skews $\left(\theta = 0^\circ, 45^\circ\ and\ 90^\circ\right)$ and three twists $\left(\alpha = 0^\circ, 45^\circ\ and\ 90^\circ\right)$, and for both cases of aspect ratios (1 and 2). The rate of increase is maximum for the combination skew= $\left(0^\circ\right)$ and twist= $\left(0^\circ\right)$, and is minimum for the combination skew= $\left(90^\circ\right)$ and twist= $\left(90^\circ\right)$. In general it has been observed that the rate of increase decrease with increase in pre-twist as well as with the increase in skew angle. At any given speed (including stationary case) and skew angle the frequency decreases with the increase in pre-twist angle. The maximum and minimum percentage increases in the frequency value, with the increase

in speed $(\bar{\Omega}\ from\ 0\ to\ 1)$ are roughly about 48% (when the skew is (0°), the twist is (0°) and $(\bar{r}=0)$) and about 6% (when the skew is (90°), the twist is (90°) and $(\bar{r}=0)$).

From **Fig. (6 and 7)** it can be seen that all the frequencies increase with increase in disc radius $(\bar{r}=r/l)$ for all cases. When the non-dimensional disc radius is increased from (0 to 1.5) the value of (β) is maximum for the combination skew=(90°) and twist=(90°), and is minimum for the combination skew=(0°) and twist=(0°). The maximum and minimum percentage increases in the frequency value, with the increase in non-dimensional disc radius (0 to 1.5) are roughly about 25% (when the skew is (90°), the twist is (90°)) and about 20% (when the skew is (0°), the twist is (0°)).

CONCLUSION:

A modal formulation for the free vibration of a pre-twist cantilever plate with setting angle is presented. Three dimensionless parameters are identified through a dimensional analysis: the aspect ratio of the plate, the ratio of hub radius to the plate length, and the dimensionless angular speed. The effects of the other parameters, such as well as the setting angle and twist angle on the natural frequencies of rotating cantilever plates are investigated. It is shown that the rotating plate's natural frequencies increase with the angular speed, that their increasing rates grow as the hub radius increases, and that the natural frequency decreases when the skew and twist angles increases. In addition, it can be noted that the frequencies of all results of are independent of skew angle and disc radius when the cantilever plate is stationary.

Table. 1 Values of fundamental non-dimensional frequency of vibration (β) for stationary and rotating cantilever plate.

	Present Work	(**Rao** 1999)	**Error %**
$(\Omega=0)$	3.403	3.437	1.0
(Ω=2000 rpm)	3.525	3.579	1.5
(Ω=4000 rpm)	3.902	3.974	1.8
(Ω=7000 rpm)	4.799	4.892	1.9

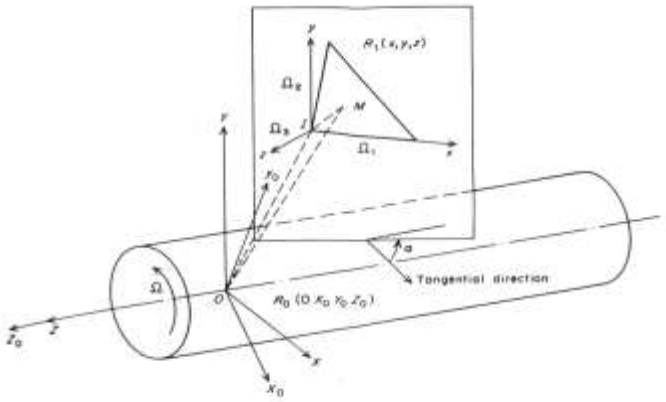

Fig.1 Cartesian co-ordinate system.

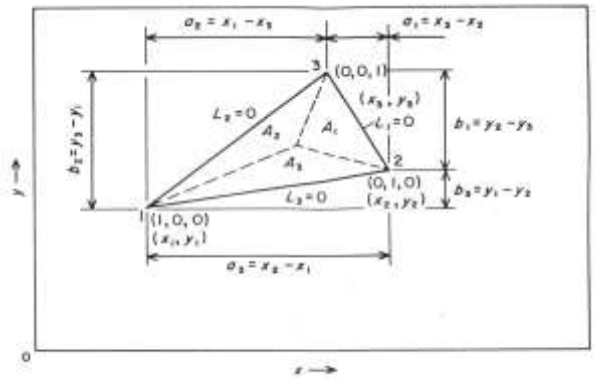

Fig. 2 Area co-ordinates.

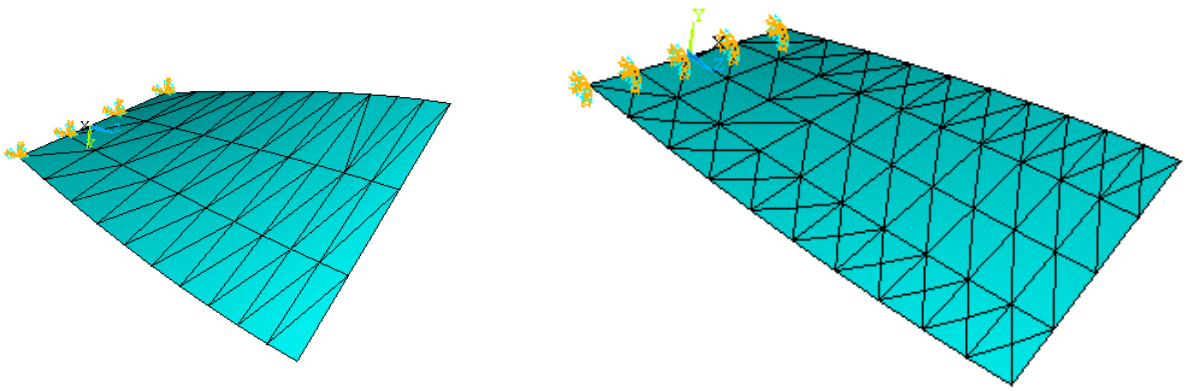

(a/b=1, No. of elements=60) (a/b=2, No. of elements=120)

Fig.3 Suitable mesh size for pre-twisted cantilever plate.

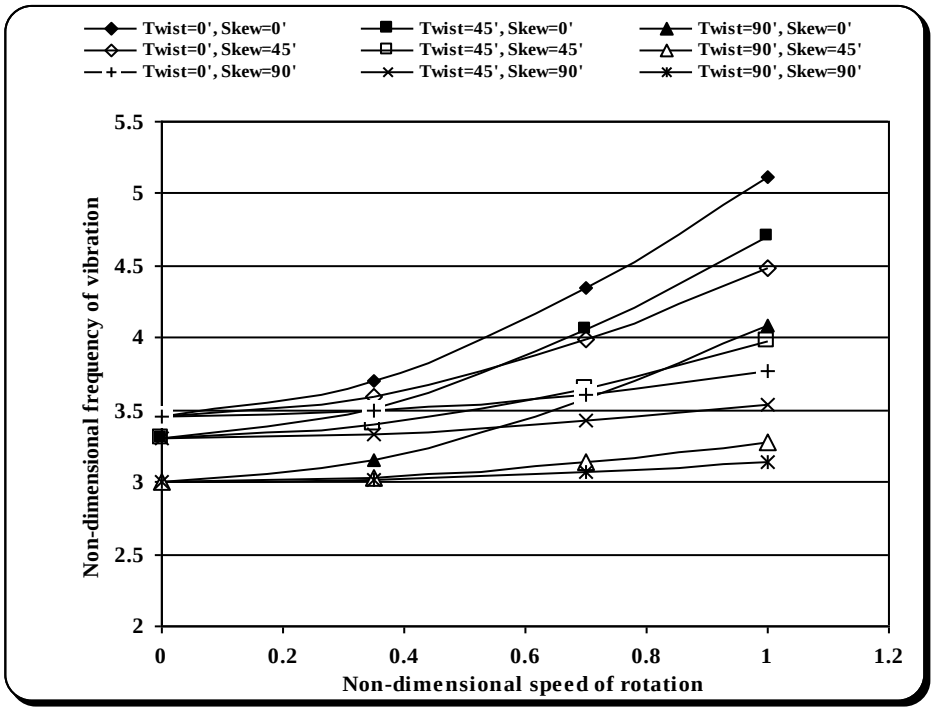

Fig. 4 Variation of non-dimensional frequency of vibration with non-dimensional speed of rotation $(a/b = 1,\ \overline{r = 0})$.

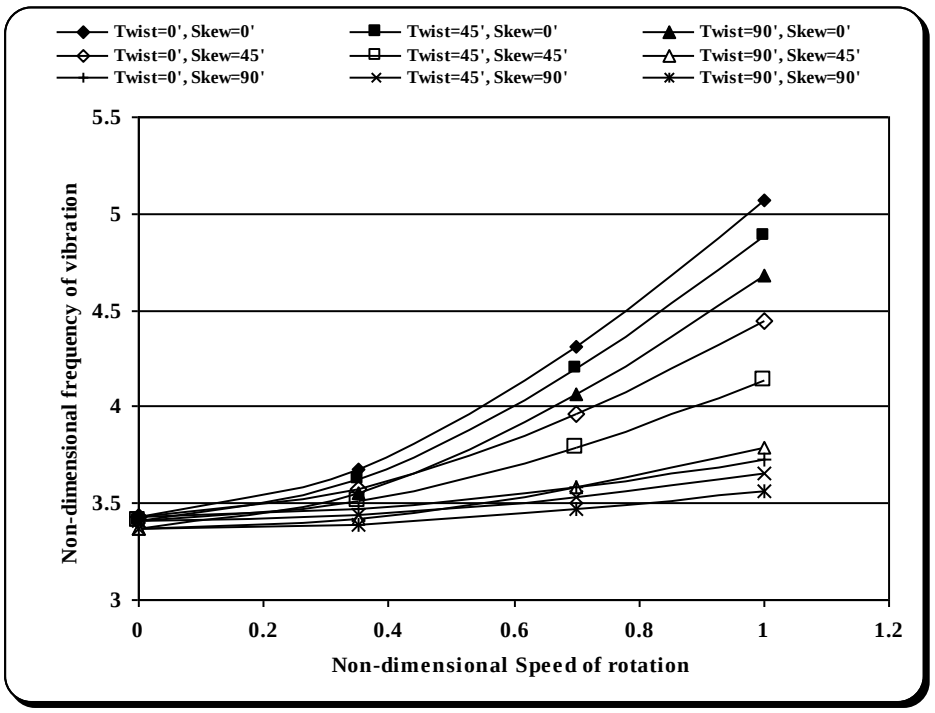

Fig. 5 Variation of non-dimensional frequency of vibration with non-dimensional speed of rotation $(a/b = 2,\ \overline{r = 0})$.

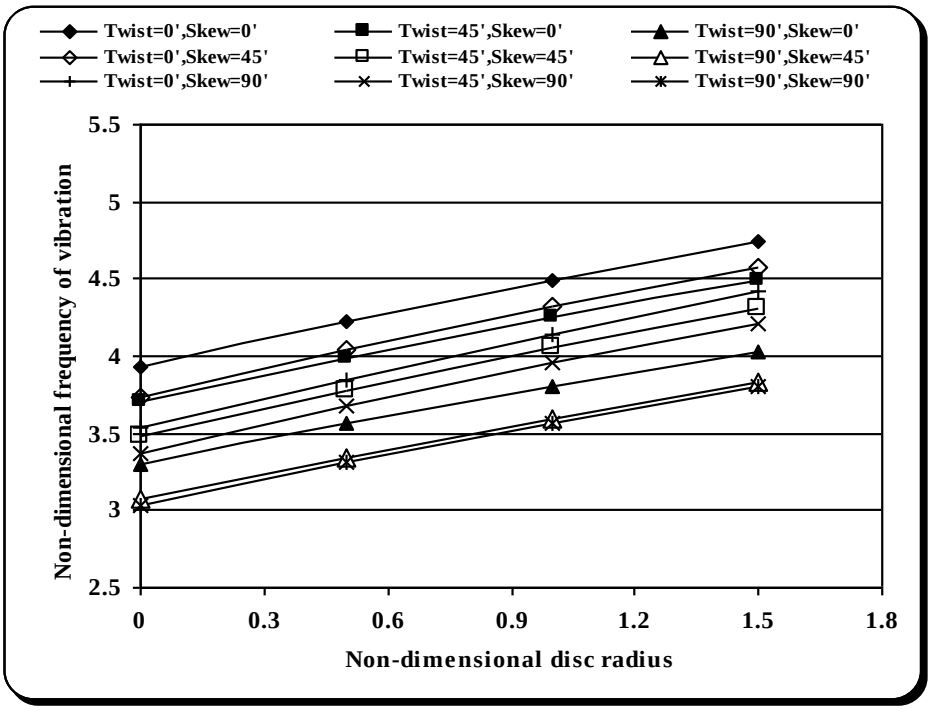

Fig. 6 Variation of non-dimensional frequency of vibration with non-dimensional disc radius $(a/b=1,\ \overline{\Omega}=0.5)$.

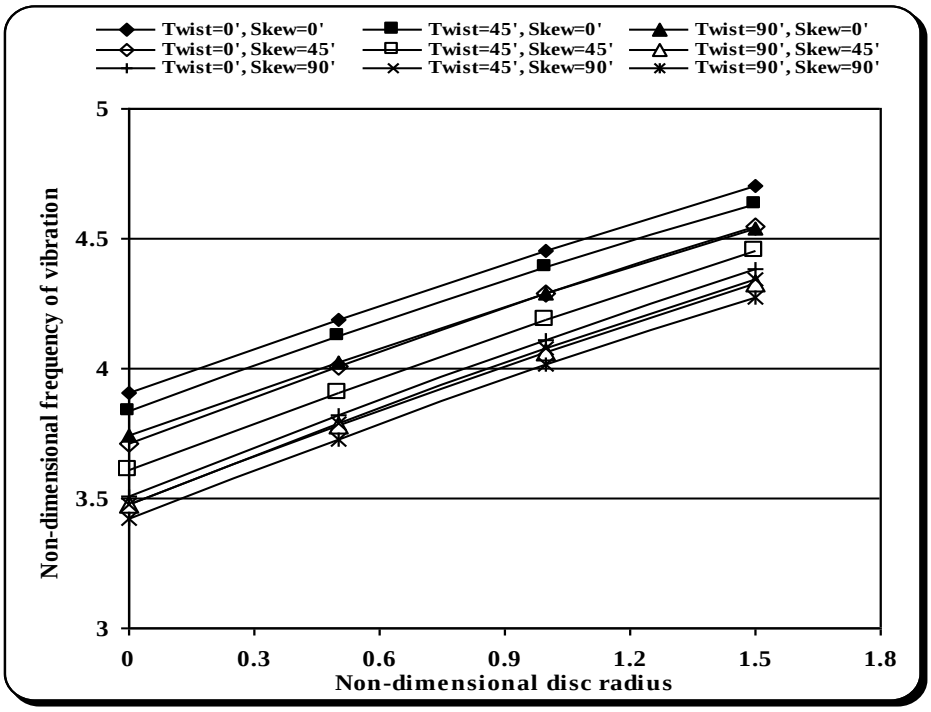

Fig. 7 Variation of non-dimensional frequency of vibration with non-dimensional disc radius $(a/b=2,\ \overline{\Omega}=0.5)$.

REFFERENCES:

-Bodley. C, A. Devers, A.Park and H. Frisch 1978 NASA ¹P-1219. A digital computer program for the dynamic interaction simulation of controls and structure.

-Bauer. H, 1980 Journal of Sound and Vibration 72, 177-189. Vibration of a rotating uniform beam.

-Christensen. E and S. Lee 1986 Computers & Structures 23, 819-829. Non-linear finite element modeling of the dynamic system of unrestrained flexible structures.

-Cowper. G. R 1973, International Journal for Numerical Methods in Engineering 7, p 405-408, "Gussian quadrature formulasn for triangle".

-Hale A. L and L. Meirovitch 1980 Journal of Sound and Vibration 69, 309-326. A general substructure synthesis method for the dynamic simulation of complex structures.

-Henry. R and M. Lalanne, 1974, "Vibration analysis of rotating compressor blade", J. of Engineering for Industry, Transactions of ASME 3, 1028-1035.

-Jennings. A and D. R. L. Orr 1977, International Journal for Numerical Methods in Engineering 3, p 13-24, "Application of The simultaneous Iteration Method to undamped Vibration Problems".

-Kuo. Y, T.wu and S. Lee 1994 Computers & Structures 22, 229-236. Bending vibration of a rotating non-uniform beam with tip mass and an elastically restrained root.

-Rao. J, 1987 Shock and Vibration 19, p 3-10. Turbomachine blade vibration.

-Rao. J. S, "Dynamic of plates", New Delhi: Narosa Publishing House, 1999, pp-532.

-Subrahmanyam. K, K.Kaza, G. Brown and C. LAWRENCE 1987 Journal of Aircraft 24, 342-352. Nonlinear vibration and stability of rotating pre-twisted preconed blades including Coriolis effects.

-Schilhansl. M, 1958 ASME Journal of Applied Mechanics 25, 28-30. Bending frequency of a rotating cantilever beam.

-Southwell. R and F. Gough 1921 British A.R.C. Reports and Memoranda, No. 766. The free transverse vibration of airscrew blades.

-Timoshenko. S and S. Woinowsky-Krieger 1959, "Theory of Plates and Sell", New York:McGraw-Hill Book Company.

-Wright. A, C.Smith, R.Thresher and J. Wang 1982 ASME Journal of Applied Mechanics 49, 197-202. Vibration modes of centrifugally stiffened beams.

-Yoo. H. H, R. R.Ryan and R. A. Scott 1995 Journal of Sound and Vibration 181, 261-278. Dynamics of flexible beams undergoing overall motion.

-Yoo. H. H and S. H. Shin 1998 Journal of Sound and Vibration 212, 807-828. Vibration analysis of rotating cantilever beams.

-Yokoyama. T, 1988 International Journal of Mechanical Sciences 30, 743-755. Free vibration characteristics of rotating Timoshenko beams.

-Zienkiewicz. O. C, "The finite element method in engineering science", New York: McGraw-Hill Book Company, Third edition, 1979.

NOMENCLATURES:

c	Coriolis matrix of the element
b	Width of the rotating plate m
a	Length of the rotating plate m
$\vec{d}$	Displacement of a typical point in the mid-surface
h	Thickness of a typical of an element
h_1, h_2, h_3	Thickness at the nodes 1, 2, 3
t	Thickness of the rotating plate
k_p, k_f, k_G	In-plane, bending and geometric stiffness matrices of an element
k_R	Additional stiffness of an element
m_E	Mass matrix of an element
q	Nodal displacements of the structure
u, v	In-plane components of the displacement $\vec{d}$
u_1, v_1	In-plane nodal displacements of node i
w	Components of the displacement $\vec{d}$ normal to the mid-surface
w_i	Bending nodal displacements of node i
x, y	Components of $\overrightarrow{IM}$ in R_i
x_1, t_i, z_i	Components of $\overrightarrow{OI}$ in R_i
A	Area of the triangular element
C	Coriolis matrix of the structure
D	Flexural rigidity of the plate, $= Et^3/12\left(1-\upsilon^2\right)$
E	Young's modulus
F	Nodal centrifugal force vector for the element
$\vec{F}\left(\Omega^2\right)$	Nodal centrifugal force vector for the structure
K_E, K_G	Elastic and geometric stiffness of the structure
K_R	Additional stiffness of the structure
L_1, L_2, L_3	Area co-ordinates of the triangle
M_E	Mass matrix of an structure
$N, N_1, N_2, N_{b1} - N_{b9}$	Shape function
P_1, P_2	Plane stress, bending strain energy
P_3	Supplementary strain energy due to the effect of bending displacement on mid-surface strains
$R(OXYZ)$	Global Cartesian co-ordinate system attached to the rotating disc
$R_0\left(OX_0Y_0Z_0\right)$	Absolute fixed Cartesian co-ordinate system
$R_1\left(IX_0Y_0Z_0\right)$	Local Cartesian co-ordinate system

T	Kinetic energy
U	Total potential energy
$\vec{V}$	Absolute velocity of M
β	Non-Dimensional frequency of vibration, $=\omega a^2\sqrt{\rho t/D}$
ε	Strains
$\varepsilon_p, \varepsilon_f$	Strain due to in-plane and bending displacements
ε_g	Effect of bending displacements on mid-surface strains
θ	Skew angle, setting angle
α	Twist angle`
υ	Poisson's ratio
ρ	Mass density Kg/m^3
σ	Stress N/m^2
σ_p	In-plane stress resultant
σ_f	Bending and twisting moment
$\sigma_x^0, \sigma_Y^0, \tau_{xy}^0$	Initial in-plane stress
ω	Frequency in rotation $(rad/\sec)$
ω_o	Frequency at rest $(rad/\sec)$
$\vec{\Omega}$	Speed of rotation $(rad/\sec)$
$\Omega_1, \Omega_2, \Omega_3$	Components of $\vec{\Omega}$ in R_1
$\overline{\Omega}$	Non-dimensional speed, $=\Omega/\omega_o$
$\bar{r}$	r/a

EFFECT OF ICE FORMATION ON AIRFOILS PERFORMANCE (PART-I)

Najdet N. Abdulla and Haitham Q. Hasoun

ABSTRACT

A numerical investigation was conducted to study the effect of simulated ice accreted on airfoil aerodynamics performance. The simulated ice shapes were tested on NACA 0012 airfoil wing at different Mach numbers. The study includes the one of the famous types of ice accreted on the airfoils called the rime ice.

The calculation of ice droplet trajectories was performed by solving the trajectories governing equations of the droplet using FVM. A numerical model based on staggered FVM is built up to solve the governing equations of a body fitted grid, trajectories equation, continuity equation and momentum equation using FORTRAN 97. The turbulence model of (k-ε) has been adopted in the programming to evaluate the turbulence effect. The program is valid for any type of 4 or 5 digits airfoil. The program is available to evaluate the rime ice accumulation. The pressure, lift, drag and pitching moment coefficients are computed and compared with that of clean case results. The program was run over different Mach numbers, to compare the results obtained at these Mach Numbers. The investigation of the work was tested on NACA 0012 in a range of angle of attack 0º to 6º, where stall starts at this angle of attack as demonstrated by the results.

The results show that the severity of ice formation could be more dangerous with increasing the angle of attack or the Mach number.

الخلاصة

أنجزت في هذا البحث الحسابات العددية لدراسة تأثير الثلج المقلد على أداء ديناميكيا الهواء المنساب على المطيار. أشكال الثلج المقلدة أختبرت على مطيار من نوع (NACA 0012) لأعداد ماخ مختلفة, وتضمنت الدراسة النوع المعروف من الثلج المتولد على سطح المطيار و هو الثلج الصقيع. لقد تم حساب مسار قطرة الثلج باعتماد المعادلة الحاكمة لمسارات قطرات الثلج وباستخدام طريقة الحجوم المحددة, و أعتمد الموديل الرياضي في ذلك طريقة (Staggered) لنظام الإحداثيات الغير المتعامدة في الشبكة المتولدة, ولمعادلة مسار القطرة, و معادلة الاستمرارية و معادلة الزخم باستخدام لغة البرمجة (فورتران 97) . تم استخدام الأنموذج الرياضي الأضطرابي (k-ε) لتحليل جريان المائع حول المطيار. ويمكن أستخدام البرنامج لأي نوع من أنواع (NACA airfoil) ذات ال 4 أو ال 5 أرقام وعلى بعدين فقط. البرنامج قادر على حساب تجمع تلك القطرات الثلجية المكونة للصقيع فوق المطيار والترويج. معاملات الضغط, قوة الرفع, قوة الكبح و عزم الترويج تم حسابها وقورنت مع حالة وجود الثلج على المطيار. أجريت الحسابات على أعداد ماخ ولزوايا مختلفة, وتم استخلاص النتائج وأخذت المقارنات للزوايا من (0º الى 6º) حيث يبدأ الانهواء بعد الزاوية (6º) كما بينت النتائج ذلك. أظهرت النتائج أن أشكال الثلج المتولد على المطيار تؤثر تأثيرا كبيرا على الأداء الديناميكي الهوائي وذلك بسبب تغير شكل الانسياب للمطيار مما يؤدي إلى زيادة معامل الكبح و نقصان معامل الرفع. كذلك أفادت النتائج بأن شدة الخطورة تكون أكثر حدة بزيادة عدد الماخ أو زيادة زاوية الهجوم.

INTRODUCTION

Icing on an airfoil or craft is defined as that condition where supercooled water droplets freeze on airframes or airfoil and form amount of ice which disturbs the airflow. In recent years, the number of icing related accidents has stimulated a renewed interest in the effect of icing on aerodynamic performance of aircraft (**Anderson, et al, 2001**). The formation of ice on aircraft components such as wings, control surfaces and engine intakes, occurs when the aircraft flies at a level where the temperature is at, or below freezing point and hits supercooled water droplets (**Anderson, et al, 2003**) and (**Anderson and Ching, 2003**).

The presence of ice accretion on unprotected aircraft components can lead to a number of aerodynamic penalties and consequently causes a serious safety problem. The most severe penalties encountered deal with decreased lift, increased drag, decreased stall angle, changes in the pressure distribution, vibration, early boundary layer separation, and reduced controllability. In fact, test data on ice effects indicate that the presence of ice on unprotected wing may increase drag by as much as 40% and reduce lift by 30% (**Bergrun, 1947**). To overcome these penalties, various practical methods have been used to remove or prevent accumulation of ice on aircraft surfaces by applying de-icing/anti-icing procedures. Modern types of airfoils have been developed, but, still needs specific ice protection systems to maintain their aerodynamic efficiency and safety margin.

Icing on aircraft occurs when the aircraft flies at a level where the temperature is at, or slightly below the freezing point and the atmosphere contains supercooled water droplets. When these droplets are hit by the aircraft they begin to freeze immediately. As the water droplets freeze, however, heat is released so that their temperature rises until 0ºC is reached. As this temperature is reached, freezing stops while the remaining liquid fraction of the droplets starts to run back along the surface of the aircraft or along existing ice and freeze downstream. The freezing fraction depends mainly on the temperature. At colder temperature a large part of a droplet freezes by impact while at higher temperature only a small part freezes while the remaining part freezes slowly (**Bragg, et al, 1982**).

The more dangerous types of ice are encountered in dense clouds, composed of heavy accumulations of large water droplets.

Icing is one of the most serious hazards for aircraft. Icing comes from the freezing of cloud droplets, or supercooled droplets which remain in liquid state even at temperatures far below freezing, when they are stuck by the aircraft during the flight. Cloud droplets may freeze instantaneously and form rime ice on unprotected surfaces or run downstream and freeze later forming glaze ice structure. Icing is most severe when temperature is near 0°C but may be encountered at temperature as low as -40 °C.

Icing is described as trace, light, moderate or severe which depends on the type of clouds, the type of aircraft, and the type of icing protection systems. The distribution of potential aircraft icing zones is mainly a function of cloud structure and temperature, which in turn vary with altitude, location and season. There are two types of clouds that may present icing conditions;

1) Stratiform clouds (continuous icing conditions) with horizontal extents up to 200 miles, altitudes 5,000 ft, liquid water content ranging from 0.1 g/m³ to 0.9 g/m³ and droplets diameter varying from 5 to 50 microns.

2) Cumuliform clouds (intermittent icing conditions) with vertical extents at altitude of 10,000 ft, horizontal extent of about 6 miles, liquid water content ranging from 0.1 g/m³ to 1.7 g/m³ and sometimes as high as 3.9 g/m³ or more, and droplets diameter similar to the case of stratiform clouds.

Icing can be serious when the cloud has high liquid water content. Some types of precipitation cause serious icing conditions while others may indicate the presence of serious icing in the vicinity. Freezing rain ahead of warm fronts presents a serious icing for aircraft flying near the top of the cold air mass beneath a deep layer of warm air. This is because rain drops are much larger than ordinary clouds droplets and may lead to high liquid water content. Icing may also comes from freezing drizzle just near the cloud base where the accretion on aircraft. Presently, more droplets are large.

Rime Ice Growth and Its Physics and Mechanism Process

The ice growth starts with the process of condensation. Water vapor condenses around particles and forms water droplet. The particles may grow up to 50μm or more. For larger droplets, such as rain drops which may exceed 1000μm, collision-coalescence and ice crystal theory must be included to explain growth process.

Rime ice is a dry, milky and opaque ice deposit which usually occurs at low airspeed, low temperature and low liquid water content. It is characterized by the instantaneous freezing of the incoming supercooled water droplets as soon as they hit the surface of the body trapping the air inside. As a consequence, the shape of the surface is altered generating performance penalties due to the loss in the aerodynamic characteristics and to the added weight which introduces an unbalance of the aircraft components during the flight, as shown in Fig. (1).

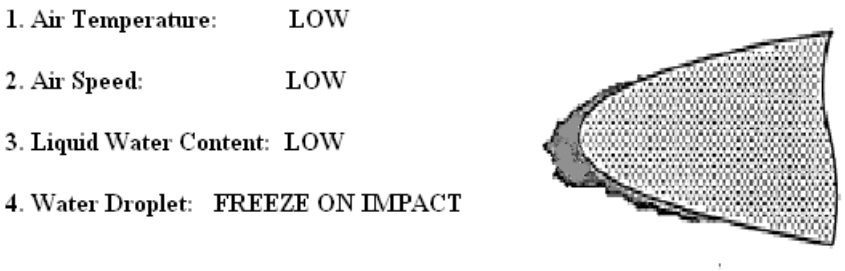

Fig. (1) Typical rime ice conditions on an airfoil [*Bergrun, N.R, 1995*].

The geometry of rime ice growth is shown below in Fig. (2);

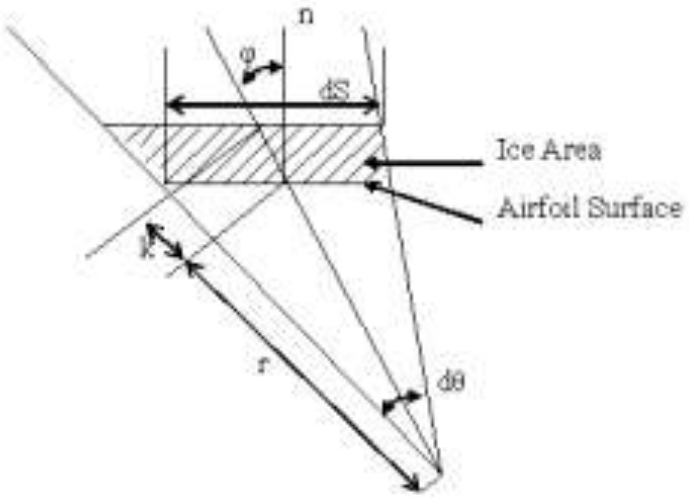

Fig. (2) Geometry of ice growth calculation [*Bragg M.B. and Kerho Michael, 1994*].

Important Factors and Parameters Affecting the Aircraft Icing

The amount and rate of icing depend on a number of meteorological and aerodynamic factors. Of primary importance are:

1- The amount of liquid water content of droplets.
2- The size of the liquid water droplets.
3- The temperature of aircraft surfaces.
4- The collection efficiency.
5- Icing intensity.
6- Air speed.

MATHEMATICAL FORMULATION

The main objective of ice simulation is the calculation of the impingement of the particles on the airfoil which determines the droplet impingement regions as well as the mass of liquid on the body surface.

The mathematical formulas are a process with a time-stepping procedure where successive thin ice layers are formed on the surface and followed by flow field and droplet impingement recalculations. The calculation of the water flux impinging on each grid forming the wing surface can be performed, then the ice accretion is calculated and the geometry is modified defining the ice shape for the first time step. The procedure is then performed for another time step to calculate a new ice layer.

Trajectory Calculations

To calculate the droplet trajectories, we assume that the volume of the droplet remains constant throughout the entire process. Although the droplet may or may not keep its spherical shape the droplet density ρ_d remains constant throughout the whole path, the initial droplet velocity is equal to

the free stream velocity U_∞ the droplets are much smaller than the body considered so that they do not affect the velocity field (**Bragg, 1988**).

The equation of motion of the droplet is given by (**Bragg and Kerho, 1994**);

$$a = \frac{1}{K}\left(\frac{C_D \,\mathrm{Re}}{24}\right)(u - v) \tag{1}$$

And K is the inertia parameter and define as;

$$K = \frac{\rho_d D_{eq}^2 U_\infty}{18 C\mu} \tag{2}$$

For Reynolds number below (1000) the following formula for Langmuir is used (**Langmuir and Blodgett, 1946**);

$$\frac{C_D \,\mathrm{Re}}{24} = 1 + 0.197\,\mathrm{Re}^{0.63} + 2.6 * 10^{-4}\,\mathrm{Re}^{1.38} \tag{3}$$

For Reynolds number higher than (1000) and below (3500) the formula (**Paraschivoiu and Brahimi, 1994);**

$$\frac{C_D \,\mathrm{Re}}{24} = 1.699 * 10^{-5}(\mathrm{Re}) \tag{4}$$

For Reynolds number higher than (3500) Hansoman formula's is used (**Hansoman, 1985**);

$$\frac{C_D \,\mathrm{Re}}{24} = 1.669 * 10^{-5}(\mathrm{Re})^{1.92} \tag{5}$$

Modified Inertia Parameter

The modified inertia parameter for (**Anderson and Ching, 2003**) formula is used in eq. (1) which is described as follows;

$$K_o = \frac{1}{8} + \frac{\lambda}{\lambda_{stokes}}\left(K - \frac{1}{8}\right) \tag{6}$$

Where

$$\frac{\lambda}{\lambda_{stokes}} = \left(0.8388 + 0.001483\,\mathrm{Re}_d + 0.1847\sqrt{\mathrm{Re}_d}\right)^{-1} \tag{7}$$

And

$$\mathrm{Re}_d = \frac{u(MVD)\rho_w}{\mu} \tag{8}$$

Turbulence Model (k-ε Model)

There are many two-equation models used in numerical today. Among them is the (k-ε) model. The reason of using the (k-ε) model is that in two-dimensional thin shear layers the changes in the flow direction are always so slow that the turbulence can adjust itself to local conditions, and if the convection and diffusion of turbulence properties can be neglected it is possible to express the influence of turbulence on the mean flow in terms of a simple model such the mixing length model, while if the convection and diffusion are not negligible (as in the case of flow around an airfoil) a compact algebraic prescription for the mixing length is no longer feasible, and the mixing length model lacks this kind of generality, so the way forward is to consider a statements regarding the dynamics of turbulence (**Versteeg and Malalasekera, 1995**).

In general form the transport equations for (k) and (ε) can be expressed in Cartesian coordinates as below (**Chung, 2002**):

$$\left(\rho u_j k\right)_{,j} = \left[\mu_k \left(k\right)_{,j}\right]_{,j} + \mu_t\left(\left(u_i\right)_{,j} + \left(u_j\right)_{,i}\right)\left(u\right)_{,j} + \frac{C_\mu \rho^2 k^2}{\mu_t} \tag{9}$$

$$\left(\rho u_j \varepsilon\right)_{,j} = \left[\mu_\varepsilon \left(\varepsilon\right)_{,j}\right]_{,j} + \frac{C_{\varepsilon 1}\varepsilon}{k}\mu_t\left(\left(u_i\right)_{,j} + \left(u_j\right)_{,i}\right)\left(u\right)_{,j} + \frac{C_{\varepsilon 2}\rho\varepsilon^2}{k} \tag{10}$$

Boundary Conditions and Properties

It is important to clear out the flying conditions and its properties, and these included the Mach number, pressure, ice density, ice intensity, air density, air viscosity, air temperature, LWC, droplet diameter, droplet effectiveness distance, and all these conditions are shown in table 3.1. Also the freezing fraction is taken 1.0, and the accretion time is taken in this work equal to 180 s. Table 1 below shows the properties and conditions of air and droplet.

Table 3.1 properties and conditions of air and droplet.

No.	Variable	Magnitude or quantity	Units
1	Mach number, M	0.3, 0.4 and 0.5	Nondimensional
2	Air pressure, P_a	101	kN/m²
3	Airfoil Chord	1	
4	Ice density, ρ_{ice}	1.2	g/cm³
5	Ice intensity	severe	non
6	Air density, ρ_a	1.2	kg/m³
7	Dynamic viscosity of Air	$17.1*10^{-6}$	N.s/m²
8	Altitude *h*	9000	m
9	Air temperature, T_a	-12.6	C°
10	LWC	1.0	g/m³
11	Droplet diameter	50	µm
12	Droplet effectiveness distance	4.5 of Chord length	Nondimensional

FLOW FIELD CALCULATION

The flow field calculation is needed to determine the velocity of air so that the droplet trajectory calculation can be solved. Where the equation of the airfoil that the flow field must flow over is;

$$y = \left(\frac{t}{0.2}\right) * \left(0.2969 * x^{0.5} - 0.126 * x - 0.3537 * x^2 + 0.2843 * x^3 - 0.1015 * x^4\right) \quad (11)$$

Where the basic equations governing incompressible and steady state fluid flow in Cartesian coordinates are the continuity and momentum equations stated as:

$$\left(u_i\right)_{,j} = 0 \quad (12)$$

$$\left(\rho u_j u_i\right)_{,j} = -P_{,i} + \left(\tau_{ij}\right)_{,j} \quad (13)$$

τ_{ij} is referring to the viscous stress tensor, and its constitutive relation in Newtonian fluid:

$$\tau_{ij} = \mu\left(\left(u_i\right)_{,j} + \left(u_j\right)_{,i}\right) - \frac{2}{3}\mu\frac{\partial u}{\partial x}.\delta_{ij} \quad (14)$$

The lift and drag equations governing the force over the airfoil are stated as:

$$C_L = \frac{2L}{\rho * V^2 * A} \tag{15}$$

$$C_D = \frac{2D}{\rho * V^2 * A} \tag{16}$$

Where the L and D is the summation of the components of the forces in the x- and y-direction:

$$L = F_y \cos(alpha) - F_x \sin(alpha) \tag{17}$$

$$D = F_x \cos(alpha) + F_y \sin(alpha) \tag{18}$$

GRID GENERATION

The O-grid type is selected to produce the grid generation using Poisson equations**.** The Elliptic grid generator is the most extensively developed method (**Hoffmann, 1989**), where it is commonly used for 2-D problems. A system of elliptic equations in the form of Poisson's equation is used, which is solved for the coordinates of the points in the physical domain:

$$\frac{\partial^2 \xi}{\partial x^2} + \frac{\partial^2 \xi}{\partial y^2} = P(\xi, \eta) \tag{15}$$

$$\frac{\partial^2 \eta}{\partial x^2} + \frac{\partial^2 \eta}{\partial y^2} = Q(\xi, \eta) \tag{16}$$

Fig. (3) shows the O-type grid generation using Poisson equation (PDE) with mesh of (71X37) at 0° angle of attack. Fig. (4) shows the O-type grid generation with mesh (151X71) at 6° angle of attack.

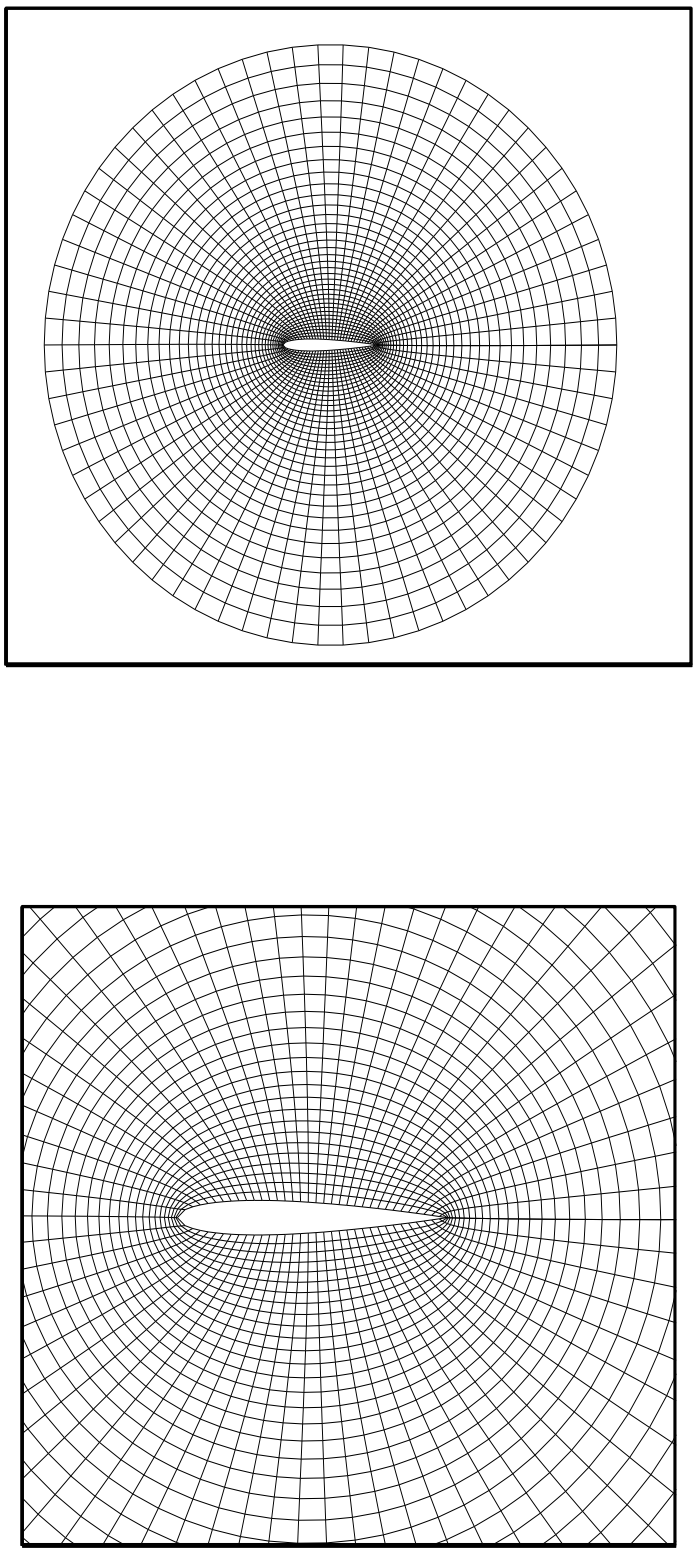

Fig. (3) PDE grid generation (O-type) of airfoil of mesh (71x37) with close view.

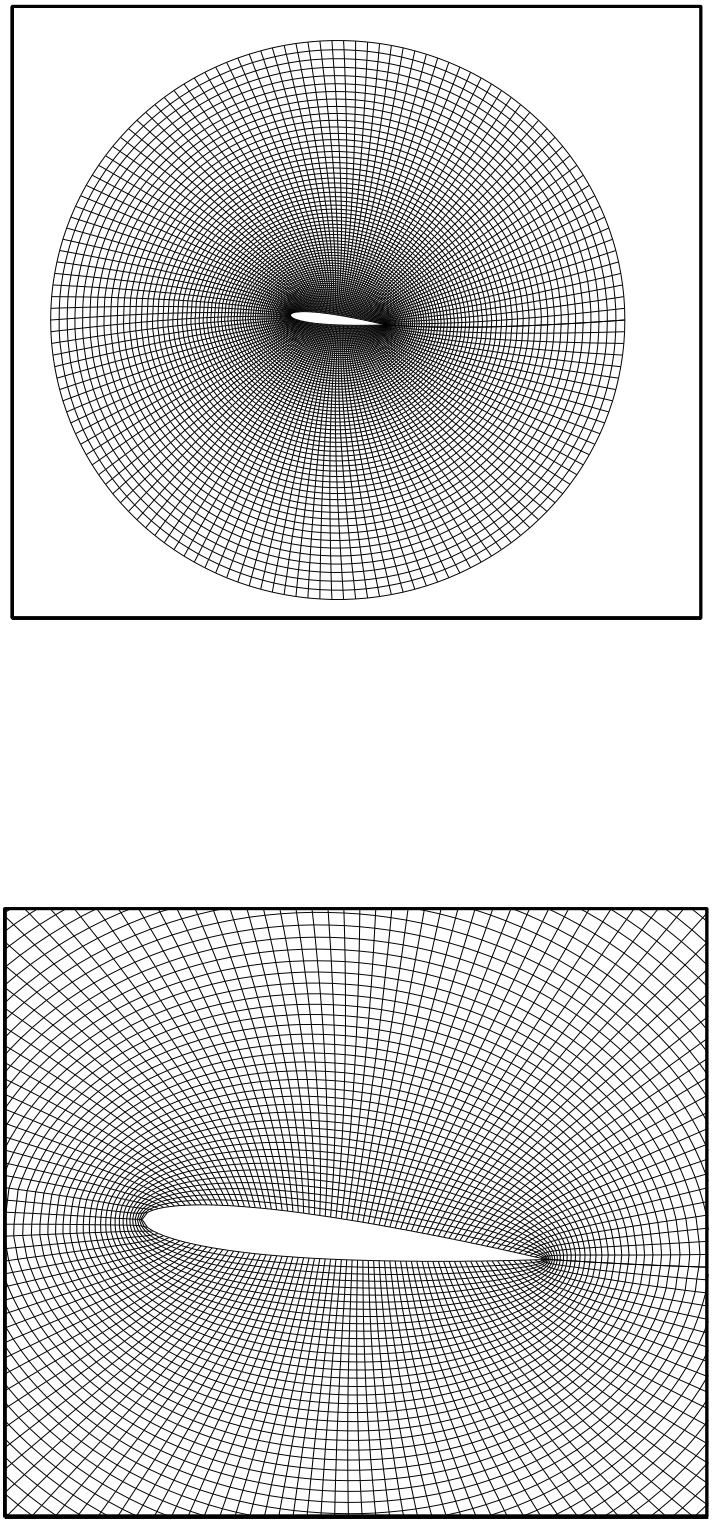

Fig. (4) PDE grid generation of airfoil at 6° angle of attack and mesh (151x71) with close view.

RESULTS

In clean case the results show that the increase in the angle of attack and Mach number cause a decrease in (C_P) on the upper surface of the airfoil, and increase the performance of the airfoil as shown in Figs. (5 through 7) at different Mach numbers (0.3, 0.4 and 0.5, respectively).

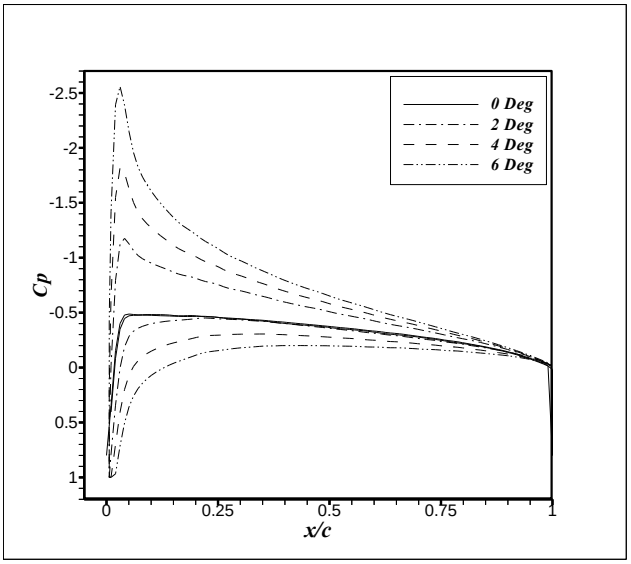

Fig. (5) Pressure coefficient distribution at M=0.3 for various angle of attack in clean case.

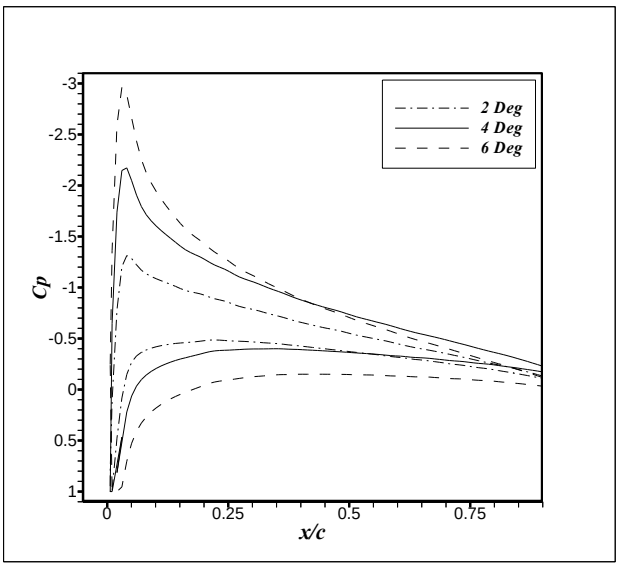

Fig. (6) Pressure coefficient distribution at M=0.4 for various angle of attack in clean case.

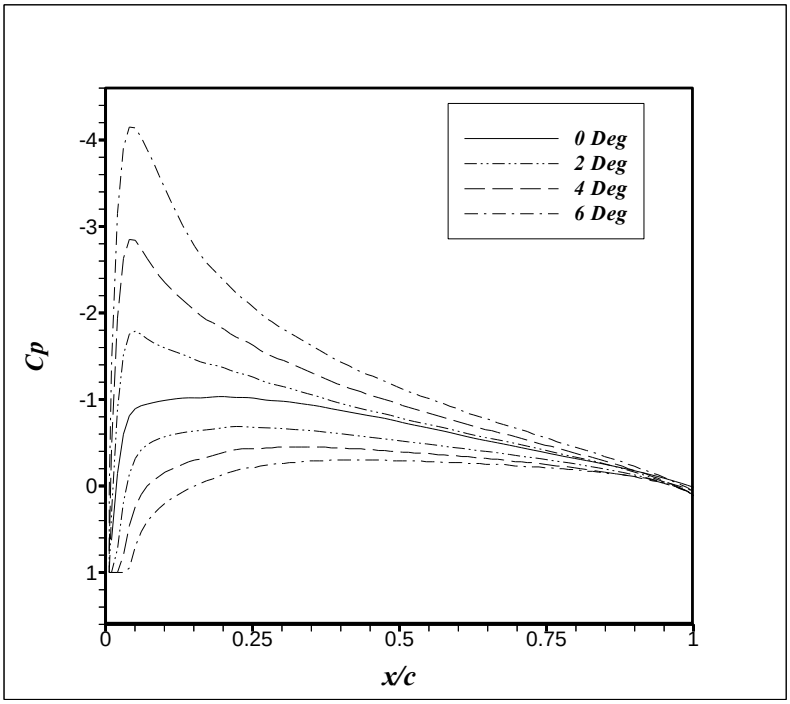

Fig. (7) Pressure coefficient distribution at M=0.5 for various angle of attack in clean case.

Figs. (8 through 11) show a comparison of (C_P) between the clean and rime ice case at different angle of attack and at constant M=0.3. The Figs. indicate that the increase in angle of attack would increase the (+ve) pressure coefficient in case of rime ice and hence decrease the airfoil performance. The ice formation at the nose of the airfoil caused a disturbance for the air flow over the airfoil and thereby cause uncouthly flow over the airfoil.

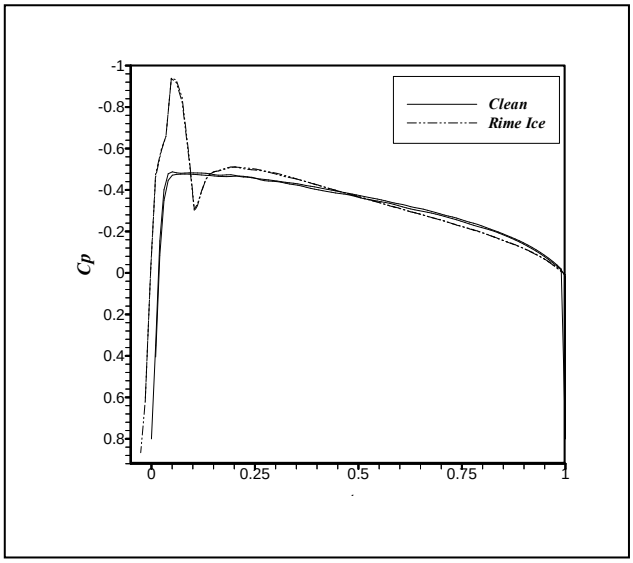

Fig. (8) Pressure coefficient distribution at (α=0°) and M=0.3 for clean and rime ice.

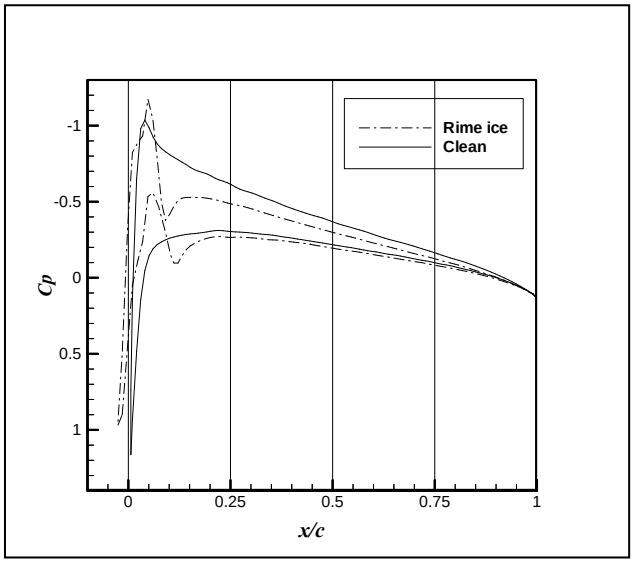

Fig. (9) Pressure coefficient distribution at (α=2°) and M=0.3 for clean and rime ice.

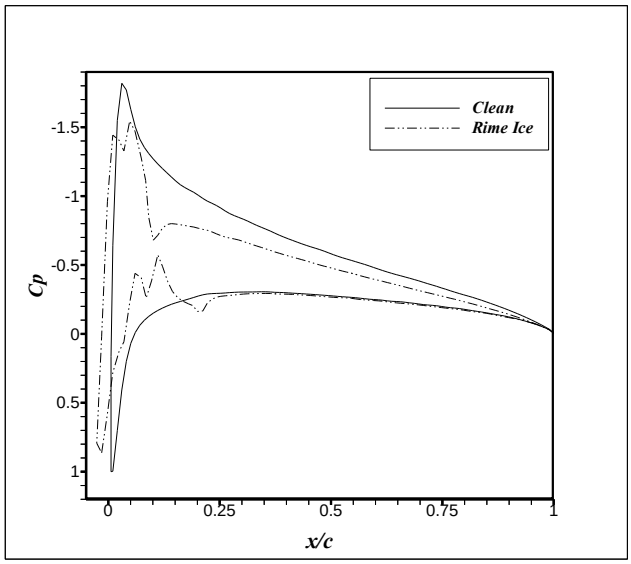

Fig. (10) Pressure coefficient distribution at (α=4°) and M=0.3 for clean and rime ice.

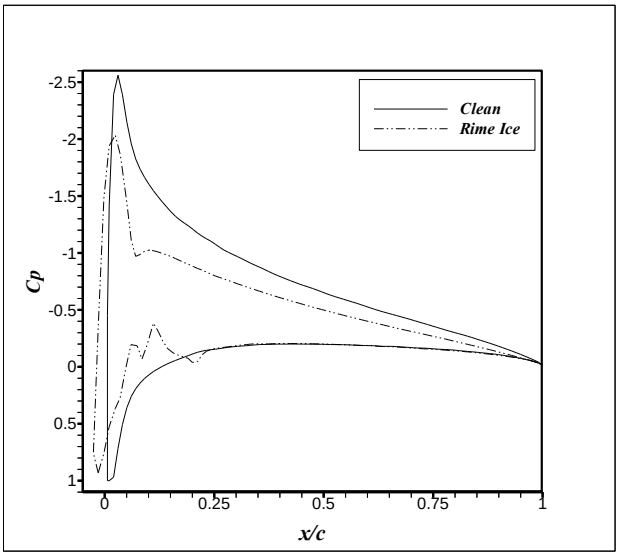

Fig. (11) Pressure coefficient distribution at (α=6°) and M=0.3 for clean and rime ice.

Figs. (12 through 15) show a comparison of (C_P) between the clean and rime ice case at different angle of attack and at constant M=0.4. Although the Figs. show that the increase in Mach number from 0..3 to 0.4 would decrease the pressure coefficient in case of rime ice, but in compassion to that in case of clean case the severity would be more dangerous than that at M=0.3. Where the difference between the clean case and that of rime ice case at M=0.3 is smaller that in case of M=0.4. Since the increase in the Mach number must lead to decrease pressure suction side, the Figs. above show that the increase in the angle of attack will not overcome the dangerous of the accreted ice on the airfoil. The performance will get worse due to the ice accretion, where the pitching moment will cause the airfoil to turn back with increasing the angle of attack which causes decrease in lift force so early.

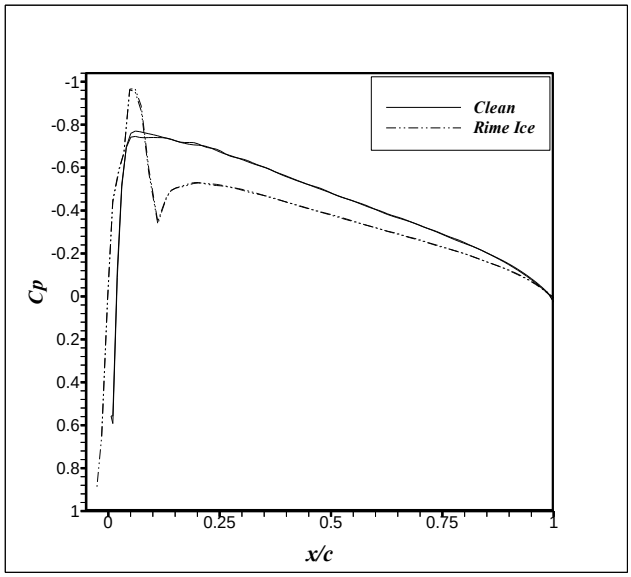

Fig. (12) Pressure coefficient distribution at (α=0°) and M=0.4 for clean and rime ice.

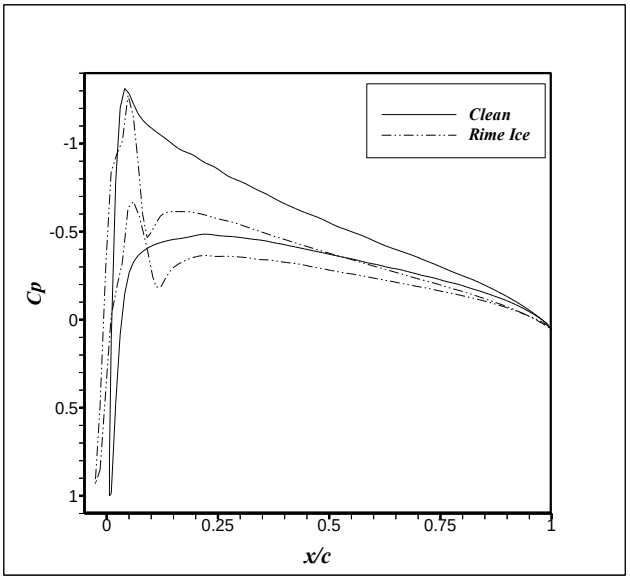

Fig. (13) Pressure coefficient distribution at (α=2°) and M=0.4 for clean and rime ice.

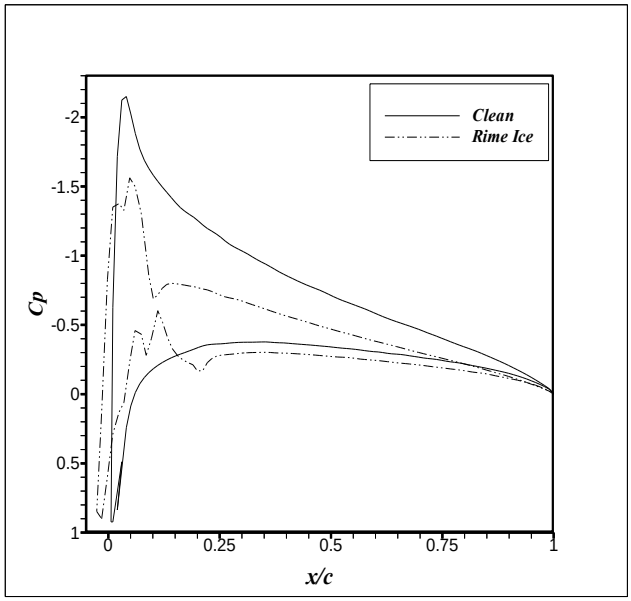

Fig. (14) Pressure coefficient distribution at (α=4°) and M=0.4 for clean and rime ice.

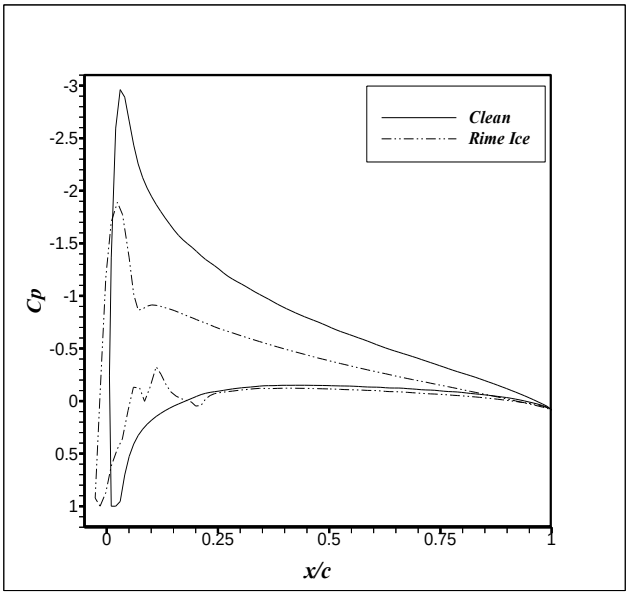

Fig. (15) Pressure coefficient distribution at (α=6°) and M=0.4 for clean and rime ice.

It is well known that any (nongeometrical) change in the airfoil shape would cause a decrease in the airfoil performance, and this can be figure out in lift and drag coefficients. Fig.(5.16) shows the decrease in lift coefficient if the rime ice accreted on the airfoil at M=0.3 when compared with the clean case. The Fig. shows that the difference in lift coefficient increases with increasing the angle of attack, while the value of C_L in the clean case increases to reach its maximum value ***0.68*** (at ***α=6°***). This value decreased from (***0.68***) to **(0.47)** at the same angle of attack when ice accreted. Also, C_L decrease from (***0.84***) to (***0.44***) for M=0.4 at the same angle of attack due to the existing of ice, where the ice disturb the smoothness flow of air over the airfoil, and from ***1.3*** to ***0.46*** for M=0.5 as shown in Figs.(5.17 and 5.18, respectively). Fig. (19) shows the lift coefficient deference is increased with increased the Mach number, which means that the increase in Mach number will not overcome the severity of the ice accumulation and will effect inversely.

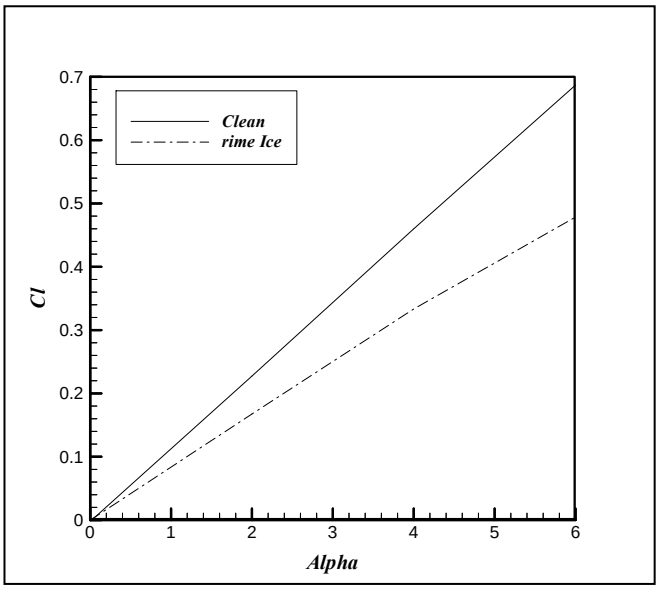

Fig. (16) Lift coefficient comparison between clean and rime ice at M=0.3.

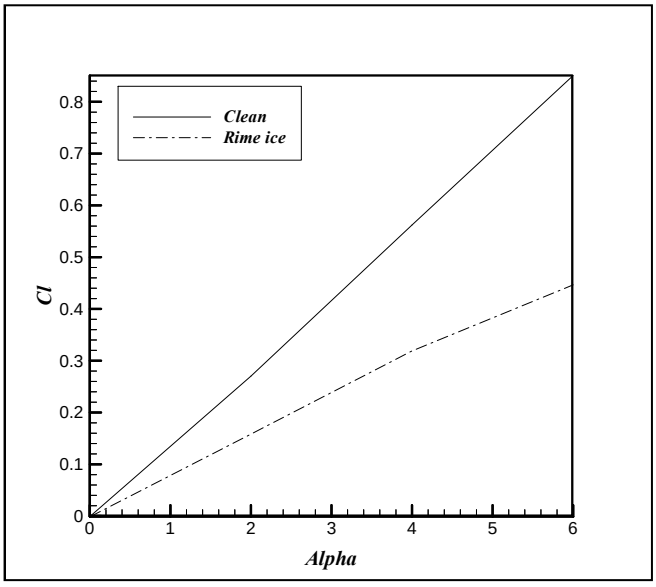

Fig. (17) Lift coefficient comparison between clean and rime ice at M=0.4.

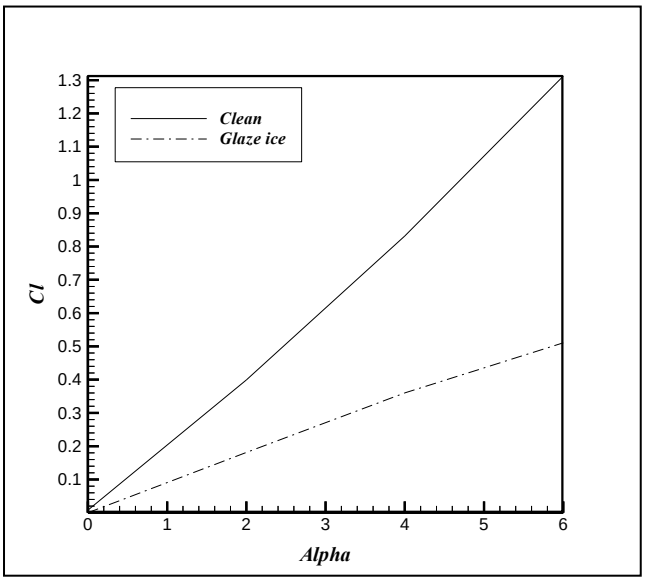

Fig. (18) Lift coefficient comparison between clean and rime ice at M=0.5.

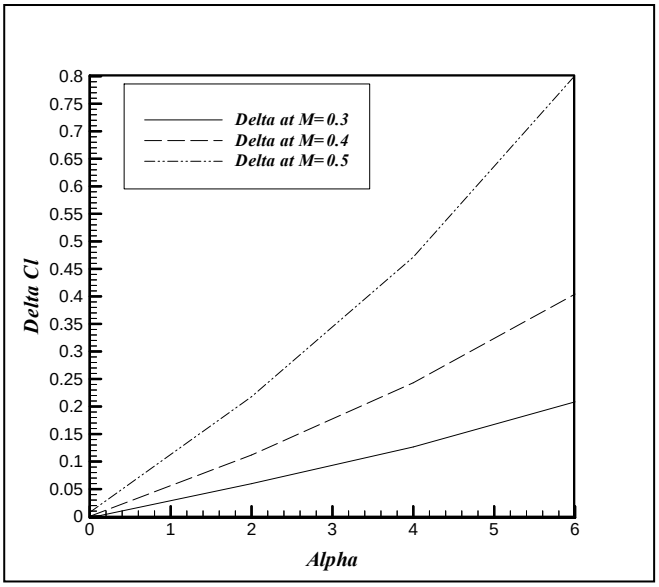

Fig. (19) Lift coefficient difference between clean and rime ice at deferent Mach numbers.

Fig. (20) shows the increase in drag coefficient due to the ice accretion compared with that of clean case, where the accreted ice cause more disturb for the air over the airfoil and thereby increase the drag force. Fig.(21) shows the increases in drag coefficient as Mach number increases along the angle of attack for the rime ice case, where the increase of velocity over the airfoil with ice accreted will lead to increase the disturbance of the flow, hence increase the drag coefficient. Fig.(22) shows the variation of (C_L) against (C_d) for rime case at different Mach number. The Fig. shows that the increase in Mach number would increase in the drag coefficient against the lift coefficient and this performance get wars as much as the Mach number increases.

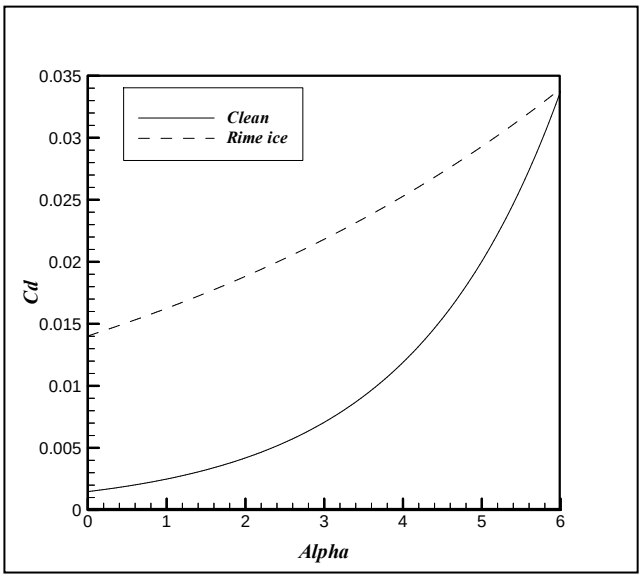

Fig. (20) Drag coefficient comparison between clean and rime ice at M=0.3.

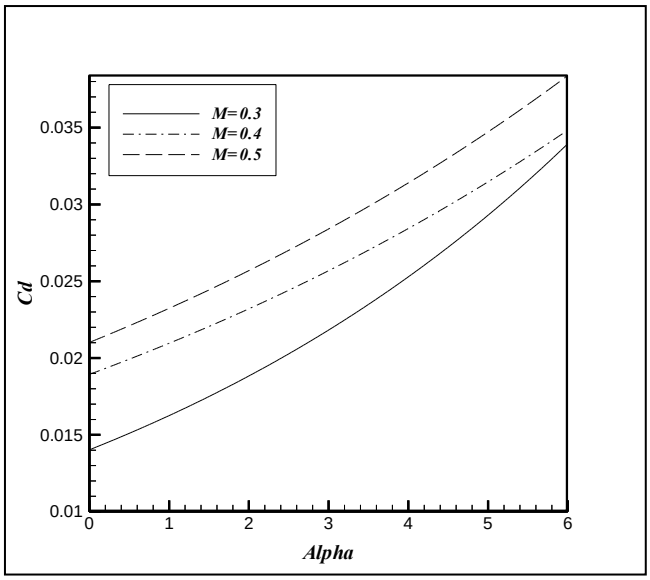

Fig. (21) Drag coefficient for rime ice at different Mach numbers.

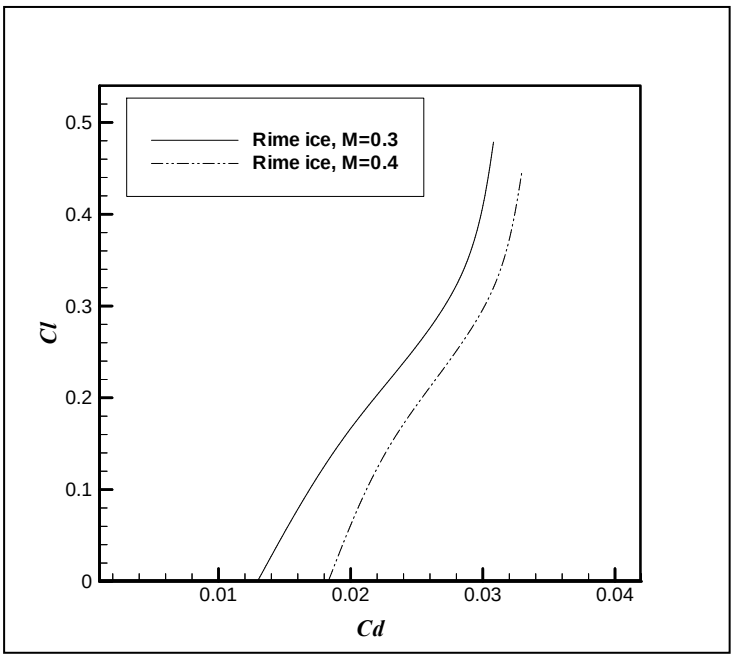

Fig. (22) Variation of C_L versus C_d for rime ice at different Mach numbers.

A comparison of a pitching moment coefficient versus angle of attack for the clean and rime ice case at Mach number (0.3) is shown in Fig.(23), it shows that the (C_m) in the iced case is higher than that in clean one, this gesticulate that the increase of instability when the shape of the airfoil is changed due to the ice accretion. This coefficient varies if the Mach number increases or decreases, especially in the ice case, while in the clean case the general behavior is the same. Fig.(24) shows the comparison at Mach number (0.4). More reliable comparison is made between the pitching moment coefficient and the lift force coefficient. This comparison shows the lift behavior versus the pitching moment as shown in Fig.(25) at M=0.3. It can be seen that the lift coefficient of the clean case is higher than that of the rime ice case and at the same time the pitching moment is higher for the ice case. Since the pitching moment is so high compare with that lifting force, the airfoil will be exposed to fall early in ice case. Fig. (26) shows the same comparison at M=0.4.

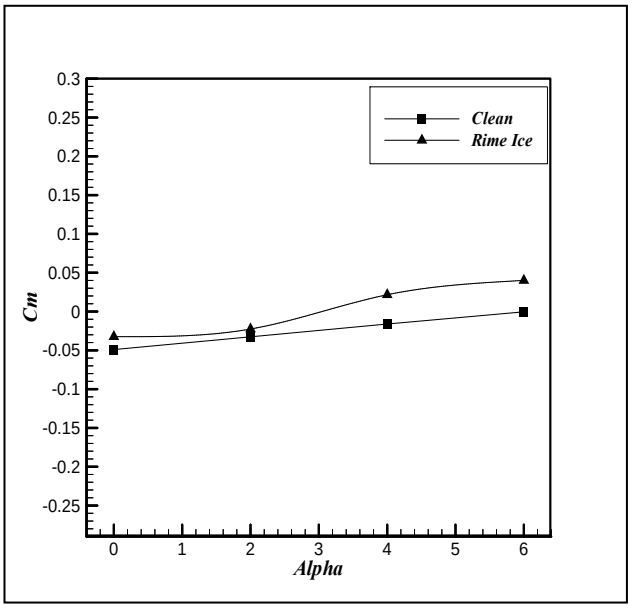

Fig. (23) Comparison pitching moment coefficient at M=0.3.

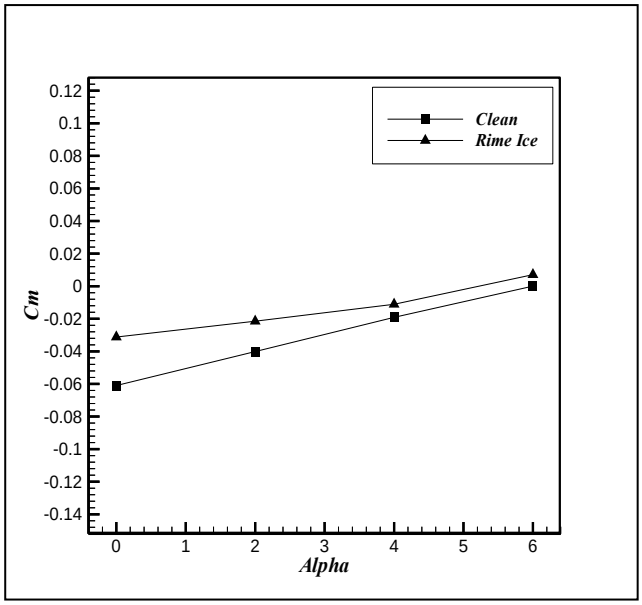

Fig. (24) Comparison pitching moment coefficient at M=0.4.

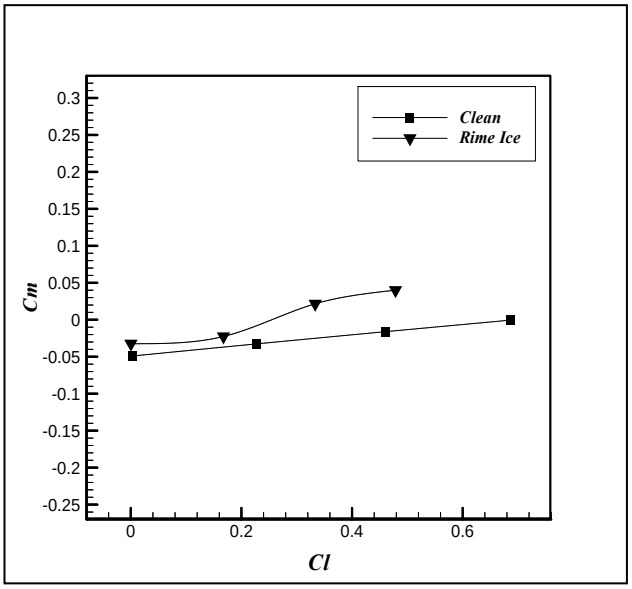

Fig. (25) Pitching moment coefficient versus lift coefficient at M=0.3.

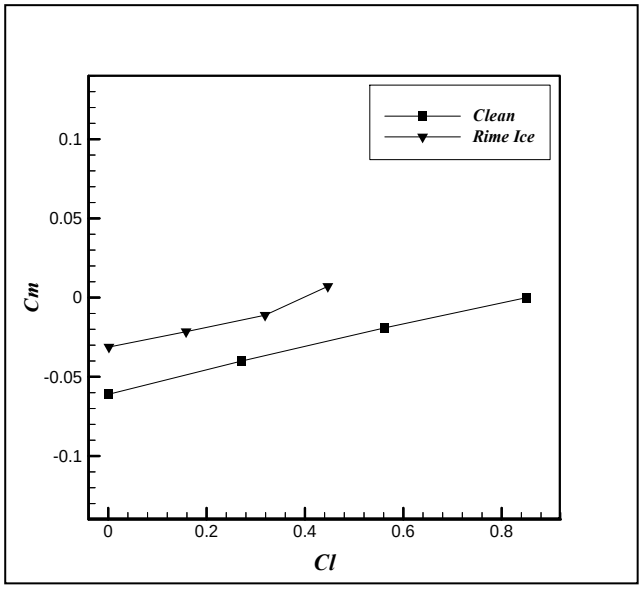

Fig. (26) Pitching moment coefficient versus lift coefficient at M=0.4.

Fig. (27) shows the effect of time accreted of ice at 6 time steps is considered, each of 30 second till reach the final steady state condition (180 s). Fig. (28) shows the distribution of pressure coefficient at that M=0.3 and α= 0°, where some one can see that the increase in time step (increase quantity of ice on the airfoil) will lead to increase the pressure coefficient, hence decrease the performance of the airfoil. Fig.(5.29) shows that the when the time step increased, the lift coefficient performance decreased. This is due to increase the disturbance of the air flow over the airfoil due to the ice. Fig.(30) shows the increase of the drag coefficient according to the increase and distortion in the airfoil nose area with increased of the ice accumulation.

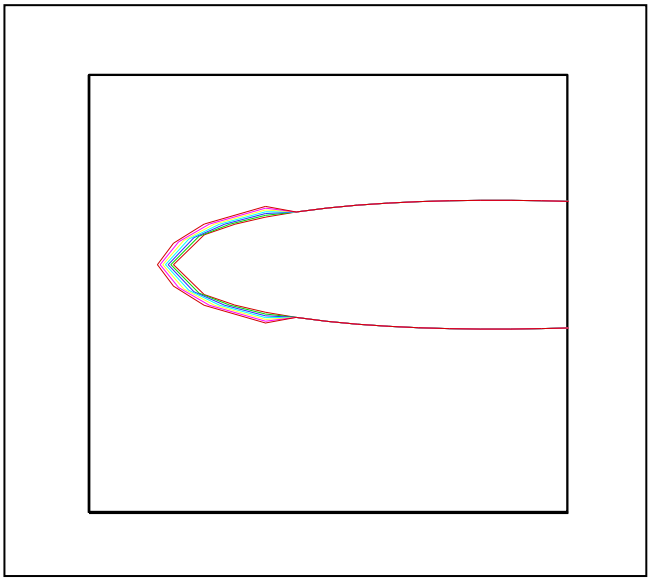

Fig. (27) Ice accreted on the airfoil of six time steps.

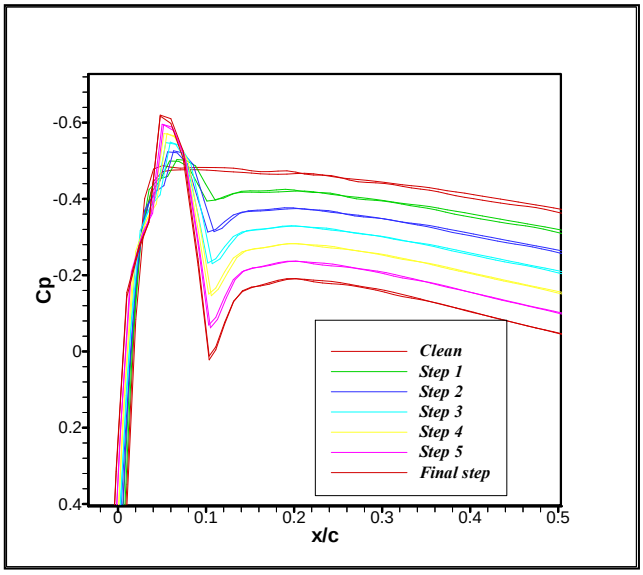

Fig. (28) Pressure coefficient distribution at M=0.3 and α=0° with different time step of ice accreted.

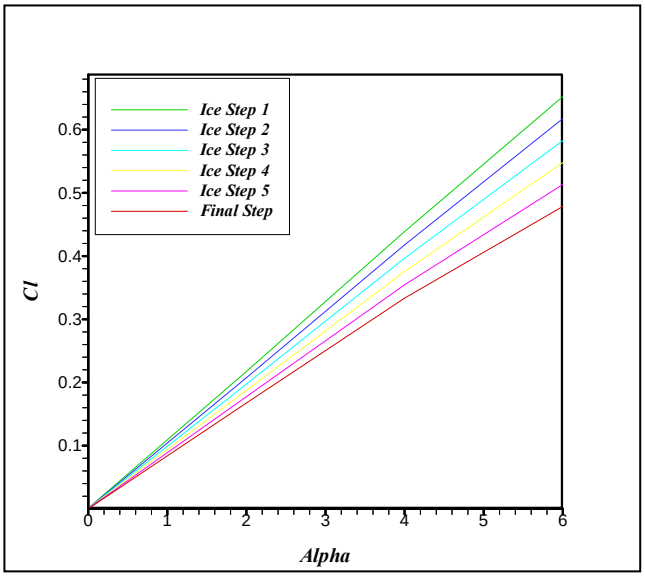

Fig. (29) Lift coefficient variation at M=0.3 and α=0° with different time step of ice accreted.

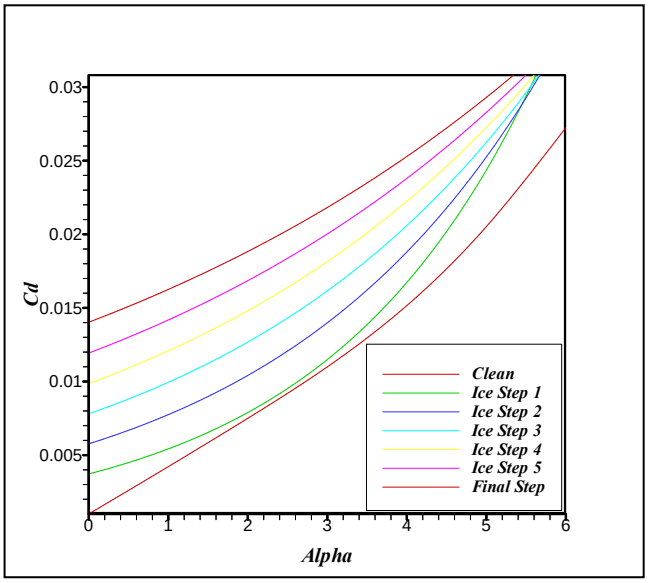

Fig. (30) Drag coefficient variation at M=0.3 and α=0° with different time step of ice accreted.

CONCLUSION

The icing on an airfoil was simulated with a renewed effect of time and collection efficiency and the airfoil performance showed severe aerodynamic penalties encountered with decrease in lift, and increase in drag and highly changes in the pressure distributions. The presence of ice on unprotected airfoil may increase drag by as much as 60% and reduce lift by 45%, where the severe adverse gradients will lower the C_l , as well as increasing the drag of the airfoil.

The drag and lift results for the ice cases show a severe deviation from that of the clean case, which indicate that the accretion ice on the airfoil is so dangerous and could cause big problems for the pilots.

The pitching moment coefficient increases in the case of ice accretion more than the clean case, where the average percentage increase of the pitching moment coefficient with the lift coefficient is 96 % and. This increase would cause an unstable condition for the flying condition.

NOMENCLATURES

a Acceleration of Ice Droplet (m/s²)

C Chord Length (m)

C_d Drag Coefficient

C_l Lift Coefficient

C_m Pitching Moment Coefficient

C_P Pressure Coefficient

D_d Droplet Diameter (μm)

D_{eq} Mean Volume Diameter (μm)

k Turbulent Kinetic Energy (m²/s²)

Re Reynolds Number

V Ice Droplet Velocity (m/s)

u Flow Field velocity (m/s)

U_∞ Free Stream Velocity (m/s)

K Inertia Parameter

Ko Modified Inertia parameter

μ Dynamic Viscosity (kg/m.s)

μ_k *Turbulent Dynamic Viscosity in k-Equation* (kg/m.s)

μ_ε *Turbulent Dynamic Viscosity in ε-Equation* (kg/m.s)

μ_t *Turbulent viscosity* (kg/m.s)

ρ_a *Air Density* (kg/m^3)

ρ_d *Ice Droplet Density* (kg/m^3)

ρ_w *Water Density* (kg/m^3)

(λ / λ_s) *Trajectory of a Droplet in Still Air to the Same Trajectory of the Droplet if the Drag is Assumed to Obey Stock's Law*

ξ , η *Curvilinear Coordinate Direction*

ε *Dissipation of Turbulent Kinetic Energy* (m^2/s^2)

σ_k *Empirical Constant in k Transport Equation*

σ_ε *Empirical Constant in ε Transport Equation*

REFERENCES

-Anderson David N., Galdemir C. Botura, Broeren Andy P., "A Study of Scaling For Intercycle Ice Accretion Tests", 39th Aerospace Sciences Meeting and Exhibit Reno, Nevada, Januarys- 11, 2001.

-Anderson David N., Hentschel Daniel B. and Ruff Gary A., "Measurement and Correlation of Ice Accretion Roughness". NASA/CR—2003-211823, AIAA–98–0486, June 2003.

-Anderson David N. and Tsao Jen-Ching, "Evaluation and Validation of the Messinger Freezing Fraction", Ohio Aerospace Institute, Brook Park, Ohio 44142. Prepared for the 41st Aerospace Sciences Meeting and Exhibit sponsored by the American Institute of Aeronautics and Astronautics Reno, Nevada, January 6–9, 2003.

-Bergrun, N.R., "A Method for Numerically Calculating the Area of Water Impingement on the Leading Edge of an Airfoil in a Cloud," NACA TN 1397, Aug. 1947.

-Bergrun, N.R., "Warming Trend for Icing Research," Aerospace America, pp. 22-27, Aug. 1995.

-Bragg M.B., Zaguli R.J., and Gregorek G.M. " Wind Tunnel Evaluation of Airfoil Performance Using Simulated Ice Shapes" Ohio State University Columbus, Ohio Prepared for Lewis Research Center Under Grant NAG3–28 NASA Contractor Report 167960, November 1982.

-Bragg, M.B., "Experimental Aerodynamic Characteristics of NACA 0012 Airfoil with Simulated Glaze Ice," AIAA Journal of Aircraft, Vol. 25, No. 9, pp. 849-854, Sept. 1988.

-Bragg M.B. and Kerho Michael F. "3-D Measurement on a 30-Degree Swept Wing with a Simulated Ice Accretion". University of Illinois, Urbana, IL, NACA Contact report, April 1994.

-Chung T. J. "Computational Fluid Dynamics", University of Alabama in Huntsville, Cambridge University Press, 2002.

-Hansoman R. john, "Droplet Size Distribution effects on aircraft ice accretion". J. Aircraft, vol. 22, No. 6, June 1985.

-Hoffmann Klaus A. "Computational Fluid Dynamics for Engineers", University of Texas at Austin, TX 78713-8148, USA, 1989.

-Langmuir, Irving, and Blodgett Katherine B.,"A Mathematical Investigation of Water Droplet Trajectories'" Army Air Process Technical Report No.5418 (Contract No. w-33-038-ac-9151), Feb. 1946.

-Paraschivoiu I., Tran P., and Brahimi M.T., "Prediction of Ice Accretion with Viscous Effects on Aircraft Wings," AIAA Journal of Aircraft, Vol. 31, No. 4, pp. 855-861, July-Aug. 1994, (also AIAA Paper 93-0027).

-Versteeg H. k. and Malalasekera W., "An Introduction to Computational Fluid Dynamics". Longman Group Ltd, 1995.

NUMERICAL INVESTIGATION OF THE CAVITATION IN PUMP INDUCER

Mishaal A. AL-Saffar
Mechanical Department
College of Engineering
AL-Mustansiriya University.

Najdat N. Abdulla
Mechanical Department
College of Engineering
University of Baghdad.

Jalal M. Jalil
ElectroMechanical
Engineering Department
University of Technology.

ABSTRACT

A numerical investigation of the non-cavitating and cavitating performance of a three-blade pump inducer under nominal and off-design operating conditions is presented. Three different simulated hydrofoils; a flat plate, "NACA0004", and "Clark-Y-6%" has been selected to represent the profile of the inducer blade. A 2D, steady, incompressible, turbulent, and isothermal flow field between the inducer blades is simulated using the FVM. The "Interface Tracking" model is selected to predict the cavity profile of the attached cavitation and the cavitating performance drop. For each blade profile, the influence of solidity in the range of (1.8 to 3.0) and blade angle in the range of (20° to 35°) on the inducer performance is studied. Comparing the present model with available experimental and numerical results, confirms that the developed model well predicts the general non-cavitating performance for an inducer having a flat plate blade profile. For "NACA0004", or "Clark-Y-6%" hydrofoil blade profiles, a reduction in the operating range of these inducers is produced. In addition, the developed model predicts the inception of cavitation earlier than the experimental results. The predicted cavitating head drop curve of an inducer having a flat plate blade profile is compared with available experimental results and a good agreement is obtained. The drop curve occurs suddenly and simultaneously with the experimental one. For "NACA0004", or "Clark-Y-6%" hydrofoil blade profiles, a smooth curves with simultaneous or gradual head drop occurs with the experimental one, respectively. Generally, the agreement between the results is satisfactory.

الخلاصة

تم عرض دراسة عددية عن خصائص الأداء لمحاثة ثلاثية الريش لمضخة تعمل عند انعدام التكهف ومع التكهف عند حالات العمل التصميمية وغير التصميمية. تم اختيار ثلاثة أشكال بطريقة منمذجة لمطيار مائي وهي: صفيحة مستوية، و "NACA0004" و "Clark-Y-6%" لتمثل شكل ريشة المحاثة. تمت نمذجة الجريان ثنائي الأبعاد, مستقر, غير انضغاطي, مضطرب، و ذو درجة حرارة ثابتة لمائع ينساب بين ريش المحاثة وباستخدام طريقة الحجم المحددة. تم اختيار نموذج "Interface Tracking" لتخمين شكل الفجوة للتكهف الملتصق و انخفاض الأداء المتكهف. لكل شكل ريشة، تمت دراسة تأثير الصلادة في المدى (1.8 الى 3.0) وزاوية الريشة في المدى (20 الى 35 درجة) على أداء المحاثة. إن مقارنة النتائج التي تم الحصول عليها من النموذج المطور مع النتائج المتوفرة من التجارب العملية ومن الحسابات العددية ,تؤكد أن النموذج المطور يحسن تخمين الأداء العام وبدون تكهف لمحاثة ذات ريشة بشكل صفيحة مستوية. لمطيار مائي بشكل "NACA0004" أو "Clark-Y-6%" سينخفض مدى التشغيل لهذه المحاثات. بالإضافة إلى ذلك, فان النموذج المطور يخمن بدء التكهف بصورة مبكرة عن تلك المتوفرة من التجارب العملية. تمت مقارنة منحني انخفاض الضغط عند تكهف المحاثة ذات ريشة بشكل صفيحة مستوية مع النتائج المتوفرة من التجارب العملية حيث تم الحصول

على توافق جيد. إن منحني انخفاض الضغط يحدث بشكل مفاجئ ومتزامن مع نضيره المتوفر من التجارب العملية. لمطيار مائي بشكل "NACA0004" أو "Clark-Y-6%" , فان منحنيا انخفاض الضغط تحدث بشكل متزامن أو تدريجي مع نضيرها المتوفر من التجارب العملية وعلى التوالي. بشكل عام, إن التوافق بين النتائج هو مرضي.

KEYWORDS

Cavitation, inducer, two-phase, Rayleigh-Plesset, NACA0004, Clark-Y-6%, interface tracking, FVM.

INTRODUCTION

Nowadays, satellite systems such as satellite broadcasting and navigation by GPS are becoming indispensable for our life. Liquid fuel rockets are mainly used to launch the satellites. In the rockets, liquefied hydrogen (LH_2) and liquefied oxygen (LOX) are used as propellants. A turbopump, which supplies the propellants to a combustion chamber with high pressure, is incorporated in the rocket engine to make the system smaller and lighter, **(Tokumasu et. al. 2003)**. It is necessary for the turbopump to run very fast to make it smaller. In this condition, cavitation occurs, because the local static pressure becomes smaller than the vapor pressure.

The performance of the pump, or other hydraulic device, may be significantly degraded. In the case of pumps, there is generally a level of inlet pressure at which the performance will decline dramatically, a phenomenon termed "Cavitation breakdown". This adverse effect has naturally given rise to changes in the design of a pump to minimize the degradation of the performance; or, to put it another way, to optimize the performance in the presence of cavitation. One such design modification is the addition of a cavitating inducer upstream of the inlet to a centrifugal or mixed flow pump impeller. Another example is manifest in the blade profiles used for super-cavitating propellers. These super-cavitating hydrofoil sections have a sharp leading edge, and are shaped like curved wedges with a thick, blunt trailing edge.

An inducer is attached to these turbopumps to increase their efficiency. The "inducer" is a device that causes a rise in the inlet head, which prevents cavitation in a pump stage following the inducer. Inducers are therefore used at the inlet portion of the main pump. They are typically designed to be axial flow impellers with a high solidity so that long narrow passages result. Cavitation bubbles collapse in these passages before they reach the main pump, **(Acosta 1958)**.

Nowadays, CFD numerical techniques are commonly used in the hydraulic design of industrial turbomachines components. Unfortunately, without a suitable numerical model, it is impossible to solve directly cavitating flows. Since 1990's, various methods have been proposed to simulate cavitating flows as two-phase flows. Three different approaches have been mainly proposed for the numerical simulation of cavitation phenomenon in hydraulic machinery, these are: (1) The Single Fluid Model: It is based on a pseudo-density function of the liquid-vapor mixture to close the equations system. A Baratropic law relating the pressure to density is mainly proposed. Assuming no-slip is present between the liquid and vapor phases, both phases are in thermal equilibrium. **(Coutier-Delgosha et. al. 2001)** has used this model to simulate numerically the cavitation behavior of beveled and sharp leading edge shapes for two-dimensional hydrofoil sections of an inducer blade at two different angles of attacks. This simulation was coded with the 3D "FINE/TURBO™" commercial code. **(Joussellin et. al. 2001)** has used this model to investigate numerically the cavitating flows in rocket engine turbopump inducers. A 2D numerical model of unsteady cavitation, developed by previous studies, was applied to a 2D blade cascade drawn from the inducer geometry. **(Coutier-Delgosha et. al. 2002)** has used this model to investigate numerically the characteristics, performance breakdown, cavitation development and vapor structures distribution of a 4-blade turbopump inducer in non-cavitating and cavitating conditions associated with quasi-steady effects. The numerical model was

coded using the "FINE/TURBO™" commercial code. (2) The "VOF" Model: It is a multiphase mixture model which has an additional equation for the volume fraction including source terms to model the vaporization and condensation processes. Using a truncated form of the Rayleigh-Plesset equation to estimate the rate of vapor production or destruction assuming that thermal and mechanical equilibrium stands between liquid and vapor phases. **(Bakir et. al. 2003)** has used this model to investigate numerically the hub shape effect on the inducers performance under cavitation. **(Reboud et. al. 2003)** has used this model to correctly simulate the unsteady cavitaing flows in 2D venturi type section implementing the influence of four turbulence models. Simulations were also performed to a hydrofoil, a foil cascade, and another venturi type section. **(Ait-Bouziad et. al. 2004)** has used this model to simulate the cavitation behavior of a 3-blade industrial inducer. **(Bakir et. al. 2004)** developed a numerical cavitation model suitable for general three-dimensional flows with extensive cavitation at large density ratios. His model assumed two-phase, three-component system with no inter-phase slip and thermal equilibrium between any of the components and phases. (3) The "Interface Tracking" Model: In this approach, the cavity interface is considered as a free surface boundary of the computation domain and the computational grid includes only the liquid phase. **(Hirschi et. al. 1998)** has used this model to predict the performance drop of a cavitating centrifugal pump and the influence of the diffuser geometry on this performance. **(Ait-Bouziad et. al. 2003)** investigated numerically the performance of "Interface Tracking" and "VOF" Models for modeling the cavitation phenomenon in the case of 3-blade industrial inducer.

This paper is presented to study and simulate numerically the non-cavitating and cavitating performance of a three-blade pump inducer under nominal and off-design operating conditions and to predict the cavity profile using the FVM. This inducer will be designed for nominal operating condition with flow coefficient (φ=0.38), rotational speed (N=1450 rpm), and head coefficient (ψ=0.15). The "Interface Tracking" model is selected to predict the cavity profile of the attached cavitation and the cavitating performance drop. Three different simulated hydrofoils; a flat plate, "NACA0004" and "Clark-Y-6%" will be selected to represent the shape of the three-blade inducer. For each blade profile, the influence of solidity in the range of (1.8 to 3.0) and blade angle in the range of (20° to 35°) on the inducer non-cavitating and cavitating performance will be studied under nominal and off-design operating conditions. The results of this paper will be compared with available experimental and numerical results of the "CFX-TASCflow" commercial code.

The details of this paper are described completely in a Ph.D. Thesis work of **(AL-Saffar 2007)**.

GOVERNING EQUATIONS

The two-dimensional governing equation of mass and momentum for steady, turbulent, incompressible flow can be written in tensor conservative form and expressed in Cartesian coordinates as follows, **(Nilsson 2002)**:

$$\frac{\partial u_i}{\partial x_i} = 0 \tag{1}$$

$$\rho_L \frac{\partial u_i u_j}{\partial x_j} = -\frac{\partial p}{\partial x_i} + \frac{\partial \left(t_{ij} + \tau_{ij} \right)}{\partial x_j} \tag{2}$$

Where (t_{ij}), is the viscous shear stress tensor that is expressed as:

$$t_{ij} = \mu\left[\left(\frac{\partial u_i}{\partial x_j} + \frac{\partial u_j}{\partial x_i}\right) - \frac{2}{3}\left(\frac{\partial u_k}{\partial x_k}\delta_{ij}\right)\right] \quad (3)$$

The Reynolds stress tensor (τ_{ij}) can be determined according to the Boussineq assumption as:

$$\tau_{ij} = -\overline{\rho_L u_i' u_j'} = \mu_t\left[\left(\frac{\partial u_i}{\partial x_j} + \frac{\partial u_j}{\partial x_i}\right) - \frac{2}{3}\left(\frac{\partial u_k}{\partial x_k}\delta_{ij}\right)\right] - \frac{2}{3}\delta_{ij}\rho_L k \quad (4)$$

The standard (k-ε) two-equation turbulence model has been selected among other turbulence models. Hence, the value of the turbulent eddy viscosity (μ_t) is estimated as, **(Wang and Komori 1998)**:

$$\mu_t = \frac{c_\mu \rho_L k^2}{\varepsilon} \quad (5)$$

"INTERFACE TRACKING" MODEL:

It is a mono-fluid model having an incompressible, single-phase transport equation, and it considers the cavity interface as a free surface boundary of the computational domain. As the cavity shape has an influence on the mean flow, an iterative process needs to be applied between the CFD code and the cavitation prediction one to modify the interface shape in order to reach a constant pressure equal to the vapor pressure along it. This shape is defined by the envelope of high number of transferred bubbles over the blade associated with attached cavitation; the bubble radius instead of its diameter is used to define this envelope. The main numerical complexity is how to predict an adaptive grid for the computational domain to update the cavity shape. This model does not compute any cavitation, which is not attached to the blade surface. Only the attached cavitation to the blade surface boundary is predicted, and the tip clearance cavitation is not considered.

This model has the advantage of being independent of the flow computation code. It is based on some version of the Rayleigh-Plesset equation that defines the relation between the radius of a spherical bubble, (R), and the pressure, (p), far from the bubble. The generalized Rayleigh-Plesset equation for bubble dynamics is given as, **(Brennen 1995, 2005)**:

$$\frac{p_v - p}{\rho_L} = R\frac{d^2R}{dt^2} + \frac{3}{2}\left(\frac{dR}{dt}\right)^2 + \frac{4\nu_L}{R}\frac{dR}{dt} + \frac{2S}{\rho_L R} \quad (6)$$

In the absence of the surface tension and viscous terms, the generalized form of this equation is truncated to predict (R) at a given (p), provided that (p_v) is known.

$$\frac{dR}{dt} = \sqrt{\frac{2}{3}\frac{(P_v - P)}{\rho_L}} \quad (7)$$

NUMERICAL TECHNIQUE

The "Interface Tracking" model has been used to simulate the hydraulic performance of a cavitating performance of a three-blade pump inducer under nominal and off-design operating

conditions using the FVM using the standard k-ε turbulence model associated with laws of the wall along solid boundaries. Steady state solutions were obtained by setting a uniform flow velocity and a constant total pressure at the inducer inlet for the boundary conditions.

A grid independency test for the three selected profiles is performed and a single-block structured mesh has been generated for each profile. Mesh sizes of (30x100), (30x99) and (30x70) are selected for flat plate, "NACA0004" hydrofoil profile and "Clark-Y-6%" hydrofoil respectively. Each mesh is made for a single passage (1/3 of the inducer).

Computations starts from the non-cavitating regime, then the "Interface Tracking" model is turned on, while the imposed total pressure at the channel inlet is decreased by a constant step of (10,000 Pa). Close to the drop zone, this step is reduced by a factor of (10) and more to overcome the high instability of the solution due to the strong non-linear behavior of the cavitation phenomenon. For each value of the imposed total pressure at the channel inlet and after entering the drop zone, the truncated Rayleigh-Plesset equation is activated to predict the cavity interface shape. The cavity interface is treated as a wall boundary of the blade-to-blade channel. Hence, the wall function will be imposed along the cavity interface. This is considered to be a major assumption of the "Interface Tracking" model. The shape of the cavity interface is inserted into the grid generator to update the grid shape. This shape is adapted step by step according to the pressure distribution obtained from the flow computation at the previous iteration in order to reach a given condition (the pressure at the cavity interface is equal to the vapor pressure). The head drop curve is created gradually. It is noted finally that the time consuming for the creation of a whole one head drop curve is about (30 min) on a P4, Celeron(R) CPU, 2.41 GHz, 256 MB of RAM. For all computations, a maximum residual is kept below 10^{-4}.

RESULTS DISCUSSION

Non-Cavitating Performance

The effects of different values of solidity and blade angle on the numerical results of the (Head-Flow) curve for the non-cavitating performance of an inducer having a flat plat, "NACA0004", and "Clark-Y-6%" hydrofoil blade profile are simulated and compared with the experimental and 3D numerical results of, **(Bakir et. al. 2004)**, using the "CFX-TASCflow" commercial code**,** of the "LEMFI" inducer, as shown in **Fig. 1**. For each case study, the optimum simulated values of solidity and blade angle are listed in **Table 1**.

Table (1) Optimum geometry configuration for different simulated shapes of blade profiles.

Case study	Blade profile	Optimum geometry configuration	
		Solidity (s)	Blade angle (β_b)
1	Flat plate	2.95	25°
2	"NACA0004"	2.95	30°
3	"Clark-Y-6%"	1.8	25°

As shown in **Fig. 1**, for the flat plate case study, a good agreement between the experimental results of **(Bakir et. al. 2004)** of "LEMFI" inducer, and the numerical results of the present work is obtained at nominal flow coefficient (φ=0.38), and high flow coefficients. At low flow coefficients, an average difference in the value of head coefficient of about (0.15) is obtained between the experimental

and two-dimensional numerical results and this due to the tip clearance effects. For "NACA0004" or "Clark-Y-6%" hydrofoil blade profiles using the optimum values of solidity and blade angle listed in **Table 1**, will result a reduction in the operating range producing a flow coefficient value of (10%) lower than that of the nominal one with an average head coefficient value of (30%) higher than that of the nominal one. This is due to the change in the blade profile and geometric parameters.

Cavitation Inception

Fig. 2 shows the comparison between the experimental and numerical results of **(Bakir et. al. 2004)** of "LEMFI" inducer, for the inception cavitation number (σ_i) versus flow coefficient (φ) and present work inducer having different simulated shapes of hydrofoil profiles, using the optimum solidity and blade angle values listed in **Table 1**. As shown, the present work numerical results predict the inception of cavitation earlier than the experimental and numerical results of **(Bakir et. al. 2004)**. This is due to the unsteady nature of cavitation inception. On the other hand, the numerical results of **(Bakir et. al. 2004)** were based on using the "VOF" model and the inception cavitation number was associated with a (3%) head drop.

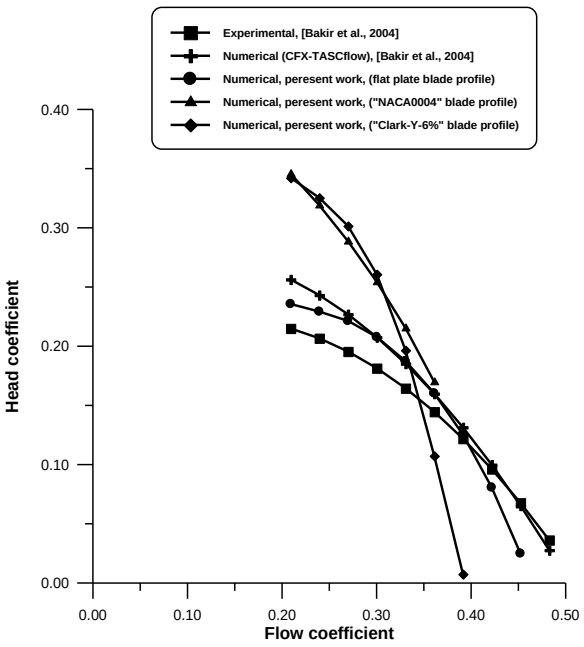

Fig. 1 : Non-cavitating performance.

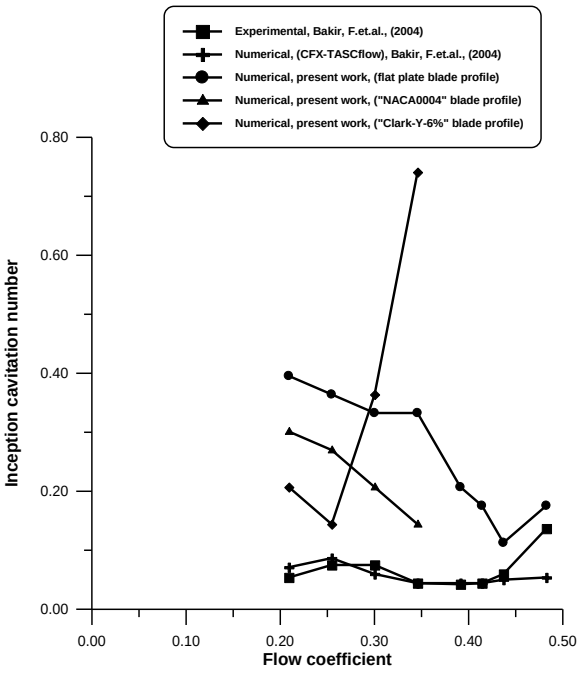

Fig. 2 : Cavitation inception curve.

Cavitating Performance

Fig. 3 and **Fig. 4** show the comparison between the developed model and the experimental and numerical results of **(Bakir et. al. 2004)**, for the head drop characteristics of an inducer having a flat plate blade shape, operating at a flow coefficient of (φ=0.346) or (φ=0.38), a good agreement is obtained between the developed model and experimental results. The drop curve occurs suddenly and simultaneously with the experimental one. The agreement between the results is very satisfactory.

For "NACA0004“ hydrofoil profile, when operating at a flow coefficient of (φ=0.346), a smooth with simultaneous head drop occurs with the experimental one, with a (30%) increase in the value of the head coefficient.

For "Clark-Y-6%" hydrofoil, a smooth with gradual head drop occurs before the experimental one, with a (30%) increase in the value of the head coefficient, as shown in **Fig. 4**.

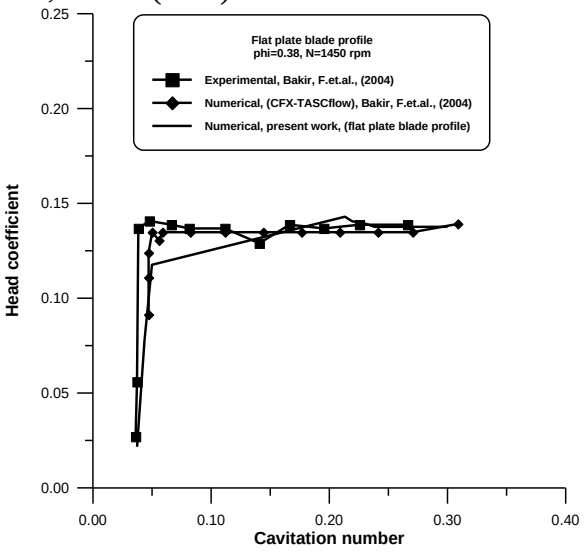

Fig. 3 : Head drop curve, φ=0.38

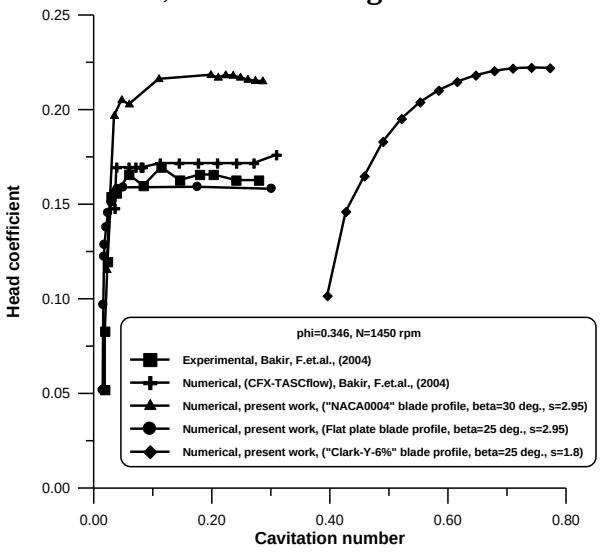

Fig. 4 : Head drop curve, φ=0.346

Fig. 5 show the evolution of the cavity profile on the suction side of a flat plate blade profile of an inducer operating at a flow coefficient of (φ=0.38) and (φ=0.346), at cavitation inception and with different cavitation numbers.

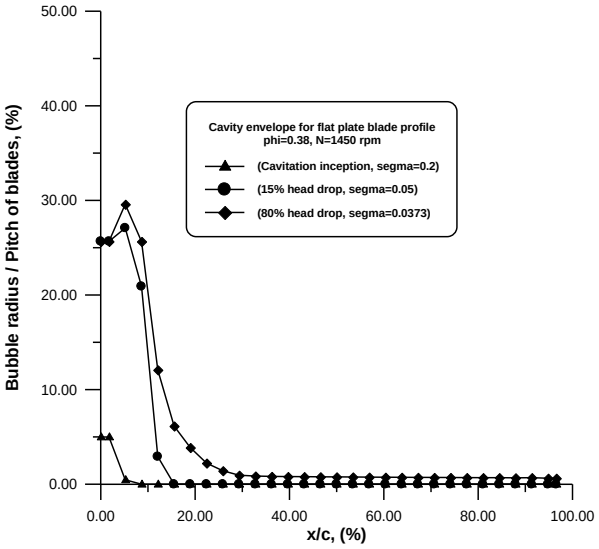

(a) Flat plate blade profile, φ=0.38

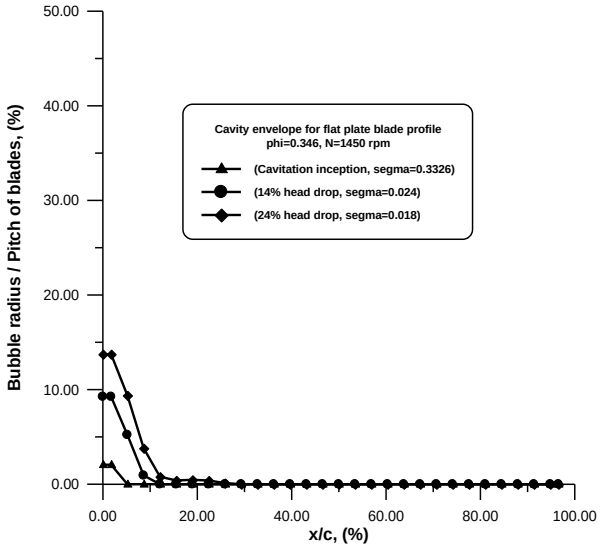

(b) Flat plate blade profile, φ=0.346

Fig. 5 : Cavity envelope evolution on the suction side at different cavitation numbers.

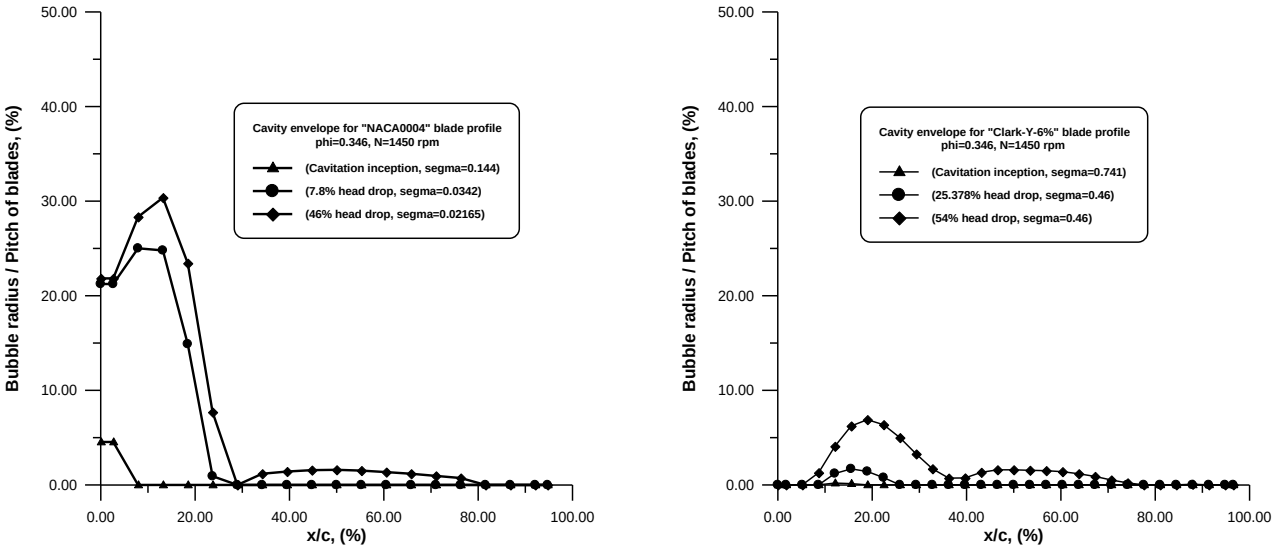

(a) "NACA0004" blade profile, φ=0.346 (b) "Clark-Y-6%" blade profile, φ=0.346

Fig. 6 : Cavity envelope evolution on the suction side at different cavitation numbers.

Fig. 6 shows the evolution of the cavity profile on the suction side of a "NACA0004" and "Clark-Y-6%" blade profile of an inducer operating at a flow coefficient of (φ=0.346), at cavitation inception and with different cavitation numbers.

CONCLUSIONS

The abnormal cavitating behavior of the "Clark-Y-6%" hydrofoil blade profile as shown in **Fig. 2** and **Fig. 4** is due to that the "Clark-Y-6%" hydrofoil blade profile is of cambered shape with a maximum thickness to cord ratio value of (6%) which is greater than that of the flat plate blade profile of a negligible constant thickness to cord ratio value and greater than the "NACA0004" hydrofoil blade profile of a symmetric shape with a maximum thickness to cord ratio value of (4%). This shape of the "Clark-Y-6%" hydrofoil blade profile will produce a greater contraction (i.e. a 2% increase above that of the "NACA0004" hydrofoil and a 6% increase above that of the flat plate shape) at its blade-to-blade channel resulting a higher velocity value at its throat and a lower pressure value which result a higher value of the inception of cavitation parameter and also a smooth with gradual head drop occurs before the head drop curve of both the "NACA0004" and the flat plate hydrofoils when operating at a flow coefficient of a value of (φ=0.346).

In general, the shape of the blade profile and its geometric parameters (i.e. the solidity and the blade angle values) has a major effect on the performance characteristics of the non-cavitating and cavitating pump inducer. Therefore, it is better to design and manufacture an inducer with a blade profile that produce a blade-to-blade channel that has no contraction (i.e. flat plate blade profile) having a relatively high value of solidity and a value of blade angle that produce a few degrees of the angle of incidence.

SYMBOLS AND ABBREVIATIONS

c=Cord length, (m).
c_μ= Empirical coefficient, (-).
h=Pitch of blades, (m).
k= Turbulent kinetic energy, (J/kg).
p= Static pressure, (Pa).
p_{in}=Inlet pressure, (Pa).
p^T= Total pressure, (Pa).
p_v= Vapor pressure, (Pa).
Q= Volumetric flow rate, (m^3/s).
R= Bubble radius, (m).
R_{hub}=Hub radius, (m).
R_{tip}= Tip radius, (m).
s= Solidity=c/h, (-).
S= Surface tension, (N/m).
t= Time, (s).
u= Cartesian velocity component, (m/s).
x= Cartesian coordinate, (m).
β_b= Blade angle, (degree).
$\delta_{ij=}$ Kroneker delta switch.
ε= Turbulent kinetic energy dissipation rate term, (J/kg).
μ= Dynamic viscosity, (N.s/$m^{2)}$.
$\mu_{t=}$ Turbulent eddy viscosity, (N.s/m^2).
ν_L= Kinematic viscosity, (m^2/s).
ρ_L=Liquid Density, (kg/$m^{3)}$.
σ= Cavitation parameter=$(p_{in}-p_v)/(0.5\rho_L\Omega^2R^2_{tip})$, (-).
τ_{ij}= Reynolds stress tensor, (N/$m^{2)}$.
φ= Flow coefficient=$Q/(\pi\Omega R^3_{tip}[1-(R_{hub}/R_{tip})^2])$, (-).
ψ= Head coefficient= $(P_2{}^T-P_1{}^T)/(\rho_L\Omega^2R^2_{tip})$, (-).
Ω= Angular velocity, (rad/s).
CFD= Computational Fluid Dynamics.
FVM= Finite Volume Method.
GPS= Global Positioning System.
LEMFI=Laboratoire d'Energétique et de Mécanique des Fluides Interne.
LOX= Liquefied Oxygen.
VOF= Volume Of Fluid.

REFERENCES

-Acosta, A.J., 1958, "An experimental study of cavitation inducers", Proceedings of 2nd Symposium on Navel Hydrodynamics, Washington D.C., pp. 533-557.

-Ait-Bouziad, Y., Farhat, M., Guennoun, F., Kueny, J.L., Avellan, F., 2003, "Physical modeling and simulation of leading edge cavitation, application to an industrial inducer", Fifth International Symposium on Cavitation (CAV2003), (cav03-os-6-014), Osaka, Japan, November 1-4.

-Ait-Bouziad, Y., Farhat, M., Kueny, J.L., Avellan, F., Miyagawa, K., 2004, "Experimental and numerical cavitation flow analysis of an industrial inducer", 22nd IAHR Symposium on Hydraulic Machinery and Systems, June 29 - July 2, Stockholm – Sweden.

-AL-Saffar, M.A., 2007, "Numerical investigation of the cavitation in pump inducer", Ph. D. Thesis, Mechanical Department, College of Engineering, University of Baghdad, Iraq.

-Bakir, F., Kouidri, S., Mejri, I., Rey, R., 2003, "Hub shape effects under cavitation on the inducers performance", Fifth International Symposium on Cavitation (cav2003), (Cav03-OS-6-001), Osaka, Japan, November 1-4.

-Bakir, F., Rey, R., Gerber, A.G., Belamri, T., Hutchinson, B., 2004, "Numerical and experimental investigations of the cavitating behavior of an inducer", International Journal of Rotating Machinery, 10: 15-25.

-Brennen, C.E., 1995, "Cavitation and bubble dynamics", Oxford University Press.

-Brennen, C.E., 2005, "Fundamentals of multiphase flows", Cambridge University Press.

-Coutier-Delgosha, O., Morel, P., Fortes-Patella, R., Reboud, J.L., 2002, "Numerical simulation of turbopump inducer cavitating behavior", IJRM paper No. 02-Y-56, (Previously presented at ISROMAC-9 Conference, Honolulu).

-Coutier-Delgosha, O., Reboud, J.L., Fortes-Patella, R., 2001, "Numerical study of the effect of the leading edge shape on cavitation around inducer blade sections", Forth International Symposium on Cavitation (CAV2001, session B7.003), California Institute of Technology, Pasadena, California, USA, 20-23 June.

-Hirschi, R., Dupont, Ph., Avellan, F., Favre, J.-N., Guelich, J.-F., Parkinson, E., 1998, "Centrifugal pump performance drop due to leading edge cavitation : Numerical predictions compared with model tests", Journal of Fluid Engineering, Vol. 120, pp 705-711, December.

-Joussellin, F., Courtot, Y., Coutier-Delgosha, O., Reboud, J.L., 2001, "Cavitating inducer instabilities: Experimental analysis and 2D numerical simulation of unsteady flow in blade cascade", Forth International Symposium on Cavitation (CAV2001, session B8.002), California Institute of Technology, Pasadena, California, USA, 20-23 June.

-Nilsson, H., 2002, "Numerical investigation of turbulent flow in water turbines", Ph.D. Thesis, Chalmers University of Technology, Sweden.

-Reboud, J.L., Coutier-Delgosha, O., Pouffary, B., Fortes-Patella, R., 2003, "Numerical simulation of unsteady cavitating flows: Some applications and open problems", Fifth International Symposium on Cavitation (CAV2003), (CAV2003-IL-10), Osaka, Japan, November 1-4.

-Tokumasu, T., Sekino, Y., Kamijo, K., 2003, "A new modeling of sheet cavitation considering the thermodynamic effects", Fifth International Symposium on Caviation, (Cav03-GS-16-003), Osaka, Japan, November 1-4.

-Wang, Y., Komori, S., 1998, "Prediction of duct flows with a pressure-based Procedure", Journal of Numerical Heat Transfer, Part A, Applications, Vol. 33, No. 7, pp.723-748, Taylor & Francis, London.

SIMULATION OF CASTING SOLIDIFICATION PARAMETERS IN METALLIC MOULD

Ayad M. Takhakh
Mechanical Engineering Department, University of Al-Nahrain, Baghdad-Iraq
Akeel D. Subhi
Department of Production Engineering and Metallurgy, University of Technology, Baghdad-Iraq

ABSTRACT

In this work, numerical method approach has been used to simulate the solidification parameters of an eutectic aluminum-silicon alloy in chilled metallic mould with copper. The approach is based on the solution of heat flow equations of the casting and mould. In addition, the latent heat is treated as a boundary condition between the liquid and solid phase. The results showed that different behaviors of solidification parameters are obtained along the casting. Furthermore, the simulation approach of solidification parameters in conjunction with the microstructure indicated that it is possible, to a large degree, giving a knowledge about the microstructural features for any alloy system.

الخلاصة

تم في هذا البحث استخدام الطريقة الرقمية في محاكاة متغيرات التجمد لسبيكة الالمنيوم–سليكون الايوتكتيكية في قالب معدني مزود بمصقع من النحاس. اذ تستند الطريقة المستخدمة على حل معادلات انسياب الحرارة للمسبوكة والقالب. اضافة لذلك فقد تم اعتماد الحرارة الكامنة كظرف للحد الفاصل بين السائل والصلب. وقد اوضحت النتائج وجود اختلاف في سلوك متغيرات التجمد على طول المسبوكة. علاوة على ذلك فقد تم التوصل من خلال الربط ما بين محاكاة متغيرات التجمد والبنية المجهرية الى امكانية الاستفادة من نتائج المحاكاة لهذه المتغيرات للتنبا بالسمات المجهرية الى حد كبير ولاي نظام سبائكي.

KEY WORDS

Solidification parameters, simulation, metallic mould, aluminum-silicon alloy, microstructure

INTRODUCTION

Casting, one of the important manufacturing processes, has been used more widely in industry **(Schey 2000)**. It is a very economic method of forming a component and in the same time a complicated process involving control the metallurgical and mechanical aspects **(Metals Handbook 1998)**. The properties of solidified metal or alloy are dependent not just on composition but also on grain size and the shape and distribution of phases **(Metals Handbook 1998 and Campbell 2004)**. These factors can be controlled and modified through controlling the solidification process. The cooling rate, temperature gradient, and local solidification time, which are the solidification parameters, govern the microstructure which in turn control the mechanical properties **(Campbell 2004)**.

The simulation of solidification has received increased attention as the computer revolution has matured. Simulation will be very important tool to optimize the casting process, to shorten the lead time, to assure the quantity, and to improve the mechanical properties of castings **(Kurz and Fisher 1986)**. A wide range of efforts is being used to simulate the solidification and microstructure evolution. These include finite element method (FEM) **(Masters et al. 1997 and Guillemot et al. 2004),** finite difference method (FDM) **(Palmer and Games dos Santos 1998 and Lu 2002)**, finite volume method (FVM) **(Warran et al. 2002 and Lewis 2004)**, cellular automation method (CAM) **(Varam et al. 2001 and Qingyan et al. 2005)**, etc.

The main research objective is to simulate the solidification parameters of Al-12%Si alloy casted in chilled metallic mould using a numerical method approach. The simulated solidification parameters are coupled with microstructure that evolved during solidification in order to develop a modified approach.

MODEL ASSUMPTIONS

The filling of metallic mould with molten metal of eutectic Al-Si alloy is assumed to be instantaneous in this work. It is also assumed that no convection in the molten metal of eutectic alloy. This is related to the redistribution of solute that takes place within the boundary layer, in which this layer is smaller than the momentum boundary layer resulting from the molten metal flow **(Flemings 1974)**. Thermal conductivity and density are considered to be variable with the temperature. While the thermophysical properties of the mould are considered to be constant.

MATHEMATICAL MODEL

Macro-Micro model is built to simulate the solidification of the eutectic Al-12%Si alloy system. The eutectic Al-12%Si alloy was prepared using pure aluminum, Al-22%Si master alloy as starting materials. The chemical composition of pure aluminum, master alloy and prepared Al-12%Si alloy are illustrated in **Table I**. After adjusting the chemical composition, the molten of Al-12%Si alloy was poured in a rectangular metallic mould made from stainless steel and chilled with copper (**Fig. 1**). The simulation of solidification requires the application of heat transfer equations and also some special technique to simulate the latent heat release. For the molten metal that undergoing from solidification, the latent heat is a new factor which needs to be incorporated into the simulation program. In this paper, the solidification range was assumed to be 10 $^{\circ}$C (565 – 575 $^{\circ}$C).

The liquid and solid phases were modeled separately in which the latent heat is treated as a boundary condition. The initial boundary conditions can be expressed as:

At t=0; T_{mold}= 30 $^{\circ}$C

T_{chill}= 30 °C
T_{air} = 30 °C

While the boundary conditions can be expressed as:
(a)- At the internal point, the general heat conduction equation in the casting for liquid phase is:

$$k_L\left(\frac{\partial^2 T}{\partial X^2}+\frac{\partial^2 T}{\partial Y^2}+\frac{\partial^2 T}{\partial Z^2}\right)=\rho_L C_{PL}\frac{\partial T}{\partial t} \qquad (1)$$

While for solid phase, the general heat conduction equation will be

$$k_S\left(\frac{\partial^2 T}{\partial X^2}+\frac{\partial^2 T}{\partial Y^2}+\frac{\partial^2 T}{\partial Z^2}\right)=\rho_S C_{PS}\frac{\partial T}{\partial t} \qquad (2)$$

- For mushy zone, the general heat conduction equation is

$$k_m\left(\frac{\partial^2 T}{\partial X^2}+\frac{\partial^2 T}{\partial Y^2}+\frac{\partial^2 T}{\partial Z^2}\right)+\rho L\frac{\partial f_s}{\partial t}=\rho_m C_{Pm}\frac{\partial T}{\partial t} \qquad (3)$$

(b)- At the mould/air interface

$$Q = h_{air}(T_{air}-T_{mold}) \qquad (4)$$

At the external surface, a constant heat transfer coefficient is taken to be 15 W/m^2.K for mould/air interface region **(Baily 1988)**.

In the solidification of a given alloy, the amount of liberated latent heat is considered to be proportional to the fraction of solid, which is calculated using the lever rule **(Rappaz 1989)**. All equations are solved using finite difference method to determine the temperatures history for casting at each determined node.

The energy equation that related to heat conduction in metallic mould can be expressed as:

$$\rho_m C_{pm}\frac{\partial T_m}{\partial t}=k_m\left[\frac{\partial^2 T}{\partial X^2}+\frac{\partial^2 T}{\partial Y^2}+\frac{\partial^2 T}{\partial Z^2}\right] \qquad (5)$$

where the subscript m represents the mould. The above equations must be solved with appropriate initial boundary conditions.

Image processing was performed using image J program. In this program, the microstructural picture of all specimens that sectioned from the Al-12%Si alloy casting at different positions was inserted to the program separately and processing was achieved.

Fisher and Kurz equation **(Fisher and Kurz 1980)** was used to calculate eutectic spacing (λ). This equation can be expressed as

$$\lambda=\frac{\lambda_e+\lambda_b}{2} \qquad (6)$$

where λ_e is the spacing at the extremity and λ_b is the branching spacing in which the range of stable eutectic growth is located between them.

RESULTS AND DISCUSSION

The cooling curve of Al-12%Si alloy at different positions along the casting can be shown in **Fig. 2**. It is clear from this figure that the solidification time is very short near the chill/cast interface and then increases until reaching a specified distance of 20 mm. Without any doubt, this distance is a transition point in which the solidification time over it has approximately a constant value (0.584 s). The ascription of differences in cooling curve behavior at different positions along the casting is related to the differences in cooling rate. As a result of using copper chill, the cooling rate will be very high at the chill/cast interface region and then decreases with ascending until reaching a specified distance of 20 mm as shown in **Fig. 3**. The constancy in cooling rate (53.093 $^{\circ}$C/s) can be shown clearly beyond a distance of 20 mm. In addition, **Fig. 3** also shows that the cooling rate at the casting corner is very high compared with that along the casting center. This is related to the mould wall which acts as a chill. This accompanied with the copper chill that already existed and conducted with the mould in comparison with that along the casting center which is affected only by the copper chill. This increasing in the cooling rate leads to modify the microstructure of Al-12%Si alloy which in turns raise the mechanical properties.

The relationship between temperature gradient and distance at different positions along the casting can be shown in **Fig. 4**. The important notice that can be recognized form this figure is that the temperature gradient is high in the region that conducted with the copper chill. This increasing in the temperature gradient does not remain the same as that in the early stage of solidification in which the distance of 20 mm that measured from the chill/cast interface is a transition point where the temperature gradient decreases beyond it. **Fig. 4** also shows that the temperature gradient laterally is too high especially at the mould wall compared with that at the casting center. This is because the mould wall acts as a chill during solidification. Because of the small thickness of mould wall used compared with the molten metal volume, this makes the mould wall unable to act as a chill through all stages of solidification. Therefore, decreases in temperature gradient laterally can be recognized obviously with departing from the mould wall toward the casting center.

Some directional solidification can be observed in the early stage of solidification as shown in **Fig. 5** which represents the relationship between local solidification time and distance. This can be demonstrated by the linear relationship between local solidification time (t_s) and distance (d) until reaching a specified distance of 20 mm according to the following relationship which can be expressed as

$$t_s = 0.033d - 0.019 \qquad (7)$$

Beyond this distance, constancy in solidification time can be recognized until completing the solidification. This means that chill effect is limited up to distance of 20 mm measured from the chill/cast interface and beyond this; no effect of chill has been occurred.

The effect of changes that occurred in solidification parameters along Al-12%Si alloy casting as a result of using copper chill was reflected on the microstructural features as shown in **Fig. 6**. It is important to recognize that flake silicon phase with different degrees of modification are presented along the Al-12%Si alloy casting. Several investigators studied the mechanism of modification in Al-Si alloys either quench or chemical **(Kobayashi and Hogan 1985)**. Because of using a copper chill, the modification of eutectic silicon phase related certainly to chill effect. As mentioned elsewhere,

quench modification was originally attributed to the repeated nucleation of the eutectic silicon phase at a reduced temperature **(Metals Handbook 1998)**. Near the chill/cast interface region, as shown in **Fig. 6a**, the greatest modification in flake silicon phase can be recognized. This is related to high cooling rate in this region that reaches to 256.676 $^{\circ}$C/s. Moderate modification can be observed in flake silicon phase with departing from the chill/cast interface region as shown in **Figs. 6b and c**. This is related to decrease the chill effect. The depletion of chill effect at distance of 20 mm, as shown in **Fig. 6d**, and over it makes the size and morphology of flake silicon phase slightly changed, as shown in **Figs. 6e-g**.

From this, the magnitude of solidification parameters at a given point along the Al-12%Si alloy casting has a strong role on determining the eutectic spacing (λ) and morphology of silicon phase. The predominant morphology of silicon phase, as explained above, is flake. As represented in **Table II**, which is essence of the results of the present work, no changes in eutectic spacing (λ) can be observed at and beyond a specified magnitude of solidification parameters that corresponding to (R=53.696 $^{\circ}$C/s, G=14.987 $^{\circ}$C/mm, t_s=0.577 s) and distance (20 mm). Of course, this is related to depleting the chill effect. This means that no modification in flake silicon can be observed at distance of 20 mm and beyond it. The most important result that can be concluded from **Table II** is that the relationship between the solidification parameters and microstructural features of Al-12%Si alloy casting can be used to predict the microstructural features for any other alloy system after determination the casting conditions, thermal properties of the casting and the mould, and system constituents used.

CONCLUSIONS

The prediction of solidification parameters using numerical method approach has been developed. The results showed that different behaviors of solidification parameters are obtained along the chilled Al-12%Si alloy casting using copper. The results also showed that the distance of 20 mm measured from the chill/cast interface is a transition point in which constancy, to a large degree, in the solidification parameters is produced. Furthermore, the numerical approach has been extended to include microstructural features. From the simulation of solidification parameters-microstructure relationship, one can predict the microstructual features for any other alloy system.

REFRENCES

-Baily, C., "Computational Modeling of Mold Design in Lead Ingot Casting", Modeling of Casting, Welding and Advanced Solidification Processes, Vol. VIII (1988) 827.

-Campbell, J., "Castings", Elsevier Butterworth-Heinemann (London) 2004.

-Fisher, D.J. and Kurz, W., "A Theory of Branching Limited Growth of Irregular Eutectics", Acta Metallurgica, 28 (1980) 777.

-Flemings, M.C.," Solidification Processing", McGraw-Hill, Inc. (New York) 1974.

-Guillemot, G. et al., "A New Cellular Automation-Finite Element Coupling Scheme for Alloy Solidification", Modeling Simul. Mater. Sci. Eng., 12 (2004) 545.

-Kobayashi, K.F. and Hogan, L.M., "The crystal Growth of Silicon in Al-Si Alloys", J. Mater. Sci., 20 (1985) 1961.

-Kurz, W. and Fisher, D.J., "Fundamentals of Solidification", Trans Tech Publication Ltd (Switzerland) 1986.

-Lewis, D., "Phase Field Models for Eutectic Solidification", JOM, (2004) 34.

Lu, Y., "Convection Effects in Three-Dimensional Dendritic Growth", ASME International Mechanical Congress and Exposition, (2002) 17.

-Masters, I. et al., "Finite Element Analysis of Solidification Using Object-Oriental and Parallel Techniques", International Journal for Numerical Methods Engineering, 40 (1997) 2891.

-Metals Handbook, Vol. 15, "Casting", American Society for Metals, Metals Park, Ohio, 1998.

-Palmer, W. and Games dos Santos, R., "Numerical Analysis of Steel Solidification Using Finite Difference Method and Finite Element Method", Modeling of Casting, Welding and Advanced Solidification Processes VIII (1998) 1063.

-Qingyan et al., "Modeling of Dendritic Structure During Solidification Process Base on Cellular Automation Model", Mater. Sci. Forum, 475-497 (2005) 3137.

-Rappaz, M., "Modeling of Microstructure Formation in Solidification Process", Intern. Mater. Reviews, 34 (1989) 93.

-Schey, J.A., "Introduction to Manufacturing Processes", McGraw-Hill Higher Education (Singapore) 2000.

-Varam, M.R. et al., "Cellular Automation Simulation of Microstructure Evolution During Austenitic Decomposition Under Continuous Cooling Conditions", Bull. Mater. Sci., 24 (2001) 305.

-Warran, W.J. et al., "Phase Field Simulation of Solidification", Annual Review of Materials Research, 32 (2002) 163.

Greek and Latin Symbols

Symbols	Definition	unit
ρ	Density	kg/m^3
λ	Eutectic spacing	mm
λ_b	Eutectic spacing at which branching occurs	mm
λ_e	Eutectic spacing at the extremity	mm
T	Temperature	$^{\circ}C$
G	Temperature gradient	$^{\circ}C/mm$
R	Cooling rate	$^{\circ}C/sec$
C_p	Specific heat	J/kg.K
K	Thermal conductivity	W/m.K
L	Latent heat	J/kg
h	Heat transfer coefficient	$W/m^2.K$
t_s	Local solidification time	sec
Q	Heat flux	W/m^2
x,y,z	Cartesian coordinates	

f	Phase fraction	

Elements (Wt.%)	Si	Fe	Pb	Cu	Mn	Cr	Ni	Ti	Al
Al	0.119	0.276	0.001	0.005	0.004	0.001	0.001	0.005	Rem.
Al-22%Si alloy	22.30	0.190	0.011	0.020	0.157	0.006	0.006	0.043	Rem.
Al-12%Si alloy	12.30	0.220	0.014	0.018	0.151	0.004	0.005	0.034	Rem.

Table I Chemical composition of pure aluminum, master alloy and prepared Al-12%Si alloy.

Table II The eutectic spacing and degree of modification as a function to the solidification parameters.

Distance from the chill/cast interface (mm)	**Microstructural features**		**Solidification parameters**		
	Eutectic spacing (λ) (μm)	Degree of modification	Cooling rate, (R) (°C/s)	Temperature gradient,(G) (°C/mm)	Local solidification time, (t_s) (sec)
At interface	-	Excellent	1501.640	51.509	0.021
5	5.6	Potent	256.676	28.569	0.121
10	8.5	Moderate	92.540	20.345	0.353
15	9.1	Moderate	59.816	17.882	0.518
20	12.5	No modification	53.696	14.987	0.577

35	12.6	No modification	53.093	14.631	0.584
50	12.6	No modification	53.093	14.631	0.584
65	12.7	No modification	53.093	14.631	0.584

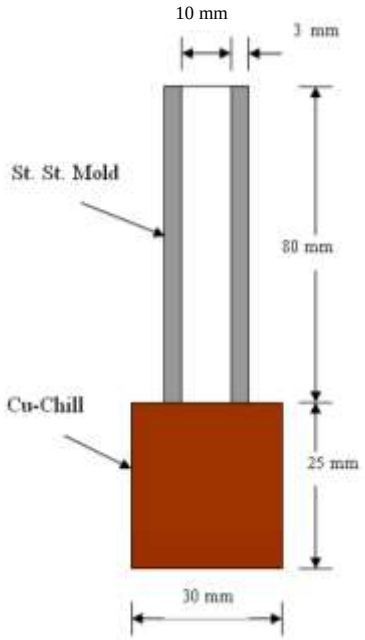

Fig. 1 Rectangular metallic mould chilled with copper.

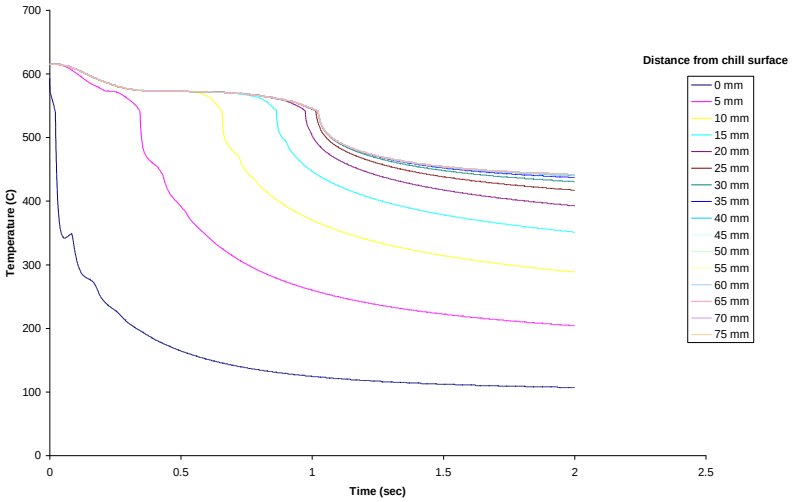

Fig. 2 The cooling curves at different positions along the casting of Al-12%Si alloy.

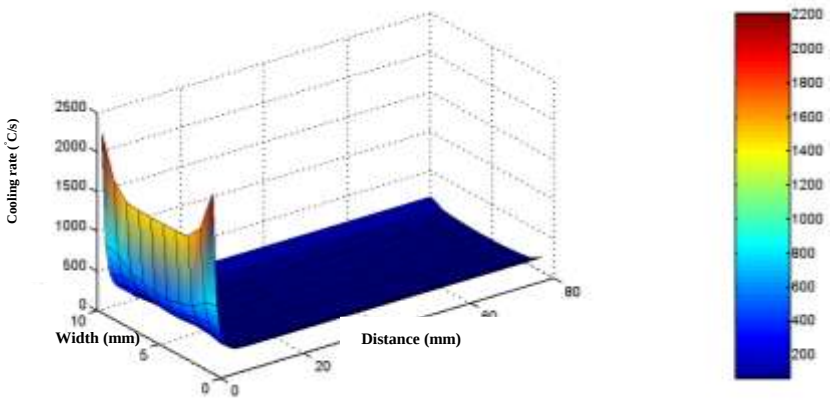

Fig. 3 The relationship between cooling rate distribution and distance along the casting of Al-12%Si alloy.

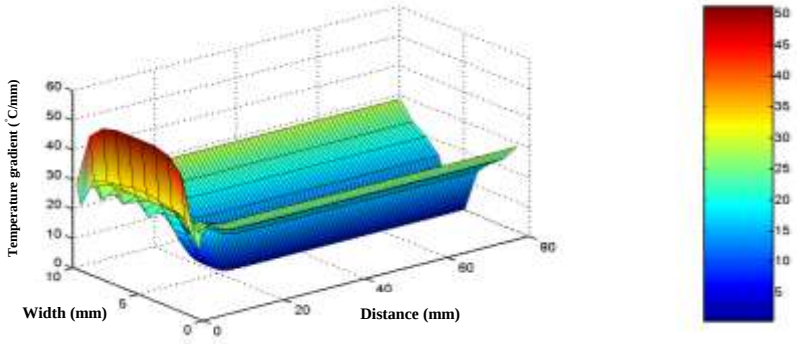

Fig. 4 The relationship between temperature gradient distribution and distance along the casting of Al-12%Si alloy.

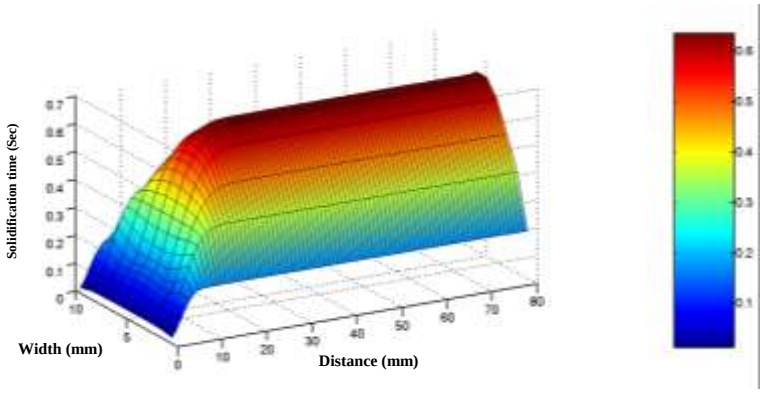

Fig. 5 The relationship between local solidification time distribution and distance along the casting of Al-12%Si alloy.

Before Image Processing	After Image Processing
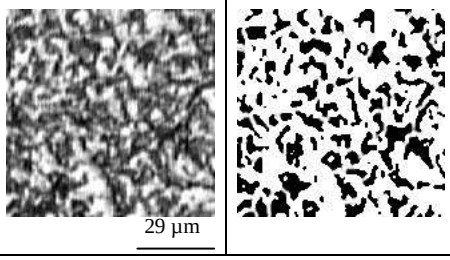	

(a)

Before Image Processing	After Image Processing
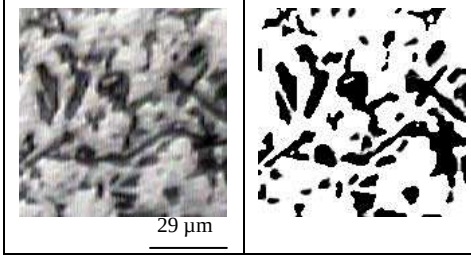	

(b)

Before Image Processing	After Image Processing
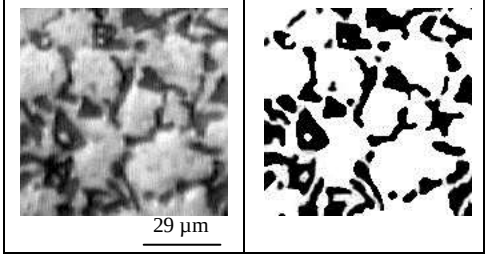	

(c)

Before Image Processing	After Image Processing
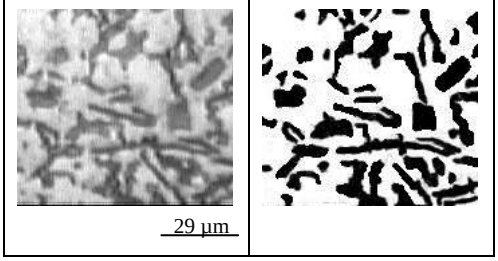	

(d)

Before Image Processing	After Image Processing
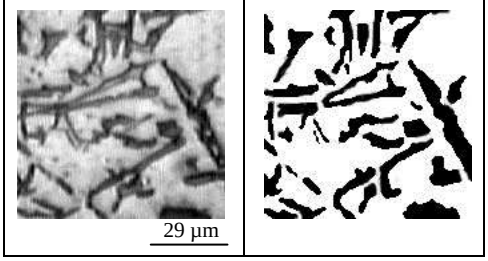	

(e)

Before Image Processing	After Image Processing
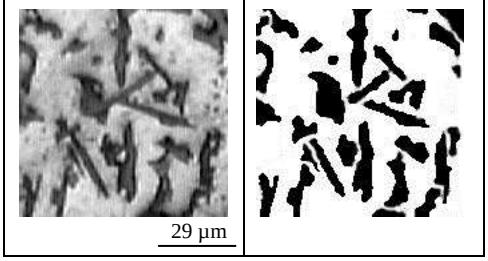	

(f)

Before Image Processing	After Image Processing
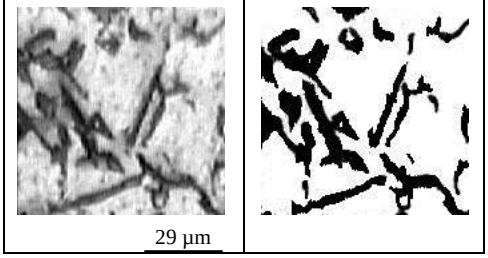	

(g)

Fig. 6 Microstructure of Al-12%Si alloy casting before and after image processing at different positions measured from the chill/cast interface; a=5mm, b=10mm, c=15mm, d=20mm, e=35mm, f=50mm, g=65mm. Optical microscopy; etched with 0.5%Vol. hydrofluoric acid.

THE DEFLECTION CONTROL OF A SIMPLY SUPPORTED THIN BEAM BY USING A PIEZOELECTRIC ACTUATOR / SENSOR

Waleed Kh. Al-Ashtari
Mech. Eng. Dept.
College of Engineering
University of Baghdad
Baghdad-Iraq

ABSTRACT

Piezoelectric transducers have become increasingly popular in vibration control applications. They are used as sensors and as actuators in structural vibration control systems. They provide excellent actuation and sensing capabilities. In this paper, the term smart beam refers to a beam with a finite number of collocated piezoelectric actuator / sensor pairs. The proposed thin smart beam governing equation was derived by the same procedure that the Bernoulli-Euler equation derived but with some additional mathematical terms to be valid for describing the smart beam. The engineering control techniques were used to obtain the solution of the proposed differential equation for the simply supported beam where with some auxiliary equations and modifications a block diagram for any type of applied load (static, or cyclic) as the input and the beam deflection as the output was constructed. For insuring an efficient reduction in the beam deflection an integrated system with a high voltage amplifier and lead controller was designed. Many cases were studied and simulated including the variation of load nature and its frequency, and the number of collocated piezoelectric actuator/sensor pairs and in all cases a valuable deflection reductions were obtained.

الخلاصة:

أصبحت محولات البيزو شائعة الاستخدام في تطبيقات السيطرة على الإهتزازات. فهذه المحولات ممكن ان تستعمل كمتحسسات اوكمحفزات في منظومات السيطرة على الإهتزاز الهيكلي حيث توفر هذه المحولات تحفيزاً وتحسساً ممتازين. في هذا البحث، يطلق تعبير العتبة الذكية على العتبة التي تحتوي على عدد محدد من ازواج المحفز / متحسسِ. لقد اشتقت المعادلة الرياضية المقترحة في هذا البحث للعتبة الذكية بنفس طريقة اشتقاق معادلة برنولي - اولر مع اضافة بعض الحدود الرياضية التي تميز العتبة الذكية. لقد تم حل المعادلة التفاضلية المقترحة بأستخدام تقنيات هندسة السيطرة حيث تم انشاء بواسطة هذه المعادلة وبعض المعادلات الاخرى مخطط صندوقي فيه القوة الخارجية المسلطةعلى العتبة (سكوني أو دوري) كمدخل و ازاحة اهتزاز العتبة كمخرج. لضمان فاعلية اداء المنظومة المقترحة والحصول على اكبر نسبة تقليص ممكنة لازاحة العتبة لقد تم اضافة مسيطر مع مضخم اشارة للمنظومة. لقد تم دراسة ومحاكاة حالات كثيرة منها تغير طبيعة الحمل و تردده عدد ازواج المحفز / متحسسِ وفي كل الحالات تم الحصول نسب تقليص مقبولة.

KEYWORDs: Smart Beam, Ordinary Beam, Bernoulli-Euler Equation, Lead Network Controller, and High Voltage Amplifier.

INTRODUCTION

Piezoelectric transducers have become increasingly popular in vibration control applications. They are used as sensors and as actuators in structural vibration control systems. They provide excellent actuation and sensing capabilities. The ability of piezoelectric materials to transform mechanical energy into electrical energy and vice versa was discovered over a century ago by Pierre and Jacque Curie. These French scientists discovered a class of materials that when pressured, generate electrical charge, and when placed inside an electric field, strain mechanically.

Piezoelectricity, which literally means "electricity generated from pressure" is found naturally in many monocrystalline materials, such as quartz, tourmaline, topaz and Rochelle salt. However, these materials are generally not suitable as actuators for vibration control applications. Instead, man-made polycrystalline ceramic materials, such as lead zirconate titanate **(PZT)**, can be processed to exhibit significant piezoelectric properties. PZT ceramics are relatively easy to produce, and exhibit strong coupling between mechanical and electrical domains. This enables them to produce comparatively large forces or displacements from relatively small applied voltages, or vice versa. Consequently, they are the most widely utilized material in manufacturing of piezoelectric transducers.

Piezoelectric transducers are available in many forms and shapes. The most widely used piezoelectric transducers are in the form of thin sheets that can be bonded to or embedded in composite structures. As actuators they are mainly used to generate moment in flexible structures, while as sensors they are used to measure strain.

Piezoelectric transducers are used in many applications such as structural vibration control, precision positioning, aerospace systems, and more recently they have been critical in advancing researches in nanotechnology. **(Moheimani and Fleming, 2006)**

To this end, many researchers have concentrated on dynamic modeling of piezoelectric materials as elements of intelligent (smart) structures (**Crawley and Luis, 1987; Clark, Saunders, and Gibbs, 1998; Smits and Choi, 1991; Wang and Cross, 1999, Kermani, Moallem, and Patel, 2004)**, while a number of others have focused on control methods of piezoelectric actuators for suppressing vibrations and noise reduction **(Bailey and Hubbard, 1986; Sun and Mills, 1999a; Halim and Moheimani, 2002)**. **(Sun and Mills 1999b)** conducted studies on the application of segmented piezoelectric transducers PZT ceramics and poly vinylidene fluoride **(PVDF)** materials for this purpose, **(Choi, Park, and Fukuda 1998)** investigated active vibration control by utilizing hybrid smart actuators constructed from PZT and shape memory alloy. **(Patnaik, Heppler, and Wang 1992)** studied stability issues in controlling a flexible beam. A quite comprehensive literature review has been given in **(Smits and Choi 1991)**.In selecting a PZT actuator for vibration control; it is useful to know how the physical parameters of a PZT can affect system performance. This issue is of paramount importance if one notes that a PZT actuator has the major drawback of limited capability to produce high torques. This fact reduces the effectiveness of the PZT usage for suppressing vibrations. There are two ways to remedy this problem. One of these calls for the use of stronger PZT actuators such as the one developed at NASA's Langley research center for alleviating the buffet load in the tail fin of the fuselage **(Moses, 1997)**.The other solution involves finding optimum values of the physical parameters to make use of the maximum strength of the actuator. Previous work has tried to address this issue, in an attempt to obtain the optimum size and location of the actuator **(Lim and Gawronski, 1993; Moore, 1981)**. **(Hamdan and Nayef 1989)** proposed a measure of modal controllability based on the angle between the normalized left eigenvectors of the system and the control input matrix. **(Kim and Junkins 1991)** presented a modal cost to rank each mode's participation in system output. **(Aldraihem, Singh, and Wetherhold, 1997)** reported a weighted controllability measure by modifying Hamdan's controllability index. They also considered a penalty for the length of the actuator in formulating the optimization problem. **(Yaghoobi and Abed, 1999)** defined a participation factor to address the

participation of a mode in a state, specified as output. **(Moheimani and Ryall, 1999)** introduced the idea of spatial controllability in order to include the effect of actuator location in the optimization problem. **(Yong, Onada, and Minesugi, 2002)** considered the effect of the adding an actuator/sensor on the mass and stiffness of the structure and combined that with the control performance index to obtain the optimum values for the location, size and feedback gains, simultaneously. However, a clear description of the actuator performance with respect to each individual mode of vibration needs to be given more attention. The degree by which a certain parameter can affect each resonance mode motivates further investigations. The use of the controllability Grammian and singular value decomposition of the system dynamics can provide practical guidelines for selecting the optimal values of the aforementioned parameters. **(Vasques, and Dias Rodrigues, 2006)** introduce an analysis and comparison of the classical and optimal feedback control strategies on the active control of vibrations of smart piezoelectric beams. **(Belouettar, Azrar, Daya, Laptev, and Potier-Ferry, 2007)** they developed a simplified and consistent theory to actively control sandwich beams (the upper and bottom surfaces are covered entirely with a piezoelectric layer) at small and large amplitude.

In this research, the term smart beam will refer to a beam with a finite number of collocated piezoelectric actuator/sensor pairs, while ordinary beam will refer simply to the beam itself without any actuators or sensors. A smart beam differential equation had been derived by the same procedure that the Bernoulli-Euler equation derived with some mathematical modifications to be applicable for the smart beam actuating by any type of applied load such as static or cyclic. The engineering control techniques was used to obtain the solution of proposed differential equation where with some auxiliary equations and modifications a block diagram as the applied load be the input and as the smart beam deflection be the output was constructed as shown later. Also in this research, a beam deflection reduction system with a lead network controller and a high voltage amplifier has been designed mainly for two reasons: the first was to amplify the voltage generated by the sensor to be able to handle and transmit it efficiently to the actuator. And the second was to enhance the system response.

THE THIN SMART BEAMS GOVERNING EQUATION

Now, the derivation of the smart beam differential equation actuated by an external load (static or cyclic) will be accomplished. Let us consider a setup as shown in **Fig.(1)**, where *m* of identical collocated piezoelectric actuator/sensor pairs are bonded to a beam. The assumption that all piezoelectric transducers are identical is only adopted to simplify the derivations, and can be removed if necessary. The i^{th} actuator is exposed to a voltage of $e_{ai}(t)$ and the voltage induced in the i^{th} sensor is $e_{si}(t)$. We assume that the beam has a length of l_b, width of w_b, and thickness of t_b Corresponding dimensions of each piezoelectric transducer are l_p, w_p, and t_p. Furthermore, we denote the transverse deflection of the beam at point *x* and time *t* by *v*(*x*, *t*).

It is well known that Bernoulli-Euler equation governs the transverse vibration of beams. Therefore, the derivation of the smart beam equation will follow the same procedure that used in derivation of Bernoulli-Euler equation but with changing the applying load condition.

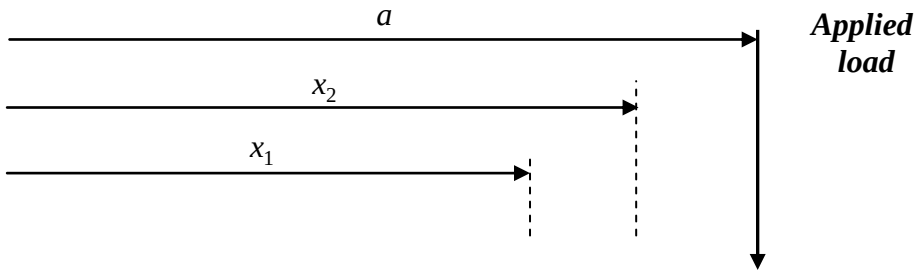

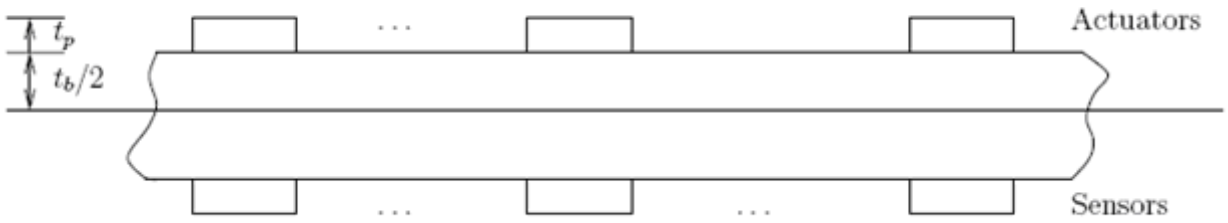

Fig.(1) A Beam with A Finite Number of Collocated Piezoelectric Actuator/Sensor Pairs and Applied Load

Consider a beam in bending, in the *x*-*y* plane, with *x* as the longitudinal axis and *y* as the transverse axis, of bending deflection, as shown in **Fig.(2)**. The required equation is developed by considering the bending moment– deflection relation, rotational equilibrium, and transverse dynamics of a smart beam element.

Rotatory Dynamics (Equilibrium)

Consider the beam element δx, as shown in **Fig.(2)**, where forces and moments acting on the element are indicated.

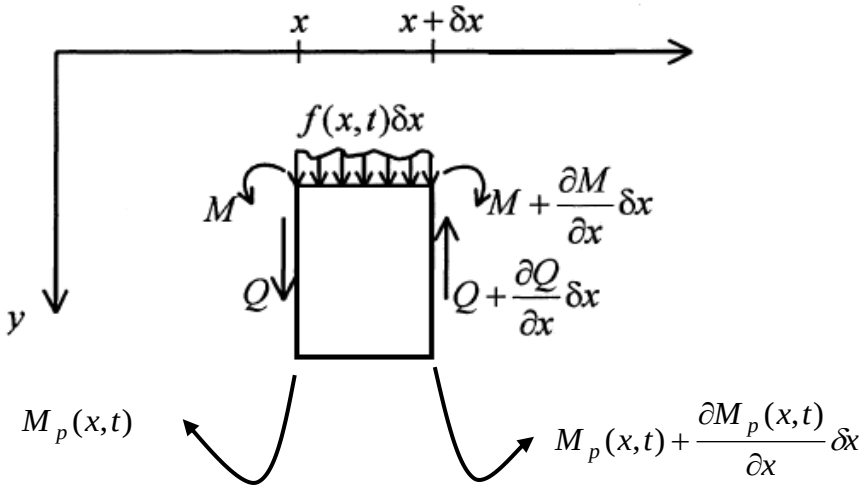

Fig.(2) Dynamic of a Beam Element in Bending

Here, $f(x,t)$ is the excitation force per unit length acting on the beam in the transverse direction at location *x*, and $M_p(x,t)$ is the total moment that generated by all the actuators and can expressed by

$$M_p(x,t)=\sum_{i=1}^{m} M_{pi}(x,t) \qquad (1)$$

Where *m* is the number of identical collocated piezoelectric actuator / sensor pairs which are bounded to the beam. The equation of the angular motion is given by the equilibrium condition of moments:

$$M - M_p(x,t) + Q\delta x - \left(M + \frac{\partial M}{\partial x}\partial x\right) + \left(M_p(x,t) + \frac{\partial M_p(x,t)}{\partial x}\partial x\right) = 0 \qquad (2)$$

where the moment deflection relation can expressed as

$$M = E_b I_b \frac{\partial^2 v}{\partial x^2} \tag{3}$$

simplifying **Eq.(2)** and substituting **Eq.(3)** into it will give

$$Q = \frac{\partial}{\partial x}\left(E_b I_b \frac{\partial^2 v}{\partial x^2} \right) - \frac{\partial M_p(x,t)}{\partial x} \tag{4}$$

Transverse Dynamics

The equation of transverse motion (Newton's second law) for element δx is

$$(\rho_b A_b \delta x)\frac{\partial^2 v}{\partial t^2} = f(x,t)\delta x + Q - \left(Q + \frac{\delta Q}{\partial x}\delta x \right) \tag{5}$$

Here, ρ is the mass density of the beam material, more simplifying will give

$$\rho_b A_b \frac{\partial^2 v}{\partial t^2} + \frac{\partial Q}{\partial x} = f(x,t) \tag{6}$$

Now, substituting **Eq.(4)** into **Eq.(6)**, one will obtain the governing equation of forced transverse vibration of smart beam with finite number of actuators

$$\rho_b A_b \frac{\partial^2 v}{\partial t^2} + \frac{\partial^2}{\partial x^2}\left(E_b I_b \frac{\partial^2 v}{\partial x^2} \right) = \frac{\partial^2 M_p(x,t)}{\partial x^2} + f(x,t) \tag{7}$$

THE ENGINEERING CONTROL SOLUTION

Now, **Eq.(7)** will be solved by using the linear engineering control techniques, but this deferential equation must be linearized to be able for handling it and this done firstly by specifying the case of study where a simply supported beam has been chosen, and follow the below procedure

Beam and Actuator Equation

If young's modules and second moment of area about the neutral axis are constant then

$$\rho_b A_b \frac{\partial^2 v}{\partial t^2} + E_b I_b \frac{\partial^4 v}{\partial x^4} = \frac{\partial^2 M_p(x,t)}{\partial x^2} + f(x,t) \tag{8}$$

As shown in **Fig.(1)** where the actuating force is applied at $x = a$, then by using Dirac delta **Eq.(8)** can be rewrite as

$$\rho_b A_b \frac{\partial^2 v}{\partial t^2} + E_b I_b \frac{\partial^4 v}{\partial x^4} = \frac{\partial^2 M_p(x,t)}{\partial x^2} + f(t)\delta(x-a) \tag{9}$$

And the moment exerted on the beam by the i^{th} actuator can expressed **(Moheimani and Fleming, 2006)** as

$$M_{pi}(x,t) = \bar{k}\, e_{ai}(t)\left[u(x-x_{1i}) - u(x-x_{2i})\right] \tag{10}$$

where $u(x)$ is a unit step input and $\bar{k}$ was formulated by **(Zhang, Meng, and Li, 2006**) as

$$\bar{k} = \frac{E_b\, E_p t_b^2 w_b\, w_p d_{31}}{E_b\, t_b\, w_b + E_p t_p w_p} \tag{11}$$

Substitute that

$$v(x,t) = \sum_{k=1}^{\infty} Y_k(x) q_k(t) \tag{12}$$

where normalized mode shapes for the simply supported beam are **(De Silva, 2000)**

$$Y_k(x) = \sin k\pi x / l_b \tag{13}$$

where $k = 1, 2, 3, \cdots$

multiply by $Y_j(x)$; integrate over $x = [0, l_b]$ and use the orthogonality of mode shapes to obtain

$$E_b I_b \left(\frac{i\pi}{l}\right)^4 \frac{l}{2} q_j(t) + \rho_b A_b \frac{l}{2} \ddot{q}_j = \bar{k}\, \psi_{ji}\, e_{ai}(t) + f(t) \sin \frac{j\pi a}{l} \tag{14}$$

where

$$\psi_{ji} = \int_0^l Y_j(x)\left[\delta'(x-x_{1i}) - \delta'(x-x_{2i})\right] dx \tag{15}$$

and using the derivative Dirac delta function property stated by **(Moheimani and Fleming, 2006)**, will have

$$\psi_{ji} = Y_j'(x_{2i}) - Y_j'(x_{1i}) \tag{16}$$

now **Eq.(14)** can be rewrite as

$$\ddot{q}_j + \omega_j^2\, q_j(t) = \gamma \psi_{ji}\, v_{ai}(t) + \alpha_j\ f(t) \tag{17}$$

Where $\omega_1 = \left(\frac{\pi}{l_b}\right)^2 \sqrt{\frac{E_b I_b}{\rho_b A_b}}$ (18)

$$\omega_j = j^2 \omega_1 \tag{19}$$

$$\alpha_j = \frac{2}{\rho_b A_b l_b} \sin j \frac{\pi a}{l_b} \tag{20}$$

$$\gamma = \frac{2\bar{k}}{\rho_b A_b l_b} \tag{21}$$

To this end we point out that the differential equation **Eq.(17)** dose not contain a term to a count for the natural damping associated with beam. The presence of damping can be incorporated into **Eq.(17)** by adding the term $2\zeta_j\omega_j\dot{q}_j$ to **Eq.(17)**. This results in the differential equation

$$\ddot{q}_j + 2\zeta_j\omega_j q_j + \omega_j^2 q_j(t) = \gamma v_{ai}(t) + \alpha_j \ f(t) \tag{22}$$

Applying the Laplace transform to **Eq.(22)**, assuming zero initial conditions and solving for beam deflection and for N mode shapes, will get

$$V(s) = \gamma \sum_{j=1}^{N} \frac{\psi_{ji} Y_j(x)}{s^2 + 2\zeta_j\omega_j s + \omega_j^2} E_{ai}(s) + \sum_{j=1}^{N} \frac{\alpha_j Y_j(x)}{s^2 + 2\zeta_j\omega_j s + \omega_j^2} F(s) \tag{23}$$

Sensor Equation

The voltage generated by the i^{th} piezoelectric sensor e_{si} can be expressed as **(Moheimani and Fleming, 2006)**

$$e_{si}(t) = \frac{d_{31} E_p W_p}{C_p} \int_{x_{1i}}^{x_{2i}} \varepsilon_{si} \, dx \tag{24}$$

The expression of the mechanical strain in sensor patch can be obtained from **(Moheimani and Fleming, 2006)**

$$\varepsilon_{si} = -\left(\frac{t_b}{2} + t_p\right)\frac{\partial^2 v_i}{\partial x^2} \tag{25}$$

Now $e_{si}(t)$ will be

$$e_{si}(t) = -\left[\frac{d_{13} E_p W_p}{C_p}\left(\frac{t_b}{2} + t_p\right)\sum_{j=1}^{N}\frac{\psi_{ji}}{Y_j}\right] v_i(t) \tag{26}$$

Applying Laplace transform to result equation, assuming zero initial condition we get

$$\frac{E_{si}(s)}{V(s)} = -\frac{d_{13} E_p W_p}{C_p}\left(\frac{t_b}{2} + t_p\right)\sum_{j=1}^{N}\frac{\psi_{ji}}{Y_j} = -\sum_{j=1}^{N} k_{ji} \tag{27}$$

ORDINARY BEAMS GOVERNING EQUATION

Starting from Bernoulli-Euler equation for constant young's modules and second moment of area about the neutral axis and for the actuating force is applied at $x = a$, and following the previous derivation procedure and for *N* mode shape, will have

$$\frac{V(s)}{F(s)} = \sum_{j=1}^{N}\left[\frac{\alpha_j Y_j(x)}{s^2 + 2\zeta_j\omega_j s + \omega_j^2}\right] \tag{28}$$

SMART BEAM BLOCK DIAGRAM

A complete block diagram representing the smart beam had been constructed, where Form the previous derived equations and with some block diagram modification, the block diagram that shown in **Fig.(4)** had obtained

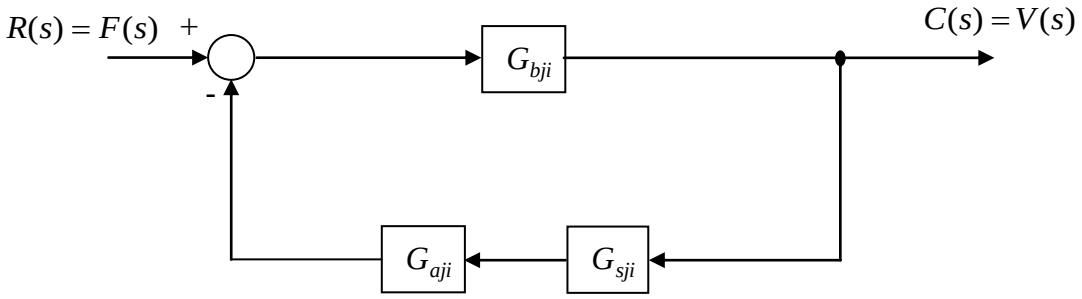

Fig.(4) The Block Diagram for Smart Beam with *m* Collocated Piezoelectric Actuator / Sensor Pairs and Infinite Beam Vibration Mode Shapes

The transfer function matrix G_{bj} shown in **Fig.(4)** consists of a very large number of parallel second order terms while the transfer functions G_{sji} and G_{aji} have a m number of parallel terms, and there values can be expressed as

$$G_{bj} = \sum_{j=1}^{N} \frac{\alpha_j Y_j}{s^2 + 2\zeta_j \omega_j s + \omega_j^2} \tag{29}$$

$$G_{sji} = \sum_{i=1}^{m} \sum_{j=1}^{N} k_{ji} \tag{30}$$

$$G_{aji} = \gamma \sum_{i=1}^{m} \sum_{j=1}^{N} \frac{\psi_{ji}}{\alpha_j} \tag{31}$$

In most scenarios, only control of a limited bandwidth is of importance. Typically N modes of the structure would fit within this bandwidth while modes $N + 1$ and above are left uncontrolled. The uncontrolled modes, however, do exist and have the potential to destabilize the closed-loop system. Therefore, the existence of these modes should be taken into account, and a controller should be designed to ensure adequate damping performance, as well as stability in the presence of these out-of-bandwidth modes.

THE PROPOSED INSTRUMENTATION

Practically, the voltage generated by the piezoelectric sensor was very small to handle and transmitted to the piezoelectric actuator, therefore, the needs for an integrated instruments system not only for amplifying purpose but also for controlling the beam response. **Fig.(5)** shows the overall proposed system components. And the block diagram representing this system is shown in **Fig.(6)**.

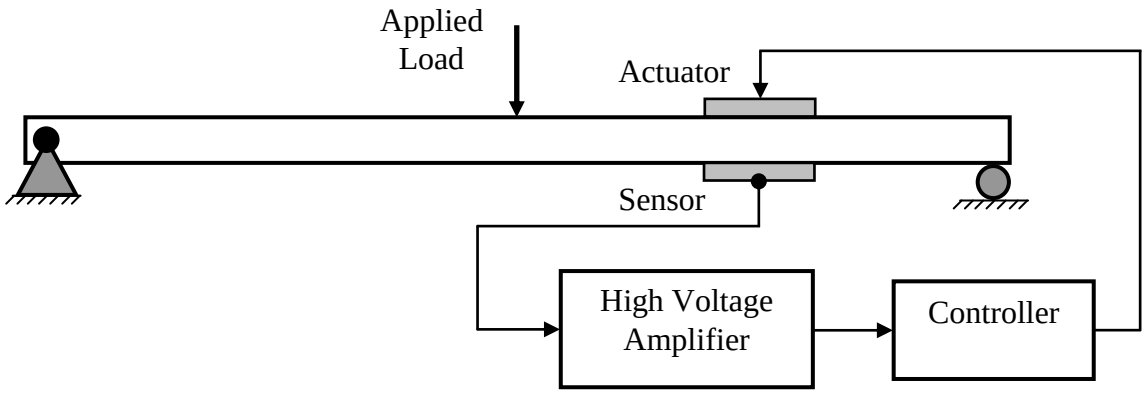

Fig.(5) The Proposed Instrumentation

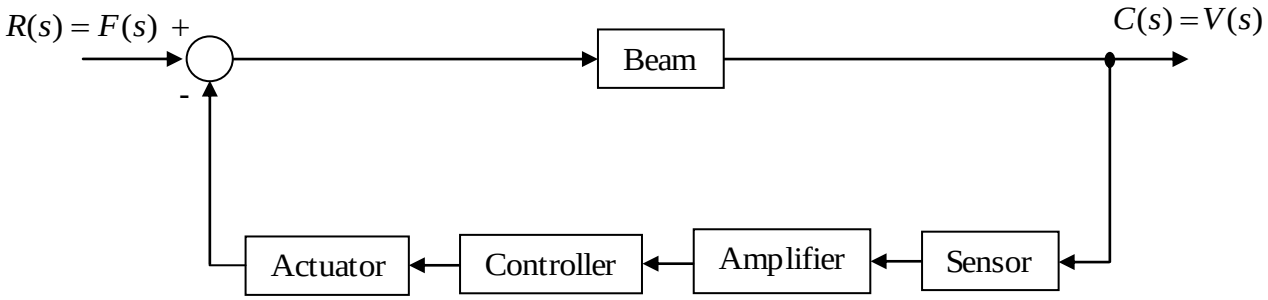

Fig.(6) Smart Beam With Controller And Amplifier Block Diagram

FIRST MODE CONTROLLER DESIGN

Because of the unique properties for the lead net work controller shown in **Fig.(7)** especially it property to accelerate the system response. For performing the controller design some physical properties for the desired system response must be assumed in order to be achieved by the controller operation.

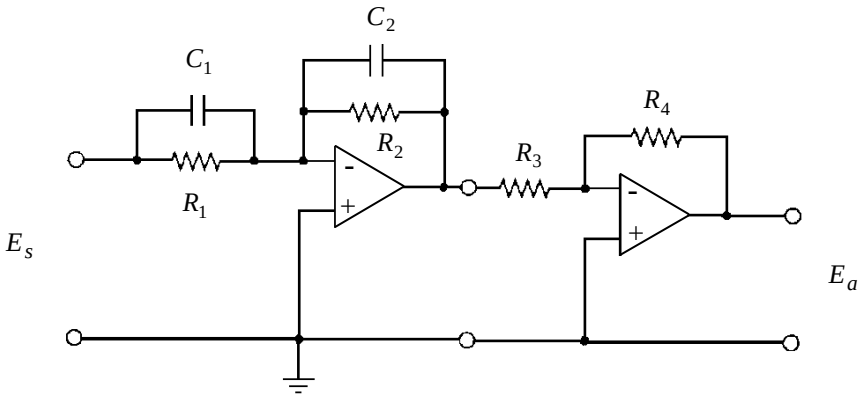

Fig.(7) Electronic Circuit of A Lead Network

The transfer function of the lead network compensator can be expressed as **(Ogata, 2002)**

$$G_c = K_c \alpha \frac{Ts+1}{\alpha Ts+1} \tag{32}$$

Referring to **Fig.(5)** , $T = R_1C_1$, $\alpha T = R_2C_2$, $K_c = \frac{R_4C_1}{R_3C_2}$, and $\alpha = \frac{R_2C_2}{R_1C_1}$

The Bode diagram for the smart beam is shown in **Fig.(8)**, and after executing the control system design by frequency response procedure as stated by **(Ogata, 2002)**, for static velocity error about $50\,s^{-1}$ and at least 100° phase margin. After calculations the following controller transfer function will obtained

$$G_c = \frac{1.4(s+47.5)}{(s+135.1)}$$

Where $K_c = 1.4$, $\alpha = 0.35$, and $T = 0.022$. The system with the controller Bode diagram is shown in **Fig.(9)**

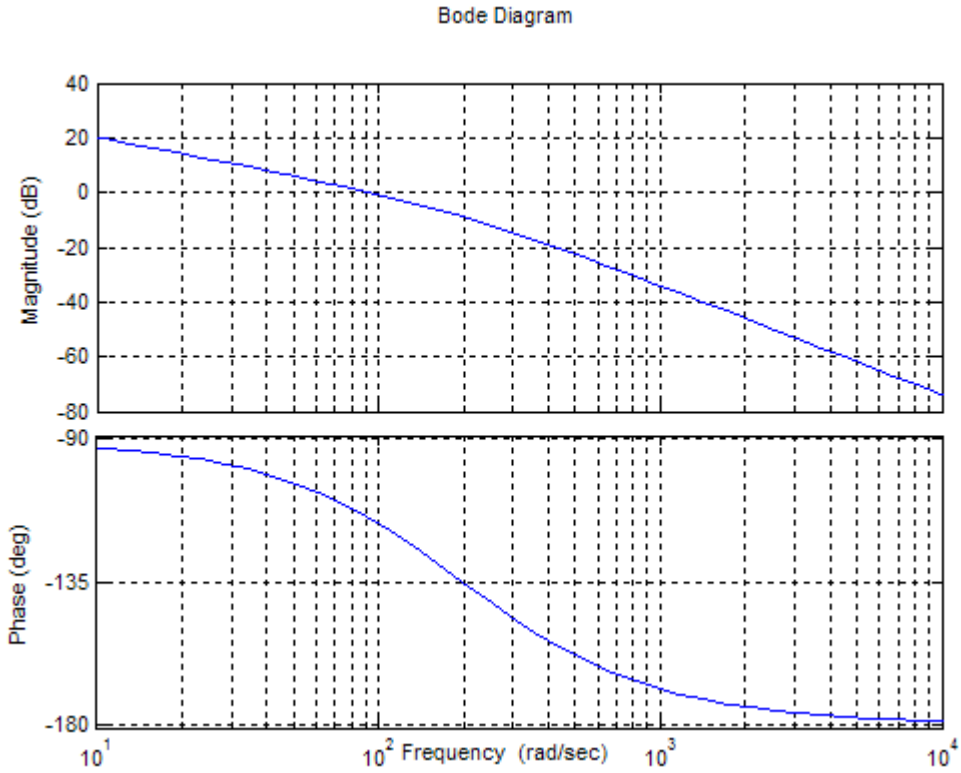

Fig.(8) Bode Diagram for First Mode Simply Supported Thin Smart Beam

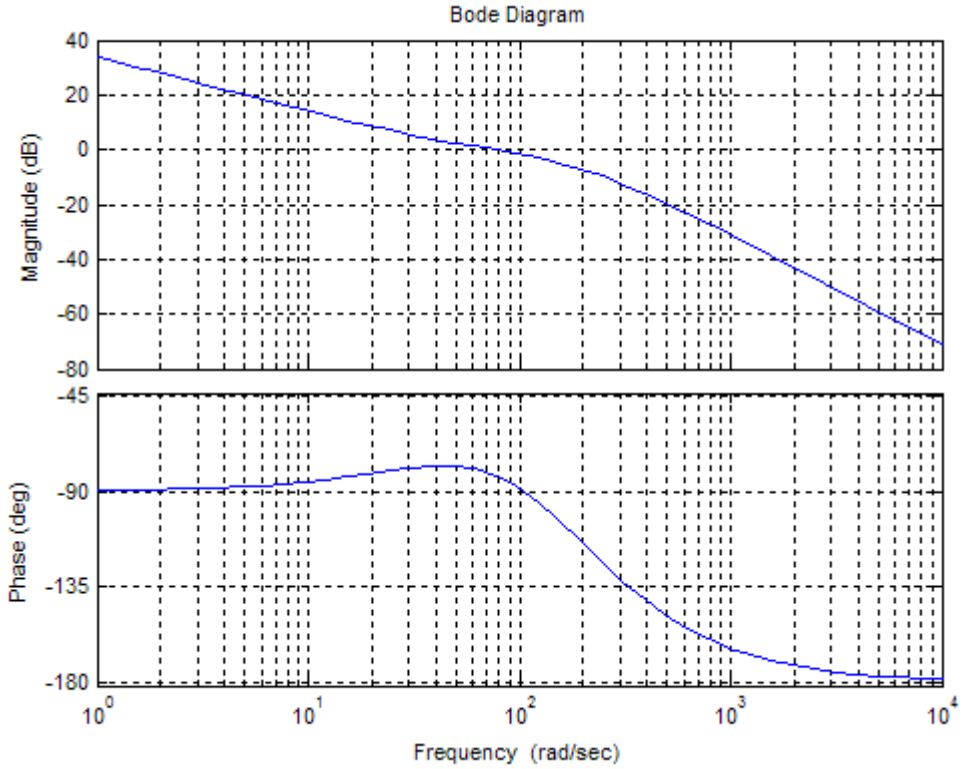

Fig.(9) Bode Diagram for Compensated First Mode Simply Supported Thin Smart Beam

FIRST MODE HIGH VOLTAGE AMPLIFIER

After studying and analyzing the block diagram of the proposed system without controller, for the first mode case. In the present paper, the voltage amplifier gain for the i^{th} collocated piezoelectric actuator / sensor pair was formulated to be

$$K_a = \frac{\omega_1^2}{\gamma \psi_{1i} k_{1i}} \tag{33}$$

RESULTS AND DISCUSSION

SIMULINK / MATLAB software was constructed to simulate the proposed system block diagram. The properties that listed in **Table (1)** which was adopted from **(Moheimani and Fleming, 2006)** had been used as numerical values for such software.

The simulation results of the ordinary beams are showing the high accuracy of the ordinary beam transfer function in comparing with the analytical solution given by any text.

Many cases had been studied for the first mode vibration and for static deflection, where the type of the applied load was changed, the number of collocated piezoelectric was varied, and the beam damping ratio also was varied. **Fig.(10)** to **Fig.(17)** show the results of the software simulations for different cases where the applied load was about 10 *N*, all the piezoelectric collocated pairs configurations exhibit a significant reduction in smart beam deflection in compare with the ordinary beam deflection, as example in the case of cyclic load with $\zeta = 0.7$ about 42% deflection reduction for single piezoelectric collocated pair at $x = l/2$, about 52% deflection reduction, for double piezoelectric collocated pairs at $x_1 = l/4$ and $x_2 = 3l/4$, and about 65% deflection reduction for three piezoelectric collocated pairs at $x_1 = l/4$, $x_2 = l/2$, and

$x_3 = 3l/4$.For the static load cases, the simulation results was decided to introduce for a very short time about 1 *s*, and this for showing the beam transient response and effect of the controller. Where with $\zeta = 0.7$ about 34% deflection reduction for single piezoelectric collocated pair at $x = l/2$, about 40% deflection reduction, for double piezoelectric collocated pairs at $x_1 = l/4$ and $x_2 = 3l/4$, and about 55% deflection reduction for three piezoelectric collocated pairs at $x_1 = l/4$, $x_2 = l/2$, and $x_3 = 3l/4$.

The simulation of the smart beam without voltage amplifier and lead controller was didn't exhibits any valuable reduction in beam deflection and this was expected because of the voltage that generated by the sensor can not initiate the actuator to be strained to the required limit, and this lead us to assemble the system shown in **Fig.(5)**, where the voltage amplifier was designed to obtain the required actuator stain while the controller was designed to obtain the desired beam response.

Beam Properties	
Length	550 *mm*
Thickness	3 *mm*
Width	50 *mm*
Density	$2.77\times10^{3}\ kg/m^{3}$
Young's Modules	$7\times10^{10}\ N/m^{2}$
PZT Properties	
Length	50 *mm*
Thickness	0.25 *mm*
Width	25 *mm*
Charge constant	$-210\times10^{-12}\ m/V$
Young's Modules	$6.3\times10^{10}\ N/m^{2}$
Capacitance	115 *nF*

Table (1) Numerical Values

CONCOLUSIONS

The principle of operation of the proposed system is to reduce the beam deflection for any external load situation and this was done by bonded a number of finite of collocated actuator / sensor pairs working to generate an additional moment operate inversely to reduce the effect of the applied load.

It has been shown practically that the best result of deflection reduction is obtained by increasing the number of the collocated actuator / sensor pairs for the case of multi collocated actuator / sensor pairs, but for single collocated actuator / sensor pair the best reduction is done if the collocated actuator / sensor pair is bonded exactly at the location of load application

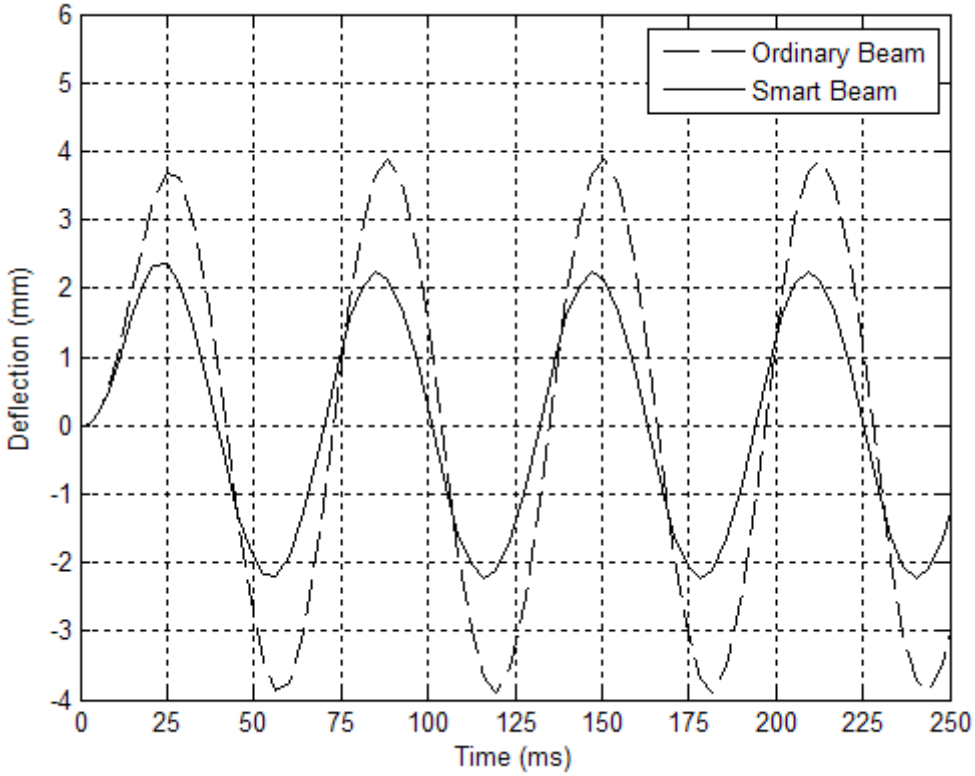

Fig.(10) First Mode Beams Vibrations with $\zeta = 0.7$. The Smart Beam with Single Collocated Piezoelectric Actuator / Sensor Pair at $x = l/2$

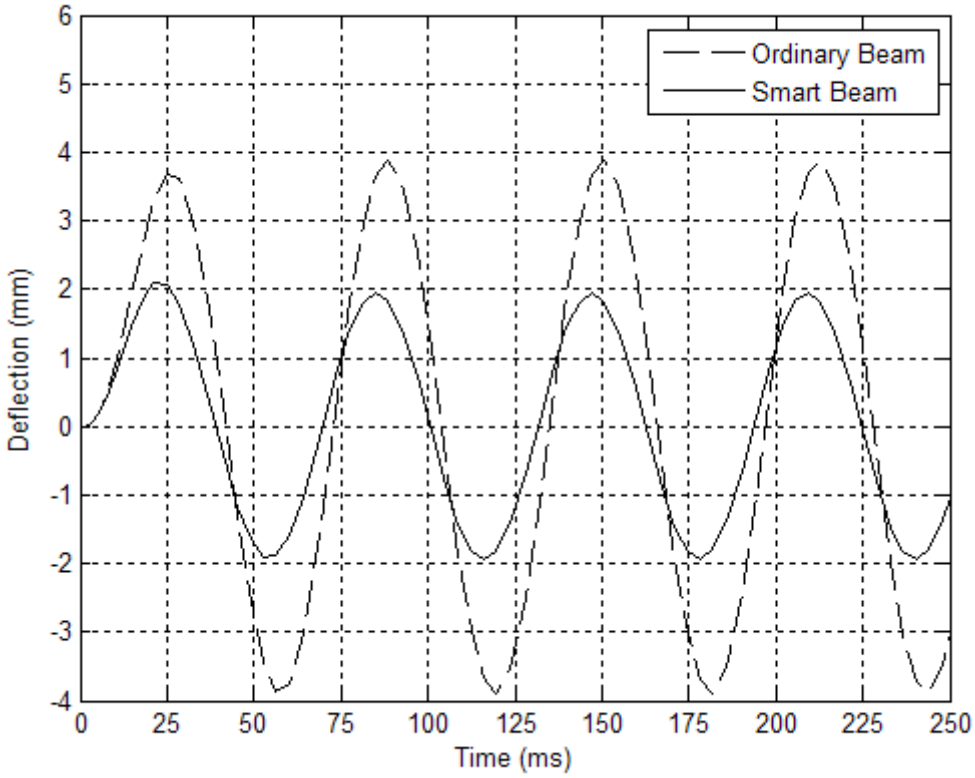

Fig.(11) First Mode Beams Vibrations with $\zeta = 0.7$. The Smart Beam with Double Collocated Piezoelectric Actuator / Sensor Pairs at $x_1 = l/4$ and $x_2 = 3l/4$.

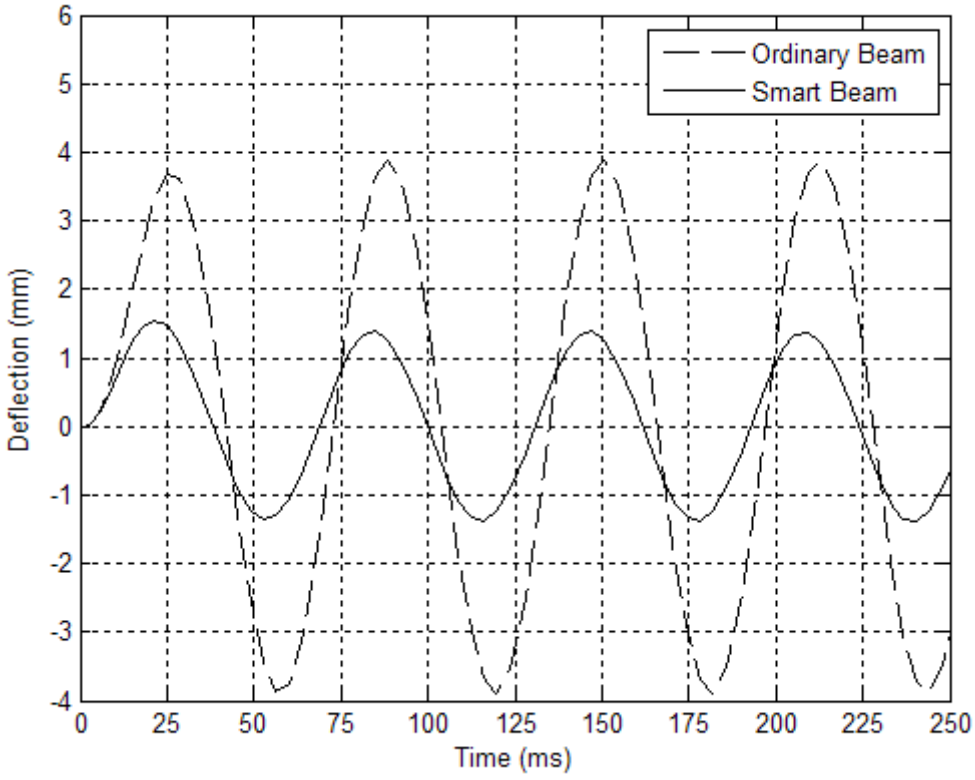

Fig.(12) First Mode Beams Vibrations with $\zeta = 0.7$. The Smart Beam with Three Collocated Piezoelectric Actuator / Sensor Pairs at $x_1 = l/4$, $x_2 = l/2$, and $x_3 = 3l/4$

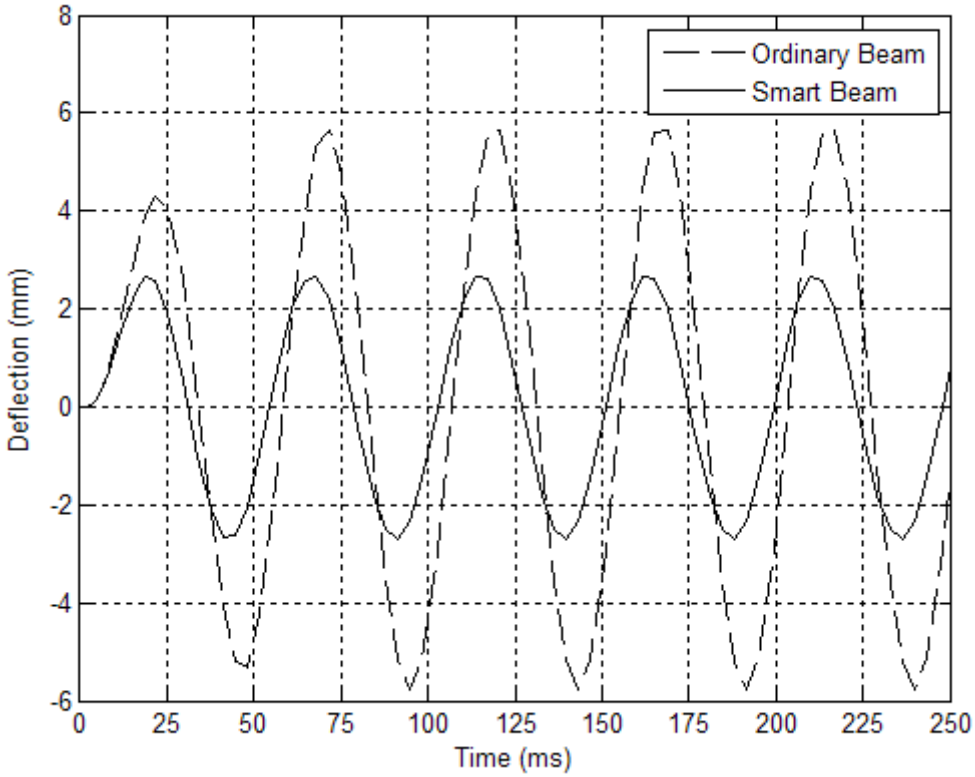

Fig.(13) First Mode Beams Vibrations with $\zeta = 0.4$. The Smart Beam with Single Collocated Piezoelectric Actuator / Sensor Pair at $x = l/2$.

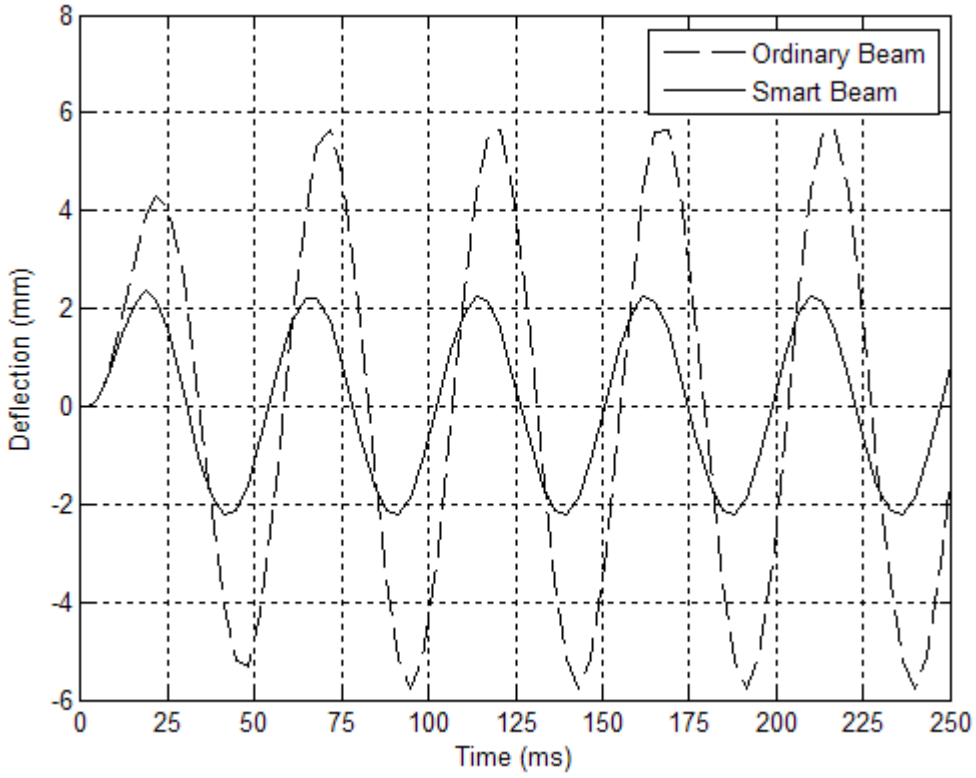

Fig.(14) First Mode Beams Vibrations with $\zeta = 0.4$. The Smart Beam with Double Collocated Piezoelectric Actuator / Sensor Pairs at $x_1 = l/4$ and $x_2 = 3l/4$

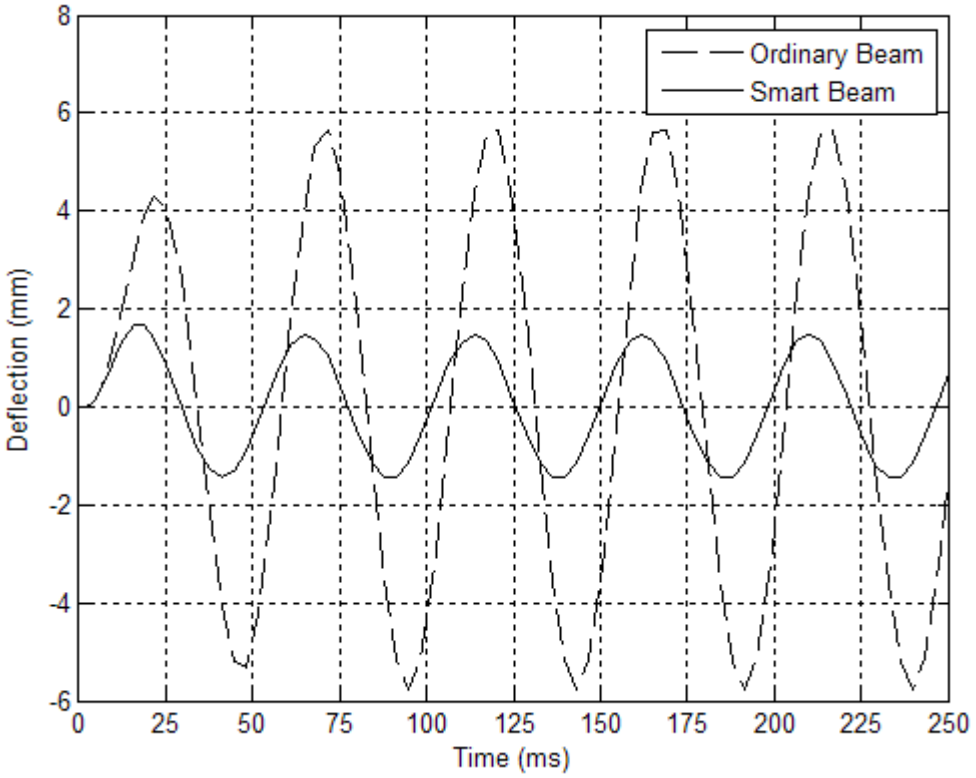

Fig.(15) First Mode Beams Vibrations with $\zeta = 0.4$. The Smart Beam with Three Collocated Piezoelectric Actuator / Sensor Pairs at $x_1 = l/4$, $x_2 = l/2$, and $x_3 = 3l/4$.

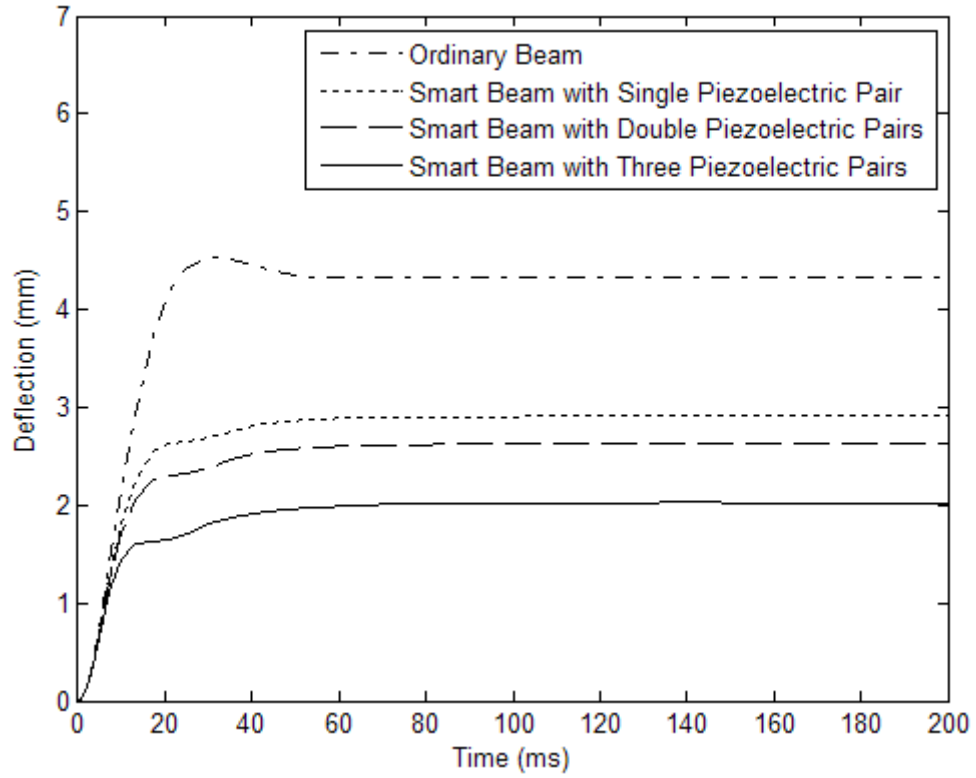

Fig.(16) Static Load Beams Deflections with $\zeta = 0.7$

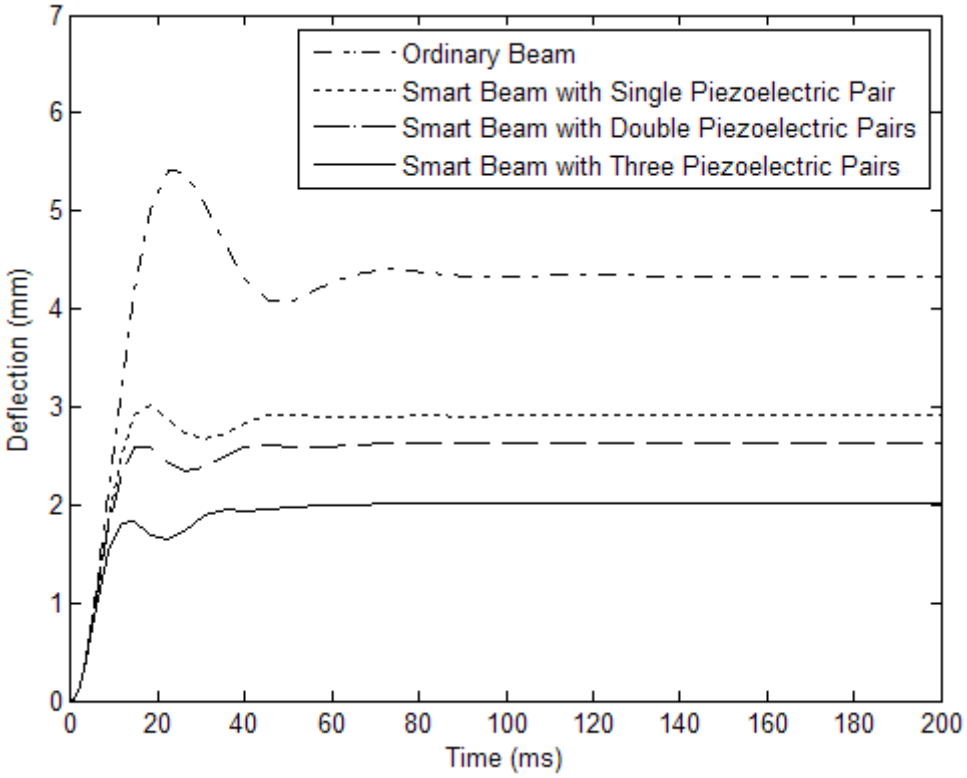

Fig.(17) Static Load Beams Deflections with $\zeta = 0.4$

REFERENCES

Aldraihem, O. J., Singh, T., and Wetherhold, R. C. (1997). Realistic determination of the optimal size and location of piezoelectric actuator/sensor. IEEE proceedings of the international conference on control applications, Piscataway, NJ (pp.435–440).

Bailey, T., and Hubbard Jr., J. E. (1986). Distributed piezoelectric polymer active vibration control of a cantilever beam. Journal of Guidance, 8(5), 605–611.

Belouettar S. , Azrar L., Daya E. M., Laptev V., and Potier-Ferry M. (2007). Active control of nonlinear vibration of sandwich piezoelectric beams: A simplified approach. Computers and Structures

Choi, S. B., Park, Y. K., and Fukuda, T. (1998). A proof of concept, investigation on active vibration control of hybrid smart structures. Mechatronics, 8, 673–689.

Clark, R. L., Saunders, W. R., and Gibbs, G. P. (1998). Adaptive structures: Dynamics and control. New York: Wiley.

Crawley, E.F. , and Luis, J.D.(1987).Use of piezoelectric actuators as elements of intelligent structures. AIAA Journal, 25(10),1373–1385.

De Silva C. W. (2000). Vibration: Fundamentals and Practice. Boca Raton, CRC Press LLC.

Halim, D., and Moheimani, S. O. R. (2002). Experimental implementation of spatial H-Infinity control on a piezoelectric laminated beam. IEEE/ASME Transactions on Mechatronics, 7(3), 346–356.

Hamdan, A.M. , and Nayef, A. H.(1989).Measure of modal controllability and observability for

first- and second-order linear systems. Journal of Guidance, Control and Dynamics (AIAA), 12(3), 421–428.

Kermani M. R., Moallem M., and Patel R. V (2004). Parameter selection and control design for vibration suppression using piezoelectric transducers. Control Engineering Practice 12, 1005-1015.

Kim, Y., and Junkins, J. L. (1991). Measure of controllability for actuator placement. Journal of Guidance, Control and Dynamics (AIAA), 14(5), 895–902.

Lim, K.B. , and Gawronski, W.(1993).Actuator and sensor placement for control of Flexible structures. In C.T. Leondes (Ed.), Control and dynamic systems, Advances in theory and applications, Vol.57(pp.109–152). New York: Academic Press.

Moheimani, S.O.R and Fleming J. Andrew (2006). Advances in Industrial Control. Copyright by Springer-Verlag London Limited.

Moheimani, S.O.R. , and Ryall, T.(1999). Consideration on placement of piezoelectric actuators that are used in structural vibration control. IEEE proceedings of the conference on decision and control, Phoenix, AZ (pp.1118–11 23).

Moore, B.C.(1981).Principal component analysis in linear systems: Controllability, observability and model reduction. IEEE Transactions on Automatic Control, 26(1), 17–32.

Moses, R.W. (1997).Vertical tail-buffeting alleviation using piezoelectric actuators—Some results of buffet-affected tails (ACROBAT) program. Proceedings of SPIE, Vol.3044 (pp.87–98).San Diego, CA, USA.

Ogata K. (2002). Modern Control Engineering. Fourth Edition, published by Prentice Hall, Inc.

Patnaik, B., Heppler, G. R., and Wang, D. (1992). Stability analysis of a piezoelectric vibration controller for an Euler–Bernoulli beam. American control conference, San Francisco, CA.

Shen, Y., Homaifar, A., and Chen, D. (2000). Vibration control of flexible structures using fuzzy logic and genetic algorithm. American control conference, Vol.1 (pp.448–452). Chicago, IL,USA.1014 M.R. Kermani et al. / Control Engineering Practice 12 (2004) 1005–1015

Smits, J.B. , and Choi, W.(1991).The constituent equations of piezoelectric heterogeneous Bimorphs. IEEE Transactions on Ultrasonics, Ferroelectrics and Frequency Control, 38(3), 256–270.

Sun, D., and Mills, J. K. (1999a). Application of smart material actuators for control of a single-link flexible manipulator. International federation of automatic control (IFAC) world congress, Beijing, China.

Sun, D., and Mills, J. K. (1999b). Study on piezoelectric actuators in control of a single-link flexible

manipulator. IEEE international conference on robotics and automation, Vol.2 (pp.849–854).Detroit, Michigan, USA.

Vasques C. M. A. and Dias Rodrigues (2006). Active vibration control of smart piezoelectric beam: J Comparison of classical and optimal feedback control strategies. Computers and Structures 84, 1402-1414.

Wang, Q.M. , and Cross, L.E.(1999).Constitutive equations of symmetrical triple layer piezoelectric benders. IEEE Transactions on Ultrasonics, Ferroelectrics and Frequency Control, 46(6), 1343–1351.

Yaghoobi, H., and Abed, E. H. (1999). Optimal actuator and sensor placement for modal and stability monitoring. IEEE proceedings of the American control conferences, San Diego, LA, pp.3702–3707.

Yong, L., Onoda, J., and Minesugi, K. (2002). Simultaneous optimization of piezoelectric actuator placement and feedback for vibration suppression. Acta Austronautica, 50(6), 335–341.

Zhang W., Meng G., Li H. (2006). Adaptive vibration control of micro-cantilever beam with piezoelectric actuator in MEMS. J Advance Manufacturing Technology, 321-327.

NOMENCLATURE

(SI units are used, unless otherwise stated)

A	The location of the applied load
A_b	The beam cross-sectional area
$C_1, and\, C_2$	The controller capacitances
C_p	The piezoelectric constant
d_{31}	The piezoelectric charge constant
e_{ai}	The exposed voltage to the i^{th} actuator
E_b	The beam Young's modules
E_p	The piezoelectric Young's modules
e_{si}	The voltage induced by the i^{th} sensor
f	The applied external force
I_b	The beam second moment of area
$\bar{k}$	A piezoelectric constant
K_a	The high voltage amplifier gain
K_c	The controller gain
l_b	The beam length
l_p	The piezoelectric length
m	The total number of the collocated piezoelectric actuator / sensor pairs
M_{pi}	The piezoelectric actuator control moment generated by the i^{th} actuator
M	The applied external moment
N	The controlled vibration mode number
Q	The external shear force
$R_1, R_2, R_3\, and\, R_4$	The controller resistances
T	The time
T	The controller time constant
t_b	The beam thickness
t_p	The piezoelectric thickness
$u(x)$	The unit step function
v	The beam deflection
w_p	The piezoelectric width
w_b	The beam width
x_{1i}	The location of the closer edge of the i^{th} piezoelectric
x_{2i}	The location of the further edge of the i^{th} piezoelectric
x_i	The location of the center of the i^{th} piezoelectric
$Y_k(x)$	The normalized mode shapes
α	The controller constant
α_j	A constant for j mode
ε_{si}	The mechanical strain of the i^{th} piezoelectric sensor
ψ_{ji}	Piezoelectric constant for i^{th} piezoelectric and for j^{th} mode
γ	A beam constant

ω_j	The j^{th} natural frequency
ρ_b	The beam density
ρ_p	The piezoelectric density
ζ	The beam damping ratio

EFFECT OF OBSTACLE IN RIVER ON THE HEAT DISSIPATION OF HOT WATER INJECTION

Ayser M. Fleh
Mech. Engr. Dept.
College of Eng. /Univercity of Baghdad
Baghdad-Iraq

ABSTRACT

Numerical analysis of the cooling process of hot water discharge from a steam power plant into a river has been carried out in the present study. A mathematical model describing the flow field and temperature distribution induced in the river as a result of the cooling process is made based upon the assumptions of steady state, two-dimensional, turbulent flow, in the horizontal plane. The governing equations are the continuity, the momentum, the (K-ε) turbulence model and the energy equation. A proper initial and boundary condition are specified to be used in the solution of the governing equations. A numerical solution of the governing equations is made by using the control volume approach, with non-staggered grid technique and modified SIMPLE algorithm. The numerical solution is capable of calculating the velocity and temperature distributions of the calculation domain. The numerical results show that the developed algorithm is capable of calculating the flow field, properly and accurately. Results are obtained for ten cases of configuration, constant aspect ratio and weather conditions for Baghdad. The results show that the injection velocity effect on the temperature distribution and stream line , the exist of obstacle and its distance from the injection zone but the increase in injection temperature cause a small effect on temperature distribution and stream line.

الخلاصة

تقدم هذه الدراسة تحليلا عددياً لعملية تبريد الماء الساخن المتدفق من مكثفات محطات الطاقة الكهربائية الى النهر. فقد تم وضع نموذجاً رياضيا يصف طبيعة الجريان والتوزيع الحراري الحاصل في النهر نتيجة لعملية التبريد تلك, وقد أعتمد هذا النموذج على فرضيات منها حالة ألاستقرار,ثنائي البعد، الجريان مضطرب في المستوى الأفقي. يتضمن النموذج الرياضي أشتقاق المعادلات التفاضلية الجزئية للمسألة، والتي هي معادلات الاستمرارية، الزخم، معادلتي نموذج ($\kappa-\varepsilon$) للاضطراب ومعادلة الطاقة. بالاضافة الى ذلك . تم تعريف ظروف أبتدائية وحدية مناسبة لاستخدامها في حل المعادلات. تم حل المعادلات عددياً بأستخدام تقنية الحجم المحكوم مع شبكة غير مزحفة وطريقة (SIMPEL) المعدلة. للحل العددي القابلية على حساب توزيعات السرع ودرجات الحرارية. أظهرت النتائج العددية ان النموذج العددي الذي تم التوصل أليه له القابلية على حساب الجريان بصورة مناسبة ودقيقة ولقيمة ثابتة(نسبة طول النهر الى عرضها aspect ratio) وللظروف الجوية لمدينتة بغداد.ولقد أظهرت النتائج مياه النهر القريب من منطقة التدفق تتأثربزيادة سرعة التدفق,زيادة درجة الحرارة,قرب وبعد الجسم العائق وكذلك وجود العائق وتتأثر قليلا بزيادة درجة الحرارة.

KEY WORDS

Obstacle in River, Velocity and Temperature Field, Steady state, two-dimension, Horizontal Plane, Constant aspect ratio.

INTRODUCTION

Cooling water for steam power plants is in most cases supplied from rivers, lakes, artificial water ponds or cooling tower. Thermal pollution of water is considered a water temperature rise due to artificial reasons. Basically the rise at temperature may be observed naturally and be caused by many natural reasons. The degree of heating expressed in temperature may vary from several degrees(e.g. run-of waters from area exposed for solar radiation) up to extremely high degree(e.g. when lava flows into the ocean). If artificial reasons are concerned, the main impact associated to water temperature rise is generated by industry. Water with its high heat capacity is considered as good cooling medium in industry. It is estimated that electric generating plants are the main source of thermal pollution in rivers and water reservoirs **(H.Inhaber 2005).** Furthermore, nuclear power plants reject all heat to the cooling water system, and emit 50% more heat than heat than a fossil fuel stations (with a similar amount of produced electricity, **(Joyce and Port 1999)**). Nowadays the opinion predominates that thermal pollution due to hot waste water badly affects aquatic environment. Thermal shock can harm fish and organisms, and thermal enrichment, in spite of several positive aspects, (e.g. melting ice snow or warm water use in green houses) may be finally harmful for biocenosis (lack of dissolved oxygen). The main advantages of river are simplicity, low maintenance, and ability to operate for extended periods without the need for make-up water and, the low power requirements, as the only mechanical equipment needed are pumps for occasional addition of make up water. Circulating water pumps are of course needed by river, as by all other systems. Hot water from the condenser is simply dumped into a river and left to cool. Cool water from the river is returned to the condenser. The river performance is important to the efficiency of the power plant itself because a condenser operating at a lower temperature results in more turbine work and operating at a lower temperature. Results in more turbine work and cycle efficiency, and less heat rejection. It was found that a difference of (5 C) in the natural temperature of a cooling river between winter and summer reduces the thermal efficiency of power plant by approximately (1%) in summer **(A. Zukauskas 1976).** The present work deals with velocity and temperature distribution in a river as a means to evaluate heat dissipation. For such analysis values are needed for eddy viscosity and diffusivity. Literature survey indicates that value for these parameters used by other workers range between ($2.5 * 10^{-4}$ to $0.1*10^{-2}$ m^2/s).

The problem was investigated in literatures with different a approaches. **(American Society of Civil Engineering.1988)** the turbulence models regarding surface water flow.

(Nogano and Tagawa. 1990) made an improvement of the K-€ model in conjunction with an accurate prediction of the near-wall limiting behavior of turbulence and the final period of the decaylaw of free turbulence. This improved $k-\varepsilon$ model has been extended to predict the effects of adverse pressure gradients on shear layers, which most previously proposed models failed to do correctly**.(Anis AL-Layla and Hasan Al-Rizzo1990),** describes the development and calibration of a mathematical model for the Tigris River downstream of AL Mosul. The river stretch studied is 75km long extending from the Al Mosul Dam to Mosul city. The field work was conducted during the period from July to September 1986. Water samples were collected bimonthly from specified sampling points. **(Michael Manga and James W.Kirchner 2004)**, circulating groundwater transports heat. If groundwater flow velocities are sufficiently high, most of the subsurface heat transport can occur by advection. This is the case, for example, in the Cascades volcanic arc where much of the background geothermal heat is transported adjectively and **(Andrzej Pozlewicz2006),** Special attention is paid to electric generating plants where cooling water are mixed with a river. The study area covers the lower part of Odra River, near Szczecin, Poland, where the main thermal pollution sources are power plants and coal combustion is used in energy production. The river

flows through Szczecin in two beds linked by several canals, lake and creates a complex hydraulic system. The mean discharge flow rate in Odra River is 500-600 m^3/s, and the mean velocity 0.3-0.5 m/s.

MATHEMATICAL MODELING

The usual system of Cartesian coordinates will be adapted, the x-axis being along the wall, and the y-axis being at right angle to it. Injection will be accounted for by prescribing non-zero normal velocity component (V_w) at the wall. In the case of and $V_w>0$ will be used for injection, see **Fig (1).** Two-dimensional flow and heat transfer (w =0, $\partial/\partial z = 0$) ,Uniform suction or injection (V_w=constant).

Negligible axial diffusion ($\partial^2/\partial x^2 = 0$) .

According to the previously mentioned assumptions, the governing conservation and constitution laws will be presented here in terms of the geometry and coordinates system of **Fig (1)**.these are the continuity, the momentum, the (**k-ε)** turbulence model and the energy equations.

Continuity Equation

$$\frac{\partial}{\partial x}(\rho u)+\frac{\partial}{\partial y}(\rho v)=0 \qquad (1)$$

Momentum Equation in X-Direction;

$$\left(u\frac{\partial u}{\partial x}+v\frac{\partial u}{\partial y}\right)=-\frac{\partial P}{\partial x}+\frac{\partial}{\partial y}\left(\mu\frac{\partial u}{\partial y}\right)+\frac{\partial}{\partial y}\left(\mu_t\frac{\partial u}{\partial y}\right) \qquad (2)$$

Momentum Equation in Y-Direction;

$$\left(u\frac{\partial v}{\partial x}+v\frac{\partial v}{\partial y}\right)=-\frac{\partial P}{\partial y}+\frac{\partial}{\partial y}\left(\mu\frac{\partial v}{\partial y}\right)+\frac{\partial}{\partial y}\left(\mu_t\frac{\partial v}{\partial y}\right) \qquad (3)$$

The standard form of (K-ε) model is as follows:-

Turbulence Kinetic Energy Equation;

$$\left(u\frac{\partial \kappa}{\partial x}+v\frac{\partial \kappa}{\partial y}\right)=\frac{\partial}{\partial y}\left(\frac{\mu_t}{\sigma\kappa}\frac{\partial \kappa}{\partial y}\right)+\mu_t\left(\frac{\partial u}{\partial y}\right)^2-\rho\varepsilon \qquad (4)$$

And dissipation of turbulence kinetic energy equation;

$$\left(u\frac{\partial \varepsilon}{\partial x}+v\frac{\partial \varepsilon}{\partial y}\right)=\frac{\partial}{\partial y}\left(\frac{\mu_t}{\sigma\varepsilon}\frac{\partial \varepsilon}{\partial y}\right)+\mu_t c_{\varepsilon_1}\frac{\varepsilon}{\kappa}\left(\frac{\partial u}{\partial y}\right)^2-c_{\varepsilon_2}\rho\frac{\varepsilon^2}{\kappa} \qquad (5)$$

According to the high Reynolds number (κ-ε) turbulence model the turbulent viscosity μ_t is related to the turbulent kinetic energy (κ) and to the dissipation of turbulent kinetic energy (ε) through the expression

$$\mu_t = c_\mu \rho \frac{\kappa^2}{\varepsilon} \tag{6}$$

The effective viscosity (μ_{eff}) is related to the turbulent viscosity (μ_t) and to the molecular viscosity (μ) through the relation :-

$$\mu_{eff} = \mu + \mu_t \tag{7}$$

In the above equations, ($c_\mu, c_{\varepsilon_1}, c_{\varepsilon_2} \sigma_k, \sigma_\varepsilon$) are constants at high Reynolds number and the model constant $c_\mu, c_{\varepsilon_1}, c_{\varepsilon_2} \sigma_k, \sigma_\varepsilon$ are set to $c_\mu = 0.09, c_{\varepsilon_1} = 1.44, c_{\varepsilon_2} = 1.92$. Usually, the constant $\sigma_k and \sigma_\varepsilon$ are assigned to $\sigma_k = 1.0 and \sigma_\varepsilon = 1.3$ **(Launder and Spalding 1974)**

Energy Equation;

$$\rho\, cp\left(u\frac{\partial T}{\partial x} + v\frac{\partial T}{\partial y}\right) = \frac{\partial}{\partial y}\left(k\frac{\partial T}{\partial y}\right) + \frac{\partial}{\partial y}\left(k_t\frac{\partial T}{\partial Y}\right) \tag{8}$$

Where;

$$k_t = \frac{\mu_t cp}{\mathrm{Pr}_t} \tag{9}$$

For the evaluation of turbulent kinetic energy and dissipation at turbulent Kinetic energy, it is sufficed to fix their values at the near wall node (P) according to the following formula:-

$$\kappa_{\mathrm{P}} = \frac{\tau_\omega}{\rho c_\mu^{1/2}} \tag{10}$$

$$\varepsilon_{\mathrm{P}} = \frac{c_\mu^{3/4}}{V_{\mathrm{K}} y_{\mathrm{P}}} \kappa_{\mathrm{P}}^{3/2} \tag{11}$$

$$y^+ = \frac{\rho y_p c_\mu^{1/4} k_p^{1/2}}{\mu_l} \tag{12}$$

Where (y_p)is the normal distance of the near wall node (p) to the solid surface. In the above formula, (k) is the Von Karman constant (0.4187) and (E) is an integration constant that depends on the roughness of the wall. For a smooth wall constant shear stress, (E) has a value of (9.793).

The initial and boundary conditions of problem are shown in **Fig (2)**. All the previously discussed differential equations can be conveniently presented in the general form.

$$\frac{\partial}{\partial x}(\rho u\phi) + \frac{\partial}{\partial y}(\rho v\phi) - \frac{\partial}{\partial y}\left[\Gamma_\phi \frac{\partial \phi}{\partial y}\right] = s_\phi \tag{13}$$

In the above equation, ϕ identifies the dependent variables, Γ_ϕ is the appropriate exchange coefficient for the variable ϕ, and S_ϕ are the source term which includes both the sources of ϕ and any other terms which cannot find place on the left-hand side of **Eq. (13)**

The derived governing equations and the initial and boundary conditions in **Fig. (2)** will be solved numerically by using the control volume approach of **(Patanker1980).** The finite difference method (F.D.M.) will be used, and the details of the numerical solution will be described in the next article.

NUMERCAL SOLUTION

The general form **Eq. (13)** may by write as;

$$\frac{\partial}{\partial x}\left[\rho u\phi-\Gamma_\Phi\frac{d\phi}{dx}\right]+\frac{\partial}{\partial y}\left[\rho v\phi-\Gamma_\Phi\frac{d\phi}{dy}\right]=S_\Phi \qquad (14)$$

By defining J as the total flux which consists of convection and diffusion fluxes, or

$$J_x=\rho u\phi-\Gamma\frac{\partial\phi}{\partial x} \qquad (15)$$

$$J_y=\rho v\phi-\Gamma\frac{\partial\phi}{\partial y} \qquad (16)$$

Where J_x and J_Y are the total fluxes through faces normal to the x and y directions respectively with these definitions, **Eq. (14)** can be written

$$\frac{\partial J_x}{\partial x}+\frac{\partial J_y}{\partial y}=S_\Phi \qquad (17)$$

Eq. (17) was integrated by using the finite volume approach of **(Patenker 1980)**, see **Fig. (3)** The source term has been linerized, and the values at the control volume faces (e,w,n,s)are assumed to be found by linear interpolation (central difference) . The resulting final form of **Eq. (17)** becomes

$$\frac{\left(\rho_P\phi_P-\rho_P^\circ\phi_P^\circ\right)\Delta x\Delta y}{\Delta t}+J_e-J_w+J_n-J_S=\left(S_c+S_P\phi_P\right)\Delta x\Delta y \qquad (18)$$

$$a_P\phi_P=a_E\phi_E+a_W\phi_W+a_N\phi_N+a_S\phi_S+b$$

$$\begin{aligned}a_E&=D_eA(P_e)+Max[-F_e,o]\\ a_W&=D_wA(P_w)+Max[F_w,0]\\ a_N&=D_nA(P_n)+Max[-F_n,0]\\ a_S&=D_sA(P_s)+Max[F_s,0]\end{aligned} \qquad (19)$$

$$a_P^\circ=\frac{\rho_P^\circ\Delta x\Delta y}{\Delta t} \qquad b=S_c\Delta x\Delta y+a_P^\circ\phi_P^\circ \qquad (20)$$

$$a_P=a_E+a_W+a_N+a_S+a_P^\circ-S_P\Delta x\Delta y \qquad (21)$$

$$\begin{aligned}\phi_e &= \phi_E f_e + \phi_p[1-f_e]\\ \phi_w &= \phi_W f_w + \phi_p[1-f_w]\\ \phi_n &= \phi_N f_n + \phi_p[1-f_n]\\ \phi s &= \phi_S f_s + \phi_p[1-f_s]\end{aligned} \quad (22)$$

Generally

$$a_P\phi_P = \sum_{nb} a_{nb}\phi_{nb} + b \qquad nb = E,W,N,S \quad (23)$$

Where: b = Absolute part of the discredited equation

COMPUTER PROGRAMS

Computer programs are developed in FORTRAN 90 to perform the numerical solution formulated previously. The program consists of 3 main parts. The first is for grid generation. The second deals with solving the five non-linear, partial differential equations and the third deals with displaying the large quantity of results in a simplified form. In the first part of the program **(MESHGEN),** the mesh distribution of the model is generated. The resulting grid is stored in an external file and plotted on the screen for visual checking. In the second part **(MODEL)**, the five non-linear, partial differential equations (u-velocity momentum equation, continuity equation, turbulent kinetic energy equation (K), turbulent energy dissipation equation (ε) and energy equation (T) are solved. The equations are solved in a sequential order after applying the appropriate boundary condition to each equation. In the third part **(PLOT)**, the displaying of the large quantity of results in simplified standard windows graphics is made. This includes plotting the made, grid the velocity vectors and contour lines in **Fig.4**.

RESULTS AND DISCUSSION

The developed computational algorithm is tested for the take part in Tigris River 1000m long, 150m width and input river obstacle variable (dimensions, near river, further river) 5m long and 3m width. The obstacle near (+15m) and obstacle further (-15m) from injection. The Mach number was taken as (0.5), the free stream velocity (1m/s). Velocity injection equals to (0.1, 0.9m/s). The Reynolds number of the flow is ($1*10^7$) the temperature surface ($25C^\circ$) with the free stream pressure and temperature (101325 pa) and ($25C^\circ$) respectively. The Iraqi standard for thermal pollution according to environmental protection law **(Ministry of health directorate genera of human environment 1967)** is that' no hot water should be discharged into natural water resources on which its temperature is greater than ($35C^\circ$) ", as well as another world wide limit at powre stations that thermal pollution should not exceed $3C^\circ$ in the receiving water at mixing zone in case of river condition **(International atomic energy1974)**. The numerical results show that the developed algorithm is capable of calculating the flow field, properly and accurately. Taken as follow:-

Case No.1 present normal section without obstacle and without injection show the **Fig (1)**
Case No.2 river region with obstacle in the middle and without injection.
Case No.3 river region with obstacle in the middle and with injection (0.3 m/s, T-inj=308 K).
Case No.4 normal region without obstacle and with injection (0.3 m/s, T-inj=308 K).
CaseNo.5without obstacle in river and increase injection velocity (0.9 m/s, constant - temperature injection).
CaseNo.6obstacle in river and increase injection velocity (0.9 m/s, constant temperature - ---- - injection.

CaseNo.7obstacle in river, increase injection velocity and increase injection temperature ---. (0.9 m/s, T-inj=313 K).
CaseNo.8 obstacle in river, increase injection velocity and increase injection temperature ---. (0.9 m/s, T-inj=318 K).
Case No.9same as 6, with obstacle closer to injection.
Case No.10 same as 6, with obstacle further to injection

The difference equations of this study were solved on a digital computer using **FORTRAN 90** program and the mat lab program was used **MAT LAB** the isotherm and streamline contours.

The Flow Field

Case1: The first water body configuration that was considered in this work has a rectangle shape without obstacle and without injection. The numerical results of the stream function were drawn as equipotent lines giving the trend of the flow all over the river which is without obstacle as shown in **Fig. (5)**

For case2: **Fig. (6)** Shows the stream lines of the flow with obstacle and without injection. The streamlines were shown to be simple diffuse in obstacle region.

In case3 higher diffuse in streamlines compared with case 2 for a large portion of the obstacle is clear in **Fig. (7)** because of the existing of the injection. After the obstacle the stream lines were equipotent lines giving the trend of the flow.

Stream lines in case4 were diffuse clearly in a large portion of the river in the zone of injection without obstacle as in **Fig. (8)**.

In case 5 for higher injection velocity (v x 3) compared with case 4 it is clear that the characteristics of the flow field is relatively similar to that in case 4 for the region far away from the injection zone as shown in **Fig. (9)**.

For case 6 which is as case 3 but with higher injection velocity (v x 3), **Fig. (10)** Shows more diffusion in flow compared with **Fig. (7).**

It is clear from **Fig. (11)** and **Fig. (12)** that the increase in injection temperature (T_{inj} =298˚ K for case 6 and T_{inj} = 343˚ K for case 7) cause the flow to move longitudinally occupying the end of the region and a disturbance will be occur in the injection zone.

In case 8 the obstacle is closer to the injection zone by 15 m for the same conditions of case 6. **Fig. (13)** shows a disturbance in the region of injection because of the imminence of the obstacle and after the disturbance region the stream lines are steady in the longitudinal direction.

When the obstacle is far away from the injection zone by 15 m (case 9) there is no effect on the stream lines as shown in **Fig. (14)**.

The velocity vector

The flow field can be demonstrated in a vector form to show the value and direction of the velocities in the river area for the 9 cases. **Figures (15) and (16)** show the velocity vector for a river without and with obstacle respectively and without injection for both cases. It is clear from **Fig. (16)** that the velocity vector is disturbed near the obstacle.

When the obstacle exist with the injection as in case 3 the velocity decrease near the injection zone as shown in **Fig. (17)** Compared with that in **Fig. (18)** for case 4 because of the existing of the obstacle

Fig. (18) for case 4 shows that the higher velocity vector is near the injection zone and its value reduced away from the injection zone.

The velocity vector increase higher near the injection zone in case 5, compared with that in case 4 because of the increase in injection velocity and this are clear in **Fig. (19)** while in **Fig. (20)** the velocity vectors are seen to be decrease and become very small near the obstacle.

In **Fig. (21)** the obstacle is closer to the injection zone which noted a shifting occurred near the injection zone compared with that in **Fig. (22)** for isle far away from the injection zone.

Temperature Field

The temperature field was obtained by the numerical solution of the energy equation for the 8 cases in configuration considered in the previous section. The net local energy rejected from each finite element of the surface of the river as a function of the finite element local surface temperature, turbulent flow (k-ε) model, incompressible fluid, different injection temperature, different injection velocity and different obstacle location (closer or farness) in river.

The results of the temperature field are clear in **Fig. (23)** and **Fig. (24)** for case 3 and case 4 which show the temperature distribution in the river region of 1000 m length and 150 m width. The injection temperature for the two cases is T_{inj} =298˚ K and a decrease in temperature of hot water injected and the isotherms are seen to be clustered around the injection zone then the temperature decays in all directions away from injection towards river due to the convection heat transfer as net energy lost from the river to the environment. The isotherms obtained by **(Seghal and Jaluria 1982)** are qualitatively similar to the isotherms obtained in this work. Comparing **Fig. (23)** and **Fig. (24)** Shows similarity due to the grate area providing bigger region of dissipating a large amount of heat transfer to the environment and obtaining lower temperature far away from injection zone.

Fig. (25) and **Fig. (26)** With grater injection velocity for cases 5 and 6 without and with obstacle respectively are shown the isotherms obtained to be clustered around the injection and to have increasing value when moving away from the injection opening toward river. The shape of the contours differs from that in **Fig. (23) and (24).** It is clear that the temperature is taken wider region due to the increase in injection velocity. Comparing **Fig. (25)** and **Fig. (26)** it is clear that there is different distance of temperature distribution or wide region of temperature distribution for the case with obstacle in the river, so the obstacle is an obstacle disturbs the temperature distribution and after this obstacle the temperature distribution will be steady.

The isotherms profiles with injection are shown in **Fig. (26)** with T_{inj} =298˚ K and in **Fig. (27)** with T_{inj} =313˚ K and **Fig. (28)** with T_{inj} =318 k. respectively. The three cases have the same condition of isle existing and velocity injection but, the variation between the three figures are very small. So the temperature distribution area increases in the last case.

Fig. (29) shows the isotherms for the river with obstacle closer to injection zone and other conditions are as in case 6 but the difference in temperature distribution region increases due to the decrease of the distance between the obstacle and the injection zone.

It is clear from **Fig. (30)** which is of the same conditions as case 6 but with obstacle existing far away from the injection zone by 15 m that the isotherms of this case is the same as in case 6 because this area is not affected by the farness obstacle.

Comparison with an Actual Case

The estimated weather conditions for cooling ponds are listed below:-

$U_{\infty} = 0.1 m/s$

$length = 300m$

$width = 10m$

$\Delta t = 10C^{\circ}$

$\mathrm{Re}t = 1000$

$Pet = 1000$

$T_{in} = 36C^{\circ}$

$T_{\infty} = 23C^{\circ}$

The inflow temperature was taken to be approximately $36\,C^{\circ}$.The contour lines close to the inflow both cases (present work and cooling ponds **(Kasim Daws)**) are seen to be clustered around the inflow and a reducing value by moving a way from the inflow opening toward the length river. Selected results and calculations concerning the thermal temperature of the cooling river under study are presented **Fig. (5, 6)** are same cooling ponds **(Kasim Daws) Fig. (31, 32)** but the temperature distribution **Fig. (33)** different between the present work **Fig.(34)** because the cooling ponds taken study the following:-

1. Solar heat flux.
2. Evaporation heat-exchange.
3. Heat flux due to back radiation
4. Surface temperature.
5. Weather different.

CONCLUSION

The contour lines close to the inflow in all cases are seen to be clustered around the inflow and reducing value by moving away from the inflow opening toward the long river. From the results of the present work it was concluded that the increase in injection velocity cause a disturb near the injection zone and affect the area of temperature distribution and stream lines and so was the obstacle exist but the in crease injection temperature cause a small effect. The closer obstacle to the injection zone by15m cause more disturbances in this area.

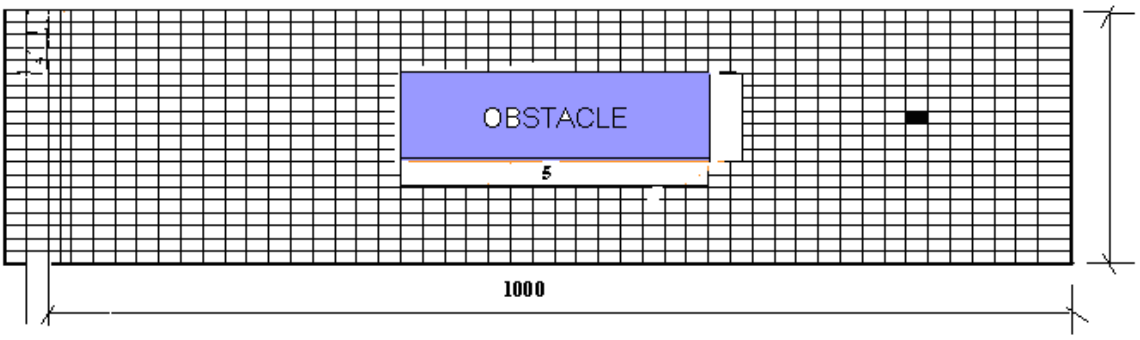

Fig.1: The Problem of the Present Work

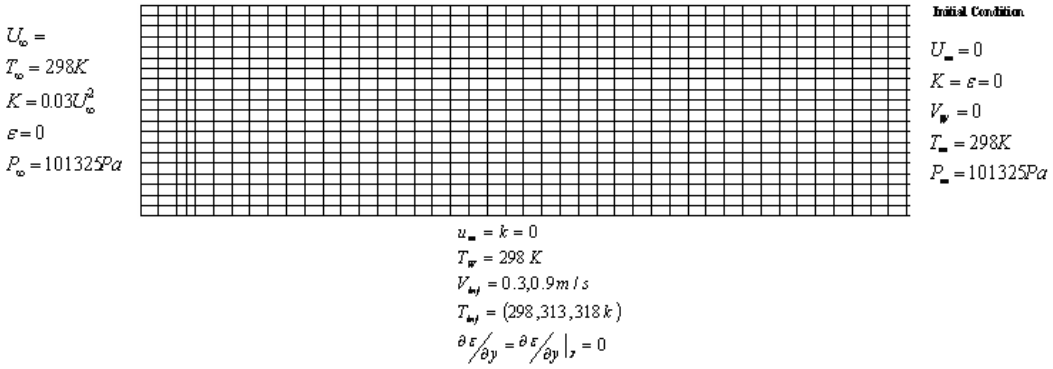

Fig.2: The Initial and Boundary Condition

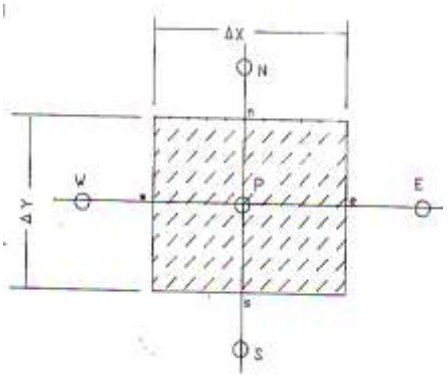

Fig.3: The Volume for Tow-Dimensional Case

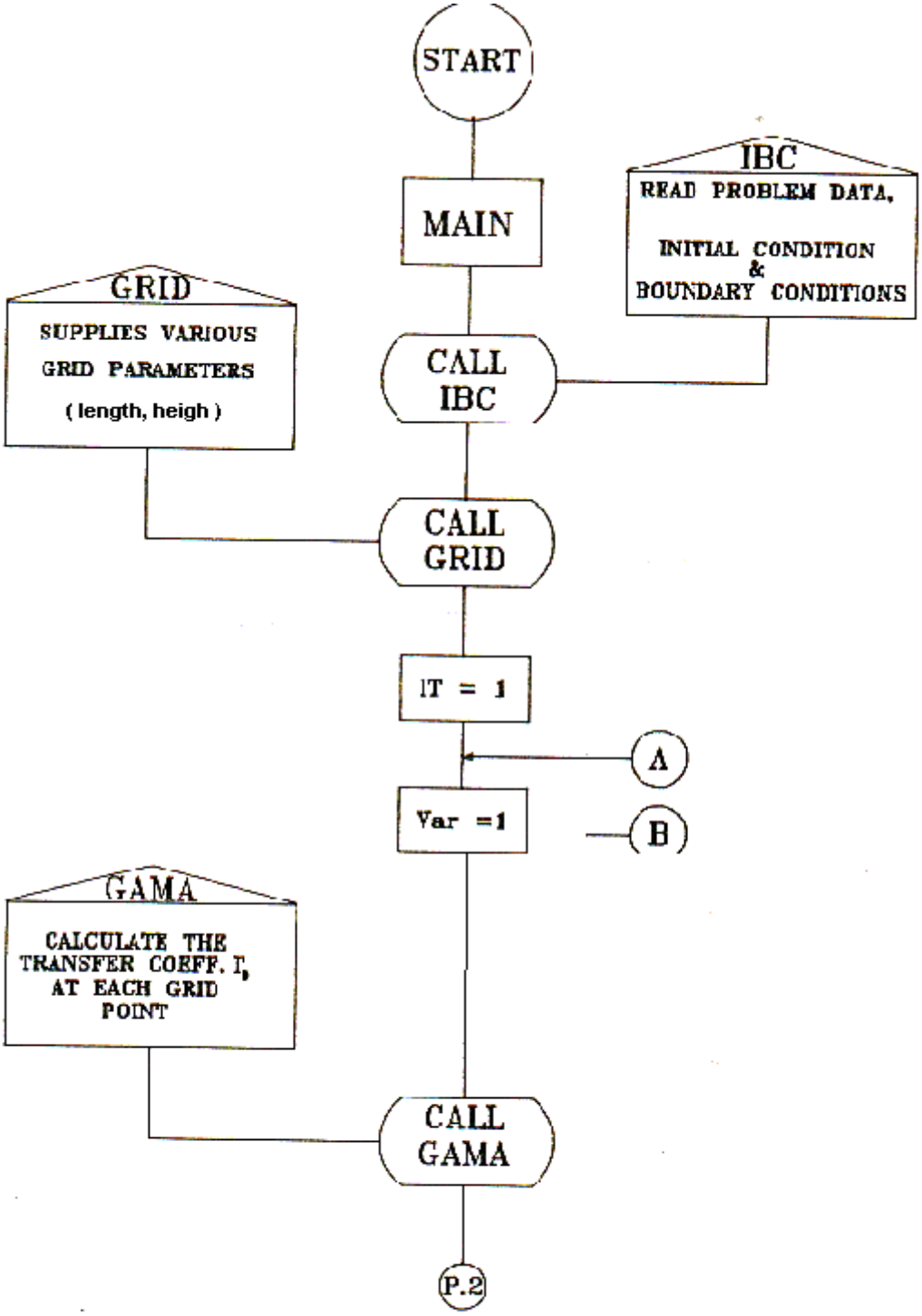

Fig.4: Flow Chart for the Numerical Model

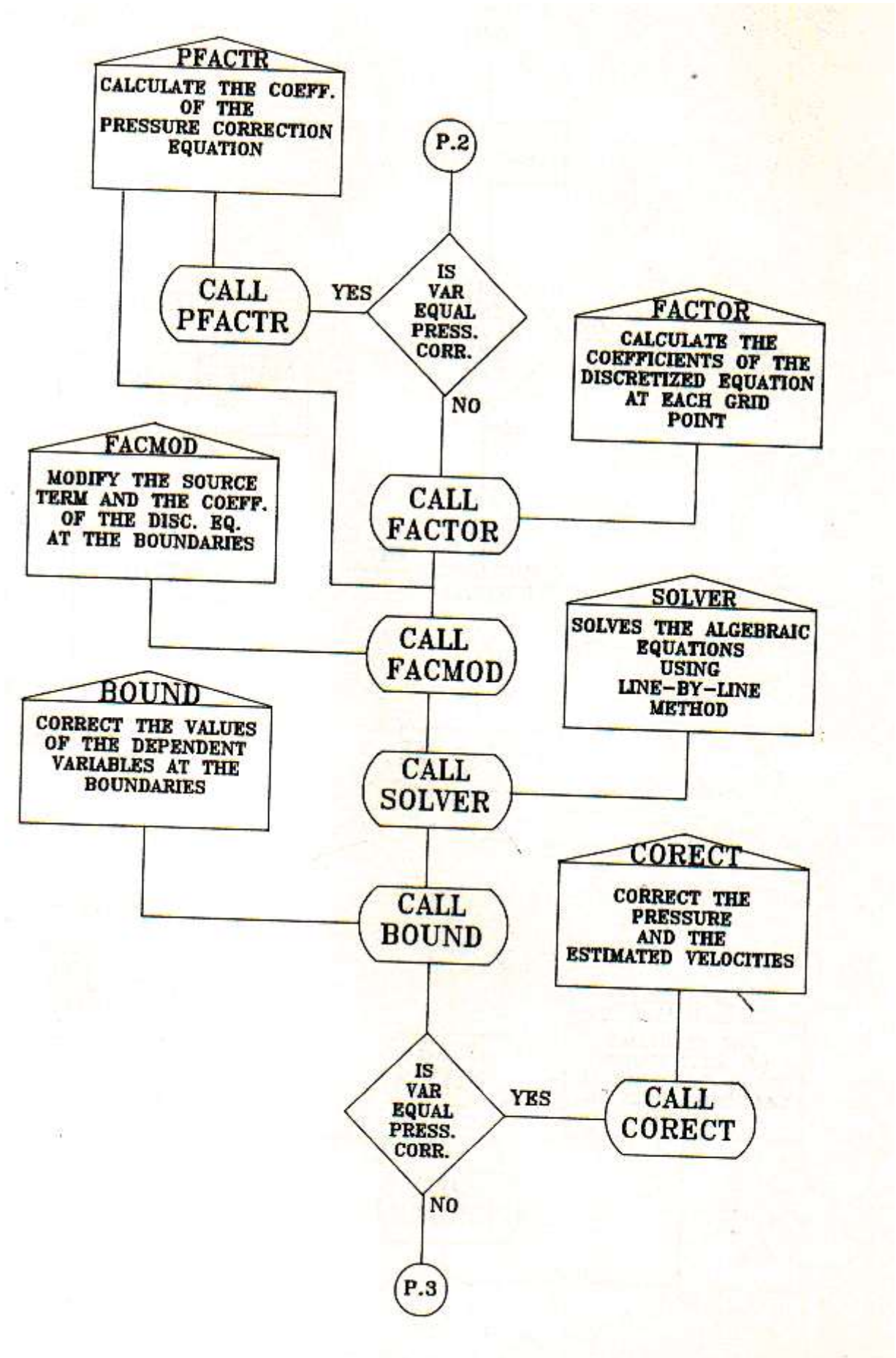
PFACTR
CALCULATE THE COEFF. OF THE PRESSURE CORRECTION EQUATION
P.2
CALL PFACTR
YES
IS VAR EQUAL PRESS. CORR.
FACTOR
CALCULATE THE COEFFICIENTS OF THE DISCRETIZED EQUATION AT EACH GRID POINT
NO
FACMOD
MODIFY THE SOURCE TERM AND THE COEFF. OF THE DISC. EQ. AT THE BOUNDARIES
CALL FACTOR
SOLVER
SOLVES THE ALGEBRAIC EQUATIONS USING LINE-BY-LINE METHOD
CALL FACMOD
BOUND
CORRECT THE VALUES OF THE DEPENDENT VARIABLES AT THE BOUNDARIES
CALL SOLVER
CORECT
CORRECT THE PRESSURE AND THE ESTIMATED VELOCITIES
CALL BOUND
IS VAR EQUAL PRESS. CORR.
YES
CALL CORECT
NO
P.3

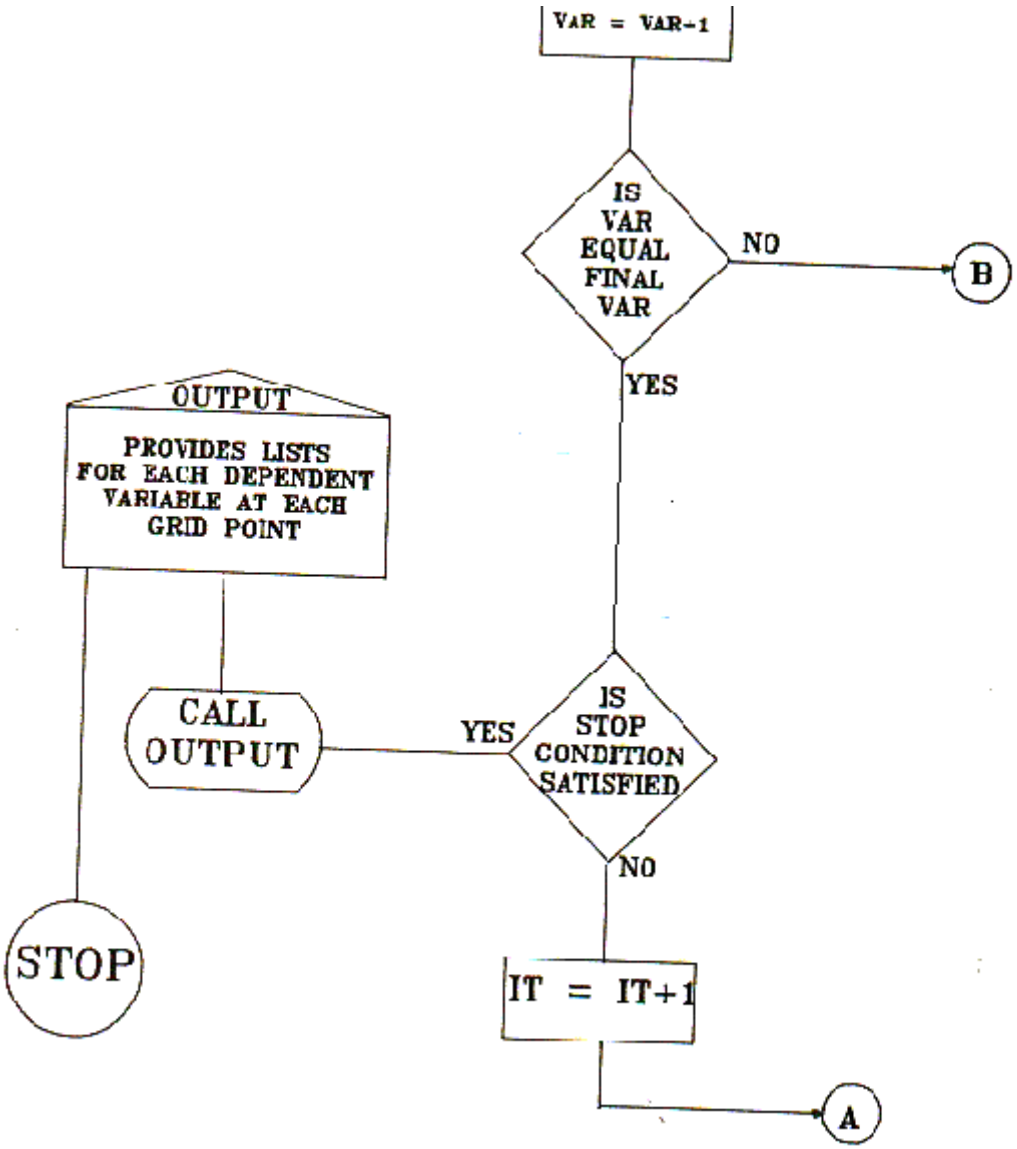
VAR = VAR-1
IS VAR EQUAL FINAL VAR
NO
B
YES
OUTPUT
PROVIDES LISTS FOR EACH DEPENDENT VARIABLE AT EACH GRID POINT
CALL OUTPUT
YES
IS STOP CONDITION SATISFIED
NO
STOP
IT = IT+1
A

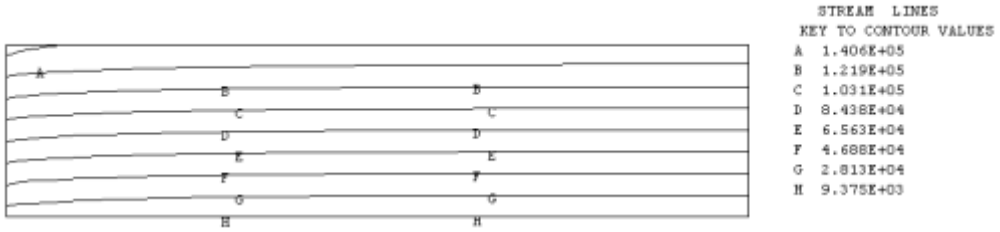

Fig. 5: Stream Lines for case 1

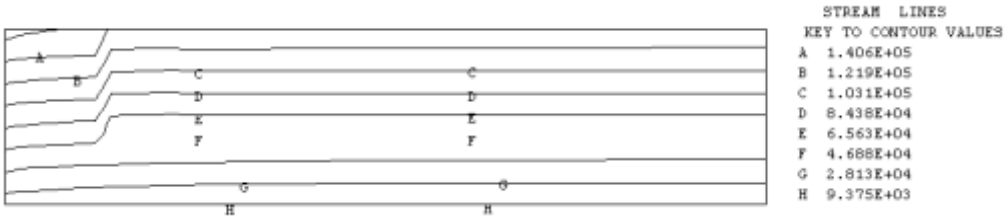

Fig. 6: Stream Lines for case 2

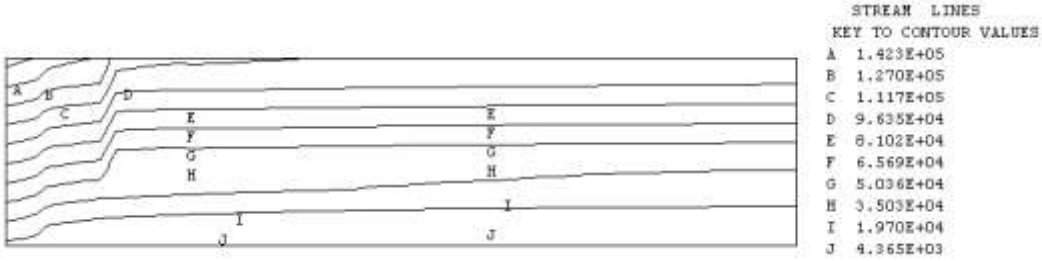

Fig. 7: Stream Lines for case 3

Fig. 8: Stream Lines for case 4

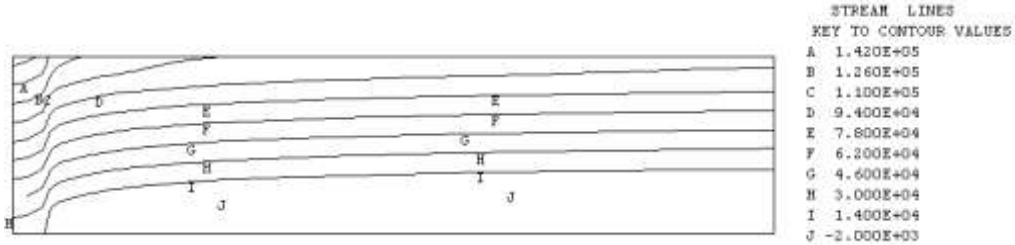

Fig. 9: Stream Lines for case 5

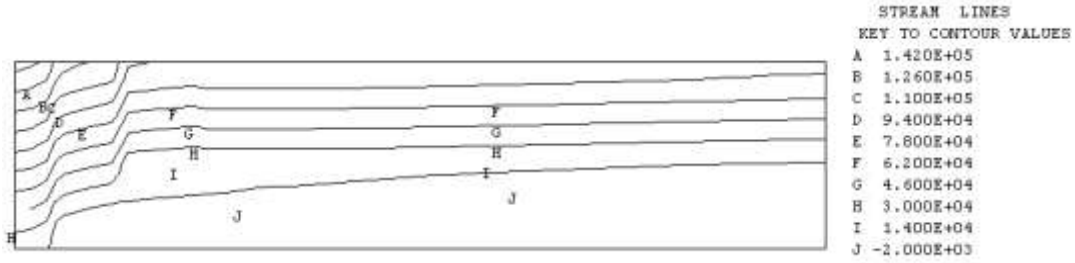

Fig. 10: Stream Lines for case 6

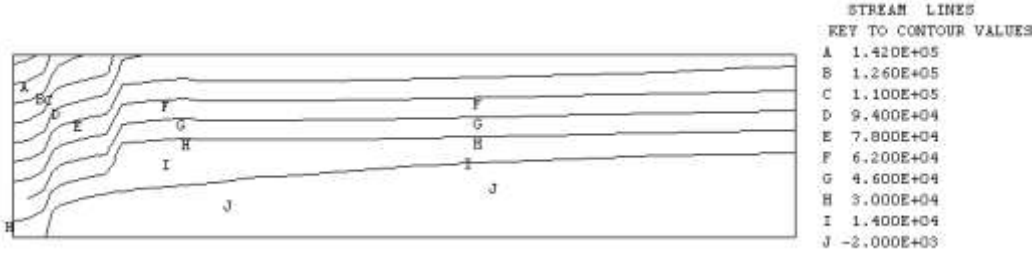

Fig. 11: Stream Lines for case 7

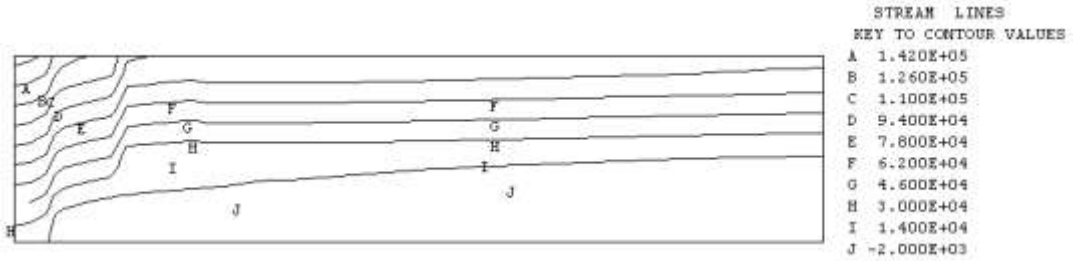

Fig. 12: Stream Lines for case 8

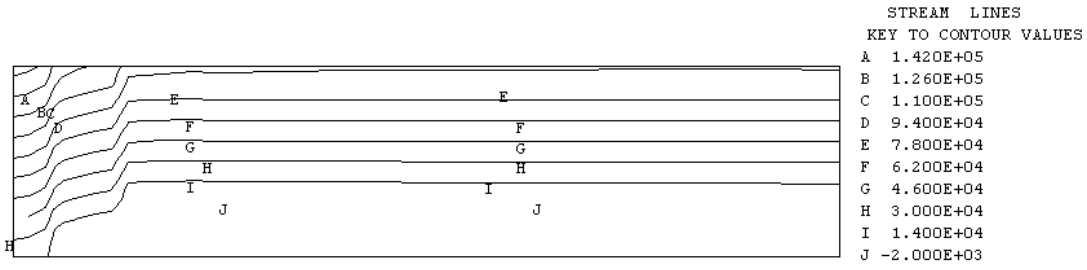

Fig. 13: Stream Lines for case 9

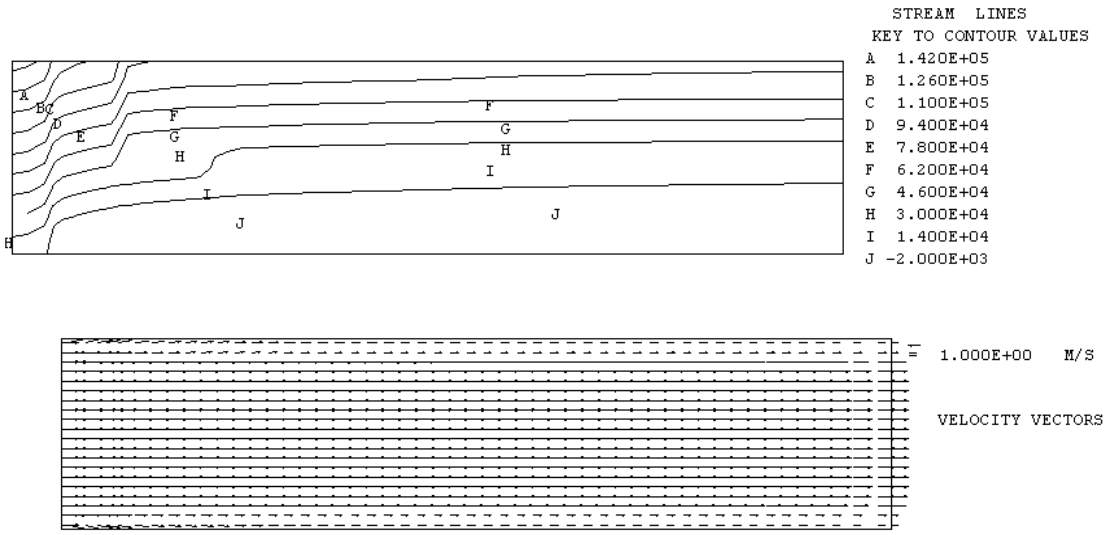

Fig. 14: Stream Lines for case 10
ig. 15: velocity Vectors for case1

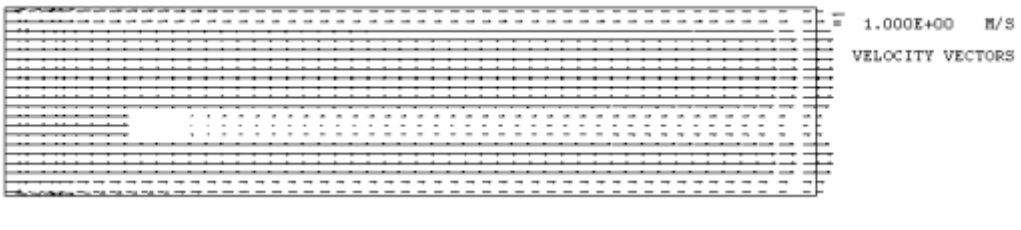

Fig. 16: Velocity Vectors for case2

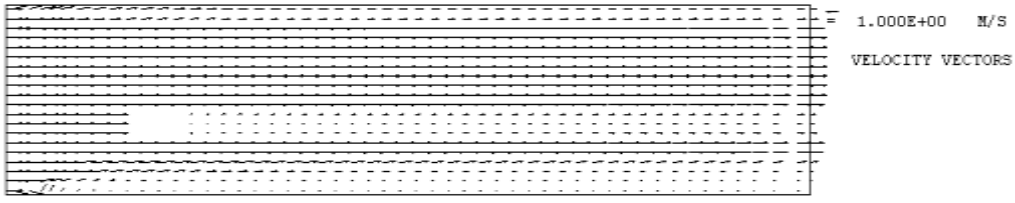

Fig. 17: Velocity Vectors for case3

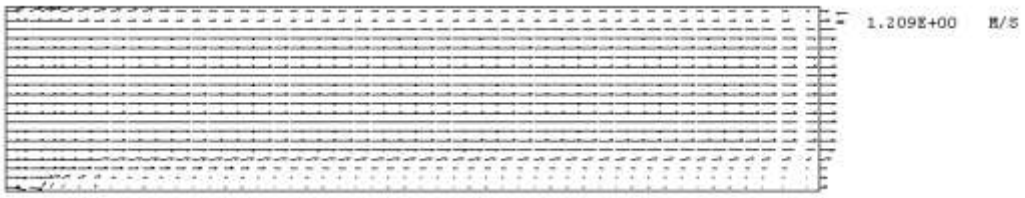

Fig. 18: Velocity Vectors for case4

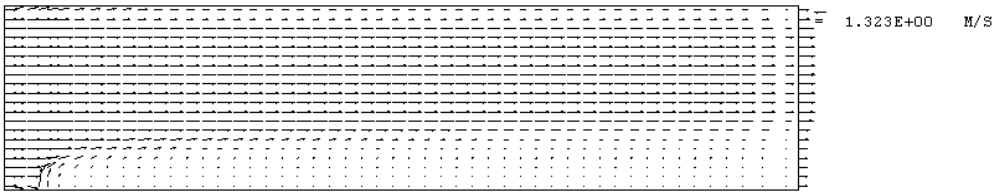

Fig. 19: Velocity Vectors for case5

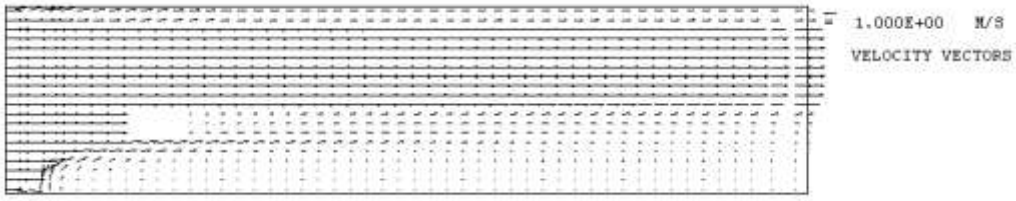

Fig. 20: Velocity Vectors for case6

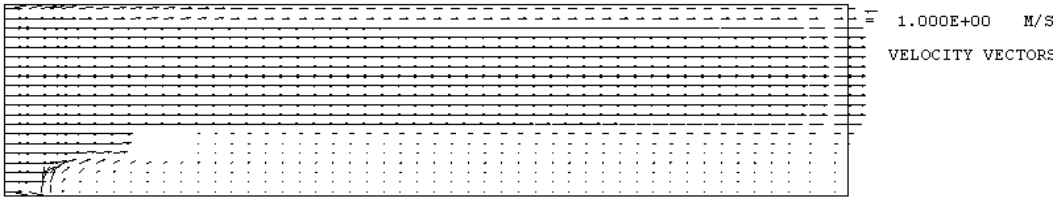

Fig. 21: Velocity Vectors for case9

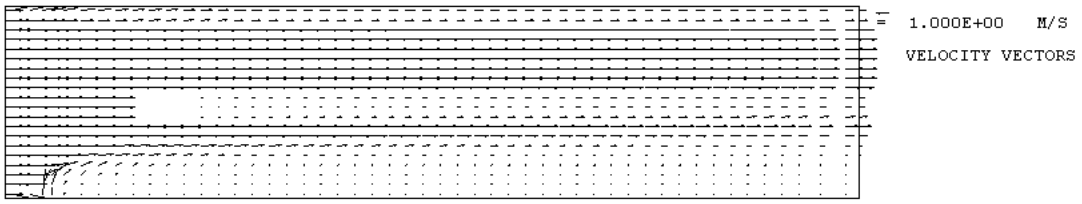

Fig. 22: Velocity Vectors for case10

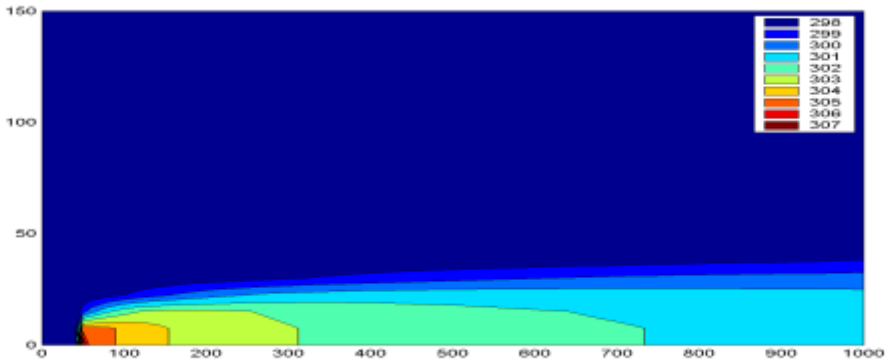

Fig.23: Isotherms for case3

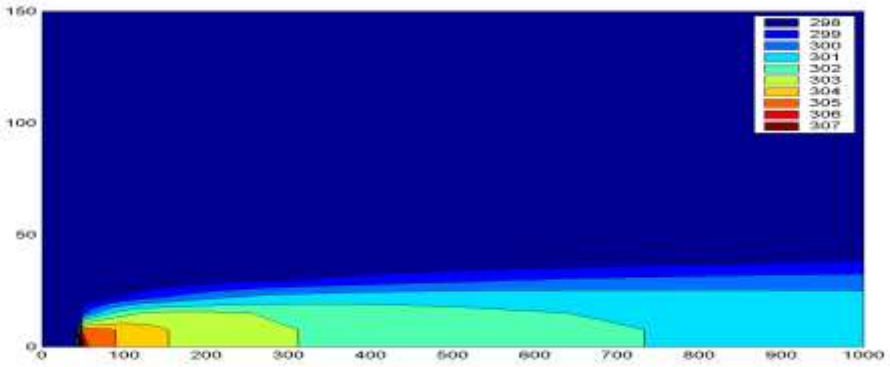

Fig.24: Isotherms for case4

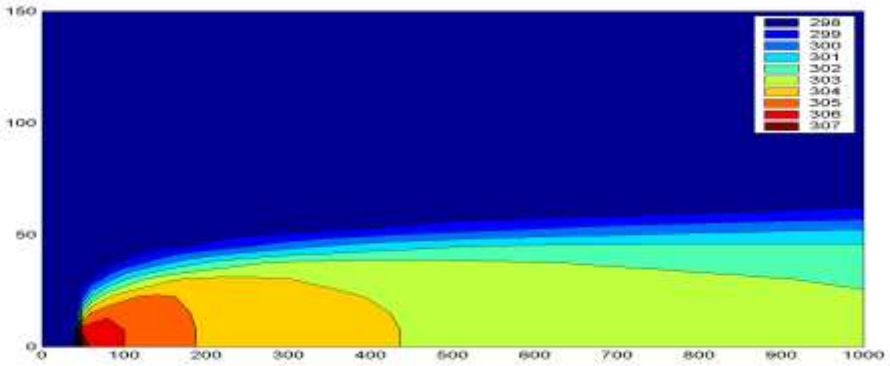

Fig.25: Isotherms for case5

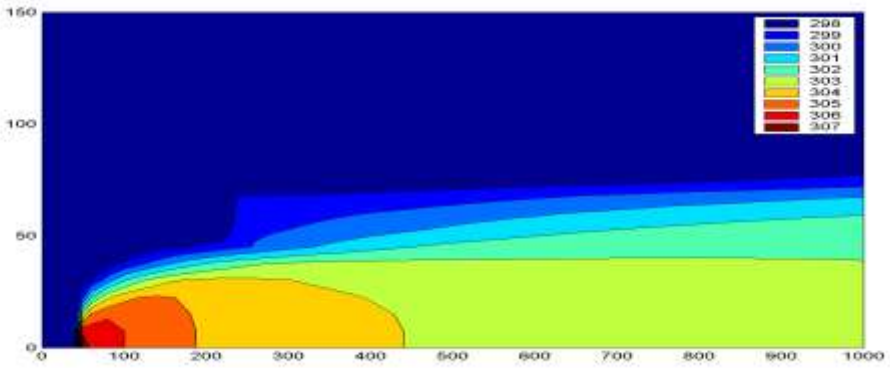

Fig.26: Isotherms for case6

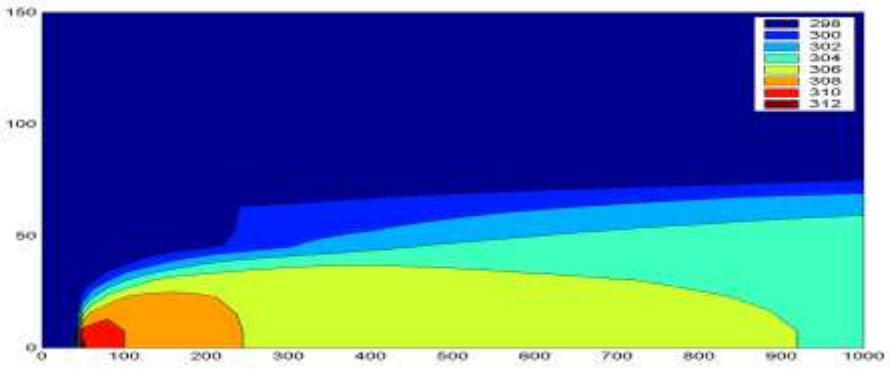

Fig.27: Isotherms for case7

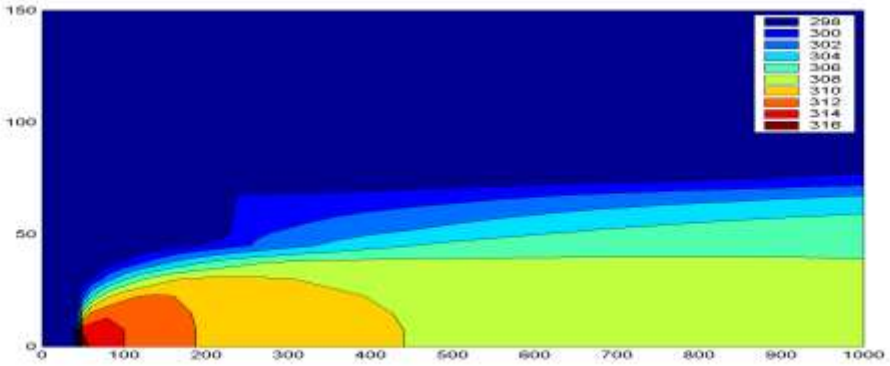

Fig.28: Isotherms for case8

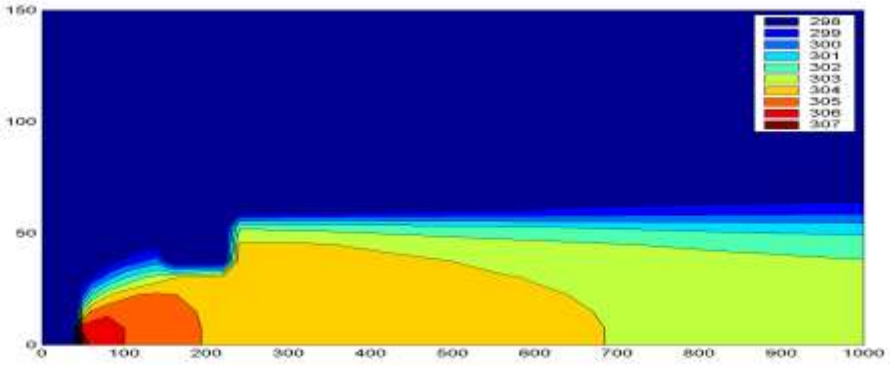

Fig.29: Isotherms for case9

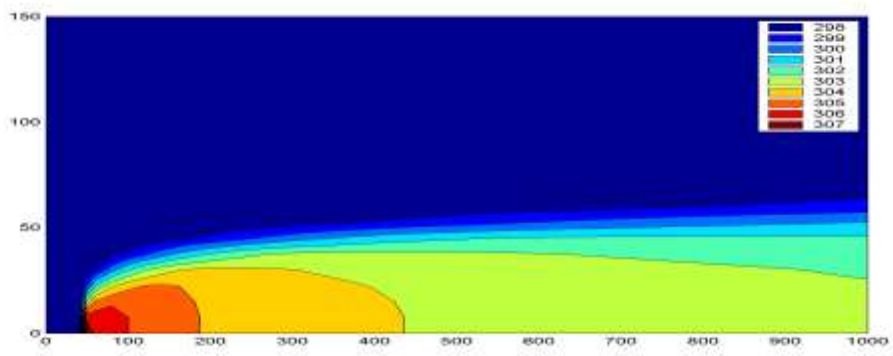

Fig.30: Isotherms for case10

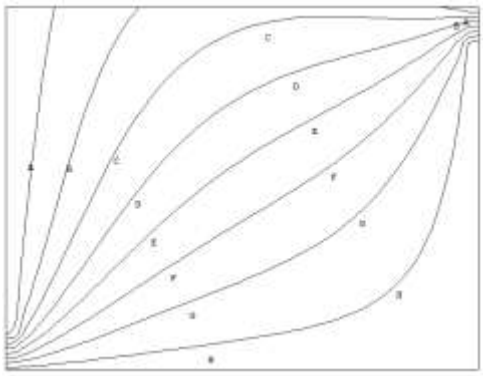

Fig. 31: Stream Lines for same (present work and cooling ponds)

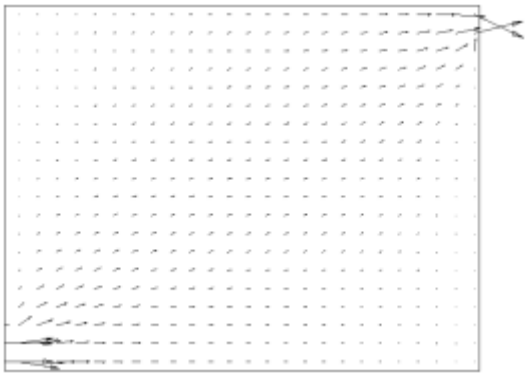

Fig. 32: Velocity Vectors for same (present work and cooling ponds)

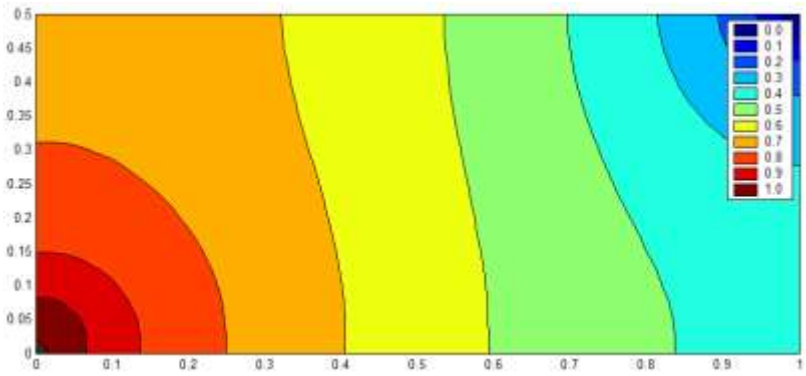

Fig.33: Isotherms for cooling ponds

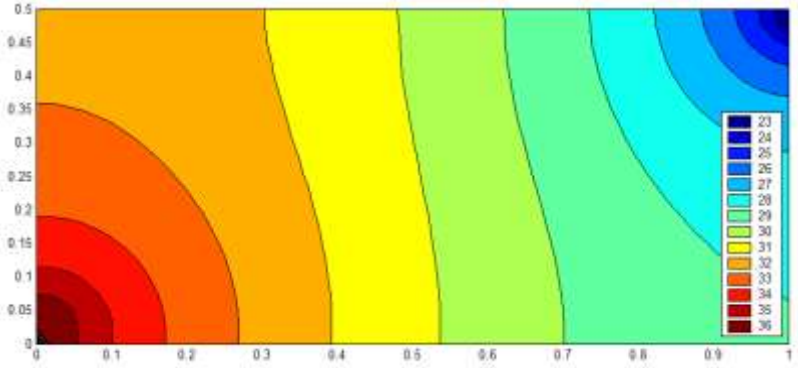

Fig.34: Isotherms for present work

REFFRENCES

- Andrzej Pozlewicz" Modeling of thermal pollution dispersion in lower Odra river" Department of Geotechnical Engineering, Szczecin Univercity of Technology, Poland,al. Piastow 50,PL 70-311 Szczecin, Poland.

-ASCE Task Committee on Turbulence Model in Hydraulic Computation "Turbulence Modeling of surface water Flow and Transports part I", Journal of Hydraulic Engineering Vol. 114, No9, sep. (1988).

-A.Zukauskas"Warm-watre spreading in cooling ponds of steam power plants" Heat transfer and turbulent buoyant convection, vol.1, pp.139, (1976).

-H.Inhaber,water encyclopedia,vol.1, wiley-interscience,pp.560-565(2005).

- International atomic energy, thermal discharge at nuclear power station, their management and environmental impacts. Technical report series 155.1974.

-Kasim Daws"Heat Exchange and Dissipation in Large Water Bodies",M.Sc. Thesis, Mech.,Eng., Dept., University of Baghdad, 1990.

- M. Anis AL-Layla and Hasan AL-Rizzo" Awater quality model for the Tigris River downstream of Al Mosul Dam, Iraq"Hydrological Sciences, Vol.34, No.1, June, PP. 687, (1990).

-Michael Manga and James W.Kirchner"Interpreting the temperature of water at cold springs and the importance of gravitational potential energy' Water Resources Research, Vol.40, W05110, doi: 10.1029/2003WR002905, 2004.

- Ministry of health directorate genera of human environment the limits of the regulation of rivers and public waters from the pollution No.25 for a year (1967).

-M. J. Joyce and S. N. Port, Environmental Impact of Power Generation, 11, Issues in Environmental Science and Technology, Royal Society of Chemistry(1999).

- Nagano Y. and Hishida M., "An Improved $\kappa-\varepsilon$ Model for Boundary Layer Flows " J. Fluid Mech., vol. 112, PP. 33-39, March (1990).

- Patanker S.V. "Numerical Heat Transfer and Fluid Flow", Mc Graw-Hill Book Company, N.Y., (1980).

- R.C. Sehgal and Y. Jaluria"Horizontal Recivculcation in Water Bodies due to Thermal Discharge" Energy, vol.7, No.5, PP. 419-428, 1982.

NOMENCLATURE

C_p	The Specific heat at Constant Pressure, (=1004.5 J/kg.K)	
F	Convective Flux Through a cell Face	m^2/sec
K	Thermal Conductivity	W/m. K
k	Kinetic Energy of Turbulence	J
K	Ratio of Specific's Heat, (=1.4 for air)	
P	Pressure	N/m^2
P	Cell Nodal Point	
R_e	Reynolds Number	
T	Temperature	K
T_w	the Wall Temperature	K
t	Time	sec
U	The Velocity Vector	m/sec
u, v, w	Velocity Components in the x, y and z	m/sec
X, x	X-Coordinate Distance	m
Y, y	Y-Coordinate Distance	m

Greek letters

ε	Dissipation Rate of Turbulent	
$\Delta X, \Delta Y, \Delta Z$	Cell Distances	
$\delta k, \delta \varepsilon$	Constant in the $K-\varepsilon$ Model	
$\delta x, \delta y$	Half the Cell Distances	
Φ	Dependent Variable in the General Form of Equation	
Γ	Transfer Coefficient	
μ	Laminar Viscosity	kg/m.s
μ_{eff}	Effective Eddy Viscosity	kg/m.s
μ_t	Turbulent Viscosity	kg/m.s
ρ	Density	kg/m^3
ν	Kinematics Viscosity	m^2/s
τ_w	Wall Shear Stress	N/m^2

Subscripts

e, w, n, s	(east, west, north, south) nodes at the cell face
l	Laminar
o	Initial Value
t	Turbulent
u, v, w	Velocity Component in x, y, and z directions
1, 2, 3	Coordinate Direction

Superscripts

t	Turbulent
*	Predicted Values
,	Fluctuation Values, Correction Values
∞	Signifies Free Stream Conditions

Abbreviations

F.D.M	Finite Difference Method
SIMPLE	Semi-Implicit Method for pressure-Linked Equation

NUMERICAL INVESTIGATION OF TURBULENT NATURAL CONVECTION IN AN INCLINED SQUARE ENCLOSURE

Qasim S. Mehdi
College of Engineering
University of Mustansiriya

Khudheyer S. Mushatet
College of Engineering
University of Thiqar

ABSTRACT

Two dimensional turbulent natural convection heat transfer and fluid flow inside an air filled inclined square enclosure differentially heated has been numerically studied. Fully elliptic Navier- Stockes and energy equations are solved using finite volume method. The problem is simulated for different angles of inclination ($0 \le \theta \le 180 \deg.$) and Rayleigh numbers ($10^8 \le Ra \le 10^{16}$). The turbulence k-ϵ model is used to model the effect of turbulence. The wall function approach is used to model the regions near the walls of the enclosure. The obtained results from this study show that the rate of heat transfer is increased with the increase of Rayleigh number and decreased with the increase of angle of inclination($0 \le \theta \le 90 \deg.$).Also the induced vortices are strongly elongated with increase of Rayleigh number. The thickness of thermal boundary layer is decreased with the increase of Ra. The validation of the present code was done by comparing the computed results with the published ones. The comparison indicated a good agreement.

المستخلص: أجريت دراسة عددية لدراسة انتقال الحرارة وجريان المائع بالحمل الحر الأضطرابي داخل حيز مربع مائل ومسخن تسخينا جزئيا. تم حل معادلات نافير– ستوكس ومعادلة الطاقة باستخدام طريقة الحجم المحدد. أجريت الدراسة الحالية لزوايا ميلان مختلفه($0 \le \theta \le 180 \deg.$) ولأرقام رايلة متعددة($10^8 \le Ra \le 10^{16}$) بينما تم استخدام نموذج الأضطراب (k-ϵ) لمعالجة تأثير الأضطراب. أستخدم اسلوب دالة الجدار لنمذجة المناطق القريبة جدا من الجدران. أظهرت النتائج التي تم الحصول عليها أن معدل انتقال الحرارة قد ازداد مع زيادة عدد رايلة ويقل بزيادة زاوية الميلان($0 \le \theta \le 90$ deg). أيضا بينت النتائج أن الدوامات الناتجة تستطيل وتتحد بقوة مع زيادة عدد رايلة بينما يقل سمك الطبقة الحرارية المتاخمة. تم التأكد من صحة الطريقة العددية المستخدمة من خلال المقارنة مع النتائج العملية المنشورة حيث بينت المقارنة توافقا جيدا.

KEYWORDS

natural convection, heat transfer, enclosed enclosure

INTRODUCTION

Natural convection heat transfer in an enclosure is of importance in many engineering applications. These include cooling of electronic systems, double windows, air gaps in unventilated spaces and solar collectors.. However turbulent natural convection in inclined enclosures is still needs more research area to understand the complex fluid flow and heat transfer behavior. In the reviewed studies on natural convection, there is a few studies relating the turbulent natural convection inside inclined enclosures, so the present study try to facillate the challenge in understanding the flow and heat transfer behavior in this type of the problems. One of the most important bench mark studies on turbulent natural convection inside enclosed cavities was an experimental study done by(**Ampofo and Karayiannis,2003**). (**Corcione,2003**) performed a numerical study on the natural convection in a rectangular horizontal enclosure differentially heated. He used various thermal conditions of the cavity side walls. Also laminar natural convection in enclosed cavities has been studied numerically and experimentally by (**Davis to Kuper et al**., **1983-1993**). (**Markatos et al.,1984**) and **(Lankhorst et al., 1991)** used a k-ϵ model to study the two and three dimensional turbulent flows inside a cavity. Some interesting studies for both laminar and turbulent flows in inclined cavities has been found by the authors (**Zhongand Young,1985**) and(**Elshirbiny,1982**).

In the present work a numerical investigation has been performed to study the turbulent 2D thermally driven air flows inside a square enclosure. The objective was to investigate how the enclosure tilted angle can effect on these flows which are found in a diverse engineering applications. The computations were performed for Ra ranging from 10^8 to 10^{16} and an angle of inclination from 0° to 180°. The enclosure is differentially heated as shown in **Fig**.**1**.

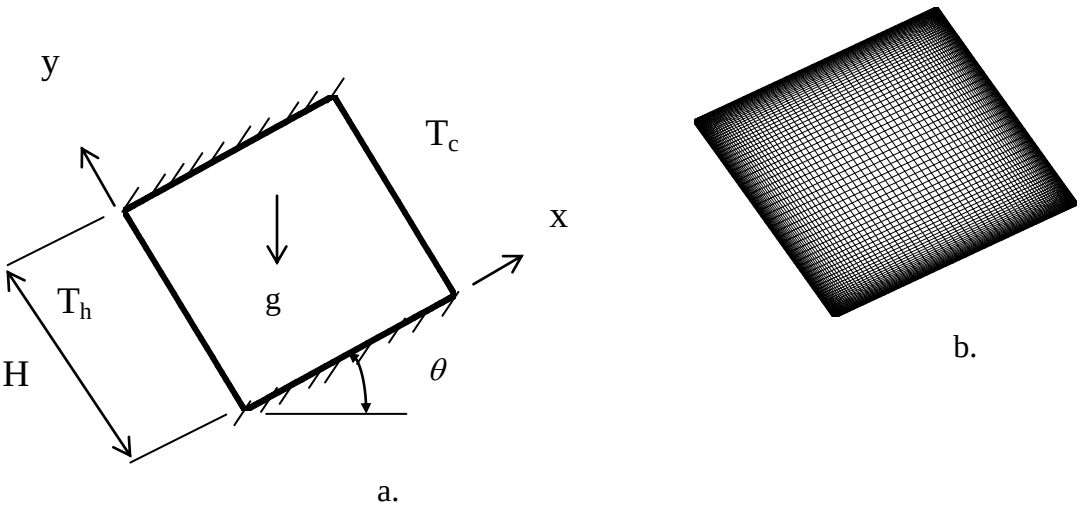

Fig.1. problem of interest; (a) physical domain , (b) computational domain

MATHEMATICAL MODEL

The turbulent viscous flow and temperature distribution inside an inclined square enclosure are described by the steady Navier-Stockes, energy and turbulence equations. The flow is assumed to be incompressible and Boussine approximation is valid. Employing the eddy viscosity concept, the time averaged governing equations are defined as follows(**Jones and Luander,1972)**:

$$\frac{\partial u}{\partial x}+\frac{\partial v}{\partial y}=0 \quad (1)$$

$$\rho u\frac{\partial u}{\partial x}+\rho v\frac{\partial u}{\partial y}=-\frac{\partial p}{\partial x}+2\frac{\partial}{\partial x}\left(\mu_{eff}\frac{\partial u}{\partial x}\right)+\frac{\partial}{\partial y}\left(\mu_{eff}\frac{\partial u}{\partial y}\right)+\frac{\partial}{\partial y}\left(\mu_{eff}\frac{\partial v}{\partial x}\right)+\rho g\beta(T-T_0)\sin\theta \quad (2)$$

$$\rho u\frac{\partial v}{\partial x}+\rho v\frac{\partial v}{\partial y}=-\frac{\partial p}{\partial y}+\frac{\partial}{\partial x}\left(\mu_{eff}\frac{\partial v}{\partial x}\right)+2\frac{\partial}{\partial y}\left(\mu_{eff}\frac{\partial v}{\partial y}\right)+\frac{\partial}{\partial x}\left(\mu_{eff}\frac{\partial u}{\partial y}\right)+\rho g\beta(T-T_0)\cos\theta \quad (3)$$

$$\rho u\frac{\partial T}{\partial x}+\rho v\frac{\partial T}{\partial y}=\frac{\partial}{\partial x}\left(\Gamma_{eff}\frac{\partial T}{\partial x}\right)+\frac{\partial}{\partial y}\left(\Gamma_{eff}\frac{\partial T}{\partial y}\right) \quad (4)$$

$$\mu_{eff}=\mu+\mu_t, T_0=(T_C+T_h)/2,\ \beta=1/T_0 \quad (5)$$

$$\Gamma_{eff,T}=\frac{\mu}{\Pr}+\frac{\mu_t}{\Pr} \quad (6)$$

The turbulent kinetic energy and the rate of its dissipation for two dimensional buoyancy turbulent flow can be written as follows(**Jones and Luander,1972**):

$$\rho u\frac{\partial k}{\partial x}+\rho v\frac{\partial k}{\partial y}=\frac{\partial}{\partial x}\left(\Gamma_{eff,k}\frac{\partial k}{\partial x}\right)+\frac{\partial}{\partial y}\left(\Gamma_{eff,k}\frac{\partial k}{\partial y}\right)+G-\rho\varepsilon \qquad (7)$$

$$\rho u\frac{\partial \varepsilon}{\partial x}+\rho v\frac{\partial \varepsilon}{\partial y}=\frac{\partial}{\partial x}\left(\Gamma_{eff,\varepsilon}\frac{\partial \varepsilon}{\partial x}\right)+\frac{\partial}{\partial y}\left(\Gamma_{eff,\varepsilon}\frac{\partial \varepsilon}{\partial y}\right)+C_{1\varepsilon}\frac{\varepsilon}{k}G+C_{2\varepsilon}\frac{\varepsilon^2}{k} \qquad (8)$$

where $$G=\nu_t\left[2\left(\frac{\partial u}{\partial x}\right)+2\left(\frac{\partial v}{\partial y}\right)+\left(\frac{\partial u}{\partial y}+\frac{\partial v}{\partial x}\right)\right] \qquad (9)$$

$$\Gamma_{eff,k}=\mu+\frac{\mu_t}{\sigma_k},\ \Gamma_{eff,\varepsilon}=\mu+\frac{\mu_t}{\sigma_\varepsilon} \qquad (10)$$

the eddy dynamic viscosity is obtained by the Prandtl-Kolmogorov hypothesis

$$\nu_t=C_\mu\frac{k^2}{\varepsilon} \qquad (11)$$

the model coefficients are (σ_k ;σ_ϵ ; $C_{1\epsilon}$; $C_{2\epsilon}$; $C\mu$) = (1.0 , 1.3 , 1.44 , 1.92, 0.09) respectively (**Jones and Luander,1972**).

BOUNDARY CONDITIONS

In order to solve the mathematical model, the following boundary conditions are used

At the walls: u = v = 0. and wall function approach (**Versteege and Meer,1995**) is used for the near wall grid points.

For perpendicular walls on the x-axis: at x = 0, T = T_h , at x =L , T = T_c and the parallel walls to the x-axis are insulated.

The local and average Nusselt numbers along the left vertical hot wall can be obtained from the following formulas:

$$Nu=\frac{\partial\Phi}{\partial X}=\frac{\partial T}{\partial x}\frac{L}{T_h-T_C};\quad Nu_{av}=\int_0^1\left(\frac{d\Phi}{dX}\right)dy\approx\frac{1}{N}\sum_{J=1}^{N}\frac{\partial\Phi}{\partial X}$$

The average Nusselt number is a function of Rayleigh and grid points. The number of grid points for $10^8 \le Ra \le 10^{10}$ is 41×41 and for $10^{10} \le Ra \le 10^{16}$ is 84×82 . The increase in Ra needs more grid points and computational time to obtain a converged solutions. The large part of grid points for all the studied Ra are found near the walls in all directions.

NUMERICAL PROCEDURE

Finite volume method is used for the discritisation of the considered governing equations. This gives a system of discritization equations which means that the system of elliptic partial differential equations is transformed into a system of algebraic equations. The solution of these equations is performed by implicit line by line Gause elimination scheme. A computer program is developed to attain the results using the pressure velocity coupling (SIMPLEC algorithm) (**Versteege and Meer,1995**). Due to this strong coupling and non-linearity inherent in these equations, relaxation factors are needed to ensure convergence. The relaxation factors used for velocity components, temperature, pressure and turbulence quantities are 0.4, 0.5, 0.45 and 0.7 respectively. These relaxation factors have been adjusted for each case studied in order to accelerate convergence. Non uniform grid with refinements near the walls is used. The computational grids are staggered for the scalar variables and not staggered for the scalar one. The accuracy of the considered code is validated by comparing the present results with published results as shown in the table 1 . The linear least square regression method is used for the correlation between Ra and Nu_{av} for the present results found in the table 1. This relation takes the form $Nu_{av} = 0.25Ra^{0.40}$

Table1. Comparison of the present results with the published results of (**Marakato,1984**) for Pr=0.71 and $\theta = 0^{\circ}$.

Ra	Nu_{av} (present results)	Nu_{av} (published results)
10^6	8.748	8.754

10^8	32.1	32.04
10^{10}	156.85	156.8
10^{12}	8 40.8	840.1
10^{14}	3627	3624
10^{16}	11229.9	11226

RESULTS AND DISCUSSION

The computed results are presented as follows for different Rayleigh numbers and angles of inclination.

Fig.**2**. demonstrates the stream function for different values of Ra and $\theta = 0^\circ$. It can be seen that at Ra = 10^8, there is two elongated vortices near the enclosure walls. When Ra increased to 10^{10}, the two vortices are stretched to one vorticity in the central part of the enclosure. However there is small vortices arises in the bottom right corner. As Ra =10^{12}, there is small secondary vortices found in the upper part of the enclosure besides the central vorticity. At Ra =10^{14} and Ra =10^{16} the secondary vortices are distributed near the walls. The increasing of Ra due to the increment in H leads to increase the buoyancy which leads to increase the vertical and horizontal velocities consequently effect on the vorticity distribution. The effect of angle of inclination on stream function distribution for Ra = 10^8 is depicted in **Fig**.**3**. As the Figure shows, when $\theta = 30^\circ$, the stretching vortices are elongated in the direction of inclination and the size of the occupied region by these vortices is less compared with the case of $\theta = 0^\circ$. When $\theta = 60^\circ$, besides to the elongated vortices, there is a small secondary vortices near the enclosure walls. The size of these vortices is larger compared with $\theta = 30^\circ$. At $\theta = 90^\circ$ there is four re-circulating secondary vorticties formed near the vertical walls and bottom surface as a result of increasing the buoyancy force because the hot wall became at the bottom . As the angle increased to $\theta = 120^\circ$, there is elongated vortices and two secondary vortices near the walls. The occupied zone by the elongated vortices is larger. For $\theta = 150^\circ$, the distribution is nearly similar to the case of $\theta = 30^\circ$. However the boundary layer is thicker. This is demonstrated at **Fig**.**6** and **Fig**.**8**.

For $\theta = 180^\circ$ there is two secondary vortices and the size of these vortices is larger compared with the case of $\theta = 0^\circ$. The temperature distribution for different Rayleigh numbers and $\theta = 0^\circ$ is shown in **Fig**.**4**. It is evident that the heat is transferred from the hot wall to the cold wall through a working fluid (air) by convection. This assessed when one observe that the isotherm lines are not perpendicular. Also it can be seen that the thermal boundary layer thickness as shown in b,c,d and e. is decreased with the increase of Ra and as a consequence of this the rate of heat transfer is faster with increasing the Rayleigh number. The temperature distribution for different angles of inclination and Ra=10^8 is shown in **Fig**.**5**. It can be seen that at $\theta = 30^\circ$, the isotherm lines are inclined with direction of the enclosure tilted angle and the rate of heat transfer is less compared with case of $\theta = 0^\circ$. The isotherm lines be thicker at the lower part of the hot wall and upper part of the cold one and this leads to the rate of heat transfer to be larger. This confirmed through **Fig**.**6**. which demonstrates the variation of the average Nusselt number with angles of inclination. As **Fig**.**5**. shows, the rate of heat transfer is continous to decrease from $\theta = 60^\circ$ to $\theta = 90^\circ$. At $\theta = 120^\circ$ to $\theta = 180^\circ$, the rate of heat transfer is noticeably increased and this confirmed at **Fig**.**6**.. Also it can be seen from **Fig**.**6** that the average Nusselt number is increased with the increase of Ra for all angles of inclination because when Ra is increased, the buoyancy induced flow is increased and that leads to increase the rate of heat transfer. The local nusselt number variation along the hot wall for different Ra and $\theta = 0^\circ$ is depicted in **Fig**.**7**. It can be seen that the the lower corner of the hot wall indicated the high value of Nu and hence the high rate of heat transfer. When the enclosure is tilted with the considered angles of inclination($0 \le \theta \le 90 \deg.$), **Fig**.**8**., the local Nusselt number values is decreased. It is evident that for $\theta = 30^\circ$ to $\theta = 90^\circ$, the lower corner(y/H=0) of the hot wall disclosed the high values of Nu while at $\theta = 120^\circ$ to $\theta = 180^\circ$, this position is shifted to y/H=0.95 as a

result of change of the location of hot and cold walls and hence changing the strength of buoyancy force.

CONCLUSIONS

In the present paper, the turbulent 2D natural convection inside inclined square enclosure has been successfully predicted. From the computed results, the following conclusions can be obtained.

- The rate of heat transfer is increased with the increase of Ra and decreased with the increase of angle of inclination($0 \le \theta \le 90 \deg.$) and converse verse at($90 \le \theta \le 180 \deg.$) .
- The local Nusselt number values along the hot tilted wall is higher at the bottom section of the wall, while for the tilted cold wall at the top section.
- The thermal boundary layer thickness is decreased with the increase of Ra
- The resulted vortices are stretched to the middle of the enclosure with the increase of Ra.

REFERENCES

-Ampofo, F., Karayiannis, T.G., " Experimental benchmark data for turbulent natural convection in an air filled square cavity", Int. J. Heat Mass Transfer, vol.46, 2003.

-Corcione, M., " Effect of thermal boundary conditions at side walls upon natural convection in rectangular enclosures heated from below and cooled from a bove", Int. J. Thermal Sci. vol.42, 2003.

-El shirbiny, S.M., Hollands, G.D., Raithby, " Nusselt number distribution in a vertical and inclined air layers", J. heat Transfer, 1983.

-Elshirbiny, S.M., Hollands, G.D., " Heat transfer by natural convection across vertical and inclined air layers", J. Heat Transfer 104, 1982.

-Ganzarolli, M.M, Milane Z, L.F., " Natural convection in rectangular enclosures heated from below and symmetrically cooled from the sides", Int. J. Heat and Mass Transfer, 1995.

-Hart,E.J., "Stability of the flow in a differentially heated inclined box", J. Fluid Mech.,1971.

-Jones, W.P., Lunder, B.E., The prediction of laminarization with a two equation model of turbulence", J. Heat and Mass transfer, 1972

-Kuyper, R.A, Van Der Meer, C.J., Henkes, R.A.," Numerical study of laminar and turbulent natural convection in an inclined square cavity, Int.J. Heat mass Transfer,36,1993.

-Lankhorst, A.M., Henkes, Hoogendoorn, C.J.,'' Natural convection in cavities at high Rayleigh numbers", second UK national conference on heat transfer, university of Strathclycle, Glasgow, 1991

-Markatos, N.C., Pericleous, K.A., " Laminar and turbulent natural convection in an enclosed cavity", Int. J. Heat mass transfer, 1984.

-Osttrach, S., " Natural convection in enclosure", J. heat Transfer Trans., ASME, 1988.

Vahl Davis, G.De., " Natural convection in a square cavity, a comparison exercises", Int. J. Numer. Methods Fluids, 1983.

-Versteege, H. and Meer, W." An introduction of computational fluid dynamics", Hemisophere Publishing Corporation, United State of Americs, 1995.

-Zhong, Z.Y., Yang, K.T., " Variable property natural in tilted cavities with thermal radiation", Numerical Methods in Heat Transfer, vol.3, 1985.

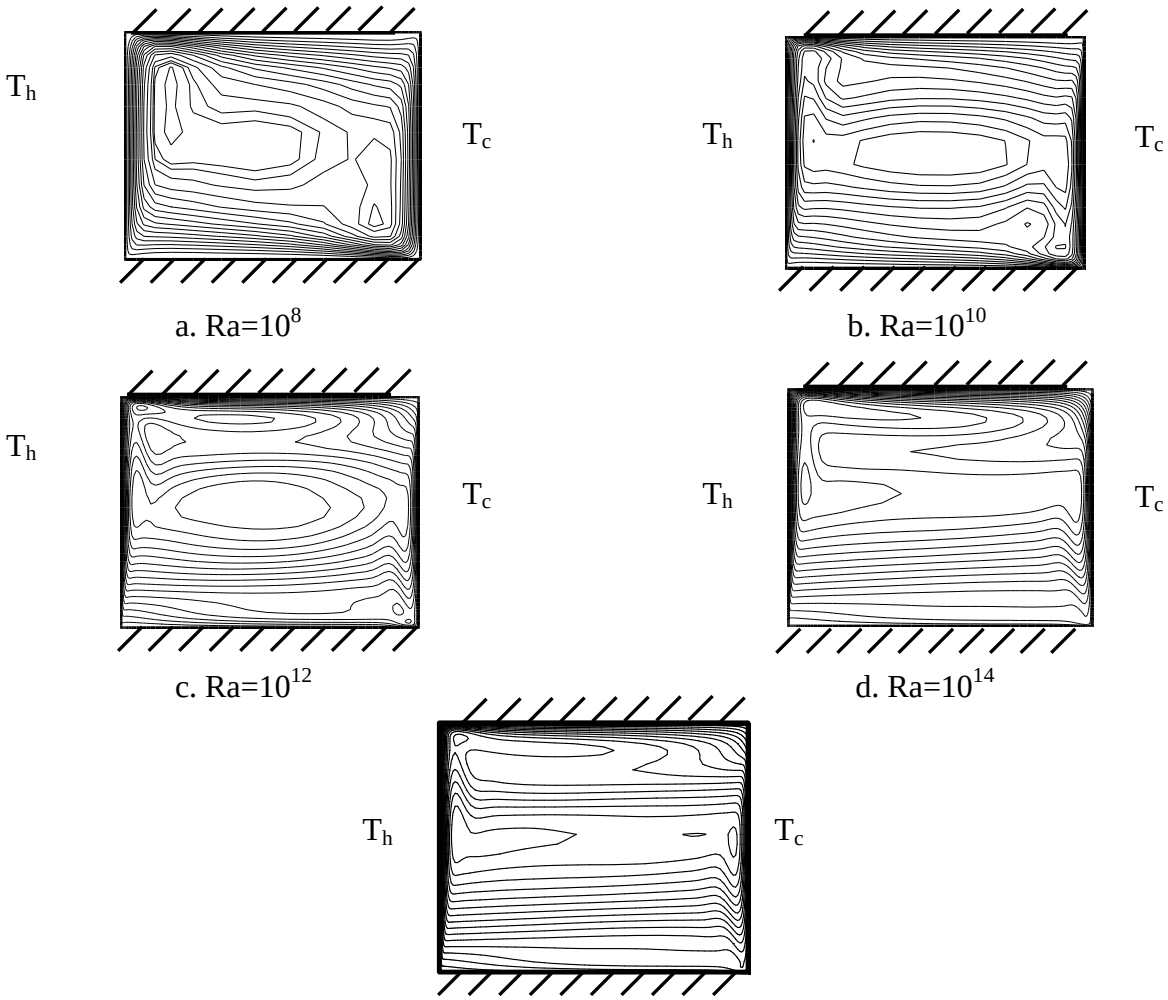

Fig.2. stream function distribution at different Ra and. $\theta = 0^\circ$

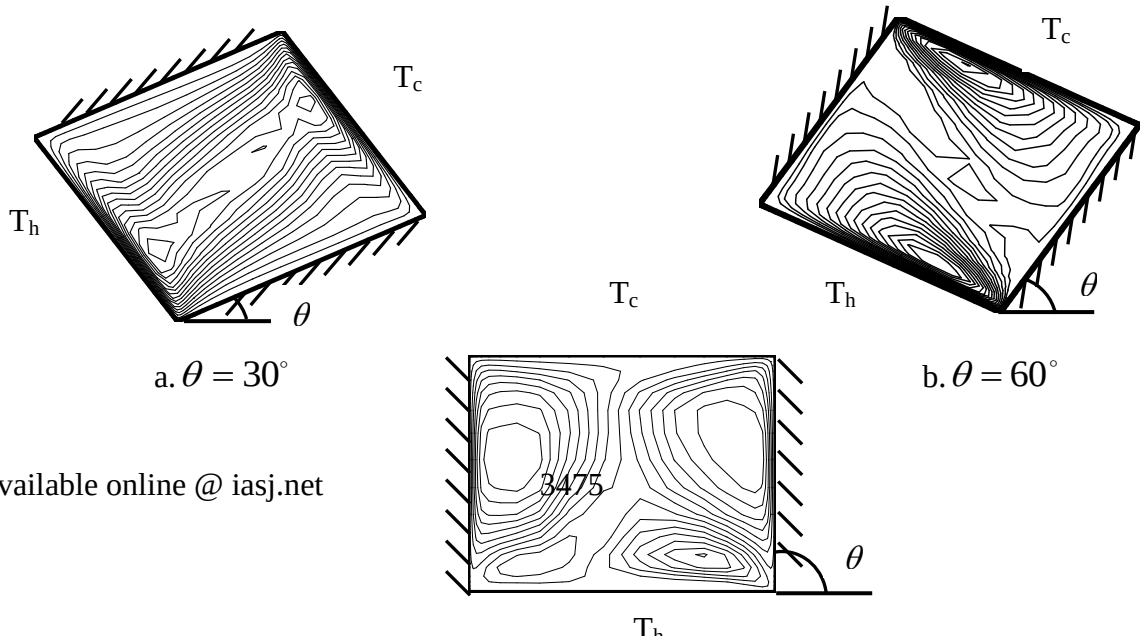

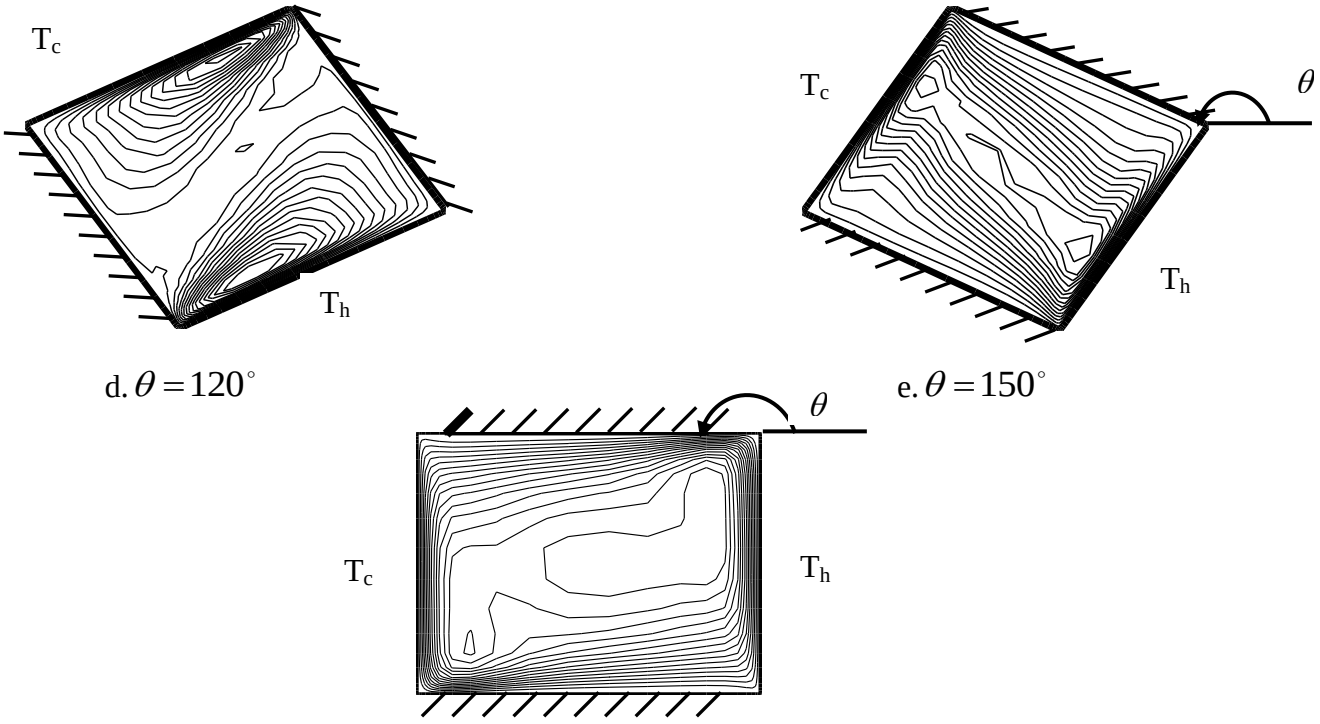

d. $\theta = 120^{\circ}$ e. $\theta = 150^{\circ}$

f. $\theta = 180^{\circ}$

Fig.3. stream function distribution at different angles of inclination and Ra=10^8

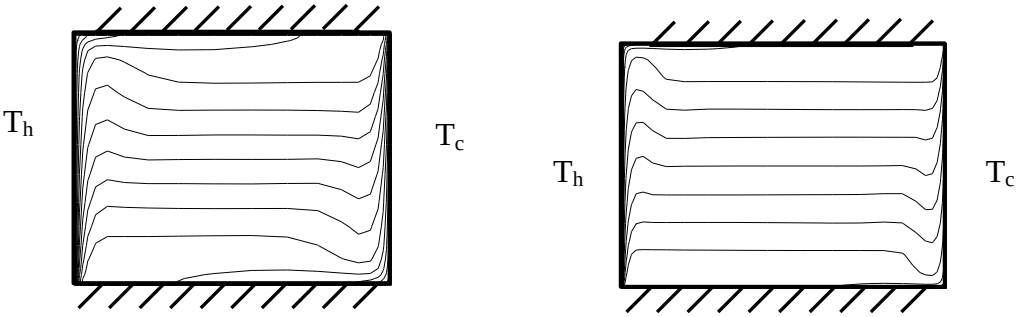

a. Ra=10^8 b. Ra=10^{10}

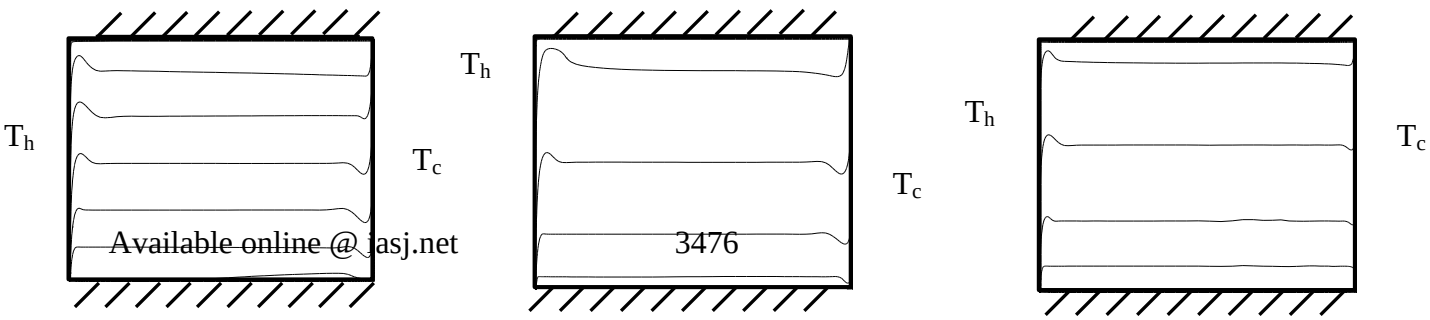

c. Ra=10^{12} d. Ra=10^{14} e. Ra=10^{16}

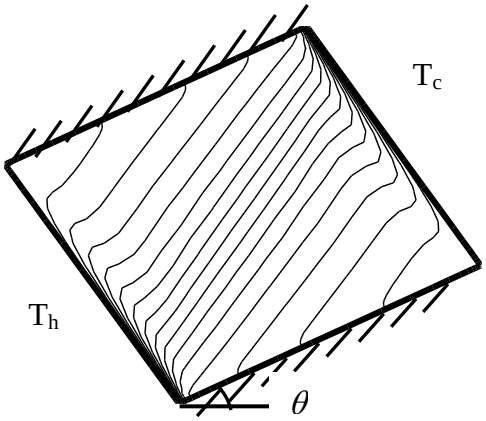

a. $\theta = 30^\circ$

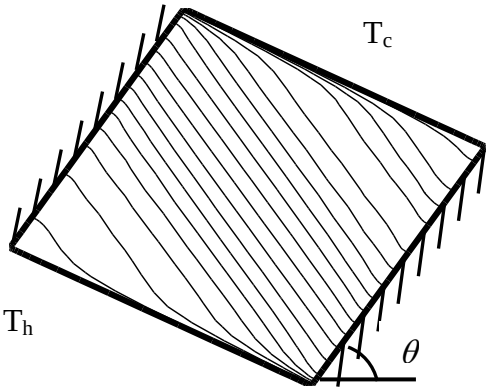

b. $\theta = 60^\circ$

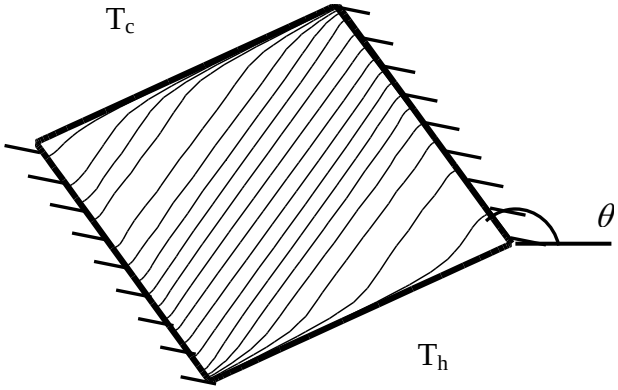

c. $\theta = 120^\circ$

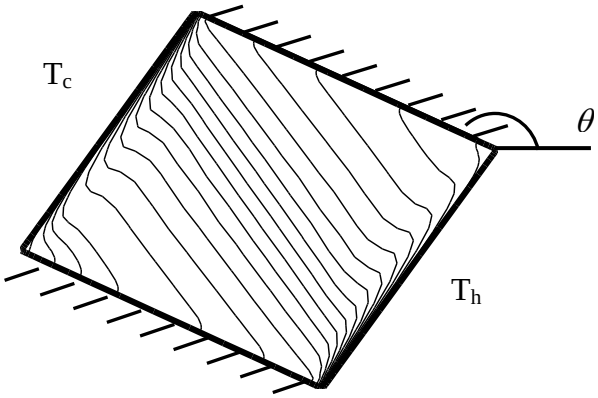

d. $\theta = 150^\circ$

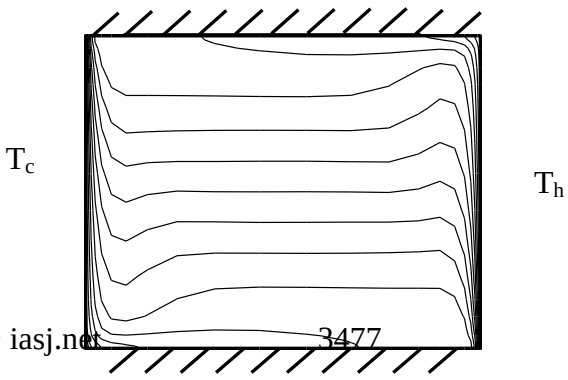

e. $\theta = 180^\circ$

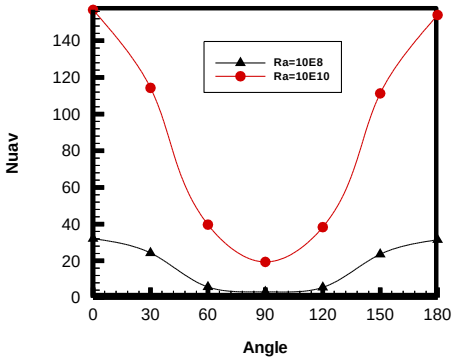

a

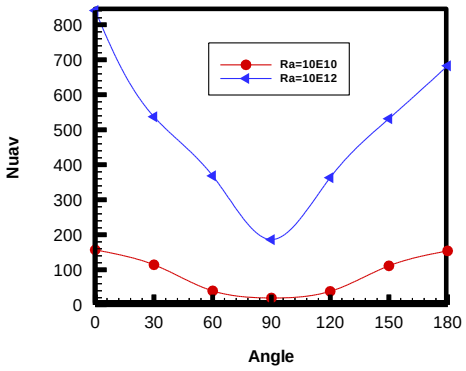

b

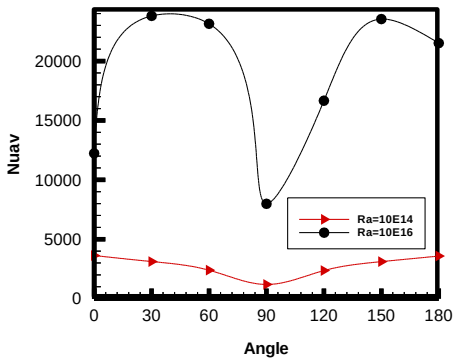

c

Fig.6. variation of average Nusselt number with angles of inclination at different Rayleigh numbers

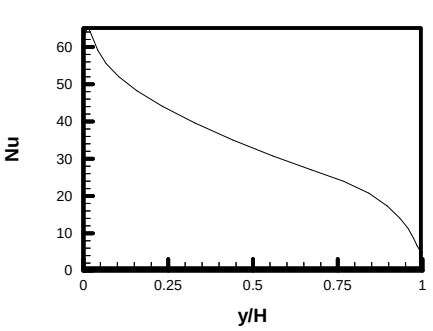

a.

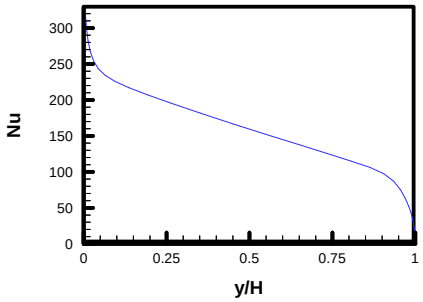

b.

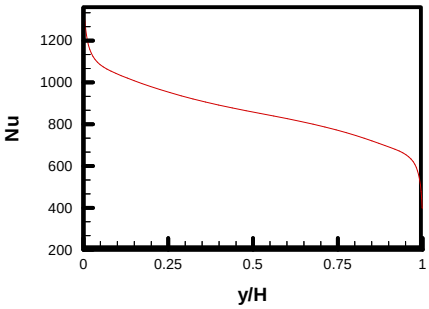

c.

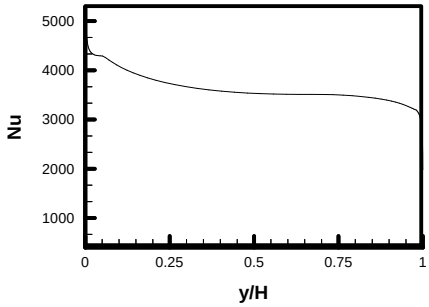

d.

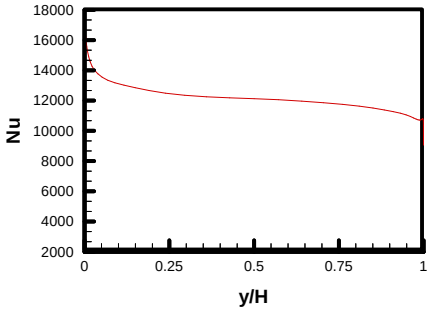

e.

Fig.7. Local Nusselt number variation at the hot wall (x=0) for different Ra; a. Ra=10^8; b. Ra=10^{10}; c. Ra=10^{12}; d. Ra=10^{14} e. Ra=10^{16}

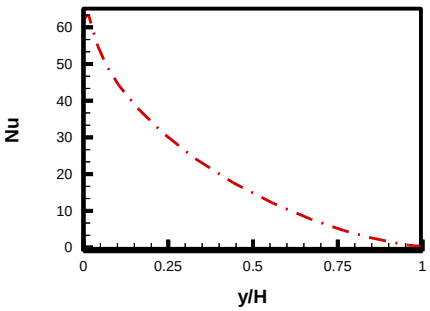

a. $\theta = 30^{\circ}$

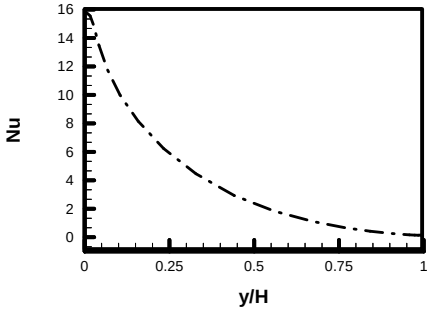

b. $\theta = 60^{\circ}$

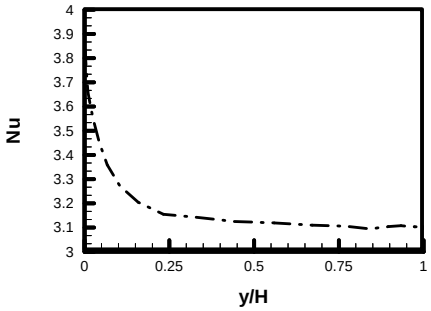

c. $\theta = 90^{\circ}$

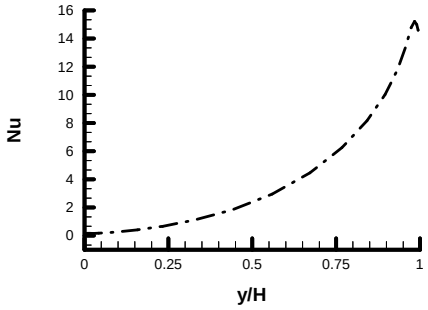

d. $\theta = 120^{\circ}$

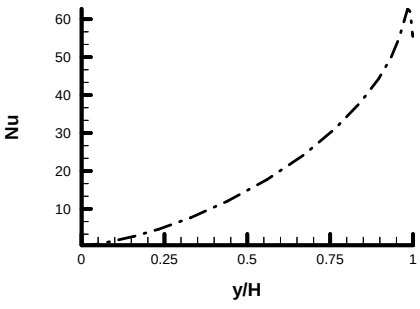

e. $\theta = 150^{\circ}$

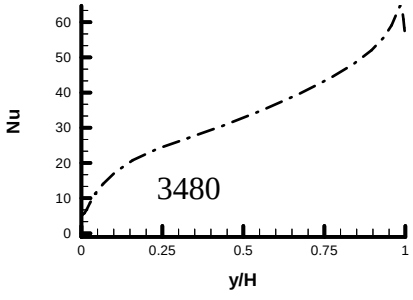

NOMENCLATURE

C_u, $C_{1\varepsilon}$, $C_{2\varepsilon}$	turbulence constants, -
G	generation term by shear, Kg/m.sec^3
H	height of the enclosure, m
k	turbulent kinetic energy, m^2/s^2
Nu	local Nusselt number, -
Nu_{av}	average Nusselt number, -
P	pressure, N/m^2
Pr	Prandtl number, -
Ra	Rayleigh number $\left(\frac{g\beta H^3(T_h - T_c}{\alpha\mu}\right)$, -
T_C	cold wall temperature, Ċ
T_h	hot wall temperature, Ċ
x, y	Cartesian coordinates, m
X	dimensionless Cartesian coordinate $\left(\frac{x}{H}\right)$,-

Greak symbols:

ϵ	turbulance dissipation rate, m^2/s^3
μ	dynamic viscosity, N.s/m^2
μ_t	turbulent viscosity, N.s/m^2
v_t	eddy dynamic viscosity, m^2/s
μ_{eff}	effective turbulent viscosity, N.s/m^2
Γ_{eff}	effective exchange coefficient, kg/m.s

Φ dimensionless temperature $\left(\frac{T-T_c}{T_h-T_c}\right)$, -

σ_k ;σ_ϵ turbulent schmidt numbers, -

α thermal diffusivity of fluid, m^2/s

DRAG REDUCTION BY USING ANIONIC SURFACTANTS

Sameera M. Hamad-Allah **Hussein H. Hussein**

University of Baghdad
College of Engineering
Petroleum Engineering Department

ABSTRACT

The aim of reducing drag is to increase the flow efficiency by using the same pipes and pumps. As a result the amount of crude oil transported will increase without using new pipes and pumps.

In the present work, the effectiveness of two surfactants (Sodium dodecyl benzene sulfonate (SDBS) and Sodium lauryl sulfate (SLS)) are studied by using a closed loop system. This system consists of three pipes made from commercial steel, each one with different diameter (0.75, 1 and 1.5 inch). The length of each individual test section of the pipe is two meters. The experimental work is achieved under three different temperatures (30º, 40º and 50°C). The concentrations of both surfactants used are ranging between 50 to 300 weight ppm.

Laboratory tests showed that there is a direct proportionality between the percentage of drag reduction (%DR) on one hand and in Reynolds number and pipe diameter on the other hand. Inverse proportionality is observed between %DR and temperature. The %DR increases as concentration increases, but at a certain higher concentration, this relation will reverse.

The final results showed that the highest drag reduction (%DR) was 23.67%. This value is obtained when 200 ppm SDBS is added at 30°C.

The calculated values of friction factor were found to be situated between Blasius and Virk asymptote adjacent.

الخلاصة:

إن الهدف من تقليل الإعاقة هو زيادة كفاءة الجريان باستخدام نفس الأنابيب والمضخات. بالنتيجة تزداد كمية النفط الخام المضخوخ بدون استخدام مضخات وأنابيب جديدة.

في هذا العمل تم دراسة فعالية نوعين من معاملات التوتر السطحي(المنظفات) وهي:

(SDBS, SLS) باستخدام منظومة جريان مغلقة. هذه المنظومة تتألف من ثلاثة أنابيب مصنوعة من مادة الستيل الصناعي ذات أقطار مختلفة وهي (0.75 و 1 و 1.5 أنج). طول كل مقطع اختبار يبلغ (2 متر). تم إجراء العمل ألمختبري تحت ثلاث درجات حرارية مختلفة وهي (30 ,40 ,50 درجة مؤية). تركيز المنظفين المستخدمين تروح بين (50-300 جزء لكل مليون جزء وزني).

الفحوص المختبرية بينت وجود تناسب طردي بين نسبة تقليل الاعاقة (DR%) من جهة وعدد رينولد وقطر الأنبوب من جهة أخرى. يلاحظ وجود تناسب عكسي بين نسبة تقليل الاعاقة ودرجة الحرارة. إن زيادة تركيز معاملات التوتر السطحي يساعد على زيادة نسبة تقليل الاعاقة ولكن هذه الزيادة تعطي مفعول عكسي عند التراكيز العالية.

أظهرت النتائج النهائية إن أعلى نسبة لتقليل الاعاقة بلغت 23.76 % .نحصل على هذه القيمة بإضافة 200 جزء لكل مليون جزء من مادة SDBS وبدرجة حرارة 30 درجة مؤية.
تقع القيم المحسوبة لمعامل الاحتكاك بين محاذي Blasius ومحاذي Virk.

INTRODUCTION

Drag is a term used to refer to pressure drop per unit length of pipe which resulted from friction. Many techniques for drag reducing were suggested by many researches. One of these techniques depends on suppressing turbulent eddies by using baffles with different heights, other techniques used layers of greasy materials or bubble layers to reduce friction. The modern techniques use small amounts of an additive in a fluid which cause a reduction in the turbulent friction compared with that of the pure fluid at the same flow rate (Jiri Myska 1997). The word "drag" may also be defined as the resistance force parallel to the direction of fluid flowing over a solid surface. Drag force may be expressed by two components: "friction component" which is equal to the stream wise component of all shearing stresses over the surface and "pressure drag component" which is equal to the stream wise component of all normal stresses (Mansour 1998).

There are many applications of drag reduction such as increasing flow rate in drilling operations, fire fighting and irrigation. In petroleum industry, drag reduction is of great importance in hydraulic fracturing of oil wells and transportation of liquid petroleum (Thomas R. 1981).

White (1967) examined flowing of a dilute solution of cetyl trimentol ammonium bromide (CTAB) at concentration 508 ppm. He concluded that the drag reduction increases by increasing pipe diameter. Hershy, Mcmillan and Boxter (1971) used aluminum dioctoate in toluene as drag reducer. Zakin (1983) used large number of non–ionic surfactants to study the effect of surfactant structure, concentration, temperature and mechanical degradation on drag reduction. Abdul–Hakeem(2000) used one type of non–ionic surfactant (nonyl phenol) and two types of anionic surfactants (sodium dodecyle benzene sulfonate, SDBS and sodium lauryl sulfate , SLES) as drag reducers in turbulent flow of Iraqi crude oil.

EXPERIMENTAL WORK AND TEST PROCEDURE

The flow system used in this work consists of reservoir tank, pump, flow meter, pipes, valves, pressure transmitters, chiller, digital thermometers and computer interface. A schematic

diagram of flow system is given in figure (1). The diameters of pipes are 0.75, 1 and 1.5 inch while the length used is two meters. These dimensions are considered suitable for laboratory work.

The following experimental procedure is carried out :

1. The crude oil is permitted to flow in only one pipe. The flow rate of solution was controlled by bypass section until this rate reaches a specific value.
2. The pressure drop is measured by transmitter which is connected with the computer.
3. Steps 1 and 2 are repeated with different flow rates, keeping in mind that this operation is carried out at constant temperature.
4. The above steps are redone but with the addition of a solution of different additives to the crude oil.
5. Steps 1 to 4 are repeated for the other two pipes.
6. Using different surfactant types, concentrations and temperatures, the above procedure is redone for the sake of observing the effect of these parameters on pressure drop.

The main properties of crude oil before and after adding are given in table (1)

Table (1) Physical properties of crude oil

Temperature °C	Specific gravity before adding	Kinematic viscosity csc before adding	Specific gravity after adding	Kinematic viscosity csc after adding
30	0.879	15.314	0.876	15.315
40	0.873	10.152	0.874	10.152
50	0.867	4.233	0.869	4.232

The velocities used are 1.7 to 5.3 m/sec. The choice of the velocities is controlled by the pump capacity.

The concentration of available surfactants are first chosen to be very small (50 ppm). As this concentration gave small drag reduction the concentration is continuously increased. At specific concentration (300 ppm), the drag reduction decreased hence the concentration increase is stopped.

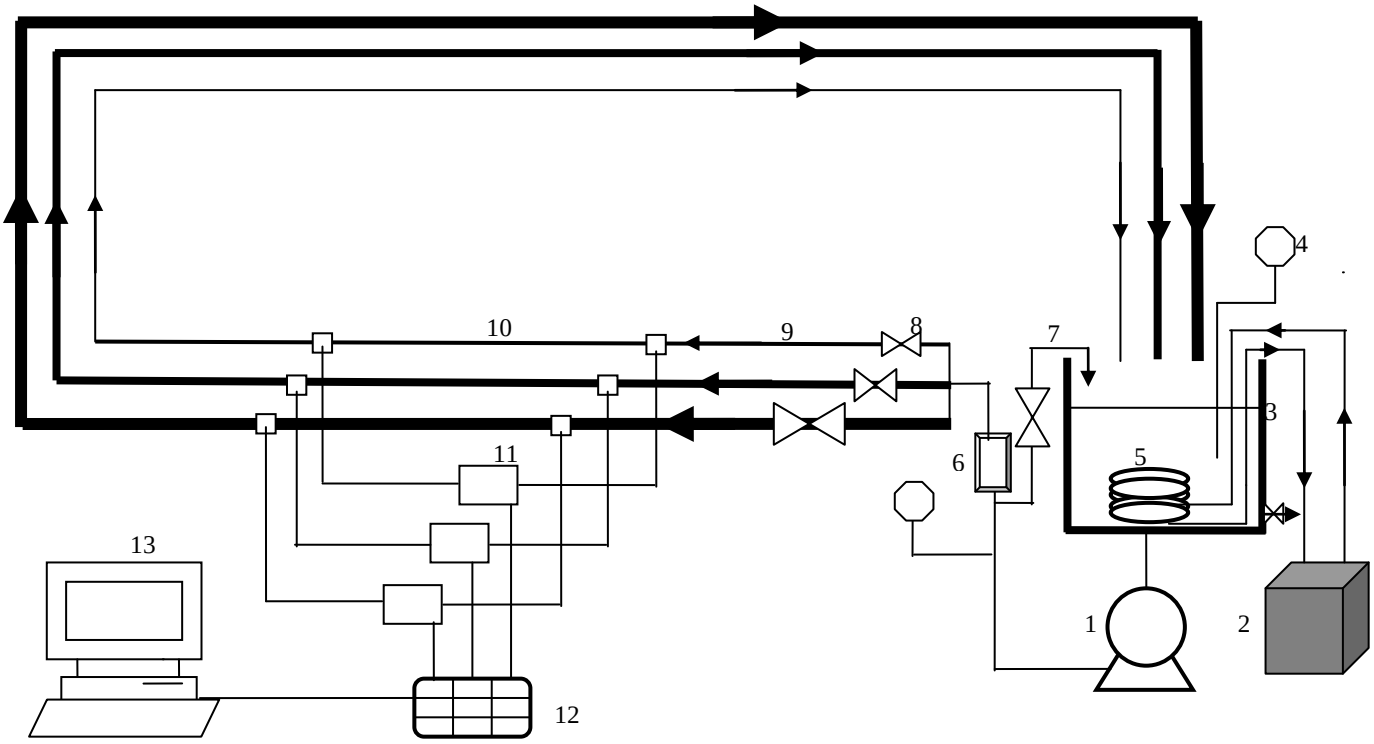

1. Centrifugal pump, 2. Chiller, 3. Tank, 4. Digital thermometer, 5. Cooling coil, 6. Flow meter, 7. By pass line, 8. Valve, 9.Entrance length, 10. Test section, 11. Pressure transducer, 12. Parallel port, 13.P/C interface.

Figure (1) schematic diagram of flow system

Experimental Calculations

The following equations are used to calculate velocity(V), drag reduction percentage(%DR) and Reynolds number(Re) respectively.

$$V = Q/\ \ A \tag{1}$$

$$\%Dr = \frac{\Delta P_b - \Delta P_a}{\Delta P_b} \tag{2}$$

$$\mathrm{Re} = \frac{\rho \cdot V \cdot D}{\mu} \tag{3}$$

RESULTS

Several runs (108) were carried out in this work to study the influence of the following variables on drag reduction:

1- Reynolds number and Pipe diameter.
2- Surfactants concentration.
3-Tempreature.

Effect of Reynolds Number and Pipe Diameter

Figures (2a-2d) shows the effect of Reynolds number and pipe diameter on %DR for concentrations (50-300) ppm for SDBS at 30°C at different pipe diameters (0.75, 1 and 1.5 inch). Figures (3a-3d) show the same effect but for SLS.

It is noticed that for a certain pipe diameter the %DR increases by increasing Reynolds number. This result is expected since the degree of turbulence inside the pipe increases as Reynolds number increases and this will provide a better media to the drag reducer (surfactant) to be more effective.

It is obvious that at the same Reynolds number, high %DR is obtained for larger pipe I.D This is because the increase in pipe diameter will give a large area for interaction between the aqueous solution of surfactant and crude oil. At temperature 40° and 50°C the same effects were observed.

Effect of Concentration

Figures (4a-4c) are plotted for SDBS at 30°C for different diameters and figures (5a-5c) for SLS at 30°C.

From figures (4 and 5), it is noticed that %DR increases as concentration increases to a certain value (about 200 ppm). This may be attributed to the formation of rod-like micelles which increases as concentration increases to some extent.

When the concentration became greater than 200 ppm, the rate of %DR increase will be less. Such behavior may be explained by the change of micelles structure from rod-like to spherical shape as explained by Virk(1967).

Effect of Temperature

The temperature of crude oil is reduced and controlled by a chiller. Figures (6a-6d) show the effect of temperature on %DR for concentrations (50-300) ppm for SDBS in pipe of 0.75 inside diameter at different temperatures, and figures (7a-7d) show similar plot but for SLS.

It is noticed that %DR decreases as the temperature increases for both additives used. This may be caused by the transformation of rod-like (or thread like) to spherical micelles these behavior noticed by Takashi(1993).

Friction Factor

The friction factor is calculated by the following equation(Bottural 1999):

$$f = \frac{\Delta P d / 4L}{\rho v^2 / 2} \quad (4)$$

The calculated value of friction factor is plotted versus Reynolds number on log-log scale as shown in figures 8 and 9. The friction factor is also calculated by using Blasius and Virk equations.

$$f = 0.0791(\mathrm{Re})^{-0.25} \quad \text{Blasius} \tag{5}$$

$$f = 0.59(\mathrm{Re})^{-0.58} \quad \text{Virk} \tag{6}$$

As can be seen from figures 8 and 9, the values of friction factor obtained by equation (4) lie between Blasius and Virk .

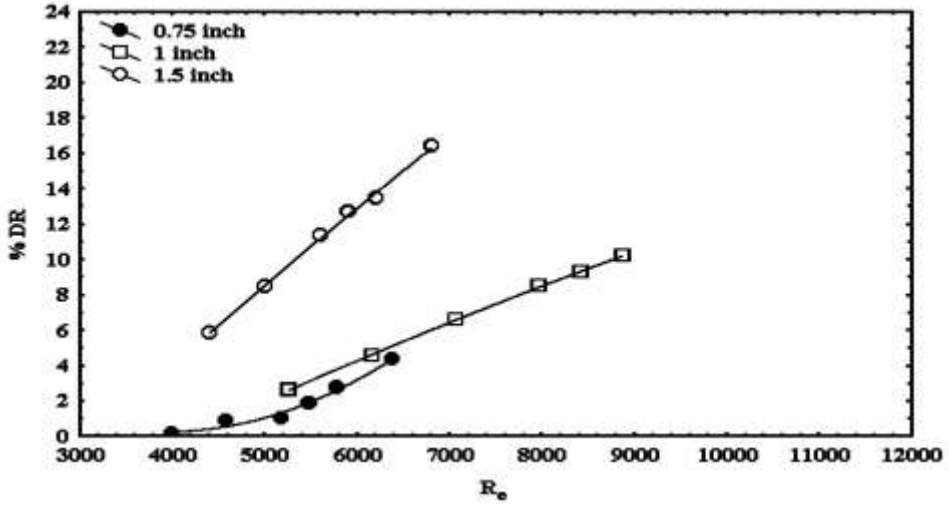

Figure (2a)

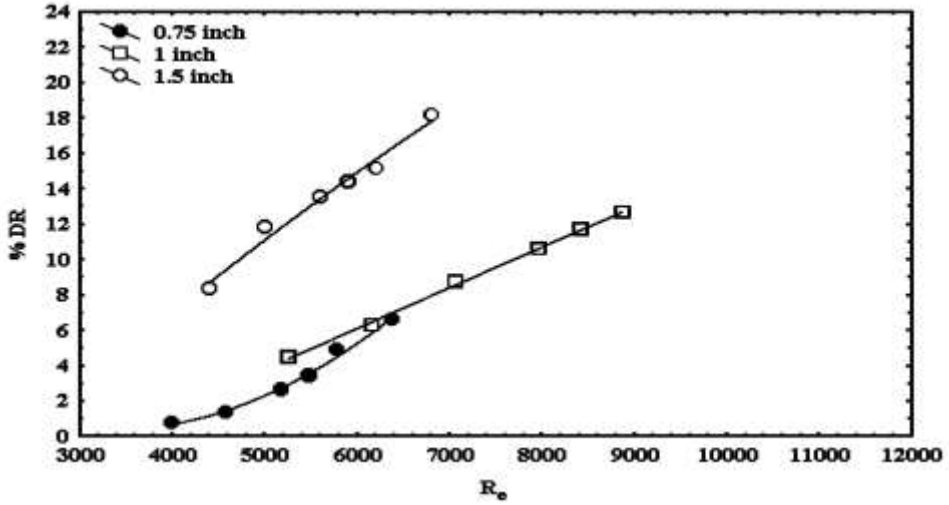

Figure (2b)

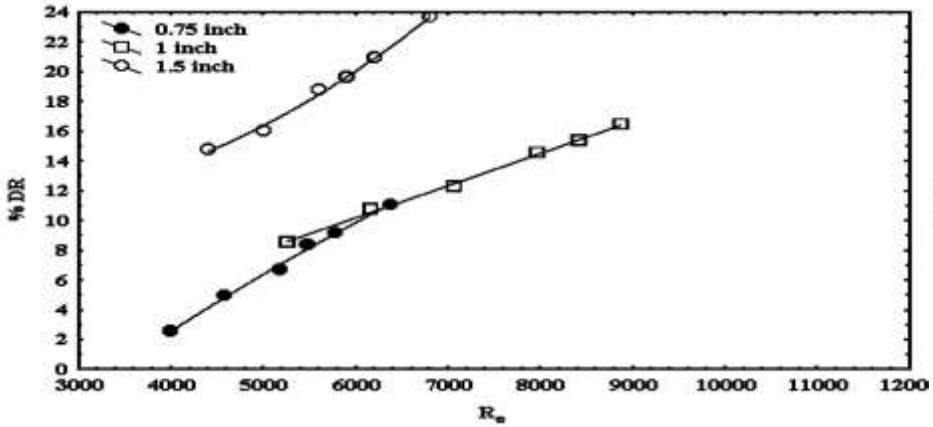

Figure (2c)

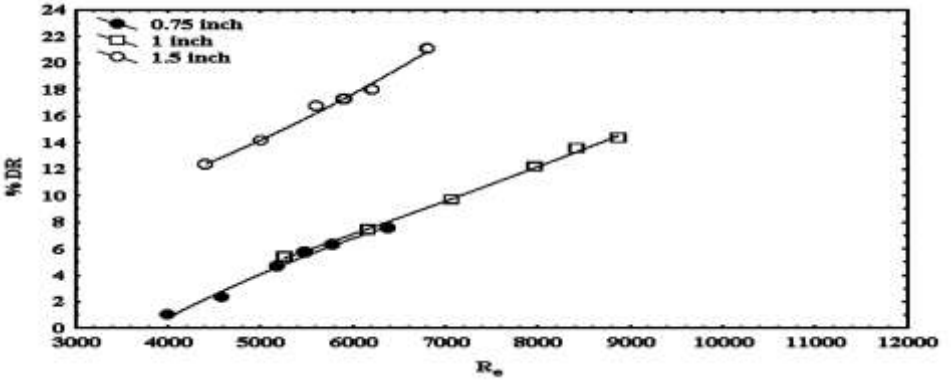

Figure (2d)

Figure (2) effect of Reynolds number and pipe diameter on %DR for SDBS at 30°C; (a): 50 ppm, (b): 100 ppm, (c): 200 ppm and (d): 300 ppm

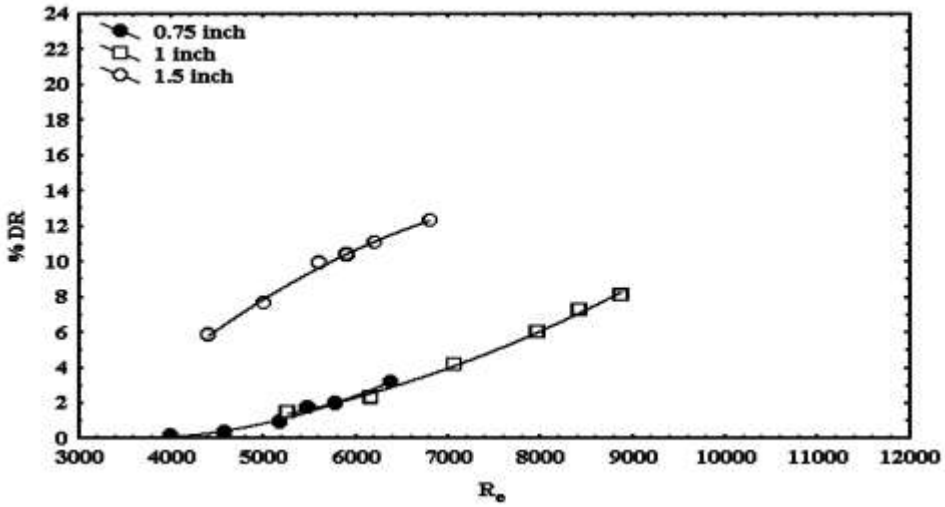

Figure (3a)

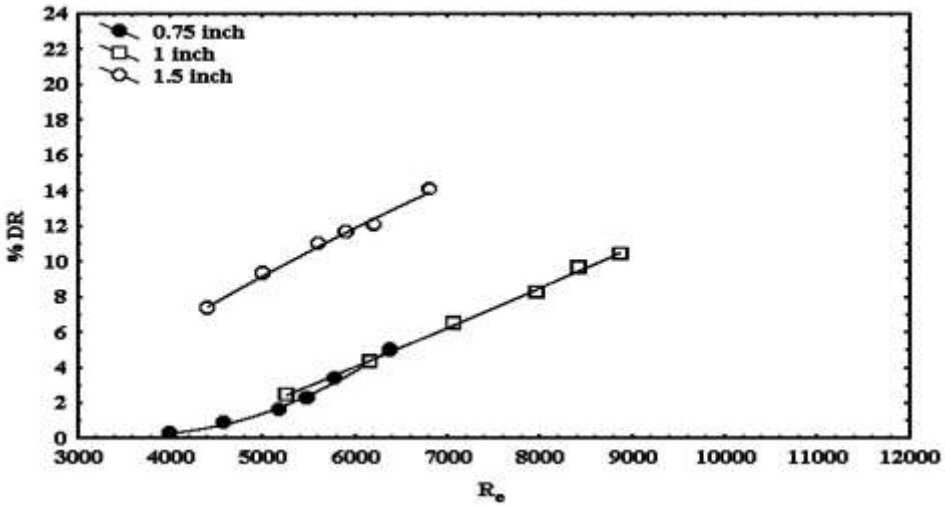

Figure (3b)

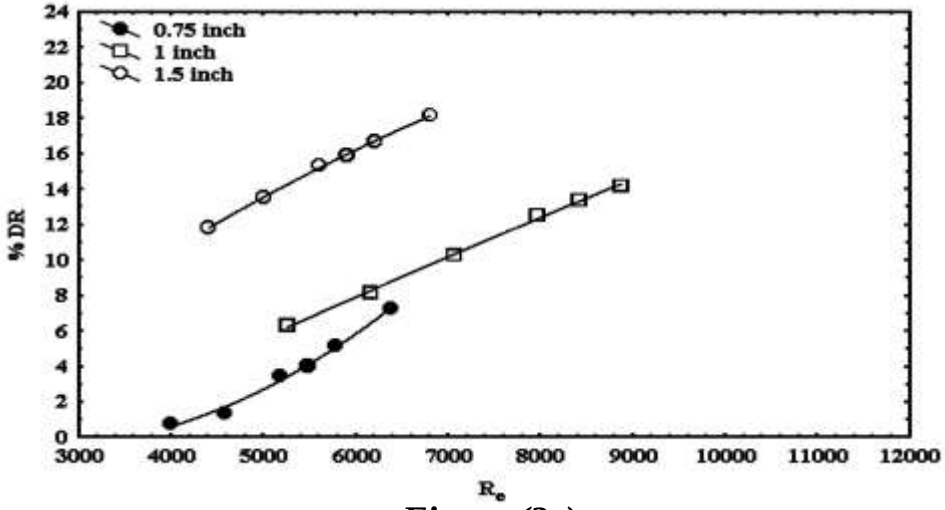

Figure (3c)

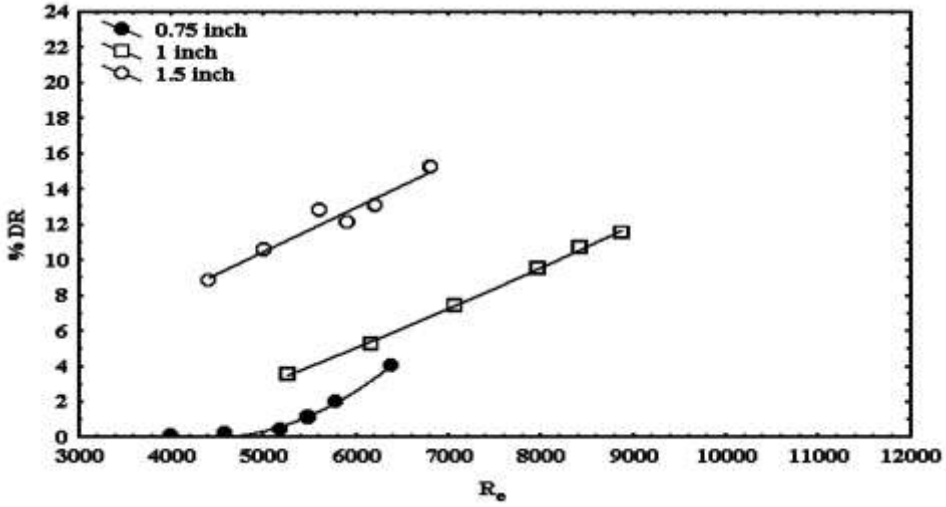

Figure (3d)

Figure (3) effect of Reynolds number and pipe diameter on %DR for SLS at 30°C; (a): 50 ppm, (b): 100 ppm, (c): 200 ppm and (d): 300 ppm

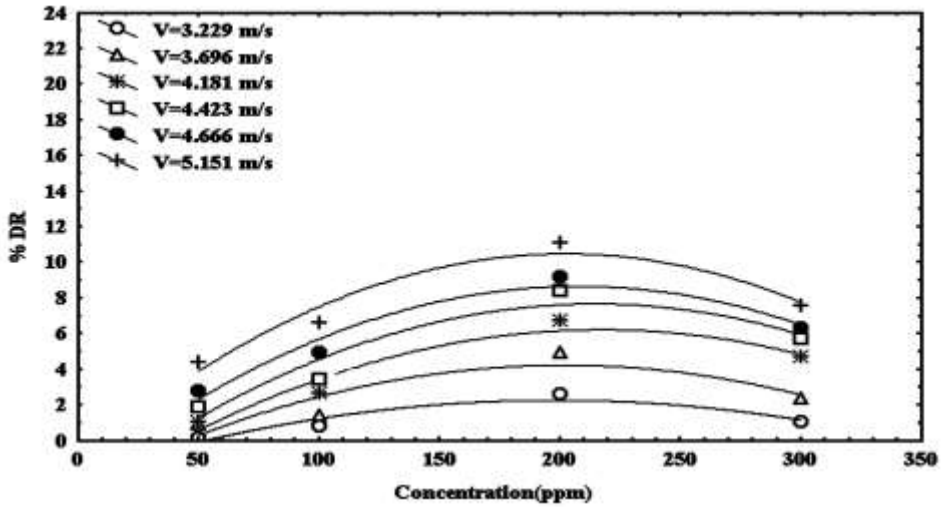

Figure (4a)

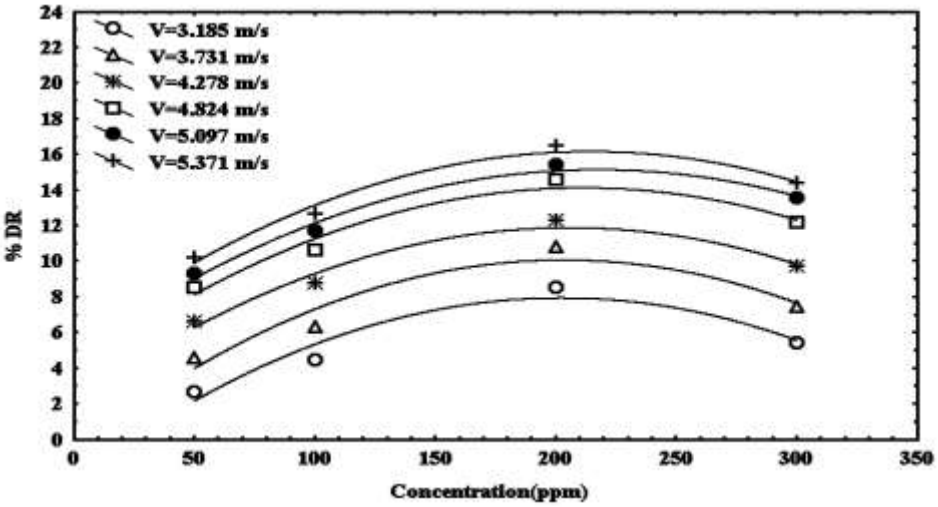

Figure (4b)

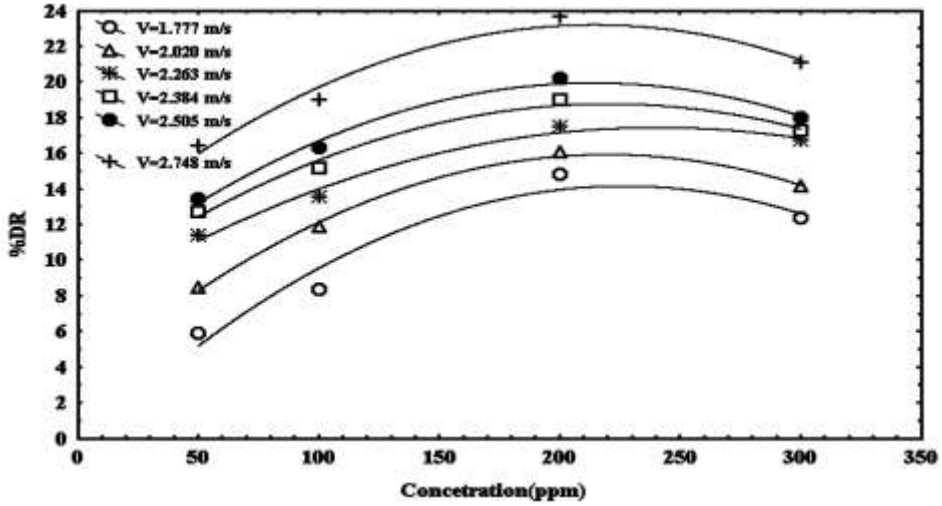

Figure (4c)

Figure (4) effect of concentration on %DR for SDBS at 30°C; (a): 0.75 inch ID, (b): 1 inch ID and (c): 1.5 inch ID

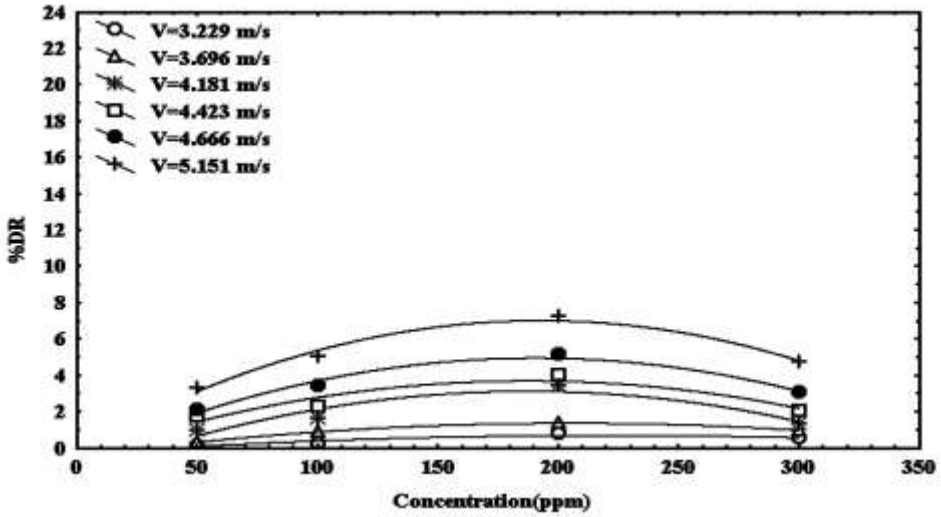

Figure (5a)

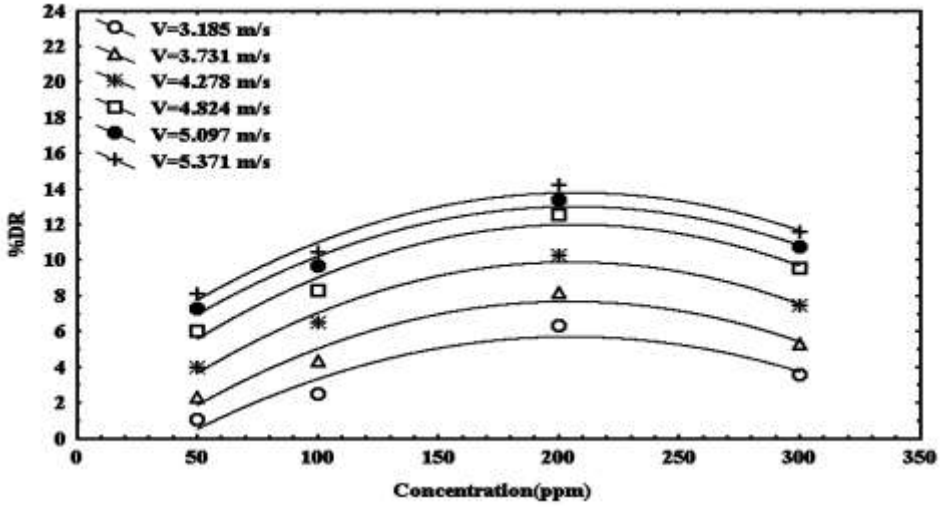

Figure (5b)

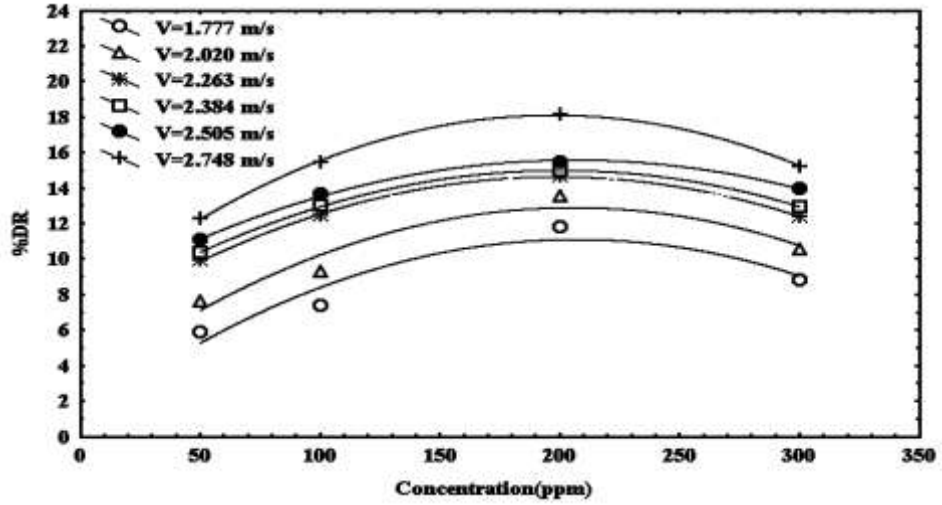

Figure (5a)

Figure (5) effect of concentration on %DR for SLS at 30°C; (a): 0.75 inch ID, (b): 1 inch ID and (c): 1.5 inch ID

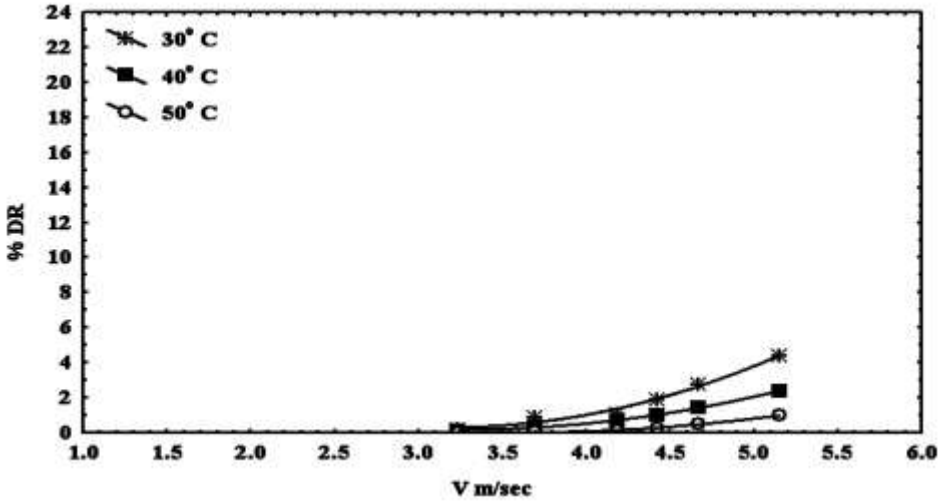

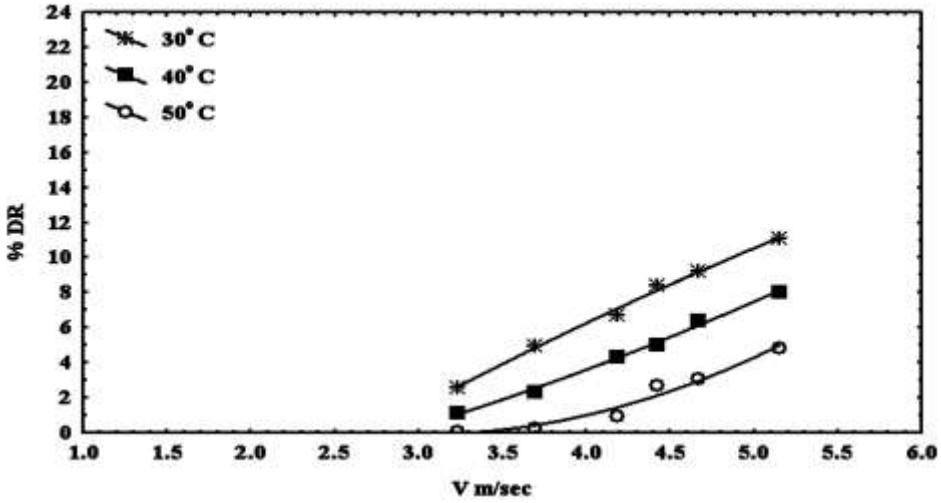

Figure (6c)

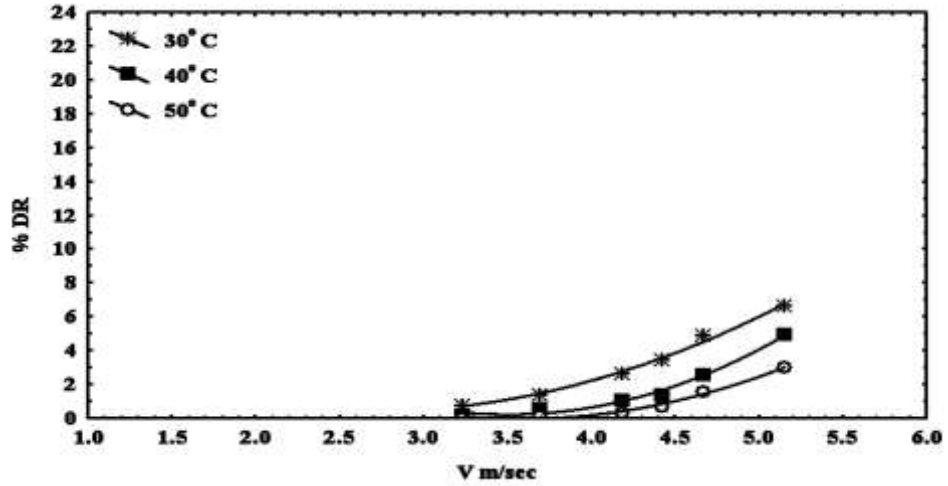

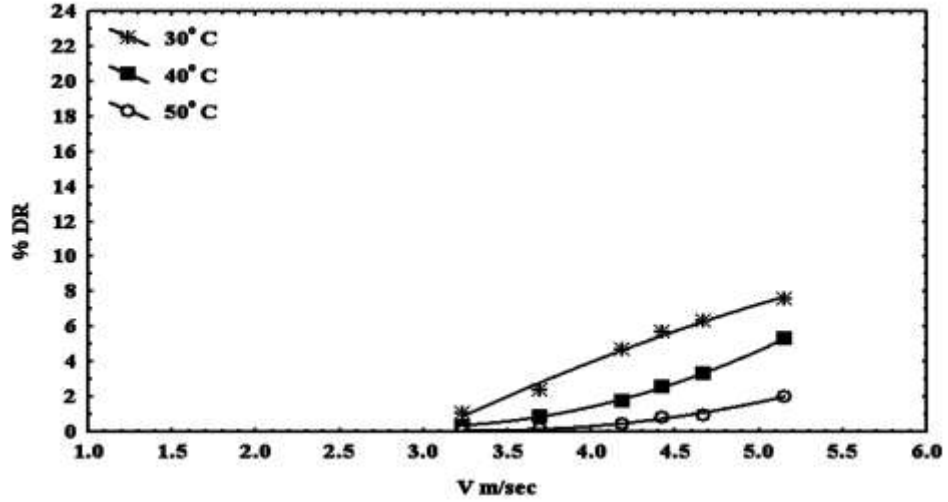

Figure (6c)

Figure (6) effect of temperature on %DR for SDBS at 0.75 inch I.D.; (a): 50 ppm, (b): 100 ppm, (c): 200 ppm and (d): 300 ppm

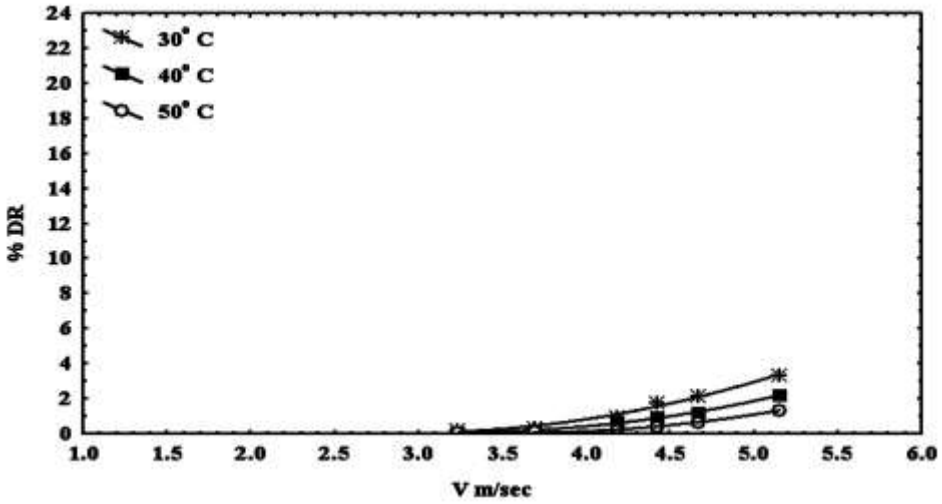

Figure (7a)

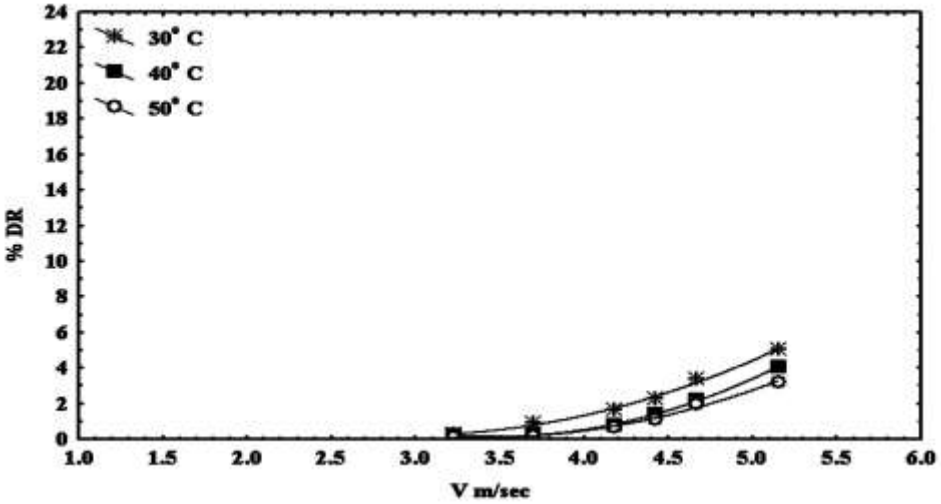

Figure (7b)

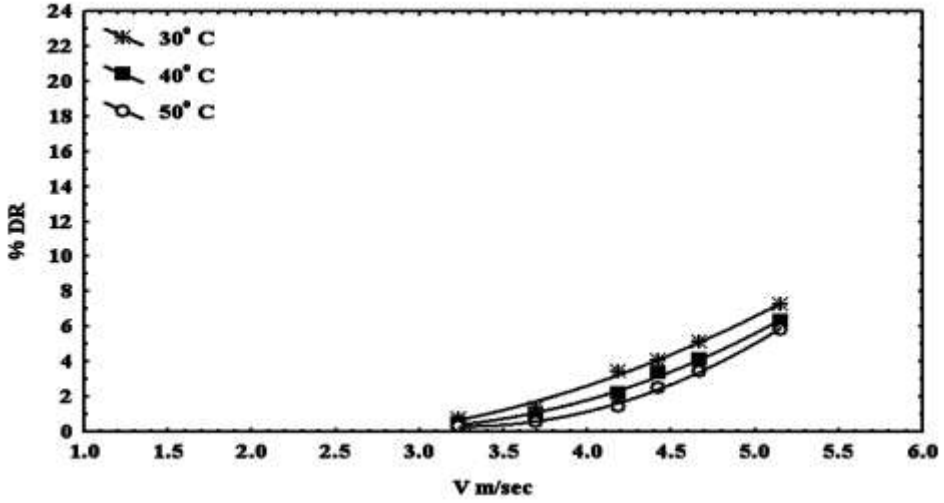

Figure (7c)

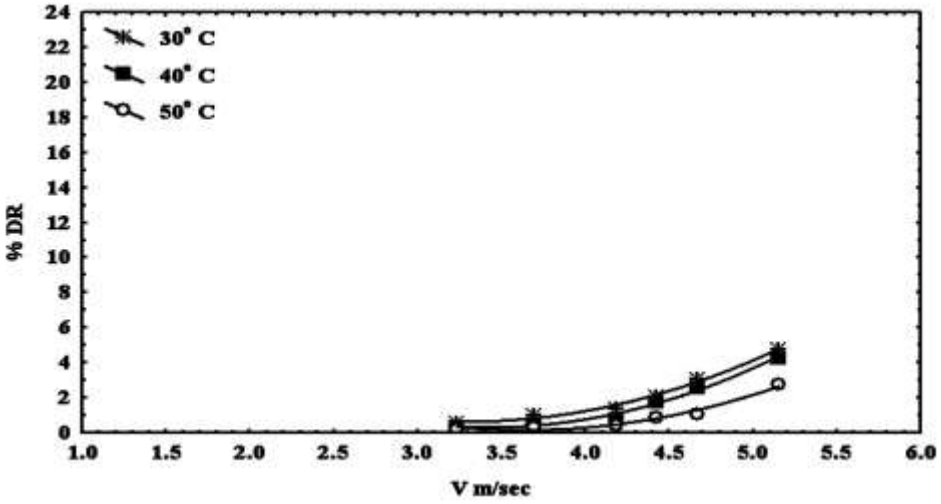

Figure (7d)

Figure (7) effect of temperature on %DR for SLS at 0.75 inch I.D.; (a): 50 ppm, (b): 100 ppm, (c): 200 ppm and (d): 300 ppm

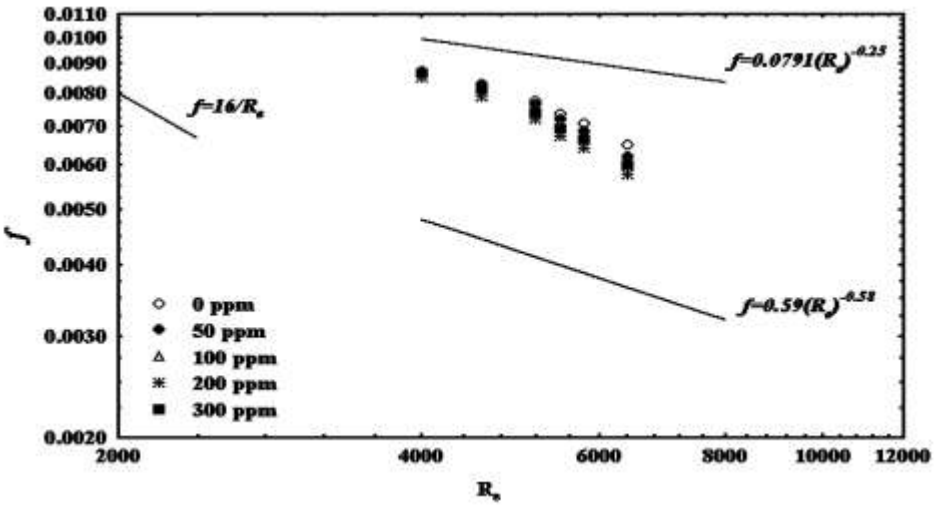

Figure (8a)

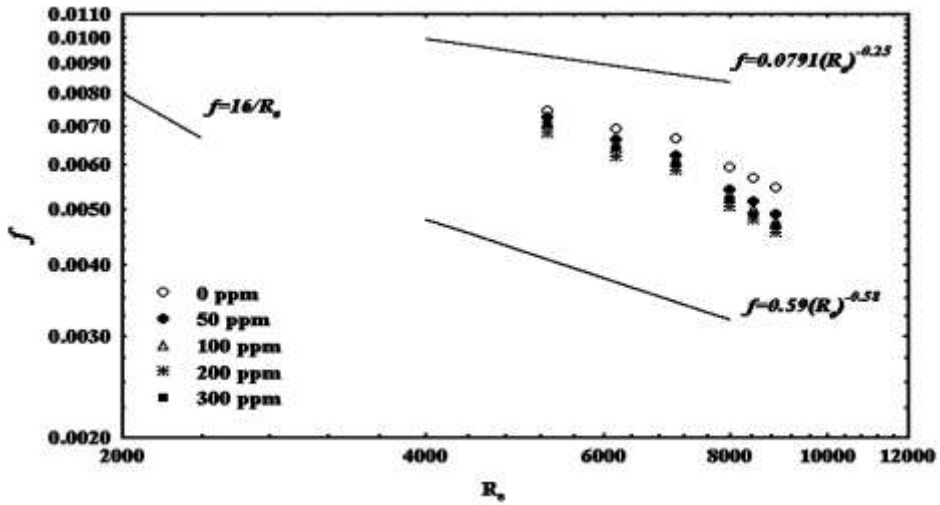

Figure (8b)

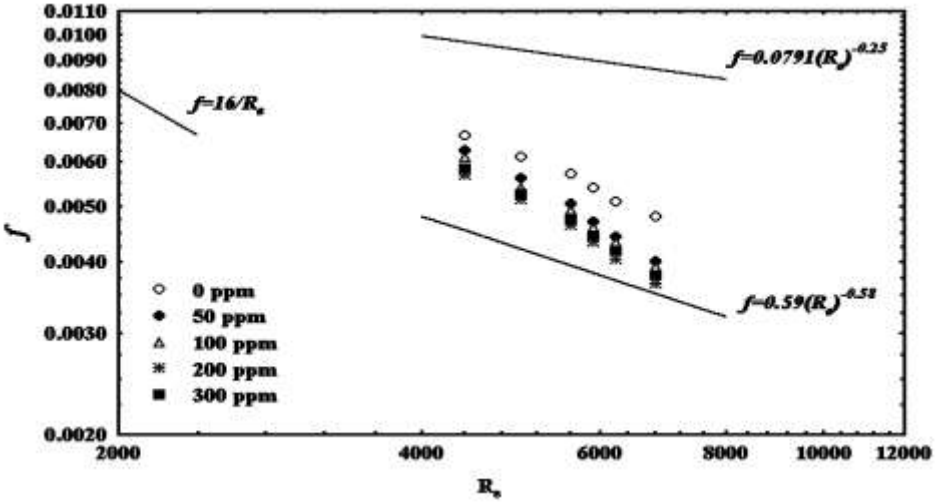

Figure (8c)

Figure (8) calculated friction factor versus Reynolds number at different concentration of SDBS at 30°C; (a): 0.75 inch ID, (b): 1 inch ID and (c): 1.5 inch ID

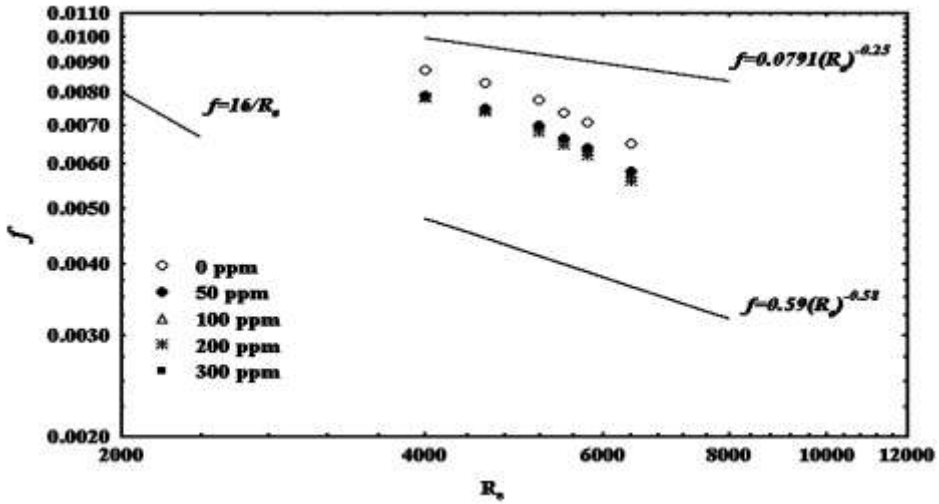

Figure (9a)

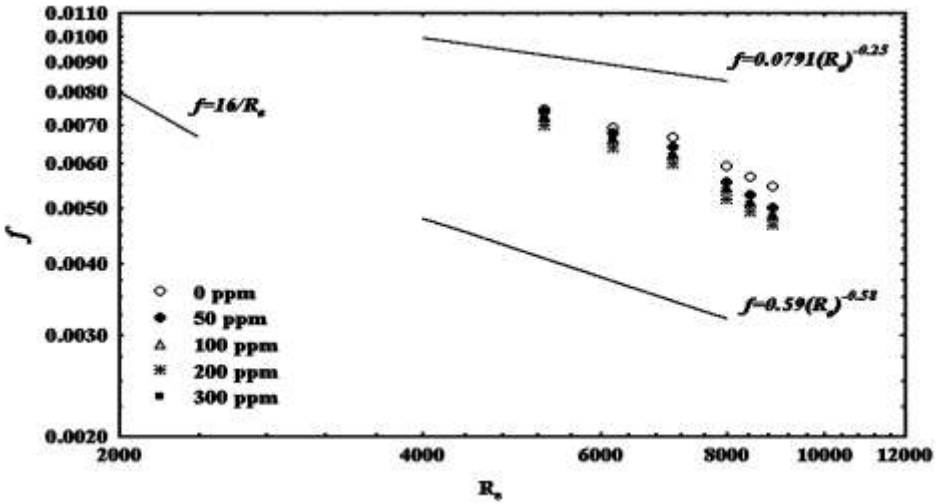

Figure (9b)

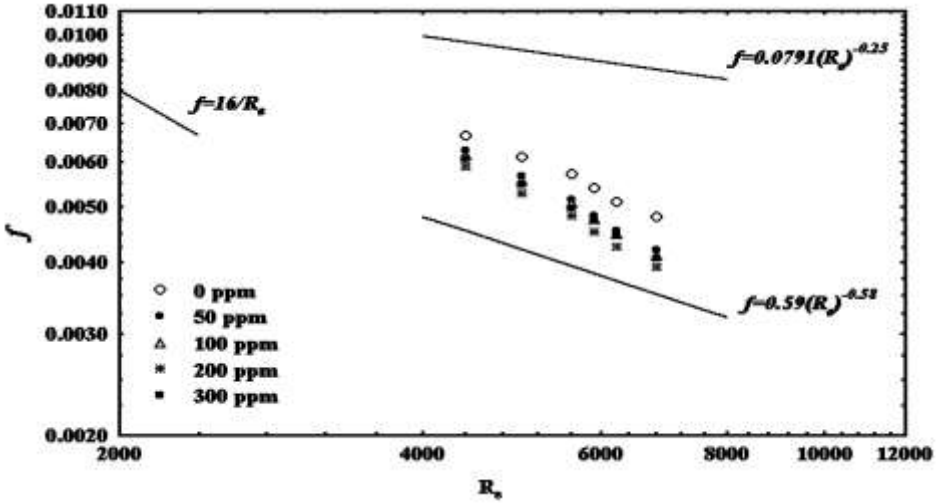

Figure (9c)

Figure (9) calculated friction factor versus Reynolds number at different concentration of SLS at 30°C; (a): 0.75 inch ID, (b): 1 inch ID and (c): 1.5 inch ID

CONCLUSIONS

1-Maximum % DR obtained in the present work was 23.67% by using SDBS surfactant at 30°C in 1.5 inch pipe diameter. This indicates that both surfactants used are effectiveness of moderate as drag reducer with the crude oil under study.

2-The drag reduction percent increases when :

- Increasing Reynolds number.
- Increasing surfactant concentration to a certain limit.
- Decreasing temperature.

3-The values of friction factor calculated lie between Blasius and Virk lines.

SYMMOLS AND ABBREVIATIONS

Symbol	Description	Unit
%DR	drag reduction percentage	-
d	Pipe inside diameter	[in]
L	Testing section length	[m]
Re	Reynolds number ($\rho VD/\mu$)	-
V	velocity	[m/s]
P	Pressure	[psi]

Abbreviations	Definition
CTAB	Cetyl tri-methyl ammonium bromide
NPH	Nonyl phenol
ppm	part per million
SDBS	Sodium dodecyle benzene sulfonate
SLES	Sodium lauryl ether sulfate
SLS	Sodium lauryl sulfate

References

- Abdul–Hakeem A.R., "Optimizing Viscous Flow in Pipes through Improved Flow Conditions and Chemical Injections", Ph. D. thesis, Pet. Eng. Dept., University of Baghdad (2000).
- Bottural L., "Friction Factor Correlations", Cryosoft, www.cryosoft.com, Feb.6 (1999).

- Hershy, H. C., Mcmillan, M. L. and Boxter, R. A., "Effect of Aging, Concentration, Temperature, Method of Preparation and other Variables on the Drag Reduction", Chem. Eng. Progr. Symp. Ser., no. 111, pp 67-74, (1971).
- Hussein H. Hussein, "Laboratory Study of Improving the Transportation Efficiency of Oil in Pipes ", M. Sc. thesis, Pet. Eng. Dept., University of Baghdad (2007).
- Jiri Myska, Jacqyes L.Zakin "Differences in the Flow Behaviors of Polymeric and Cationic Surfactant Drag-Reducing Additives", Ind. Eng. Chem. Res. 1997, 36, 5483-5487.
- Munsour, R. B., Yong, D. F. and Okilishi, H. T., "Fundamental of Fluid Mechanics", 3rd edition update, John Whily, New York, (1998).
- Thomas R. and Robert A., "Drag Reduction in Three Distinctly Different Systems", paper SPE 8722, December (1981).
- White A., "Flow Characteristics of Complex Soap Systems", Nature, 214, pp. 585–586 (1967).
- Zakin J.L., "Variables Affecting Drag Reduction by non–Ionic Surfactant Additives", Chem. Eng., Common, 23, pp. 77–88 (1983).